PROCEEDINGS
FOURTH SYMPOSIUM ON
ELECTRON BEAM TECHNOLOGY

March 29-30, 1962

Boston, Mass.

EDITOR - R. BAKISH

alloyd electronics corporation
CAMBRIDGE 42, MASSACHUSETTS

Proceedings of the Fourth Symposium on Electron Beam Technology

March 29 and 30, 1962

Somerset Hotel, Boston, Massachusetts

R. Bakish
Editor

Sponsored
By

ALLOYD ELECTRONICS CORPORATION
35 Cambridge Parkway
Cambridge 42, Massachusetts

The Aims of the Electron Beam Symposia are:

1) To promote the establishment and renewal of personal contacts among engineers and scientists working in the field.
2) To promote the exchange of experiences and cooperation among scientific and engineering groups working independently both in this country and abroad.
3) To promote the application of electron beams to new and unique areas and thus affect technological progress.
4) To disseminate information pertinent to electron beam processes.

Robert Bakish
Chairman

PROCEEDINGS OF THE 4TH SYMPOSIUM

ON ELECTRON BEAM TECHNOLOGY

TABLE OF CONTENTS

TABLE OF CONTENTS
(continued)

TABLE OF CONTENTS
(continued)

PREFACE

In the preface to the Proceedings of the 1961 Symposium, I said that it was highly probable to see the growth in electron beam technology which had taken place from 1959 to 1961 to be exceeded at time of the 1962 meeting. Although I don't have the exact numbers of scientists and engineers working in this technology today, the indications that I do have make me believe that their total number most likely exceed the sum total of all those active in this technology the three preceding years.

I cannot but feel highly flattered at the response given to the IVth Symposium as it reflects for a third consecutive year the confidence that a competent audience places upon me in regard to my judgment to organize and ability to conduct a meeting at the level that scientists, engineers and their respective employers find interesting, worthwhile and profitable.

True to my last year's statement the Symposium has remained of the same size. Three hundred and fifty people is, in my opinion, the largest number of scientists and engineers who could get together and benefit from such a gathering.

The participants of this meeting remain the nucleus of men active in this technology, men who can listen, learn and question, men who maintain the high level of competence needed for full realization of the benefits of a meeting like this.

I present these Proceedings to the public as a product of cooperative effort of scientists and engineers, researchers working independently in widely separated locations, yet bound together by the desire to further this technology. Gentlemen, these Proceedings belong to you, as only through your effort could they become a reality.

Every corporation of group which has lent support to this undertaking, by sending a speaker, should know that it shares the achievement of this IVth Symposium in fostering the dissemination of information and progress in the field of electron beam technology.

Many hours of concerted thought and painstaking work have been vested so that you, the reader, can build upon this and contribute further to progress in this technology.

I, as an individual, cannot express sufficient gratitude to you, the participants, who made this volume possible.

I would like, however, to take the liberty and express to you the gratitude of the many prospective readers. Gratitude for helping them to short circuit the arduous path of scientific progress and bring them closer to newer and more exciting discoveries.

The reader will also find here two papers which were not presented at the conference; an additional paper by Dr. Namba and one by Professor Rexer. They have been included to broaden the scope of this volume.

In conclusion I wish also to convey greetings to the readers from all who were present here at this Symposium, all who helped with their questions and discussions to bring even greater meaning to these presentations.

I said, last year, that it was my hope that these Proceedings will bring to the reader, if not the spirit of the conference, at least its factual essence. I hope that this volume will do likewise for the 1962 meeting.

Last but not least, I wish to thank my secretary, Miss Juliet Hartley, for her assistance both in the course of organization of the Symposium and in the preparation of the manuscript.

R. Bakish,
Symposium Chairman

INTRODUCTORY REMARKS

R. Bakish

Ladies and Gentlemen, it gives me great pleasure to welcome you to the Fourth Electron Beam Symposium. As the person who has been responsible for all arrangements in connection with this meeting, my feelings at this moment are no different from what they were at kick-off time at the two prior meetings which I arranged for you. I am excited and happy with the overwhelming confidence that you continue to place upon my judgement by your presence here today. I am also apprehensive in anticipating your approval of the presentations and the Symposium details.

For your information some 300 participants representing 7 countries, 120 companies and 20 government agencies and educational institutions are present with us today. Some of you have but walked a fraction of a mile while others have flown distances exceeding 7000 miles to be here. I do hope that all of you will find your participation in the Symposium well worthy of the effort.

I do believe that the corporations, government agencies and educational institutes who have supported this

Symposium by encouraging their staff to be here today as guest speakers are a cross-section of the leaders of this technology. Even though they do not include all of the physical entities having capable teams working in this field, the work presented does indicate the direction in which electron beam applications technology is progressing today.

All of the Symposium speakers have voluntarily assumed an additional burden on their extremely crowded schedules so that they may tell us of their new work. I wish, for a minute, to assume the role of your representative and thank them. Many are individuals of international reputation while the others are likely to acquire such in the future. Some of the speakers have been active in the field for a number of years while others have become members of this "electron beam community" only of recent date. All of them, I am sure, will be conveying to you information at a high level of technical competence, information which I hope will be new and of interest to you.

But let me now go to the program and give you some of the perhaps subjective reasons as to why the topics to be presented were selected.

Physics has played a major role in all technological developments which surround us. In electron beam technology physics are most important because they underline both its fundamentals and applications. It is then, only natural to initiate the activities of this Symposium by discussing them!

Work studying the interactions of electron beams with materials continues to expand bringing justification for the second group of talks. Electron beam welding in essence belongs to the group of talks discussing the interaction of electron beams and materials, yet its rapid growth justifies a separate treatment. Although not fully accepted by industry at large, it has made substantial strides and is certain to be adopted more generally in the next few years. By discussing this topic I hope to further and hasten its acceptance.

As to microelectronics, I believe that there is no need to expound upon the important role that they play today and the even greater role that they will play in the future. My belief that electron beams are to become, in the long run, the screwdriver, the insulation tape and calibration meter for the electronics engineer, is being asserted with each of the new developments being made in this technology.

There are, no doubt, in the program, a few papers which are of no interest to some of you in the audience. Rather than initiate simultaneous sessions of the different subject matter, I have decided to give those of you so inclined an additional breather during those presentations. Thus you can discuss matters of real interest with colleagues with similar thoughts whom you may not have encountered under other circumstances.

But so much about the program. Let us now look into a few mechanical details pertaining to the operation of the meeting. First and foremost, I wish to request once again the cooperation of the speakers in their most strict adherence to the times allowed for their presentations. Second, I wish to encourage an active participation of the audience in the discussions and state that discussions will not appear in the conference record. I believe that off the record discussion is more spontaneous and allows people who might have restrained under other circumstances to make contributions to participate. Furthermore, recording of the questions and answers and their verification by the authors, in particular the latter, is extremely time-consuming and can substantially delay the

publication of the Proceedings.

It is my feeling that in a technology as dynamic as electron beam technology the need for timely publication is of foremost importance and that no effort should or could be spared to achieve this promptly.

In conclusion, I would like to say that as in any other scientific meeting, directly or indirectly, the content, the speakers and achievement of the conference reflect on the individual responsible for it. As in the past, I am prepared to bear my responsibility. But I know you did not come here to listen to me so without further delay I will turn the meeting over to Mr. John Morley who will moderate the first session.

ON THE LIMIT THEORY OF CIRCULAR ELECTRON BEAMS

By

Hilary Moss
Advisory Engineer
Electronic Tube Division
Westinghouse Electric Corporation
Elmira, New York

ABSTRACT

By disregarding mere detail and concentrating on scientific essentials it is often possible to determine upper limits of performance to physical systems. Such an approach often illuminates a whole technology in a way impossible by a more detailed study.

This technique is applied to circular electron beams. The basic density limitations imposed on even an ideal system by diffraction, space charge and thermal emission energies are discussed both physically and in precise mathematical form. Graphs are given indicating the quantitative relationship between limiting beam current, cathode loading and spot size in terms of various design parameters. Some discussion is given of the practical nearness-of-approach to these theoretical performances.

List of Principal Symbols Used

V	-	beam voltage in region of convergence and work piece
I	-	beam current focussed onto work
z	-	distance between exit plane of lens and work
r_i	-	radius of beam at exit plane distant z from work
r_s	-	radius of beam at work (defined also as radius of "equivalent" Gaussian distribution at ρ_o/e amplitude)
r_m	-	minimum radius of beam between exit plane and work
ρ_o	-	peak beam density at work
ρ_c	-	cathode emission density
ρ_s	-	electron beam current density at radius r
k	-	Boltzmann constant
e	-	electron charge
T	-	cathode temperature in degrees absolute
$\frac{e}{kT}$	=	$\frac{11,606}{T}$
λ	-	electron wavelength
θ	-	beam semi convergent angle

Normally the work to be welded or bombarded will be placed at the beam image plane. The terms "image" and "work" refer to this same plane and are used interchangeably.

Note. If $\rho_s = \rho_o \exp -Br^2$, which is the usual form of the image current density distribution, then simple integration shows that the total beam current contained in this image is $I = \frac{\pi}{B}\rho_o$

ON THE LIMIT THEORY OF CIRCULAR ELECTRON BEAMS

Introduction

One of the risks of detailed technological study is the mental myopia it can so easily induce. The details of most physico-electronic processes are very intricate. Detailed study is indeed essential but it needs to be supplemented by broad overall vision. It is not easy to develop a mental attitude where very detailed knowledge co-exists happily with broad understanding.

It is the conviction of the author that limit theory is useful in gaining this dual perspective. Its philosophy can be simply stated. To gain overall vision we temporarily abandon all considerations of the details by which a given "result" is being achieved. Instead we direct attention to the basic science on which it rests. This basic science will be circumscribed by immutable* natural laws which in turn set upper limits on the device performance. Such limits are usually quite independent of mere technological detail. By thus excluding such detail from our field of view we can gain a width of outlook not otherwise readily attained.

A classic example is Carnot's expression $(T_1-T_2)/T_1$, for the

---

* Perhaps this is excessively strong language. It might be safer to add "immutable within the context of present knowledge". Sometimes limit theorems rest on values of engineering constants which are not absolutely defined in upper value[1]. But in any event, such analysis directs a searchlight on the whole technology and may indicate the possibility of conditional advances.

maximum possible conversion efficiency of any heat cycle working between temperature T_1 and T_2. Study of such expressions not only disentangles the essentials from what are generally very intricate details, but also establishes a yardstick by which we may assess the merits of any particular arrangement.

Although we shall not succeed in matching the elegance of Carnot's work when applying a similar philosophy to the study of circular electron beams, yet this study will assuredly illuminate the field in a way impossible by any other approach.

Innumerable similar examples occur throughout science. We may cite diffraction theory in limiting resolution, information theory in limiting the capacity of a channel of given bandwidth, and noise theory in defining upper limits to the useful sensitivity of detecting devices. In fact a study of science through limit theory provides a generalized approach of the greatest value especially to those guiding industrial research investigations[1].

General Nature of the Problem

Fig. 1 shows the essentials of any circular electron beam generator. S is the electron source, usually thermionic, which feeds electrons into an arbitrary "lens system" L. In accordance with our general philosophy we are disinterested in its details. Eventually electrons emerge at a certain volt-velocity V and converge through an angle 2θ into a focussed spot where the work is situated.

In looking at the overall physics of the system of Fig. 1 the

following variables seem of obvious significance; (1) the distance z between lens exit hole and the work, (2) the radius of the beam r_i at exit, r_s the spot radius (with some suitable definition), ρ_c the density of electron emission at the source S, V the beam voltage in the convergence space and I the beam current being focussed into the spot. These basic variables define at least two derived ones of interest, namely spot density $\rho_s = f(r_s, I)$, and Θ the convergent beam semi angle $\simeq r_i/z$.

Someone with a more sophisticated eye would also detect that the emission velocity spread is likely to be involved - it transpires that this can be expressed in terms of cathode temperature T. Finally someone with a knowledge of wave mechanics would expect electron wavelength to be involved in setting a diffraction limit to the spot size. However, this wavelength can be expressed in terms of V and the consequential diffraction spot size limit expressed in terms of lens aperture angle Θ, so that no new variables are introduced. Here then are our basic parameters which we would expect to exert overall control on the problem and which are not merely technological.

The question now posed and answered is this - how does the total current, spot size and spot density depend on the above quantities? What limits, if any, exist and how do they arise? The answers to such questions are not only of the greatest significance in assessing the whole future of electron beam welding but they also <u>illuminate the total field of its technology</u> and indicate the general course toward system optimization.

PERFORMANCE LIMITS - PHYSICAL DISCUSSION

If, in the system of Fig. 1, it were possible for all electrons in the plane of the circular hole P to have uniform axial speed and a perfect lens system gave them an inward radial speed exactly proportional to their distance from the beam axis, then, in the absence of space charge, and diffraction effects, an infinitely small spot and an infinitely large image density would be achieved. This is obvious on simple geometrical grounds.

Our failure to achieve such perfection is not due primarily to inability to make a focussing lens having an inward force proportional to distance from axis. Such lenses can be very closely approximated[2*]. Failure arises from three more basic causes:

(1) Diffraction effects

(2) Space charge in beam

(3) Finite initial emission velocity of a random nature

Mathematical statements of the effects of (1), (2) and (3) will be given later. At the moment we are concerned with physical principles.

A long and distinguished line of physicists including Fresnel, Kirchhoff, Abbe and Lord Rayleight were instrumental in evolving a numerical understanding of the diffraction error due to a wave or wave guided particle system. Electron flow is essentially a wave guided

---

* We are greatly helped here by the small apertures common in electron optical lenses.

particle system. With reference to Fig. 1, the image of radius r_s is being "illuminated" by flow through the hole P which subtends only a very small angle $\theta \cong {}^{+r}/_{z}$ at the image. The minimum possible image "size" is given by eqt. (3). As shown it is negligibly small in the present state of the art even though θ is very small. The situation is saved by the very short wavelengths associated with the electron flow - a mechanism which accounts for the superiority of the electron over the light optical microscope.

Space charge effects can be physically visualized as follows. In Fig. 2 suppose that the beam emerging from the hole P is "laminar" i.e. no electron crossovers occur and each electron maintains its relative position so that the beam is uniformly compressed. Consider an electron at the outer edge of this beam. The lens L gives it a certain initial inward velocity v_r proportional to initial radius r_i, and a corresponding kinetic energy. The radial outward flux due to the charge in the beam (considered "smeared" over the whole beam) exerts an <u>outward</u> force on this electron. The latter dissipates its initial inward kinetic energy against this force which rises inversely as the beam radius. After some flight time its initial inward velocity is reduced to zero and the beam reaches its minimum section or "waist" W in Fig. 2. Subsequently it expands again. At the waist W the radius must be finite since the outward radial force tends to infinity as the beam radius tends to zero. In this physical picture, if the electron density at P is uniform, it will remain uniform throughout the whole flow.

In the preceding paragraph it has been assumed that the "perfect

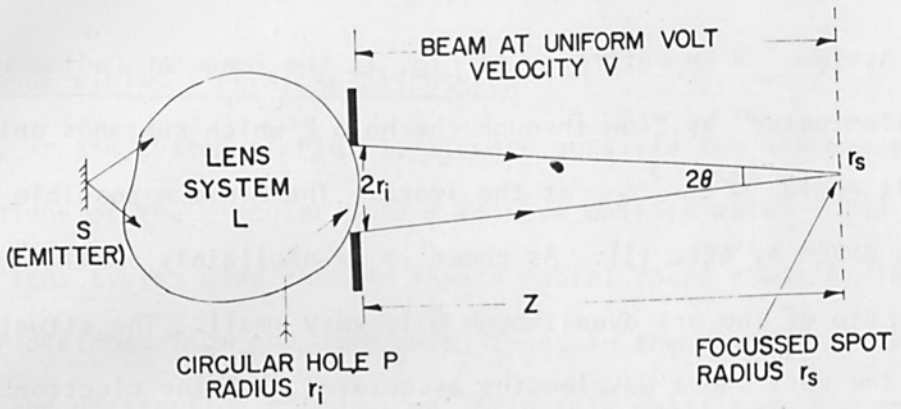
BEAM AT UNIFORM VOLT
VELOCITY V
LENS
SYSTEM
L
S
(EMITTER)
2r_i
2θ
r_s
Z
CIRCULAR HOLE P
RADIUS r_i
FOCUSSED SPOT
RADIUS r_s

FIG. 1

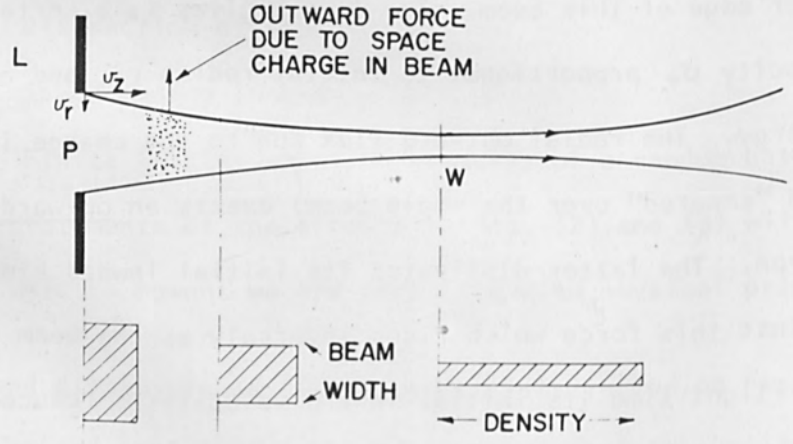
L
OUTWARD FORCE
DUE TO SPACE
CHARGE IN BEAM
v_z
v_r
P
W
BEAM
WIDTH
DENSITY

FIG. 2

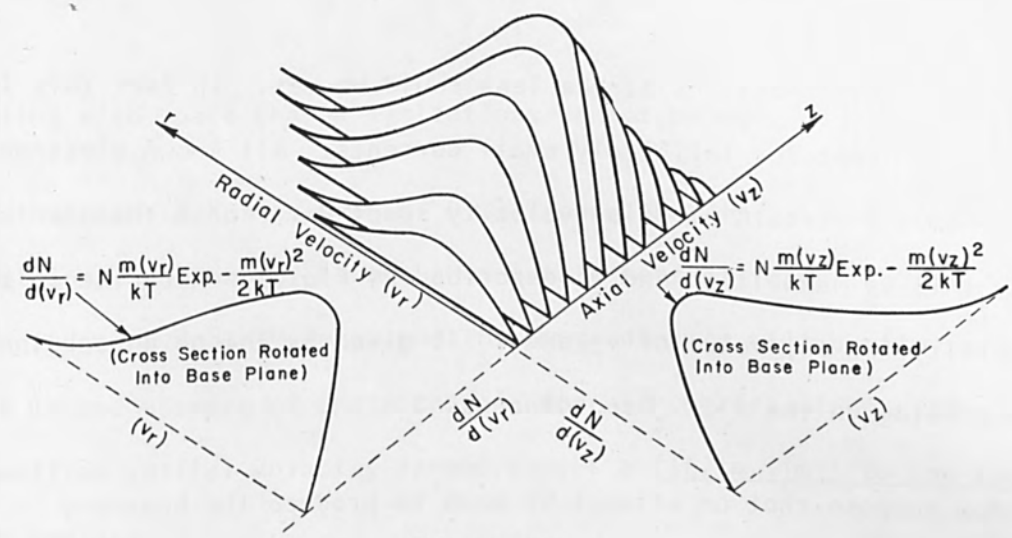
r
Radial Velocity (vr)
z
Axial Velocity (vz)
dN/d(vr) = N m(vr)/kT Exp. - m(vr)²/2kT
(Cross Section Rotated Into Base Plane)
(vr)
dN/d(vr)
dN/d(vz)
dN/d(vz) = N m(vz)/kT Exp. - m(vz)²/2kT
(Cross Section Rotated Into Base Plane)
(vz)

FIG. 3

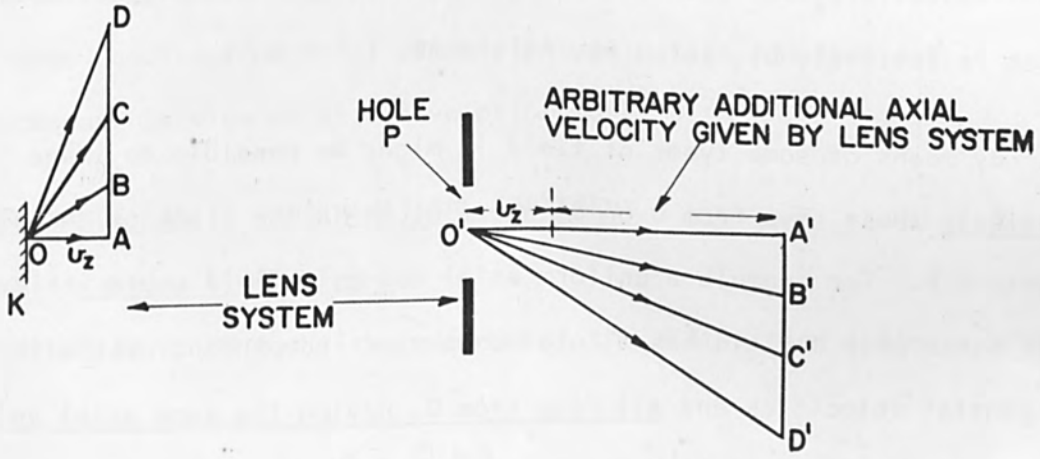
D
C
B
A
O
uz
K
HOLE
P
ARBITRARY ADDITIONAL AXIAL VELOCITY GIVEN BY LENS SYSTEM
uz
O'
A'
B'
C'
D'
LENS SYSTEM

FIG. 4

focus" boundary conditions at the lens could be met. In fact this is impossible except for infinitely small currents. All known electron sources have a certain emission velocity spectrum. For a thermionic source this is Maxwellian and is described by Fig. 3. Here the emission probability for any value of v_r and v_z is given by the height ordinate corresponding to the v_r, v_z coordinates.

Now suppose that an attempt be made to produce the boundary conditions postulated at a circular aperture P in Fig. 4. To do this an electron source with the Maxwellian velocity spectrum might be placed at K and some lens system interposed between K and P. Consider four electron tracks OA, OB, OC and OD emerging from O each with the same axial velocity v_z but with differing tangential emission velocities, given respectively by, zero, AB, AC and AD.

By means of some types of field it might be possible to image precisely these rays from O on O' where O' is in the plane of the circular aperture P. For example a uniform axial magnetic field could achieve this since such a field has a rotation period independent of the initial tangential velocities and all rays from O, having the same axial velocity v_z, would be imaged at O'. On the other hand, this does not meet our requirements since the rays at O' would then have varying inward velocities. In addition we have considered only one group of electrons all having the same axial speed v_z whereas Fig. 3 shows that the axial speeds are also scattered in a Maxwellian distribution. This argument indicates in physical terms why the assumed boundary conditions postulated when

dealing with space charge limitations cannot be met.

But consideration of Fig. 4 will show that if the ideal boundary conditions at P cannot be met then even a perfect focussing lens will not produce a "point" focus and the image density will be finite. Thus even in the absence of space charge, and with perfect lenses, the Maxwellian initial velocity spread causes a <u>finite limit to the focussed beam density</u>.

These general physical arguments show therefore that at least three fundamental upper limits to focussed beam density must exist <u>even if the system indicated in Fig. 1 is supposed "perfect"</u>. A precise mathematical form will now be given to these limitations. Derivation of these results from first principles would take too long and is unnecessary in view of extensive prior work[3,4,5,6,7].

PERFORMANCE LIMITS - MATHEMATICAL STATEMENT

1. Diffraction Limitation

The radius of the first minimum of the diffraction image is given by

$$r_s\Big|_{diff} \cong \frac{0.6\lambda}{\theta} \quad ----(1)$$

where λ is the electron wavelength and is equal to

$$\lambda \cong \frac{12.3}{\sqrt{V}} \quad -----(2) \quad \left\{\begin{array}{c}\lambda \text{ in Angstroms for} \\ V \text{ in volts}\end{array}\right\}$$

Substituting (2) in (1) gives

$$r_s\Big|_{diff} \cong \frac{7.4}{\theta\sqrt{V}} \text{ Å} \quad -----(3)$$

For $V = 10^4$ and $\theta = 5 \times 10^{-3}$ this yields a diffraction radius limit in the order of 1.5×10^{-7} cm. Obviously this is negligible in the present state of beam technology.

2. Space Charge Limitation

The mathematics of the physical picture given in the previous section was worked out first by Headrick and Thompson[3]. The matter was re-examined in 1952 by Hollway[4] and again independently in 1957 by Schwartz[5] who both produced normalized curves permitting rapid numerical solutions to the integral equations involved.

Fig. 5 is such a curve reproduced and extended by the present author.[11] It contains inset numerical values, calculated by Hollway,[12] should greater accuracy be required. For a given focussing lens aperture, expressed by $\theta = r_i/z$, and a given beam voltage V, Fig. 5 permits rapid calculation of the space charge limited spot size r_s in terms of total beam current I. For values of $r_s/r_i > .04$ the curve is doubled-valued. Here, where the space charge effects are appreciable, a plane of minimum sectional area exists between the screen and the lens when the minimum focussed spot condition is achieved. For our purposes the upper curve is the one of usual interest, but the lower curve permits calculation of the condition where the image plane at distance z is also the plane of minimum section $\dot{r} = 0$. The table also shows values of minimum beam radius (r_m) when the smallest spot exists at the work.

3. Thermal Limitation

D. B. Langmuir[6] in 1937 first completed the mathematical description

r_i/r_m	r_s/r_m	r_s/r_i	$(z/r_i)\ (I/V^{3/2})^{1/2}$
54.60	1.030	0.0189	0.00350
44.81	1.038	0.0232	0.00363
36.97	1.048	0.0283	0.00378
30.65	1.059	0.0345	0.00393
25.53	1.072	0.0420	0.00410
21.38	1.088	0.0509	0.00429
17.99	1.106	0.0615	0.00449
15.22	1.128	0.0741	0.00470
12.94	1.153	0.0891	0.00494
11.05	1.182	0.1070	0.00520
9.488	1.216	0.1282	0.00549
8.187	1.256	0.1534	0.00580
7.099	1.302	0.1833	0.00615
6.187	1.354	0.2189	0.00653
5.419	1.415	0.2612	0.00696
4.771	1.486	0.3115	0.00743
4.221	1.568	0.3715	0.00796
3.753	1.664	0.4433	0.00856
3.353	1.775	0.5294	0.00923
3.012	1.906	0.6329	0.00999
2.718	2.060	0.7577	0.01086
2.562	2.165	0.8450	0.01143
2.3491	2.3491	1.0000	0.01242
2.165	2.562	1.183	0.01353
2.060	2.718	1.320	0.01433
1.906	3.012	1.580	0.01578
1.775	3.353	1.889	0.01743
1.664	3.753	2.256	0.01930
1.568	4.221	2.691	0.02143
1.486	4.771	3.210	0.02386
1.415	5.419	3.829	0.02664
1.354	6.187	4.569	0.02984
1.302	7.099	5.455	0.03354
1.256	8.187	6.518	0.03782
1.216	9.488	7.799	0.04280
1.182	11.05	9.345	0.04862
1.153	12.94	11.22	0.05544
1.128	15.22	13.49	0.0635
1.106	17.99	16.26	0.0730
1.088	21.38	19.65	0.0842
1.072	25.53	23.82	0.0977
1.059	30.65	28.94	0.1138
1.048	36.97	35.29	0.1332
1.038	44.81	43.16	0.1567
1.030	54.60	52.99	0.1852

FIG. 5

of the image density limitation due to thermal emission energies at the cathode. He proved the following theorem:

> Electrons originate from a unipotential cathode having a Maxwellian velocity distribution corresponding to a uniform absolute temperature T. The emission density is supposed uniform and equal to ρ_c. Some or all of these electrons are subsequently converged into a focussed spot by a rotationally symmetric lens system, of any form whatever, such that the cone of convergence is in a region of uniform volt-velocity V, and is free from external magnetic fields. In these conditions the maximum attainable peak density in the image, due, and only due to those electrons lying inside the cone of semi angle θ is given by
>
> $$\rho_o = \rho_c \left\{ \frac{eV}{kT} + 1 \right\} \sin^2 \theta \quad ----(4)$$

A simplified justification for this result is given in ref. 7. The limiting image density ρ_o defined by (4) can be attained only if all lenses are aberration free and in addition if space charge forces are negligibly small. Some measurements made by the author show that the

---

* It will be noted that the "limit" implied by eqt. (4) is of a different and less fundamental nature from that implied by space charge. For if ρ_c is unbounded, so also is ρ_o, and in this sense no true thermal limit exists at all. However, eventually such considerations as cathode resistance and cathode voltage gradients do impose an upper bound on emission density. Hence ρ_o is also bounded although in an inexact manner.

theoretical density can be approximately reached provided θ is sufficiently small[8]. This condition insures negligible aberrations. In the author's measurements the current was sufficiently low to insure negligible space charge.

The primary physical situation leading to eqt. (4), i.e. a Maxwellian emission velocity distribution corresponding to cathode temperature T, can be shown to lead to a Gaussian current density distribution in the image. This means that the flow conditions in the beam between the lens exit plane and image are <u>not</u> laminar. However the derivation of the space charge limitation in the previous section has implicity assumed laminar flow. It is natural to ask how we are to combine the effects of the space charge and thermal limitations when the physical assumptions on which they are separately based are so different.

To this the simple answer must be that an exact analysis of the combined effects of space charge and thermal limitations is very intricate. Attempts in this direction have been made[9,10] but it is doubtful whether these complex analyses are worthwhile at least in the context of beam welding studies. Our cruder but very easy procedure is as follows.

First, we work out from Fig. 5 the consequence of the space charge laminar flow conditions where the current density is everywhere uniform across any beam section and r_s is simply the radius of the sharp edge of the image. Obviously for this case we may write exactly

$$\rho_o = \frac{I}{\pi r_s^2} \quad -----(5)$$

Fig. 6 shows some results indicating the space charge limited maximum possible values of I and ρ_o in terms of r_s.

But for any value of ρ_o in Fig. 6 eqt. (4) yields a corresponding value of cathode loading ρ_c when $\theta = r_i/z$ is defined. This is shown in Fig. 7. Here it is assumed that the peak density ρ_o of the Gaussian distribution exactly equals the uniform beam density ρ_o in the laminar flow space charge analysis. This is indicated in Fig. 8(a).

However since eqt. (4) explicity defines only ρ_o in terms of ρ_c, from this viewpoint any Gaussian image density curve of peak value ρ_o would require the same value of ρ_c. On the other hand the space charge limitation calculations are based on a definite total beam current I associated with a definite spot radius r_s.

To complete the description of the "equivalent" Gaussian image we need therefore to define not only its peak density ρ_o but also its total current. It is reasonable to make this exactly equal to the current I carried when investigating the space charge limitation. Very simple mathematics[11] shows that this will be the case if the Gaussian curve is defined as having a radius r_s at the point where its current density has fallen to ρ_o/e. This is shown in Fig. 8(b).

The following statement now seems possible. "In most practical beam forming systems, the image density will be Gaussian. For a given

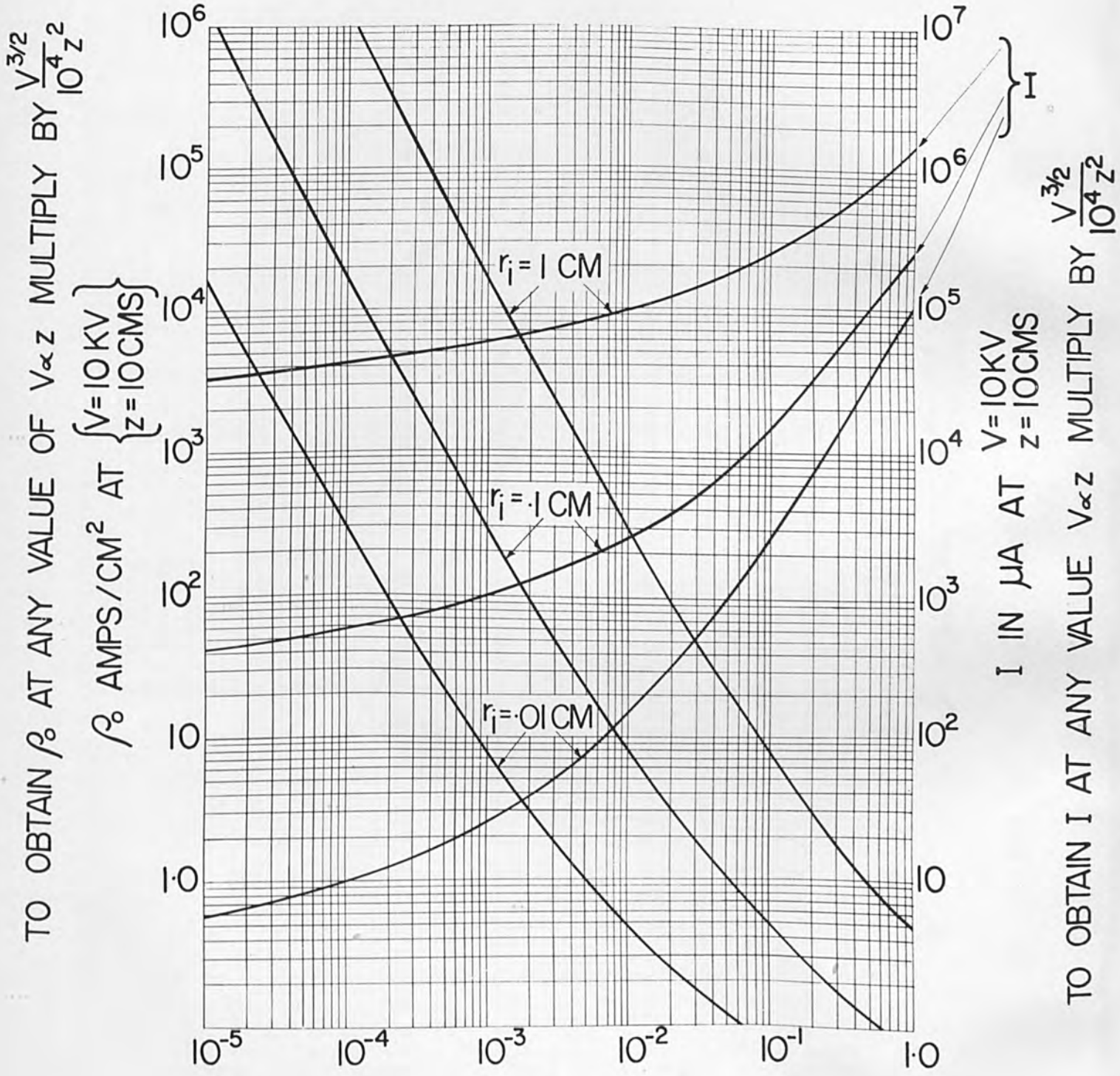
TO OBTAIN ρ_o AT ANY VALUE OF V∝z MULTIPLY BY $\frac{V^{3/2}}{10^4 z^2}$
ρ_o AMPS/CM² AT {V=10 KV, z=10CMS}
r_i = 1 CM
r_i = ·1 CM
r_i = ·01 CM
10^6
10^5
10^4
10^3
10^2
10
1·0
10^7
10^6
10^5
10^4
10^3
10^2
10
1·0
I
I IN μA AT V=10KV z=10CMS
TO OBTAIN I AT ANY VALUE V∝z MULTIPLY BY $\frac{V^{3/2}}{10^4 z^2}$
10^{-5}
10^{-4}
10^{-3}
10^{-2}
10^{-1}
1·0
r_S (CM)

FIG. 6

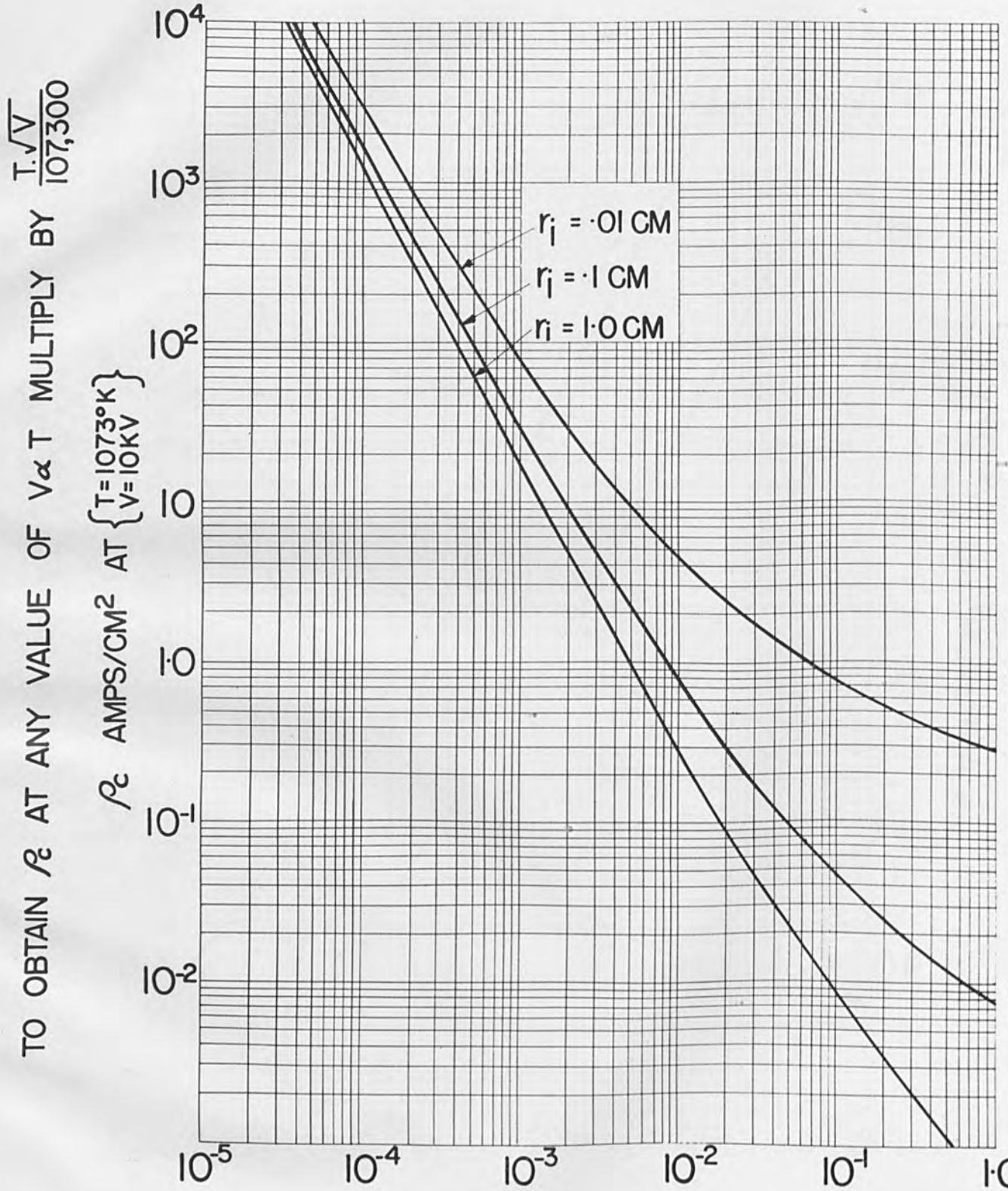
TO OBTAIN ρ_c AT ANY VALUE OF V & T MULTIPLY BY $\frac{T.\sqrt{V}}{107,300}$
ρ_c AMPS/CM^2 AT $\{^{T=1073°K}_{V=10KV}\}$
10^4
10^3
10^2
10
1·0
10^{-1}
10^{-2}
r_i = ·01 CM
r_i = ·1 CM
r_i = 1·0 CM
10^{-5}
10^{-4}
10^{-3}
10^{-2}
10^{-1}
1·0
r_s (CM)

FIG. 7

value of V, z, r_i I and ρ_c as given by Figs. 6 and 7 the space charge effects will limit the spot size to a somewhat <u>smaller</u> value of r_s (defined at ρ_o/ϵ point) than that given from Figs. 6 and 7. This must be true since in the practical Gaussian image case, Fig. 8(b) shows that some of the beam current is being carried <u>outside</u> the radius r_s and the space charge forces are thus somewhat less than calculated. Hence the curves of Figs. 6 and 7 yield errors in the <u>safe</u> direction."

If the beam converging onto the work has a narrow angle due to a severe stop limit at the initial radius r_i, so that only a small fraction of the total cathode emission is being used, then the above approximation is a very close one. For in this event direct measurement will show that the current density across any beam section is reasonably uniform except around the focus plane. Thus the assumed uniform density for the space charge analysis is approximately met for a large fraction of the electron transit time from exit aperture to the work.

<u>Some General Comments</u>

Figs. 6 and 7 permit the desired performance estimations almost at a glance. They cover the ranges of primarily interest. Fig. 5 permits any extension desired. The results could be presented as an alignment chart. Dr. Hollway[12] has recently done this. On the other hand alignment charts give no "feel" for the variations involved. Also it will be noted that normalized coordinates have been avoided on Figs. 6 and 7. These again have the drawback of conveying no immediate information. Our ordinates on Figs. 6 and 7 include multipliers to deal with any values of V, z and T.

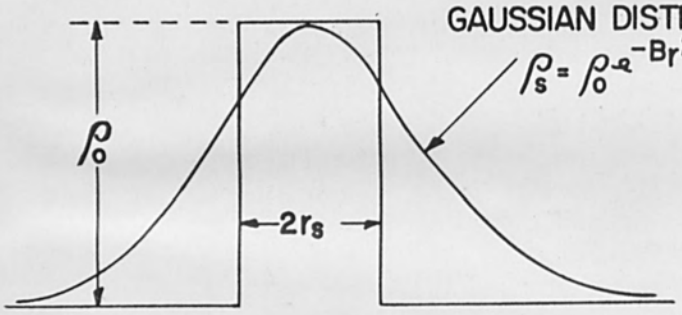
GAUSSIAN DISTRIBUTION
$\rho_s = \rho_0 e^{-Br^2}$
ρ_0
$2r_s$

FIG. 8(a)

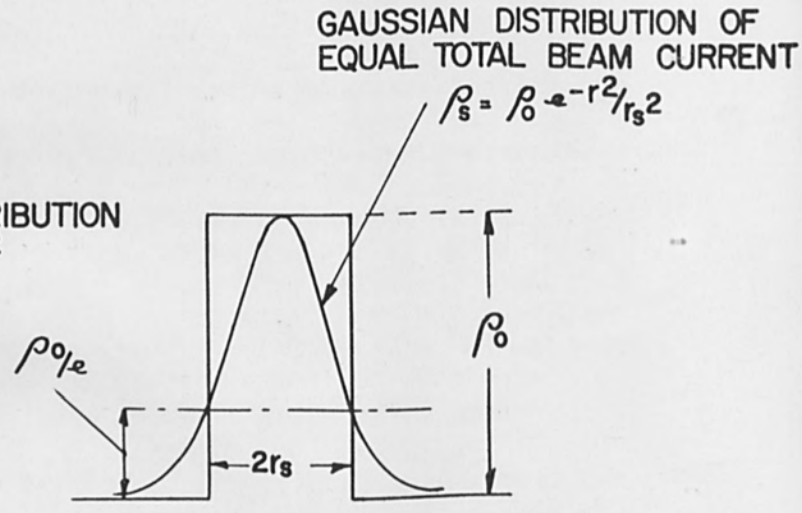
GAUSSIAN DISTRIBUTION OF
EQUAL TOTAL BEAM CURRENT
$\rho_s = \rho_0 e^{-r^2/r_s^2}$
$\rho_{0/e}$
ρ_0
$2r_s$

FIG. 8(b)

Misunderstandings occasionally still exist about the physical nature of the thermal density limitation. Sometimes it appears to be imagined that a Pierce type electron gun by "focussing down" from a comparatively large area cathode on to a small area or aperture can achieve densities in excess of that indicated by eqt. (4) for a given ρ_c , V and T. This is simply not so. High densities can be so achieved but <u>are due to use of a large value of Θ</u> as will be evident from simple consideration of geometry. Of course this may indeed be a most valuable technique but it in no way violates Langmuir's concept.

The exact meaning of Θ must be fully understood. It is the half angle-of-arrival-spread <u>at the plane where ρ_o is being defined.</u> Our paper relates to the case where the electrons converge into the focussed spot in a conical region <u>free from external fields</u>. Here $\Theta \leqq {}^{r_i}/_{z}$. On the other hand Θ might be much larger if fields existed between the exit aperture of radius r_i and the image plane at distance z.

For example in many types of microwave tube an electron beam is constrained by a suitable external field system (usually magnetic) into a roughly cylindrical shape. Superficially we might be tempted to imagine that here $\Theta \rightarrow 0$. Of course in such a case only the overall beam envelope has a roughly parallel sided form. <u>Within</u> the beam the arrival angles may be very large especially if a high magnetic field is applied so that the electrons have a pronounced helical trajectory. This fact explains why large currents and current densities can be achieved in such beam devices without the necessity for very large

values of emission density.

In cathode ray tubes however such techniques are difficult since the beam must be deflected without excessive distortion. Conventional practice thus converges a thin beam in an external field-free drift space as has been here considered. On the other hand in electron beam welding, little or no beam deflection may be needed and the use of beam confining fields may well be advantageous, if the highest beam densities are sought.

A better physical grasp of the thermal limitation can perhaps be attained by a simple transposition on eqt. (4). Dividing both sides by $\sin^2\theta$ and writing image density as the quotient of current and area gives

$$\frac{\text{beam current}}{\text{image area} \times \sin^2\theta} \propto \rho_c \cdot \frac{eV}{kT} \quad \text{-----} \quad 4(a) \quad \left\{ \frac{eV}{kT} >> 1 \right\}$$

The left hand side is current/unit area/unit solid angle (for small angles) and is thus a measure of image "brightness". Eqt. 4(a) then says that this brightness is proportional to the emission density multiplied by the ratio of image volt velocity to object space average volt velocity. Since this last ratio is the square of the ratio of image and object space "refractive indices" we see that 4(a) is the equivalent of the well known optical law: image brightness equals object brightness multiplied by the square of the ratio of the refractive indices of image and object spaces. (ρ_c is the object density but is proportional to object brightness since the cathode emits into a constant solid angle of 2π).

It is well known from thermodynamic reasoning that no system of optics can increase the brightness of any source if the refractive indices of image and object spaces are the same. By the same reasoning no electron-optical system can do so either. The effect of higher voltages is to increase brightness by reducing arrival angles.

Nearness of Approach to Theoretical Limits

It is natural to ask how closely we may approach the theoretical performance limits discussed.

So far as the space charge limit indicated in Fig. 6 is concerned, observations on a variety of cathode ray tubes lead the author to the conviction that this limit can indeed be approached. The analysis leading to it is direct and straightforward - it would be surprising if actual measurements were in substantial disagreement.

Much more controversial is the thermal limit indicated in eqt. (4), mainly because measurement of ρ_c is quite difficult.

The author has made some studies here[8] but they relate to conditions rather far removed from those obtaining in beam welding. The author was concerned with very narrow angle guns as used in ultra high resolution cathode ray tubes.

Briefly it seems that for values of $\theta \leqslant 2 \times 10^{-3}$ radian we may closely approach the theoretical thermal limit of eqt. (4), in standard oscillograph type flat cathode electron guns. For larger values of θ the practical performance fell away rapidly in a way depending on geometry

and which is difficult to summarize. With high negative control grid bias i.e. operating towards cut-off, some measurements showed that θ could be increased to about 5×10^{-3} radians before departure from theoretical performance.

Theory has only this to say about the "breakway" value of θ i.e. the maximum value of θ at which the Langmuir relation is still satisfied:

For <u>any given geometry</u> it will be the <u>lesser</u> value of θ at which <u>either</u>

(a) The lenses start to show appreciable aberrations (mainly spherical) (Including the triode immersion lens)

(b) That value of θ at which the final exit aperture of radius r_i begins to be incompletely "filled" i.e. beyond which the beam current is less than proportional to aperture area πr_i^2

Now the design of the whole electron gun will vitally affect this value of θ. For our artifical gun it was, as we have seen, only about 2×10^{-3} radian. Probably this can be greatly increased by adoption of some sort of gun construction in which the cathode and anode system is part of a sphere. This seems intuitively apparent and indeed the well known Pierce gun is of this broad description. In principle what we achieve here is a dissection of the total beam angle θ into a composite system of small component angles each contributing an increment of current. With spherical geometry all these composite ray systems are physically identical (this is not so with <u>flat</u> systems) and it is

therefore reasonable to suppose that their contributions add directly to achieve a high density (at a high θ value!). At present though it must be admitted that exact knowledge of wide angle gun design and performance is scanty.

Such measurements as are available, made on TV electron guns with values of $\theta \backsim 10^{-2}$ radian seem to show that cathode emission densities of 10 to 100 times that indicated by eqt. (4) may be needed under high drive conditions. On the other hand this may not matter much in practice since as Fig. 7 shows only quite low values of emission density can be reached - for spot sizes common in TV practive - before the onset of space charge limitation. Only for very fine focus tubes can high emission densities be usefully employed. It is a mistake to imagine that normal TV electron gun performance would be revolutionized even if sources of unlimited emission density were discovered.[13]

Bibliography

1. Moss, H., Research and Engineering, February 1956
2. Schlesinger, K., I.R.E. Trans. Electron Devices 8 224 (1961)
3. Headrick, L. B. and Thompson, B. J., Proc. I.R.E. 28 318 (1940)
4. Hollway, D. L., Australian Journal Sci. Research Series A 5, 430 (1952)
5. Schwartz, J. W., R.C.A. Review 18, 3 (1957)
6. Langmuir, D. B., Proc. I.R.E. 25 977 (1937)
7. Moss, H., Journal of Electronics 6 403 (1959)
8. Moss, H., Journal of Electronics 10 341 (1961)
9. Cutler, C. C. and Hines, M. E., Proc. I.R.E. 43 307 (1955)
10. Danielson, W. E., Rosenfeld, J. L. and Saloom, J. A. B.S.T.J. 35, 375 (1956)
11. Moss, H., Journal Brit. I.R.E. 21 35 (1961)
12. Hollway, D. L., Electronics 35, 7, (1962)
13. Haine, M. E., Journal Brit. I.R.E. 17, 211 (1957)

THE USE OF INTENSE MAGNETIC FIELDS AT THE POINT OF IMPACT IN HIGH RESOLUTION ELECTRON BEAM PROCESSING

By

E. A. Ash
Head
Electron Devices Laboratory
Standard Telecommunication Laboratories Limited
Harlow, Essex
England

ABSTRACT

One of the main factors limiting the maximum attainable performance in high resolution electron beam processing is the thermal velocity spread of electrons. This conclusion is valid in the case when, at the point of interest, there is no applied magnetic field. The situation has now been analyzed in cases where there is such a magnetic field.

The second part of the paper discusses how these potentially larger current densities can be best exploited in electron beam processing tools. A number of possibilities are discussed in which the object to be processed, is, in essence, immersed in the field of the objective lens. An attempt is made to compare the resolution limit in the various cases. These possibilities all represent variants of the basic arrangement derived from electron microscopy electron optics.

THE USE OF INTENSE MAGNETIC FIELDS AT THE POINT OF IMPACT IN HIGH RESOLUTION ELECTRON BEAM PROCESSING

I. INTRODUCTION

The electron optical systems used in electron beam machines are generally of the type indicated in Fig. (1). The ultimate performance of such machines is subject to some quite general restrictions with respect to maximum current density and minimum spot size, restrictions which have for long been familiar in electron microscopy and electron beam probe X-ray analysis. For many applications performances well below the limiting values are adequate, but in a number of cases an advance beyond the present frontier would greatly extend the range of applications of the electron beam technology.

There are two factors which are involved in the basic performance of the system of Fig. (1). The first is the limitation on the maximum attainable current density derived by Langmuir[1] and Pierce[2]. This result, valid for a focus in field free space, may be written in the form

$$j_m = j_o(1 + \frac{eV}{kT} \sin^2\theta \qquad (1)$$

where

j_m is the maximum attainable current density

j_o the current density at the cathode

V the beam voltage

T the cathode temperature

k the Boltzmann constant

θ the angle of covergence at the focus (Fig. 1)

The second factor which comes into play is thespherical aberration constant, C_s, of the objective lens. In seeking to optimize a design, the thermal velocity limitation demands a large aperture, the spherical aberration a small one. Combining these two considerations, one can derive (see e.g. ref. 3) an equation for the current falling in a spot of diameter d:

$$i = \frac{\pi}{4} (d - \tfrac{1}{2} C_s \theta^3) \frac{eV}{kT} j_o \theta^2 \qquad (2)$$

These considerations apply when the focus of the beam is in field free space. In this paper we will examine the possibility of attaining an improved performance when this restriction is removed.

II. THE EFFECT OF A MAGNETIC FIELD ON THE LIMITING CURRENT DENSITY.

We now consider a different type of electron optical system, such as indicated in Fig. (2). Here a magnetic field extends over the whole length of the beam, gradually increasing in magnitude from the cathode onwards. The conditions are those that in the context of microwave tubes are known as "confined flow"; if the magnetic field is sufficiently strong, and the increase in field strength sufficiently gradual, the flux threading a cross-section of the beam will remain approximately constant, and the beam area will shrink directly as the magnetic field increases. Suppose we start with a field at the cathode which is strong enough to control the space charge forces, and make the field at the "working plane" R times greater than the cathode value. As we increase R, the current density at the working plane will at first rise proportionally. However, as R is further increased, another effect comes into play: an increasing number of electrons will be reflected before reaching the working plane. This effect, identical with that exploited in mirror fusion machines, is due to the increase in the transverse energy and tha attendent decrease in the

longitudinal energy, which takes place as an electron with a given initial transverse energy penetrates into the converging field. This effect can be analyzed by using the abiabatic invariance principle[4], which states that an electron with an initial thermal transverse energy of E_{tr} at the cathode will have a transverse energy $R.E_{tr}$ at the working plane. The maximum current density which can be attained in a system of this type can be derived in a manner very similar to that used by Pierce[2] in deriving equation 1. The starting point in Liouille's theorem, and this in combination with the adiabatic invariance theorem leads to the following result.*

$$j_m = j_o \left(R - (R-1) - \frac{eV}{kT(R-1)}\right) \qquad (3)$$

For sufficiently large R this expression attains the limiting value

$$j_m = j_o \left(1 + \frac{eV}{kT}\right) \qquad (4)$$

This expression suggests that very large current densities are, in principle, attainable. Thus if V = 10 kV and T = 1000°K, j_m is of the order of 10^5 times the cathode current density.

* A detailed account of this calculation is being prepared for publication.

Physically equation 4 becomes very plausible when it is appreciated that in the presence of a very strong magnetic field, some of the electrons can reach the axis at right angles, corresponding to $\theta = \frac{\pi}{2}$ in equation 1. It must be emphasized that equation 3 represents only an upper limiting value; the actual current density achieved in practical system must be calculated taking the detailed circumstances into consideration.

III. CURRENT DENSITY IN A CONVERGENT BEAM

There are a number of different systems which one might use in order to approach the large limiting current densities predicted by eqn. 3. For the present we will confine our attention to the simplest system, that of Fig. (2).

If there were no limit on the available magnetic field, the electrons could be made to follow the magnetic lines of force with any desired precision, and under these conditions the limiting current density of eqn. 3 could be reached. This idealized situation might be relevant to the case of low voltage, low power density applications. In general, however, the available magnetic field sets a practical limitation. The field must in the first instance be sufficiently strong to overcome the space charge forces. In practice

this means that it must be several times the value of the Brillouin magnetic field for the beam[5]; it will be assumed in the following that this condition is fulfilled. The field must also be strong enough to limit the excursion of the electrons, due to their transverse thermal velocities, to a small fraction of the nominal beam diameter. Now an electron with a transverse energy corresponding to eV_{tr} in a uniform field B will complete orbits, which, in a transverse plane travelling with the electron, are circles of radius r,

$$r = 3.37\ V^{\frac{1}{2}}_{tr}/B \qquad (5)$$

where B is in webers per m^2, V in volts and r in microns. The adiabatic theorem allows us to write V_{tr} as

$$V_{tr} = \frac{RkT}{e}$$

For a cathode temperature of 1000°K, and a magnetic field of 20 kilogauss eqn. 5 becomes

$$r = 0.55R^{\frac{1}{2}} \qquad (6)$$

This shows that for large values of R the excursions of the electrons may well be of the same order or even exceed the desired beam diameter.

Fortunately, eqn. 6 does not necessarily define the smallest beam diameter which can be achieved. The reason lies in the well known property of a uniform magnetic field, that the time for completion of one circular orbit is inde-

pendent of the velocity. This fact leads to the phenomenon, observed and discussed by a number of authors[6,7] of periodic images of the cathode surface along the length of the beam. Electrons initiating from the same point on the cathode, will, according to their particular thermal velocity, follow different trajectories, - trajectories which, however, cross periodically to form the cathode images. This fact has led one writer[7] to the suggestion that at these images the thermal velocities do not decrease the current density at all. This will be approximately true for relatively small values of R, but as indicated by the quite fundamental argument which led to eqn. 3, the conclusion must break down for large values of R.

In practice the formation of the images along the beam does not proceed without aberration. There are two types of aberration which may come into play. The first is concerned with space charge effect; these we will ignore the moment, as they cannot represent the most fundamental feature of the question; for sufficiently low cathode density the space charge can always be made negligible. The other source of aberration lies in the longitudinal components of the thermal velocities. Even in a uniform magnetic field these will eventually lead to a complete loss of the cathode images;

although the transverse orbits of electrons initiating at the same point on the cathode will still be completed in the same time, the effect of the different longitudinal velocities will cause them to be at different points along the beam. The greater the spread in longitudinal velocities, the sooner will the cathode images deteriorate. This effect therefore becomes particularly pronounced in the case of a convergent magnetic field, Fig. (2). Here the transverse energies are continually increasing, with a resultant increase in the spread of the longitudinal velocities.

An approximate analysis of this result leads to the following conclusion. If the aberration of the cathode image at a point z_1 from the anode is to be relatively small we must satisfy the condition,

$$R = 1 + 2 \left(\frac{eV}{kT}\right) \left(\frac{t_c}{t_1}\right) \qquad (7)$$

where t_c is the time to complete one cyclotron orbit corresponding to the field strength at the working plane, and t_1 is the time taken by an electron with a forward velocity corresponding to V to reach z_1. A numerical example will be considered in section 4. Generally it turns out that at high voltages (order of 10^4 or higher) this condition is easily satisfied, but at low voltages the cathode images are blurred to extinction rather rapidly. It should be noted that R in eqn. 7 is proportional to $V^{3/2}$ The expression

is valid only if the variation of field is truly adiabatic, which for fairly large R implies that $t_c/t_1 \quad 1$.

IV. NUMERICAL EXAMPLE

The above considerations suggest that confined flow electron optical systems may be of value both in high power density applications such as machining as well as in lower power density applications. The following example has been chosen more to illustrate some of the discussion rather than that it represents any sort of optimum situation.

The example is illustrated in Fig. (3). The aim is to achieve a power density of 10^7 w/cm^2 with a beam diameter of 5 μ using an accelerating voltage of 10 kv and a magnetic field of 20 kg. The latter figure has been chosen simply because it represents the maximum easily attainable using iron pole pieces.

The magnetic field at the cathode is 80 gauss so that R = 250. The current density at the working point is assumed to be R times that at the cathode, and eqn. 3 indicates that this is well below the theoretical maximum density. Equation 6 shows that the radial excursion of the electrons amounts to 8.8 μ so that if we do not make use of the cathode image phenomenon we will be unable to achieve our target diameter of 5 μ. Reference to eqn. 7 now shows

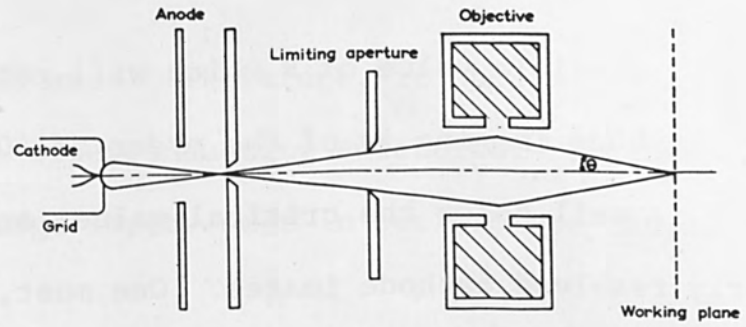

FIG.1 ELECTRON BEAM MACHINE ELECTRON OPTICAL SYSTEM

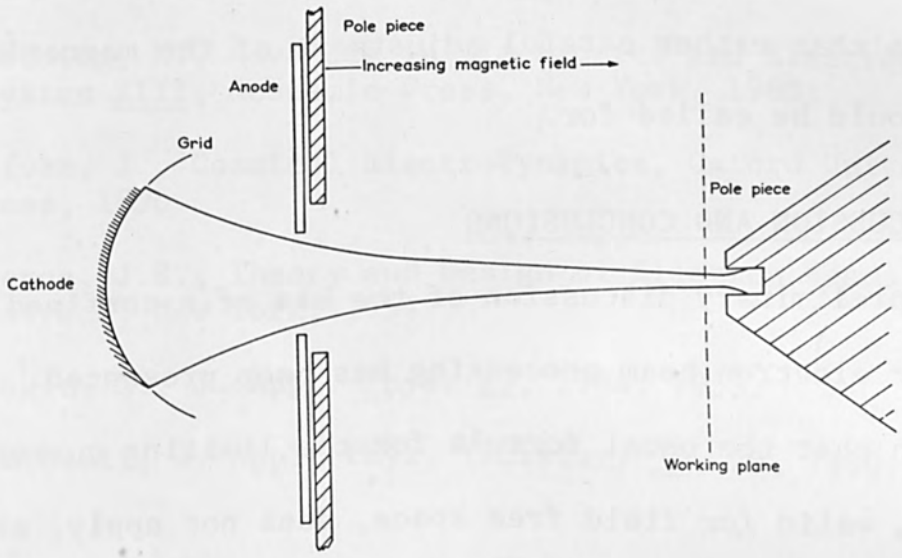

FIG.2 CONFINED FLOW SYSTEM

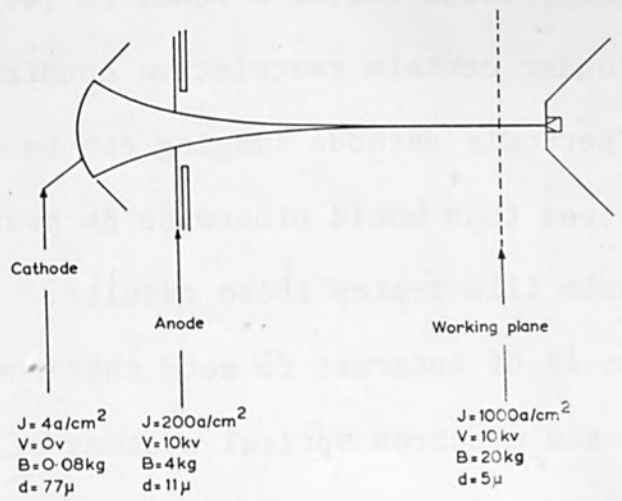

FIG.3 CONFINED FLOW - A NUMERICAL EXAMPLE

that the maximum permissible value of R which will retain some significant cathode imaging is of the order of 4000. Thus the actual R is well below the critical value, and one may expect clearly resolved cathode images. One must, however, retain some reservations as we have not yet examined the effect of space charge. A further practical difficulty is that the cathode images would be separated by only about 1 mm, so that rather careful adjustment of the magnetic field would be called for.

V. DISCUSSION AND CONCLUSIONS

A preliminary discussion of the use of a confined flow beam for electron beam processing has been presented. It is shown that the usual formula for the limiting current density, valid for field free space, does not apply, and is replaced by an expression which, for very large values of the field compression factor R tends to $(eV/kT)j_o$. It is shown that under certain restrictive conditions, the phenomenon of periodic cathode imaging can be used to obtain smaller spot sizes than would otherwise be possible. A numerical example illustrates these results.

Finally it is of interest to note that the confined flow system, unlike the electron optical systems of the electron microscope type, requires no rapid variation of field strength

with distance. Therefore, it should prove possible to use it with superconducting solenoids. In this way a further very large improvement in performance can be anticipated.

VI. REFERENCES

1. Langmuir, D.B., Proc. I.R.E., 25, 977, 1937.
2. Pierce, J.R., J. Appl. Phys. 10, 715, 1939.
3. Castaing, R., Advances in Electronics and Electron Physics XIII, Academic Press, New York, 1960.
4. Alfven, J., Cosmical Electrodynamics, Oxford University Press, 1950.
5. Pierce, J.R., Theory and Design of Electron Beams, Van Nostrand, New York, 1954.
6. Ashkin, A., J. Appl. Phys. 29, 1954, 1958.
7. Troitskii, J. Appl. Phys. (Russian) 30, 25, 1960.

POINCAIRE INVARIANT AND BEAM SPOT SIZE

By

R. F. Donovan
Senior Project Engineer
Hamilton Standard Division
United Aircraft Corporation
Windsor Locks, Connecticut

ABSTRACT

Utilizing the Poincaire Invariant, one can calculate the minimum spot sizes to be expected from a given cathode source for a given axial symmetric electron optical system or converse problem of given the spot size and power density requirements, calculate cathode source requirements and size. Calculated solutions are given to illustrate both of these problems and general curve data is included.

Poincaré Invariant and Beam Spot Size

Perhaps it is facetious to say that electron optical system designers are interested in beam spot size. A method for calculating beam spot sizes which has not received much attention in the literature is based on the Poincaré invariant. The full significance of this invariant has not been explored, but it can be a useful tool in electron optical design, for example, in the establishment of preliminary cathode specifications. The designer generally knows what is desired in terms of final beam spot size, current, and voltage as well as the design characteristics of various cathodes, electron guns, and electromagnetic lens systems. At this point, one usually draws upon experience to try to decide whether space charge or thermal velocity effects will predominate. If the goal is to obtain small spot sizes or high current densities, one will also be concerned with lens aberrations. Even in the simplest problems, one performs a few engineering judgement calculations. All of these calculations help formulate the problem, but skip around the pertinent calculation relating cathode and beam spot specifications.

This paper illustrates the Poincaré invariant method for calculating minimum spot size to be expected from a given cathode source for a given axially symmetrical electron optical system or the converse problem of calculating the cathode source specifications for given spot size and power density specifications. Although the calculations are done for an axially symmetrical system, the method is applicable to other coordinate systems and is not restricted relativistically. Other aspects of this paper are the discussion of some of the implications of the Poincaré invariant and beam spot size and a way towards correcting relativistically Langmuir's thermal velocity limitations for an axially symmetrical system.

Based on the principle of least action, P. Sturrock has developed from the Lagrange invariant some of the imaging relations for electron optical ray assemblies such as the Poincaré invariant which can be written as

$$I = \oint \overline{P} \cdot \overline{ds} \tag{1}$$

where $\overline{P} = p\overline{l} - \overline{A}$ is the electron optical ray vector, p is the scalar momentum, $\overline{l}$ is a unit vector in the direction of motion, $\overline{A}$ is the magnetic vector potential, and $\overline{ds}$ is the incremental path length vector. All quantities are in terms of electron optical units[1].

The integral is invariant when taken around any closed curve encircling a given tube of rays.

Since electron optical units are not common, it is appropriate to point out that the scalar kinetic momentum, p, is expressible as

$$p = \sqrt{2\phi + \phi^2} \tag{2}$$

where ϕ is the electrostatic potential and the magnetic vector potential, $\overline{A}$, retains its symbol when the unit of electrostatic potential is 511,200 volts and the unit of magnetic field strength is 1704 gauss.

For a more complete discussion of these units, see section 1.2 in Sturrock, reference #1.

Considering Figure 1, it is easy to show that for a circular integration path where $\overline{ds} = r\, d\theta\, \overline{l}_\theta$ for an axially symmetrical system,

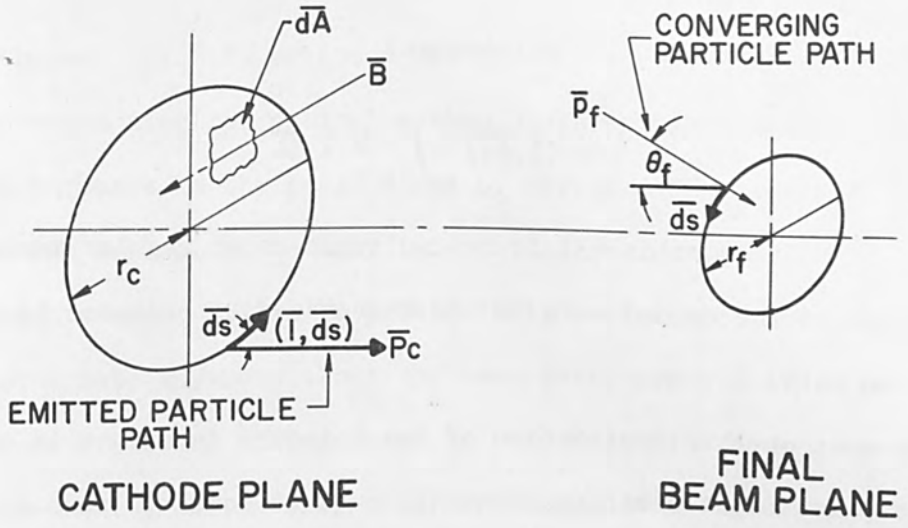

$I = \phi \bar{P} \cdot \bar{ds}$

FOR CATHODE PLANE

$I = 2\Pi r_c p_c \cos(\bar{l}, \bar{ds}) - \int_c \bar{B} \cdot \bar{dA}$

Figure 1. Definition of Terms for Rotationally Symmetrical Beam Systems

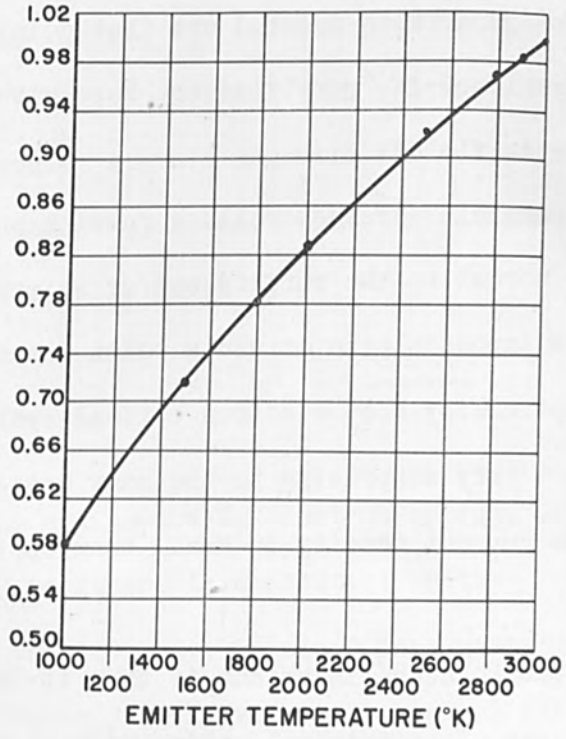

$p_c = \sqrt{2\phi_c + \phi_c^2}$

(MULTIPLY GRAPH VALUE BY 10^{-3} FOR TRUE p_c)

Figure 2. Graph of $p_c = \sqrt{2\phi_c + \phi_c^2}$ Where $\phi_c = \frac{V_c}{511{,}200}$ And $V_c = \frac{T}{11{,}600}$ vs T, The Emitter Temperature

the Poincaré invariant can be written as

$$I = 2\pi r_c p_c \cos(\overline{l},\overline{ds}) - \int_c \overline{B} \cdot d\overline{A} \qquad (3)$$

The first term in equation (3) is recognizable as an angular momentum - like term while the second term is the magnetic flux enclosed by the integration path.

The most obvious implication of the Poincaré invariant is that to achieve a point focus beam the invariant must be equal to zero at that point. This is only a necessary condition and, of course, does not guarantee a point focus since the cosine term may also be zero.

The implication of the cosine term being equal to zero is that a parallel beam path is formed for an axially symmetrical system. H. R. Fechter showed that if particles are emitted from a single point, a parallel beam path can not be produced unless the flux is zero at that region[2]. H. Fechter in the same paper also pointed out that point focus or parallel beams can be achieved if "particles are born with zero motion in a region of zero magnetic field".

Since electrons or other particles are generally born with a finite velocity not necessarily normal to the surface and/or in magnetic fields from area emitters, it is impossible to obtain a point focus even under the laws of geometrical optics for most electron optical systems. Of course, this conclusion is not very surprising to the many designers who have tried to produce a high current density in small beam spot sizes.

One of the advantages of the Poincaré invariant is that it is derivable from the fundamental laws of geometrical optics without restriction based on current density. Hence the question whether the spot

size is thermal velocity or space charge limited is academic for several questions which electron optical system designers are interested in for practical purposes in the early stage of design. In practice, the invariant can be applied to many interesting regions of electron or particle beam systems. It can be particularly useful when used with known experimental data anywhere along the beam path, especially if beam stops or apertures are being contemplated to help determine beam geometry. Some of the real problems are: one, what could a designer expect to achieve from a given cathode source in terms of beam spot size, convergence angle and voltage; or two, the converse problem, given goals of final beam spot size, convergence angle, and power density; what are the minimum cathode source specifications?

To illustrate problem one for an axially symmetrical system, a designer may have a cathode in a magnetic field-free region with an emitting radius, r_c, operating under space-charge limited flow at temperature, T. Given a final beam voltage and a desired beam half-cone convergence angle, θ, in a magnetic field free region, one can apply invariance and equation (3) to show that the minimum spot radius for 100% beam transmission is given by

$$r_f = \frac{r_c p_c}{p_f \sin \theta} \qquad (4)$$

where p_c and p_f are in electron optical units and other terms are in consistent units.

To aid the designer, Figure 2 is a graph of p_c versus emitter temperature while Figure 3 is a graph of p_f versus final beam voltage in electron optical units. For example, for a cathode emitting radius of one milli-

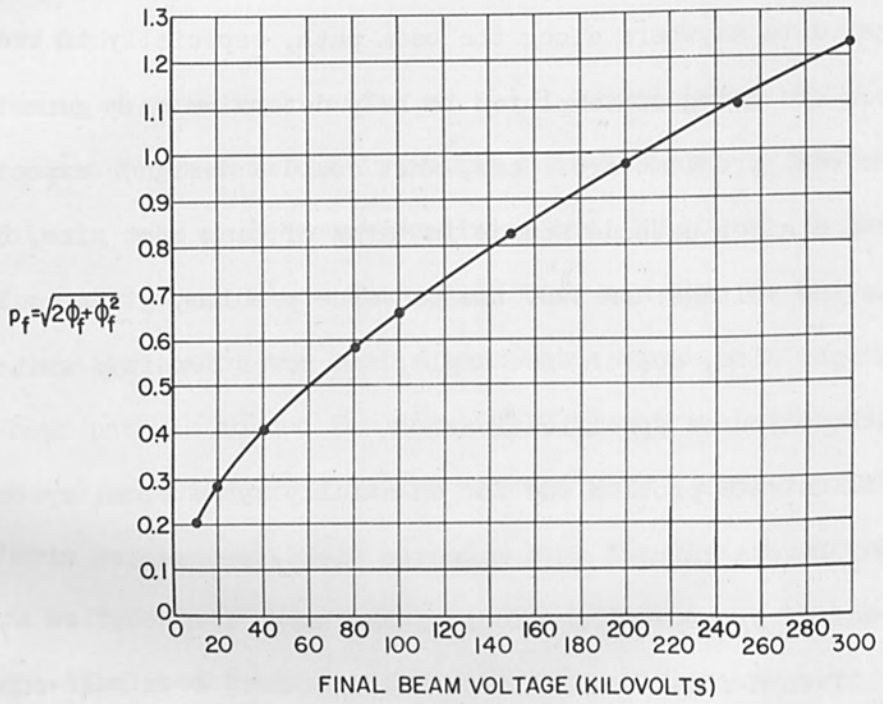

Figure 3. Graph $p_f = \sqrt{2\phi_f + \phi_f^2}$

Where $\phi_f = \frac{V_f}{511,200}$ vs V_f,

The Final Beam Voltage

meter operating at a temperature of 1000°K, if the final voltage is 100 kilovolts with a convergence angle of 1°, one could obtain a final beam diameter of 0.096 millimeters or approximately 0.004 inches even under the most extreme emitting condition where the electrons leave the emitting surface tangentially perpendicular to the surface normal vector at the circumference.

To reduce spot size further, the designer must usually accept a lower beam transmission efficiency along with the consequent beam interception heating problems at various stops or apertures.

Final beam currents depend then on how much can be achieved from the given source and how much is wasted. This latter aspect is generally more of a measure of the seriousness of the lens aberration problems than of the design competence.

To illustrate problem two for an axially symmetrical system, a designer may wish to meet a given goal of final beam spot size, power density, and beam convergence angle and may prefer to have this cathode operating under space charge limited flow in a magnetic field-free region. His problem is then to calculate a cathode source specification generally within the limits of some final beam voltage supply. For 100% transmission systems, the current density in the final spot, j_f, can be expressed in terms of cathode current density, j_o, by

$$j_f = j_o\left(\frac{r_c}{r_f}\right)^2 \qquad (5)$$

where equivalent terms are in consistent units.

For the illustrated problem, one can apply invariance and equation (4) and rewrite (5) to give

$$j_f = j_o \frac{p_f^2}{p_c^2} \sin^2 \theta \qquad (6)$$

where p_f and p_c are expressed in electron optical units and other terms are in consistent units.

The final power density requirements, W_f, can then be expressed in terms of final current density and beam voltage to give

$$W_f = V_f j_f = j_o \left(\frac{p_f^2}{p_c}\right)\left(\sin^2 \theta\right) V_f \qquad (7)$$

where p_f and p_c are expressed in electron optical units and other terms are in consistent units.

Since allowable current densities from known cathode sources are known as functions of temperature and the final power density and beam convergence angle specifications are given, equation (7) can be solved to give the required minimum beam voltage for desirable cathode sources. Knowing this voltage and previously given quantities, equation (4) can be used to specify the minimum cathode radius required. Note that this procedure emphasizes once again the dominant role of the cathode source in electron optical calculations. For example, given a cathode source which has a cathode current density of 1 ampere per square centimeter operating at a temperature of 1000°K where a ten billion watt per square inch power density is desired with a 5° beam convergence angle, one finds, utilizing equation (7), a minimum voltage of 125 kilovolts is required. For a final spot size radius of 0.00005 inches, a minimum emitting radius of 0.0055 inches is needed.

It is interesting to point out a new implication of equation (6) by rewriting it non-relativistically. Sturrock further pointed out that the non-relativistic form of the scalar momentum, p, is expressible as

$$p = \sqrt{2\phi} \tag{8}$$

where ϕ is in electron optical units.

Substituting appropriate terms in equation (8), equation (6) can be rewritten as

$$j_f = j_o \frac{eV_f}{kT} \sin^2 \theta \tag{9}$$

Equation (9) is recognizable as the practical modified form of Langmuir's well known thermal velocity limitation[3]. Hence, one may note that new information on thermal velocity limitations is contained in the Poincaré invariant. One may speculate, then, that the correct relativistic modification of Langmuir's thermal velocity limitation would follow from using the relativistically correct form of p expressed in equation (2). If this is done, equation (9) becomes

$$\begin{aligned} j_f &= j_o \frac{e}{kT} V_f (1 + .98 \times 10^{-6} V_f) \sin^2 \theta \\ &= j_o \frac{e V^*}{kT} \sin^2 \theta \end{aligned} \tag{10}$$

where V^* is the effective relativistic potential such as tabulated in Electron Physics Tables[4].

In summary, some of the implications of the Poincaré invariant relative to spot size have been discussed. Specific examples of how the Poincaré invariant method can be applied to some beam spot size and cathode source problems have been given. Finally, a relativistic

modification of Langmuir's thermal velocity limitation on current density for an axially symmetrical system has been given.

The author would like to express his thanks to Mr. O. Leisure for calculating the curves in Figures 2 and 3, and to Drs. R. O. Haxby and H. R. Fechter for many interesting discussions on the Poincaré invariant.

References:

1. Sturrock, P. A., Static and Dynamic Electron Optics, University Press, Cambridge, 1955, p. 32.
2. Fechter, H. R.,"Poincaré's Invariant and Particle Optics", Argonne National Laboratory Paper #HF-7.
3. Langmuir, D. B.,Proc. of IRE, 25, 977 (1937).
4. Morton, L. et al, Electron Physics Tables, NBS 571, Washington, 1956, p. 1.

THE USE OF ELECTRON BEAMS AS MEASURING TOOLS IN HIGH VACUUM PHYSICS

By

C. K. Crawford
Department of Electrical Engineering
Massachusetts Institute of Technology
Cambridge, Massachusetts

ABSTRACT

The use of mass spectrometers and ionization gauges to measure and control processes occurring in high vacuum is discussed. It is shown that the method is very sensitive and extremely versatile but a good method of calibration is currently lacking and a remedy is suggested. New mass spectrometers designed for evaporation control are described.

THE USE OF ELECTRON BEAMS AS MEASURING TOOLS IN HIGH VACUUM PHYSICS

Processes which involve atomic beams in high vacuum are difficult to study at present due to a lack of suitable measuring devices. Such processes as the deposition and analysis of thin films, the study of flash desorption, high temperature thermodynamics, reaction rates, and the study of electron induced reactions in thin films, all require a method of measuring the absolute flow rates and of identifying the constituents in a mass flow. One solution to this problem would be the construction of a mass spectrometer with an electron ionizer which is calibratable directly from fundamental ionization cross section data. Present day mass spectrometers cannot do this. This paper will consider the advantages and limitations of such a device and describe work being done along these lines at M.I.T.

Electron ionization has several significant advantages which make it particularly suitable for atomic beam detection and measurement. The most important of these is its complete generality. Any species of atom may be detected in the vapor state with approximately equal ease. Also, the sensitivity is very good; mass spectrometers are ultimately capable of detecting single particles, while electron ionizers have been built which can ionize up to ten percent of the incident atomic beam.[1]

Electron ionization measures the instantaneous value of the flow rate, not an integrated total of the flow. Thus no differentiation is ever required. If an integrated total is desired, such as a thin film thickness, integration is much simpler than differentiation would have been.

Construction of a linear, analyzable, calibrateable electron ionizer has proved to be somewhat difficult. The geometry of the intersection of the electron beam with the atom beam must be carefully controlled, so that the linear equation:

$$I = i\ell nq$$

can be used, see Fig. 1. Here I is the ion current resulting from the passage of an i ampere electron beam through an atomic beam ℓ cm wide. The atomic beam contains n atoms per cubic centimeter, and each atom has an ionization cross section of q square centimeter. Ultimately this equation is to be inverted, solving for n. A knowledge of n plus the source temperature is sufficient to calculate the mass flow rate. To use this equation the following conditions must be met.[2]

1.) Secondary electrons must be suppressed at the electron collector, to prevent any electron from passing through the atomic beam more than once, and to insure proper measurement of the electron current.

2.) The atomic beam must be wider than the electron beam because the atomic beam density can be made constant across its width. This cannot be done with the electron beam because of space charge. In this way every electron has an equal opportunity to form an ion while it does not matter that all atoms do not have equal opportunity to

become ionized.

3.) The electron beam should be sufficiently monoenergetic to permit operation at a single point on the cross section curve. If a significant spread in energy occurs, then a difficult weighted integration must be made over the appropriate part of the cross section curve. Deep space charge wells must be avoided, hence low ionizing currents must be used.

4.) The electron path length through the atomic beam, ℓ, must be a known constant, therefore the atomic beam must be defined by a rectangular aperture.

5.) Either all the ions, or a known fraction of them must be collected. A simple way of extracting all ions from the ionizer is to make the ion generating region about $\frac{5kT}{e}$ volts negative with respect to the ionization chamber wall, where T is the source temperature. It is then electrostaticly impossible for the positive ions to be collected on the chamber wall.

6.) The mass spectrometer must have a known transmission. At M.I.T. a Paul type quadrupole mass filter has been used.[3] At the expense of resolution, these filters may be adjusted to give 100 per cent transmission, providing an excellent calibration point.

7.) If an electrometer type ion collector is used, Auger electron emission and ion reflections must be suppressed, i.e., a Farady

collector should be provided.

8.) If an electron multiplier ion detector is used, a means must be found to calibrate it. The most accurate way is to use pulse counting and to ignore the fluxuating gain.

9.) The electron ionization cross section, q, must be known for the material under study. Otherwise the gauge cannot be calibrated without an additional calibration experiment.

At the present time, the last requirement, a knowledge of q, presents the most serious problem. The absolute values for ionization cross sections have been measured for many gases and for a few high vapor pressure metals.[4-11] These vapors can be contained in a glass vacuum system as a background gas. No studies, however, have been made on the absolute cross sections of ordinary metals or other interesting materials. To measure them requires some type of crossed beam experiment in which n is known. Otherwise, we have one equation and two unknowns, q and n. Relative cross section values can be measured by simply holding n constant. This has been done for copper, gold, and silver.[12]

Considerable work has been done using electron ionization gauges for proportional control and for the feedback stabilization of evaporators without knowing the absolute magnitude of either n or q.[13-17, 2] The ion current from a gauge is amplified and used to control the evaporator generating an atomic beam, as in Fig. 2a. If the gauge is to be used

in a relatively poor vacuum, 10^{-5} mm Hg or so, then a second gauge may be used to buck out the ion signal arising from the background gas, Fig. 2b. The author is working with the Alloyd Electronics Corp. on developing gages based on these principles.

The author's work at M.I.T. is currently directed toward implimenting an independent method of obtaining n, and thus toward measuring q. There are several methods of obtaining n. The simplist way is to use a Knudsen cell as an evaporator source and to measure the weight loss for a long run at a constant effusion rate. The density n may then be calculated from the weight loss, the geometry, and the cell temperature. Another way would be to install a Faraday cage type atom trap above the gauge and to measure the weight gain. Neither of these two methods can be used when the material being studied evaporates as a mixture of different species.

We would like to propose a new method which can do this, and in addition is entirely electronic. No weighing or other auxiliary operations are required. It must be emphasized that this method has not yet been tried, and so far works on paper only. A test is imminent at M.I.T.

As an atomic beam passes through an ionization gauge, the strength of the beam is decreased minutely by the loss of the atoms which are ionized and swept out. If a second gauge is placed after the first, it should in principal be capable of detecting this decrease, see Fig. 3. In fact, the decrease is so small in comparison to the other losses, that it is undetectable on a D.C. basis. However, if the electron current in the first gauge is periodically pulsed, then the modulation resulting in the seond gauge can be detected quite easily. Figure 4 indicates the appropriate pulse shapes. The equations have been somewhat simplified here,

for sake of clarity. The subscript j indicates the mass number under consideration. The Φ's designate equivalent currents, i.e., the currents which would flow in the atomic beam if each atom carried an elemental charge. It can be seen that both the ionization cross sections and the absolute flow rates, can be calculated from the gauge currents and known constants. Note that the constant k depends on the source temperature, thus requiring that this also be known. Figures 5 to 7 show a quadrupole mass spectrometer which was built at M.I.T. for the purpose of making ionization cross sections measurements. It is in this instrument that a double gauge ion source will be tried. More details on this instrument will be published at a later date.

Because of its complexity, this kind of equipment can require considerable time to build. We have reduced this time substantially by the use of punched metal parts stacked between aluminum oxide insulators. Figure 8 shows some of the parts which we now stock. They fit together in an erector set fashion and are particularly suited for crossed beam experiments where right angle intersections are required. Aperture alignments of $\pm$.001 inch can be maintained with stock parts. One of their major advantages is that design changes can be made very quickly. The parts can also be salvaged when the experiment is completed. So far we have made ionization gauges, evaporators, electron guns, an RF mass spectrometer, and two quadrupole mass spectrometers from them. We have also given some of them to other laboratories for use in various experiments. They save about one half on construction time and considerable design time as well.

References:

(1) Weiss, R., Rev. Sci. Instr., 32, 397 (1961).

(2) Crawford, C. K., Thesis, E. E. Dept. MIT, 1960.

(3) Paul. W., Reinhard, H. P., and von Zahn, U., X. Physik, 152, 143 (1958).

(4) Nottingham, W. B., Phys. Rev., 55, 203 (1939).

(5) Hagstrum, H.D., Rev. Sci. Instr., 24, 1122 (1953).

(6) Fox, R. E., et al., Rev. Sci. Instr., 26, 1101 (1955); J. Chem. Phys., 32, 385 (1960); J. Chem. Phys., 33, 200 (1960); (many others).

(7) Shultz, G. J., Phys. Rev., 106, 1179 (1957); Phys. Rev., 112, 150 (1958); Phys. Rev., 113, 816 (1959) Phys. Rev., 116, 1141 (1959).

(8) Marmet, P. and Kerwin L., Canadian J. Phys., 38, 787 (1960); J. Appl. Phys. 31, 2071 (1961)

(9) Brown, S. C., Basic Data of Plasma Physics, The Technology Press, Cambridge Mass., 1959.

(10) Field, F. H., and Franklin, J. L., Electron Impact Phenomenon, Academic Press, New York 1957.

(11) Massey, H.S.W., and Burhop, E.H.S., Electronic and Ionic Impact Phenomena, Oxford Clarendon Press, London, 1952.

(12) Blais, N. C., and Mann, J. B., J. Chem. Phys., 33, 100 (1960).

(13) Metzger, D. D., Thesis, E. E. Dept. M.I.T., 1958.

(14) Shoulders, K. R., Publication No. PB171027, Office of Technical Services, 1960.

(15) Thun, R. E., Proceedings of the Second Symposium on Electron Beam Processes (Alloy Corporation), 1960, page 70.

(16) Giedd, G.R., and Perkins, M.H., Rev. Sci. Instr., 31, 773 (1960).

(17) Schwarz, H., R v. Sci. Instr., 32, 194 (1961).

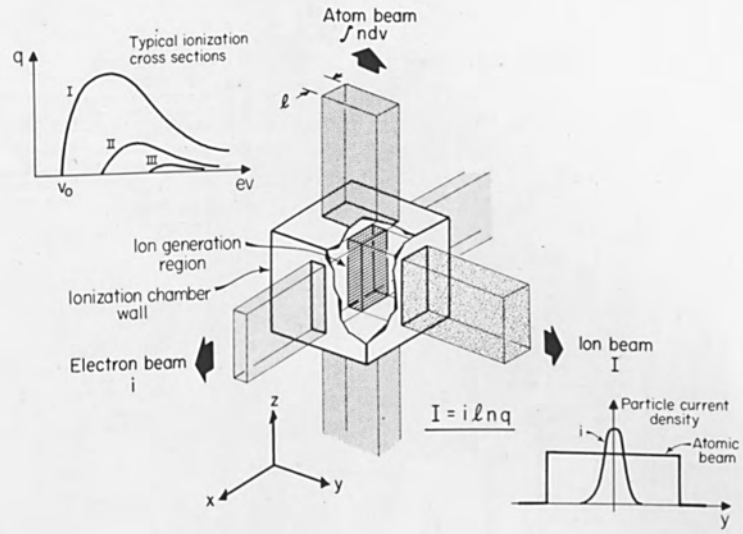

Fig. 1. Beam Intersection Geometry

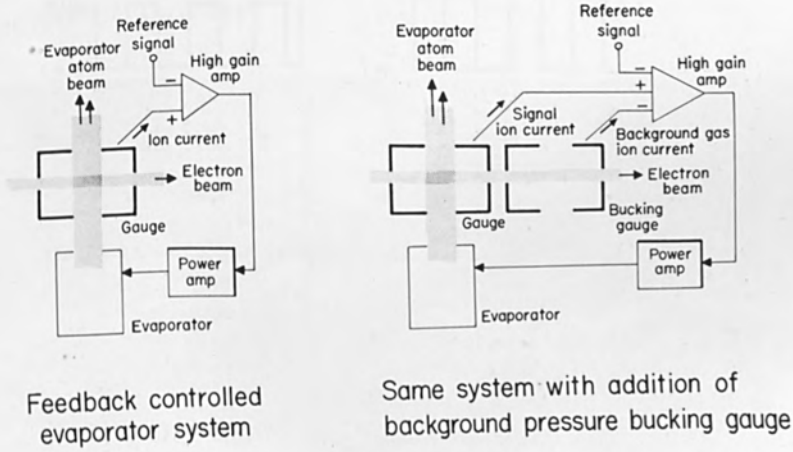

Fig. 2. Use of Ion Gauges to Stablize an Evaporator System

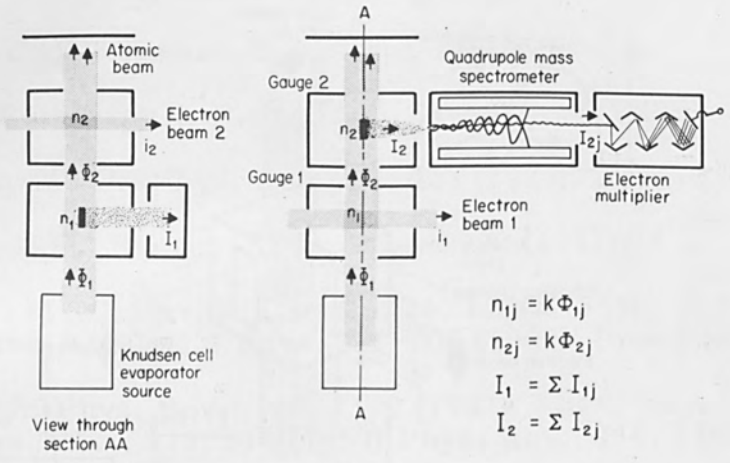

Fig. 3. Double Gauge Method of Obtaining Both the Ionization Cross Sections and the Absolute Flow Rates of a Beam with Several Components.

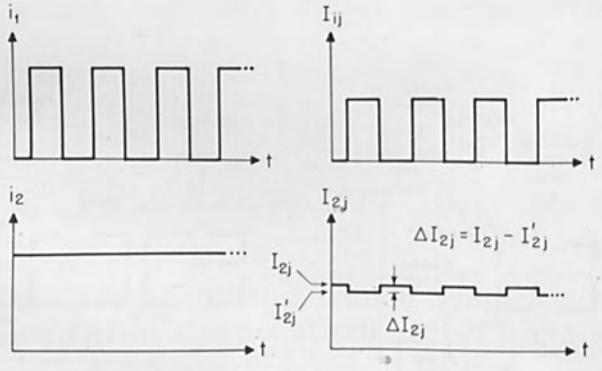

$$I_{2j} = i_2 \ell n_{2j} q_j = i_2 \ell k \Phi_{2j} q_j$$

$$I_2 = i_2 \ell \sum_j n_{2j} q_j = i_2 \ell k \sum_j \Phi_{2j} q_j$$

} Likewise for I_{1j} and I_1

$$\Phi_{2j} - \Phi_{1j} = I_{1j}$$

$$\frac{I_{1j}}{I_1} = \frac{I_{2j}}{I_2} \longrightarrow I_{1j} = \frac{I_1}{I_2} I_{2j}$$

$$\frac{\Delta I_{2j}}{I_{2j}} = \frac{I_{1j}}{\Phi_{1j}} \longrightarrow \Phi_{1j} = \frac{I_{2j}}{\Delta I_{2j}} I_{1j} = \left(\frac{I_1}{I_2}\right) \frac{(I_{2j})^2}{\Delta I_{2j}}$$

$$q_j = \left(\frac{I_2}{I_1}\right) \frac{\Delta I_{2j}}{i_2 \ell k I_{2j}}$$

Fig. 4. Pulse Shapes for Double Gauge

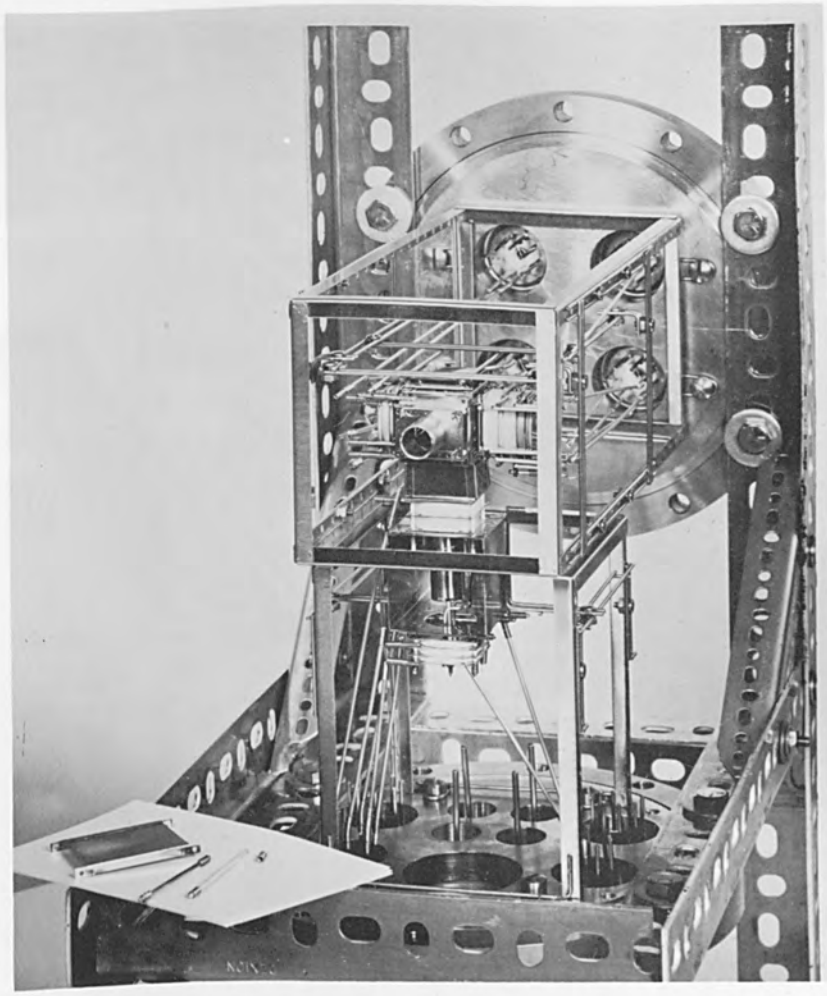

Fig. 5. Crossed Beam Ion Source for Quadrupole Mass Spectrometer

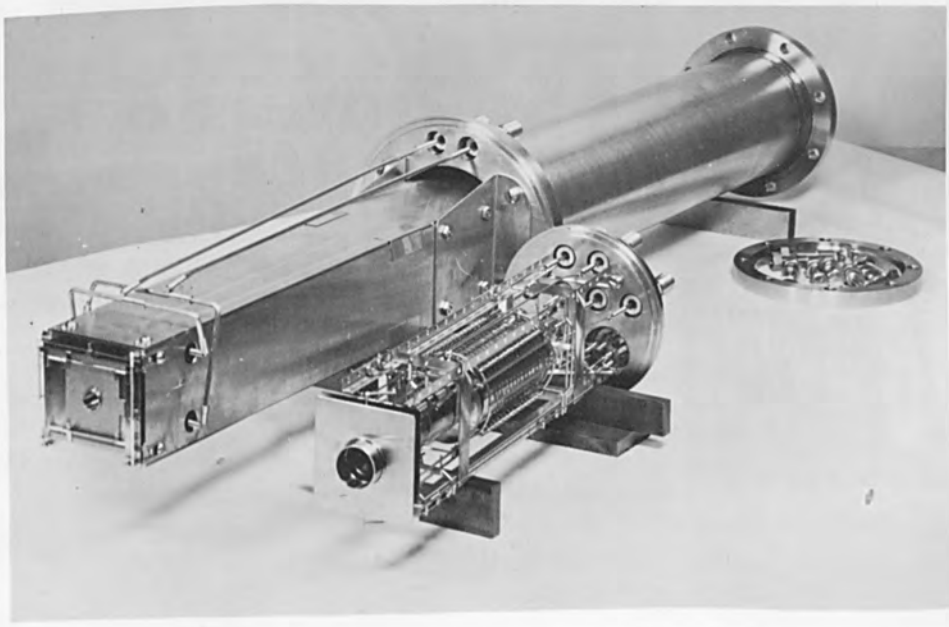

Fig. 6. Quadrupole Mass Filter with Electron Multiplier Ion Detector

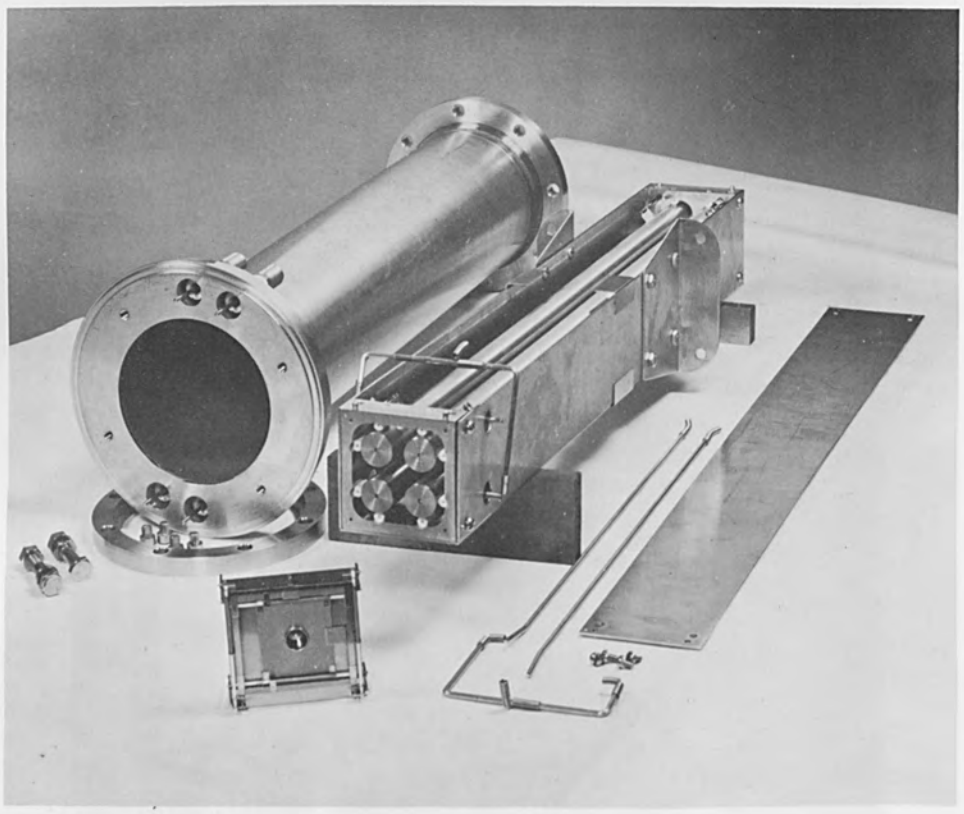

Fig. 7. Mass Filter Disassembled

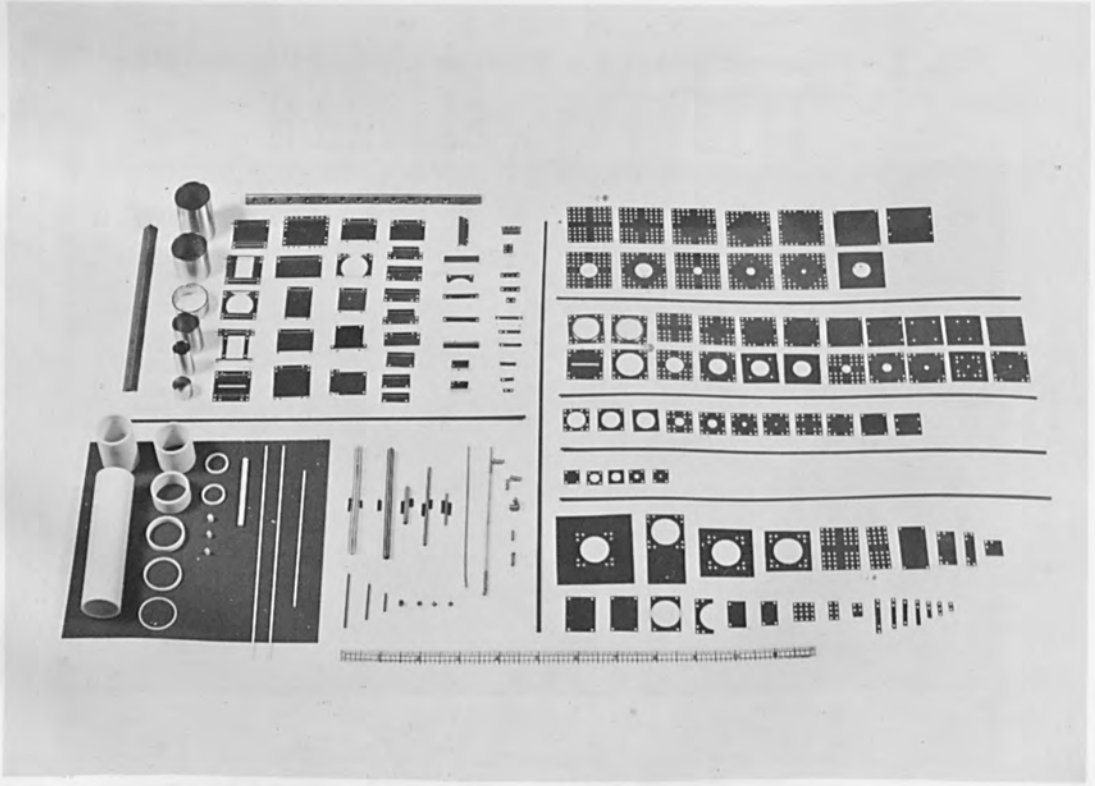

Fig. 8. M.I.T. Standard Electron-Atom-Ion Beam Parts

EVALUATION OF C.R.T. TYPE ELECTRON-GUNS AND THEIR MODIFICATION FOR USE IN KINETIC-VACUUM SYSTEMS

By

A. H. Andrews
Engineering Specialist
C.B.S. Laboratories
Stamford, Connecticut

ABSTRACT

A short survey of presently available electron/ion guns is presented showing typical operating parameters. Also discussed is the design of a demountable electron gun, having an easily replaceable oxide cathode, this gun has operated in a hydrocarbon contaminated vacuum of 10^{-5} Torrs with good life, yielding spot densities of several amperes per cm^2, at accelerating potentials of less than 20 KV.

EVALUATION OF C.R.T. TYPE ELECTRON-GUNS AND THEIR MODIFICATION FOR USE IN KINETIC-VACUUM SYSTEMS

Before any development program is undertaken, it is usual to list equipment requirements, and then survey the field for existing components that may be employed. This is always cheaper and easier than developing your own designs for everything that is required. These obvious statements are made here to stress the fact that persons requiring electron-guns for experimental purposes, have no criteria upon which to choose one type of C.R.T. gun over any other.

I mention only C.R.T. guns, because our experience at CBS, was that most people, in the early development states of their programs, would ask for performance data on existing cathode-ray tubes. These inquiries were from people with no method of determining electron-gun performance as to electron beam size and current densities, from data referring to lines of resolution on the phosphor face. Another characteristic that gives a misleading estimate of overall C.R.T. performance is the fact that some high resolution, high current, C.R.T.s employ aperturing of the beam

at ultor potential and the indicated current is the total beam current, not just that appearing at the screen.

A useful but admittedly approximate method for C.R.T. gun evaluation will now be described. Though of less interest here, but still of consequence, it is also a test of the ultimate capability of the phosphor screen. It may be used in comparative tests, with standardized procedures, in the further development of phosphor screens in addition to C.R.T. electron guns.

The first requirements are resolution figures, taken at screen currents in the range of interest, with the resolutions measured under half power point conditions.

Figure 1 shows the algebra associated with two simple assumptions. These assumptions are that for small changes in beam current, both the electron beam density and the scatter within the phosphor remain constant. The units chosen are not coherent, but are those usually used and most easily recognizable, all that is required now are two sets of conditions of current and resolution to derive the unknown.

The curve on **Figure 2** shows the results obtained by applying an expression derived from the previous algebra, that the gradient = $\frac{BT^2}{4I}\ 10^{-3}$. This curve was the response obtained from an experimental C.R.T. having a fine P.11 phosphor when using a shrinking E.I.A. test pattern at TV rate. The values for current have been multiplied by 1.43 to indicate high-light values rather than mean current, this factor was arrived at from the fact that the E.I.A. test chart used was bright over only 70 per cent of its area.

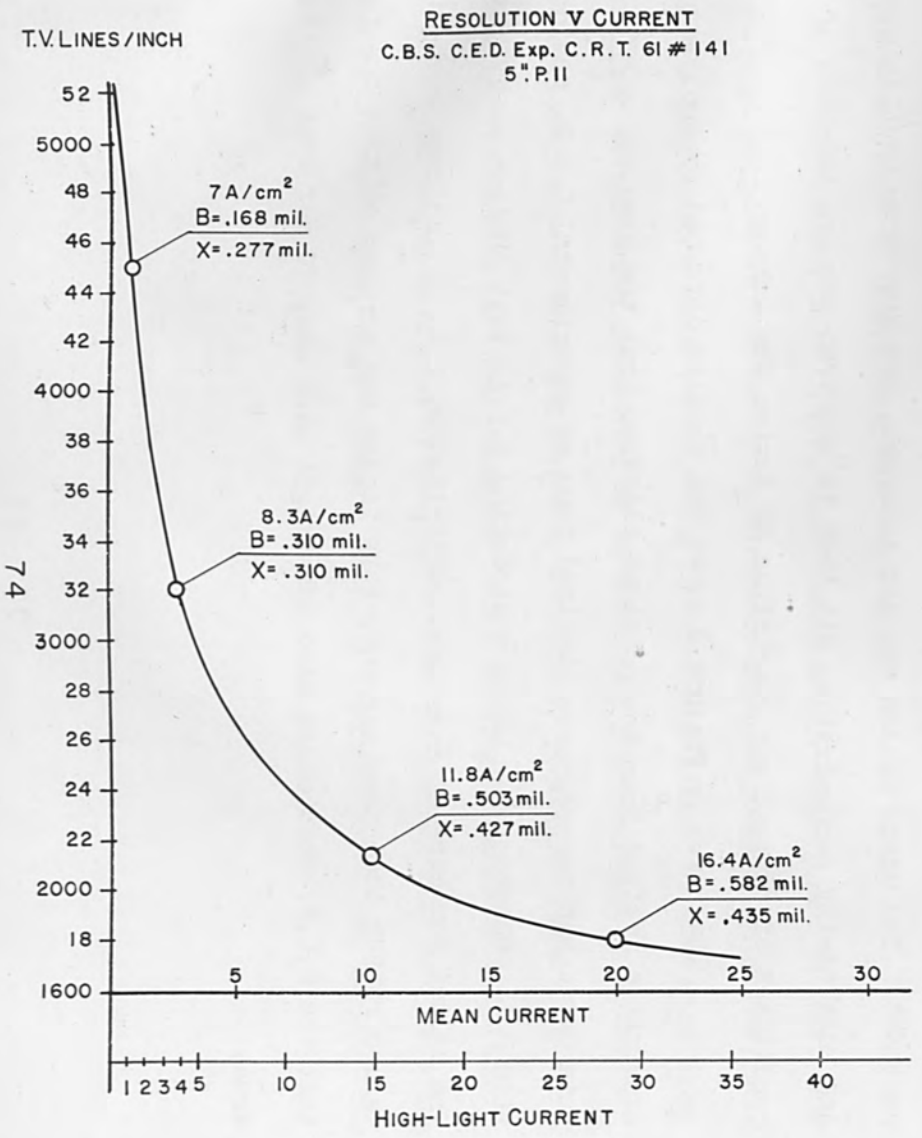

FIGURE 2.

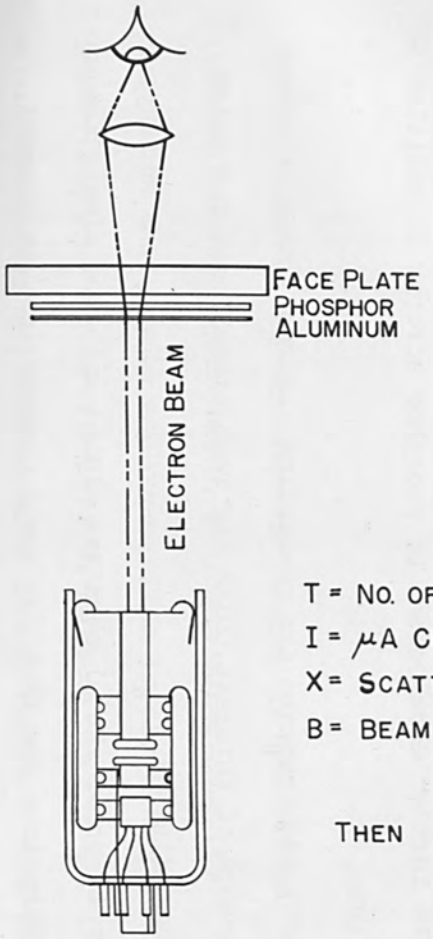

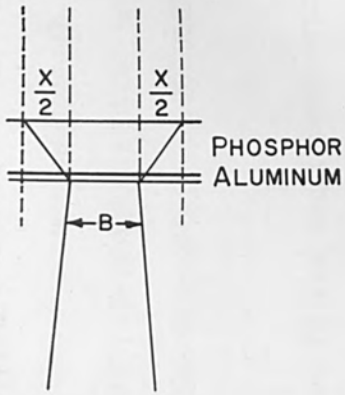

T = NO. OF T.V. LINES PER INCH.

I = μA CURRENT TO THE SCREEN.

X = SCATTER IN PHOSPHOR (mils.)

B = BEAM WIDTH (mils.)

THEN $X + B = \frac{2.10^3}{T}$

$$A = \frac{I \cdot 10^{-6}}{(2.54)^2 \cdot \frac{\pi B^2}{4} \cdot 10^{-6}} = \frac{I}{5.06B^2}$$

$$B = \sqrt{\frac{I}{5.06A}}$$

$$X = \frac{2.10^3}{T} - \sqrt{\frac{I}{5.06A}}$$

FIGURE 1.

The figures quoted show increasing current density and phosphor scatter through the current range, this is understandable and to be expected when some of the variables are considered. It is known from experiments conducted at CBS that the phosphor scan line, in cross section, approaches Gaussian at very low currents, although it is essentially square with small tails at higher current values. This will be one source of error, as the calculation assumes an essentially square cross section throughout. Also as the current is varied over a wide range of values the diameter of the beam in the final lens will alter so varying the angle of beam convergency and the current density possible at any particular ultor voltage. The raster size of the test pattern alters, for differing resolution figures, so altering the rate of beam travel although the error from this source is very small, effecting mainly the size of the tails. These objections can be removed when using this method of evaluation in a C.R.T. laboratory under reproducible test conditions.

None of these limitations, however, are half so frustrating as the endeavor to obtain response curves from manufacturers, and have them state, fully, their methods of measurement. For the ones amongst you who may obtain such data, I can say that this simple calculation has shown good correlation, in the current range above 1 micro-amp, with results obtained by a fine-wire method of beam sizing, which I will describe now.

Close to the phosphor face of the tube, parallel to it and to each other, several fine wires of different sizes are mounted with separate leadouts through the face plate, their other ends being common but insulated from the screen. The C.R.T. was run for these tests with the gun at high negative potential relative to the screen with the screen and

wires at ground. Also shown is a typical response, obtained when the beam is swept in line-scan perpendicular to these wires. The oscilloscope response shown here is that obtained when crossing the 1 mil diameter wire at 15 KV 3 μA. The pickup current was fed into a Dumont 440, the marked sections of the curve can be identified as follows, **Figure 3.**

A. Presence of secondaries and any halo around the beam.

B. The electron beam traversing onto the wire and

C. The exponential decay of the external R.C. circuit to the scope.

D. The electron beam leaving the wire and

E. The resultant of halo, R.C. decay and secondaries.

This fine wire method of spot sizing has the advantage of simplicity in that beam velocity need not be known and the only precaution to observe is that the line scan is at right angles to the wire. Sixty cycle sinusoidal A.C. has been employed for deflection and then a long scan length should be used compared with the wire diameter (1000:1) and the wire should be at centre of the scan to give a response showing equal widths in sections B and D.

Perpendicularity of the line scan to the wires, is achieved by rotating the deflection coils until sections B and D have minimum widths. Correlation between this form of measurement and the calculated values shown earlier are good, certainly less than 10 per cent difference between the two, so that either method can be considered as giving a good indication of beam size.

The electron gun, used in the experimental U.H.R.C.R.T., has been used successfully in the method of recording, described at the outset

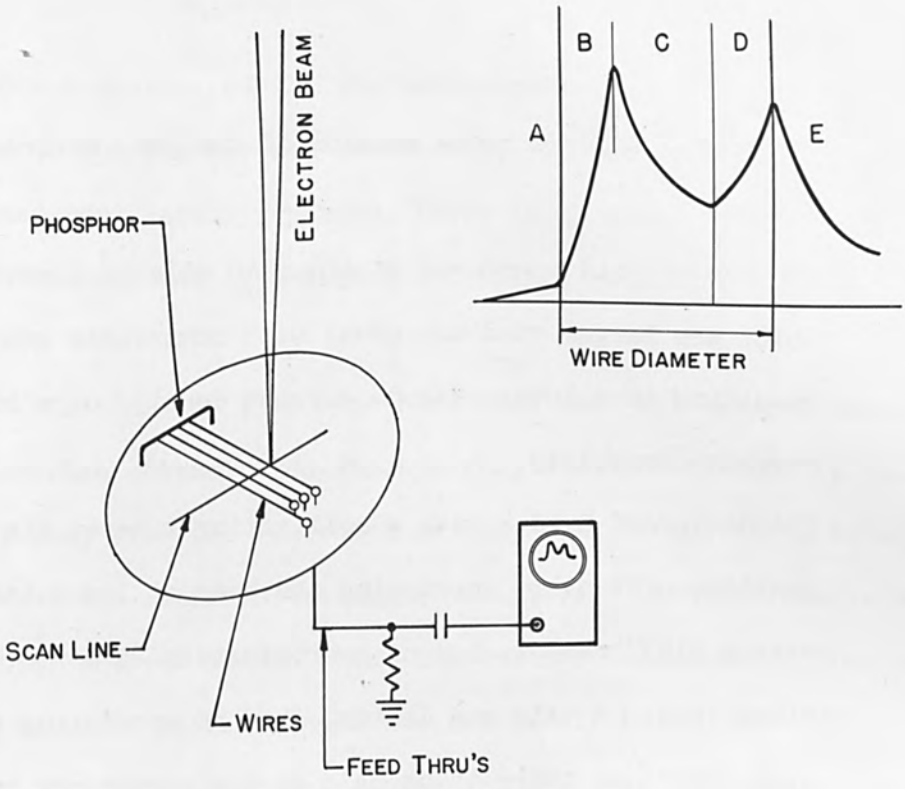

A. PICK UP OF SECONDARIES & BEAM HALO
B. BEAM TRAVERSING ONTO THE WIRE
C. R.C. DECAY OF CIRCUT
D. BEAM LEAVING THE WIRE
E. R.C. DECAY, BEAM HALO & SECONDARIES

FIGURE 3.

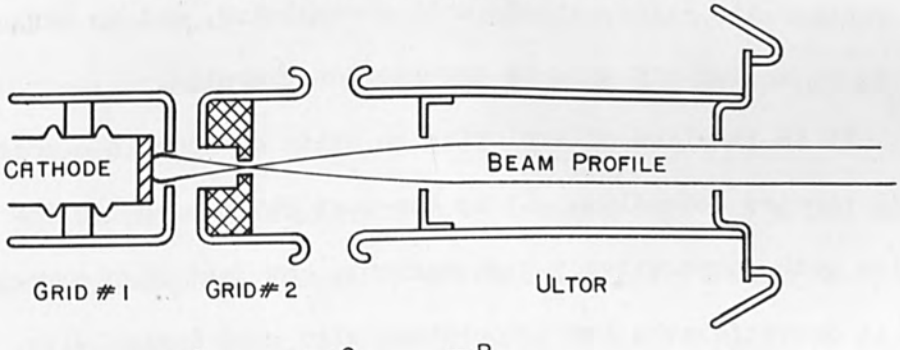

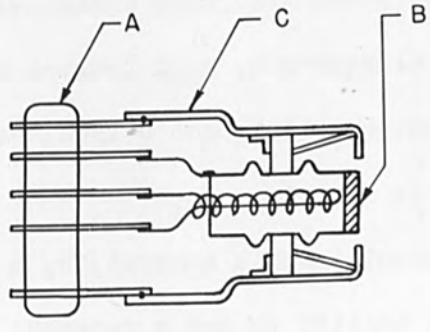

A. GLASS BEADED ASSEMBLY WELDED TO METAL CUP "C".
B. C.R.T. TYPE CATHODE .110" DIA.

FIGURE 4. OXIDE CATHODE PLUG-IN UNIT

of this paper. **Figure 4** shows a cross section of the gun, several points are worthy of notice.

1. The use of grid apertures of about 40 mils in diameter which are larger than are usual with comparable guns, resulting in a lower cathode current density or a higher current capability.
2. The design of Grid 2 with a collimating tube at the mean position of X over, aperturing the beam at low voltage but with a high transmission of approximately 25 per cent. The final lens, in this gun design, does no aperturing at voltage above 7 KV, so there is no halo at the screen nor outgassing of gun parts nor are there any variations in tube-characteristics as a final aperture is burnt away.

Modifications for use in a kinetic system were the change to the plug-in replaceable oxide-cathode unit shown below, and in arranging for the gun to be angled off axis to provide ion trapping.

It is the idea of employing an oxide cathode in a poor vacuum, that will require defending. It is the most obvious choice for high resolution with comparatively high current, not just high current density, because it operates at a low temperature with good emmissivity. It has other advantages of fair mechanical strength, good thermal efficiency and above all cheapness. The important question that arises then, what sort of life will it have?

Let us define what is meant in this context, by a reasonable life. In a research project, the ability to get a coherent set of test results is probably all that is required. This may take less than an

hour. For a system feasibility demonstration, the equipment may be required to run for several hours only. If the cathode is cheap enough and very easily replaced, there is no reason why commercial equipment should not be designed and built, requiring a cathode change everyday.

Cathodes of this type have been used for several hundred hours, in hydrocarbon contaminated atmospheres, when the cathode is mounted a long way away from the recording medium, as is required to obtain a good object to image ratio in the magnetic-optics. When the gun is also angled with respect to the axis, the cathode is protected from ions arising anywhere other than in the gun itself.

Differential pumping over orifices has often been employed to improve the electron gun environment. Cathode poisoning can be decreased in its effect by running the cathode at temperatures nearer 900°C than the normal 780° and an automatic activation circuit should be employed for the initial activation. Under these conditions the oxide cathode is a reasonable type of cathode to specify and is economically to be preferred over other types.

Until there is a significant "breakthrough" to a low temperature, high emissivity, rugged, thermally-efficient, highly stable and, above all, a cheap cathode, the oxide cathode can be called upon to perform under adverse conditions. As a further example, it has been found possible to operate a C.R.T. type oxide-cathode, 1/8" in diameter, in a grid controlled Pierce gun, giving 60 mAs at 4 KV, for 20 hours of welding on stainless steel. A Müller configuration with a 1 1/2" diameter annular

oxide-cathode is used in our laboratories to deliver 2 amps at 10 KV, for welding and melting, and has a similar lifetime.

SUMMARY

Many people present, I'm sure, have been frightened away from the idea of using oxide cathodes, by the copious literature on cathode-poisoning phenomena. A sense of proportion should be maintained however, and it should be remembered that the authors are usually concerned with thousands of hours of reliable life at low noise levels in sealed off tubes.

The method of C.R.T. gun evaluation should be useful to anyone wishing to choose an existing commercial C.R.T. gun design, for their own experimental purposes. This evaluation procedure is more useful in a C.R.T. laboratory using C.R.T.s, of the same geometry with similar operating parameters where it may be used to evaluate progress in the development of both guns and high-resolution phosphors.

PROBLEMS OF MICROSPACE INFORMATION STORAGE

By

S. P. Newberry
Physicist
General Engineering Laboratory
General Electric Company
Schenectady, New York

ABSTRACT

The microspace approach to information storage is now generally accepted as one of the more attractive possibilities for a needed breakthrough in data storage and retrieval. Essentially it is a method which makes practical use of the high storage density capabilities (over 10^{10} bits/cm^2) of the electron microscope.

After a brief review of the basic approach, the present paper will attempt to make a realistic appraisal of the major problem areas, and indicate probable best solutions for many of them.

PROBLEMS OF MICROSPACE INFORMATION STORAGE

The need for high capacity, rapid, random-access memories is now generally recognized. It is difficult to recall the technical climate, ten years ago, when the chief problem of developing high capacity memories was to dramatize the need for improvement. This need is now self-dramatized, for example, by the library problem wherein the technical information published each day throughout the world is equivalent to seven complete sets of the Encyclopedia Britannica[1]. We have already passed the point in generation of technical papers, and business records at which an individual can read, or even find all those papers, letters, and other written materials pertinent to his performance. In addition, industrial control must now be too precise to depend upon human memory and its pace too rapid for manual recall of pertinent data. This and other staggering problems with written work, clearly point to the conclusion that the technological word is building a Tower of Babel which will completely bog down because of impossible information handling problems, unless a new approach is adopted.

The development of an ultra high density memory is the first (and a key) step in the new approach needed to overcome this mounting data handling problem. Development of proper memory techniques, can therefore serve the same purpose today as the invention of the printing press did in its day. This new approach must be built in our time if we are to avoid complete intellectual chaos and frightful waste of human effort. Let us examine, in brief review, the microspace approach[2] to large capacity, rapid, random-access memories as one of the more attractive possible solutions to the memory problem.

By use of electron optical information storage capabilities, a sheet of material one-fifth the size of a printed page could contain the memory capacity of the human mind. However impressive this accomplishment may be in its own right, it is proper to ask, what does greater storage density contribute toward solution of the memory problem? Couldn't one find ample floor space for an expanded memory based on ordinary techniques? If necessary, the whole American desert is available for files of key punched cards. This ridiculous extreme (Fig. 1), combining our least condensed memory device with the largest available space, serves to emphasize the advantage of compact storage media in reducing access time. Even with a jeep to collect the key punch cards, the access time is limited by the physical remoteness of some of the data from the processing center. If one must interrogate the memory at nanosecond rates[3], then even with an access channel operating at the speed of light, the most remote part of the memory could not be more than six inches away because light can only travel about one foot round trip in one nanosecond. By use of a buffer storage, a much slower access time, for example one microsecond, might be compatible with nanosecond access. This would extend the theoretical limit to 500 feet but practical considerations such as switching time, interelectrode capacities, etc., bring the operating distance for microsecond response into the buffer down to a few feet at most.

Microsecond random access (or faster) is impossible with tape or drum memories, but it can be accomplished by thin film memories or by optical memories. A circulating optical memory such as a vacuum path optical delay line, could be 1000 feet total length but it would

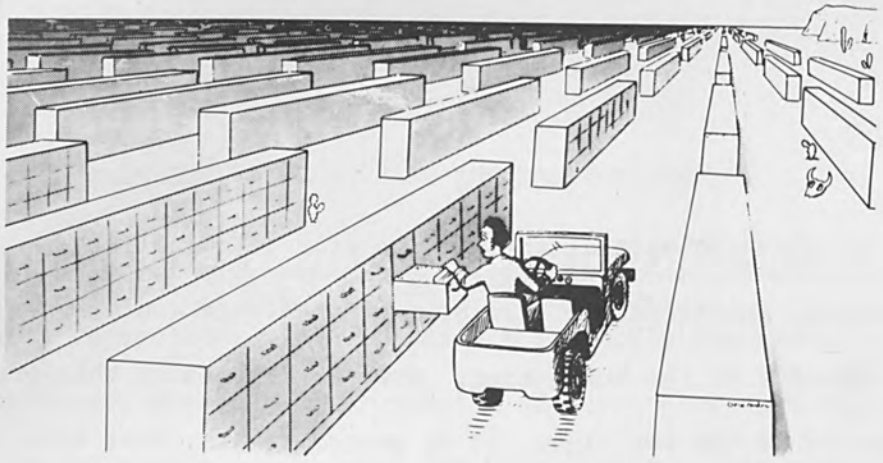

Figure 1 - More filing space does not solve the data storage problem even with all the space in the desert and a jeep for data pickup, access is too slow to search a large memory randomly.

Figure 2 - High density photographic data storage is an old art. This is a picture of English rulers recorded in a microscopic dot. Although this picture was made nearly a century ago, we have not been able to use this recording density for data storage.

have an approximate total capacity of only 10^8 bits. To match the capacity of the human mind would require 10^4 such delay lines with 10^4 switches, sources, detectors, etc. Perhaps some economy could be effected by circulating more than one message in a given delay line. The important point is that a close limiting relationship exists between memory-density and access time.

The problem is not, however, to achieve greater storage density; we aren't using the memory capacities already available in photographic film. Why then be concerned about the storage density available with the electron microscope? The capabilities of photography were demonstrated nearly a century ago when photographers made pictures so small a microscope was needed to see them (Fig. 2). But "as a watch is more difficult to make than an alarm clock" even so this high density could not be used for recording because of dirt, blemishes, scratches, tedious processing, and difficult relocation. Sixty times magnification is generally considered the ultimate practical resolution for microfilm even though it has an inherent resolution reaching down to or below the light microscope limits.

The problem now faces a potential mountain - what is needed is a giant step beyond this mountain. If we take this giant step in storage density then:

1. The entire memory can be stored in a clean enclosure free of dust.
2. The storage surface is so small that it does not become scratched by being rolled or folded upon itself.

3. Access time is brought down orders of magnitude by reduction or elimination of mechanical motions.
4. Accuracy of location of data can be accomplished with micro-inch precision by use of optical coupling, detection of location error in a magnified image plane, and successive refinements of coincidence.

A pseudo quantitative picture of the relation between storage density and system reliability is given below (Fig. 3). A similar picture could be drawn for the relation between density and access time. This giant step is the essence of microspace storage technique.

To attain this giant step, it is proposed to employ electron beam storage and readout techniques for the following reasons:

1. The writing beam of electrons can be at least 100 times smaller than an optical, mechanical or magnetic "pencil".
2. An electron "pencil" has no perceptible inertia.
3. Readout can be directly translated into electrical signals.
4. The depth of focus is roughly 25 times as great as optical or magnetic recording systems - thereby relaxing the tolerance on vertical memory position.
5. It permits an increase in writing and reading speed because the energy density of the electron beam is three orders of magnitude greater than that possible with optical or magnetic recording systems.*

*If lasers can be employed, they will produce energy densities approaching electron optical values within their resolution range.

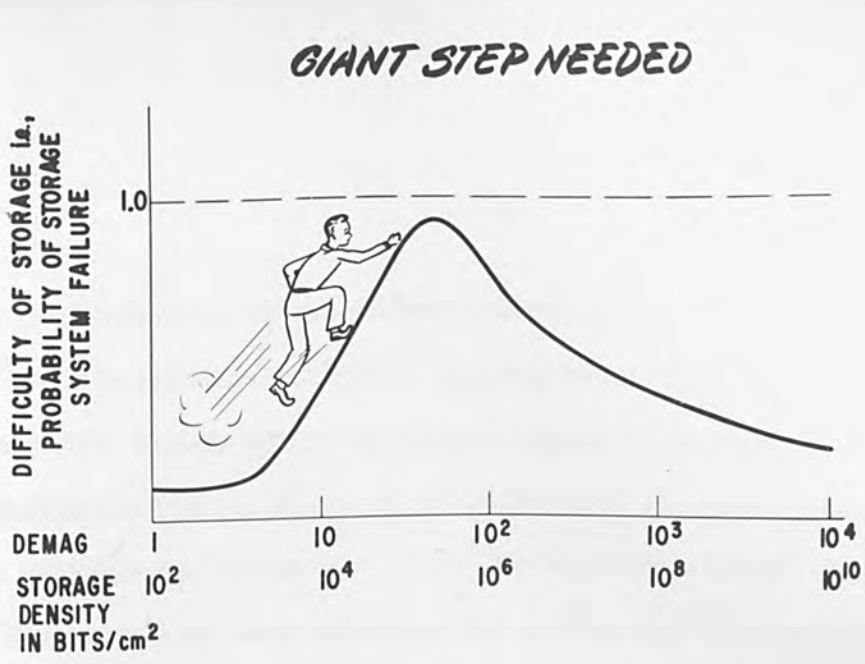

Figure 3 - A giant step in storage density is required to overcome practical limitation of dust, scratches, and slow access. For very large capacity memories the probability of dropouts reached a maximum at some value less than 100 times demagnification.

Figure 4 - Mollenstedt's recording achievement. Guiding a minute electron beam across a thin collodion film he could engrave letters or outline drawings at will. The beam evaporates some of the collodion leaving a groove whose contrast is enhanced by a metal vapor coating. Half-tone picture recordings should be possible by his technique. It does not, however, answer all our needs for a microspace memory plate.

A wide choice of electron beam techniques is available for devising memory systems. The most obvious is a micro-microfilm which can be viewed in a standard electron microscope. The modern electron microscope can resolve detail down below 10 Au which appears to permit storage densities of more than 10^{14} bits per square centimeter; a density which places the dignity of the human mind on .01 square centimeter or about equal to the useful area of two standard 1/8" dia. electron microscope specimen grids.

No recording medium has yet been demonstrated to have this kind of resolution. There is no immediate urgency to reach this ultimate goal because the electron microscope occupies several cubic feet, thus the specimen chamber might as well accommodate a memory plane several square cm. in area. Professor Möllenstedt of the University of Tubingen, Germany, demonstrated electron beam recording of letters 1/2 micron high and digital bits 0.05 micron dia. at last year's meeting of this assemblage.[4] The same kind of resolution has been demonstrated by Shoulders[5] using a different recording medium. The resolution they have obtained (Fig. 4) gives a density of 10^{10} bits/cm^2. At this density the human mind is now elevated to the size of 1/5 of a printed page as mentioned earlier. This is still a very impressive storage density. It can record the entire Encyclopedia Britannica on less than a postage stamp. For a great many practical reasons, which cannot be explored in the time available in this paper, 10^{10} bits/cm^2 is the density which we have chosen as a design goal for our first microspace devices. At this level of resolution, the basic system parameters are in general comfortably removed from fundamental limitations. How-

ever many serious problems exist between now and the day of providing complete copies of the Encyclopedia on a postage stamp. These problems are the concern of the present paper.

Recording Material Problems

The development of an "ideal" recording material will probably become a never-ending pursuit but even the production of compromise recording materials, limited to specific applications, is beset with many problems. The normal electron microscope specimen must be less than 200 Au thick which makes it very fragile. We prefer recording on a substantial, solid surface which is incompatible with the normal transmission electron microscope. However, both the mirror electron microscope (Fig. 5) and the scanning electron microscope (Fig. 6) can read from a solid surface. The mirror microscope[6] has been troubled by interference from the incoming electron beam which normally requires a hole in the middle of the image screen. This can be avoided by use of an electron prism[7]. It has also suffered from marginal resolution for this application but this is not due to fundamental electron optical limitations but rather to lack of sufficient attention to the development of this equipment. The output of the mirror microscope is an image. Location of specific information and conversion to electrical output can best be accomplished by an image tube as described by the author[2].

The scanning microscope[8] gives a direct electrical output and has been demonstrated to have adequate resolution if the specimen can be viewed at a 25 degree angle. This angle causes serious instrumentation problems when scanning a memory plate several centimeters in each

MIRROR TYPE ELECTRON MICROSCOPE

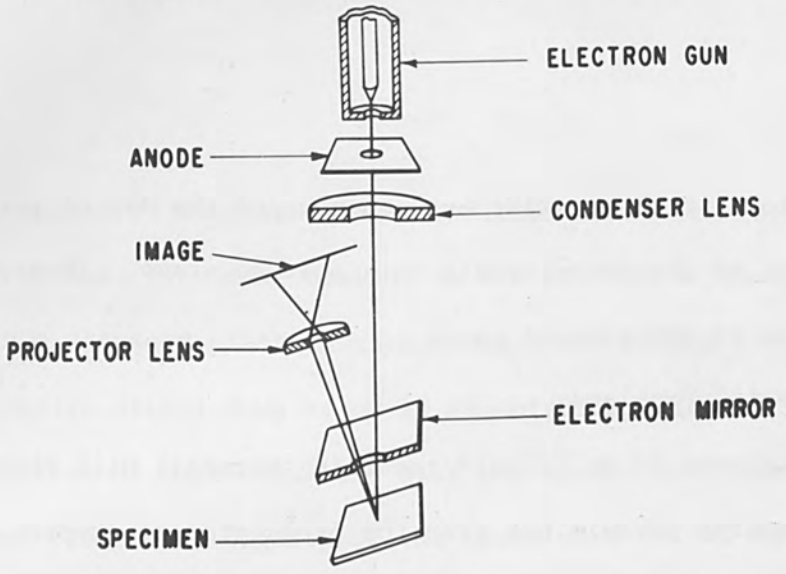

Figure 5 - Schematic diagram of a mirror electron microscope. Small surface differences in the specimen have an enormous effect upon the electron beam as it comes to its turn around point in the electron mirror. This microscope can read from a solid surface. It needs further practical improvement - especially in resolving power.

SCANNING TYPE ELECTRON MICROSCOPE

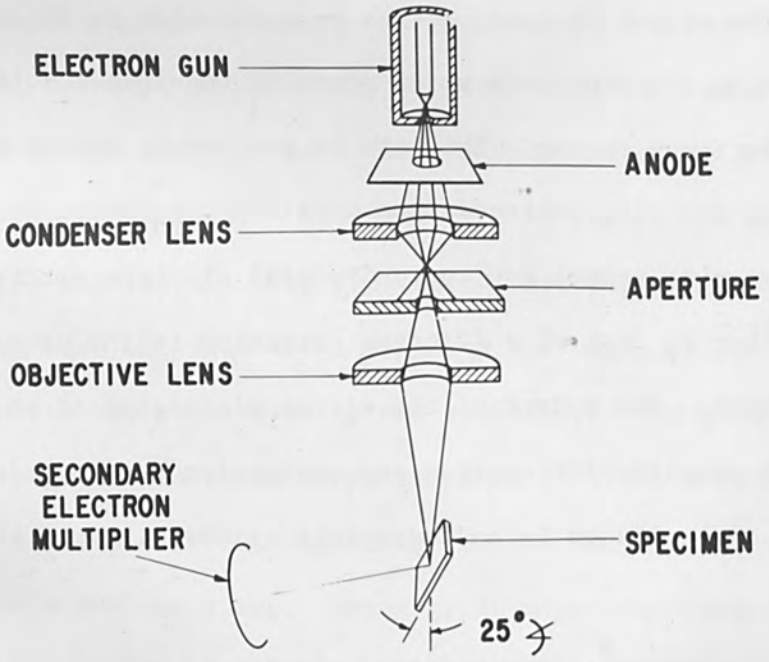

Figure 6 - Schematic diagram of scanning electron microscope. This microscope images a solid surface with adequate resolution. The 25^{o} angle is an impediment for its use in memory systems.

direction. Considerable improvement is needed in the resolution of the scanning microscope when the specimen is normal to the beam. This problem is difficult but not considered to be serious. The ideal solution would be development of a combination scanning-mirror microscope. The difficulty in producing a combination microscope is that the spot size becomes too large as the electrons are slowed down and reversed in direction. The spot size can only be improved by starting with a smaller, brighter electron source. If current attempts to employ the field emission source are successful, this combination system will be possible.

Even if the problem of normal incidence readout of a solid surface is thus solved, a more serious problem of electron scattering is encountered in recording on a solid surface. No matter how fine an electron spot is used for recording, the effect of the electrons will be spread over a diameter equal to the electrons penetration length in the material (Fig. 7). At 5 kilovolts this penetration is of the order of 0.3 micron or ten times the spot size we wish to record. This problem has been avoided by Möllenstedt, Shoulders, and others who have demonstrated 10^{10} bits/cm^2 resolution by recording on very thin materials, with high voltage electrons. The high voltage electrons are not scattered in passing through the thin film. This solution is not compatible with our goal of recording on a solid surface and also suffers from the difficulty that it employs a very small fraction of the electron's energy.

There are a number of possible ways of getting around the scattering problem which are all compromises between resolution and full

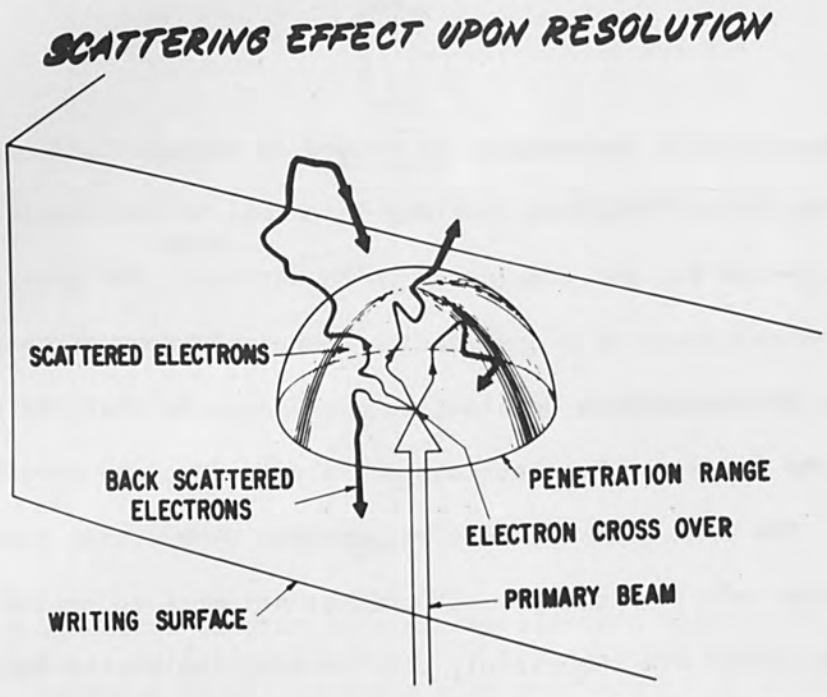

Figure 7 - Electron scattering is one of the more difficult problems in a storage system based on a substantial thickness of recording surface. Several means are available for avoiding this problem, hopefully some of them will be compatible with desirable memory systems.

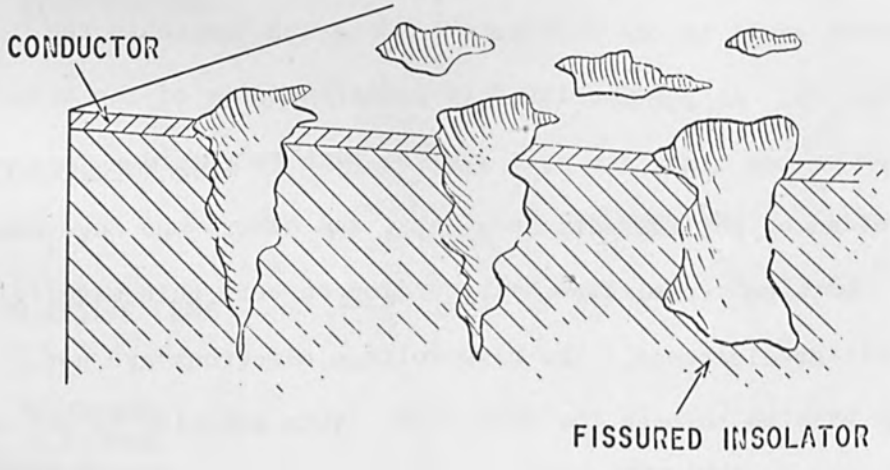

Figure 8 - One possible surface structure for recording material which minimized the effect of electron scattering. Several industrial materials have this structure; the conducting layer is added to the surface of the base material.

utilization of the available beam energy density. It is not possible to discuss these solutions in the time available so we must be content to list a few of the more attractive possibilities as follows:

1. Reduce the landing energy but keep the spot size small by use of the small bright field emission source (further complicated by space charge repulsion).
2. Use an ion beam for recording since the penetration will be reduced at least four fold, for the same landing voltage, by this substitution. (Space charge repulsion and beam generation are both more difficult for ion beams than for electron beams).
3. Use a recording medium with a high voltage threshold so that it can only be triggered by incoming electrons - not by electrons scattered back through the surface or by secondary effects from electrons captured below the surface. (This severely restricts the choice of recording materials and requires compromises in the choice of other system properties).
4. Use a material with surface traps[2] which becomes charged by secondary emission at the point of entry of the electron beam (Fig. 8). (This system lacks storage permanency for the materials, known to form traps of the proper 50 Au size range, lose charge in a few minutes. Other materials which hold charge for years may possibly be prepared with traps of the correct size and distribution.)

In addition to these fundamental recording material difficulties, we desire that the material can be; updated section at a time, or at

least recorded section at a time, permanent until intentionally erased, very sensitive for recording by electrons, but not changed by readout, and easily reproduced by mass copying.

The Recording Speed Problem

The greater the recording speed the more useful the memory device becomes. It is desirable that it either be able to record in parallel from a buffer store or record spot by spot at the incoming data rate. Let us consider the extreme case of nanosecond input rates since logic circuit elements are rapidly approaching these operation times.[3] For the purpose of discussion, let us further assume that adequate signal-to-noise can be obtained by use of ten electrons per spot. This then requires 10^{10} electrons per second or 6×10^{-8} amps beam current, which is possible to obtain in the 500 Au spot sizes required. However, if each electron converts only one molecule, of the 10^{4} molecules present on the surface of a 500 Au spot, it will not be visible with the resolution limit imposed by the equipment. What must be accomplished, is nearly total conversion of the molecules in the 500 Au spot by the ten incoming electrons either by multiple interaction of the incoming electrons - by chain reactions in the recording materials, by development, or by a combination of these effects. Furthermore, it must not be possible for a single electron to cause conversion of the entire area. These considerations are fundamental to a recording system which produces a chemical or structural change in the recording medium. These basic principles have been thoroughly explored through the development of silver-halide photography.

Systems such as xerography, which add material in proportion to charge density, or thermoplastic recording*, which causes deformation in accord with the charge present, depend only on the number of charges deposited per spot and, in general, requires the same surface charge density regardless of spot size. The recording speed is therefore not dependent upon the spot size chosen. Both of these recording systems require entirely different approaches to their normal form in order to be applied at electron microscope levels of resolution. Because they cannot depend upon chain reactions or development, they must have higher current densities (than photography) of the order of 10^{-5} amperes at least for nanosecond recording at 10^{10} bits/cm^{-2}. This would require development of brighter electron source than the currently used thermionic sources.

Slower recording rates pose a different kind of problem. Suppose we must use a recording system such as direct conversion (without chemical development) of silver halide which requires about ten millisecond exposure per spot. To record a 10^{10} bit memory would require 30,000 hours or roughly 3-1/2 years - day and night - holidays and Sundays. One hundred square centimeters (capacity of the human mind at 10^{10} bits/sq. cm.) would therefore require 3-1/2 centuries to record. The need for fast response of parallel input becomes quite obvious.

It is interesting to recall that the maximum usable input rate from the outside world to the human mind is considered to be about

*Trademark of General Electric Company

the same rate, namely, 50 to 100 bits per second. This rate limitation of the human decision maker, which would require 3-1/2 centuries for him to survey the complete memory, clearly points out the need for machine processing of data if he is to have time to make use of all the pertinent data.

The Data Capacity Per Field of View Problem

The best electron optical performance to date has been about 10^9 image points per field of view or roughly 10^7 bits per field of view. If we are to make use of the memory capacity available in a reasonable memory plane area, (e.g., 10^{14} bits), then we must have 10^7 separate fields of view or a matrix of fields of view 3,200 x 3,200 fields wide with mechanical motions up to 30 cm. This would slow down access to all parts of the memory to fractions of a second. One of the ways we are attempting to surmount this problem is by use of a matrix of lenses, like the compound eye of the fly, all energized by a common electron source (Fig. 9). This solution keeps the number of signal wires down to a small number and substitutes electron deflection for mechanical motion. However, it severely increases the instrument construction problems; places severe restriction on maintaining registration between the memory plate and the lens plate; and slows down the response in a given field of view because of the large increase in interelectrode capacity.

The Problem of Location of Data

The problem of data location in a microspace system usually evokes the greatest concern from the casual observer yet it is one of our least difficult problems. We find data by the same method that a

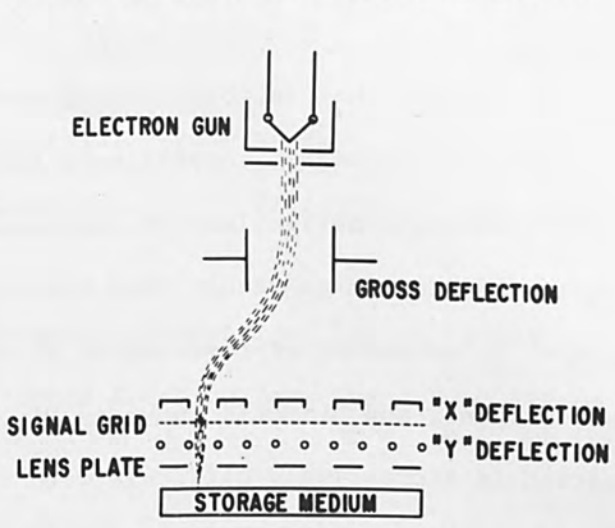

Figure 9 - Possible storage system which entirely eliminates need for mechanical motions in the memory system by switching beam to individual recording lenses of a compound objective lens similar to the eye of the fly.

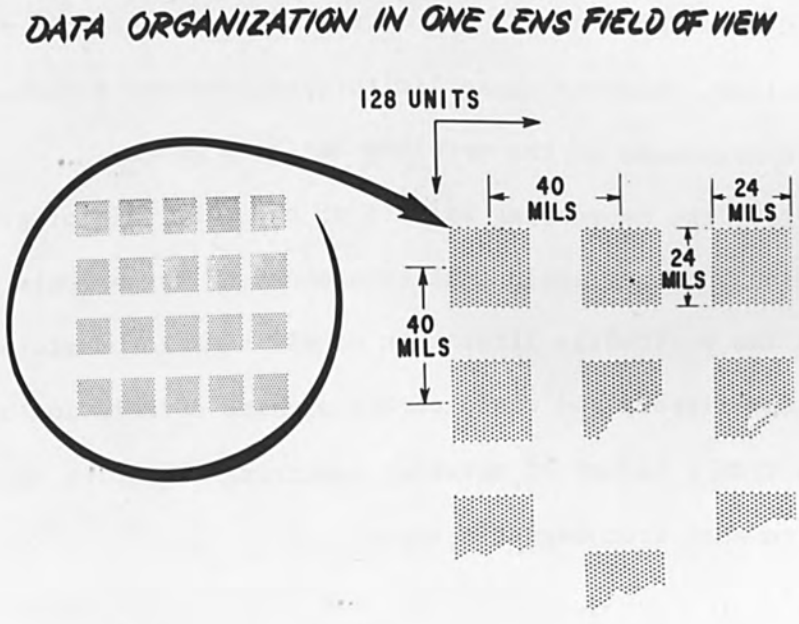

Figure 10 - Schematic representation of data organization into rows, columns, and blocks as an aide to data location. By working through an optical magnification linkage and by successive quantization (or optical indexing), one percent accuracy is adequate for location of one part in 10^{12}.

street address is located, that is, by counting rows and columns of data from a recognizable landmark. Approximate location can be made of the landmark by analogue deflections or displacements. It is better to work with the magnified image rather than the actual storage medium wherever possible. A schematic representation of the separation of data into rows, columns, and blocks is shown in Fig. 10.

Data location is increasingly difficult with increasing storage capacity regardless of which storage system is employed. From our experience it appears to be considerably less difficult with microspace systems.

In this brief review of the problems facing exploitation of microspace potentialities, we have only been able to explore the chief problems in a cursory fashion and have failed to mention a host of lesser problems. Despite these limitations, perhaps a better appreciation of the magnitude of the problems has been given.

To offset the depressing effects of the multitude of problems, may we remind you once again that attainment of these goals would permit all the worthwhile literature of all time to be stored in a small village library and would permit machine correlation of data in minutes from a volume of material requiring centuries to read or even days to scan from magnetic tape.

BIBLIOGRAPHY

(1) Sharp, H. S., Industrial Research, April 1961, p. 33.

(2) Jurgen, R. K., Electronics, 31, 72 (1958), "Technical Highlights of '58 Wescon".

(3) Staff Report, Electronic Industries, 21, 14 (1962).

(4) Mollenstedt, G., Third Electron Beam Symposium, Alloyd Corp. Boston, 1961, p. 340.

(5) Shoulders, K. R., Office of Tech. Services, Dept. of Commerce, PB 171027, (Sept. 1960).

(6) Mayer, L., J. Appl. Phys., 26, 1228 (1955).

(7) Klemperer, O., Electron Optics, Second Edition, Cambridge U. Press, London, 1953, p. 345.

(8) Smith, K.C.A. and Oatley, C. W., Brit. J. Appl. Phys., 6, p. 391 (1955).

MEASUREMENT OF SURFACE TENSION OF MOLTEN METALS BY ELECTRON BOMBARDMENT HEATING

By

Susumu Namba
Senior Physicist

Takehiro Isobe
Physicist
The Institute of Physical and Chemical Research
Tokyo, Japan

ABSTRACT

An electron beam system for measurement of surface tension of metals is described. Results obtained with this system using the drop weight method for Tantalum, Molybdenum, Zirconium and Titanium are presented.

MEASUREMENT OF SURFACE TENSION OF MOLTEN METALS BY ELECTRON BOMBARDMENT HEATING

I. Introduction.

Though the surface tension of molten metals is of interest from technological and theoretical points of view, it has been measured only for about a half of all the metallic elements excluding those of the rare-earth group, and for many of the remaining metals, scarcity of materials, chemical reactivity and refractoriness have given rise to difficulty of measurement.

Values of the surface tension on twenty-seven metals have been estimated by Taylor[1] with a probable error of ± 10% in some cases. The values for titanium and tungsten have been measured to be 1510 dyne cm^{-1}[2] and 2300 dyne cm^{-1}[3] respectively.

The drop-weight method, which measures the weight of molten metal drops that fall from the bottom end of a vertically supported metal rod, is most accurate of all the methods of measuring the surface tension, but refractory materials are difficult to be made into controllable molten drops.

Electron bombardment heating method is suited for making molten drops in easily controllable manner; it has first been used by Calverley[3] for measuring the surface tension of

molten tungsten. In the present work, this method was used to measure the surface tension of various refractory metals in molten state.

II. Method of experiment.

The apparatus used for the experiment is shown schematically in fig. 1. A vertically supported metal rod, which is the anode, is connected to a positive high tension supply of $2 \sim 5$ kV. Cathode system consisting of a circular tungsten filament and a set of tantalum focusing plates is at earth potential. The metal rod is bombarded from below by electrons from the heated tungsten filament accelerated by the created field, the beam of electrons being directed by the tantalum focusing plates. The accelerating voltage is raised to increase the power of the electron beam until the tip of the rod becomes molten and hangs down in a form of a drop which grows in size and eventually falls down into a molybdenum cup of known weight when the weight of the drop overcomes the surface tension of the molten metal. The required beam power, which depends on the material of the rod and the configuration of the whole system, is estimated at $15 \sim 100$ Watt for a rod of $1 \sim 4$ mm in diameter. The mass of the fallen drop is obtained by weighing. The whole arrangement is enclosed in an evacuated chamber shown by dotted lines of the figure, the evacuation during the experiment being $2 \times 10^{-5} \sim 1 \times 10^{-4}$ mmHg pressure which is read on an ion guage.

Forming of the drop shortens the rod. This necessitates the raising of the cathode system. A titanium rod of 1 mm diameter, for example, was shortened by as much as 10 cm beyond the adjustable range of the system. In such cases, end of the rod was made in advance in a form of a drop of appropriate size.

With some metals, considerable outgassing occurred causing a shower of sparks. For this reason, the loss in mass of the rod cannot be used for determining the mass of the drop. To avoid such sparks falling into the molybdenum cup to upset the weighing, the cup was shielded with a nickel sheet until the drop became large enough to fall.

The apparatus is shown in fig. 2. The whole electrode system is hung from a steel top plate enabling the initial adjustments to be made before setting into the vacuum apparatus. The cathode system and the shield for the cup are manipulated from outside by rotary shafts with O-ring vacuum seal through the top plate. In the photograph, a molten drop of titanium is seen about to fall.

III. Calculation of surface tension.

Fig. 3 is a photograph of a molten drop hanging from the lower end of a titanium rod. The shape of the molten drop is not the same for all materials; it is a function of surface

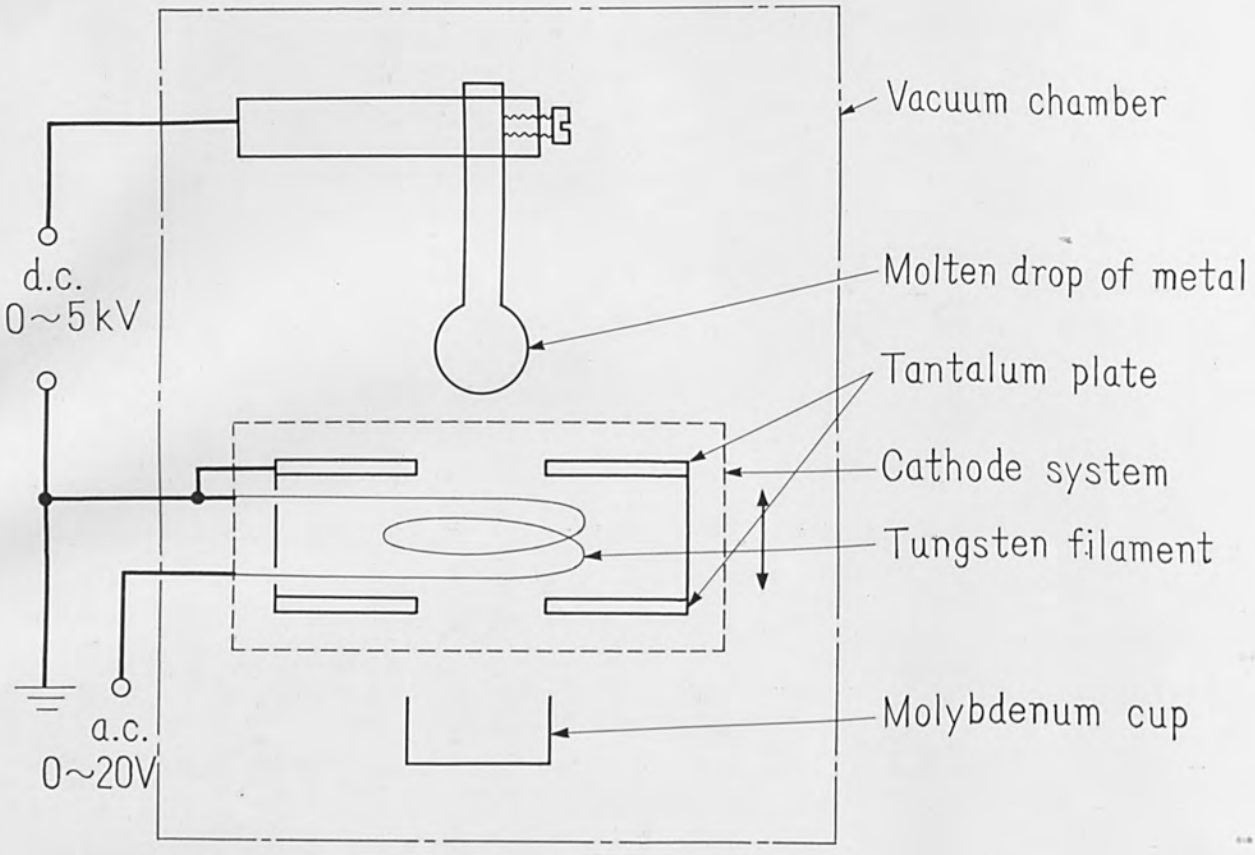

FIGURE 1. Schematic diagram of the apparatus.

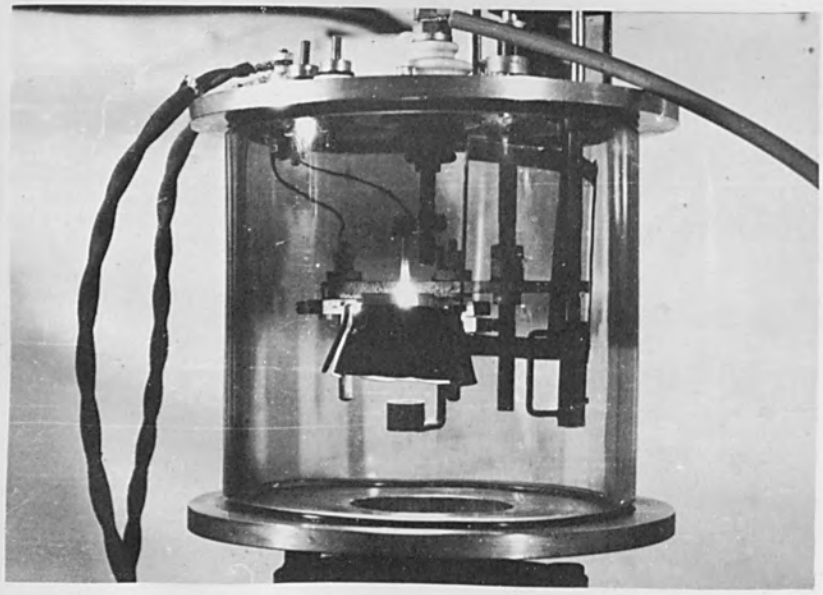

FIGURE 2. Photograph of apparatus under operating condition.

FIGURE 3. Molten drop of titanium.

tension and density of the material. Though there is a method by which the surface tension is obtained from the shape of drops,[4] its accuracy was thought not enough for our experiment, and the drop-weight method discussed by Harkins was adopted.

By the theory of Harkins,[5] surface tension is given by

$$\gamma = F\ m\ g/r$$

where F is a function of V/r^3 (or $m/\rho\ r^3$), γ is the surface tension of the molten metal in dyne cm^{-1}, m the mass of the drop in grammes, g the acceleration due to gravity in cm sec^{-2}, r the radius of the rod in cm, V the volume of the drop in cm^3 and ρ the density of the molten metal in g cm^{-3}. F is a correction factor to obtain the true mass of the molten drop from the mass of metal that falls down and is a function of V/r^3 by Harkins and Brown; its values are given in International Critical Table Vol. IV and are plotted in fig. 4.

IV. Results.

Table 1 shows the result obtained on titanium measured by the drop-weight method. The values found on titanium rods of various diameters do vary, yet no direct effect of the rod size is apparent. The mean value 1460 dyne cm^{-1} can therefore be taken as the value of surface tension of molten titanium.

Results on various metals are summarized in Table 2. The fourth column shows the number of successful measurements.

Refractory metals, such as Ta, Mo, Zr, contain tolerable amounts of gases losing the weight of the molten drop in the form of a shower of sparks. For this reason, measurement of surface tension on these metals was difficult.

V. Discussions.

There are many sources of error as mentioned below in determining the surface tension.

(1) The density and the expansion coefficient of metals are not measured at their melting temperature, and estimation of ρ and r cannot be exact. Since the variation of V/r^3 does not affect very much the value of F, if volume change between solid and liquid states is not very large, the effect of error on F will be small. For example, the variation of F is only about 1% when the variation of V/r^3 is 10%. Therefore, the values found at room temperature were used for the estimation of F.

The value of r in denominator of Harkins' equation was estimated on the assumption of linear expansion between the room temperature and the melting temperature, which is, however, more or less questionable. The correction factors based on linear expansion used for obtaining the values of γ are given in Table 2 for reference.

(2) Premature falling of the drop leads to low values of γ. Therefore the rotary vacuum pump was stopped to avoid

the vibration before the drop became large enough to fall. But there was some vibration induced by the outgassing from molten drop or originated from the room floor. The amount of error caused by vibration could not be estimated.

(3) The drop-weight method is only valid when the solid-liquid interface is perfectly flat and horizontal. With our apparatus, the verticallity of the metal rod could not be assured and the bombardment of the rod by electron beam was not truely axially symmetrical. These lead to the possibility that the obtained values of γ are too large.

(4) Electro-static force between the drop and the cathode is estimated to be smaller than 1 dyne and can be neglected.

(5) Temperature of the molten metals was measured by a pyrometer from outside of the vacuum chamber. Measured temperatures were very close to known melting points. On the surface of the molten drops, continuous revolving motion by convection was observed. The value of the surface tension decreases as the temperature rises; its temperature coefficient was estimated at about $-0.03 \sim -0.1$ dyne $cm^{-1}/°C$. Therefore, it is reasonable to regard γ in Table 2 as the value measured at the melting temperature.

Though the amount of overall error of the measurement cannot be ascertained, it would not be beyond $\pm 5\%$.

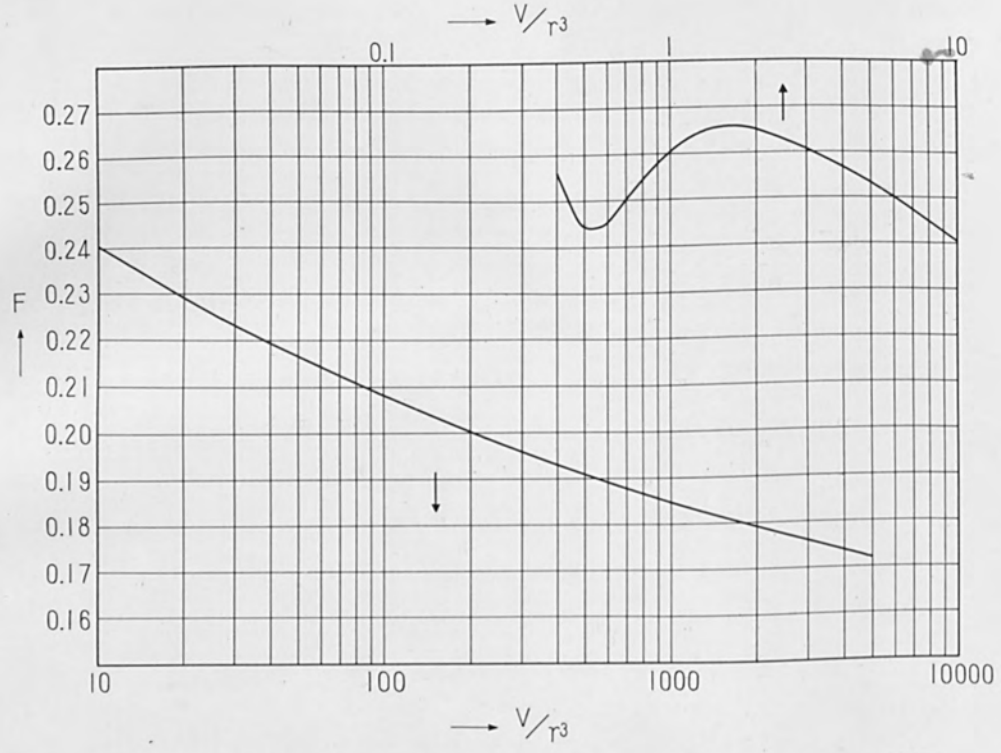

FIGURE 4. Graph of F for drop-weight correction (Harkins and Brown[5])

TABLE 1.

SURFACE TENSION OF TITANIUM

Rod Diameter (at Room Temperature)	m	γ	mean γ
mm	gram	dyne cm^{-1}	dyne cm^{-1}
4.0	1.414	1500	1515
"	1.443	1530	
3.0	1.031	1420	1453
"	1.065	1460	
"	1.081	1480	
2.0	0.747	1460	1467
"	0.745	1460	
"	0.757	1480	
1.0	0.378	1420	1425
"	0.387	1430	

TABLE 2.

SURFACE TENSION OF METALS

Metal	Melting Temperature (°C)	Surface Tension (dyne cm^{-1})	Number of Successful Measurements	Correction Factor for γ $\frac{\gamma_m - \gamma_0}{\gamma_0} \times 10^2$ *
Ta	2996	1910	5	1.92
Mo	2622	2080	3	1.3
Zr	2127	1390	5	1.0
Ti	1727	1460	10	1.55
Fe	1535	1510	2	1.85
Ni	1455	1670	4	1.85

* γ_m : rod diameter of melting temperature.
γ_0 : rod diameter of room temperature.

References

(1) Taylor, J.W., Metallurgia, Manchr., 50, 161 (1954).

(2) Yelyutin, V.W., and Maurakh, M., Investiya Akad. Nauk., SSSR, Otdelenic Technicheskikh Nauk, 4, 129 (1956).

(3) Calverley, A., Proc. Phys. Soc., 70, 11-B (1958).

(4) Andreas, J.M., Hauser, E.A., and Tucker, W.B., J. Phys. Chem., 42, 1001 (1938).

(5) Harkins, W.D. and Brown, F.E., Amer. Chem. Soc., 41, 499 (1919).

A Note on the Physical Principles Underlying the Formation of the Cavity in Electron Beam Welding

by

Oliver C. Wells

Westinghouse Research Laboratories

Pittsburgh 35, Pennsylvania

and

Professor Thomas E. Everhart

Department of Electrical Engineering

University of California, Berkeley, California

Abstract

Calculations are given of the momentum transported by the vapor from the weld zone in electron beam welding, and the conclusion is reached that the formation of the weld cavity may be explained by this means.

A Note on the Physical Principles Underlying the Formation of the Cavity in Electron Beam Welding

I. INTRODUCTION

In this note some calculations will be presented which are an elaboration of those made prior to the publication by Wells[1,2] of a suggested mechanism for the formation of the cavity in electron beam welding. The basis of this method (as described in reference 1) is to equate the momentum that leaves the cavity per second in the evaporating vapor molecules to the volume of the cavity multiplied by the density of the molten metal in a manner that is analogous to Archimedes' Law. (The justification for this procedure is discussed below.) Although the consideration is a very elementary one, so far as it has been possible to discover there is no mention of the part played in the electron beam welding process by the momentum of the evaporating vapor molecules in any account of weld cavity formation published prior to reference 2 (references 3, 4, 5, 6, 7, 8, 9).

In a paper published by Schwarz[10] an explanation of weld cavity formation was given but in which the classical electron penetration had been assigned a role that is more significant than the role assigned to it here. Seeler[11] has also discussed the characteristics of the cavity, but without reference to the physical principles involved. The significance of electron reflections from the sides of the cavity and the gas refocussing effect have been pointed out by Meier.[8] In the present note no discussion is given of the alternately widening and contracting weld cross-sections that are sometimes observed (and which were discussed by Schwarz).

II. THE FORMATION OF A CAVITY

To explain the deep welds that are obtained with electron beam welding it is generally agreed that a cavity is formed under the beam. Thus for example, the classical depth of penetration of electrons into a piece of stainless steel is of the order of 40 microns only, and yet welds over one-half inch (12,500 microns) can be accomplished using 100 kV electrons. In the present note the factors affecting the formation of this cavity are discussed.

To form an estimate of the volume of the cavity from published cross-sections of welds is not always easy inasmuch as it is not obvious how much of the weld cross-section was occupied by the cavity. For the purpose of making an estimate (probably a conservative estimate) it will be assumed that the cavity is of inverted conical shape, having the base diameter equal to approximately two thirds of the weld width, and having the apex located at the center of curvature at the bottom of the cavity. The volumes of the cavities, and the downwards forces that these represent, are shown for a number of welds described in the literature in Table I. (In Table I an artificially small value of weld width is quoted in some cases to avoid the possibility of overestimating the cavity size.)

In Table I the expression "displacement force" F_D dynes is used to denote the estimated volume of the cavity in cm^3 multiplied by the density of the liquid metal in $gm.cm^{-3}$ multiplied by 981 $cm.sec.^{-2}$. The definitions of F_E and F_T are given below.

III. THE FORCES ACTING ON THE CAVITY

The situation in the weld cavity is shown in a simplified form in Fig. 1, taken without modification from reference 1. In an actual case this cavity will be in motion across the workpiece, either in a uniform or else in a nonuniform manner, and therefore at the very least it would in all probability be distributed in an asymmetrical manner about the vertical axis. It is also quite possible that the shape of the cavity would change (either periodically or nonperiodically) with time (as suggested by the apparently nonperiodic irregularities that are sometimes observed in the profiles of electron beam weld beads) but for the purpose of an initial discussion it will be assumed that the cavity is stationary and symmetrical about the axis.

If it is assumed that the cavity is lined entirely with a liquid that is in equilibrium, then by a derivation that is similar to that generally given for Archimedes' Law it can be shown that there must be a downwards force or forces acting on the surface of the liquid, such that the total downwards force is equal to the volume of the cavity multiplied by the density of the liquid. (A discussion on whether it is necessary to postulate the existence of a liquid lining and whether it must be considered to be in equilibrium with the vapor in the cavity is given below.) In the present case there are four possible forces to be considered, namely (1) due to the momentum possessed by the impinging electrons F_E dynes (2) due to the momentum possessed by the evaporating molecules F_M dynes (3) due to the momentum possessed by the droplets of metal that are seen in a practical case to be ejected from the cavity, and (4) due to surface tension.

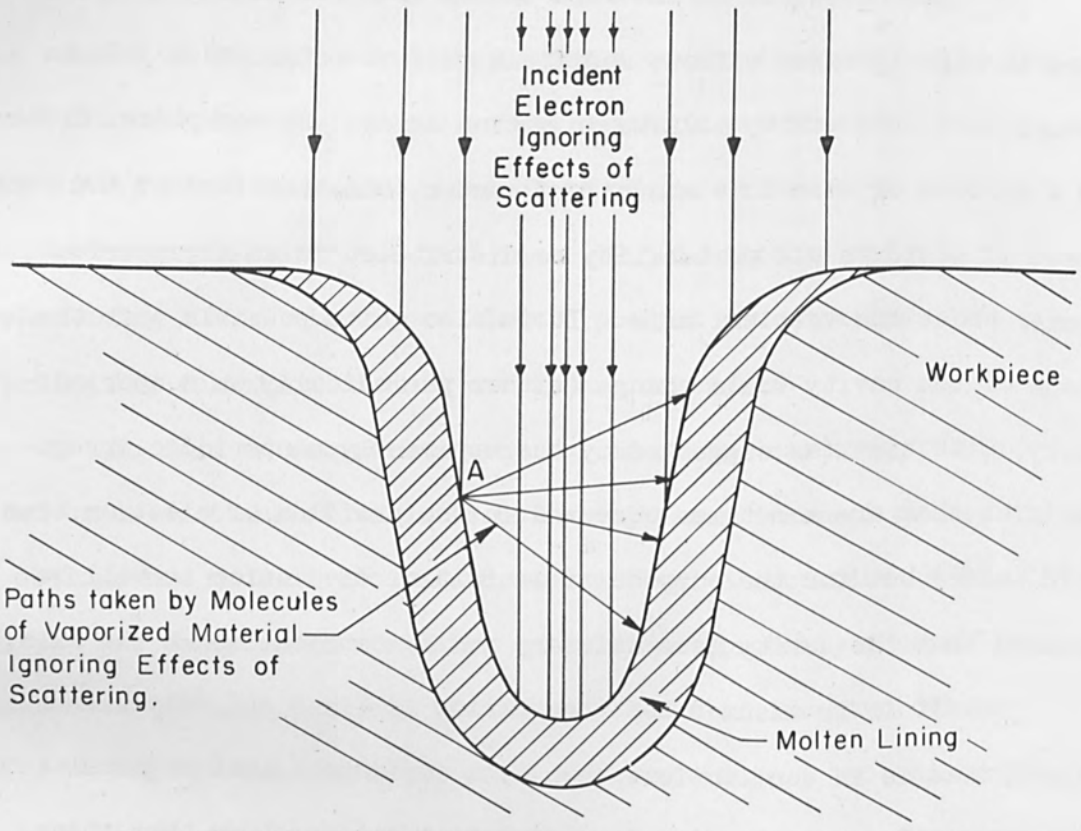

Rocket action theory to explain the formation of a crater under the beam in electron beam welding apparatus.

FIGURE 1.

In a practical case the liquid lining will not be stationary, but will be in motion. At the very least it is to be expected that the effect of the electron pressure, which acts only on a thin surface layer of the liquid, will be to cause a stirring of the liquid, but it is not easy to see how motion of the liquid or of the cavity (from this or any other cause) can affect the necessity for a downwards force as stated above.

At an incident energy of 100 KeV the classical penetration of electrons into a material of density 10 gm. cm^{-3} will be of the order of 30 microns, which is two orders of magnitude smaller than the depths of the weld cavities that are observed. From an analysis published by Steigerwald[12] it is clear that for the conditions existing in electron beam welding thermal conduction will predominate over the classical electron penetration for the distribution of heat. Thus in the case of an incident electron energy of 500 keV or above, the classical penetration depth will be of the order of 250 microns or greater, which might therefore be large compared both with the beam diameter and with the distance through which heat conduction will occur to melt a "pear shaped" zone as discussed by Schwarz[10]. With electron energies of the order of 100 keV and beam diameters of the order of 200 microns and with the levels of intensity commonly used with electron beam welding the melted zone will be tens of microns in depth and hundreds of microns in sideways extent. It is not correct to say that the existence of the classical penetration was ignored by Wells in reference 2.

(a) Electron Pressure

The effect of electron pressure has been discussed by Platte[5], Bas and Cremosnik[6], Hablanian[7] and others, and is well known. Thus the downward pressure p gm. cm.$^{-2}$ due to an electron stream of energy V volts and current density J amp.cm^{-2} is

$$p = J\sqrt{V(2m/e) \times 10^7} \quad \text{gm.cm.}^{-2} \qquad (1)$$

where m = mass of electron = 9.1×10^{-28} gm

e = charge of electron = 1.6×10^{-19} coulomb

and the force F_E is

$$F_E = I\sqrt{V\,(2m/e) \times 10^7} \quad \text{dynes}$$

$$= 0.34\ I\sqrt{V} \quad \text{dynes} \qquad (2)$$

where V is in volts and I is the electron current in amps. (In the above non-relativistic formulae the electron's momentum is in error by less than 3 per cent at 100 kV, and by less than 18 per cent at 500 kV.)

The magnitudes of the electron forces for five welds taken from the literature are shown in Table I. In each case the electron force is smaller than the displacement force, i.e., the force required to hold the cavity open against hydrostatic pressure as calculated from Archimedes' Law. From this result it is concluded that the electron pressure, although possibly significant as far as the motion of the

liquid in the cavity is concerned, is in all probability minor from the point of view of cavity formation. (The balance of force, $F_D - F_E$ dynes, to be provided by the vapor momentum in the absence of surface tension effects is given in Table I.)

(b) Force Due to Evaporated Atoms of Metal

We consider only single atoms which are evaporated. The reaction force F_M dynes due to escaping atoms is $F_M = v\,(dM/dt)$ where v cm.sec^{-1} is the mean escaping velocity of the atoms, and dM/dt gm.sec^{-1} is the mass lost in unit time. If the average number of atoms per second which escape is n_o, and the number which escape with velocities between v and v + dv cm.sec^{-1} is n(v), then if M_o gm. is the mass of one atom the following relations hold.

$$\bar{v}n_o = \int_o^\infty n(v)\ dv \qquad (3)$$

$$F_M = M_o \int_o^\infty v\ n(v)\ dv \text{ dynes} \qquad (4)$$

As a rough approximation, we set v equal

$$\bar{v} = \sqrt{2kT/M_o} \quad \text{cm.sec}^{-1}$$

where k = Boltzmann's constant = 1.380×10^{-23} joule. deg^{-1}

and T = absolute temperature of gas. Then

$$F = M_o\, n_o \sqrt{(2kT/M_o)}$$

or, solving for n_o

$$n_o = F_M / \sqrt{2\ kT\ M_o} \quad \text{atoms sec.}^{-1} \qquad (5)$$

For iron (or stainless steel); $M_o = 5.1 \times 10^{-26}$ gm., and for T near the melting point of 1540°C = 1813°K and assuming as a typical value that $F_M = 40$ dynes we have

$$n_o \approx 3 \times 10^{20} \quad \text{atoms sec.}^{-1}$$

$$\approx 1.5 \times 10^{-5} \quad \text{gm. sec.}^{-1}$$

from which, on the basis of a weld in which the metal is melted and resolidified at the rate of 1 gm. sec^{-1}, the ratio of the volume of metal evaporated to the volume welded each second (or per inch of weld) $\approx 10^{-5}$.

In the above calculations it was assumed that the velocity with which the gas molecules escape from the cavity is equal to the thermal velocities with which they are emitted from the interface between the liquid and the gaseous zones. In fact the mean free path of the gas molecules at the lowest part of the cavity, will be small compared with the dimensions of the cavity, and therefore it is important to consider what the behavior of the gas in the cavity would be taking these collisions into account. Such a calculation can be made on the basis of the conservation of energy and momentum in the gas molecules leaving the cavity (and on the assumption that the gas emitted from the cavity expands to zero temperature and zero density at infinity). Thus in the cavity the gas molecules (on the average) will have energy $(1/2)\, M_o\, \bar{v}^2 + (1/2) M_o\, v^2$ where $\bar{v}$ cm.sec^{-1} is the mean square thermal velocity and v cm.sec^{-1} is the velocity of the gas (considered as an ideal gas) sweeping up the cavity. (For

Archimedes' Law it is the second of these velocities that is significant.) At infinity the thermal energy will be zero, and the gas will therefore possess a radial translational velocity V cm. sec^{-1} given by $V^2 = \bar{v}^2 + v^2$. The net upwards momentum per molecule will be (on the average) $(2/3) M_o V$, where the (2/3) term arises from the radial motion of the gas.

In the above calculation it was assumed that the molecules of the evaporating material do not strike the surface of the weld specimen subsequent to being ejected from the cavity. If this assumption can be taken as correct then it is concluded that it is a not unreasonable procedure to calculate the momentum leaving the cavity per second in terms of the thermal velocities of the gas (although in fact it will be the translational velocity of the gas at the mouth of the cavity that will be the important factor).

As a method for estimating the temperature of the liquid lining necessary to produce such a flux of momentum in the evaporating material, it could be argued that since a part of the vapor in the cavity is escaping into the vacuum then it can be expected that the gas pressure in the cavity will lie somewhere between 0.5 and 1.0 of the vapor pressure of the liquid at that temperature. For iron, to obtain a vapor pressure of 100 mm. Hg a rise in temperature of less than 100 degrees above the melting point is required (reference 13, p. 750) from which it can be concluded that these pressures are of the correct order of magnitude to explain the effects that are observed even without the necessity for assuming extremely high temperatures in the weld cavity.

(c) Force Due to Momentum of Metal Droplets

From observation of the welding process it can be seen that there is a continuous stream of metal droplets thrown out from the weld cavity to a height of several inches above the weld. Typically 20 such droplets of diameters 0.05 cm. or less might be thrown to a height of 10 cm. per inch of weld length. On the basis of 10" per minute weld speed a material density of 10 gm. cm^{-3} this works out at a force of the order of 2.8 dynes (see Appendix 1). It is therefore a possibility that the momentum possessed by these droplets is a significant factor in the formation of the weld cavity.

From an examination of Table I it can be seen that a force of this magnitude might be sufficient to contribute to the formation of the cavity (if surface tension can be excluded) in the last two cases. However, the part that is played by this momentum will be a consequence of the manner in which the momentum of the droplets is derived. Thus if the droplets are ejected from the liquid lining as a result of air pockets originally trapped in the material, then it would appear to be legitimate to regard the momentum that is carried by them as being of significance from the point of view of cavity formation, but if (as has been pointed out by R. L. Longini, private communication) the momentum of these droplets is a consequence solely of the motion of the vapor past them, then the momentum of the droplets should be disregarded in the calculation. It is for this reason that no allowance is made for the momentum of the droplets in Table I.

(d) Surface Tension Force

Following the procedure used by Platte[5] an estimate (probably an upper estimate) of the total vertical component of surface tension force F_T can be made by multiplying the circumference of the cavity by 1000 dynes cm^{-1}. In Table I an estimate of F_T is given made in this way, from which it can be concluded that if indeed surface tension forces are present of this magnitude then they can be expected to be comparable or even greater in magnitude than F_D, so requiring an increased transport of momentum in the vapor leaving the cavity.

IV. THE STABILITY OF THE LIQUID LINING

In the above discussion it was assumed that the thickness of the liquid lining was sufficiently great so that the liquid could flow to take up hydrostatic equilibrium with the gas in the cavity. Under any "steady-state" theory it would appear to be essential to postulate that this is so. For it is an observed fact that the volume of metal lost from the weld is only a small fraction of the metal that has been melted and resolidified, and therefore the liquid must be allowed to collect at the trailing edge of the cavity before being resolidified. For this liquid to accumulate the gas pressure at the trailing edge of the cavity must certainly be no greater than the hydrostatic pressure of the liquid at a given depth, and it would appear to be a necessary conclusion that the gas pressure and the liquid pressure are equal (or very nearly equal) leading to Archimedes' Law.

As an alternative it could be argued there is no need to postulate the existence of a liquid lining, at least at the lower parts of the cavity, the transfer of material from the leading to the trailing sides of the cavity being in gaseous rather than in liquid form. On the basis of the amount of heat available (in comparison with the latent heat of vaporization of materials commonly welded) such a situation would not appear to be impossible, and, as pointed out by R. L. Longini (private communication), a similarity might be thought to exist between the condition that would exist at the bottom of the cavity in such a case (where material liquified by the electron bombardment would be swept away instantaneously by the current of gas) and on the surface of a meteorite entering the earth's atmosphere, in which material liquified by air friction is swept away instantaneously by the air flow. In this case the need for gas pressure at the bottom of the cavity would be greater than would be the case if a liquid lining were to exist, from which it follows that the value of momentum per second leaving the cavity as given by Archimedes' Law will represent a <u>lower limit</u> to what is required.

As a further alternative it might be supposed that the cavity, instead of being stable with time, oscillates in either shape or depth. But even in this case it is not easy to see how the requirement for momentum to be projected from the cavity could be avoided.

V. CONCLUSION

In conclusion it is considered that the momentum conveyed from the cavity in the evaporating material is of greater importance than

electron pressure in explaining the formation of the cavity in electron beam welding.

VI. ACKNOWLEDGEMENTS

Acknowledgement is due to Dr. R. L. Longini, Mr. R. E. Davis, Mr. R. Byrne and Dr. H. F. John for detailed discussion and to Dr. R. Bakish for permitting us to submit this paper to the symposium at such a late date.

REFERENCES

1. Wells, O. C., Internal company memorandum dated 21 Oct. 1959.
2. Wells, O. C., "Electron Beams in Micro-Electronics," Proc. Third Symposium on Electron Beam Technology (Alloyd Corporation), p. 291 (1961).
3. Burton, G., and Matchett, R., "Electrons Shot from Guns Make High Purity Welds," American Machinist 103, (No. 4) 95, (1959).
4. Burton, G., and Frankhouser, W. L., "Electron Beam Welding," Welding J., 38, 401S (1959).
5. Platte, W. N., "Electron Bombardment Welding Gun," Westinghouse Research Report, 401-FF-309-R1 (Internally Published Report) 14 Nov. 1958.
6. Bas, E. B. and Cremosnik, G., "High-Vacuum Electron-Beam Welding" (in German), Vakuum-Technik, 7, 181 (1959).
7. Hablanian, M. H., "Some Aspects of Electron Gun Design for Welding," Proc. Third Symposium on Electron Beam Technology (Alloyd Corporation), p. 42 (1961).
8. Meier, J. W., "Electron Beam Welding Characteristics of Several Materials," Proc. Third Symposium on Electron Beam Technology (Alloyd Corporation), p. 145 (1961).
9. Hoffman, H. H., "Electron Beam Welding at High Voltage," Proc. Third Symposium on Electron Beam Technology (Alloyd Corporation), p.117 (1961).
10. Schwarz, H., "Electron Beam Processes at Different Voltages," Proc. Second International Vacuum Congress, Washington, D.C. (1961).

11. Seeler, H., "Investigations into the Penetration Behaviour of the Electron Beam during Electron Beam Welding," (in German), Schweiben u. Schneiden, 13 (No. 12) 581 (1961).

12. Steigerwald, K. H., "Electron Beam Milling," Proc. Third Symposium on Electron Beam Technology (Alloyd Corporation), p.269 (1961).

13. Dushman, S., Scientific Foundations of Vacuum Technique, New York (1949).

TABLE I

Electron beam weld / Weld Parameters	Ref. 7 Fig. 3 (p. 52)	Ref. 7 Fig. 4 (p. 52)	Ref. 7 Fig. 5a (p. 52)	Ref. 9 Fig. 4 (p. 124)	Ref. 9 Fig. 10 (p. 130)
Material	s. steel	s. steel	s. steel	Zirc-2	s. steel
Density ρ gm. cm^{-3}	8	8	8	6.5	8
Depth D cm	1.25	1.9	0.62	1.0	1.25
Width W cm	0.25	0.15	0.16	0.1	0.07
Cavity vol. $DW^2/8$ cm^3	0.01	0.005	0.0019	0.0012	0.0008
Table speed cm. sec^{-1}	0.42	0.42	0.42	0.63	0.63
Metal Melted cm^3 sec^{-1}	0.065	0.060	0.02	0.031	0.025
gm. sec^{-1}	0.52	0.48	0.16	0.20	0.20
Electron beam Conditions V volts	2×10^4	2×10^4	10^4	1.5×10^5	1.5×10^5
I amps	0.15	0.1	0.1	0.009	0.0095
Force in electron beam F_E $0.34\ I\sqrt{V}$ dynes	7.2	4.8	3.4	1.2	1.3
Displacement force F_D $DW^2\ \rho\ g/8$ dynes	78	39	14.7	7.6	6.3
$F_D - F_E$ dynes	71	34	11	6.4	5.0
Total vertical component of surface tension force F_T 2000 W dynes	500	300	160	200	140
$F_D + F_T - F_E$ dynes	571	334	171	206	145

Appendix I

Force due to Momentum of Metal Globules

Velocity of weld = 10" per minute

= 1" per 6 secs.

Mass of metal ejected per inch of weld seam

$= 20 \times (413) \times \pi \times (0.025)^3 \times 10$

= 0.013 gm. per inch of weld

$= 0.02 \text{ gm. sec}^{-1}$

Height of ejection = h = 10 cm

$\therefore$ velocity $= \sqrt{2 g h}$

$= \sqrt{2 \times 981 \times 10}$ cm. sec^{-1}

$= 140 \text{ cm. sec}^{-1}$

$\therefore$ Force $= (\text{gm. sec}^{-1})(\text{cm. sec}^{-1})$ dynes

= 0.02 x 140 dynes

= 2.8 dynes

COMPARISON OF VARIOUS ELECTRON BEAM GUN CONFIGURATIONS AS APPLIED TO THE LOW VOLTAGE MELTSTOCK CATHODE TECHNIQUE

By

Joseph W. Griffith
President and Chief Engineer

and

William M. Van Datta
Development Engineer

Electro-Glass Laboratories, Inc.
Beaverton, Oregon

ABSTRACT

The low voltage meltstock cathode offers advantages over high voltage means for maintaining molten pools in casting crucibles. Heating of the meltstock cathode can be accomplished by combining the best features of present electron gun configurations. A comparison of annular guns of two types versus remote multiple gun configurations will be made.

COMPARISON OF VARIOUS ELECTRON BEAM GUN CONFIGURATIONS AS APPLIED TO THE LOW VOLTAGE MELTSTOCK CATHODE TECHNIQUE

Electron beam processing of materials has become a rapidly expanding field. Thanks to the excellent job of education performed by Dr. Bakish and his symposia, the advantages, abilities, advances and techniques of this versatile tool are becoming the watchword of progressive laboratories throughout the world. It is indeed a privilege to present a small contribution to the state of the art.

In order to be brief, let us accept the process of electron bombardment melting as being useful. Successful melting facilities are already producing high purity metals. The quantity of electron beam melted metals is increasing and the decreasing cost per melted pound is placing the electron beam method closer to a favorable economic position with respect to competition. Since new techniques generate new interest, a regenerative usage schedule is anticipated, making more room for the utilization of new techniques, ideas and new equipment. With increased usage comes a demand for larger sized parts, larger castings and larger ingots. The megawatt electron beam furnace is a reality[1]. However, the appetite for increased size appears insatiable, and even larger ingots are in demand.

Arc cast ingots have a size advantage at present. The arc process, however, suffers a disadvantage in the conversion of sizes. It is always

necessary to have the consumable electrode smaller than the cast ingot so that desired pressure environments can be maintained in the region of the molten metal. The large ingot size is a function of the high power, which in the arc melting case is easier to obtain. Low voltage systems are standard mass production items.

High voltages are presently used in the electron beam systems for melting metals. Electrons generated from a hot surface are propelled at 15 KV, or higher, toward both meltstock and molten pool. A plurality of electron pencil guns has been used as well as one or more annular guns[2, 3]. These guns utilize high voltage electrons to bombard the meltstock material as well as supplying the energy to maintain the molten pool. Remote guns operate for longer periods of time without contamination and at higher tank pressures. High voltage arcs still provide problems and current limiting systems are essential to prevent permanent damage to furnace and the power packages associated with them.

There are also practical limits to the power available at high voltages. The ac to dc conversion units, at the high voltages used, are the main limitations. Circuit protection devices also provide unsolvable problems at higher voltages. At high voltages, arc suppression systems are essential and equipment has been damaged due to lack of, or faulty design of, devices to extinguish high voltage, high current arcs.

The use of an electron cloud or space charge surrounding heated meltstock has been reported[4]. This technique attempts to utilize the

enormous emission capability of the molten refractory metals to maintain a molten pool. The large emission current available is accelerated to the cast ingot by low voltage - high current power supplies. A simple line isolation transformer can be used in conjunction with easily available, off the shelf, rectifiers to generate high powers needed for large ingots. No high voltage arcs have to be suppressed or extinguished. Normally available circuit protectors can be used. High speed control over the power available is also possible using readily available electrical components.

Several methods of heating the meltstock to emission (and melting) temperatures can be used. Induction heating of the meltstock is possible but it offers problems of directing the heat and heat penetration. Single gun, (remote), multiple gun, (remote), work accelerated annular gun and self accelerated annular guns offer heating possibilities. Each has advantages. This report offers a comparison of these electron bombardment devices when used to heat the meltstock to melting and emission temperatures.

A single gun can be used to achieve emission and dripping temperatures, (Figure 1). To erode the meltstock uniformly required rotation. Since only one area is heated, radiation heat losses boost the power required for emission. Electrons impinging upon the side of the meltstock can be reflected into undesirable regions. The location of the hot zone is not ideal, since the best emission area is directed at a significant angle to the desired direction.

FIGURE 1 SINGLE GUN MOUNTED ON MELTING TANK

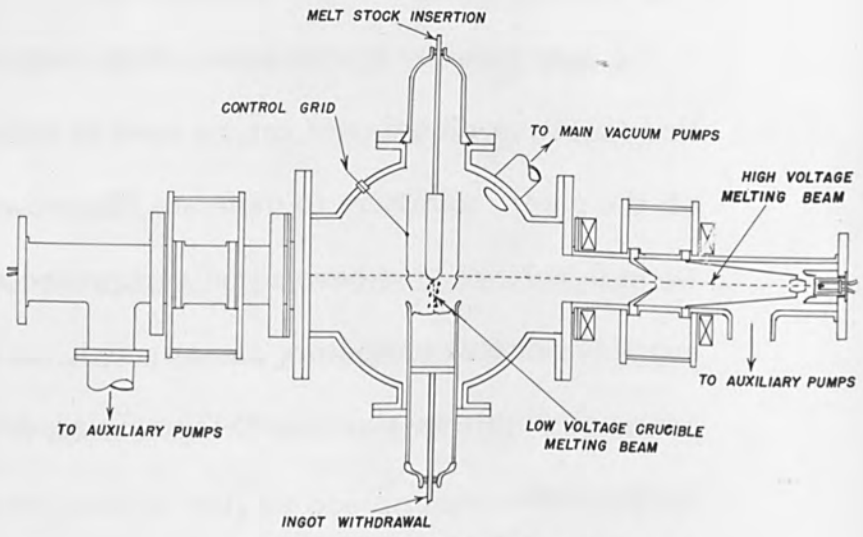

FIGURE 2 SCHEMATIC OF DOUBLE GUN CONFIGURATION

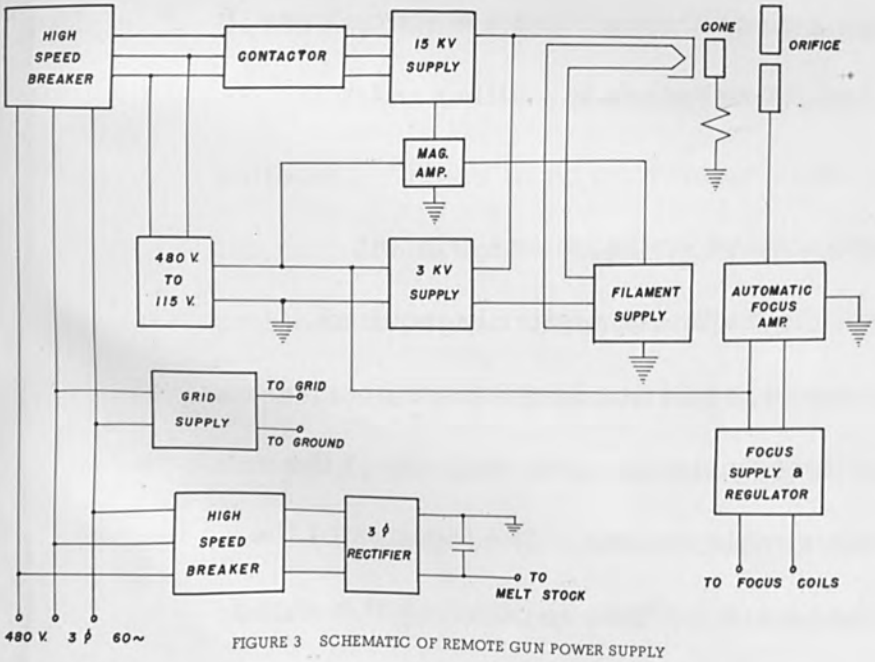

FIGURE 3 SCHEMATIC OF REMOTE GUN POWER SUPPLY

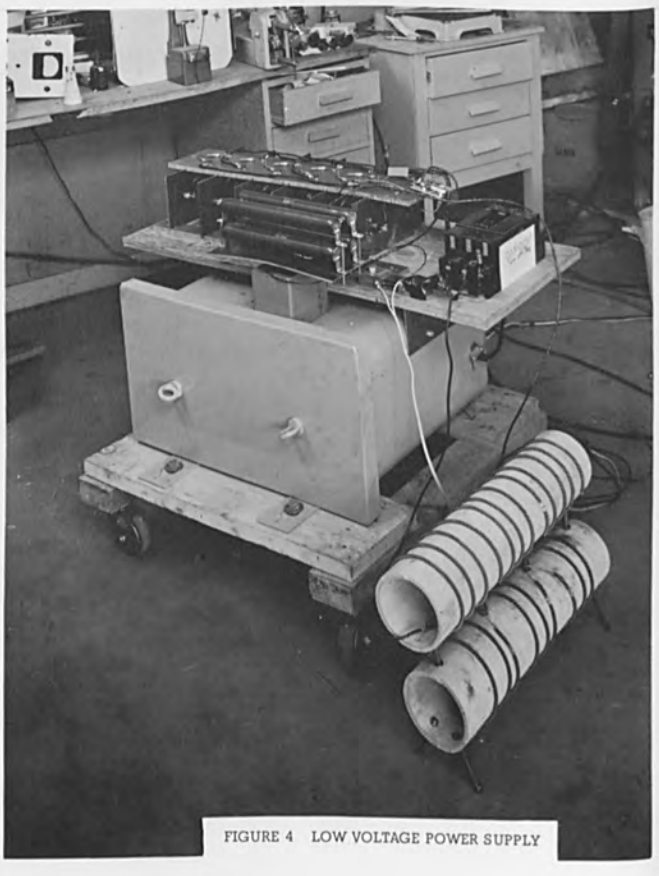

FIGURE 4 LOW VOLTAGE POWER SUPPLY

Bombardment of the bottom of the meltstock can be accomplished by repositioning of the gun, or by beam deflection. Since mechanical changes to the chamber are not necessary with beam deflection, the latter was tried with improved results.

However, if one gun is good, two should be better. (Figure 2). More uniform heating results and heat losses are somewhat reduced. Again, rotation of the meltstock is necessary and the use of beam deflection to heat the bottom of the meltstock is an improvement. This also improves the electron illumination of the cast pool. The system used is shown schematically. (Figure 3). The meltstock cathode power supply is exceedingly simple and occupies very little space. This same supply is used for all of the melting experiments. (Figure 4).

The next experiment is an attempt to simplify the power supply further. (Figure 5). A simple work accelerated gun (Temescal 4") gun configuration was used. This gun was somewhat larger than required for the tank used and the filament was reduced from .050" to .020" in diameter. This reduced the power required to heat the filament and allowed smaller filament controls to be used.

The schematic diagram of this experimental configuration, (Figure 6), shows the use of a control grid. As previously reported, this control grid provides an internal crucible current (or heating) control as well as extremely fast action protection for power supplies. Most of the experiments performed in this comparison used temperature limitation control for simplicity.

The picture, (Figure 7), shows the work accelerated gun mounted above a water cooled crucible. This gun configuration improved the heating of the meltstock and reduced the need for meltstock rotation. Alghough probably due to the large size of this gun, meltstock emission temperatures were obtained more quickly and more uniformly.

Arcing problems were present with this configuration. The entire gun is mounted within the vacuum chamber. Since the body and filament of the gun are maintained at a potential negative to the chamber, meltstock and crucible, arcs could occur in many places. Field emission from sharp corners of the gun caused ionization and discharges (low pressure arcs) which easily transferred to the low voltage area of the tank. Alghough this method offers simplification, it did not eliminate the problems of an enclosed gun configuration.

A self accelerated electron "gun" was designed, (Figure 8). Care was taken to eliminate possible points and field emission. It was designed so that the sheet of electrons emitted from the hot filament followed a funnel shaped path to the meltstock. This was done to minimize back bombardment of the hot cathode by charged particles leaving the meltstock. No direct line of sight path existed between the hot zone on the meltstock and the filament.

Meltstock cathode illumination was greatly improved over all other methods of heating. Excellent control of the temperature and width of the hot zone was possible since it was possible to focus the beam

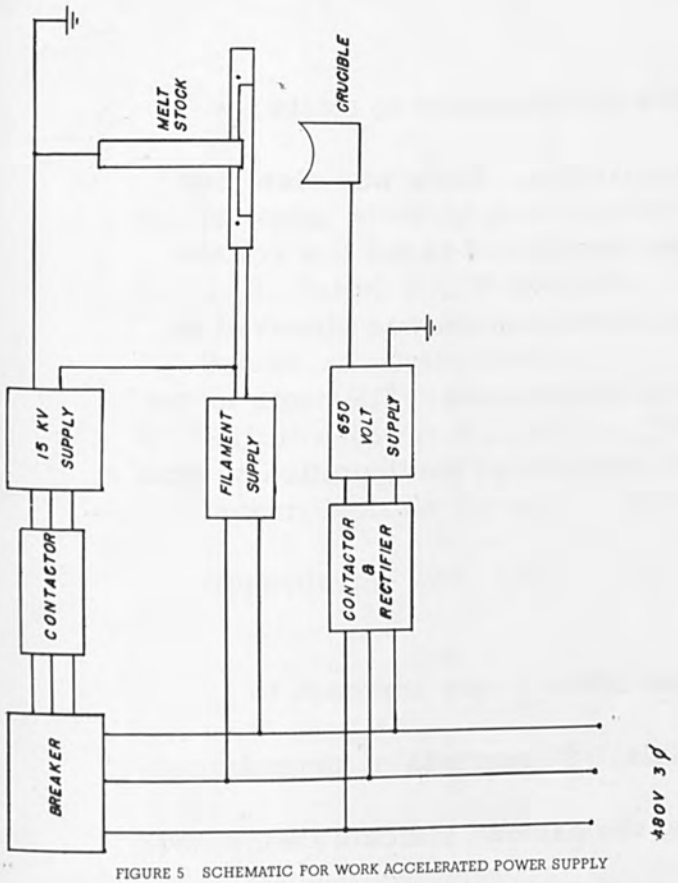

FIGURE 5 SCHEMATIC FOR WORK ACCELERATED POWER SUPPLY

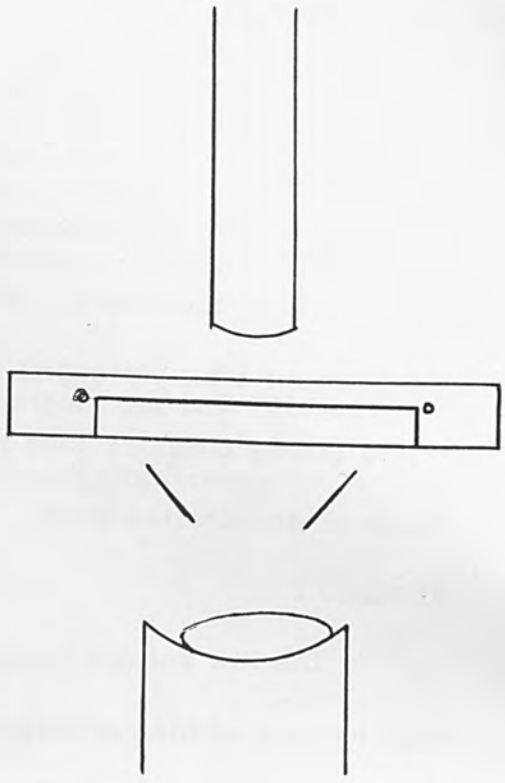

FIGURE 6 SCHEMATIC OF WORK ACCELERATED CONFIGURATION

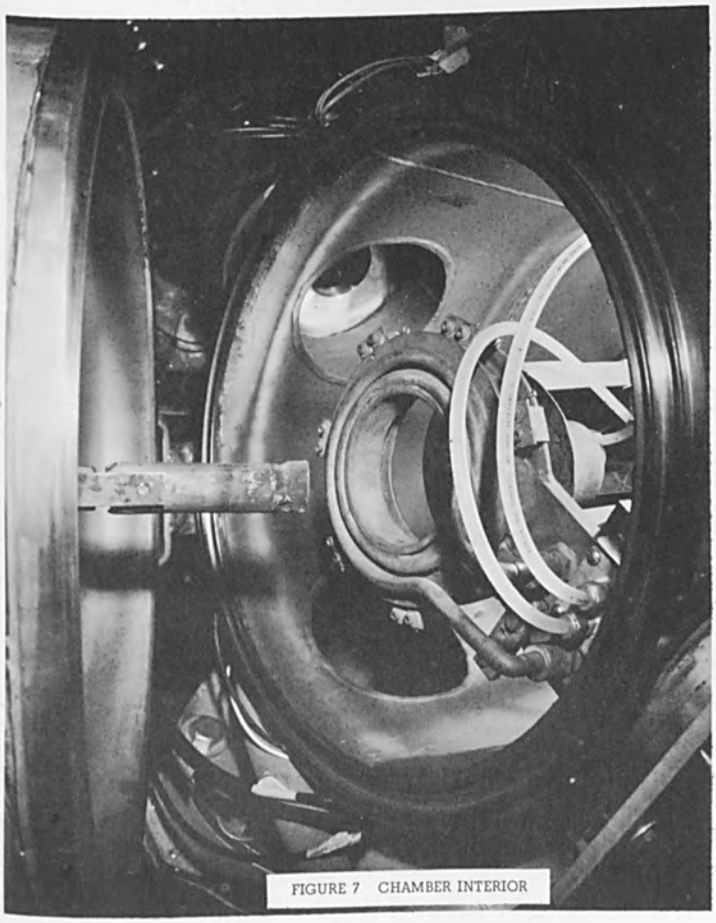

FIGURE 7 CHAMBER INTERIOR

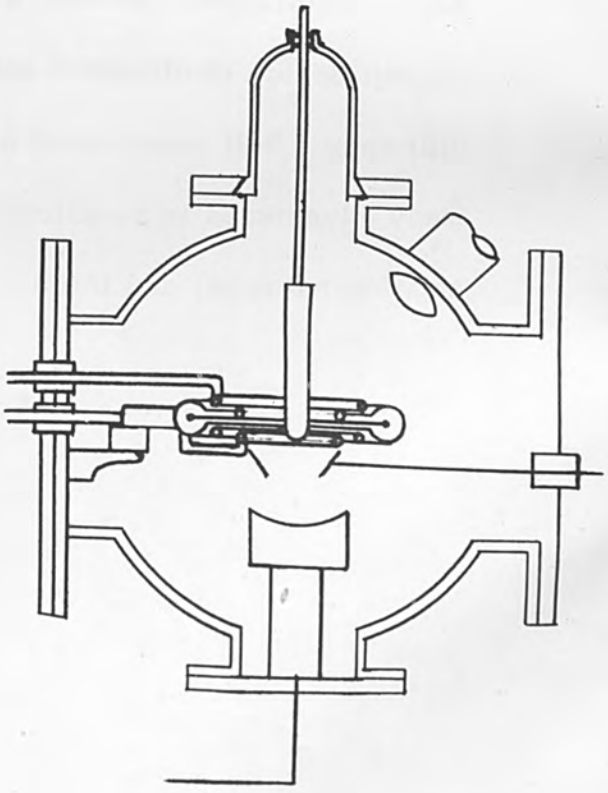

*FIGURE 8 SCHEMATIC OF SELF ACCELERATED ANNULAR CONFIGURATION

striking the work. With this system, it is not necessary to rotate the meltstock although some improvement is possible. There was also less tendency to arc, but such arcs were again transferred to the low voltage region of the experiment. No significant contamination was observed on the filament after prolonged usage in other experiments. Filaments lasted ten to twenty times as long with the self accelerated configuration as with the work accelerated guns.

SUMMARY

The low voltage meltstock cathode offers a new approach to high vacuum melting of refractory materials. Comparison of several electron bombardment methods of heating the cathode indicate that remote guns (exterior to the chamber) require work rotation but are easily maintained. Annular guns of the work accelerated type require careful design to eliminate arcing problems but heat the meltstock more uniformly. Self accelerated annular guns with beam deflection offer many advantages in simplicity, less arcing problems than the work accelerated type, and infinitely better meltstock heating than all others.

REFERENCES

1. Temescal Metallurgical Corporation. Advertisement.
2. U. S. Patent No. 2,942,098. Stauffer Chemical Corporation.
3. Heraus. Bulletin ES-2.
4. Griffith, Joseph W., et al. "Melt Stock Cathode for Low Voltage Vacuum Melting Furnace," International Vacuum Conference Proceedings, Oct. 1961.

GENERAL

Klemperer, O., "Electron Optics," University Press. 1953.

Spangenberg, K. R., "Vacuum Tubes," McGraw Hill. 1948.

Zworykin, V. K., et al. "Electron Optics and the Electron Microscope," Wiley. 1945.

Bakish, R. (editor). "Proceedings of the Third Symposium on Electron Beam Technology," 1961.

PROPERTIES OF ELECTRON-BEAM PURIFIED MATERIALS

By

Alan Lawley
Senior Research Scientist
The Franklin Institute Laboratories
Philadelphia, Pennsylvania

ABSTRACT

In recent years there have been many detailed investigations of the physical and mechanical properties of materials (metals, alloys, non-metals) prepared by electron-beam melting or refining. The present paper deals specifically with the purity, workability, and mechanical properties of the group V A refractory metals niobium and tantalum, the group VI A refractory metals molybdenum and tungsten, and the platinum group metals (group VIII A, B, C) ruthenium rhodium, palladium, osmium, iridium, and platinum. The properties of these materials are compared and contrasted with those of the materials prepared by the more conventional sintering, arc-casting, and other consolidating techniques.

Properties of Electron-Beam Purified Materials

Abstract

In recent years there have been many detailed investigations of the physical and mechanical properties of materials (metals, alloys, non-metals) prepared by electron-beam melting or refining. The present paper deals specifically with the purity, workability and mechanical properties of the group VA refractory metals niobium and tantalum, the group VIA refractory metals molybdenum and tungsten, and the platinum group metals (group VIII A,B,C) ruthenium, rhodium, palladium, osmium, iridium, and platinum. The properties of these materials are compared and contrasted with those of the materials prepared by the more conventional sintering, arc-casting, and other consolidating techniques.

1. Introduction

The recent advances made in the fields of aeronautical engineering, nuclear energy, and space and missile technology have greatly increased the demands made on structural materials. As a result of this, there has been a substantial increase in the research effort devoted to what may be termed the lesser known metals and their alloys. This group of metals is comprised of tantalum, niobium, molybdenum, tungsten, and vanadium. In addition, the platinum group of metals offer advantages in specific applications, despite the relatively high materials cost.

The fields of study of the lesser known metals include: (1) An evaluation of the flow and fracture properties of the body-centered cubic lattice. (2) A determination of the electronic structure of these transition elements. In either field it is essential to work with ultra-pure material in order not to mask any inherent effects caused by

impurities. Further, from technological considerations, it is necessary to obtain a relatively pure material consistent with sufficient fabricability and the desired mechanical strength. These demands on purity have in turn led to the development of the Van Arkel iodide process, solid state purification, vacuum distillation, electron-beam melting, and electron-beam vertical floating zone refining.

In the present paper, interest is centered on the properties of material consolidated by electron-beam melting and electron-beam zone refining. Purity, workability, and mechanical properties are the parameters of direct concern. With the exception of vanadium, it is possible to make a detailed comparison between the properties of high-purity material and those of material consolidated by other techniques.

Tantalum

Tantalum is located in group VA of the first long series of the periodic table. Hitherto, pure tantalum has been used almost exclusively in electrical applications (rectifiers, capacitors, tubes), and for chemical equipment involving corrosive media. Currently, however, much interest centers on the use of tantalum as a basis for high temperature alloy development since the metal combines a high melting point (2990°C) with excellent fabricability. However, the limitations of only moderate high-temperature strength properties and poor oxidation resistance must be fully considered. Several extensive investigations are under way concerning the workability and mechanical properties of tantalum consolidated by electron beam melting or refining, and comparisons have been made with sintered and arc-cast material.

Purity

Impurity levels reported for tantalum in various forms (reduced powder, sintered, arc-melted, electron-beam melted or refined) are assembled in Table 1. In the electron beam zone-refining of tantalum, zoning speeds ~2 mm per min. are common , and this results in a total interstitial impurity content (carbon, nitrogen, oxygen, hydrogen) of some 50-70 weight parts per million. In the standard refining units, a single turn horizontal tungsten wire surrounds the specimen. With this arrangement, it is possible for cross contamination to occur between filament and sample. Thus Ferriss[5] reports a tungsten pick-up of 1000p.p.m. in this way. The removal of many of the metallic impurities (iron, molybdenum, nickel, silicon, aluminum, titanium, copper) to a level below the limiting value for spectral analysis is due to volatilization rather than a true zoning action.

As may be seen from Table 1, it is possible to purify tantalum by vacuum sintering to a level equal to that of electron beam melted stock provided the correct times and temperatures are adhered to. Essentially the thermodynamics are the same in both operations and only the kinetics vary. Thus Michael[1] observes that in solid state vacuum sintering, hydrogen is removed in the temperature range 600-1200°C, carbon-monoxide at 1600-2000°C, and oxygen and nitrogen above 2000°C. Similarly, Schmidt et al[2] report oxygen contents below 5p.p.m. for sintering treatments (5 hours) at 2860°C. With electron beam melting, outgassing occurs from the molten state at ~ 3000°C.

Workability

Unlike the other body-centered cubic refractory metals, tantalum does not possess a ductile-brittle transition temperature

Table 1 Analysis Data for Tantalum

Impurity - parts per million - ND: Not Detected

	C	O_2	N_2	H_2	Nb	Fe	Mo	Si	W	Ti	Cr	Cu	Ni	Mn	Al	Ref.
Reduced Powder	100/1000	50/2000	50/100	100/1000	<20	100/200	50	100/500	<100	<100						1
	900	1360	130	71	20/200	4/40						<10		<5		2
Sintered Powder	200	56	130	-	1000	150	-	-	100							3
	<100	20/50	10/30	<10	<200	50/100	<50	<100	<100	<100						1
	14	80	60	-												4
	-	<5	10	<0.6												2
Arc-Melted Ingot	30	100	35	-	45	20	25	50	-	10	10	50	40	50	50	5
	150	280	60	<10	<100	<100	-	<50	56	<100	<100	<10	<100			6
	35	12	12													7
	8	14	100													7
	3	96	12													7
Electron-Beam Melted Ingot	50	60	60	1												6
	30	16	10	1.4	100/300	8				3	30	3				2
	20	<6	30	3.2												2
	<10	7	18													7
	<30	<30	8													8
	<100	20/50	10/30	<10	<200	50/100	<50	<100	<100	<100						1
Electron-Beam Zone Refined Crystal	10/30	30	10	-	10	ND*	ND	ND	1000	ND	-	ND	ND	1	ND	5
	-	3	ND	2.5												9
	8	40	20	-												7

range so that even for relatively impure material (~99.9%) there is a certain amount of ductility at all temperatures. It is, therefore, not surprising that single crystal rods 1/8" dia., produced by electron beam zone refining may be cold swaged to wire sizes below ~ 0.030" dia. without intermediate annealing stages.

High-purity polycrystalline electron beam melted tantalum may be converted into standard mill products by a combination of cold forging and rolling. When cracking is observed with cold working operations, it may be directly related to localized concentrations of interstitials in the material. As a general guide to the purity requirements for cold workability, McCullough[10] gives maximum tolerance levels for carbon, nitrogen, and oxygen as 150, 50, and 200 p.p.m. respectively; for tantalum satisfying these requirements, cold reductions > 90% are common.

Holden et al[11] report that coarse-grained electron beam melted ingot ~ 2" dia. may be cold-rolled to ~0.035" strip (~98% reduction in thickness) without cracking. However, because of 'banding' in the material, optimum conditions are obtained with intermediate annealing at ~1200°C, followed by a final cold reduction of 75%.

Schussler and Brunhouse[6] examined the formability of tantalum in the arc-cast, electron-beam melted, and sintered conditions in relation to the more common metals. A measure of the potential formability may be obtained from the true stress- true strain behavior[12]. The flow equation gives:

$$\sigma = K\delta^n \qquad (1)$$

where σ is the true stress, K is a constant (strength coefficient), δ is the true strain, and n is a constant known as the strain-hardening

exponent, and the equation is only valid up to the limit of uniform elongation.

The "formability index" is defined as $\frac{\sigma}{n}$, the ratio of true stress at the limit of uniform strain to the maximum uniform strain. For optimum formability $\frac{\sigma}{n}$ should be as small as possible, i.e., a large n value combined with a small σ value. In Table 2, values of n, K, σ and $\frac{\sigma}{n}$ are given for cold-worked and recrystallized tantalum in the arc-cast, electron-beam melted, or sintered condition. From the table, it is clear that electron beam melted tantalum has superior general formability to the arc-cast or sintered stock. From a comparison of the $\frac{\sigma}{n}$ index with that for other materials, it is found that recrystallized electron-beam melted tantalum has formability characteristics similar to those of annealed 2024 aluminum alloy. Recrystallized arc-cast tantalum requires a somewhat higher forming stress than annealed low carbon steel, but has better formability than recrystallized sintered tantalum[3].

In the development of tantalum and niobium base alloys, using electron beam melting techniques, Smith et al[13] have been primarily concerned with the properties of high-temperature strength coupled with good fabricability, i.e., the ability of the alloy to be rolled or otherwise worked at relatively low temperatures. Tantalum base, tantalum-tungsten alloys with up to ~ 15% tungsten possessing these requirements have been produced in this way, the alloys having a low level of interstitial and metallic impurities. As a specific example, the tantalum-10% tungsten alloy is completely fabricable and may be forged from 4-6" dia. ingots at temperatures around 1200°C. Fully annealed

Table 2 The "Formability Index" for Tantalum (6)

Condition	Max. Uniform Strain n	Strength Coeff. K, p.s.i.	True Stress at Max. Uniform Strain p.s.i(σ)	$\frac{\sigma}{n}$ ($\times 10^{-5}$)
Arc-Melted Cold Worked 87%	0.03	131,000	118,100	39.4
Arc-Melted Recrystallized, 0.1 mm grain dia.	0.23	92,000	65,900	2.9
Electron-Beam Melted Cold Worked 98%	0.03	48,000	43,000	14.3
Electron-Beam Melted Recrystallized, 0.2 mm grain dia.	0.22	42,000	35,000	1.6
Sintered Recrystallized 0.025 mm grain dia.	0.164	108,000	80,000	4.9

alloy slabs may be rolled at temperatures as low as 260°C to ~ 88% reduction in thickness before requiring a re-annealing treatment.

Since tantalum is inherently more ductile than the other refractory metals, the difference in fabricability between the electron-beam melted, arc-cast, and sintered grades is less pronounced. Thus for many applications it may be economically desirable to use arc-cast material. Morgan and Butler[14] have recently analyzed the problems encountered in attempting to operate consumable-arc furnaces at pressure conditions resembling those in electron-beam melting (~ 10^{-4} mm Hg). It is concluded that it is in fact possible to obtain material of equivalent purity using either melting technique.

Mechanical Properties

The mechanical properties of electron-beam zone-refined single crystals of tantalum have been studied by Ferriss et al[5] and Adams[15] at temperatures down to -196°C. At low temperatures the plastic strain becomes extremely localized and leads to a ductile shear rupture and reductions in area ~ 100%. Below about -100°C, material which has yielded is unable to support any further increased load; i.e., the material has zero uniform strain and deforms continuously at the region of initial deformation. Single crystal hardness values of 65 V.D.H.[16] and 68 V.D.H.[9] have been reported. These values are to be compared with a figure of 85 V.D.H. for polycrystalline electron-beam melted tantalum and 120 V.D.H. for recrystallized arc-cast tantalum[6].

For polycrystalline electron-beam melted material, hardness, recrystallization, and tensile behavior have been studied by Schussler and Brunhouse[6] and Schmidt et al[2]. The dependence of hardness on the degree of cold reduction of electron-beam melted, arc-cast, and sintered tantalum is illustrated in Fig. 1. Arc-cast material work hardens rapidly in the initial 20% reduction and then undergoes little further hardening up to ~ 60% reduction. The rate of work-hardening then increases to give a hardness of 230 V.D.H. at 93% reduction. Electron-beam melted tantalum with a recrystallized hardness of 85 V.D.H. work-hardens slightly to 97 V.D.H. in the initial 20% reduction. Myers[17] data on sintered tantalum show that hardness increases over the whole range of reductions with a value of 202 V.D.H. at 95% reduction.

The effect of annealing on the hardness of cold-worked tantalum is shown in Fig. 2. As may be expected, the sintered material has a higher recrystallization temperature than the electron-beam melted stock. Specific temperatures for complete recrystallization, as a function of degree of cold work, are given in Table 3. For arc-cast tantalum given 87% reduction, Schussler and Brunhouse[6] report 1230°C as a minimum temperature for complete recrystallization.

A comparison of the yield strength, ultimate tensile strength and elongation to fracture is made for various grades of tantalum in Fig. 3, a,b,c. Consistent with hardness and recrystallization observations, the higher-purity electron beam melted material has the lowest yield and ultimate tensile strength but the highest ductility. This is particularly true at sub-zero temperatures where the increase in strength with decrease in temperature is most marked.

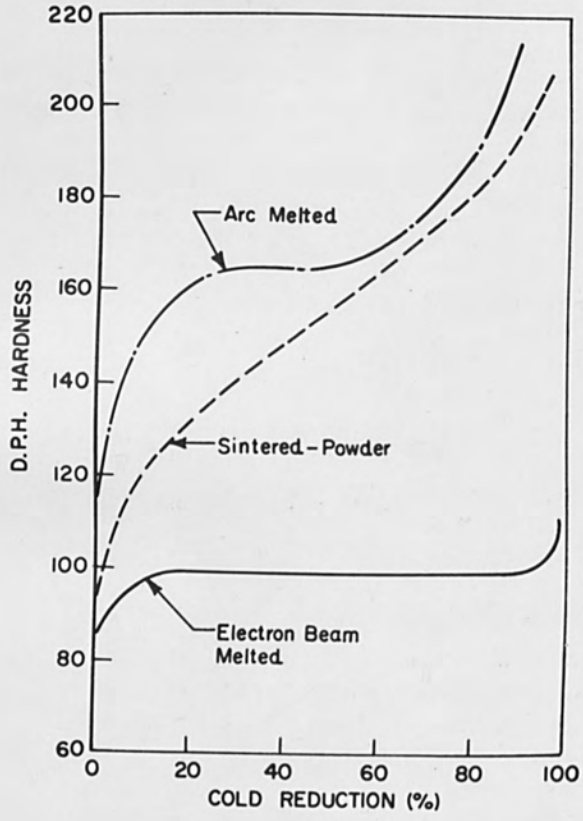

Fig. 1 The hardness of tantalum as a function of degree of cold-work[6,17].

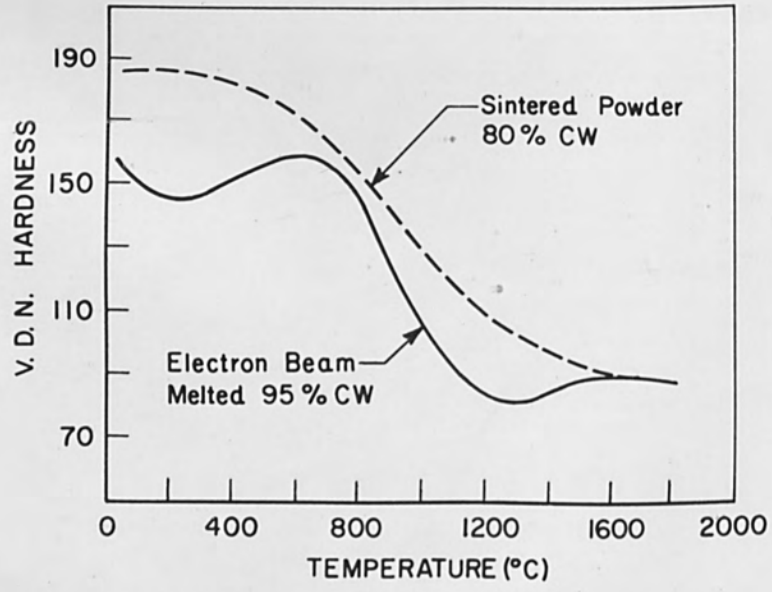

Fig. 2 Isochronal annealing curves for tantalum[11,17].

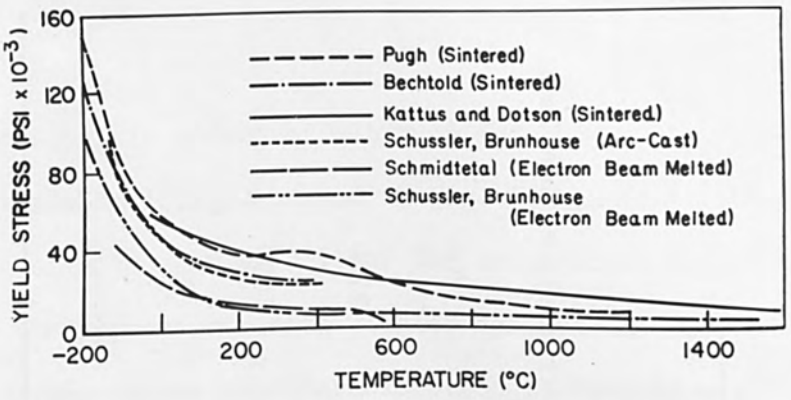

Fig. 3(a) The effect of temperature on the yield strength of tantalum.

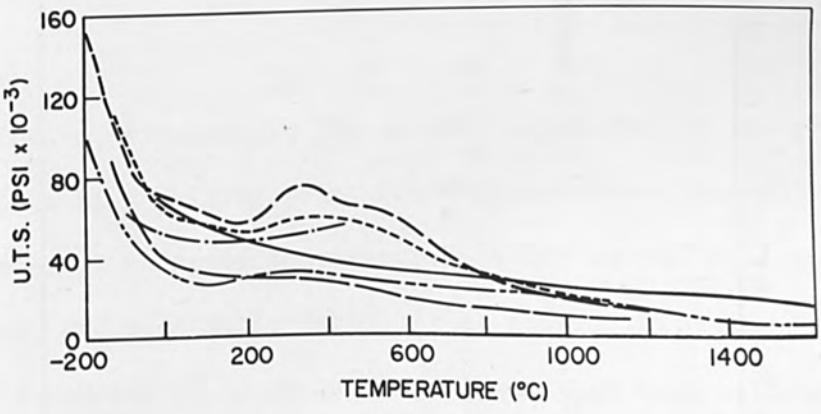

Fig. 3(b) The effect of temperature on the ultimate strength of tantalum.

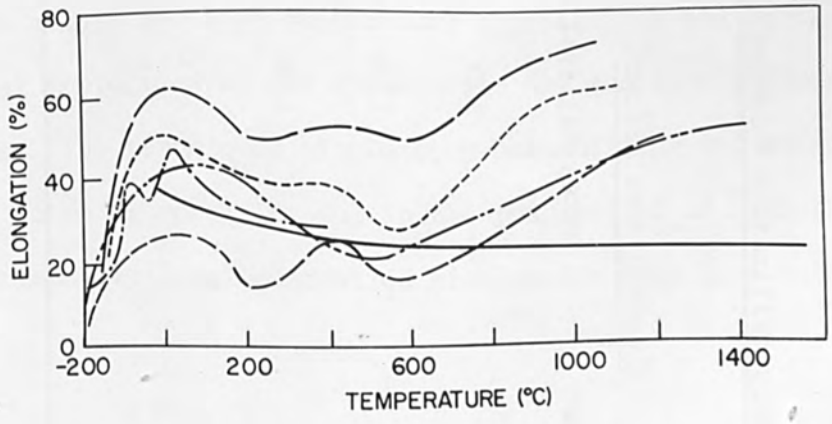

Fig. 3(c) The effect of temperature on the ductility of tantalum.

Table 3 Recrystallization Behavior of Electron-Beam Melted[2,6] and Sintered Tantalum[17]

Electron-Beam Melted		Sintered	
% Cold Reduction	Recrystallization Temp. °C	% Cold Reduction	Recrystallization Temp. °C
50	1400	40	1700
75	1200	60	1700
95	1300	80	1600
98	1200		

The specific effect of nitrogen and oxygen on the rupture strength of tantalum is illustrated in Fig. 4. The data are taken from the work of Holden et al[11] for the temperature range 750°C to 1200°C, with the rupture strength plotted against the Larson-Miller parameter. Oxygen causes considerable strengthening at ~350°C. At higher temperatures, however, nitrogen is the more effective strengthener of the two, the strengthening effect decreasing with increased time and temperature of test.

Niobium

Niobium, situated in the second long series of the group VA elements, has a high melting point (2468°C), good resistance to liquid metal corrosion at moderate temperatures, a low thermal neutron capture cross section, and reasonable ductility at ambient temperatures. In addition, its density (8.57 $gm.cm^{-3}$) is lower than that of tungsten, molybdenum, or tantalum.

Considerable effort has been devoted to the development of niobium-base alloys for high temperature applications and to the study of mechanical properties at sub-atmospheric and moderately elevated temperatures. The techniques of electron-beam melting and refining have proved to be extremely useful in the preparation of high-purity niobium, or impurity level-controlled niobium for base line data studies.

Purity

Representative impurity levels for niobium in differing forms are listed in Table 4. The list is by no means exhaustive,

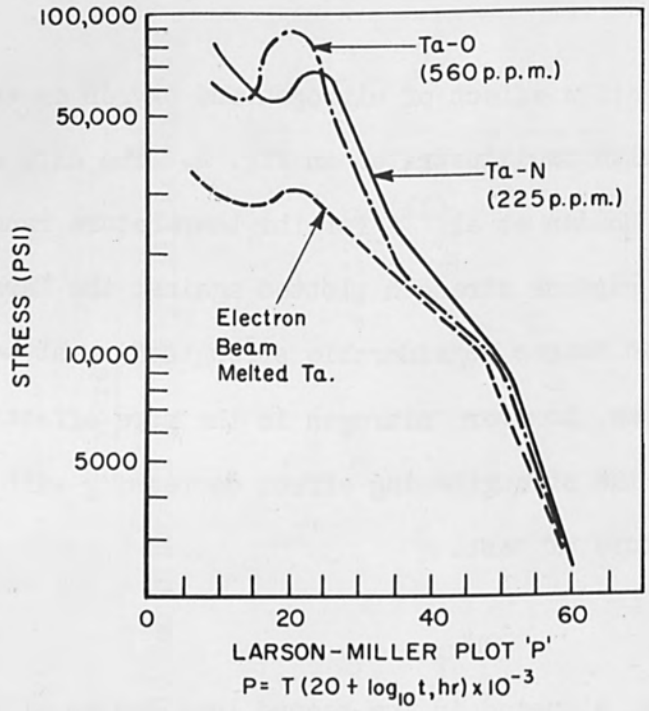

Fig. 4 Rupture properties of tantalum, Ta-O and Ta-N: Larson-Miller plot[11].

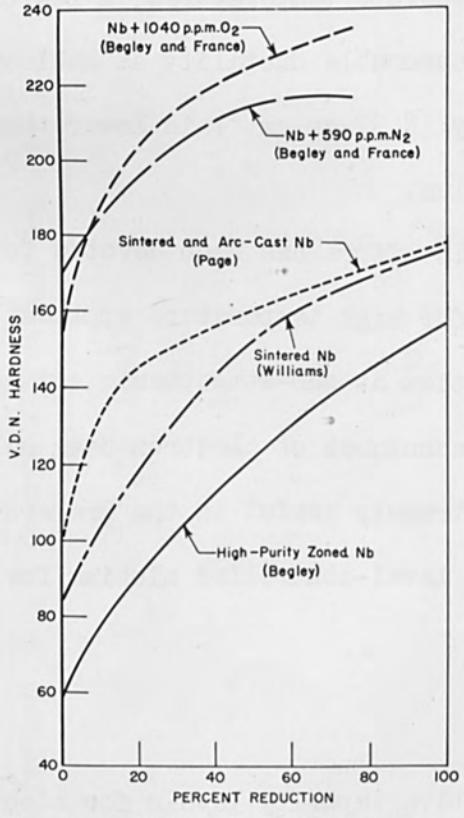

Fig. 5 The hardness of niobium as a function of degree of cold work.

Table 4 Impurity levels for Niobium

- parts per million -

	C	O_2	N_2	H_2	Si	Fe	Ta	Ti	Zr	B	W	Al	Mo	Ref.
Powder	1900	~5000	-	-	10/100	20/200	1600	-	8200	-	-	70/700	-	18
	2500	5000	700	-	800	500	3000	500	-					19
Sintered	35	600	300	-	<100	<150	400	<150	<500	<1	100	<20	<20	20
	114	210	120	-	-	-	3380	-	<1000					21
	220	650	220	9	-	-	1600	-	6200					18
	150	1200	200	-										22
Arc-Melted	300	400	200	<10	<150	<150	1000	<150	<150	1				23
	240	360	190	-	-	-	<500							24
	16	625	76											7
Cage Zone-Melted (H.F.Heating)	101	100	180				1440	400						18
Floating Zone (H.F. Heating)	240	30	80											18
Electron-Beam Melted	15	100	80											7
	700	100	500	200	1500	3000	3000							25
	210	100	90	8	<150	<150	1000	<150	<150	1				23
	<30	100	90	-	<100	<150	400	<150	<500	<1	100	<20	<20	20
	180	200	110	1	200	40	2000	1700	<300					26
	27	140	130	2	-	20	1930	20	<300					24
	200	670	70											18
	198	15	60											18
Electron-Beam Zone-Refined	33	7	25	-	<10	<10	1000	<50	1000	5	-	<5	-	27

however, it gives adequate information as to the effect of the various consolidation procedures on the overall purity. With electron-beam melting the most important factor determining purification is the relative vapor pressures of the various metals and impurities at the working temperature. As a general rule, any impurity with a vapor pressure of ten times or more that of the niobium will be removed effectively. Other factors determining the purification process include the equilibrium concentrations of the impurities in the molten state, intermetallic compound formation, and physical bonding forces.

Aschoff and Baroch[20] have applied electron-beam melting to the production of both unalloyed niobium and the F-48 alloy (15% W, 5% Mo, 1% Zr). With a melting rate between 10 and 20 lbs per hour, it is found that purification occurs by the evaporation of the metal oxides of molybdenum, boron, tungsten, zirconium, thorium, hafnium, tantalum and yttrium. Carbon is removed as carbon monoxide. In the melting of the F-48 alloy, the ratio of both molybdenum and tungsten to niobium decreases, the reverse of their respective pressures. This is due to the higher vapor pressures of the molybdenum and tungsten oxides. Aschoff and Baroch report that electron-beam melting may be profitably used for the recycling of scrap niobium, contaminated with oxygen, nitrogen and other processing impurities.

From an earlier evaluation of the electron beam melting of niobium, Smith et al[28] conclude that vanadium and metals of greater volatility than vanadium evaporate rapidly to concentrations less than a few hundredths of a percent by weight. Thus iron, aluminum, nickel, and chromium will be removed, but the impurity levels for zirconium,

molybdenum, and tantalum will be relatively unaltered. It is observed that the loss of oxygen as NbO proceeds at a rate about four times faster than that of oxygen as CO or nitrogen as N_2. At an initial melting rate of ~10" of ingot per hour, the oxygen content decreases from 2500 p.p.m. to ~500 p.p.m. Remelting at the same rate causes a further reduction to ~150 p.p.m. The rate-limiting mechanism in the removal of CO and N_2 is the diffusion of carbon, nitrogen, and oxygen in the liquid niobium. In order to reduce the nitrogen content to a satisfactory level, it is necessary to either melt at reduced rates, or to use niobium stock having an initially lower nitrogen content. As noted above, part of the carbon is removed in the form of CO and part as NbO. However, if the initial oxygen: carbon ratio is greater than 5:1, and the initial carbon content is ~ 500 p.p.m., the carbon content is reduced to ~ 150 p.p.m. for the above melting rate. Although zirconium alone is not noticeably removed, it is found that a 1% Zr - niobium alloy loses 90% of the zirconium in the form of ZrO on electron-beam melting. In this way, the oxygen content decreases from 0.15-0.2 to 0.02-0.03 wt. %.

Begley[18] finds an effective reduction in the oxygen and nitrogen content of niobium. The electron-beam melting was carried out at Temescal Metallurgical Corporation using a feed supply of 20-80 mesh niobium powder. Although the carbon level is greatly reduced, the magnitude of the decrease in carbon and oxygen does not correspond to the formation of CO. Again the formation of volatile oxides is primarily responsible for the decrease in the oxygen and metallic impurity content. Summarizing, the electron-beam melting technique is superior to vacuum arc-melting in reducing

interstitial impurities, particularly when the starting material has a relatively high overall interstitial content.

For electron beam zone-refined single crystals of niobium, Wellings and Maddin[27] obtain an extremely pure product following six zone passes. The impurity levels of the important elements in the as-received, one zone-pass, and six zone-pass material are listed in Table 5. The significant reduction in the zirconium and oxygen content is again evident.

Workability

McCullough[10], Begley[18], and Mincher and Sheely[23] have examined the working properties of niobium consolidated by electron-beam melting. As in the case of tantalum, the pure material is cold ductile, and the remarks made concerning tantalum apply equally well to niobium. Thus, in general, the material can be reduced by cold working > 90% reduction without an intermediate annealing stage. This holds true for both fine and coarse-grained ingot material. It is in the initial ingot break down stages that the danger of cracking is highest. The limitations on cold working actually lie with the size of the available equipment rather than with the niobium. To give specific examples of workability, Begley[18], starting with 3" dia. ingot produced sound 0.010" thick sheet by a combination of cold-forging and rolling. Similarly, 1.5" dia. ingot was cold rolled and cold-swaged to 0.3" dia. rod. Mincher and Sheely[23] successfully cold worked electron-beam melted niobium to 75% reduction by cold groove-rolling, followed by cold swaging to 95% reduction. Adams et al[25] Smith et al[28], and Wessel et al[26] have also cold reduced

Table 5 The Purification of Niobium Single Crystals By Electron-Beam Floating Zone Refining(27).

Impurity	As-received	1 Pass	6 Passes
	p.p.m.	p.p.m.	p.p.m.
C	51	35	33
O_2	460	84	7
N_2	82	38	25
Si	10	< 10	< 10
Fe	10	< 10	< 10
Ta	1000	1000	1000
Zr	5000	-	1000

high purity niobium to sheet or wire form without tearing or cracking.

By comparison, attempts to cold roll vacuum arc melted niobium[18] were not successful, it being necessary to either roll at ~ 1000°C, or forge at ~ 950°C in order to avoid material break-up. However, once the initial break down of the ingot was accomplished (~ 60% hot working), it was possible to proceed with cold working operations. Similarly, Mincher and Sheely[23] found it necessary to either hot extrude (1260°C) or hot forge (1145°C) vacuum arc-cast niobium ingot prior to cold swaging. In the material examined by Begley[18] the oxygen and nitrogen interstitial impurity levels in the electron-beam melted and arc-melted niobium were comparable. However, the latter had, in most cases, a higher carbon content, and this was believed to account for the poor cold workability.

Smith et al[13] examined the workability of many niobium base alloys prepared by electron-beam melting. As a general rule, it was found that 15% tungsten and 4% molybdenum represented the practical limits for alloying with niobium. Alloying above these limits caused the ductile-brittle transition temperature to rise above room temperature. As may be expected, additions of tantalum up to 30% had little effect on the impact properties.

Mechanical Properties

The relationship between hardness and % reduction (cold rolling) for high-purity cage zone melted niobium* (Begley[18]) is given in Figure 5. This relationship has not been established for electron-beam melted niobium. However, because of the similarity in impurity content in the two cases, it is anticipated that this curve

* High frequency heating.

will be representative of the strain-hardening behavior of electron-beam melted material. For purposes of comparison, hardness curves are included for commercial purity sintered niobium (Page[29], Williams[30]) and for niobium-oxygen and niobium-nitrogen alloys prepared by levitation melting (Begley and France[31]). The lower rate of strain hardening and the lower final hardness of cage zone-melted material is attributed to its higher purity.

Recrystallization of electron-beam melted niobium cold rolled 60%, 80%, and 95% (Begley[18]) is illustrated in Figure 6. The isochronal softening curves are for 1 hr. annealing periods. For complete recrystallization, the temperatures required (1 hour anneal) are 960°C, 1080°C, and 1150°C, for prior reductions of 60%, 80%, and 95%, respectively. Consistent with Figure 5, the annealing curve for a 99.8% purity sample cold worked >50% (Lement et al[32]) lies well above the curves for high-purity material.

Tensile data for recrystallized electron-beam melted[23,26], arc-cast[23], and sintered[22] niobium are compared in Figure 7 a,b,c. In the lower temperature range, all materials show the characteristic strong temperature dependence of yield stress and ultimate tensile strength.

The ductile-brittle behavior of electron-beam melted niobium has been studied by Begley and Platte[24] and Mincher and Sheely[23]. The former workers used a modified Izod specimen, and the data obtained are compared with that for recrystallized arc-cast and sintered material in Fig. 8. The ductile-brittle transition range is seen to be $\sim$ -125°C for the beam melted stock, close to room temperature for arc-cast stock and $\sim$150°C in the case of sintered niobium. Surprisingly, the

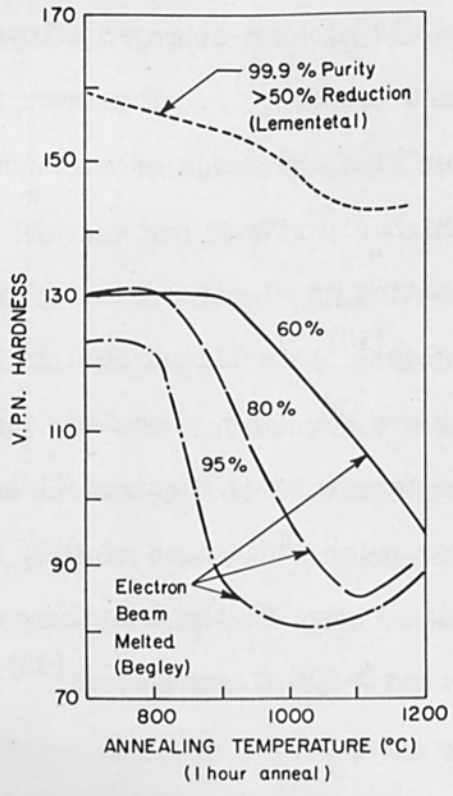

Fig. 6 Isochronal annealing curves for niobium as a function of degree of cold-work.

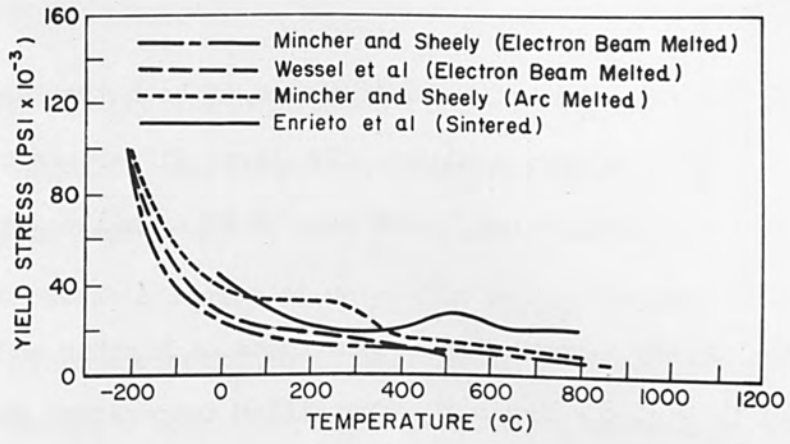

Fig. 7(a) The effect of temperature on the yield strength of niobium.

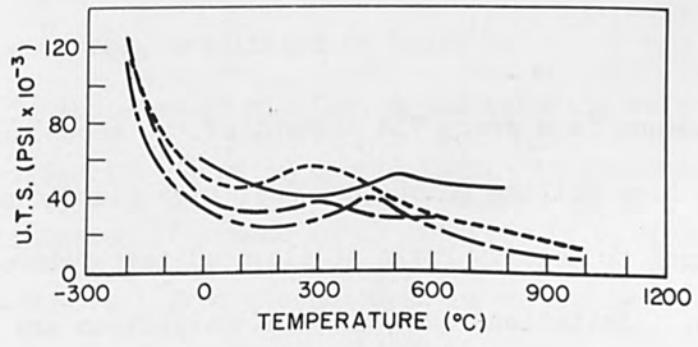

Fig. 7(b) The effect of temperature on the ultimate strength of niobium.

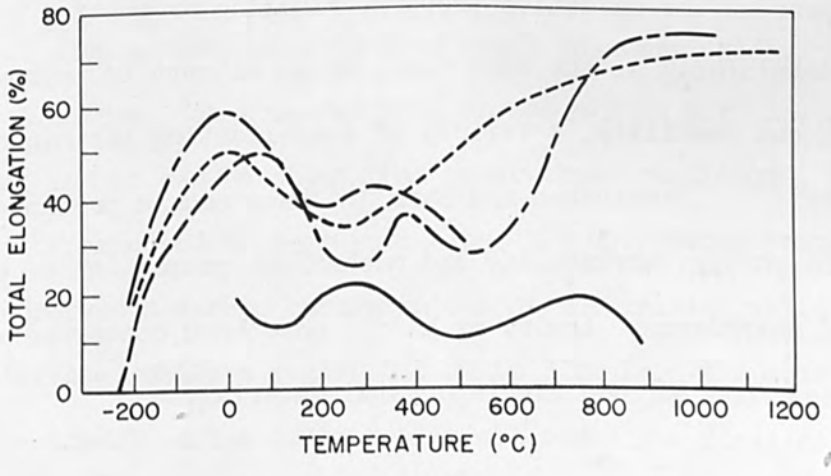

Fig. 7(c) The effect of temperature on the ductility of niobium.

interstitial impurity content and grain size of both the beam-melted and arc-melted material are similar. The large difference in transition temperature is attributed to variations in metallic impurity content.

The Charpy V-notch impact test data of Mincher and Sheely are included in Fig. 8. Again the transition temperature for the beam-melted material is at least 100°C below that of the arc-melted stock. In this case, however, the difference is consistent with the higher degree of purity in the beam-melted niobium.

Molybdenum

Molybdenum is a group VIA element of the second long series and possesses a high melting point (2610°C), high elastic modulus, and excellent strength to density ratio at elevated temperatures with small alloy additions. Limitations in the use of molybdenum are imposed by its poor oxidation resistance at temperatures $> \sim 600^{\circ}C$ and by limited low temperature ductility; cf. tantalum, niobium and vanadium. In order to overcome the oxidation problem; cladding or coating systems are being developed. At the same time, in an attempt to improve workability and ductility, a variety of consolidating techniques are under survey[33]. Semchyshen and Barr[34] have made a preliminary study of the purity, workability and mechanical properties of electron-beam melted molybdenum. Lawley et al[35] have been concerned with electron-beam zone refined single crystal material.

Purity

Theoretical calculations indicate that at the temperatures and pressures operative in electron-beam melting it should be possible

to remove practically all impurities from molybdenum, with the exception of rhenium, tantalum, and tungsten. Analyses made on such material show that this is in fact true; in most instances, the impurity levels are at or below the reliable limits of detection set by the method of analysis. Thus, for quadruple electron-beam melting of 3" dia. ingots, Wah Chang Corporation report a total interstitial content below 40 p.p.m.[44] In the case of six zone pass electron beam refined 1/8" dia. rod, Lawley et al[35] obtain a total interstitial content $\sim$ 15 p.p.m. Representative impurity levels for molybdenum, following various consolidating procedures, are listed in Table 6.

As in the case of niobium, metal suboxide volatilization is an extremely effective means of deoxidation. At the same time, almost complete distillation of excess metal impurity (e.g. aluminum, titanium) takes place. However, from a consideration of the observed changes in carbon content, Semchyshen and Barr[34] conclude that for effective deoxidation, at least $\sim$ 0.022% carbon is necessary, in addition to titanium or aluminum. In the absence of carbon, vacuum melting per se will not give a material free from grain boundary oxide.

Electron-beam zone-refining speeds $\sim$3 mm per min. are in common use, and it can be shown that under these conditions, only carbon may be expected to segregate along the molybdenum sample. Belk[42] observed a carbon concentration at the initial solid -- liquid interface, while a region 0.5 cm to 3 cm from the starting end had the lowest carbon content. In all cases the final solidified zone had a carbon content in excess of that of the starting material (0.008 wt. %). An overall reduction in the impurity content of iron,

Table 6 Analysis Data for Molybdenum

- Impurity level in parts per million -

	C	N	O	H	Fe	Si	Al	Cr	Cu	Ni	W	Co	V	Be	Ti	Ref.
Powder	10/300	20/30	500/1500		10	10	10	10	10	20	10					36
Sintered	7	60	80													37
	140	56	17		10/1000	5/500										39
Arc-Melted	20	<10	22	0.6		Total Metallics ~3510 p.p.m.										8
	260	<10	9	0.6		Total Metallics ~3510 p.p.m.										8
	500	10	30	3	-											38
	400	-	30	-	-											40
Zone-Refined H.F. Heating	-	-	-	-	<1	50	<0.2	<0.1	-	<0.2	50	<0.1	1	5		41
Electron-Beam Melted	30	-	2	0.3											<80	34
	170	-	8	0.8	1	30	8	<1	<1	<1	<100	<5	-	-	<1	34
Electron-Beam Zone-Refined	12	<1	<1	<1	5	<5	<5	<5	<2	<3	-					35
	55	-	1	-	<1	10	-	<20	11	<1	-	2				42
Electron-Beam Zone-Refined Mo-Re alloys	18	17	0.4	0.2	5	5	<5	<5	<2	<3	-	-				43

copper, and nickel was due to vaporization from the molten molybdenum.

Lawley and Maddin[43] were able to electron-beam zone refine high-purity alloy single crystals of molybdenum -- rhenium over the composition range 5-35 at. % Re. By using the zone-levelling technique it was possible to maintain a homogeneous distribution of rhenium along the single crystals. The analysis for a 35 at. % Re alloy is included in Table 6. Again it is seen that the total interstitial impurity content is < 40 p.p.m.

Workability

Several examples serve to illustrate the excellent cold workability of electron-beam consolidated molybdenum. Lawley et al[35] were able to cold-swage 6 zone-pass single crystals ($\sim$ 0.1" dia.) to 80% reduction in area before the onset of cracking. Likewise, Spacil and Wulff[45] enclosed 1/4" dia. single crystals in thick steel tubing prior to swaging at room temperature, and in this way were able to obtain reductions $\sim$90% in area. Moreover, it was found that annealing at 2100°C, followed by slow cooling, gave a highly ductile material in spite of the coarse grain structure.

The cold-rolling of high-purity single crystal molybdenum has also proved successful. Wah Chang Corporation[44] rolled 3" dia. single crystal bar to sheet $\sim$ 0.010" thick. The ductility of the single crystals grown by Belk[42] was such that they could be cold rolled to reductions $\sim$ 30% without cracking. Ogawa and Maddin[46] cold-rolled 0.1" dia. single crystal molybdenum bar directly to 0.010" strip, followed by sandwich rolling to 0.005" foil without intermediate

annealing. The crystals were given an initial annealing treatment in the electron-beam floating zone unit at 2500°C.

In order to assess the room temperature workability of polycrystalline electron-beam melted molybdenum ingot, Semchyshen and Barr[47] subjected transverse discs, cut from two separate ingots, to cold pressing. Carbon content and grain size were the only variables. It was found that linear reductions ~ 40% and ~14% were obtained prior to cracking for carbon contents of 20 p.p.m. and 170 p.p.m. respectively. The higer ductility of the low carbon ingot is apparent. The grain-size of the 0.002% ingot was ≃ 2.5 times greater than that of the 0.017% C ingot. Had the grain sizes been comparable in the two cases, the difference in ductility would undoubtedly have been greater.

Mechanical Properties

The effect of electron-beam zone refining on the hardness of single crystal molybdenum is illustrated in Figure 9 (Lawley[48]). The hardness figures refer to average values for the single crystal structure. Even though the lattice is cubic, there is a definite dependence of hardness on orientation. In the softest orientation the Knoop figure is as low as 145 (VDH ≃132). The minimum average hardness is ≃142 VDH. For comparison, the hardness figure for unalloyed polycrystalline arc-cast molybdenum is about 180 VDH. Hardness values reported for single crystal zone-refined tantalum, niobium, and vanadium are 68, 37, and 62 VDH respectively. It is interesting to note that the Knoop hardness decreases continuously over the first five zone passes, indicating a progressive increase in

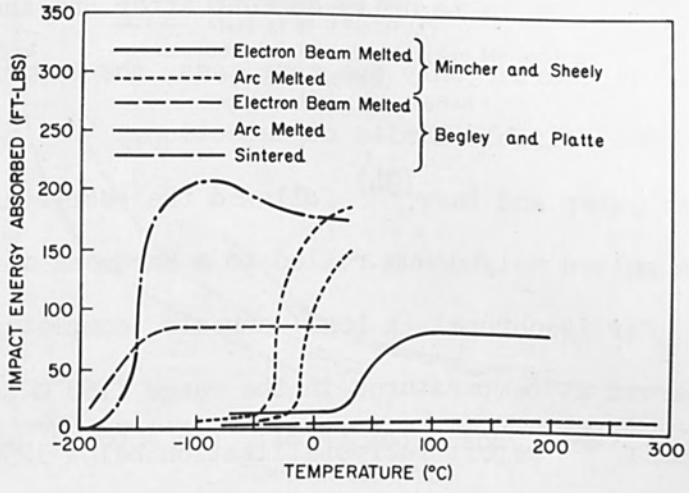

Fig. 8 The impact strength of niobium as a function of temperature.

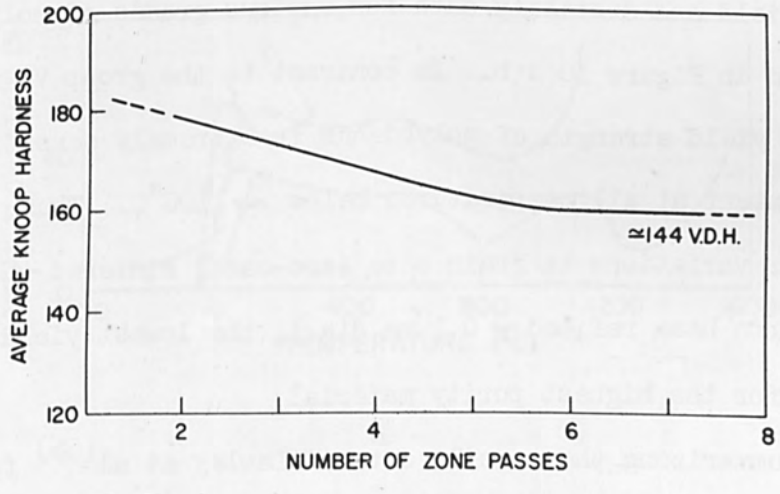

Fig. 9 The effect of zone-refining on the hardness of molybdenum[35].

purity. Spectrographic and gas analyses on the other hand show no systematic differences in impurity content after one and six zone-passes. Evidently, after only one zone pass, the impurity levels are at, or below, the reliable limits of detection.

Semchyshen and Barr[34] followed the recrystallization of electron-beam melted molybdenum rolled to a hardness in the range 236-254 VDH. For isochronal (1 hour) anneals, complete recrystallization was observed at temperatures in the range 1150°C to 1180°C. Spacil and Wulff[45] report recrystallization below 1250°C in similar material initially cold swaged to ~90% reduction in area. These values are somewhat lower than those reported for commercial purity molybdenum but are higher than the value reported by Wong[49] for cold -worked Pentachloride molybdenum. The rate of grain growth observed in the beam melted material is higher than that of powder metallurgy or arc-cast molybdenum.

Yield and ductility data for various grades of molybdenum are compared in Figure 10 a,b. In contrast to the group VA refractory metals, the yield strength of molybdenum is extremely sensitive to impurity content at all temperatures below ~ 400°C. Thus, after allowing for variations in grain size (arc-cast, sintered ~0.05 mm dia., electron beam refined ~ 0.1 mm dia.), the lowest yield stress values are for the highest purity material.

Summarizing the tensile data of Lawley et al[35] for single crystal and polycrystalline electron beam zone-refined material, over the temperature range 4.2°K to 373°K: (1) Molybdenum > 99.995% purity behaves in a ductile manner down to 4.2°K, at which temperature the material is still capable of withstanding ~5% uniform strain

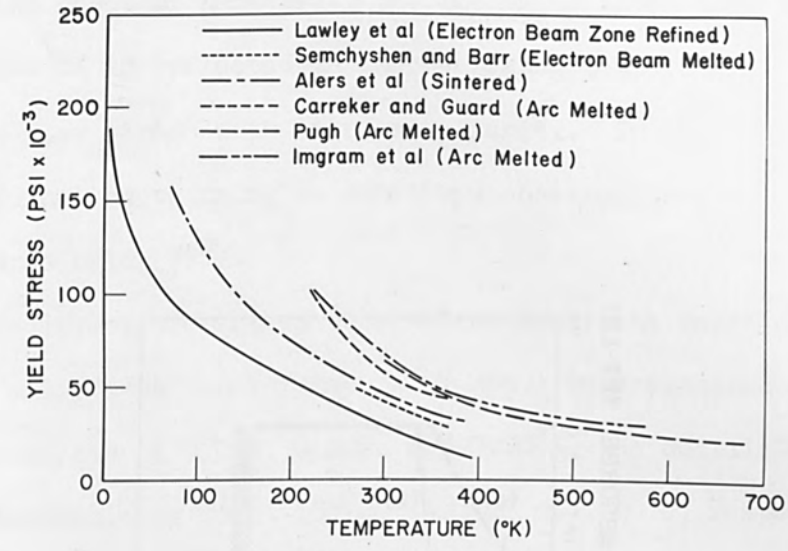

Fig. 10(a) The effect of temperature on the yield strength of molybdenum.

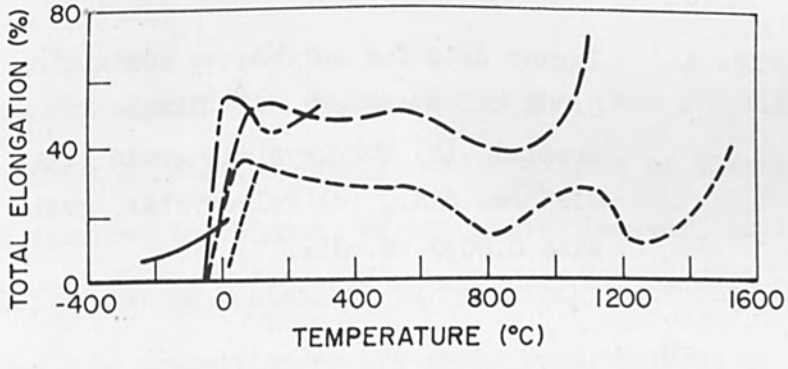

Fig. 10(b) The effect of temperature on the ductility of molybdenum.

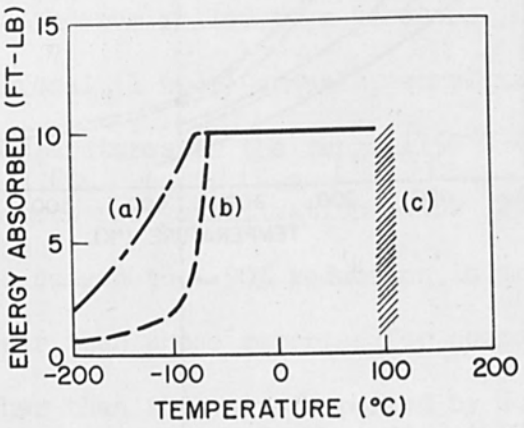

Fig. 11 Impact data for molybdenum containing 0.002 wt. % carbon: (a) Single crystal, (b) Polycrystal, grain size 0.25 cm. dia., (c) Polycrystal, grain size 0.0032 cm. dia.

(strain to the onset of necking). (2) The important effect of impurities $< 0.001\%$ is reflected in the decreased temperature dependence of yield and flow stress with increasing purity. In the highest purity material deformation twinning is sometimes observed in single crystals at temperatures below $77^{\circ}K$.

The impact properties of electron beam zone refined single crystals of molybdenum (un-notched, 1/4" dia.) were examined by Belk[42]. For carbon contents of 0.001, 0.002, and 0.008%, the ductile-brittle transition temperatures were $-180^{\circ}C$, $-140^{\circ}C$, and $-40^{\circ}C$, respectively. The effect of grain boundaries on the transition properties may be estimated from the fact that a forged and recrystallized 0.002% C crystal (grain dia. $\simeq 0.25$ cm.) gave a transition temperature of $-80^{\circ}C$, Figure 11. Arc-cast unalloyed molybdenum, having the same carbon content (0.002% C) but a finer grain size (0.032 mm dia.), shows a corresponding transition temperature of $\sim 100^{\circ}C$[8].

Tungsten

Tungsten (Group VIA, third long series) has a melting point of $3410^{\circ}C$, highest of all the metals, and a modulus of elasticity higher than that of niobium, molybdenum, or tantalum. However, as in the case of molybdenum, oxidation resistance is relatively poor, and in addition, the ductile-brittle transition occurs above room temperature, thereby imposing limits on structural applications. Consolidating techniques aimed at improving the purity and cold-workability of tungsten are still largely in the experimental stage. Several investigations have been carried out on single crystal tungsten grown by electron-beam zone refining, but there have been few specific studies of the work-

ability and mechanical properties of electron beam melted ingot. This is, of course a reflection of the practical difficulties involved in such a venture.

Purity

Impurity levels found in the various grades of tungsten are listed in Table 7. From the data of Schadler[53] on material given two zone passes at 3 mm per min., it is apparent that of the common impurities only carbon and molybdenum are detected after zoning. The 298°K to 4.2°K resistivity ratio (Bean, DeBlois, Nesbitt[54]) along the zoned sample gives a measure of the amount of impurity in solid solution, and it is found that the crystal is purified both by vacuum distillation and by zone-refining. Spectrographic analyses of zoned tungsten listed by Atkinson[50] are in general accord with these observations. A carbon level in the range 20-40 p.p.m. appears common to all electron-beam zone refined single crystals[50,51,53]. This is about twice the level attained in tungsten following a short-time anneal in high vacuum at temperatures ~2000°C. It is believed that carbon contamination occurs from back-streaming of diffusion-pump oil, or from gaskets in the working chamber. Votava and Berghezan[55] are actually constructing electron-beam zone refining apparatus with a hydrocarbon-free working chamber, and in this way it is hoped to obtain total interstitial concentrations of the order of one part per million.

Workability

Very little data are available concerning the workability of electron-beam refined tungsten. Orehotsky[56] mentions the cold working of zone-refined rods, but no specific reduction figures are

Table 7 Analysis Data for Tungsten

- Impurity levels in parts per million -

	C	O_2	N_2	H_2	Ca	K	Na	Fe	Mo	Si	Al	Mg	Cu	Ni	Mn	Réf.
Powder	70	-	-	-	22	180	-	2	-	21	5	7	1/10	1/10	<2	50
Sintered	63	15	5	-												51
	70	9	8	2	10	10		38		30	5	<3	<1	-	<2	50
Arc-Melted	-	7	6	6	nil			nil		10/30	nil	1/10	<1	nil	nil	50
	30	20	3	1				40		26			2	5		52
	70	3	0.3	0.1	10	40	20	10	40	20						53
Levitation-Melted	-	3	1	2				1/10		10/100		1/10	nil			50
Electron-Beam Zone-Refined	-	2	0.5	0.6	1/10			1/10	10/100	nil	10/100	10/100	<1	-		50
	32	<0.2	<0.4						30							51
	20	10	<1	-	<1				1	<1						53
	40	50	30					10	10							5

available. Allen et al[51] observe cracking in single crystals rolled at 400°C and 600°C. However, at 800°C it was possible to reduce material to a total 50% reduction, using 10% reductions per rolling pass.

Mechanical Properties

The recrystallization behavior of electron beam refined and sintered tungsten (Allen et al[51]) is illustrated in Figure 12. It is apparent that recrystallization occurs at a lower temperature in the beam refined material (1300°C) than in the sintered grade (1700°C). Arc-melted tungsten of comparable purity (Atkinson[50]) recrystallizes at approximately 1350°C. The trend towards a lower recrystallization temperature with increasing numbers of zone passes indicated that trace metallic impurities exerted a more potent effect than did interstitials, since the concentrations of the latter remained approximately constant following the first zone pass. Orehotsky[57] reports that zone-purified, cold worked tungsten recrystallizes at temperatures ~1100°C. Without zone-purification, the corresponding temperature is above 1500°C.

Atkinson and Koo[50], Schadler[53], and Ferriss et al[5] have made detailed studies of the effect of electron-beam zone refining on the mechanical properties of single crystal tungsten. These studies include aspects of slip, twinning, cleavage, and the effect of orientation. In general, it is found that the critical resolved shear stress decreases with increasing purity, and crystals may withstand 2-4% plastic strain at temperatures down to 20°K. For crystals of constant orientation, the proportional limit, measured under four-point bending, increases from 78,000 p.s.i. at the starting

end to 98,000 p.s.i. for material at the finishing end of zoned material. These crystals are sufficiently ductile that they can be bent or twisted into circular forms at room temperature. Quantitatively, Pugh[58] showed conclusively that the high ductility of electron-beam refined single crystals is directly related to the reduction in impurity content. Thus, single crystals grown by the strain-anneal method were found to be more ductile than polycrystalline material, but significantly less ductile than electron-beam refined crystals of similar orientation. In the particular case of an orientation close to (100) at room temperature, the strain anneal crystal had an elongation to fracture ~2% compared with a value ~ 22% for beam refined material.

Atkinson and Koo[50] obtained a ductile-brittle transition at ~ -110°C for electron-beam refined crystals with an orientation close to (011). Allen et al[51] also report that the ductile-brittle transition occurs below room temperature for single crystals. The absolute value of the transition temperature is extremely sensitive to surface imperfections so that great care is necessary in specimen preparation.

Bend ductility data for powder-metallurgy tungsten and recrystallized zoned material are given in Figure 13[51]. The ductility curve for the recrystallized zone-purified material is only 50-100°C lower than that of recrystallized powder-metallurgy material and gives a transition at ~ 320°C. This is significantly higher than the value of 230°C found for the wrought-stress relieved powder-metallurgy material. Therefore, it is apparent that the

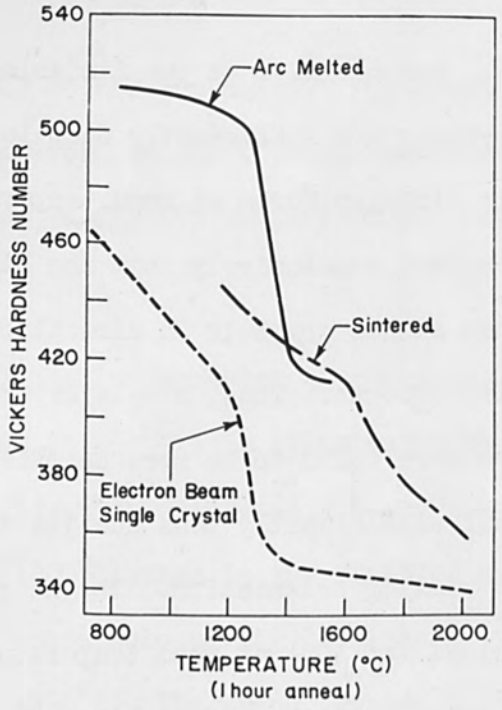

Fig. 12 Isochronal annealing curves for tungsten[50,51].

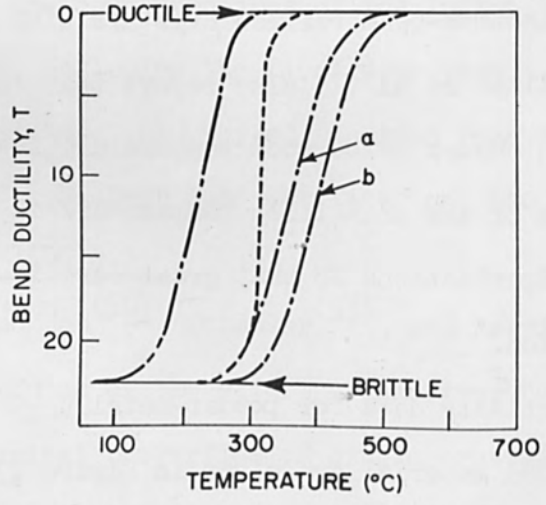

--------- Electron Beam. 50% Reduction.
Recrystallised 1 hr. 1400-1600°C

——·——· Sintered. 75% Reduction.
Recrystallised 1 hr. (a) 1800°C
(b) 2600-2800°C

——·--—— Sintered. Wrought and Stress
Relieved 1 hr. 1200°C

Fig. 13 Ductile brittle transition behaviour of tungsten[51].

presence of high angle grain boundaries is more detrimental to low-temperature ductility than is the presence of impurity elements. In agreement with these findings, Orehotsky[57] observes a lowering of the transition temperature with increasing purity, for comparable grain sizes.

The Platinum Group Metals

The platinum-group transition metals consist of ruthenium, rhodium, palladium, osmium, and platinum. In the periodic table, ruthenium, rhodium, and palladium fall in groups VIIIA, VIIIB, and VIIIC, respectively of the second long series, while osmium, iridium, and platinum are positioned in groups VIIIA, VIIIB, and VIIIC, respectively of the third long series. Compared with the refractory metals and alloys, the platinum group metals are higher in cost and relatively scarce. Nevertheless, in certain areas, these materials offer advantages over refractory materials. Thus, in general, the platinum group metals are resistant to mineral acids and certain oxidizing acids. Specifically, iridium maintains its strength at high temperatures, and this is coupled with good oxidation resistance and resistance to carbonaceous atmospheres[59]. Ruthenium[60] on the other hand shows poor oxidation characteristics but possesses the lowest neutron cross-section of any of these metals. The outstanding attribute of rhodium is its excellent high-temperature oxidation resistance[61]

Unfortunately, with the exception of platinum and palladium, it is extremely difficult to work these materials into strip or wire form unless reductions are carried out at high temperatures. While

this is not totally unexpected in the case of osmium and ruthenium (metals having a hexagonal close packed lattice structure), the lack of room temperature ductility in rhodium and iridium (face-centered cubic lattice structure) is contrary to expectation. It is, therefore, desirable to understand the inter-relation between workability, mechanical properties, and purity in this group of metals.

With high melting points ($>1500^{\circ}C$) and relatively low vapor pressures at the melting point ($< 10^{-2}$ mm Hg), the platinum group metals are ideally suited to electron beam floating zone-refining. Several studies have been carried out concerning the purity and workability of platinum-group metals produced in this way, although it should be stressed that the data available at the present time constitute a relatively incomplete study.

Purity

In Tables 8-11, a comparison is made of the metallic impurity levels present in ruthenium, rhodium, iridium, and platinum for various forms of each metal (i.e., powder, sintered stock, arc-melted, electron beam zone-refined). These figures are intended only as a general guide to the overall impurity spectrum. For a specific sample, the final impurity levels, following electron beam floating zone refining, will depend on the number of zone passes, on the speed of zoning, the working pressure, and to some extent on the purity of the starting material. With regard to the oxygen, nitrogen, and hydrogen content, Table 12, based on the data of Jaffee et al[61], illustrates the effectiveness of the floating zone techniques on purification. In general, purification by the electron beam floating zone technique

Table 8 Spectrographic Analysis - Ruthenium

- parts per million -

Impurity	Powder (60,65) (~99.0%)	Sintered (~99.9%) (62,60,63)	Electron Beam Melted* (From Sintered Stock) First Zone	Last Zone (62,60,63)
Os	< 1000	< 100	< 100	< 100
Pd	10-200	10-200	< 5	3
Rh	10-100	10-100	< 10	10
Pt	10-100	10-100	~ 10	~ 10
Ir	100-1000	100-1000	-	-
Fe	100-1000	20-200	< 50	100
Si	10-100	2-20	< 10	~ 1
Cu	100-1000	2-20	< 10	~ 1**
Au	10-100	2-20	< 20	< 1
Sn	10-100	5-50	-	-
Pb	10-100	5-50	-	-
Ni	10-100	< 20	< 20	1
Mg	10-100	2-20	1	-
Mo	100-1000	-	40-400	-
Co	1000-10,000	~ 1	< 1	< 1**
Ti	1000-10,000	~ 1	~ 1	~ 1

* Zoning speeds 2.5 mm/min.

** Probable limit of detection for Cu and Ni is 1 p.p.m.

Table 9 Spectrographic Analysis - Rhodium

- parts per million -

Impurity	Sintered[64] ≃99.8%	Bar Stock[65] ≃99.93%	Electron Beam Melted* (From Bar Stock)[65] First Zone	Last Zone
Pt	<100	10	500	500
Pd	100	-	-	-
Ru	260	100	100	100
Ir	800	100	100	2000
Fe	160	100	500	200
Pb	< 1	-	-	-
Si	trace	30	20	30
Ag	trace	1	1	1
Cu	trace	50	10	10
Ca	trace	30	5	5
Al	trace	10	10	10
Ni	trace	40	100	10
Co	not detected	10	100	20

* Zoning speeds in excess of 2.5 mm per min.

Table 10 Spectrographic Analysis - Iridium

- parts per million -

Impurity	Sintered[62] ≃99.85%	Arc-Melted[59] ≃99.9%	Electron Beam Melted* (From Sintered Stock)[62] First Zone	Last Zone
Pt	210	100	10	30
Pd	370	10	not detected	140
Rh	330	500	10	90
Ru	not detected	-	not detected	not detected
Au	trace	-	not detected	not detected
Ag	trace	50	not detected	not detected
Fe	520	30	10	20
Ni	10	-	not detected	130
Pb	1	-	not detected	not detected
Co	trace	-	not detected	not detected

* 15 Zone passes at 2.5 mm per min.

Table 11 Spectrographic Analysis - Platinum

- parts per million -

Impurity	Air Melted[62] Bar Stock (commercial purity) ≃ 99.95%	Air Melted[65,62] Bar Stock (high purity) ≃ 99.998%	Electron Beam Melted* (From High Purity Stock)[62] First Zone/	Last Zone
Pd	80	9	4	5
Rh	20	not detected	not detected	not detected
Ru	200	not detected	not detected	not detected
Ir	not detected	not detected	not detected	not detected
Au	1	1	not detected	not detected
Ag	100	2	not detected	not detected
Ca	3	1	2	2
Cu	3	-	-	-
Fe	150	10	10	10
Ni	20	< 100	-	-
Pb	2	< 100	-	-
B	not detected	-	-	-
W	not detected	not detected	not detected	trace

* 15 Zone Passes at 2.5 mm per min.

Table 12 Vacuum Fusion Analyses of Platinum Group Metals

	-parts per million*-		
Ruthenium[63]	Oxygen	Hydrogen	Nitrogen
99% Powder	3280	20	118
Sintered Bar (Vacuum)	63	0.4	< 2
Electron Beam Melted	7	<0.2	< 3
Rhodium[65,63]			
99.9% Bar Stock	27	0.2	3
Electron Beam Melted	2	0.2	3
Osmium[61]			
99.5% Powder	947	22	-
Sintered (hydrogen)	38	0.7	-
Electron Beam Melted	20	1.2	-
Iridium[65]			
99.9% Bar Stock	760	52	-
Electron Beam Melted	4	0.5	-
Platinum[63]			
Bar Stock (Air-Melted)	5	0.1	<2
Electron Beam Melted	< 1	< 0.1	< 1

* Sensitivity limits for the analyses are approximately: $H_2 \pm 1$ p.p.m., $O_2 \pm 7$ p.p.m. $N_2 \pm 1$ p.p.m.

may be attributed chiefly to preferential evaporation of volatile metallic impurities, and to outgassing at the usual working pressures, $\sim 10^{-5}$ mm Hg.

For ruthenium, Rhys[60,62], using a zoning speed of 2.5 mm per min. observes that nickel and rhodium are segregated in the end zone to a level above that present in the original material. Also in ruthenium Himes et al[63], using a slower zoning speed $\sim$0.2 mm per min. obtain effective segregation of iridium, molybdenum, palladium, and rhodium. For true zone-refining, speeds of this magnitude are considered necessary. As indicated in Table 12, the oxygen, hydrogen, and nitrogen contents are extremely low following electron beam floating zone melting.

In the electron beam treatment of rhodium, severe outgassing occurs. Rhys and Calverley[64] report that upwards of seventeen zone-passes ($\sim$12 mm per min.) are required for zoning without further gas evolution. Under these conditions, the overall level of palladium and iron impurity is reduced, but the platinum, ruthenium, and iridium levels are unaltered. Himes et al[63] and Holden et al[65] report a sharp reduction in oxygen content (Table 12) but little change in the metallic impurities. Only the calcium and copper impurities appear to be reduced to any extent. The similarity in the impurity levels at the front and end zones again indicates that the main source of purification is volatilization rather than segregation.

Little data are available for iridium. After fifteen zone passes at 2.5 mm per min., Rhys[62] observes that only nickel is concentrated (in the final zone) to any great extent. This is

rather surprising since the latter would be expected to volatilize in common with the other metallic impurities. By comparison with commercial-purity iridium, the electron-beam refined material has an extremely low oxygen and hydrogen content (Holden et al[65], Table 12).

With relatively impure platinum (~99.94%) as starting material, zoning at speeds up to 10 mm per min. causes considerable purification by evaporation, and this is accompanied by segregation of rhodium, ruthenium (elements not preferentially removed by evaporation), and beryllium[62]. As would be expected, with higher purity starting material (platinum ~99.998%), the removal of impurities is less marked, even if the zoning speed is reduced to 2.5 mm per min. In the usual experimental beam melting arrangement, the filament (tungsten) "sees" the metal, and in this case tungsten contamination may occur.

Workability

Preliminary studies have been made concerning the fabricability of rhodium, ruthenium, and iridium, as prepared by electron beam floating-zone refining. In each case, the fabricability is considerably enhanced over arc-cast or sintered material, particularly when the material is in single crystal form.

Single crystals of rhodium so prepared may be cold rolled or swaged to ~90% without cracking[66,64]. For the swaged material, Rhys and Calverley[64] find that the recrystallized polycrystalline form is no longer ductile, intercrystalline fracture occurring with further cold work. From this observation it is considered that grain boundaries and impurities localized at these boundaries determine the

mode of plastic deformation in rhodium. The electron beam melted polycrystalline material may be readily swaged (~80% reduction) at temperatures ~ 900°C. By comparison, less pure rhodium, as prepared by sintering, is more difficult to fabricate . A carefully controlled hot working procedure ~1500°C, followed by moderate amounts of cold work, is required.

According to Holden et al[65], polycrystalline ruthenium, produced by electron beam zone-refining, may be readily hot rolled ~85% reduction without cracking. This is a capacity for workability better than that of arc-melted material and equal to that of sintered stock. Rhys[60] reports that single crystal bars of electron beam zone refined ruthenium may be readily bent, at room temperature, to a circle of radius ~six times the bar diameter (3/8"). Arc-cast and sintered ruthenium, when treated in this manner, show brittle behavior. Again by comparison extremely careful procedures are necessary in the preparation of powders and in the sintering process prior to hot working (~1400°C - 1500°C). With sintered compacts, cold working (pressing and rolling) is limited to ~10% reduction between anneals with a possible total reduction of only ~50%. Rhys[60] concludes that electron beam heating offers the best possibilities in obtaining high-purity ruthenium with reasonable ductility. It appears that oxygen is the impurity most responsible for lack of ductility at ambient temperatures.

Similar considerations apply to iridium. Polycrystalline electron beam melted material may be readily swaged at 1500°C[65]. In single crystal form reductions ~25% are possible at room temperature prior to cracking (cf. rhodium ~90% reduction). On the other hand,

arc-melted and sintered materials require a working temperature~1500°C, while at room temperature, only very thin sections may be worked.

Mechanical Properties

Only in the case of rhodium and iridium are tensile data available for electron-beam zone-refined material. Tensile strength and elongation values for rhodium are given in Figure 14, a,b[65]. For both metals the elevated temperature strength properties of recrystallized zoned material are significantly higher than those of the as-received recrystallized rod stock. Commonly, the more pure material has a lower strength coupled with higher ductility at low temperatures*. In the present case there is, as yet, no meaningful explanation for the reverse behavior although it could be that the effects of grain size and of the nature of prior deformation are responsible.

The occurrence of a ductile-brittle transition at~500°C in iridium is surprising. In fact, this is the only face-centered cubic metal in which the transition has been reported. Holden et al[65] observe the transition in high and low purity material. It therefore appears likely that extremely small levels of certain impurities, segregated at grain boundaries, are responsible for the extreme intergranular cracking at low temperatures.

The strengths of rhodium, iridium, and ruthenium, when plotted against the homologous temperature, are approximately equivalent and are higher than those of platinum and palladium, and on a par with values for molybdenum and tungsten[65]. Data for rhodium, iridium, and platinum are given in Fig. 15.

* This effect is most marked in the refractory body-centered cubic metals.

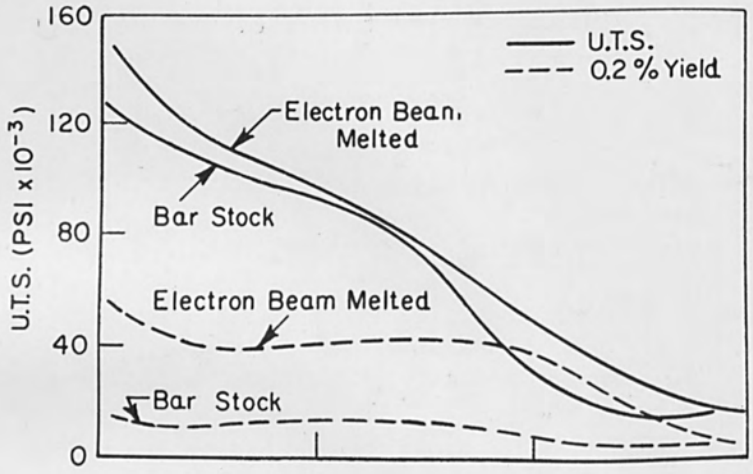

Fig. 14(a) The effect of temperature on the ultimate strength of rhodium[65].

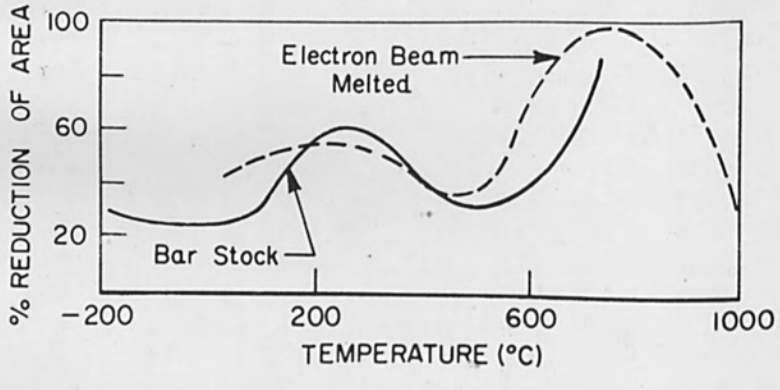

Fig. 14(b) The effect of temperature on the ductility of rhodium[65].

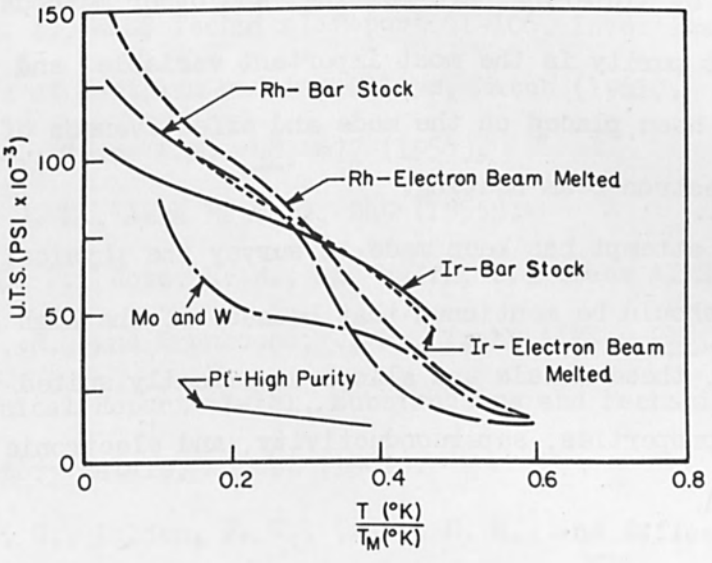

Fig. 15 Tensile Strength as a function of the homologous temperature, for annealed platinum group metals[65].

Summary

The workability and mechanical properties of the refractory and platinum group metals, prepared by electron-beam melting or refining, have been compared and contrasted with those of materials consolidated by sintering, arc-melting, and other methods. It is apparent that purity is the most important variable, and particular emphasis has been placed on the mode and effectiveness of purification by electron-beam heating.

No attempt has been made to survey the physical properties. However, it should be mentioned that because of the high state of purification, these metals and alloys are ideally suited to studies of magnetic properties, superconductivity, and electronic structure.

References

(1) Michael, A. B., Refractory Metals and Alloys, Interscience Publishers, New York/London, 1960, p. 357.

(2) Schmidt, F. F., Klopp, W. D., Maykuth, D. J., Ogden, H. R., and Jaffee, R. I., WADD Technical Report 61-106, Investigation of the Properties of Tantalum and its Alloys, March (1961).

(3) Pugh, J. W., Trans ASM., 48, 677 (1956).

(4) Bechtold, J. H., Acta Met., 3, 249 (1955).

(5) Ferriss, D. P., Rose, R. M., and Wulff, J., Trans AIME., in press.

(6) Schussler, M., and Brunhouse, J. S., Trans AIME., 218, 893 (1960).

(7) WADD Technical Report 61-181, Substructure and Mechanical Properties of Refractory Metals, August (1961).

(8) Imgram, A. G., Holden, F. C., Ogden, H. R., and Jaffee, R. I., Trans AIME., 221, 517 (1961).

(9) Calverley, A., S.E.R.L. Electron Beam Symposium, Baldock, England, 1959, p. 1.

(10) McCullough, H. M., Symposium on Newer Metals, ASTM Tech. Publication No. 272, Philadelphia, 1960, p. 160.

(11) Holden, F. C., Douglass, R. W., and Jaffee, R. I., Symposium on Newer Metals, ASTM Tech. Publication No. 272, Philadelphia, 1960, p. 68.

(12) Low, J. R., Properties of Metals in Materials Engineering, ASM, Cleveland, 1949, p. 17.

(13) Smith, H. R., Hum, J. Y. K., Donlevy, A., and Hunt C. d'A., J. Less Common Metals, 2, 69 (1960).

(14) Morgan, R. P., and Butler, T. E., AIME Fall Meeting, Detroit (1961).

(15) Adams, M. A., Private Communication.

(16) Mordike, B. L., Z. für Metallkunde, 52, 587 (1961).

(17) Myers, R. H., Metallurgia, 41, 301 (1950).

(18) Begley, R. T., WADD Technical Report 57-344, Development of Niobium Base Alloys, March (1959).

(19) O'Driscoll, W. G., and Miller, G. L., 85, 379 (1956-57).

(20) Aschoff, W. A., and Baroch, E. F., AIME Fall Meeting, Detroit (1961).

(21) Wessel, E. T., and Lawthers, D. D., The Technology of Columbium, J. Wiley and Sons, N. Y., 1958, p. 66.

(22) Enrietto, J. F., Sinclair, G. M., and Wert, C. A., Columbium Metallurgy, Interscience Publishers, New York/London, 1961, p. 503.

(23) Mincher, A. L., and Sheely, W. F., Trans AIME., 221, 19 (1961).

(24) Begley, R. T., and Platte, W. N., WADD Technical Report 57-344, Development of Niobium-Base Alloys, May (1960).

(25) Adams, M. A., Roberts, A. C., and Smallman, R. E., Acta Met., 8, 328 (1960).

(26) Wessel, E. T., France, L. L., and Begley, R. T., Columbium Metallurgy, Interscience Publishers, New York/London, 1961, p. 459.

(27) Wellings, J., and Maddin, R. M., Private Communication.

(28) Smith, H. R., d'A Hunt, C., and Hanks, C. W., J. Metals, 11, 112 (1959).

(29) Page, J. P., Oak Ridge National Laboratory Report 2372, September (1957).

(30) Williams, L. R., J. Inst. Metals, 85, 385 (1956-57).

(31) Begley, R. T., and France, L. L., Symposium on Newer Metals, ASTM Tech. Publication No. 272, Philadelphia, 1960, p. 56.

(32) Lement, B. S., Allen, S., Parsmore, E. M., Boyd, J. E., Andersson, C., and Vilks, I., WADD Tech. Report 61-181, August 1961, p. 28.

(33) DMIC Memorandum 129, Battelle Memorial Institute, October (1961).

(34) Semchyshen, M., and Barr, R. Q., Refractory Metals and Alloys, Interscience Publishers, New York/London, 1960, p. 283.

(35) Lawley, A., Van den Sype, J., and Maddin, R., J. Inst. Metals, In Press.

(36) Toensing, C. H., The Metal Molybdenum, ASM, Cleveland, 1958, p. 31.

(37) Alers, G. A., Armstrong, R. W., and Bechtold, J. H., Trans AIME., 212, 523 (1958).

(38) Pugh, J. W., Trans. ASM., 47, 984 (1955).

(39) Bechtold, J. H., Trans. AIME., 197, 1469 (1953).

(40) Carreker, R. P., and Guard, R. W., Trans. AIME., 206, 178 (1956).

(41) Buehler, E., and Kunzler, J. E., Trans. AIME., 221, 957 (1961).

(42) Belk, J. A., S.E.R.L. Electron Beam Symposium, Baldock, England, 1959, p. 9.

(43) Lawley, A., and Maddin, R., Trans. AIME, In Press.

(44) ASM Metals Review, 34, 20 (1961).

(45) Spacil, H. S., and Wulff, J., The Metal Molybdenum, ASM, Cleveland, 1958, p. 262.

(46) Ogawa, K., and Maddin, R., Private Communication.

(47) Semchyshen, M., and Barr, R. Q., Arc-Cast Molybdenum and Tungsten Base Alloys, Climax Molybdenum Co., 1957-59, p. 125.

(48) Lawley, A., Refractory Metals and Alloys, Interscience Publishers, New York/London, 1960, p. 316.

(49) Wong, J., Sc.D. Thesis in Metallurgy, Mass. Inst. Tech., (1955).

(50) Atkinson, R. H., and Koo, R. C., WADD Technical Report 60-37, Physical Metallurgy of Tungsten and Tungsten Base Alloys, May (1960).

(51) Allen, B. C., Maykuth, D. J., and Jaffee, R. I., J. Inst. Metals, 90, 120 (1961).

(52) WADD Technical Report 60-144, Investigation of the Properties of Tungsten and Its Alloys, May (1960).

(53) Schadler, H. W., Trans. AIME., 218, 649 (1960).

(54) Bean, C. P., DeBlois, R. W., and Nesbitt, L. B., J. Appl. Phys., 30, 1976 (1959).

(55) Votava, E., and Berghezan, A., Private Communication.

(56) Orehotsky, J. L., AIME Fall Meeting, Philadelphia, (1960).

(57) Orehotsky, J. L., AIME Fall Meeting, Detroit, (1961).

(58) Pugh, J. W., Electron Beam Melting Symposium, Alloyd Corporation, Boston, 1959, p. 89.

(59) Mordike, B. L., and Brookes, C. A., Plat. Metals Rev., 4, 94 (1960).

(60) Rhys, D. W., J. Less Common Metals, 1, 269 (1959).

(61) Jaffee, R. I., Maykuth, D. J., and Douglass, R. W., Refractory Metals and Alloys, Interscience Publishers, New York/London, 1960, p. 383.

(62) Rhys, D. W., S.E.R.L. Electron Beam Symposium, Baldock, England 1959, p. 22.

(63) Allred, W. P., Hines, R. C., and Goering, H. L., S.E.R.L. Electron Beam Symposium, Baldock, England, 1959, p. 27.

(64) Calverley, A., and Rhys, D. W., Nature, 183, 599 (1959).

(65) Holden, F. C., Douglass, R. W., and Jaffee, R. I., Symposium on Newer Metals, ASTM, Tech. Publication No. 272, Philadelphia, 1960, p. 68.

(66) High-Temperature Properties and Alloying Behavior of Refractory Platinum Group Metals, ONR Tech. Report 39-067.

GROWTH OF TUNGSTEN SINGLE CRYSTALS BY THE STRAIN-ANNEAL METHOD USING ELECTRON BEAM HEATING *

By

S. R. Maloof
Principal Scientist
Research and Advanced Development Division
Avco Corporation
Wilmington, Massachusetts

ABSTRACT

Tungsten single crystals 45 and 60 mil in diameter up to three inches in length were grown by the strain-anneal method using electron beam heating both for the recrystallization treatment prior to straining and for the elevated temperature heating. The steep temperature gradient obtained with electron beam heating, measured with an optical pyrometer to be greater than 1000°C per inch, is largely responsible for the high yield of crystals obtained (~80 per cent). The effects of the recrystallization treatment, straining, high temperature heating, speed of zone travel, etc. on the perfection of the crystals grown will be discussed and compared with crystals grown by the floating-zone method.

The ductility of single crystal tungsten is discussed and compared to that of polycrystalline tungsten. The yield behavior of single crystal tungsten is shown to be anisotropic.

---

* This work was carried out at M.I.T. in 1961 under the supervision of Professor E. Orowan while the author was Institute Guest in the Department of Mechanical Engineering.

GROWTH OF TUNGSTEN SINGLE CRYSTALS BY THE STRAIN-ANNEAL METHOD USING ELECTRON BEAM HEATING

INTRODUCTION

Single crystals of fine tungsten wire were made by the firm of Julius Pintsch in 1913.[1] In this process finely divided tungsten powder containing 2 per cent thoria is mixed with an organic binder and extruded through a diamond die into thin threads. The thread is converted into a single crystal by moving it at 50 mm/min through a narrow hot zone (2000-2200°C). Goucher[2] in 1920 described the making of single crystal wires by a somewhat different method. The starting material is drawn tungsten wire (3 mil) containing 0.60 per cent thoria. The wire is held at 1600°C for one second to obtain an equiaxed grain structure, then reduced 5-7 per cent in area by drawing it through a die heated to 300°C. Heating of the wire under the conditions described above converts it into a single crystal.

In both processes the main objective was not necessarily to produce a single crystal, but to obtain a creep-resistant wire containing a few large interlocked crystals.

It is more fashionable today to grow pure tungsten single crystals by the floating-zone method.[3] Crystals 1/8-inch in diameter are commonly produced by this method. Difficulties in zone stabilization are

encountered on smaller diameter rods. The present program required single crystals 45-60 mils in diameter. To avoid the necessity for centerless grinding of crystals grown by the floating-zone method to size and to minimize the danger of introducing additional dislocations into the crystals by the cold working, it was decided to produce the crystals by the strain-anneal method.[4] Furthermore, crystals grown by recrystallization and grain growth methods are reported to be freer from defects such as mosaic or subgrain structures than crystals grown from the melt.[5]

EXPERIMENTAL

Tungsten rod (99.95 per cent pure) was obtained from the Sylvania Electric Company in the ground and polished condition. The rod was recrystallized by moving it at 60 mm/min. under an electron beam, the beam power adjusted ($\sim$ 450 watts) so as to heat the rod to about 1550°C (Brightness temperature). This work was carried out in the modular electron beam laboratory unit at the Alloyd Corporation. All rods were recrystallized over about a three-inch length. Microscopic examination of the transverse section indicated the recrystallized grains to be quite uniform and about 0.05 mm in diameter. The temperature of 1550°C was found to be optimum from the point of view of insuring

complete recrystallization of the fibered structure as well as obtaining a fine and uniform starting grain size.

The recrystallized rods were heated in air by a small resistance wound furnace to a temperature between 600 to 800°F and strained by the required amount in a tensile testing machine. Strains of 3 to 6 per cent were given. A strain of about 5 per cent was found to give the best results.

After the rods were strained, they were heated by an electron beam to temperatures of 2000 to 2400°C (Brightness).* In the work carried out at M. I. T., the electron gun was moved downward relative to the stationary sample held in a vertical position by a pair of Jacobs chucks. At the Alloyd Corporation the sample was supported in a similar way, but was moved upward relative to a stationary electron gun. The heated rod was free to expand through a bushing held in the upper chuck. The quality of the crystals produced was not affected by whether the electron gun was moved relative to the sample or vice-versa. The temperature of the hot zone did not appear to be too critical, and in most cases a temperature of 2100°C was used. The speed of travel of the hot zone

* Some of the rods were heated in an electron beam unit at M. I. T. in the laboratory of Professor J. Wulff; the remainder were processed at the Alloyd Corporation in the AMEBA.

however, was found to be critical. Speeds in excess of 2 mm/min. produced an excessive amount of parasite grains. A speed of about 1 mm/min. was found to give consistently good results and was adopted throughout.

In the majority of the crystals grown under what was considered to be the optimum conditions as described above, a single crystal was produced over the three-inch length and was free of any parasite grains. It is not uncommon for single crystals produced by the strain-anneal method to contain many parasite grains or to consist of several large crystals "studded" with parasites. Such a situation cannot be tolerated in the case of tungsten, since the presence of only one small parasite grain causes fracture at the boundary after a strain of only 1 to 2 per cent. The success achieved here, 80 per cent parasite-free among some twenty-five crystals produced by the strain-anneal method, is attributed to the steep temperature gradient obtained with electron beam heating. Furthermore, the x-ray back-reflection Laue diagrams consisted of single spots indicating very few subgrains.

The testing of these crystals was carried out in a "soft" tensile machine. The details of testing, recording of the data, etc. will be published elsewhere.

DISCUSSION OF RESULTS

It is not possible at this time to discuss the experimental findings in any detail, since certain aspects of this work are still under investigation. Consequently, I would like only to touch on some of the more interesting findings. First of all, single crystal tungsten, in contrast to the polycrystalline rod, exhibits considerable ductility at room temperature. It can be easily bent into the form shown in figure 1 and, for orientations of the tensile axis within about 20° of $[01\bar{1}]$ and close to the $[001]$ - $[01\bar{1}]$ line in the standard stereographic triangle, reductions in area of 100 per cent are possible resulting in a "chisel-edge" fracture as shown in figure 2. The stress-strain curve for this crystal tested at room temperature is shown in figure 3. Even cleavage fracture at room temperature may be preceded by large plastic strains of 20 to 25 per cent. As the temperature is lowered below room temperature, the range of ductile fracture narrows. Finally, at the temperature of liquid nitrogen, the fracture mode is cleavage for all orientations with strains of 1 to 3 per cent before fracture.

The improved ductility of single crystal tungsten compared with the polycrystalline rod used in the present work* cannot be due to any significant lowering of the interstitial content (Table I), but must in some way be related to the absence of grain boundaries.[6] As mentioned earlier, the presence of only one parasite grain as small as 1/16-inch in diameter will cause the single crystal to fail after a strain of only 1 to 2 per cent, whereas much larger strains are obtained with parasite-free crystals. In every instance where premature fracture occurred, the origin of fracture could always be traced back to a grain boundary.

The perfection of the crystals grown by the strain-anneal method was good as judged by the appearance of the back-reflection Laue spots. Preliminary etch-pit studies on a crystal whose orientation was within 3° of [011] did not show any well defined substructure (Fig. 4). An examination of a crystal in the cube orientation grown by the floating-zone method did, however, reveal well-defined sub-boundaries (Fig. 5). This particular crystal was electropolished and etched twice in 2% NaOH. The first time it was polished and etched the sub-boundaries were delineated by etch pits. The second polish and etch left grooves at the

* The polycrystalline rod tested at room temperature fractured after a strain of about 5 per cent.

original dislocation sites and new pits were formed which appeared to be displaced from these sites. Similar effects have been noted by Gilman[7] in his work on ionic crystals. It is interesting to note here that the dislocation etch pits are produced on the cube (100) faces of single crystal tungsten as in the case of ionic crystals.

Finally, the initial yield stress and the form of the stress-strain curves are orientation dependent as shown in figure 6. Crystals within 5° of an [011] orientation yield in the manner shown by crystal No. 33. The crystals are initially stronger and show little or no work hardening in contrast to crystals whose orientation are close to the other two "corner orientations". Crystals in these orientations are initially softer, yield in a smooth manner, and appear to work harden more than crystals near a [011] orientation. Single crystal No. 37 was obtained from the Philips Research Laboratories in Eindhoven and was produced by a different method.* This variation of the yield behavior with orientation appears to be a singular characteristic of single crystal tungsten and is independent of how the crystals are produced, composition, strain rate, or specimen size. Rose[8] in a recent publication reported similar findings on single crystal tungsten

* This crystal was produced by the deposition of tungsten on a "hot" Pintsch wire from the decomposition of tungsten hexachloride. Crystals grown by the strain-anneal are generally confined to within 20° of an [011] orientation.

made by the floating-zone method. This is particularly interesting in view of the fact that the shear stress-strain curves of tantalum and niobium do not depend substantially on the orientation.[9]

ACKNOWLEDGEMENTS

The author is greatly indebted to the Research and Advanced Development Division of the Avco C orporation for their support of this work. The many stimulating discussions with Professors E. Orowan and A. Argon of the Mechanical Engineering Department of M. I. T. in the course of this work is gratefully acknowledged.

REFERENCES

1. Smithells, C. J., "Tungsten, Its Metallurgy, Properties, and Applications", 143, Chemical Publishing Co., Inc., New York, N. Y. (1953)
2. Goucher, F. S., British Patent 174,714, October 28, 1920 .
3. Calvery, A., Davis, M., and Lever, R., "The Floating-Zone Melting of Refractory Metals by Electron Bombardment" J. Sci. Instr., 34, 142-6(1957).
4. Schmid, E. and Boas, W., "Plasticity of Crystals", F. A. Hughes & Co. Limited, London , 23 (January, 1950).

REFERENCES (continued)

5. Honeycombe, R. W. K., "Growth of Metal Single Cyrstals", Metallurgical Reviews, 4 (13), 1-47(1959).

6. Jones, F. O. "Annealing of Worked Tungsten", Journal of of the Less-Common Metals, 2, 161-71(1960).

7. Gilman, John J. and Johnston, William G., "The Origin and Growth of Glide Bands in Lithium Fluoride Crystals", 117-61, Dislocations and Mechanical Properties of Crystals, John Wiley & Sons, Inc., N. Y. (1957).

8. Rose, R. M., Ferriss, D., and Wulff, J., "Yielding and Plastic Flow in Single Crystals of Tungsten", Submitted for publication to A. I. M. E.

9. Rose, R. M., Private Communication.

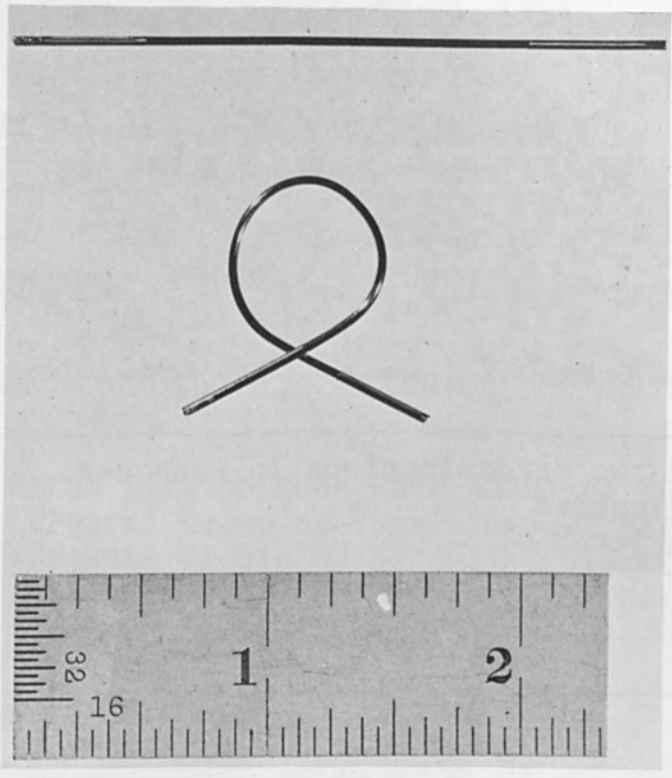

Figure 1. 0.045 - Inch Diameter Tungsten Single Crystal Grown by the Strain-Anneal Method

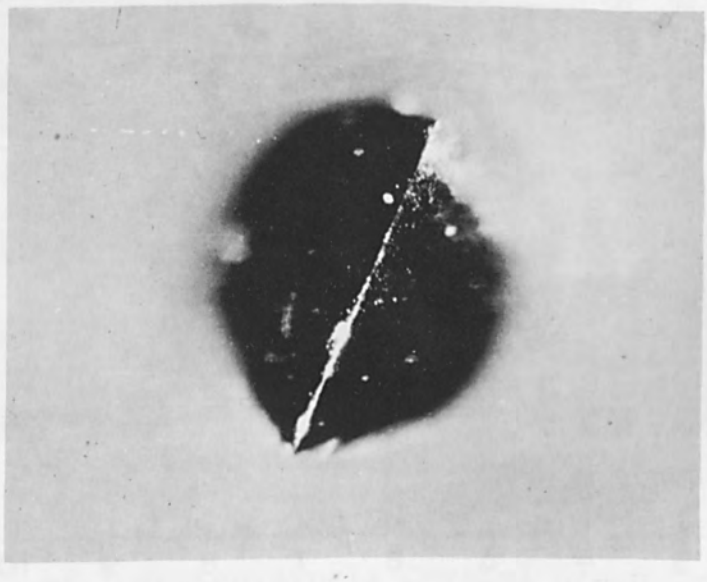

Figure 2. Chisel-Edge Fracture of Tungsten Single Crystal Tested at Room Temperature (50X)

TABLE I

Chemical Analysis in Weight Percent*

	C	O	N
As-Received Polycrystalline Tungsten Rod	0.001	0.003	NR
Single Crystal	0.001	0.002	ND

* Average of two determinations in each case.
NR = None Reported
ND = Not Detected

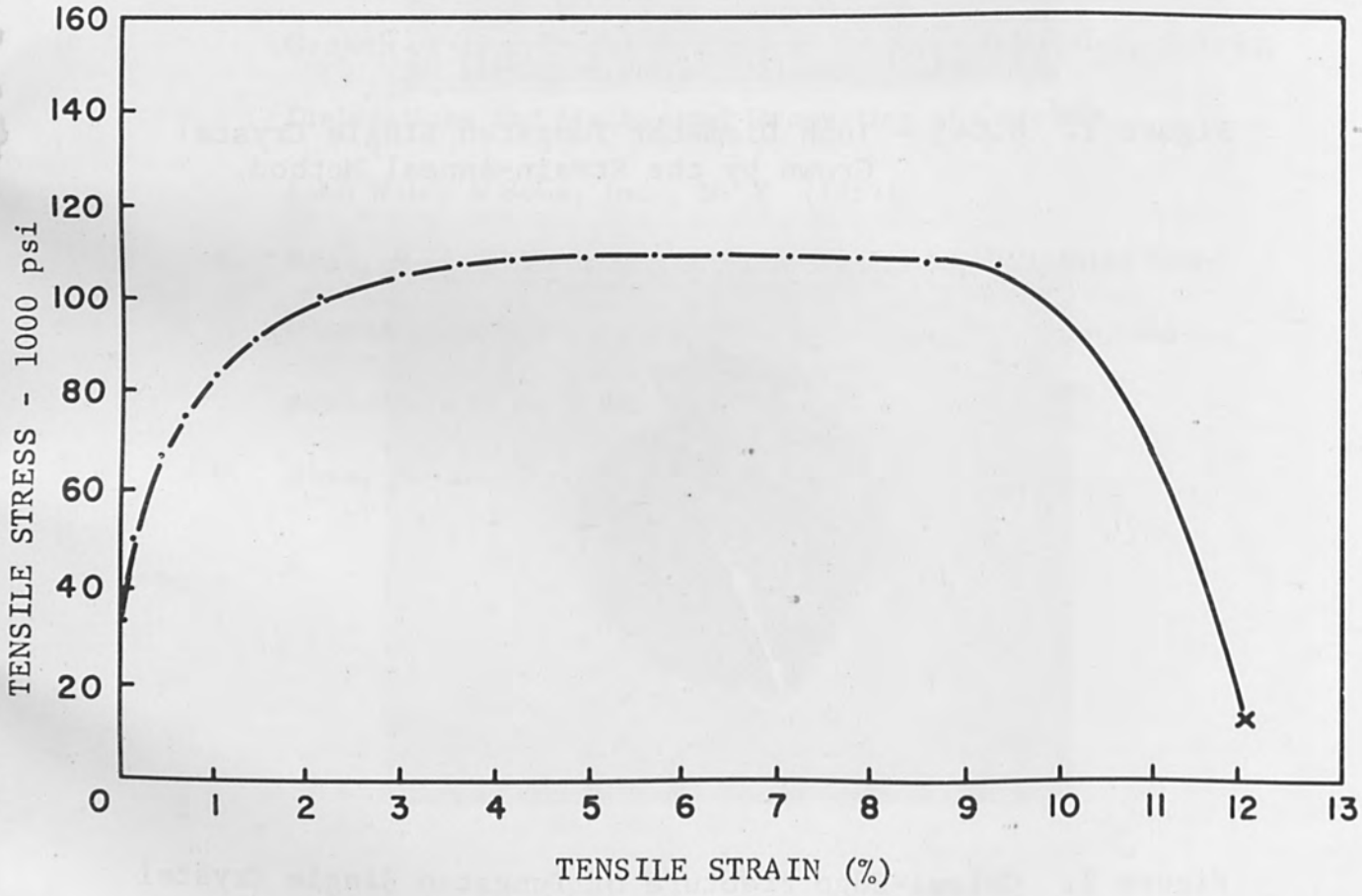

Figure 3. Stress-Strain Curve for Single Crystal No. 28 Tested at Room Temperature.

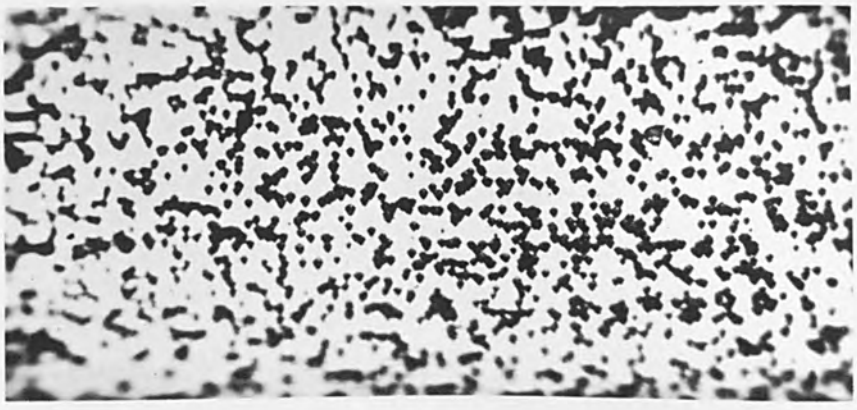

Figure 4. Etch Pits on Cube Face (100) of Tungsten Single Crystal Grown by Strain-Anneal Method. Axis of Crystal Within 3° of [011]. Electrolytically Polished and Etched with 2% NaOH. (250X)

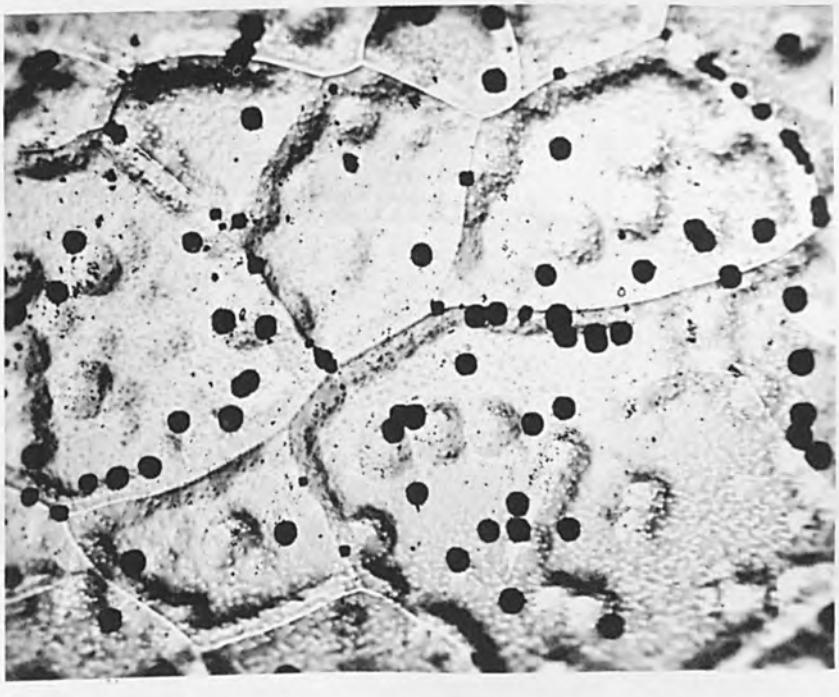

Figure 5. Etch Pits and Substructure on Cube Face (100) of Tungsten Single Crystal Grown by Floating-Zone Method. Axis of Crystal Within 2° of [001]. Electrolytically Polished and Etched With 2% NaOH. (250X)

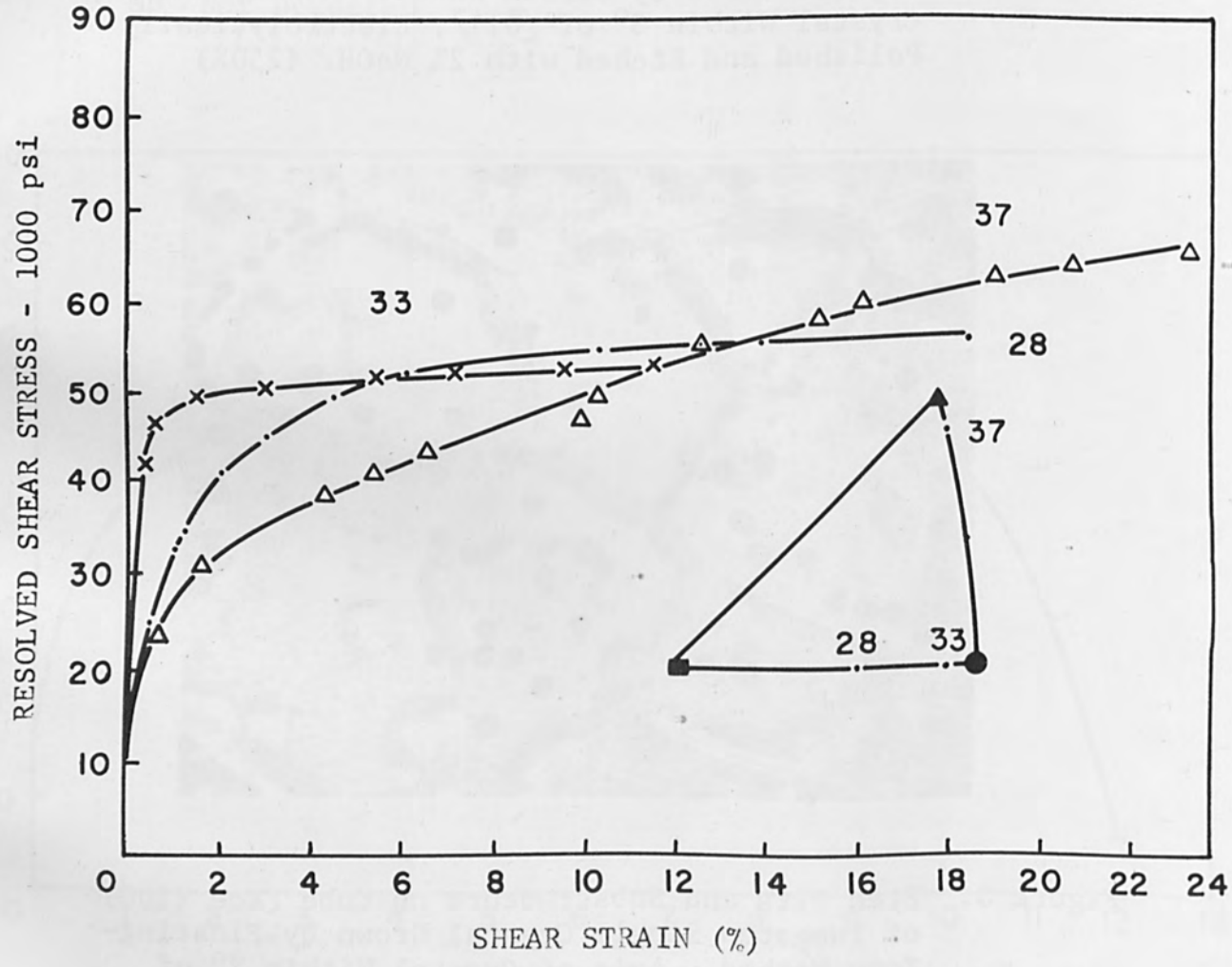

Figure 6. Shear Stress - Shear Strain curves for 0.045-Inch Diameter Tungsten Single Crystals Tested at Room Temperature. Orientation of Stress Axis Indicated.

SOME OBSERVATIONS OF ELECTRON BEAM-INDUCED RECRYSTALLIZATION OF SILICON-IRON

by

J. I. Medoff
Research Specialist
Materials Sciences Section

and

Arnold Miller
Chief, Materials Sciences Section
Research and Development Division
Autonetics, A Division of North American Aviation, Inc.
Anaheim, California

ABSTRACT

As part of a continuing program on the application of electron beams to microelectronics, the role of beam-induced structural modifications and transformations is being assessed. Using a silicon iron model system, microstructural evidence of unusual grain growth character as compared with normal diffusion time-temperature dependence is presented. The implications of such recrystallization and grain growth behavior are discussed.

SOME OBSERVATIONS OF ELECTRON BEAM-INDUCED RECRYSTALLIZATION OF SILICON-IRON

I. INTRODUCTION

The development of sophisticated devices and systems of the future will depend on the ability to control crystal structure and purity, dopant concentration and gradient, spatial characteristics, etc. Better understanding of the relationships between structure, composition and resultant electronic properties is mandatory. Autonetics has been engaged in a broad research and development effort in microelectronics. As part of that program, studies on electron beam processes in microelectronics are being carried out.

The inherent qualities of control and programming using an electron beam source coupled with its spatial selectivity has suggested a wide variety of applications in microelectronics. An exciting area of research with far-reaching implications to microelectronics is the use of the dissipation energy of the electron beam in a controlled fashion to effect various microstructural modifications in solids. This paper deals with one aspect of our study on electron beam induced metallurgical transformations. A silicon-iron model system was chosen as a convenient vehicle for the initial studies because of its inherent microstructural thermal sensitivity and the availability in the literature of extensive prior work using traditional thermal techniques.

Series of 3% silicon-iron specimens with controlled levels of induced strain were studied to develop the nature and rate of recrystallization, grain boundary movement, and grain growth induced by beam impingement under various conditions. Microstructural evidence is presented of unusual grain growth character and rapid grain boundary

movement induced by electron beam exposure. Comparison with grain growth and grain boundary movement as determined by traditional thermal techniques suggests a much higher degree of mobility in the electron beam induced case than characterized by normal solid state diffusion.

II. FUNDAMENTAL CONSIDERATIONS

Recrystallization has been defined as the process whereby cold-worked polycrystalline metal is returned to a strain-free condition upon annealing by the formation of strain-free nuclei and growth by boundary migration at the expense of the strained material (1). Primary recrystallization covers the formation of strain-free grains; grain growth or normal growth refers to uniform increase in the average grain size matrix; and secondary recrystallization or abnormal or discontinuous grain growth is the process whereby a few large grains are nucleated and grow at the expense of the strain-free, fine-grained matrix.

The rate of growth during recrystallization is not time dependent but increases with annealing temperature and the degree of deformation. Growth ceases when all the cold-worked metal has been replaced by strain-free grains, and recrystallization is then said to be complete. The recrystallization temperature is not an exact point but is taken as that temperature at which a highly cold-worked metal recrystallizes in about one hour. The rate of recrystallization is reduced by impurities, soluble and insoluble, and thus, pure metals are seen to have higher rates and lower recrystallization temperatures than their alloys.

If boundaries are in equilibrium and are equal in surface

energy, they tend to straighten and assume angles of 120° at three-boundary intersections. Early observations by Carpenter and Elam (2) and by other investigators, (3,4,5) indicated that curved boundaries between undistorted grains migrate toward their centers of curvature; the more curvature, the higher the rate. The atoms of the concave surface, being more completely surrounded, are considered more stable than those on the convex surface. Normal interchange occurs through atomic mobility but a net flow to the more stable concave surface will result and it will migrate toward its center of curvature. Since the free energy decrease associated with transferring an atom from a curved to a flat surface is inversely proportional to the radius of the curvature, the rate of transfer and thus the rate of boundary migration is also probably inversely proportional to the radius of curvature of the boundary. Verification will have to wait upon experiments giving quantitative data on the rate of migration of a single grain boundary as a function of its curvature and surface tension.

In a strained matrix, equilibrium considerations do not apply. Thus, where a recrystallized grain is growing into a deformed matrix, the direction of migration is opposite to that observed when surface tension is the driving force.

As early as 1906, Osmond and Cartaud (6) in a study of the austenite structure observed and identified four grain networks on a single specimen surface as representing the transition stages from the austenite gamma phase to the alpha phase. Similar investigations (7,8) distinguished between original alpha-iron boundaries and the higher temperature austenite network in low carbon steel. Techniques and equipment to directly observe and record the microstructural evidence

of structural modifications and transformations at the temperatures of occurrence have been improved in recent years.

By means of high temperature or vacuum metallography, the surface alterations and movements that occur during extended periods of heating and subsequent cooling in a vacuum are made visible. A description and illustration of hot-stage metallographic equipment was presented recently by Kasen and Polonis (9). In addition, an English translation of a comprehensive volume by Lozinskii (10) devoted to high-temperature metallography in the Soviet Union has recently become available.

Various types of contours are observed on the surfaces of metals heated in vacuo. There are essentially three ways in which such heating produces contours on smooth surfaces: thermal etching, surface tilting, and surface distortion. Thermal etching results from selective vaporization of atoms where a grain boundary or an interface between phases intersects the surface. Surface tilting is a distortion of the surface in a shear type of movement and surface distortion is an irregular type of surface upheaval involving change of volume. During elevated temperature exposure, the surface of the metal changes its shape in two ways. Wherever a crystal boundary intersects the surface, the intersection becomes a groove. At favorably oriented crystal planes a series of flat surfaces, joined by steps, is formed. Additional contour types which have been noted are: boundary traces, banded contours, striations, twin boundaries, serrations and fissures. Walter and Dunn (11) have noted the orientation dependence of thermal etching and the character of the striations to be a function of the disorientation from the simple plane.

In surface observations of grain boundary migration, both initial and final positions of the boundaries or parts of them, are revealed by thermal grooves. Occasionally the rate of boundary migration is too rapid for the entire growth front to be made visible by the time dependent thermal grooving process. Pinning of a segment of a grain boundary by an inclusion may also occur.

III. ELECTRON BEAM SYSTEM

An electron beam system was designed and constructed during the course of this work to carry out the metallurgical studies. A view of the overall system is given in Fig. 1, while Fig. 2 shows the details of the gun assembly, housing and reaction chamber. A schematic of the system, including the various power, control and measuring circuitry is given in Fig. 3.

The electron beam gun assembly is a modification of gun components from the Superior Electronics Company in a magnetically focused, magnetically deflected array. Through a combination of reduction in grid apertures and control in component spacings, focal spot size and uniformity were significantly improved. A cathode cup structure was introduced to control the separation between the filament and first grid. A reduced-section, flat tungsten filament structure, consisting of a 0.005" thick by 0.115" wide ribbon electro-polished at the aperture to 0.001" thick by 0.075" wide, is providing excellent service. The electron gun housing is a demountable system using flanged pyrex pipe sections with appropriate vacuum fittings.

The reaction chamber is a four-inch spherical glass chamber fitted with two view ports and four flanged pyrex pipe sections. A

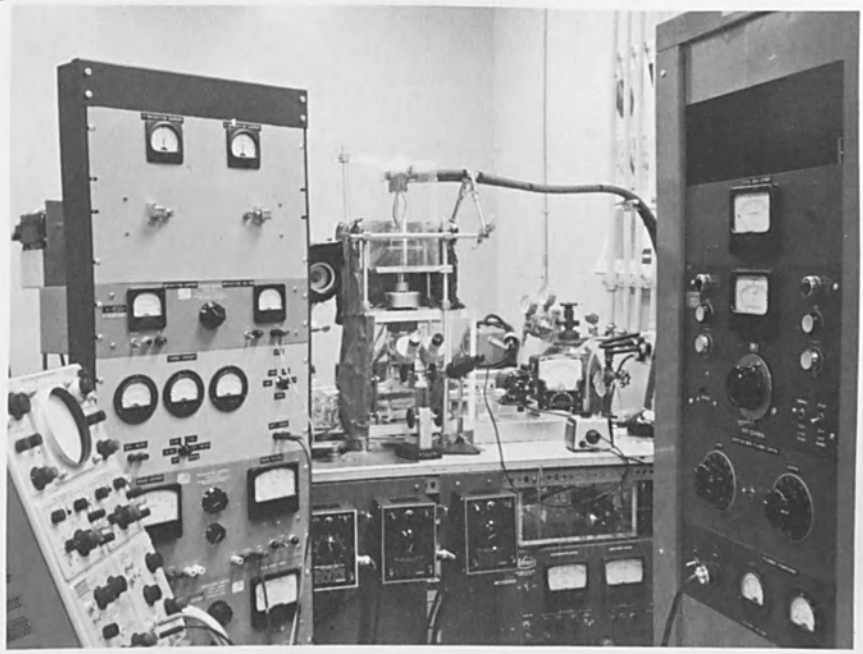

Fig. 1. Autonetics Electron Beam System and Auxiliary Equipment.

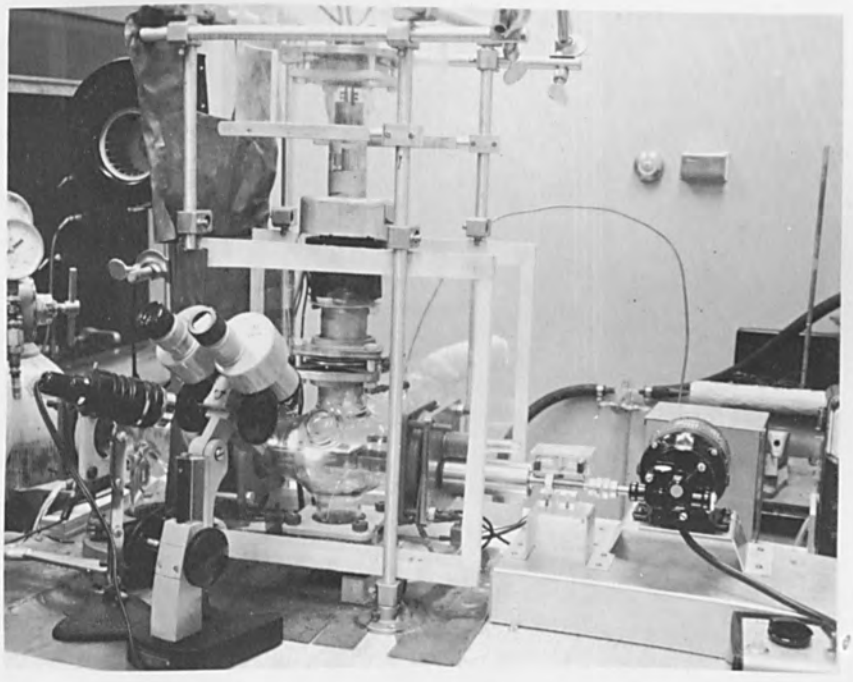

Fig. 2. Electron Gun Assembly, Reaction Chamber and Motorized Stage.

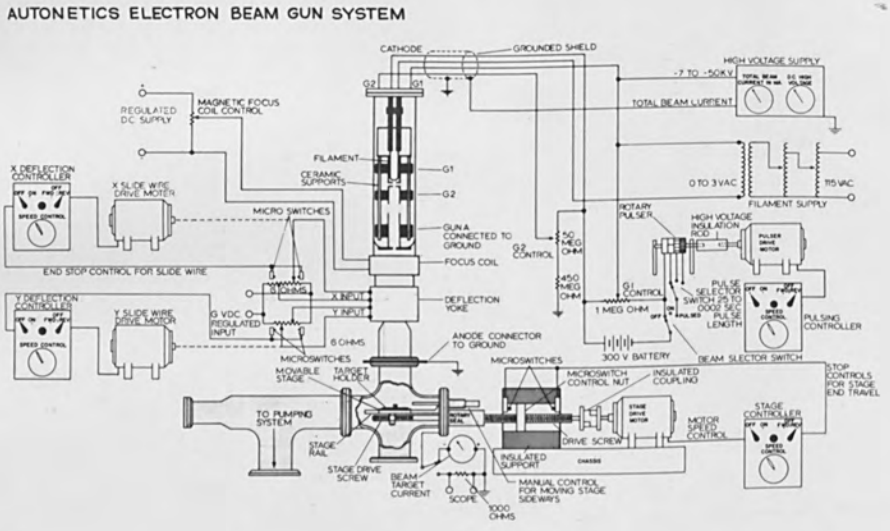

Fig. 3. Schematic of the Autonetics Electron Beam System.

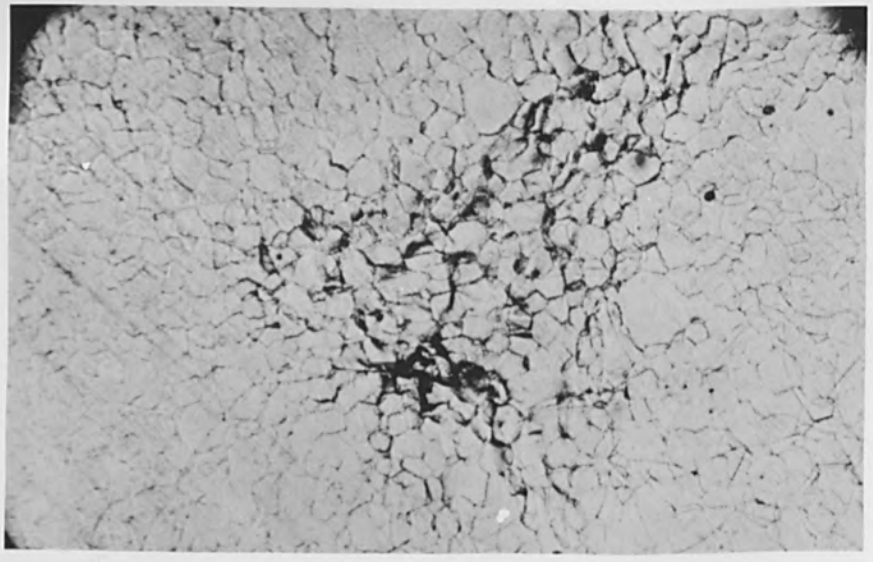

Fig. 4. Grain Boundary Network Developed on Surface of Unpolished Annealed Silicon Iron. (X100)

moveable stage allows total displacement of three and one-half inches in the x-direction and 5/8 inch in the y-direction. The x-displacement is motor controlled with an SH-12 Minarik reversible controller system operating through a rotary bellows seal. The y-displacement is controlled manually through a bellows seal. The system is fitted with a binocular microscope for focusing and positioning. Connection is made to the pumping system through a two inch vacuum gate valve. The pumping system consists of a CVC Model 115 diffusion pump, fitted with a Johns and Frame Model SL-1 liquid nitrogen trap, and backed by a Kinney Model KC-5 mechanical pump.

The high voltage supply is a GE XRD-5 full wave dc system, modified with a special filament transformer capable of delivering 25 amps at 3 volts. The high voltage supply is rated at 7 to 50 kv at 50 ma load current.

The magnetic focus coil for the electron beam gun is powered by a Dressen Barnes regulated dc supply. Controls for the x and y magnetic deflection coils are provided by slide wire circuits, individually motor driven with Minarik SH-12 reversible controllers.

For pulsing studies, a rotary pulser system was designed and fitted with a variable drive, providing a range of pulses from 0.002 to 0.25 sec. The beam can be operated under continuous, pulsed or intermittent conditions. A measuring circuit to measure target currents in the range of 0.1 to 10 ma is provided. For our metallurgical studies, beam currents in the range of 0.1 - 8 ma at 8 - 15 kv accelerating voltages with a focal spot size of approximately 20 mils are employed.

IV. RESULTS AND DISCUSSION

Initially, samples of .014" and .013" oriented and non-oriented

annealed 3% silicon iron sheet in coarse and fine grained condition, received through the courtesy of the Armco Research Laboratory, were used in the study. Subsequently, a nominal 3% silicon iron hot-rolled, strip-annealed electrical sheet .014"thick, was procured from a commercial source for the critical strain evaluation. A chemical analysis was made and showed 2.95, 2.92, and 3.06% silicon, respectively.

Samples of the coarse and fine-grained annealed silicon iron were exposed to beam impingement to develop a range of operating parameters for inducing rapid recrystallization, grain growth, and surface melting. For convenience in operation and to eliminate the possibility of X-ray generation, the beam was operated at 10 kv for much of this work. Although surface roughening and the grain boundary delineation occurred, no primary recrystallization was apparent in the annealed specimens. The stability of the grain boundaries in these unstrained specimens indicated the absence of any appreciable surface energy driving force.

Figure 4 shows the grain boundary network outlined on a roughly polished specimen surface by thermal etching and grain boundary sliding, from exposure to the 10 kv beam for ten seconds. The advantages of using well-polished specimens became evident from these early tests. Subsequent samples were lightly etched to reveal the grain orientation just before insertion into the target chamber. With heavier impingement, more deformation occurs, and Fig. 5 shows the extensive localized surface distortion from increased beam heating, with a limited amount of grain boundary migration. The dark area in the center shows selective deformation on certain crystallographic planes, given in greater detail at 1000 magnifications in Fig. 6. The large-

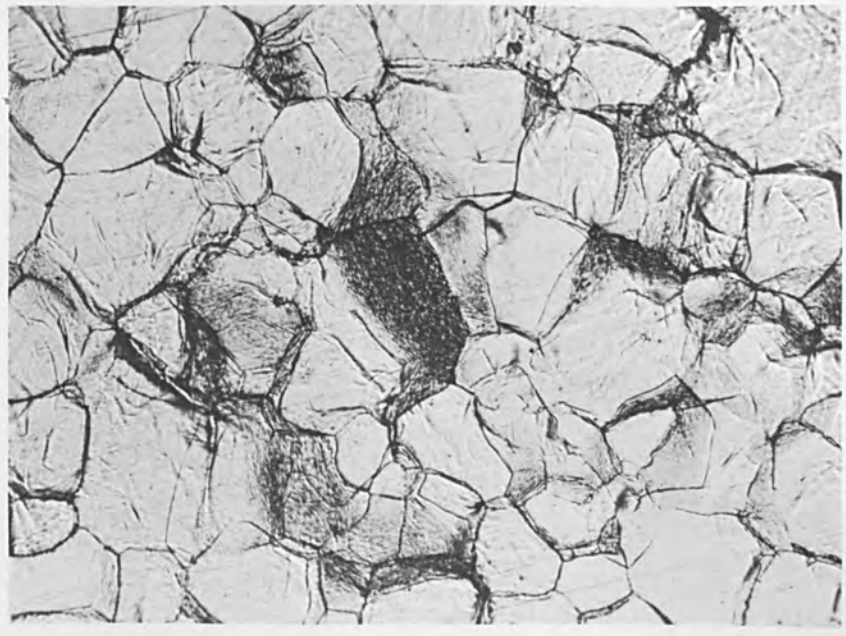

Fig. 5. Surface Distortion and Grain Boundary Delineation on Annealed Silicon Iron by Electron Beam Impingement. (X500)

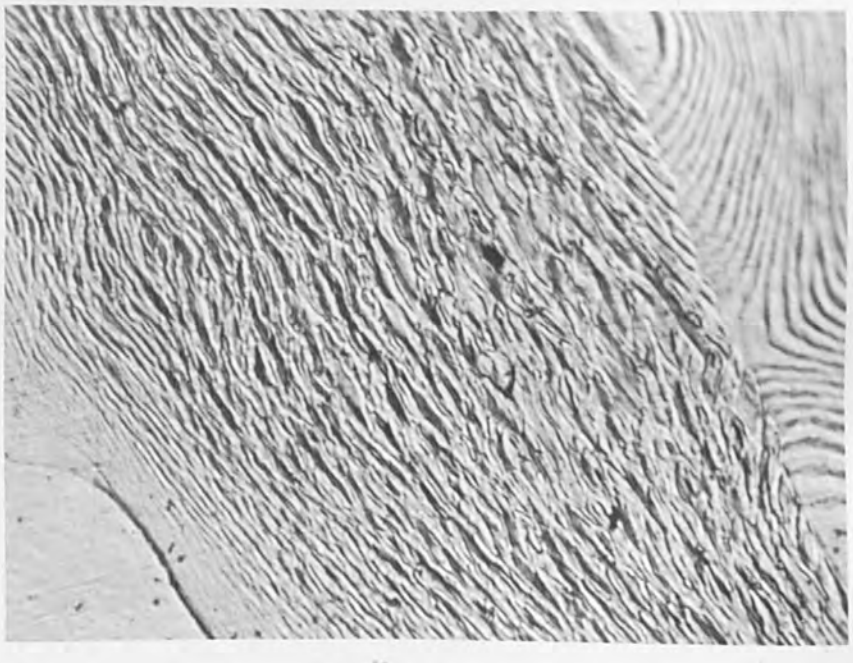

Fig. 6. Enlarged View of Dark Area At Center of Fig. 5 Showing Banded Contours. (X1000)

grain annealed samples showed much greater amounts and variety in the extent of grain boundary migration, as shown in Figs. 7 - 10. In all three figures, the ideal angular position for equilibrium is being approached. Fig. 7 shows progressive positions during the boundary movement. The high degree of curvature of these large boundaries indicates the potentiality for change. Fig. 8 shows a three-boundary junction where migration has developed an almost equilibrium relationship at the junction. Fig. 9 shows rotation of adjacent grains as well as an equilibrium junction. An excellent example of the formation of a new grain boundary during grain growth by migration of boundaries is given in Fig. 10. This is strikingly similar to the schematic diagram used by Fullman (12) to illustrate how curved boundaries between undistorted grains migrate toward their centers of curvature and form new boundaries (Fig. 11). An inclusion often impedes migration by pinning a segment of a grain boundary, as shown in Fig. 12 particularly when surface tension is the driving force for migration. It interferes with the boundary migration since part of the interface is the inclusion itself. Thus, to break away, boundary area equal to the inclusion cross-section must be re-formed.

To determine the degree of critical strain for maximum growth response to annealing, a series of specimens with controlled deformations from 3% to 18% was prepared at the Los Angeles Division of North American Aviation, Inc. by cold-rolling specimens from the fine-grained commercial 3% silicon iron.

Beam trace and spot impingements were run on this series and it was determined that the specimens with 3% and 6% strain were the most sensitive to extensive grain growth in this series. Figures 13

Fig. 7. Grain Boundary Migration on Annealed Silicon Iron Showing Progressive Positions During Movement. (X75)

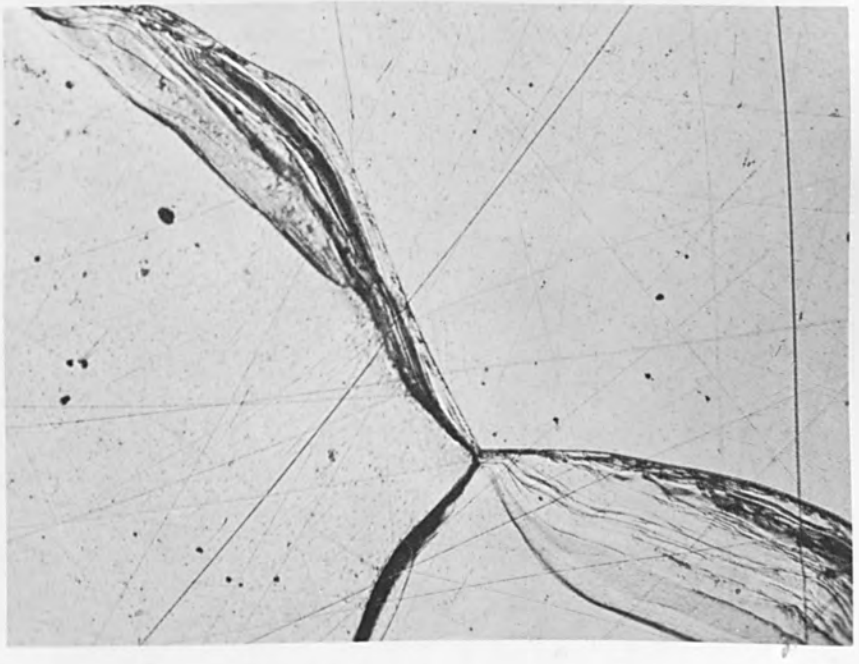

Fig. 8. Migration of Grain Boundaries on Annealed Silicon Iron at a Three Boundary Junction. (X150)

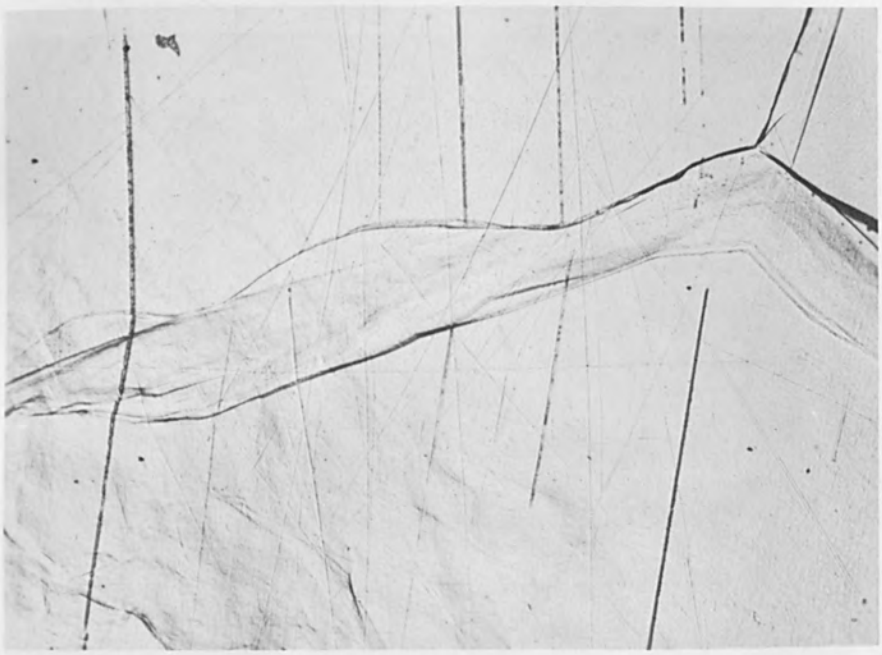

Fig. 9. Rotation of Adjacent Grains During Boundary Movement on Annealed Silicon Iron. (X150)

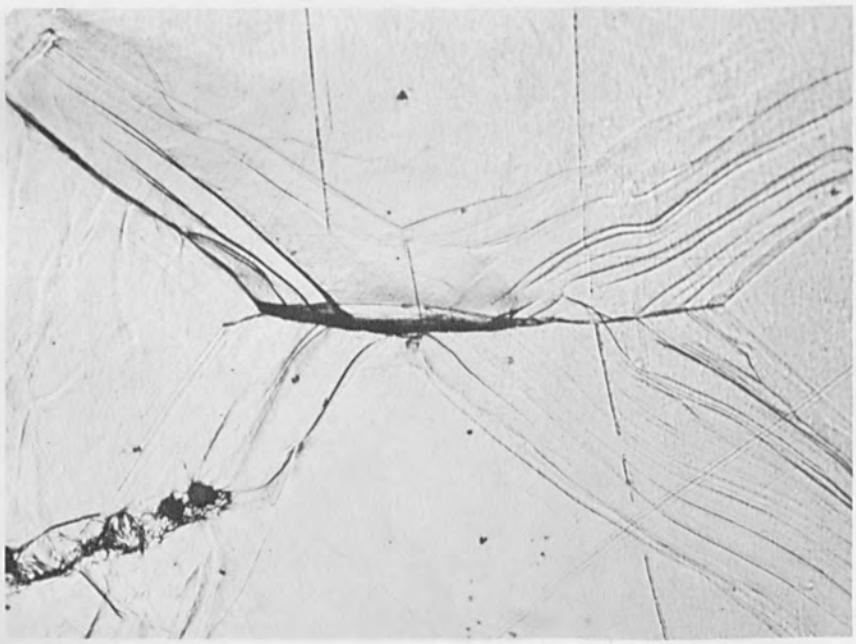

Fig. 10. Formation of New Grain Boundary During Growth on Annealed Silicon Iron. (X180)

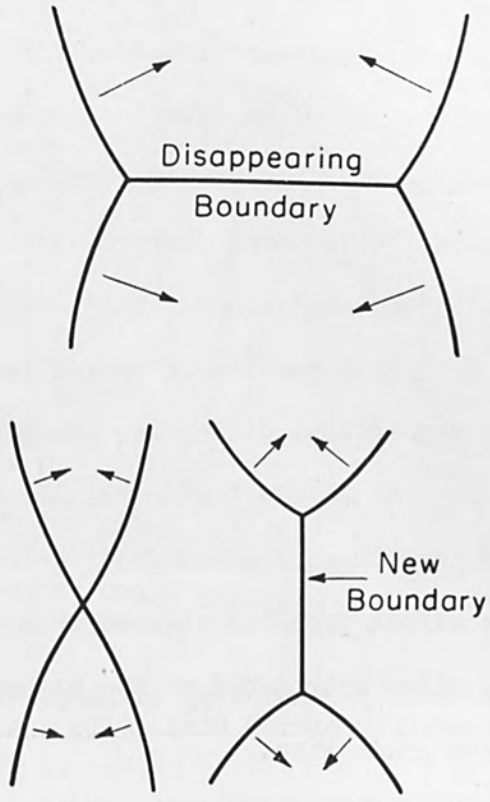

Fig. 11. Representation of Formation of a New Grain Boundary During Grain Growth. **(Ref.12)**

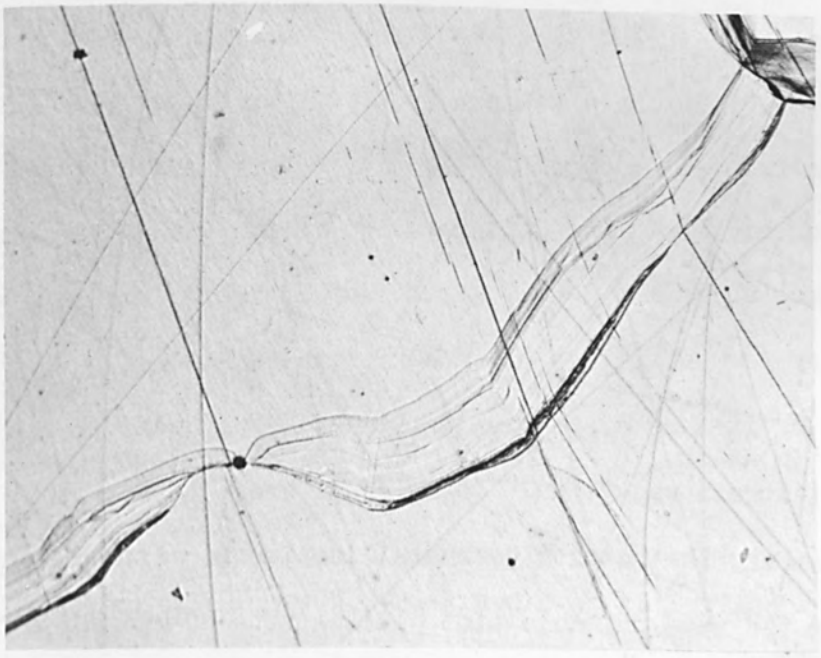

Fig. 12. Pinning of Grain Boundary by Inclusion in Annealed Silicon Iron (X75)

and 14 show the developing large-grain boundary network superimposed on the original surface small grain structure for 3% and 6% cold-worked samples, respectively. These grains show crystallographically oriented planes with fine lamellar banded contours. Comparing the results for these latter cold-worked samples with the corresponding and annealed specimens discussed above, it may be seen that the introduction of 3% cold-working results in marked increase in grain growth. There is no significant difference between the response of the 3% and 6% samples. At levels higher than 6% cold-work, beam impingement resulted in more widespread grain growth but fewer large grains. This latter effect probably stemmed from the increased number of nucleating sites introduced at the higher strain levels, restricting the ultimate grain size.

It is of interest to compare the above critical strain values for recrystallization as a function of cold work after beam impingement for periods of one to two minutes with reported values determined with conventional methods. Dunn (13) reported a value of 2.5% critical strain for high purity silicon iron. Other values have been reported to range from 2% to 6% for silicon iron for varying degrees of purity and prior history. The data reported in the literature were obtained by furnace annealing for long periods of time. Koh (14) reported rapid secondary recrystallization in commercial silicon iron for varying periods by isothermal heating in a salt bath, but no value for the critical strain was given. It is of interest to note that early work on describing the rate of recrystallization in silicon ferrite in terms of the rate of nucleation and the rate of growth as functions of the most important variables was carried out by Stanley and Mehl (15).

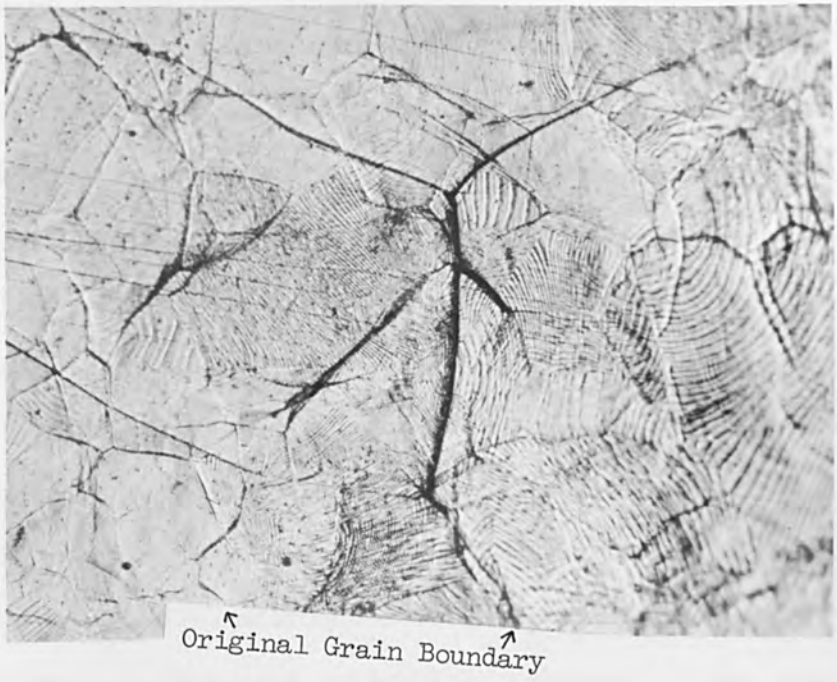

Fig. 13. Grain Boundary Network Developed on Surface of 3% Cold Worked Silicon Iron (X500)

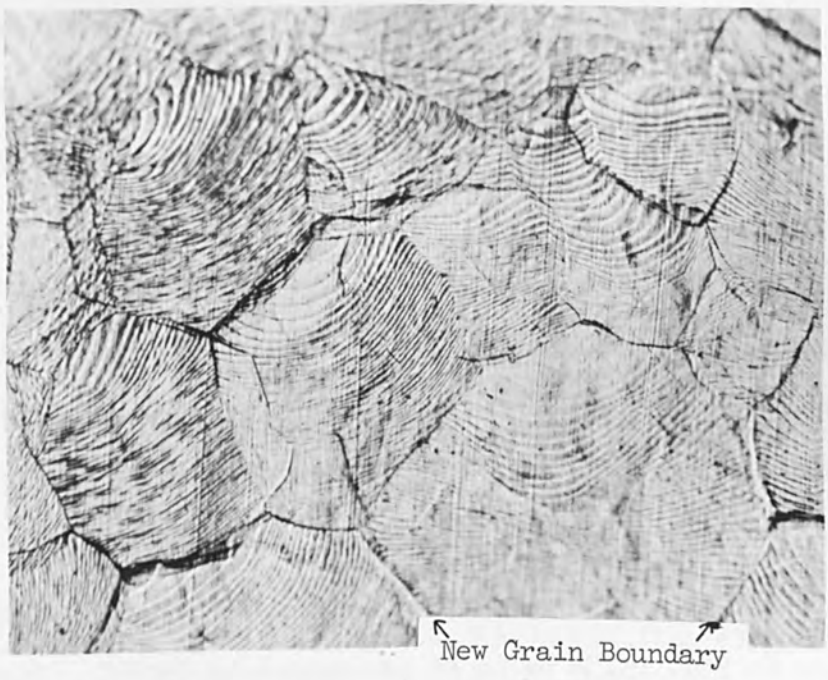

Fig. 14. Grain Boundary Network Developed on Surface of 6% Cold Worked Silicon Iron. (X500)

A nominal 3% critical strain series was prepared by cold-working the annealed sheet to between 3% and 4% cold reduction. Various combinations of electron beam power input were used to determine the grain growth rates and ultimate sizes on specimens polished and etched to either 0.011" or 0.007" thick. Fig. 15 is a graph of the heating power as determined with a chromel-alumel thermocouple spot welded to the specimen, of the focused electron beam with a spot size of the order of 20 mils. Figure 16 is a comparison of the grain growth effected with steady beam and pulsed beam for five-minute periods of impingement on .007" thick specimens as a function of beam current. Focal spot size was of the order of 20 mils, at a ten millisecond pulse rate, with constant 10 kv accelerating voltage.

Various combinations of power input were used to develop the conditions for rapid grain growth and many examples of multiple stage growth were encountered. Figure 17 is an example of a stable grain structure showing at least three grain networks of increasing size and configuration.

The most effective combination of beam parameters with this system to achieve the maximum growth in the shortest time was determined to be a steady beam current of 0.8 ma at 10 kv accelerating voltage for two minutes with a beam spot size of the order of 20 mils. The grain growth directly under the beam was 27 x 38 mils in size. The temperature at which the growth occurred can be obtained from the 10 kv current curve in Fig. 15, a value of approximately 800° C. Figure 18 is a photomicrograph showing a large ten-sided grain superimposed on the original prior grain boundary network. The new boundaries are relatively clear as though they formed rapidly with very little addi-

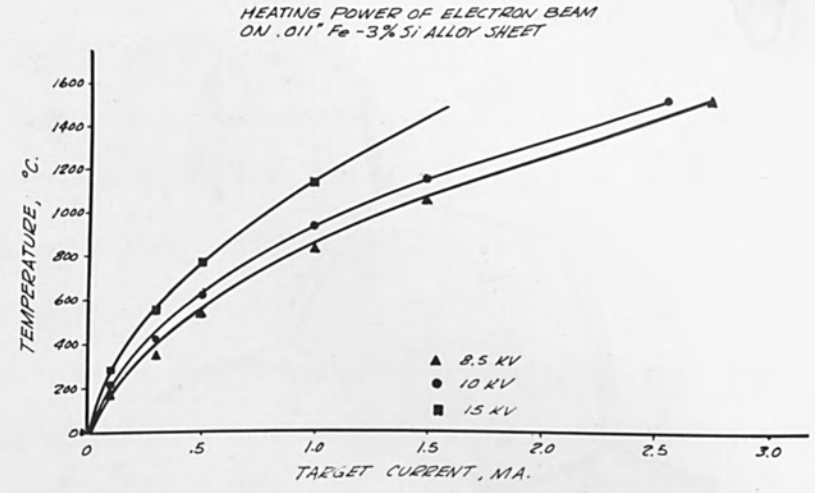

Fig. 15. Heating Power of Electron Beam as a Function of Beam Current.

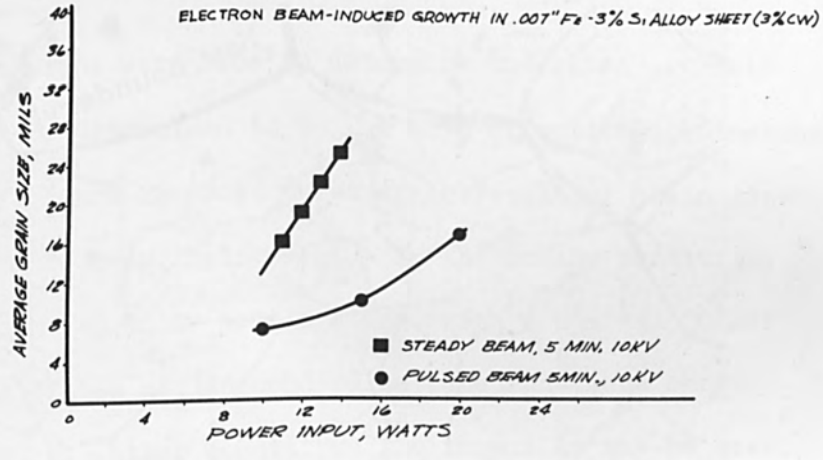

Fig. 16. Rate of Grain Growth in Silicon Iron (3% C.W.) as a Function of Power Input.

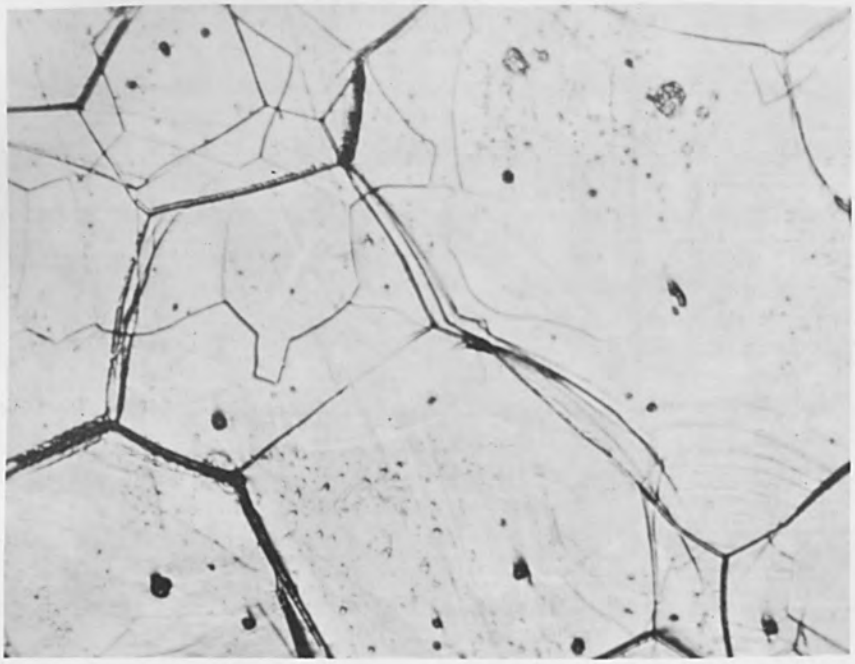

Fig. 17. Multiple Grain Boundary Network at Successive Stages of Grain Growth on 3% Cold Worked Silicon Iron.

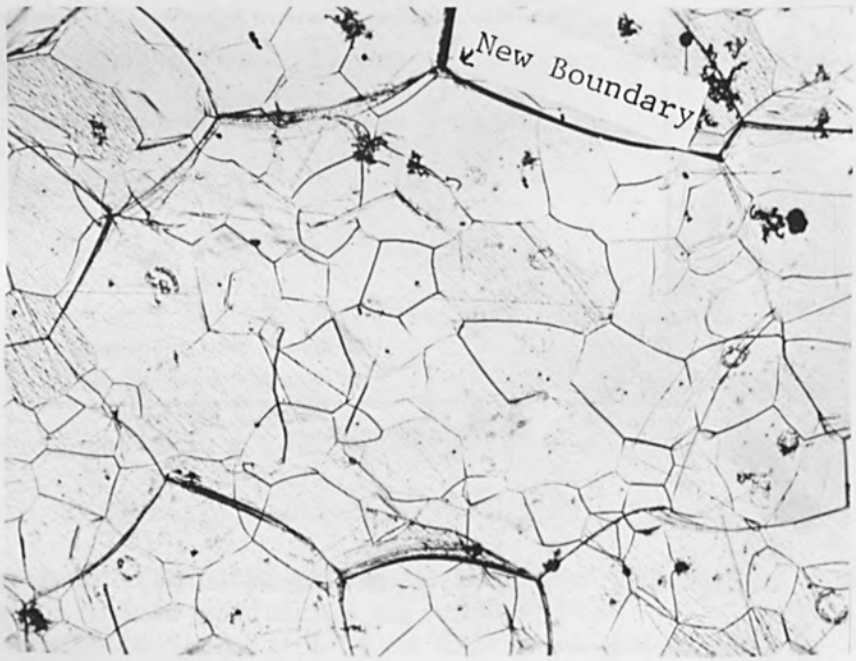

Fig. 18. Large Grain Developed on 3% Cold Worked Silicon Iron After 2 Min. at 10KV and 0.8 ma Beam Current. (X100)

tional movement. To verify the single crystallinity of this large grain, the surface was polished down approximately one and one-half mils and the same field of view is shown in Fig. 19. Additional verification was afforded by Laue back-reflection diffraction pattern taken with cobalt radiation, shown in Fig. 20.

In sheet fabrication practice, an empirical limitation on normal grain growth is commonly acknowledged, i.e., growth ostensibly stops when the grains have grown to approximately the specimen size or thickness of sheet. Figure 21 shows polished and etched cross-sections of a silicon-iron specimen before and after exposure. It is obvious that grain growth did not stop when the grains grew large enough to traverse the sheet thickness, but continued to grow laterally to many times the thickness, approximating the diameter of the electron beam itself.

A series of runs were made to determine the rates of grain growth under conditions determined to be the most effective combination of beam parameters. Figure 22 shows the average resultant grain size as a function of time of beam impingement. In the steady condition, beam current was 0.8 ma at 10 kv acceleration. with a nominal 20 mil spot size. A series of ten millisecond pulse rate runs were carried at 2 ma beam current, all other conditions the same. As may be seen, both series resulted in growth to an average grain size approximating the impinging beam diameter. After the peak average grain size value is attained, continued impingement does not result in further grain growth. This suggests that a limiting factor to maximum grain size is this configuration in the nominal impinging beam diameter, and thereby the zone of uniform temperature exposure.

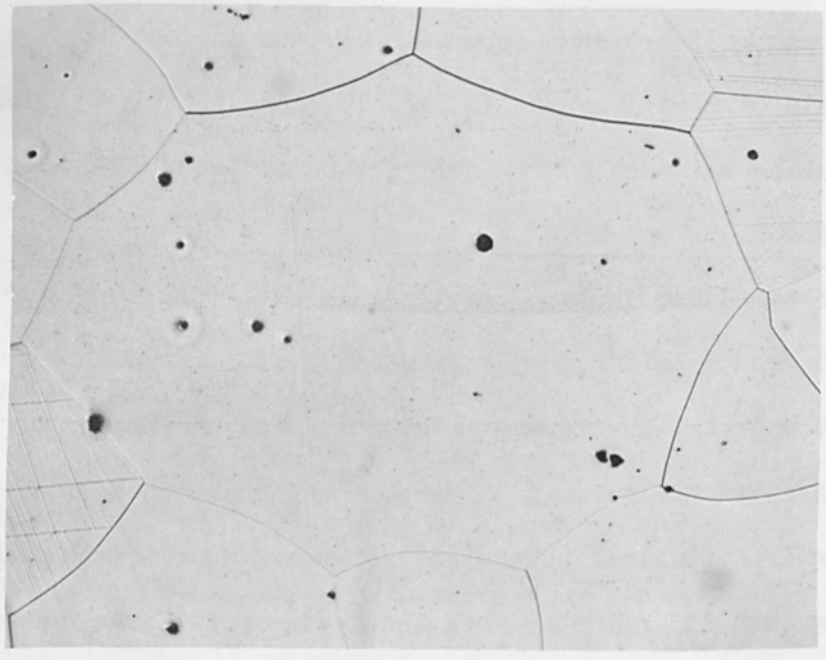

Fig. 19. Same Field of View as Shown in Fig. 18 After Repolishing and Etching. (X100)

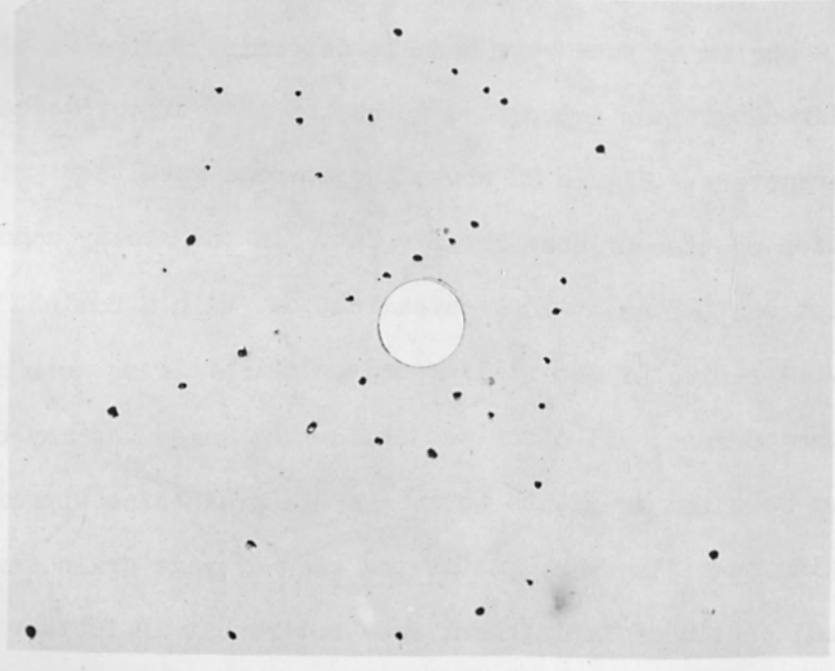

Fig. 20. Back-Reflection Laue Pattern of Large Grain Shown in Fig. 17 Using Cobalt Radiation.

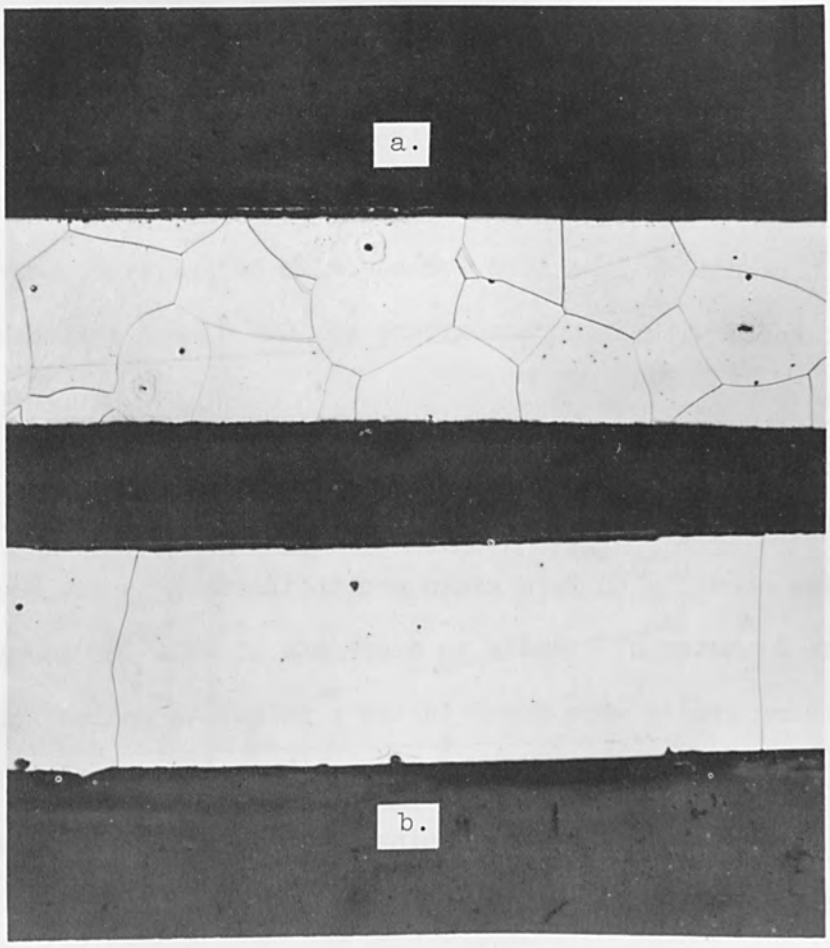

Fig. 21. Etched Cross-Section of 3% Cold Worked Silicon Iron. (X150)

a. Original Grain Structure.

b. After E-Beam Impingement.

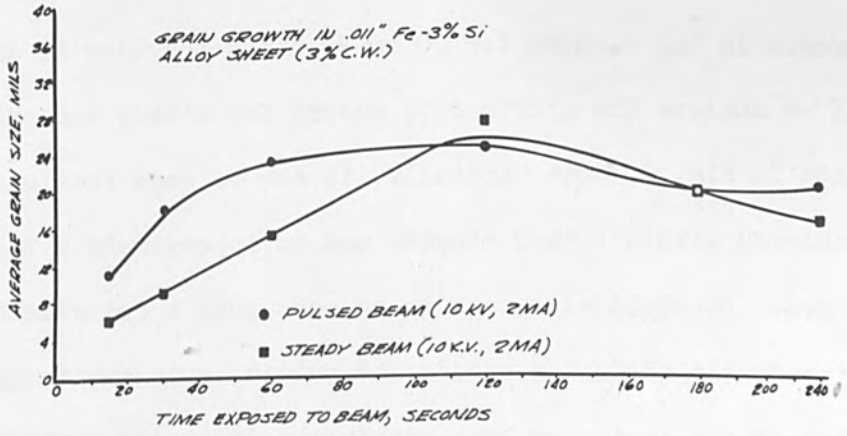

Fig. 22. Rate of Growth of Average Grain Size for Fixed Power Input, as a Function of Time of Beam Impingement

To establish a basis of comparison with results from traditional heating techniques, similar specimens were prepared and evaluated for grain growth reactions in a tube furnace with helium atmosphere at 700°C, a tube furnace with argon atmosphere at 1000°C, and a vacuum furnace at 1000°C.

The 700°C furnace anneals in helium showed no noticeable change in average grain size for periods up to 60 minutes. The grain size of the 1000°C series showed a uniform grain growth increase in one hour to an average grain diameter of 12 mils in argon and 15 mils in vacuum. A few large secondary grains were found in the specimens annealed for 45 and 60 minutes at 1000°C in argon. The largest was a single 100-mil grain at 45 minutes and a few 40-mil grains at 60 minutes. These values can be compared with work of Walter and Dunn (11) on oriented high-purity silicon iron showing a 34-mil grain at 1100°C after 30 minutes in dry argon and an 80-mil grain after 4 hours.

The results of the furnace treatments are plotted in Fig. 23. The growth rate curve for steady beam heating from Fig. 22 has been included for comparison. It can be seen to be startlingly steeper than for grain growth in the furnace for 20 to 30 times the time of annealing.

If we analyze the growth rate curves for steady and pulsed beam operation in Fig. 22 more carefully, it can be seen that maximum growth is achieved within 1 to 3 minutes and to approximately the same range of values. It would also seem to be more than a coincidence that the grain size developed during steady and pulsed impingement approximates the size of the impinging beam within the limits of experimental variation.

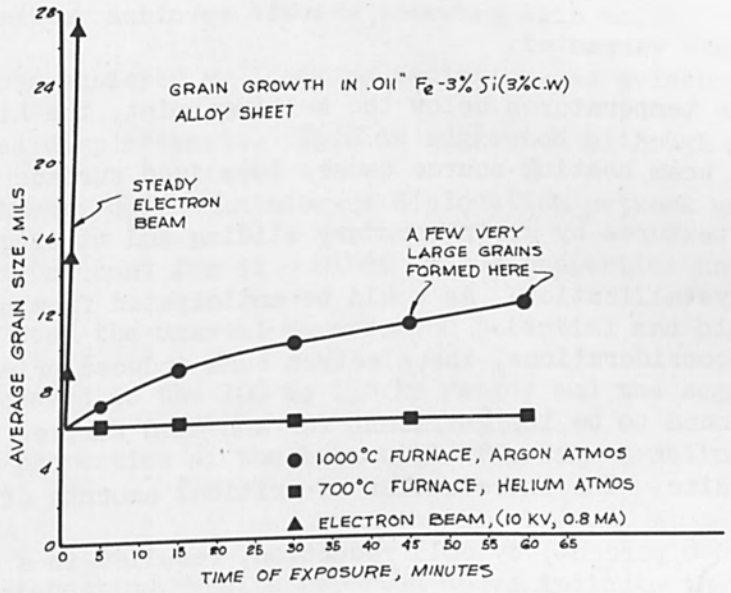

Fig. 23. Rate of Grain Growth of Silicon Iron Heated in Furnace and by Electron Beam.

V. CONCLUSIONS

The electron beam has been found to be an effective means of inducing sharply localized transformations in a model 3 percent silicon iron system. Based on the results of the study described above, a number of conclusions are warranted.

For temperatures below the melting point, the highly concentrated electron beam heating source causes localized surface distortions and deformation textures by grain boundary sliding and tilting, thermal etching and recrystallization. As would be anticipated from normal diffusion and lattice considerations, the electron beam induced primary recrystallization was found to be insignificant for annealed samples regardless of prior grain size. The introduction of critical amounts of strain, in the range of 3 to 6 percent, by cold reduction, resulted in a marked change in grain growth response to beam impingement and the development of large secondary grains by discontinuous grain growth. The range of effective critical strain determined correlates well with reported strain-anneal practice by more conventional heating methods.

It was found that above 6 percent cold work, more general grain growth occurred during beam impingement, as a result of increased nucleation with smaller overall grain size. However, when the 3 percent critical strain series was subjected to grain growth studies using a variety of beam power parameters, rapid grain growth occurred. These rates were much faster than was determined for furnace annealing treatments.

It is difficult to avoid the conclusion that such extensive and rapid grain boundary movement and growth induced by electron beam exposure suggests a higher degree of atomic mobility than is characterized by normal thermal considerations and solid state diffusion. If a high state of

disorder exists from interaction with a high energy electron beam, then the thermal dependence of grain growth might be more like liquid diffusion during beam impingement. It may well be that the interaction of energetic electrons with matter achieves effects somewhat akin to, but not as destructive as, those achieved by ionizing radiation, as evidenced by thermal spikes or thermal displacements. This is suggested although no evidence of structural damage, defect lattice or dislocation network generation has been presented to account for it. Other unique properties noted for electron beams have been the unusual penetration potential and high depth-to-width ratios achieved in the 100 to 150 kv range; and the suggestion of electromagnetic properties of the beam with effects resembling levitation melting.

The interesting results reported above indicate that the availability of electron beam sources may open up whole new areas for research in the field of metallurgical transformations in solids with the possibilities of new and unexpected phenomena.

VI. ACKNOWLEDGEMENTS

The authors are pleased to acknowledge the assistance of E. H. Abrams and W. F. Watt with the electron beam experiments, L. A. Moudy for the X-ray analysis, D. Medellin for the metallographic preparations, and W. C. Cannon for his contributions in the early stages of the work.

VII. REFERENCES

(1) Mehl, R. F., Metals Handbook, 1948 Edition, American Society for Metals, Cleveland, p. 261.

(2) Carpenter, H. C. H. and Elam, C. F., Institute of Metals, 24, 83 (1920).

(3) Vogel, R., Leit. Fur Anorg. Chem., 126, 1 (1923).

(4) Bragg, W. L., Proc., Phys. Soc. (London), 52, 105 (1940).

(5) Harker, D. and Parker, E. R., Trans. ASM, 34, 156 (1945).

(6) Osmond, F. and Cartaud, G., J. Iron Steel Inst., 71, No. 111, 444 (1906).

(7) Burgess, G., AISI 1920 Yearbook, p. 154.

(8) Reid, G. and Scott, G., Trans. AIME, 67, (1922).

(9) Kasen, M. B. and Polonis, D. H., The Trend in Engineering, January 1961, p. 15.

(10) Lozinskii, M. G., High Temperature Metallography, Pergamon Press, 1961, p. 241.

(11) Walter, J. L. and Dunn, C. G., Trans. AIME, 218, 914 (Oct. 1960).

(12) Fullman, R. L., Metal Interfaces, American Society for Metals, Cleveland, 1952, p. 179.

(13) Dunn, C. G., The Cold Working of Metals, American Society for Metals, Cleveland, 1949, p. 113.

(14) Koh, P. K., Trans. AIME, 215, 1043 (Dec. 1959).

(15) Stanley, J. K. and Mehl, R. F., Trans. AIME, 150, 260 (1942).

DIVERSE APPLICATIONS OF ELECTRON BEAM FLOATING ZONE APPARATUS

By

S. Hurwitt
Development Supervisor
Materials Research Corporation
Orangeburg, New York

ABSTRACT:

An apparatus for the floating zone refining of refractory metals and other materials by means of electron beam bombardment is described with emphasis on the basic simplicity of the equipment, the properties of the resulting specimens, and the diverse operations which may be performed thru the use of various experimental techniques.

The capabilities of a work accelerated gun of the simplest design are shown to include purification, crystal growth, alloying, welding, and thin film evaporation.

DIVERSE APPLICATIONS OF ELECTRON BEAM FLOATING ZONE APPARATUS

INTRODUCTION

Since the introduction of the electron beam as a tool for research and industry, the trend has been towards more complex systems, generally using self accelerating guns of high resolution. However, for floating zone refining, where circumferential melting of a thin cylindrical specimen is required, it was found that a single loop emitter, operating in the work accelerated mode has many advantages over a more complex system. These include even heating over 360° of specimen surface, small size, and ease of servicing.

Attesting to the flexibility inherent in this type of gun, it was found that proper experimental techniques could widely diversify the uses of the basic apparatus so as to include many laboratory operations such as alloying, annealing, sintering, specimen welding, and thin film evaporation. Such a versatile system is shown in Figure 1.

THE GUN STRUCTURE AND SPECIMEN MOUNTING

The work accelerated gun (fig. 2) consists of a formed loop emitter (30 mil thoriated tungsten wire is used in most instances), enclosed in a molybdenum cylinder at close to ground potential. The cylinder provides an electrostatic focussing field to shape the beam and confine

Material	O_2	H_2	C	N_2	Metallic
Tungsten	2.6	0.4	0.0	7.0	-
Molybdenum	4.5	0.7	15.0	1.0	Fe - 5
Tantalum	4.0	0.3	10.0	8.0	Fe - 5; Mo - 15; Nb - 50.
Iron	8.5	0.1	0.1	15.0	Cu - 1; Mg - 1; Si - 5.
Nickel	0.9	0.07	0.02	25.0	Fe - 15; Si - 10

Table I - Typical Chemical Analyses of Electron Beam Zone Refined Specimens. Impurity levels in parts per million.

Material	Single Pass Electron Beam Refined	Typical Starting Material
Tungsten	333	450
Molybdenum	159	225
Tantalum	76.1	150
Niobium	52.4	170
Nickel	87.6	200
Vanadium	76.0	170

Table II - Vickers Hardness Numbers

Figure 1. Electron Beam Floating Zone Apparatus

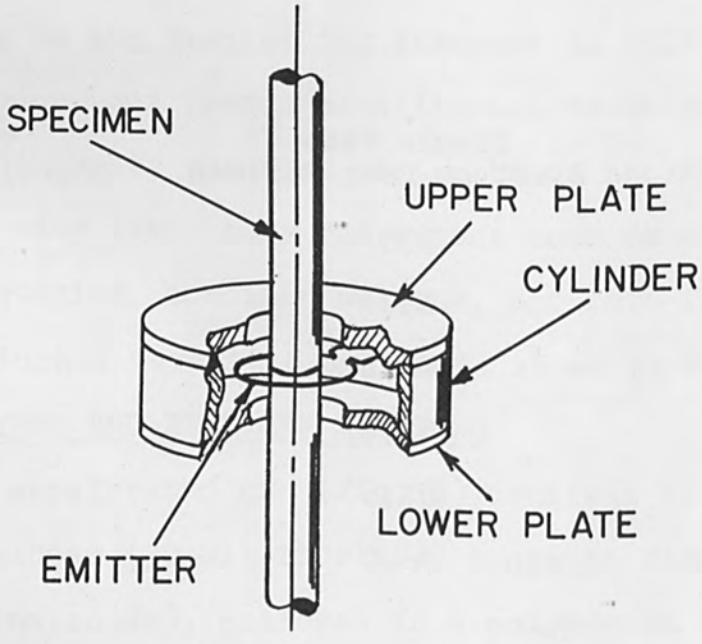

GUN STRUCTURE
FIG. 2

it to the area midway between the upper and lower plates. A small hole in the cylinder wall permits observation of the molten zone during operation.

A traversing stage, on which the gun is mounted, is driven upwards or downwards by a leadscrew at scanning speeds of 2 inches to 30 inches per hour.

To assure strain free mounting, the specimen rod is inserted in the apparatus in two sections, which are then adjusted by means of universal motion grips, for parallel and concentric alignment. The section lengths are chosen such that the welded joint will be at the end of the finished crystal.

OPERATING CONDITIONS

The apparatus is powered by a 10,000 volt, 500 milliamp supply, with the specimen held at a high positive potential. The full 5,000 watts of power are not required, but the flexibility in voltage and current available is important for such uses as the melting of ceramics, whose poor conductivity requires a higher beam voltage. A feedback system, controlling the filament emission, provides beam current regulation which results in smooth, regular crystals even if the starting material is highly gassy.

A 1500 liter per second diffusion pump maintains a vacuum of 10^{-6} - 10^{-7} Torr during melting, with an optically dense liquid nitrogen trap preventing backstreaming of pump oil vapors.

Specimen size is limited mainly by the melting point and surface tension of the material. Single crystals of the refractory metals are commonly grown to 1/4 inch diameter by 12 inches long, while single crystals of nickel and polycrystals of iron may be grown to 1/2 inch diameter by 12 inches long.

SPECIMEN PROPERTIES

Some typical single crystal specimens are shown in figure 3. Table I lists typical chemical analyses of zone refined specimens in parts per million of impurities. The specimens were prepared from starting materials containing nominally several hundred ppm impurities. As additional indication of purity, single crystal niobium processed as above has exhibited a superconducting transformation of 9.8 degrees as compared to commercial Nb of 9.1°K, while a tungsten crystal has shown a resistance ratio from 4.2°K to 296°K of 2,365.

CONTROLLING CRYSTAL ORIENTATION

Reproducing the crystallographic orientation of an existing specimen is relatively easy. The end of a crystal is used as the lower part of the specimen rod, the upper part being the polycrystalline rod to be processed, (fig. 4). The seed end is welded to the end of the polycrystalline specimen, and as the molten zone is traversed along the rod, the crystal that is formed follows the orientation of the seed.

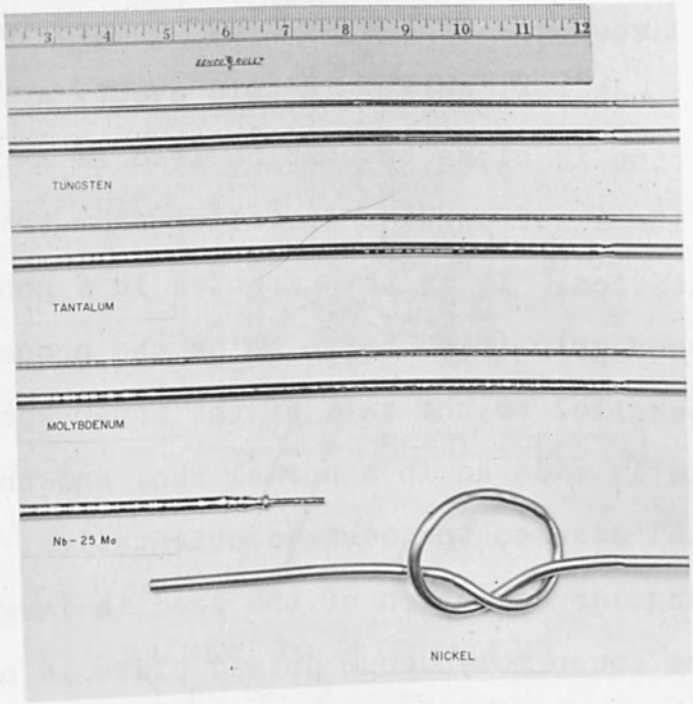

Figure 3. Typical Single Crystals

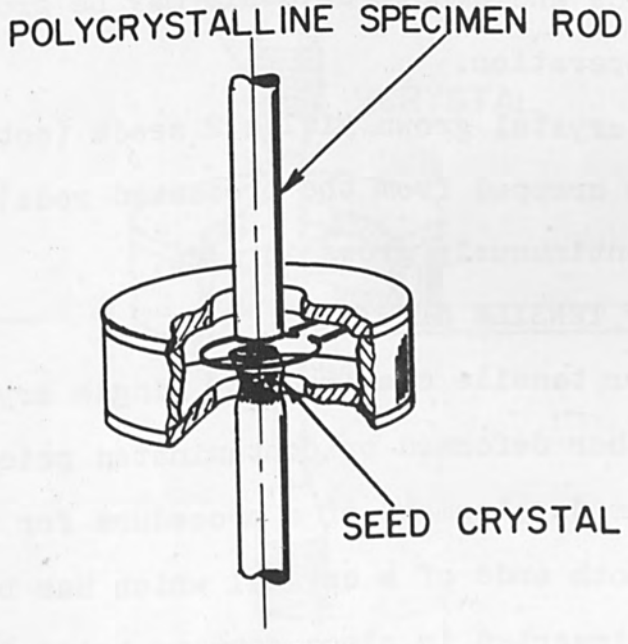

SEEDING
FIG.4

In many cases, however, a seed of the desired orientation is not available. In this event, a seed whose orientation is close to that desired is x-rayed to determine its exact angular deviation from the desired orientation. It is then mounted in a goniometer type lower grip (fig. 5) to bring the proper orientation parallel to the axis of the upper specimen rod. The weld is made as in a normal run, and the growing crystal assumes the desired orientation.

If the angular deviation of the seed is large, removal of the lower molybdenum shield plate is necessary to allow entry of the seed. This usually results in crystals of irregular surface, unsuitable for use as specimens; however these may be then used assecond generation seeds and smooth crystals may be grown in a subsequent operation.

As every crystal grown yields 2 seeds (both top and bottom are cropped from the processed rods), a seed "bank" continuously grows in size.

PREPARATION OF TENSILE SPECIMENS

A need for tensile specimens of single crystals that were neither deformed or contaminated prior to test led to the development of a procedure for attaching end-bosses. Both ends of a crystal which has been cut to length are inserted in close fitting holes drilled in threaded stainless steel rods (fig. 6). The

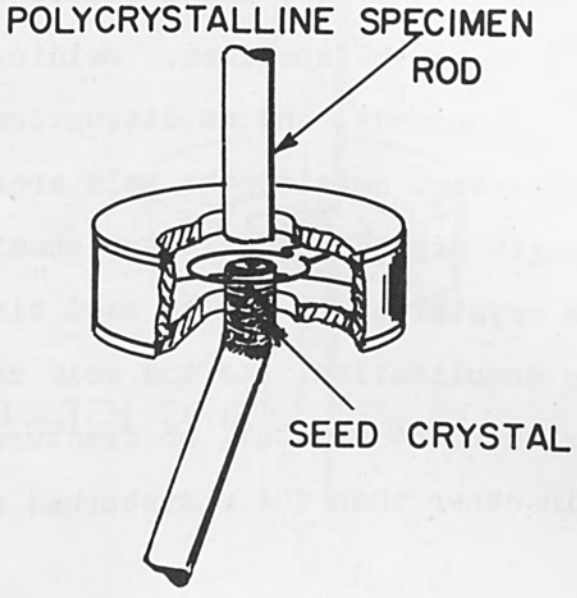

SEEDING TO ORIENTATION
FIG. 5

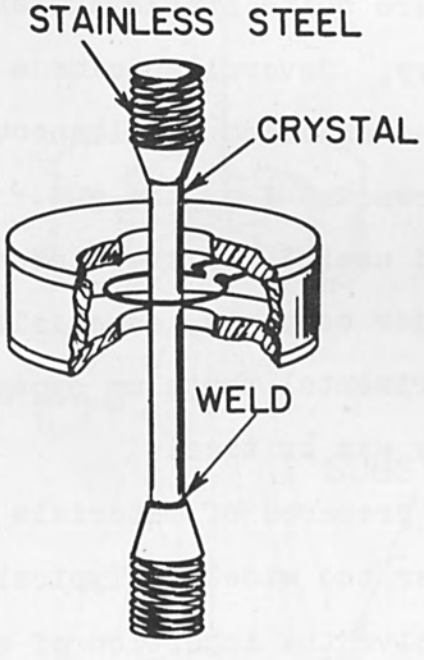

TENSILE SPECIMEN WELDING
FIG. 6

assembly is placed in the gun, and a fillet on the steel rod is welded to the specimen. Welding time is approximately 2 seconds, and no disruption of the specimen is evident outside the weld area.

A gauge length may then be electro-chemically machined in the crystal or it may be used directly without further complication. As the weld zone is always stronger than the crystal, no fractures have ever occurred in other than the undisturbed specimen area.

ANNEALING AND ALLOYING

Annealing and recrystallization are achieved by traversing the gun along a single specimen section, suspended from the upper grip. Temperatures below the melting point are quite stable and are determined by optical pyrometry. Several specimens may be bundled together and annealed simultaneously with the shield plates removed from the gun. This method has also been found useful for the sintering of refractory metal powder compacts, especially in the production of experimental tantalum capacitor slugs where final density was critical.

Alloys may be prepared of materials whose melting points do not differ too widely. Typical techniques (fig. 7) would involve the insertion of a rod or powder of one constituent in a tube of the other, or

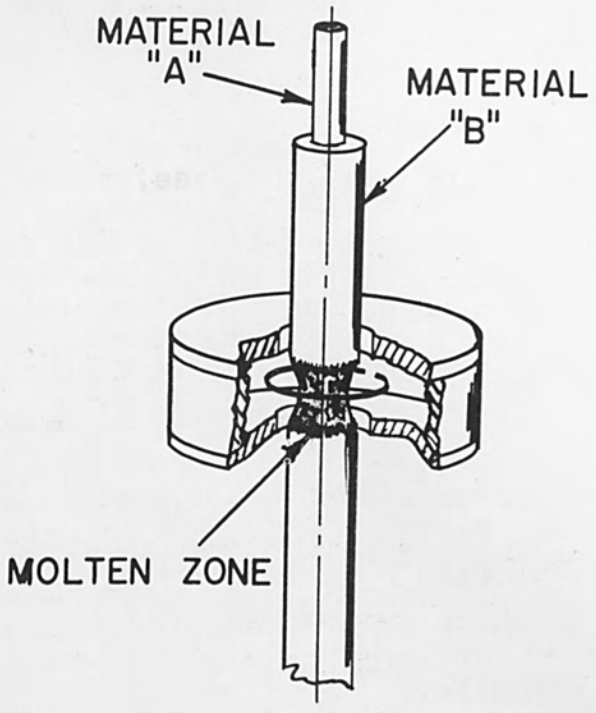

ALLOYING
FIG. 7

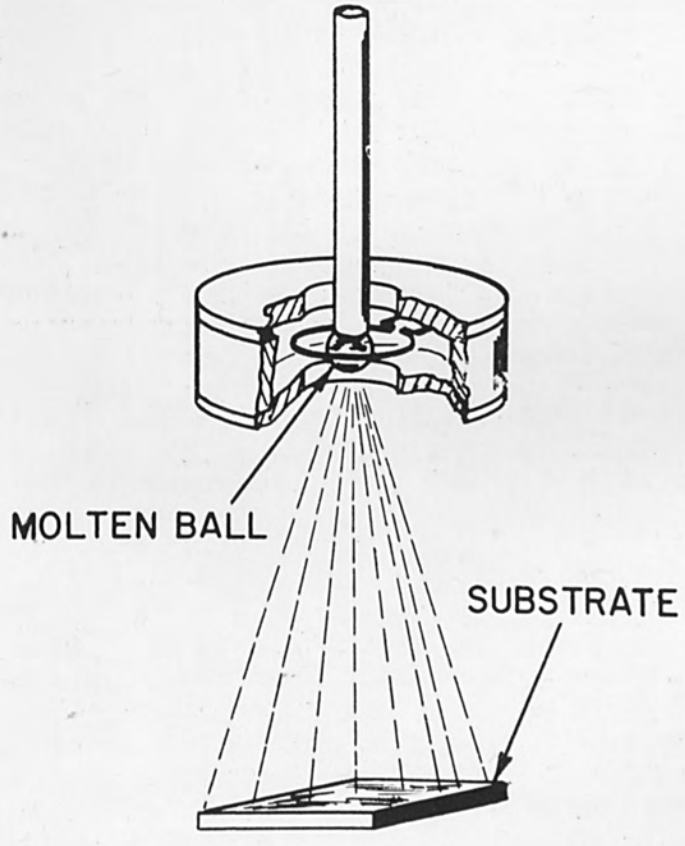

VAPOR DEPOSITION
FIG.8

wrapping a wire around a rod. In either case, the assembly is zone melted as if a single rod. By passing leveling zones in both directions, at rapid rates, segregation is reduced, yielding a homogeneous alloy.

Dilute alloys of refractory metals with carbon have also been produced by coating the rod with a colloidal graphite prior to zoning.

THIN FILM DEPOSITION

Highly adherent thin films of refractory metals, borides, carbides, and oxides have been deposited in thicknesses from 25 Å up to several thousand Å. A substrate holder, which may be heated, is placed on the lower specimen grip (fig. 8). The material to be deposited is placed with one end in the gun, and a molten ball is formed at the end of the rod. Deposition rates of several hundred angstroms per minute have been achieved with tantalum, and the adherence of film to substrate is such that hard scraping with a sharp tool is necessary to scratch the film.

SUMMARY

For the needs of our laboratory, which have been many and varied, the apparatus described here has been invaluable as a research tool. Three units are presently in constant operation filling the

requirements of some 45 research personnel on such projects as fundamental investigations of refractories, development of thin film devices, superconducting materials and protective coatings for refractory metals.

Future efforts will be directed towards improved handling of ceramics and production of refractory metal crystals with impurity levels measured in parts per billion.

ON SOME PROPERTIES OF ELECTRON BEAM MELTED METALS

By

E. Rexer
Professor and Director
Institute for Applied Physics of Pure Materials
Dresden, East Germany

ABSTRACT

Systems, at the Institute of Physics of Pure Metals in Dresden, for the electron beam melting and refining of metals are presented. Some properties of Nickel, Zirconium, Niobium, Tungsten, Molybdenum, Tantalum, Rhenium and Rhenium Molybdenum alloys processed in these installations are discussed.

Einleitung

Die Laboratorien des Institutes für angewandte Physik der Reinststoffe Dresden sind 1958 fertiggestellt worden. Seit dieser Zeit wird, neben der Bearbeitung vieler anderer Aufgaben, von einer Arbeitsgruppe den Fragen des Elektronenstrahlschmelzens Beachtung geschenkt. Der vorliegende kurze Bericht soll einen Überblick über die bisher durchgeführten oder noch laufenden Arbeiten geben. Natürlich muß dabei auf Einzelheiten verzichtet werden.

Über die Arbeiten an einem Elektronenstrahlschweißgerät ist an anderer Stelle zusammenfassend berichtet worden [1].

Der Elektronenstrahlofen

Das Laborgerät mit einer maximalen Leistung von 15 kW wird mit einer Spannung bis zu 60 kV betrieben. Diese für Elektronenöfen ungewöhnlich hohe Spannung wurde gewählt, da mit einem vorhandenen Hochspannungsaggregat auch noch ein Elektronenstrahlschweißgerät versorgt wird. Dabei muß natürlich die auftretende Röntgenstrahlung beachtet werden. Die Schmelzkammer 1 (Abb. 1) wurde deshalb aus 30 mm dicken Stahlplatten hergestellt. Außerdem befindet sich vor dem Ofen eine verschiebbare Bleischutzwand.

Die Schmelzkammer wird über ein Eckventil 2 von einer Diffusionspumpe 3 mit einer Sauggeschwindigkeit von 2 000 l / s evakuiert. Auf dem Rezipienten befindet sich, 7° gegen die Senkrechte geneigt, eine Säule 4 mit einem Fernfokussystem nach Steigerwald [2] und einer elektromagnetischen Linse. Die Wolframbandkathode arbeitet im Sättigungsgebiet,und die Regelung des Strahlstromes geschieht mit Hilfe der Kathodenheizung. Der durch eine Blende vom Rezipienten getrennte Kathodenraum wird zusätzlich durch eine Öldiffusionspumpe mit einer Sauggeschwindigkeit von 120 l/s evakuiert.

Der an der Unterseite der Schmelzkammer durch Exzenter angedrückte wassergekühlte Revolvertiegel 5 besitzt drei Vertiefungen für Knopfschmelzen. Dieser Tiegel kann durch eine Blockabzugsvorrichtung ersetzt werden. Die Materialzugabe erfolgt dann durch ein an den Rezipienten angeflanschtes Zusatzgerät.

Abb. 2 zeigt die Gesamtansicht der Anlage, Abb. 3 den Knopfschmelztiegel.

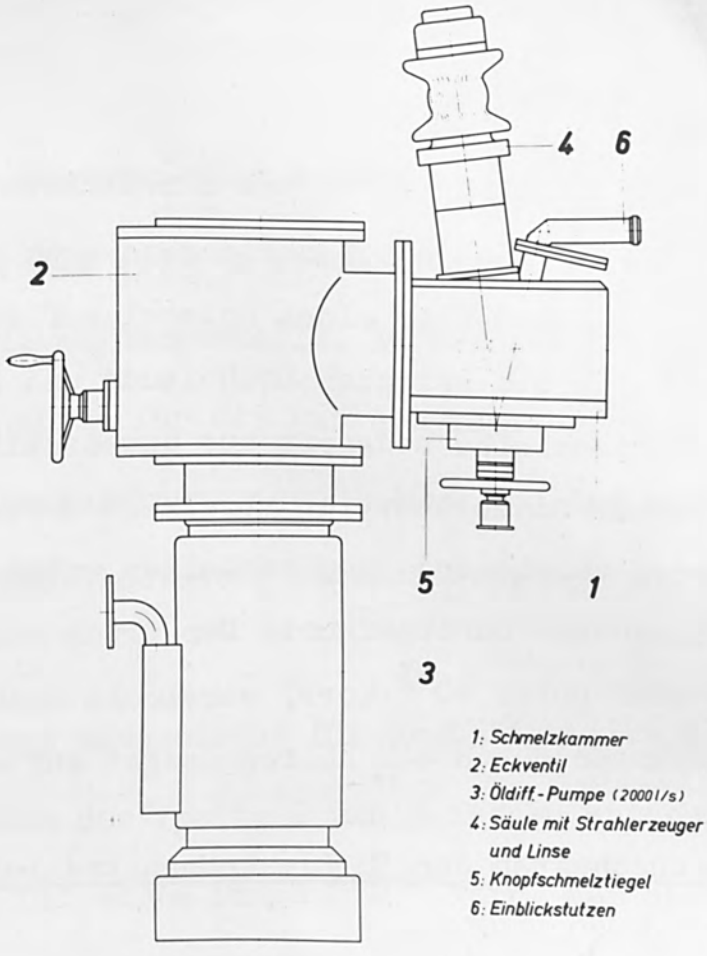

Fig. 1. Schematic of the electron beam furnace

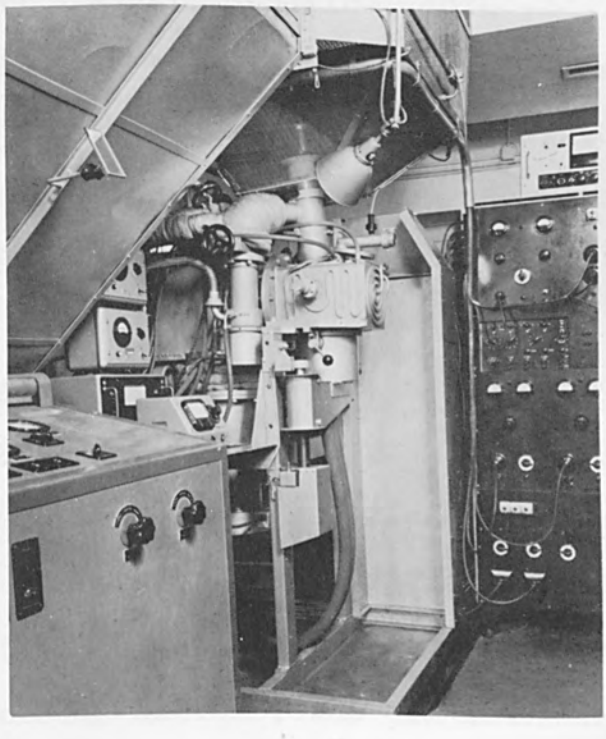

Fig. 2. The electron beam furnace

Der Schmelzvorgang wird durch den Einblickstutzen 6 (Abb. 1) beobachtet. Dabei hat sich ein Lochblendensystem bewährt, mit dessen Hilfe der Schmelzsee über einen Spiegel auf einer Mattscheibe abgebildet wird. Die zwischen Lochblende und Spiegel angebrachte drehbare Schutzscheibe bedampft nur unwesentlich und muß erst nach mehreren Wochen Schmelzbetrieb gereinigt werden.
Bisher wurden vorwiegend Knopfschmelzen unter möglichst guten Schmelzbedingungen durchgeführt. Der Druck während des Schmelzens liegt bei oder unter 10^{-5} Torr, wobei die Ölabscheider beider Diffusionspumpen durch ein Kälteaggregat auf - 50° C gekühlt werden.

Einige Eigenschaften der im Elektronenstrahlofen geschmolzenen Metalle

Die bisher durchgeführten Versuche erstreckten sich auf die Metalle Nickel, Zirkon, Niob, Molybdän, Tantal, Rhenium und Wolfram. Der mit dem Gasanalysengerät GA 01 der Firma E. Leybold's Nachf., Köln, bestimmte Gasgehalt nach dem Schmelzen ergab im Mittel für Sauerstoff Werte in der Größenordnung um 10 ppm, für Stickstoff und Wasserstoff um 1 ppm. Der Kohlenstoffgehalt lag bei 5 ppm. Spektralanalytisch wurde festgestellt, daß die in den Ausgangspulvern mit unterschiedlichen Anteilen enthaltenen Elemente Aluminium, Calcium, Chrom, Kupfer, Magnesium, Mangan, Nickel, Blei, Silicium, Zinn, Titan und Zink bis auf Restgehalte unter 10 ppm verdampfen. Dagegen konnte zum Beispiel beobachtet werden, daß sich Molybdän, Tantal und Zirkon im Niob bzw. Eisen, Molybdän und Niob im Tantal sowie Molybdän und Wolfram im Rhenium nur unwesentlich abreichern.

Eine Kaltverformung der Molybdän- und Wolframknöpfe war erwartungsgemäß nicht möglich. Für die anderen Metalle ist in Abb. 4 der Härteanstieg beim Kaltwalzen dargestellt. Auffallend ist der fast waagerechte Verlauf der Kurve für die kubisch-raumzentrierten Metalle Niob und Tantal für Dickenverminderungen > 10 % und der steile Anstieg für das in hexagonal dichtester Kugelpackung kristallisierende Rhenium.

Eine Übersicht über einige mechanische Eigenschaften gibt Tabelle 1. Aus den Härteunterschieden der Spalte 2 und 3 ist zu entnehmen, daß, nach der Glühbehandlung bei einem Druck $< 10^{-5}$ Torr, der nach dem Schmelzen vorliegende Zustand nicht wieder erreicht wurde. Die Gasanalyse des geglühten Niobmaterials ergab einen erhöhten Sauerstoffgehalt von 80 ppm, während der Stickstoffgehalt auf 6 ppm angestiegen war.

Der Einfluß der Schmelzenergie auf die Härte der Metalle Niob und Tantal ist aus Abb. 5 ersichtlich. Während des Schmelzens lag der Druck bei $5\ 10^{-6}$ Torr.

Der Einfluß des Druckes ergibt sich aus Versuchen, bei denen dieser über ein an den Ofen angeflanschtes Nadelventil variiert wird. So steigt zum Beispiel die Härte des Niobs bei $5 \cdot 10^{-4}$ Torr bei einer

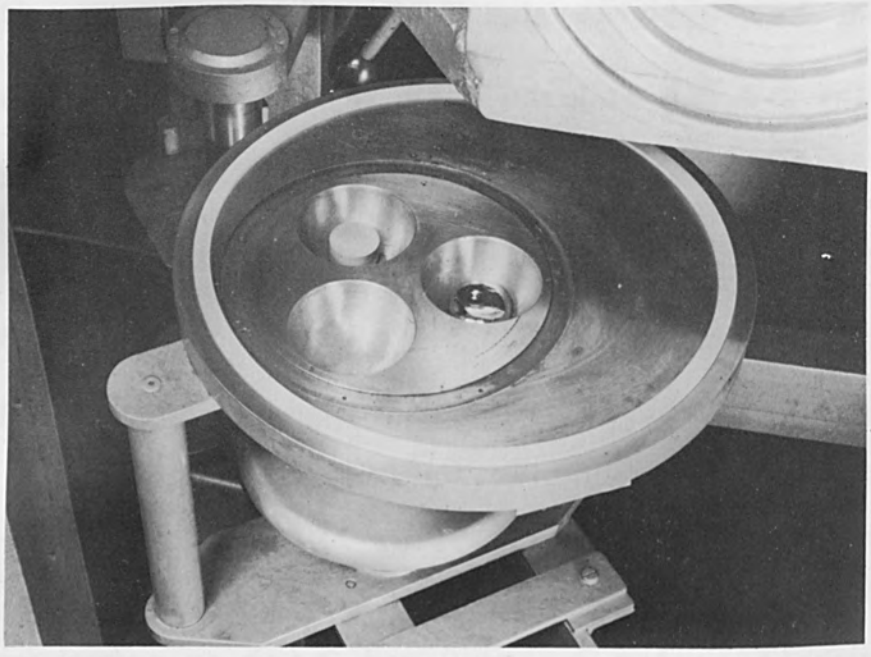

Fig. 3. Buttonmelter

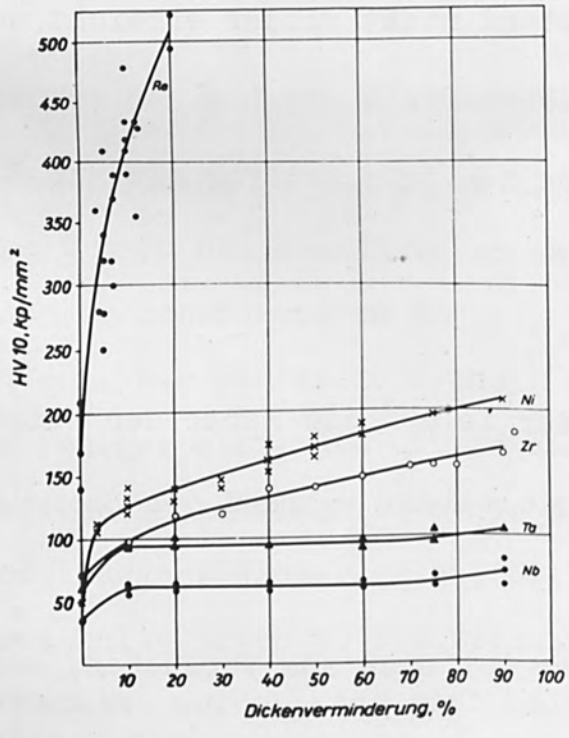

Fig. 4. Hardness as a function of cold rolling of Niobium, Tantalum, Zirconium, Nickel and Rhenium

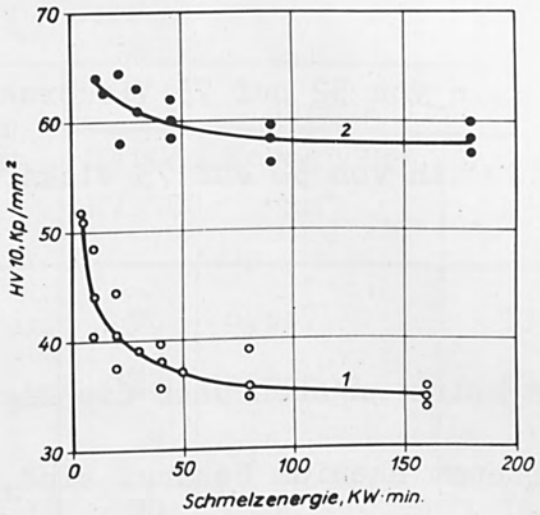

Fig. 5. Hardness as a function of fusion energy of Niobium and Tantalum

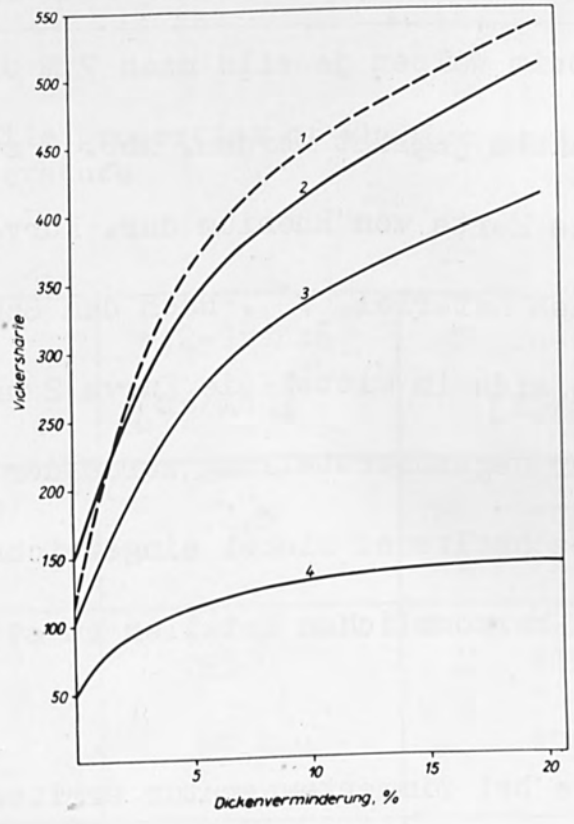

Fig. 6. Hardness as a function of cold rolling for: 1) arc melted Rhenium, 2) & 3) electron beam melted Rhenium and 4) Nickel

Schmelzenergie von 4 kW · min von 52 auf 75 Vickerseinheiten, die des Tantals bei 90 kW · min von 58 auf 75 Vickerseinheiten an (vgl. Abb. 5).

Da uns aus der Literatur keine Angaben über die Eigenschaften von elektronenstrahlgeschmolzenem Rhenium bekannt sind, sollen hierzu noch einige Werte mitgeteilt werden [6] . Rhenium wird kaltverformt, da es beim Erwärmen außerordentlich heftig oxydiert. Wegen der starken Verfestigung (Abb. 4) mußten die im Elektronenstrahlofen geschmolzenen Knöpfe beim Walzen jeweils nach 7 % Dickenverminderung bei 1 500° C im Hochvakuum geglüht werden. Abb. 6 stellt den Einfluß des Kaltwalzens auf die Härte von Rhenium dar. Kurve 1 gilt für im Lichtbogen geschmolzenes Material [7] . Nach dem Schmelzen im Elektronenstrahlofen ergab sich im Mittel die Kurve 2 und als untere Grenze die Kurve 3. Zur Gegenüberstellung wurde der Härteverlauf für elektronenstrahlgeschmolzenes Nickel eingezeichnet (Kurve 4), welches sich unter den herkömmlichen Metallen am stärksten verfestigt.

In Tabelle 2 werden die bei Zimmertemperatur ermittelten mechanischen Eigenschaften mit Literaturangaben verglichen. Das im Elektronenstrahlofen geschmolzene Rhenium hat eine geringere Zugfestigkeit

Table 1. Mechanical properties in electron beam melted metals

	Härte nach dem Schmelzen HV 10	Nach Kaltwalzen und Glühen				
		Härte HV 10	Korngröße mm^2	o,2-Grenze kp/mm^2	Zugfest. kp/mm^2	Dehnung %
Ni	48	56	o,oo7	10	34,4	43
Zr	70	122	o,ooo08	19	24,6	33
Nb	35	41	o,6	7,4	10,3	38
Ta	55	70	o,o5	14,1	19,5	40
Re	135	223	o,oo1	31,5	85	32
Mo	153	nicht kaltverformbar				
W	313	nicht kaltverformbar				

Table 2. Tensile properties of Rhenium at Room Temperature

	o,2-Grenze $[kp/mm^2]$	Zugfestigkeit $[kp/mm^2]$	Dehnung [%]
gesintert. Stab nach [3]	32,5	115	24
gesintert. Blech nach [4]	95	118	28
nach [5]	27,4	105	19
elektronenstrahl-geschmolzen, Blech	31,5	85	32

und eine größere Dehnung als pulvermetallurgisch hergestelltes Material.

Geach und Mitarbeiter [7] haben gefunden, daß sich eine im Lichtbogenofen geschmolzene Molybdänlegierung mit 35 Atom% Rhenium bis über 90 % einwandfrei ohne Zwischenglühungen kaltverformen läßt. Allerdings liegt die Dehnung derart verformten Materials nach einer Glühbehandlung bei 1 600° C bei nur 2 % [8]. Die im Elektronenstrahlofen geschmolzenen Knöpfe der gleichen Legierung lassen sich ebenfalls bis über 90 % kaltwalzen. Die Dehnung nach einer Glühbehandlung bei 2 000° C beträgt aber 20 %. Ob die günstigeren Dehnungseigenschaften auf die höhere Glühtemperatur oder die größere Reinheit des elektronenstrahlgeschmolzenen Materials zurückzuführen sind, konnte noch nicht entschieden werden.

In Tabelle 3 werden einige mechanische Eigenschaften der elektronenstrahlgeschmolzenen Mo-35 At% Re-Legierung mit nach anderen Verfahren hergestelltem Material verglichen.

Zu den bisher durchgeführten metallographischen Untersuchungen der im Elektronenstrahlofen geschmolzenen Knöpfe sollen drei Bilder als Beispiel dienen. Sie sind an einzelnen Körnern aufgenommen worden, deren Orientierung röntgenographisch bestimmt wurde.

Table 3. Tensile properties of the Mo-35 (At-%) Rhenium alloy

	o,2_Grenze kp/mm^2	Zugfestigkeit kp/mm^2	Dehnung %
Im Lichtbogen geschmolzen warm-u.kaltgewalzt, nach [5]	148	169	1
dto. geglüht 1/2h, 1650°C	86,5	105	22
Im Lichtbogen geschmolzen 95 % kaltgewalzt nach [8]	-	180	<1
dto. geglüht 2h, 1600°C	-	125	2
Im Lichtbogen geschmolzen, warm- u. kaltgewalzt, nach [8]	-	174	2
dto. geglüht 1 h, 1700°C	-	98,5	22
Herstellungsverfahren unbekannt, nach [9]	39	91,5	25
Im Elektronenstrahl geschmolzen 90% kaltgewalzt	-	174	<1
dto. geglüht 4 h, 2000°C	38	85	20

Abb. 7 zeigt eine Ätzfigur auf der Basisfläche von Rhenium, während die Abb. 8 und 9 auf einer (111)-Fläche von Niob beziehungsweise (100)-Fläche von Tantal erhalten wurden. Auf die Problematik solcher Ätzversuche im Zusammenhang mit dem Nachweis von Versetzungen kann hier nicht näher eingegangen werden.

Die Elektronenzonenschmelzapparatur

Für die Herstellung von einkristallinen Stäben steht eine Elektronenzonenschmelzapparatur zur Verfügung, die in Anlehnung an die von Calverley und Mitarbeitern [10] entwickelte Anlage aufgebaut wurde (Abb. 10) [11] . Sie besteht aus dem Rezipienten mit Eckventil und Diffusionspumpe (2 000 l/s), einem 10 kV Gleichrichter und einer Regeleinrichtung. Der Zonenschmelzeinsatz ist am oberen Flansch des Rezipienten befestigt. Die Fokussierungsbleche sind so ausgebildet, daß ein Bedampfen der Kathode von der Schmelzzone her weitgehend vermieden wird.

Bisher wurden einkristalline Stäbe aus Zirkon, Niob, Molybdän, Tantal, Rhenium und Wolfram hergestellt. Bei Bedarf kann die Orientierung mit Hilfe eines Keimes vorgegeben werden. Die Ringkathode besteht jeweils aus dem gleichen Metall wie der zu reinigende Stab.

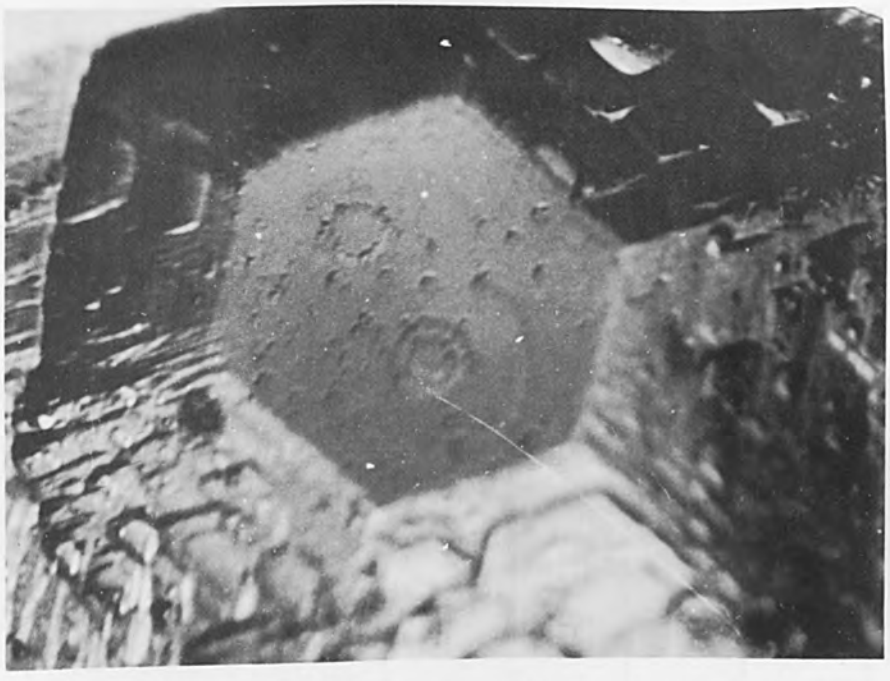

Fig. 7. Etch figure in the basal plane of Rhenium (electrolytically polished and etched with 10V-1 amp/cm^2 in 1 part CrO_3 + 4 parts CH_3 COOH + 1 part H_2O)

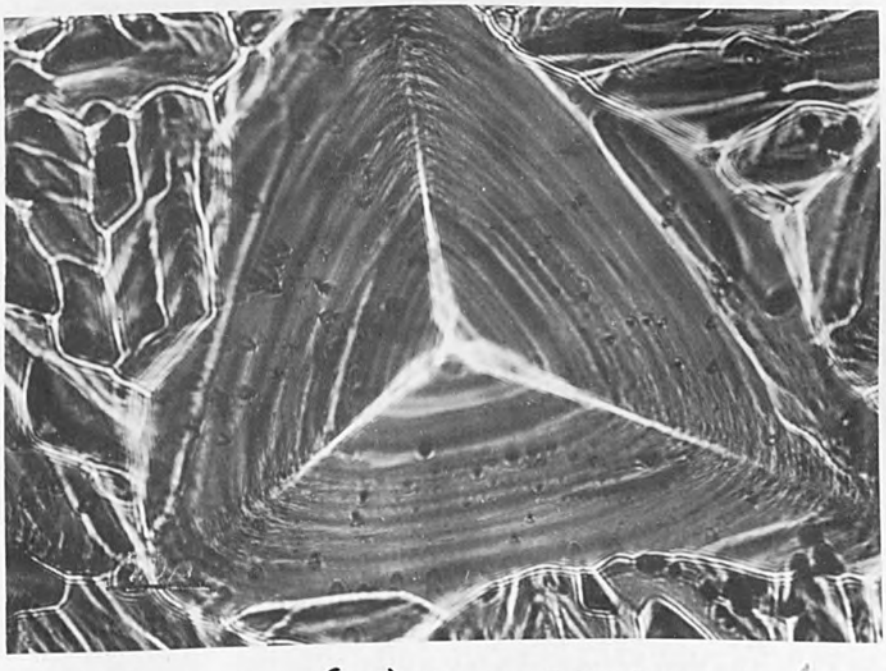

Fig. 8. Etch figure on a (111) plane of Niobium (electrolytically polished with 10-15V-1.5 amp/cm^2 in 2 parts lactic acid + 1 part H_2SO_4 + 1 part HF and chemically etched in 10 parts H_2O and 10 parts HF + 10 parts H_2SO_4 + 1 part H_2O_2 for 30 minutes)

Einige Eigenschaften elektronenzonengeschmolzenér Einkristalle

Zur schnellen Charakterisierung der elektronenzonengeschmolzenen Einkristalle wird die Härte länges der Stablänge gemessen. Abb. 11 zeigt den entsprechenden Verlauf für Tantal- und Niobeinkristalle (Kurve 1 bzw. Kurve 2). Der gleiche Gang wurde für das Widerstandsverhältnis R (80° K) / R (273° K) festgestellt (Kurve 3). Der stetige Abfall vom Stabanfang zum Stabende ist noch ungeklärt, da er offenbar nicht mit der Verteilung von Verunreinigungen mit einem Verteilungskoeffizienten > 1 erklärt werden kann.

Die Reinheit von elektronenzonengeschmolzenen Wolframeinkristallen konnte durch das freundliche Entgegenkommen von Herrn Dr. Waldron mit dem Festkörpermassenspektrometer MS 7 der Associated Electrical Industries, Manchester (England), überprüft werden (Tab. 4). Es handelt sich um eine Versuchsserie mit unterschiedlichen Schmelzbedingungen (Probennummern vgl. auch Tab. 6). Die dazu notwendigen Elektroden mit einem Durchmesser von 2 mm wurden in der Elektronenzonenschmelzapparatur gezogen. Die in Tab. 4 zu einer Gruppe zusammengefaßten Verunreinigungen Jod, Chlor, Schwefel, Fluor und Bor sind sicher auf die Ätzbehandlung vor der massenspektrometrischen Analyse mit Fluß- und Salpetersäure zurückzuführen.

Table 4. Emission spectrometry analysis of trace impurities and resistivity ratio $Z = \frac{R(o)}{R(273)}$ of zone refined tungsten samples

Proben-Nr.		14	2	7	8	1	13	11
Verun-	Indium	0,05	0,1	0,05	0,1	0,05	0,05	0,05
reini-	Molybdän	0,4	0,4	0,4	0,4	0,4	0,7	0,4
gungs-	Arsen	0,03	0,1	0,2	0,07	0,1	0,03	0,1
gehalt	Zink	1,5	2	3	2	2	2	3
[ppm]	Kupfer	0,3	0,05	0,2	0,05	0,1	0,3	0,15
(1 ppm =	Nickel	0,25	0,5	0,5	0,2	0,2	0,5	0,2
10^{-4} Atom-	Kobalt	0,03	0,03	0,03	0,03	0,03	0,03	0,15
prozent)	Eisen	0,1	1	0,6	0,2	0,15	0,6	0,15
	Chrom	0,1	0,6	0,6	0,5	0,1	1,5	0,07
	Kalzium	1,5	0,4	1,7	0,3	2,5	1	2
	Aluminium	0,03	0,1	0,6	0,15	0,06	0,6	0,2
	Tantal	7	7	10	10	7	10	10
	Jod	0,5	0,15	0,05	0,1	0,5	0,2	0,35
	Chlor	0,6	0,5	0,3	1	1,5	1,0	0,6
	Schwefel	5	2	0,5	2	6	1,6	5
	Fluor	1	3	3	7	3	10	3
	Bor	0,1	0,03	0,06	0,15	1	0,2	0,3
z $[10^{-5}]$		1,5	1,8	2,5	3,7	3,2	6,2	3,2

Der hohe Tantalgehalt erklärt sich durch die Tatsache, daß die Ionenquelle des Massenspektrometers aus Tantalbauteilen gefertigt ist. Andere als die angegebenen Elemente konnten nicht nachgewiesen werden, wobei die Nachweisgrenze zwischen 0,03 und 1 ppm lag.

Das Restwiderstandsverhältnis $z = R\,(0^{\circ}K) / R\,(273^{\circ}\,K)$ dieser Wolframeinkristalle liegt zwischen $6{,}2 \cdot 10^{-5}$ und $1{,}5 \cdot 10^{-5}$. Der beste bisher gemessene Wert beträgt $7 \cdot 10^{-6}$. Diese Werte liegen etwa eine Größenordnung unter den in der Literatur bekanntgegebenen Restwiderstandsverhältnissen [12]. Im Rahmen einer Versuchsserie, bei der die einzelnen Zonenschmelzparameter variiert wurden, sollte geprüft werden, worauf dieser Unterschied zurückzuführen ist [13].

Variiert wurden die Temperatur, die Zonengeschwindigkeit, der Druck im Rezipienten und die Anzahl der Zonendurchgänge. Schwierigkeiten traten bei der Temperaturmessung auf. Am geeignetsten erwies sich zur nachträglichen indirekten Bestimmung der Temperatur der Verdampfungsverlust während des Schmelzens.

Die Variationsmöglichkeiten für die Temperatur sind nicht groß. Es existiert eine optimale Temperatur, bei der die Schmelzzone einwandfrei stabil bleibt. Bei tieferen Temperaturen friert die Zone leicht ein, beziehungsweise der Stab ist nicht ganz durchgeschmolzen.

Bei höheren Temperaturen dagegen wird das Wolfram so dünnflüssig, daß die Zone instabil wird. Es soll deshalb innerhalb der Grenzen, in denen die Zone durchgeschmolzen und stabil gehalten werden kann, jeweils von einer tiefen, normalen und hohen Temperatur gesprochen werden.

In Tab. 5 sind die Verdampfungsverluste α und die zugehörigen Restwiderstandsverhältnisse z eingetragen. Man erkennt, daß bei großem Verdampfungsverlust und damit einer höheren Schmelztemperatur das Restwiderstandsverhältnis abnimmt, während es mit größerem Ausgangsdruchmesser zunimmt. Vermutlich spielen hier Diffusions- und Durchmischungseffekte in der flüssigen Zone eine Rolle.

Der Einfluß der Zahl der Zonendurchgänge, der Zonengeschwindigkeit und des Druckes im Rezipienten ist aus Tabelle 6 zu entnehmen.

Das kleinste Restwiderstandsverhältnis von $8 \cdot 10^{-6}$ erhält man für dreimal geschmolzene Stäbe. Weitere Zonendurchgänge haben keine Wirkung. Vermutlich ist der Einfluß der Gitterfehler schon so groß, daß der Restwiderstand von ihnen bestimmt wird.

Die Feinheiten, die sich aus dem Restwiderstand für die unterschiedliche Behandlung der Proben ergeben, sind aus den massenspektrometrischen Analysen nicht zu erkennen.

Table 5. Influence on the melting temperature on equivalent zone motion velocities and vacuum and the residual resistivity ratio $Z = \frac{R(o)}{R(273)}$ and the evaporation loss of zone melted Tungsten samples

Durchmesser des Ausgangsmaterials [mm]	2		3		5	
	a/%	$z/10^{-5}$	a/%	$z/10^{-5}$	a/%	$z/10^{-5}$
Temperatur der geschmolzenen Zone						
niedrig	19	6,2	20	7,o	20	9,o
normal	28	3,2	32	4,5	30	6,o
hoch	33	2,5	40	3,2	43	4,o

Table 6. The effect of different melting parameters on the resistivity ratio $z \frac{R(o)}{R(273}$ and weight loss of zone melted Tungsten bar

	Proben Nr.	Ausgangsmat. [mm]	Vakuum [10^{-6}Torr]	Anzahl d.Zonendurchg.	Zonengeschw. [mm/min]	Temperatur	a [%]	z [10^{-5}]
Einfluß der Anzahl der Zonendurchgänge	1	2	5	1	o,25	normal	43	3,2
	2	2	5	2	o,5	normal	43	1,8
	3	5	5	1	o,25	normal	44	4,3
	4	5	5	2	o,5	normal	44	1,2
	5	5	5	3	o,5	normal	57	o,8
Einfluß der Zonengeschwindigkeit	6	2	5	1	o,25	hoch	52	2,o
	7	2	5	1	o,5	hoch	33	2,5
	8	2	5	1	1,o	hoch	23	3,7
	3	5	5	1	o,25	normal	44	4,3
	9	5	5	1	o,5	normal	30	5,9
	10	5	5	1	1,o	normal	24	11,o
Einfluß des Vakuums	7	2	5	1	o,5	hoch	33	2,5
	11	2	70	1	o,5	hoch	33	3,2
	9	5	5	1	o,5	normal	30	5,9
	12	5	70	1	o,5	normal	30	6,4

Mein Mitarbeiter, Herr Wadewitz, untersucht im Rahmen seiner Dissertation die Substruktur zonengeschmolzener Wolframeinkristalle, vor allem in Abhängigkeit von den Zonenschmelzbedingungen [14] . Die mit vorgegebener Orientierung hergestellten einkristallinen Stäbe wurden quer zur Längsachse in Scheiben von 5 mm Dicke parallel zu (100) und (110)-Flächen getrennt und elektrolytisch poliert. Die Gefügeuntersuchung wird bevorzugt nach der Parallelstrahlmethode von Berg [15] in der von Barth [16] angegebenen Technik durchgeführt. Danach bildet man eine parallel zur Kristalloberfläche liegende Netzebenenschar auf einer parallel zur Kristalloberfläche angebrachten Fotoplatte ab. Bringt man zwischen Kristall und Fotoplatte ein feinmaschiges Gitter an, so wird dieses, falls die reflektierende Netzebene keinerlei Störungen aufweist, unverzerrt auf der Fotoplatte abgebildet. Besteht der Kristall aber aus gegeneinander verdrehten Subkörnern oder sind die Netzebenen verbogen, so wird das Gitter verzerrt wiedergegeben. Abb. 12 zeigt links als Beispiel Parallelstrahlaufnahmen ohne und rechts mit Gitter. Die beiden oberen Bilder wurden an einem zweimal geschmolzenen Kristall am Stabanfang aufgenommen und zeigen ein bis auf die Randgebiete wenig gestörtes Gefüge. Auf den beiden unteren Bildern dagegen kann man, ebenfalls am Stabanfang, eine Aufspaltung in viele Subkörner mit Winkel-

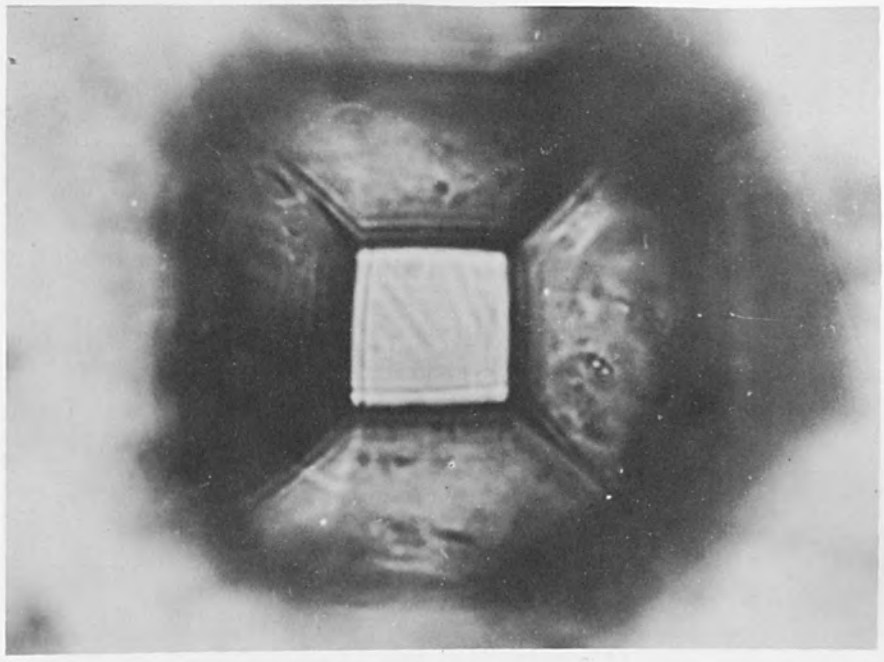

Fig. 9. Etch figure on a (100) plane of Tantalum (electrolytically polished with 10-15V-1.5 amp/cm^2 in 2 parts lactic acid + 1 part H_2SO_4 + 1 part HF and chemically etched in 10 ml Br_2 + 90 ml CH_3OH + 10 gr acetic acid for 30 hours)

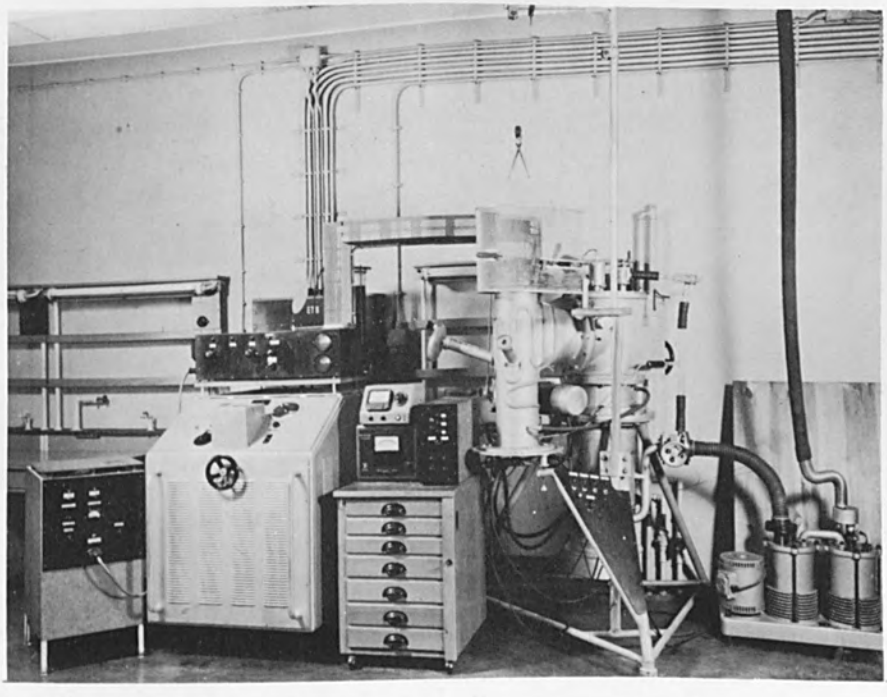

Fig. 10. Electron beam melting installation

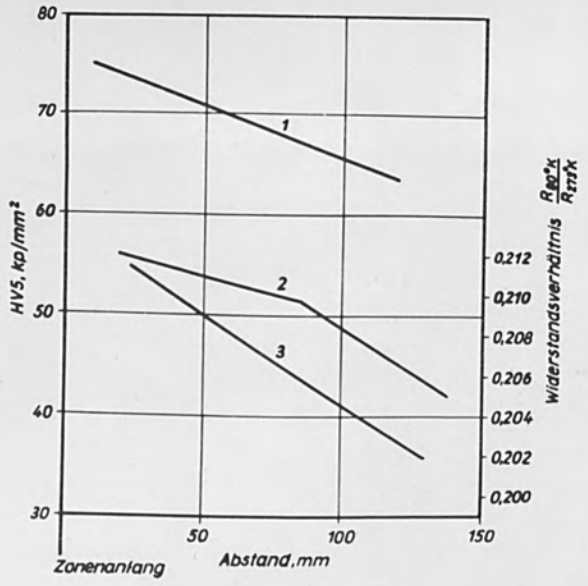

Fig. 11. Hardness of Tantalum (1) and Niobium single crystals (2). Resistivity ratio R(80°K)/R(273°K) of Niobium single crystals (3).

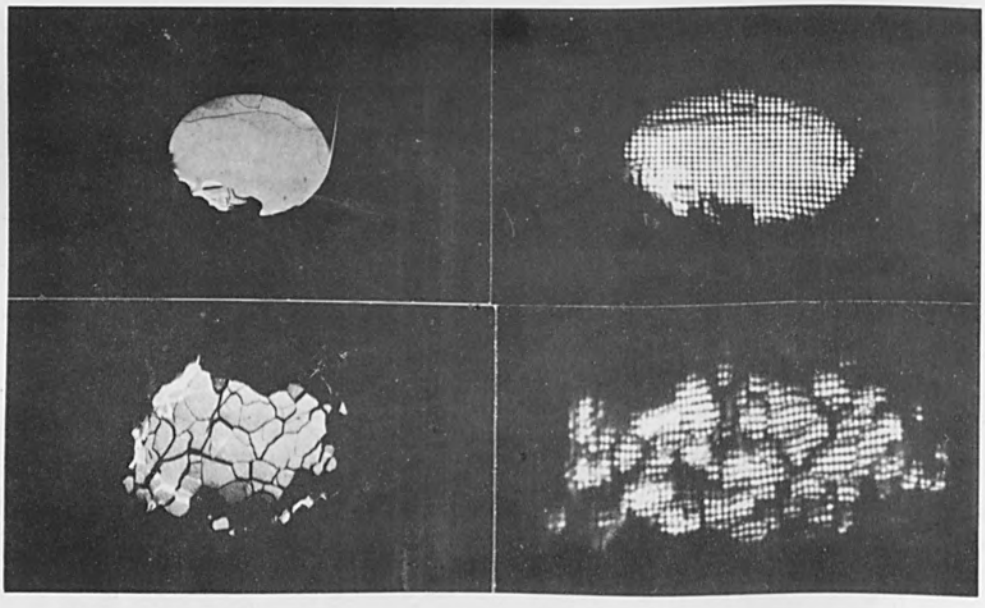

Fig. 12. Parallel beam photograph of a W crystal, left without, and right with lattice network.

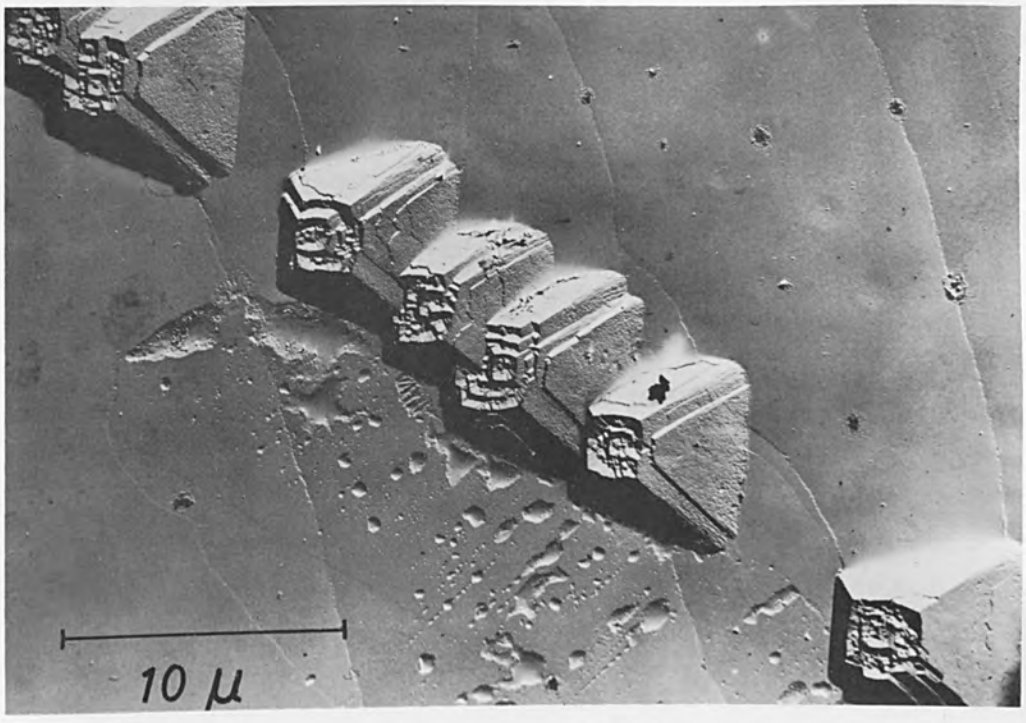

Fig. 13. Etch figures on a W-(100) face (electrolytically polished with 15V with 5% KOH solution, etched a few seconds with Murakami Reagent, photographed with Elmi D2 - Zeiss, Jena)

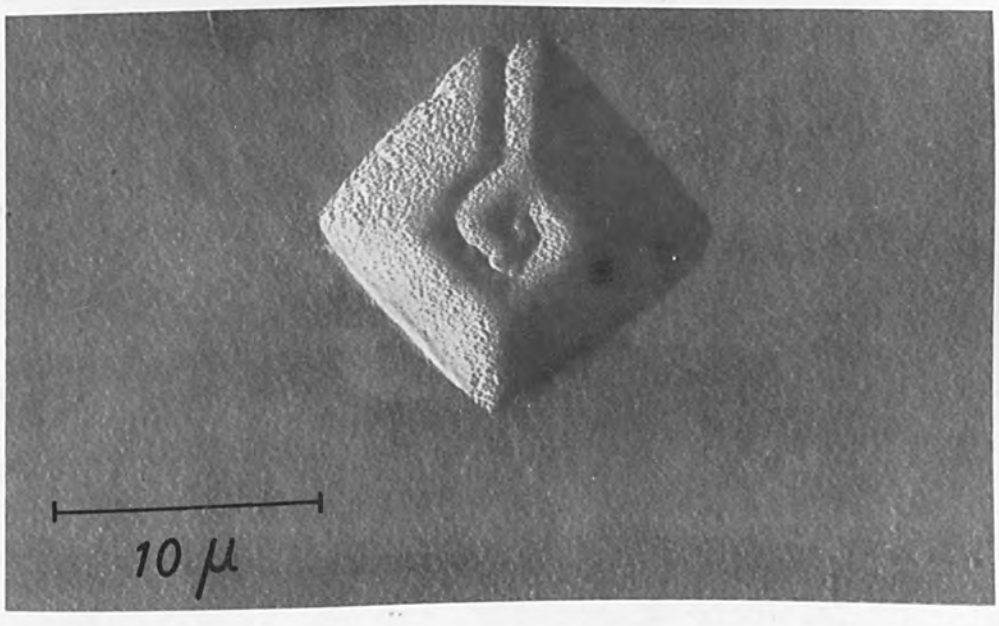

Fig. 14. Etch figure on a W-(100) face (electrolytically polished with 15V and 8% KOH solution, etched a few seconds electrolytically with 2V with 2% KOH solution, photographed with Elmi D2 - Zeiss, Jena)

unterschieden bis zu 1° über den gesamten Kristallquerschnitt beobachten. Dieser Kristall ist einmal geschmolzen worden, wobei die obere Kristallhalterung zur besseren Durchmischung der Schmelzzone gegen die untere mit 15 Umdrehungen / min rotierte. Offenbar führt diese mechanische Bewegung zu einer starken Gefügestörung.

Parallel zu diesen röntgenographischen Betrachtungen durchgeführte Ätzversuche, auf die hier nicht näher eingegangen werden soll, haben ergeben, daß sich die Subkorngrenzen reproduzierbar anätzen lassen, während dies für auf den Flächen statistisch verteilte Ätzgrübchen nicht zutrifft. In diesem Zusammenhang interessiert auch die Feinstruktur der Ätzfiguren, die mit Hilfe des Elektronenmikroskopes näher untersucht wurden. Als Beispiele dafür zeigen die Abb. 13 und 14 Ätzgrübchen auf einer Wolfram-(100)-Fläche, die Abb. 15 auf einer Wolfram-(111)-Fläche. Die von einer Aluminiumaufdampfmatrize erhaltenen Kohleschichtpräparate wurden zur Kontraststeigerung in der üblichen Weise mit Gold-Palladium schräg bedampft.

Weiterhin soll noch erwähnt werden, daß sich Arbeiten, die erst begonnen wurden, mit der Plastizität kubisch-raumzentrierter Einkristalle befassen. Bei dieser Gruppe von Metallen herrscht, völlig abweichend von der Situation bei den kubisch-flächenzentrierten und hexagonalen Metallen bis heute zum Beispiel noch keine endgültige Klarheit darüber, welche Gleitsysteme betätigt werden und ob diese kristallographisch bestimmt sind [17] [18] . Fragen dieser und anderer Art sollen in einer Zugprüfmaschine näher untersucht werden, die sich noch im Aufbau befindet. Die Einkristalle können damit bei konstanter Last und mit konstanter Geschwindigkeit verformt werden. Für Plastizitätsuntersuchungen bei sehr hohen Temperaturen wird auch hierbei die Elektronenheizung eingesetzt werden. Der Probekörper wird bis auf etwa 2 000° C mit Hilfe eines direkt geheizten Tantalheizrohres durch Strahlung erhitzt. Höhere Temperaturen erreicht man, indem die aus dem Heizleiter austretenden Elektronen auf den Probekörper hin beschleunigt werden [19] [20] .

Improvisierte Verformungsversuche in der Elektronenzonenschmelzapparatur, wobei die Elektronen nicht fokussiert wurden, ergaben zum Beispiel bei 2 000° K auf der Stirnfläche eines Wolframeinkristalles das in Abb. 16 gezeigte Gleitspurenbild. Diese Spuren verlaufen abweichend zu denen auf der Seitenfläche nicht geradlinig,

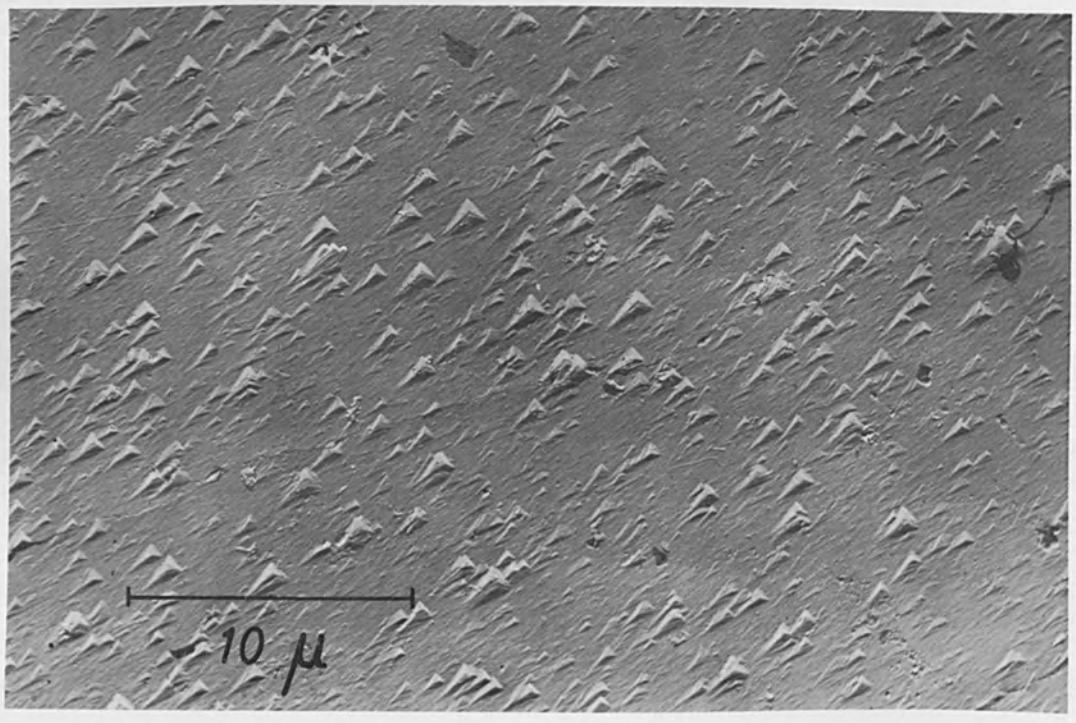

Fig. 15. Etch figures on a W-(111) face (electrolytically polished with 15V with 5% KOH solution, etch 20 seconds with Murakami Reagent, photographed with Elmi D2 - Zeiss, Jena)

Fig. 16. Slip lines on a Tungsten single crystal

sondern gewellt, was auf das Herauswandern von Schraubenversetzungen aus ihren Gleitebenen zurückzuführen ist [21]. Laue-Aufnahmen der verformten Bereiche lassen auf eine während der 10-stündigen Versuchsdauer wirksam werdende Polygonisation mit Verdrehungen der Polygonisationskörper um 3 bis 4° schließen. Das zugehörige Ätzbild zeigt Abb. 17.

Das Gleitsystem wurde bei diesen Vorversuchen, bei denen die Stabachse mit der <110> Richtung zusammenfiel, zu $\{211\}$ <111> bestimmt.

Schluß

Der Bau der beschriebenen Apparaturen und die Durchführung der einzelnen Untersuchungen wurde von einer Gruppe von Physikern, Ingenieuren und Mechanikern durchgeführt, denen ich für ihre Mitarbeit herzlich danke. Meinem Mitarbeiter, Herrn Schlaubitz, danke ich besonders für die Unterstützung bei der Abfassung dieses Berichtes.

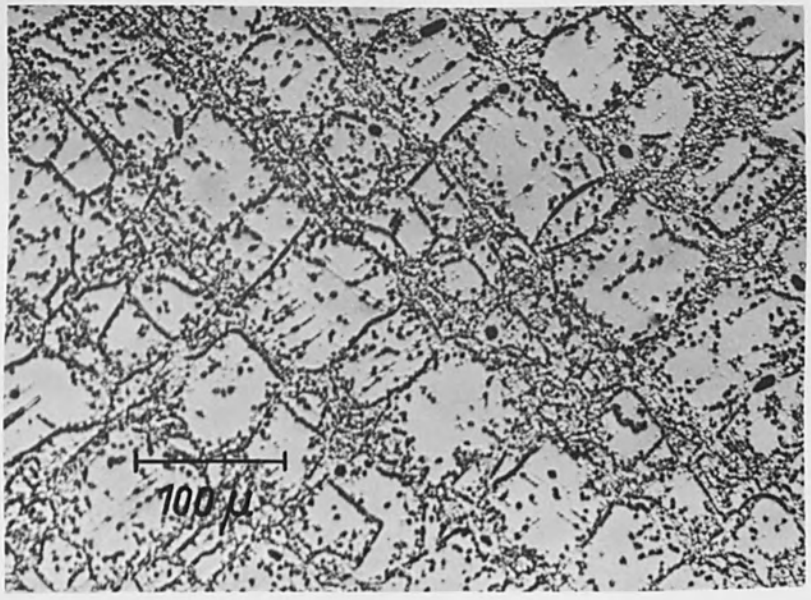

Fig. 17. Etch pattern in a Tungsten crystal deformed at 2000°K (110) face, etched with equivalent parts HF, HNO_3, and H_2O

Literaturverzeichnis

[1] Göbel, R., E. Heinze, W. Neumann, E. Rexer und K. Schlaubitz
Kernenergie, im Druck

[2] Steigerwald, K. H.
Optik 5 (1949) 469

[3] Sims, C. T., C. H. Craighead und R. I. Jaffee
Trans. AIME 203 (1955) 168

[4] Sims, C. T. und R. I. Jaffee
J. Metals 8 (1956) 913

[5] Port, J. H. und J. M. Pontelandolfo
Met. Soc. AIME Conf. Vol. 2 "Reactive Metals", 1958
S. 555

[6] Zedler, E., D. Kraut, K. Schlaubitz und D. Müller
Veröffentlichung in Vorbereitung

[7] Geach, G. A. und J. E. Hughes
2. Plansee-Seminar, 1955, S. 245

[8] Jaffee, R. I., C. T. Sims und J. J. Harwood
3. Plansee-Seminar, 1958, S. 380

[9] Jaffee, R. I., D. J. Maykuth und R. W. Douglass
AIME Refract. Met. Symp., Detroit, Mai 1960

[10] Calverley, A., M. Davis und R. F. Lever
Journ. Scient. Instr. 34 (1957) 142

[11] Longo, H. E., und K. Schlaubitz
Festkörperphysik, Akademieverlag Berlin, 1961,
S. 253

[12] Schadler, H. W.
Proceedings of the First Symposium on Electron-Beam-Melting, Boston (1959), S. 27

[13] Berthel, K. H., H. E. Longo und K. Schlaubitz
Vortrag auf dem Internationalen Symposium "Reinststoffe in Wissenschaft und Technik", Dresden 1961 (Tagungsbericht erscheint im Akademieverlag, Berlin)

[14] Wadewitz, H.
loc. cit. [13]

[15] Berg, W.
Naturwiss. 19 (1931) 391

[16] Barth, H.
Z. Naturforsch. 13 a (1958) 680

[17] Leber, S. und J. W. Pugh
Trans. AIME 218 (1960) 791

[18] Schadler, H. W.
Trans. AIME 218 (1960) 649

[19] Manjoine, M. J., L. L. France und R. T. Begley
ASTM spec. techn. publ. No 272, 1960, S. 3

[20] Kraut, D., D. Müller, K. Schlaubitz und E. Zedler
Vortrag auf dem Internationalen Kongress "Technik und Anwendung des Vakuums", 20. bis 24. Juni 1961, Paris

[21] Low, J. R. jun. und R. W. Guard
Act. Met. 7 (1959) 171

HORIZONTAL ZONE MELTING OF REFRACTORY METALS BY REMOTE GUN ELECTRON BOMBARDMENT

By

T. Hikido
Metallurgist
Oak Ridge National Laboratory
Oak Ridge, Tennessee

ABSTRACT

An electron bombardment button and ingot melting furnace has been adapted to zone melt refractory metals by designing a water cooled copper cavity of 4-1/4-in. -i.d. x 7-in.-o.d. which can contain approx. 1.2 kg of metal.

One of the objectives of the zone melting work is to produce single crystals of refractory metals for mechanistic studies pertaining to corrosion, oxidation, and deformation.

Compared to floating zone melting techniques, horizontal zone melting has the advantage of permitting larger specimens to be refined.

THE HORIZONTAL ZONE MELTING OF REFRACTORY METALS BY REMOTE GUN ELECTRON BOMBARDMENT

T. Hikido
Metals and Ceramics Division
Oak Ridge National Laboratory*

*Operated for the U. S. Atomic Energy Commission by Union Carbide Corporation.

THE HORIZONTAL ZONE MELTING OF REFRACTORY METALS BY REMOTE GUN ELECTRON BOMBARDMENT

INTRODUCTION

At the Oak Ridge National Laboratory columbium and other refractory metals of very high purity are required for research programs on the mechanisms of corrosion, oxidation, and deformation. An electron-bombardment melting furnace has been quite effective for preparing suitable starting materials for much of this work. However, in order to achieve higher purities and, if possible, to grow single crystals, the furnace was adapted for zone melting. This paper describes the zone-melting apparatus and presents the results of preliminary experiments.

THE BASIC ELECTRON-BOMBARDMENT FURNACE

The electron-bombardment furnace used in these experiments was built by the NRC Equipment Corporation and is of the type described by E. S. Candidus.[1] Its salient features, which are illustrated in Fig. 1, include a remote, self-accelerated, Pierce-type electron gun, magnetic focusing of the electron beam, and separately pumped gun and melting chambers. A second solenoid, not shown in Fig. 1, is mounted below the aperture to provide more precise control of the electron beam. The 18-in.-diam by 18-in.-high cylindrical melting chamber has an 8-in.-diam opening in the bottom plate through which the cold mold or button hearth is installed. The two 10-in. oil diffusion pumps backed by a 30 cfm compound mechanical pump maintain normal operating pressures of approx 1×10^{-5} torr.

Three circuits compose the power supply which is capable of producing a 60-kw (20 kv, 3 amp) electron beam. First, a variable autotransformer is used to heat a tungsten filament in the electron gun. Second, a 3-kv, 0.5-amp circuit is used to accelerate the electrons emitted by the tungsten filament to bombard and thus heat a tantalum disk, which is the main beam cathode. Third, the output of a motor driven 0–480 v variable transformer feeds a step-up transformer and a three-phase full-wave rectifier to produce the main beam accelerating potential.

Both the accelerating potential and the beam current can be controlled to obtain the desired electron-beam power. Generally, the potential is raised to the operating level and left constant. The beam current is then brought to the desired level and controlled by manually adjusting the filament transformer or by means of an emission regulator designed by C. B. Sibley of NRC. This regulator has proved to be very effective for providing the stable beam power required for producing a constant molten zone.

ADAPTION OF THE FURNACE FOR ZONE MELTING

In order to use the electron-bombardment furnace for zone melting, a rotatable, water-cooled, copper hearth was installed through the 8-in.-diam opening normally used for the cold mold or the button plate. The material to be refined is contained in an annular 4-in.-ID by 7-in.-OD cavity in the hearth and the molten zone is caused to move along the bar by rotating the hearth beneath the stationary electron beam. This arrangement permits the refining of a relatively long bar in the limited area

available and also the use of simple rotation to achieve movement of the molten zone. The main disadvantage lies in the nonuniform travel rate along the solid-liquid interface; the travel rate increases with radius.

A concentric tube arrangement is used for the hearth-cooling water-flow system. The water enters through the inner tube, flows through a channel machined in the copper hearth below the annular sample cavity, then discharges through the annulus between the inner and outer tubes. These tubes also serve as the drive shaft for the hearth assembly. The hearth is mounted on an adapter flange with the shaft passing through a standard double O-ring vacuum rotating seal.

Rotation of the hearth is achieved by an electric gearmotor coupled to a stepwise adjustable transmission. This transmission consists of a series of three gear boxes which provide rotation speeds of 1/16, 1/8, 1/4, 1/2, 1, and 2 rph. These rotation speeds correspond to mean zone travel rates (at the midradius of the ring specimen) of 1-1/8 to 36 in./hr.

MAGNETIC SHAPING OF THE ELECTRON BEAM

The electron beam normally produces a circular molten zone. In order to obtain a zone with a straight liquid-solid interface, experiments were conducted using magnetic fields to shape the beam. The magnets used were solenoids containing Armco iron cores with mild steel parallel end plates. Two of these magnets were mounted on the top plate of the furnace, one on each side of the 4-in.-diam tube through which the electron beam enters the melting chamber. The parallel end plates were oriented normal to the beam axis. Direct current was supplied to the solenoids, which were connected in series, from a variable power supply with a maximum output of 3 amp at 100 v.

It was found that the beam shape could indeed be altered by adjusting the power applied to the solenoids. Data are not yet available on the effect of zone shape on the purification achieved. However, one immediately apparent effect of beam shaping was to reduce the loss of material by vaporization. One columbium sample which was zone-melted at a travel rate of 1/4 rph with a 17.6-kw beam without shaping lost slightly more than 24% of its original weight by vaporization. Two similar samples which were zone-melted at the same travel rate, but with a shaped beam, had losses of only 3 to 4% even through a somewhat higher beam power (19 kw) was used. This effect of beam shaping on the loss of material by vaporization is illustrated in Fig. 2 which is a photograph of a zone-melted columbium ring. The ring received a total of six zone passes. On the last two passes, beam shaping was used on the top half but not on the bottom. The beam power was 17.6 kw and the travel rate 1/4 rph for these two passes. Further experiments are planned to optimize the beam shape for purification and crystal growth.

EXPERIMENTAL RESULTS

Most of the effort to date has been directed toward developing the mechanics of the zone-melting operation with columbium used primarily as the sample material. The result of one experiment is shown in Fig. 3 which is a photograph of a columbium ring zone melted at approx 1 rph with an unshaped 10.4-kw beam. One grain in the lower right-hand quadrant extends the full width of the ring for approx 2-1/2 in. and through the full, approx 3/8-in. thickness. Preliminary x-ray diffraction data indicate

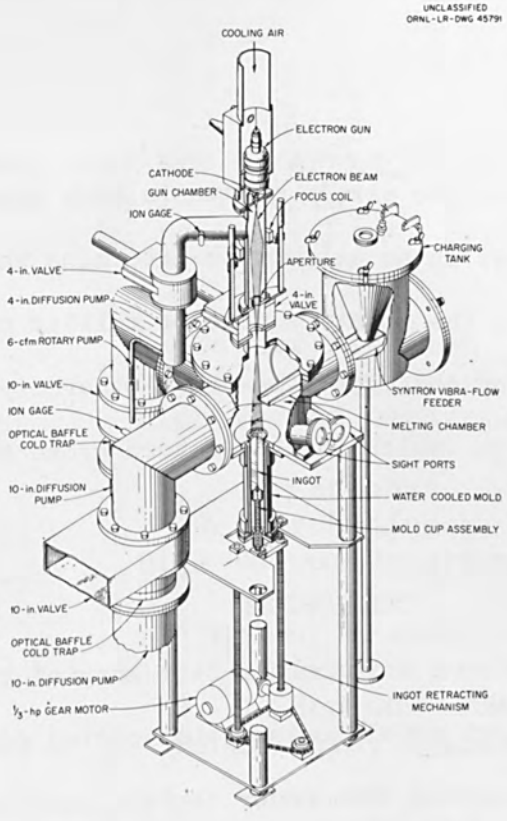

Fig. 1. Schematic Cutaway Drawing of Electron-Bombardment Furnace.

Fig.2. Columbium Ring Zone Melted at ¼ rph with a Shaped (Top) and Unshaped 17.6-kw Electron Beam.

Fig.3. Columbium Ring Zone Melted at 1 with an Unshaped 10.4-kw Electron Beam.

some substructure and lattice strain exists in this crystal. Further evaluation is in progress in an attempt to determine whether the structural defects are due to the rotating mode of melting or to the temperature gradients imposed by the copper hearth. Other crystals over 1 in. by 1 in. by 1/4 to 3/8 in. thick have also been grown and are being evaluated.

CONCLUSIONS

An electron-bombardment furnace has been adapted to the horizontal zone melting of refractory metals using water-cooled copper as a container. It has been observed that under certain, not yet clearly defined, conditions single crystals of columbium can be grown by this technique. Evaluation of zone melted samples is currently in progress.

ACKNOWLEDGMENTS

The author wishes to make the following acknowledgments: to G. E. Angel for operating the apparatus, to R. H. Jones for designing and supervising the construction of the drive mechanism, and to J. V. Cathcart, E. E. Hoffman, and C. J. McHargue whose research programs provided the incentive and support for this work.

REFERENCES

(1) Candidus, E. S., Proceedings of First Symposium on Electron-Beam Melting, March 20, 1959, Alloyd Research Corporation, Watertown, Mass., 1959, p. 27.

SOME VARIANTS OF APPLICATION OF ELECTRON BEAM GUNS IN INDUSTRIAL MELTING FURNACES

By

Walter Dietrich
Senior Engineer
High Vacuum Department

H. Stephan
Senior Engineer
High Vacuum Department

Helmut Gruber
Director
W. C. Heraeus GMBH
Hanau/Main, Germany

ABSTRACT

Recently, where electron beam melting of metals has become an important process for industry and for research, the "classic" electron beam gun has proved to be the most versatile electron source in this field. For installation equally well in smaller research furnaces as in large furnaces for production, electron beam guns were developed by us from a laboratory stage into compact and robust technical units. These guns are separately pumped and provided with water-cooled magnetic focusing and deflecting systems. Different types from 25 kW up to the 100 kW range, manufactured in our works, are shown. The larger guns are equipped with tantalum block cathodes, indirectly heated by electron bombardment.

SOME VARIANTS OF APPLICATION OF ELECTRON BEAM GUNS IN INDUSTRIAL MELTING FURNACES.

Due to the great interest in high purity refractory metals and their alloys, electron beam melting has gained a wide acceptance as research and production technique. The process itself has been known since 1905, but not until the need for the high melting temperatures for the processing of the refractory metals and the development of high pumping speed diffusion pumps could it become a commercial process.

The realization of this process on a large technical scale was shown for the first time by Dr. Smith and his team from Temescal Metallurgical Corporation. In these furnaces mostly two types of ring cathode systems are used as electron sources. Recently, the so-called "transverse gun" system has also been used.

When starting with electron beam melting three years ago, we had two points to consider:

1) The ring cathode systems, used in the existing furnaces, were not flexible enough to satisfy all requirements of research. For larger production furnaces, these systems, although they proved useful in technical respects, had in

practice also some disadvantages which could not be overcome without changing the entire system.

2) When using a "classic" electron beam gun or better a system of 3 or 4 such guns, for research furnaces the most versatile application was possible; for larger production furnaces practically no limitation on power was given, because it was known that perveances of guns up to 4.10^{-6} AV^{-3} could be reached.

These considerations and also the fact that we have been doing research work since 1952 on electron beam guns with magnetically focussed electron beams and separately evacuated cathode space made it advisable for us to adapt such beam guns to electron beam melting.

Now, different gun types are used in our furnaces. The principle design is shown on a sample, used in production furnaces, which is shown in Fig. (1).

The special characteristics of this unit are: tantalum block cathode, indirectly heated by electron bombardment, pierce electrode for concentrating the beam, water-cooled anode, two water-cooled magnetic lenses and one one-dimensional magnetic deflection system, the coils of which are also water-cooled. This gun has a beam power in the 100 kW range at 20 kV. That means a perveance of $1,8.10^{-6}$ $AV^{\frac{3}{2}}$. At present the upper limitation is only given by the cooling problem. So,

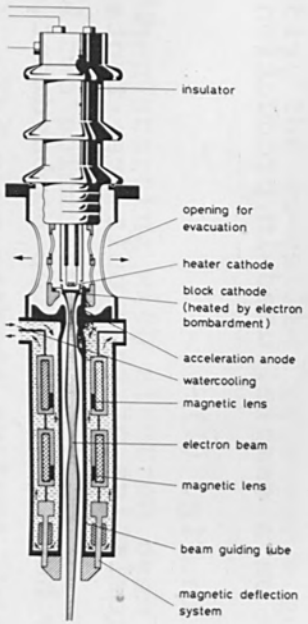

Fig. (1) Electron beam melting gun
acceleration voltage 20 kV
beam power 100 kW
perveance 1.8×10^{-6} AV $^{-\frac{3}{2}}$

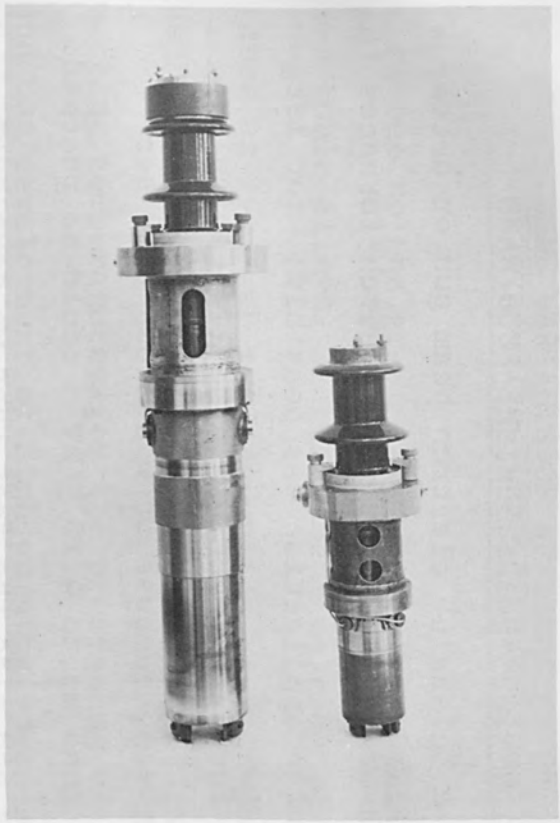

Fig. (2) a b
Manufactured electron beam melting guns of a beam power of a) 100 kW, b) 30 kW, for installation in a common and separately evacuated gun chamber.

naturally, this gun type can be used for quite some time up to 150 kW and there is no reason for the system itself not to reach perveances up to 4.10^{-6} which corresponds to a beam power of more than 200 kW.

The smaller guns in the range of 20 to 30 kW are using only one magnetic lens as focussing system and have direct heating of the cathode.

As you can also see from this sketch, the guns are designed to be mounted in a common, separately evacuated gun chamber. The cathode space has large holes for effective evacuation.

In fig.(2) the manufactured units are shown:

On the left side, a 100 kW gun for production furnaces, on the right side a 30 kW gun for smaller research furnaces. Each gun represents an independent robust technical unit which can easily be exchanged as a whole. For exchanging the cathode, only the insulator has to be taken off.

In the electron beam melting furnaces usually several guns are arranged symmetrically to the axis of the crucible by vertical mounting in the common and separately evacuated gun chamber. This is shown in fig. (3). By the deflecting systems of the guns the beams are directed to the molten pool.

In order to judge the advantages of such a gun system, let us view the electron beam melting process itself.

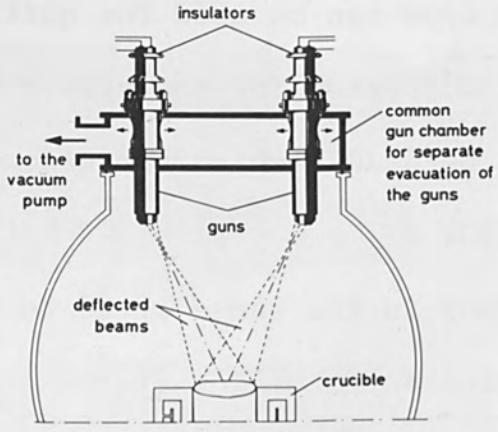

Fig. (3) Vacuum chamber for common connection of all guns to the vacuum pump.

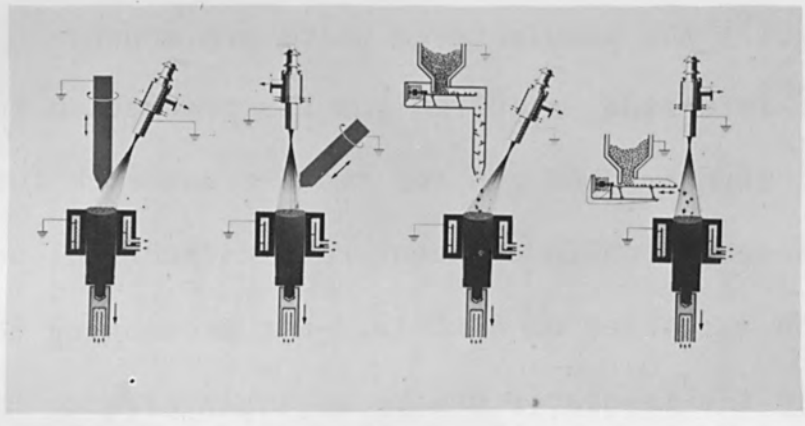

a b c d

Fig. (4) Variants when drip and pool melting with one electron beam gun.
a) Drip melt, inclined direction of beam
b) Drip melt, vertical direction of beam
c) Pool melt, central feed stock, inclined direction of beam
d) Pool melt, lateral feed stock, vertical direction of beam.

The two ways to produce ingots are the drip melting and the pool melting in a crucible with retraction of the crucible bottom.

In fig. (4) the cases are shown where drip melting of a consumable electrode and pool melting of scrap or granules is carried out by using only one gun. When using a consumable electrode, and this is absolutely necessary during the second or third melt, always an energy shadow will occur, that means that the ingot surface will not be excellent on one side.

This is overcome when using the system of multiple guns, also there is no problem in reaching the required power of 200, 300 or 500 kW.

In fig. (5) you see drip melting and pool melting, carried out with this gun system, where the molten pool or consumable electrode and molten pool are bombarded by deflected beams at a suitable angle.

The gun system offers several advantages as for instance in comparison to the known ring beam systems.

a) We can use one common beam system for all crucible diameters and also for drip melt and pool melt. Our system can be completely adapted to the different crucible diameters by modification of the magnetic beam deflection. This is done electrically without

mechanical change at the system itself.

b) The guns can be placed at a relatively long distance from the molten pool. The exactly straightened electron beams, successfully focussed by magnetic electron lenses attain a high yield of energy in spite of the great distance. The long distance guarantees good protection of the cathode against splashes and metal vapours.

c) Furthermore, it is important that melting is performed in a configuration held at ground potential so that deflected beams can be used. By this the ion current is minimized to a negligible value. The occurrence of glow discharges in the melting chamber, when degassing the melting material, is considerably hampered.

d) The possibility is given to separately evacuate the electron generating chamber. The beams can be led through relatively narrow tubes. These guide-tubes form such a gaskinetic resistance that already a small diffusion pump for the electron generating chamber is sufficient to keep the pressure therein essentially lower than in the melting chamber. High stability of the electron beams is so achieved. Bursts of gas practically do not result in glow

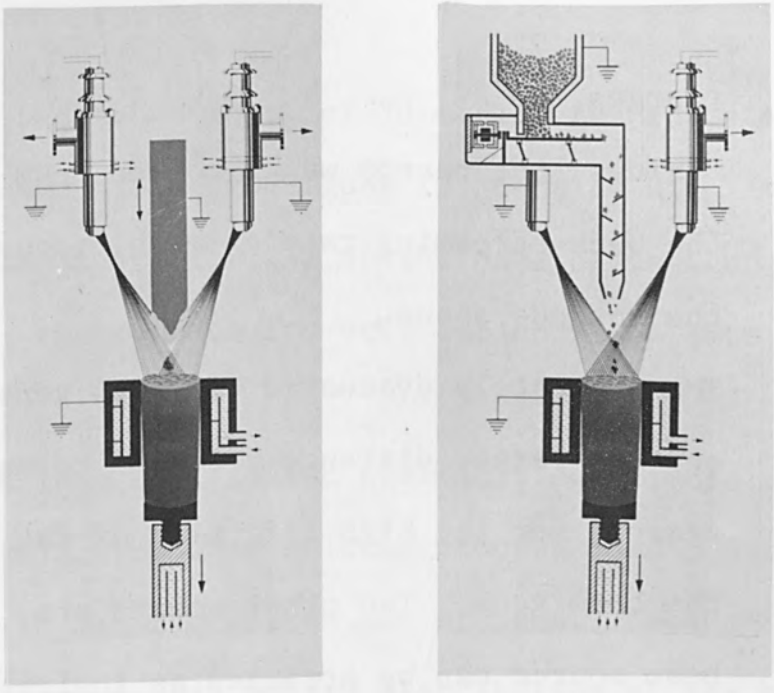

Fig. (5) Drip melting and pool melting with a system of multiple guns and deflected beams.

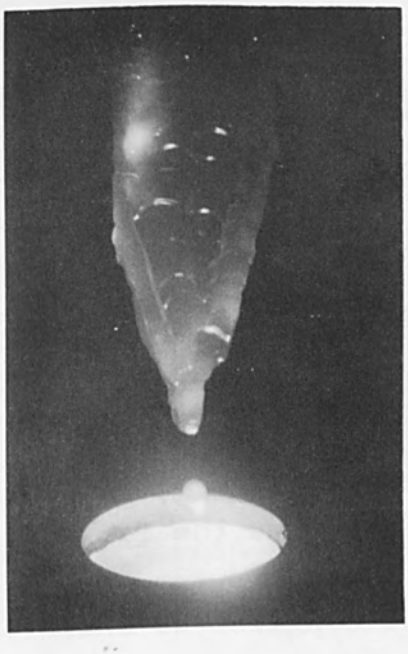

Fig. (6) Drip melt with four electron beam guns.
Electrode of columbium 50 mm diameter
Crucible 70 mm diameter

charges.

Besides, the narrow water-cooled beam tube reduces the back-streaming rate of metal vapours reaching the cathode space.

e) The separately evacuated electron generating space and the larger distance from gun to melt are two reasons for the high life time of the cathodes in the beam guns. Two other points are, that electron beam source can be arranged as indirectly heated robust block cathode and be placed in a dead angle of the melt, owing to the deflection of the beam.

In this manner cathode life exceeding 100 hours can be attained. The melting technique of multiple beam guns with deflected beams offers various possibilities to influence the energy distribution on the melt. For instance electron spots on the molten pool can be suitably formed by the pole piece shape of the deflecting system. There are also some small electric trimmers to adjust each gun of the simultaneously controlled system to correct the first differences in focussing and deflecting from gun to gun, on the first operation of the furnace.

In fig. (6) a photograph of a drip melt is shown.

A consumable electrode of Columbium with a diameter of

50 mm is remelted to an ingot of 70mm diameter in this case. The melting power of the four guns is about 80 kW. It can be seen how the drops are forming at the base of the cone. Then they run along the cone to its very end and drop into the molten pool.

Ingot surface quality and purification effects attainable with our electron beam melting process hardly differ from the results with other electron gun systems. Because we can provide an axialsymmetric energy distribution of the beam in the molten pool, the ingot surface is primarily given by the retraction technique. In order to obtain good surfaces, it is necessary to keep the molten pool in the crucible rim and to provide a uniform supply of energy and material. This is, of course, easier to be attained under constant electron beam conditions, as they are realized with our guns.

Fig. (7) shows ingots of tantalum and columbium, produced with our process.

Fig. (8) shows an electron beam melting furnace of 75 kW with a system of three electron beam guns, vertically mounted in one vacuum chamber. The plant is designed for research and pilot scale tests.

All three guns can be used together, or if need be the individual guns can be operated separately. The latter in

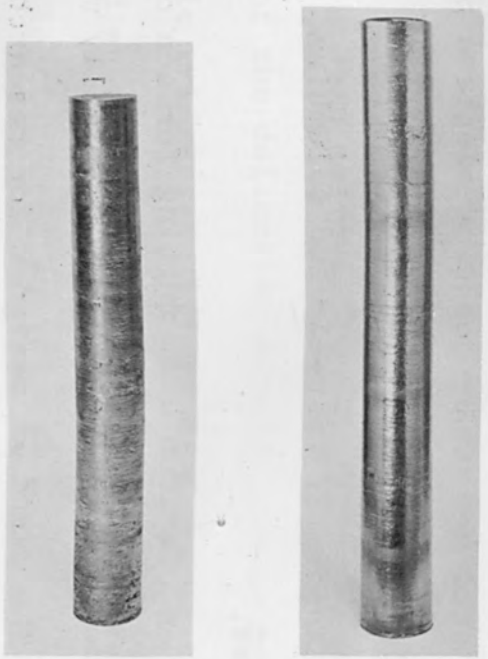

a b

Fig. (7) Electron beam melted metal ingots, second melt with consumable electrode.
a) Tantalum 70 mm Ø
b) Columbium 75 mm Ø

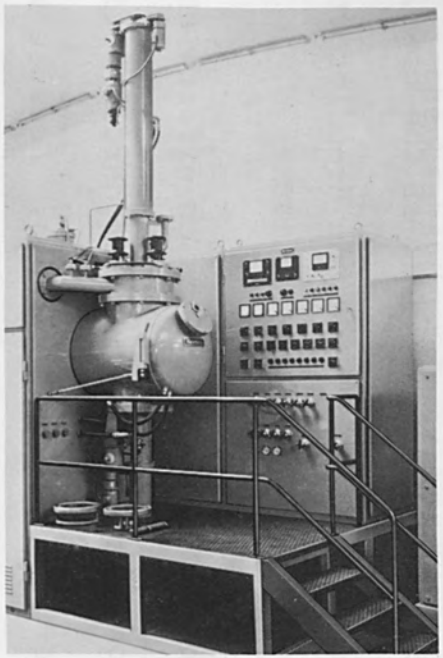

Fig. (8) Electron beam melting furnace for research with three guns
Max. acceleration voltage 20 kV
Max. beam power 75 kW

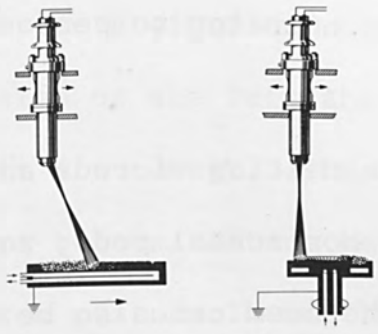

a b

Fig. (9)
a) Melting of rods
b) Melting of buttons or rings

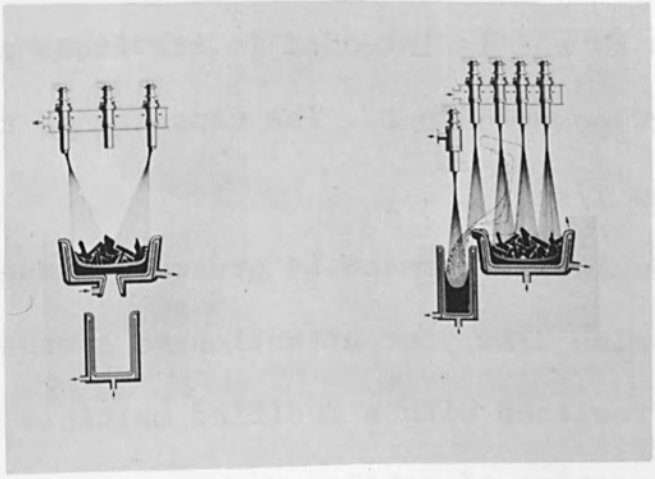

Fig. (10) Variants of electron beam casting furnaces
a) with bottom tapping; heating of the molten pool by electron beam guns. The middle gun is cut in just before casting begins melting through the bottom plate.
b) with tiltable crucible; heating of the casting flow and of the cast metal in the mold.

combination with special crucibles and deflection system available enables the operator to perform individual melting tasks.

In fig. (9) the melting of rods and of buttons and rings is demonstrated. On horizontal rods, zone melting by continuous deflection of the beam can also be made.

We have had a 260 kW power furnace with five older guns in operation for a considerable time. The vacuum is produced by two oil diffusion pumps, each pump with 8000 l/sec.

Another production furnace with four guns has been in operation for three weeks. It has been running at the power level of 260 kW and is intended in its final configuration to have a 520 kW power output. The capacity of the oil diffusion pump is 36000 l/sec.

An even larger furnace is presently under construction.

May I also draw your attention to another process which can be well realized with a modified multiple gun system. This is the casting of metals.

The electron beam is particularly suited for the introduction of energy during casting process in the crucible, in the casting metal itself, and even into the mold. With multiple guns energy can be suitably distributed during each phase of the process by either deflecting the beams or

switching on or off single guns.

Fig. (10) shows two designs of electron beam casting furnaces. In the design on the left the crucible is provided with a casting hole in its center. The third middle gun is to be switched on just before casting begins, in order to melt through the bottom plate. The method on the right with tiltable crucible shows how energy can be supplied on the molten pool and the casting flow even during casting. With this electron beam casting process we hope that we shall not only be able to cast these metals in differently shaped molds but we should also be in a position to effect grain refinement and better structure.

BACKSCATTERED ELECTRONS AS AN ANALYTICAL TECHNIQUE

By

R. E. Ogilvie
Professor
Department of Metallurgy
Massachusetts Institute of Technology
Cambridge, Massachusetts

ABSTRACT

When a specimen is irradiated with an electron beam, an x-ray spectrum is produced which is characteristic of the energy of the incident electrons and the elements present in the irradiated area. There is, however, a fraction of the incident electrons backscattered from the specimen. This fraction backscattered is a function of the average atomic number of the irradiated area. The measurement of the backscattered electrons opens up a new technique for high resolution chemical analysis.

It is the purpose of this paper to discuss the principles and applications of this new technique.

Backscattered Electrons as an Analytical Technique

by

R. E. Ogilvie

Massachusetts Institute of Technology

When a specimen is irradiated with an electron beam, an x-ray spectrum is produced which is characteristic of the energy of the incident electrons and the elements present in the irradiated area. There is, however, a large fraction of the incident electrons backscattered from the area of impact. These backscattered electrons may be divided into two groups, the primary reflected electrons and the secondary electrons of low energy (less than 50 V). The secondary electrons will not be considered here. The fraction of primary backscattered electrons is a function of the average atomic number of the irradiated area. The measurement of these backscattered electrons opens up a new technique for high resolution quantitative chemical analysis in binary or pseudo-binary systems or qualitative analysis of multicomponent systems.

The incident electrons will penetrate the sample a particular distance (R) which is a function of the accelerating voltage and the atomic number of the specimen. This electron-specimen interaction is illustrated in Figure 1. The range (R) of the electrons in several materials as calculated from the theoretical data of Nelms[1] is illustrated in Figure 2. From this data it is easily shown that the volume contributing to Kα x-ray production (R_c) for 30 KV electrons

would be about 2.5 microns in depth. However, since the backscattered electrons can only come from a depth of one-half the total range (R_B) there is a marked increase in the possible resolution of the system. The resolution can be improved even more if low energy electrons (2-5 KV) are used. In order to take advantage of the shorter range of the low energy electrons it is necessary to have an electron optical system capable of focussing the electron beam to sub-micron sizes.

At present there is not an appropriate theory for the primary backscattered electrons. However, if one uses the equations of Birkhoff[2] and Nelms[1] for the variation of electron velocity with distance traveled in the specimen, and Rutherford's equation for elastic scattering of electrons by the nuclei, an expression for the fraction of backscattered electrons (η) may be derived:

$$\eta = \frac{a - 1 + (0.5)^a}{a + 1}$$

where $$a = \frac{\pi z^2 e^4 N_A}{m^2 c A}$$

This same expression has been derived by Everhart[3] in a similar way.

Figure 3 illustrates the variation of η with atomic number. Figure 4 shows typical calibration curves for Au-Cu - Au-Ag alloys. Here it is illustrated that the technique is well suited to the analysis of diffusion couples or any bonded interface. The possibility of measuring the composition at bonded interfaces with a resolution of a few hundred angstroms is not too far off.

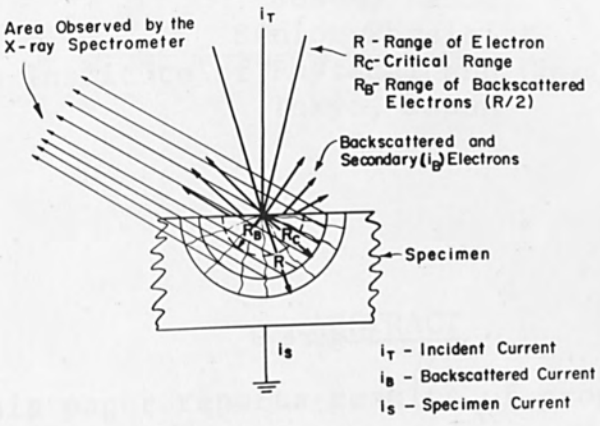

Figure 1

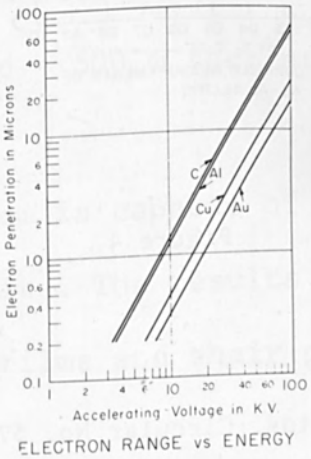

ELECTRON RANGE vs ENERGY

Figure 2

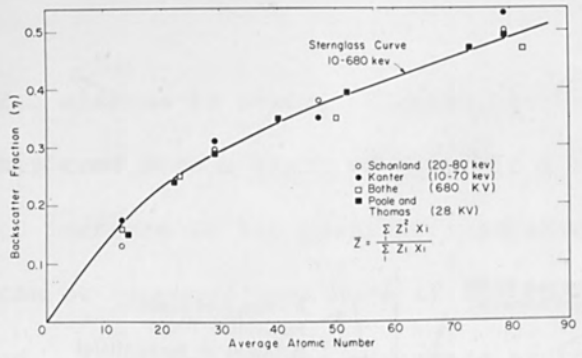

Figure 3

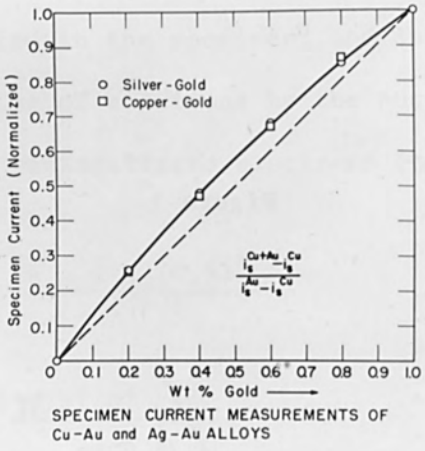

Figure 4

References

1. A. Nelms, Nat. Bur. Stds. Circular No. 577, (1956)

2. R. D. Birkhoff, Hanbuck der Physik, Vol. XXXIV, p 53 (1958)

3. T. E. Everhart, J.A.P. 31, 1483 (1960).

APPLICATIONS OF ELECTRON BEAMS FOR EVAPORATION AND MACHINING OF MATERIALS

By

Susumu Namba
Senior Physicist
The Institute of Physical and Chemical Research
Tokyo, Japan

ABSTRACT

This paper reports results of property studies on electron beam evaporated Zirconium, Titanium and Silicon thin films. It also discusses a newly developed electron beam machining system with the following specifications:

Beam current concentrated on work piece is of about 10 and 0 - 2 mA; accelerating voltage is 10-50 KV; the beam can be continuous or pulsed with frequencies of 1 - 10,000 cps and pulse durations of 50 μsec - 500 m sec; attained power density is above 10^8 watt/cm^2.

This system is capable of drilling and cutting fine shaped holes and slits. The results from studies on electron beam evaporated silicon films and their processing parameters are presented.

THE APPLICATION OF ELECTRON BEAMS FOR EVAPORATION AND MACHINING OF MATERIALS

I. Electron Bombardment Evaporation.

Vacuum evaporated thin films of titanium, zirconium and silicon have been studied for several years in our laboratory.[1][2][3][4] Until recently, titanium and zirconium films have been prepared by resistance heating method. Since these refractory metals become very active at high temperature, prolonged evaporation by tungsten heater charged with evaporant is not desirable. If electron bombardment could be applied for the preparation of pure evaporated films of these metals, it would be better than any of the other methods, because, by the electron bombardment method, the highest temperature region is on the vapour emitting surface but not, as is usual, on the evaporant heating material, and therefore there will be no contamination of the film from the heater material. This section describes the design of an electron bombardment evaporation apparatus and the properties of the films produced.

(1) Evaporation Procedure.

A very simple evaporator by means of electron beam heating was devised as shown schematically in fig. 1.

A rod of metals to be evaporated is vertically supported and connected to a positive high tension supply of

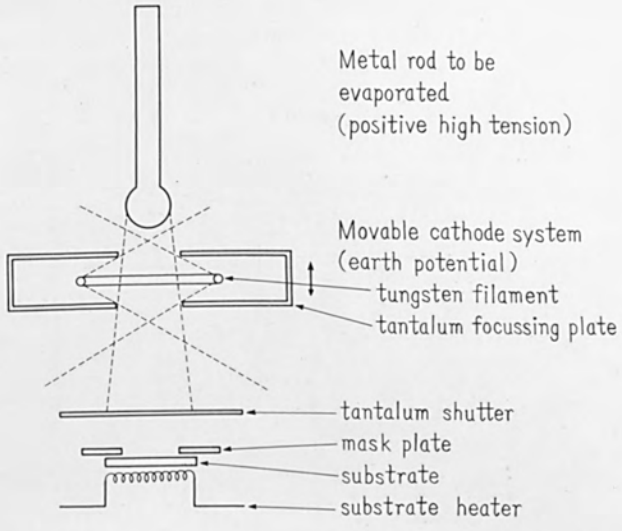

Fig. 1 Schematic Diagram of The Apparatus

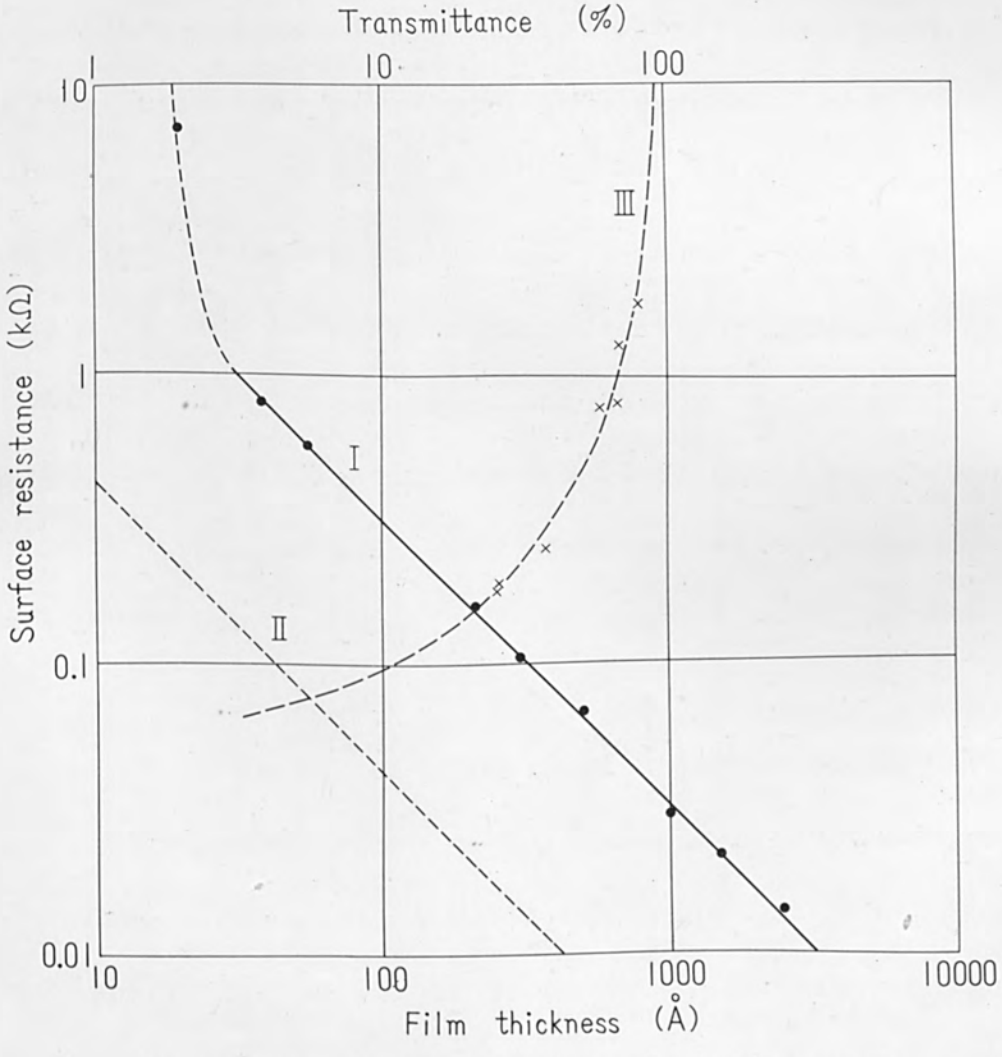

Fig 2 Relation between Surface Resistance (R), Transmittance (T) and Thickness (D) of Titanium Films

1 : R - D Relation
11 : ρ/D - D Relation
111 : T - R Relation

1 ~ 5 kv. The cathode system consists of a circular electron-emitting 0.5 mm tungsten filament of about 1.5 cm in diameter and a set of tantalum focusing plates with holes of 1 cm diameter, placed about 1 cm apart from the filament, and is at earth potential.

The metal rod is bombarded by electrons from the heated tungsten filament accelerated by the applied field, the beam of electron being directed by the focusing plates. The accelerating voltage is raised to increase the power of the electron beam until the tip of the rod becomes molten and hangs down in a form of a drop from which the metal is evaporated.

A tantalum shutter is placed between the lower tantalum plate and a heated substrate holder which is held at a distance of 5 cm to 15 cm from the molten drop. The tantalum focusing plates effectively screen the substrate and molten drop from being contaminated by evaporated filament tungsten.

The whole arrangement is enclosed in an evacuated metal chamber.

The cathode system is made to be lifted up by manipulation from outside to make up for the shortening of the rod due to drop forming and evaporation and to enable prolonged evaporation operation. The power required for evaporation, which depends on the material of the rod and the configuration of the whole system, is estimated at 15 ~ 100 Watt for a rod of

1~4 mm in diameter. For example, evaporation from a 3 mm titanium rod requires only about 10 mA at 2 kv (20 Watt).

(2) Titanium and Zirconium Films

The electric conductivity of deposited metal films is known to differ from that of bulk metals and vary with film thickness. Curve 1 of fig. 2 shows the surface resistance R of deposited titanium films measured as a function of film thickness D. To measure the film resistance during deposition of the films, the glass substrates were provided with two electrodes of aluminium film previously deposited at a given distance apart. The film thickness was determined by multiple beam interferometer method.

Evaporation speed is estimated from the film thickness and evaporation time. Constancy of speed is attained by controlling the size of molten drop, supplied power and distance of the substrate from the drop. Curve 1 shows the surface resistance of titanium films evaporated with the speed of 3Å/sec at $1\sim2 \times 10^{-5}$ mmHg. In this case film thickness was estimated by evaporation time. Curve 2 of fig. 2 shows the surface resistance of bulk metal ρ/D calculated from its resistivity ρ and film thickness D. The ratio of R to ρ/D is about ten which increases steeply at small thickness of about 30Å. Curve 3 shows transmittance of films as a function of surface resistance. From the figure, we see that an evaporated film of titanium of 50Å thick-

ness has the surface resistance of 700 Ω and the transmittance of 60% under these evaporation conditions.

Evaporation speed of zirconium was slower than that of titanium.

In general, the resistance of deposited metal films changes with the time. Surface resistance of deposited titanium or zirconium films left in air increases gradually. If deposited titanium or zirconium films are exposed to glow discharge produced between two electrodes by high voltage in a low pressure enclosure ($10^{-2} \sim 10^{-3}$ mmHg), they are oxidized from the surface by ionbombardment, thus stabilizing the films.

Curve I, I', I" of fig. 3 show the aging of resistance of titanium films of various thickness left in vacuum for a half hour after deposition then oxidized in free air. Curve II and III show the aging of resistance of a 50Å thick titanium film deposited simultaneously with the others, then oxidized by ion bombardment to different degrees. As shown in Curve I, I' I" the film resistance changes remarkably during the first few minutes of exposure to air. This change is perhaps due to considerable decrease in number of conduction electrons by surface oxidation. The oxidized surface layer of the film protects the film from further degradation when left in air. Films once thus

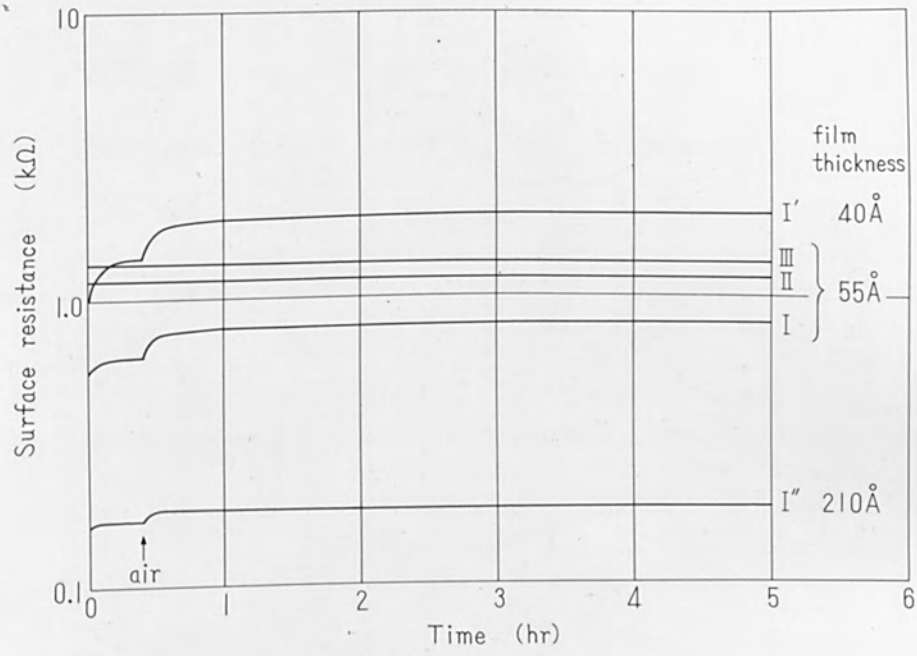

Fig. 3 Variation of Surface Resistance of Titanium Films with Time

1, 1', 1'' : Untreated Films
II : Enforced Oxidized Film (1 hr)
III : Enforced Oxidized Film (3 hr)

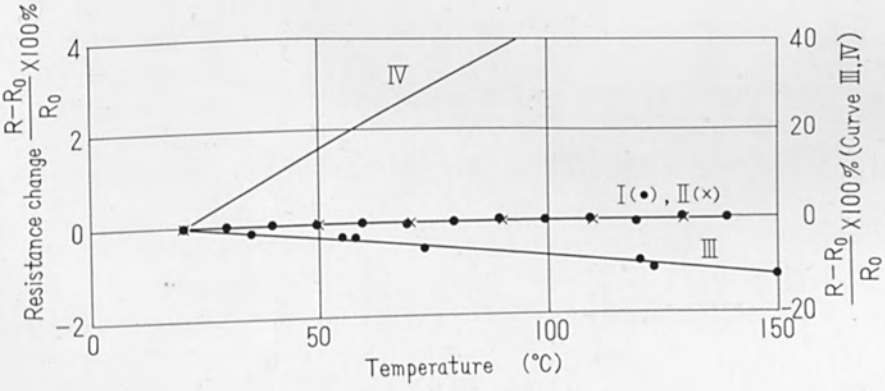

	Resistance at room temperature (Ro)	Temperature Coefficient of resistance
I	200 Ω	0
II	65 Ω	0
III	330 Ω	-1×10^{-3}
IV	Bulk metal property	$+5.5 \times 10^{-3}$

Fig. 4 Resistance-Temperature relation of Titanium Films

oxidized remained stable over several months.

Temperature coefficient of resistance of deposited titanium or zirconium films is noticeably dependent on the evaporation condition and oxidation degree, and so it is possible to prepare films with positive or negative temperature coefficient.

Fig. 4 and fig. 5 show the temperature dependence of resistance of deposited titanium and zirconium films. Negative temperature coefficient was obtained on oxidized films.

Fig. 6 shows the reflection electron diffraction pattern of a vacuum deposited 350Å thick titanium film subjected to forced oxidation for 1 hr. The structure of the film was that of rutile with diffraction spots of (110) orientation. The diffraction pattern of oxidized zirconium film was very similar to the pattern of oxidized titanium film. It was not possible to tell whether the lattice is face-centered cubic (a=5.07A°) or tetragonal (c/a=1.015, a=5.07Å) dioxide because of very broad diffraction rings.

The surface of oxidized films is extremely hard and mechanically durable. Science crystalline rutile is very hard and chemically stable, if we assume that the surface of deposited titanium film is covered uniformly with titanium dioxide layer due to forced oxidation, hard and durable state of oxidized film surface is naturally expected. It

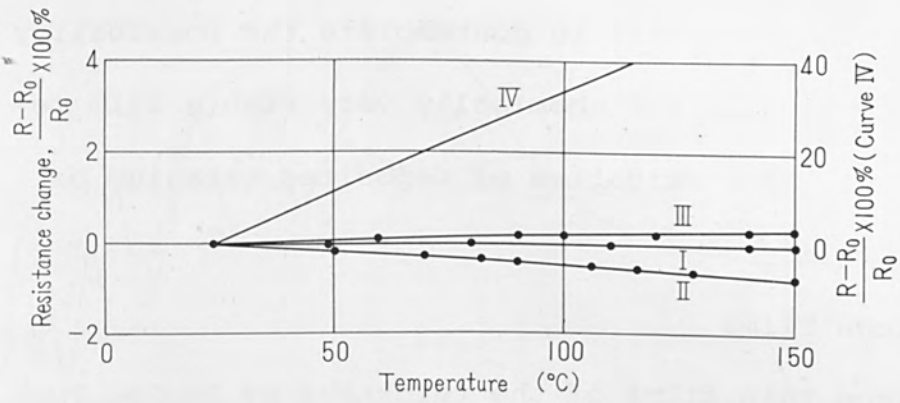

	Resistance at room temperature (Ro)	Temperature coefficient of resistance
I	280 Ω	0
II	1900 Ω	-6×10^{-5}
III	250 Ω	$+2 \times 10^{-5}$
IV	Bulk metal property	$+4.4 \times 10^{-3}$

Fig. 5 Resistance-Temperature relation of Zirconium Films

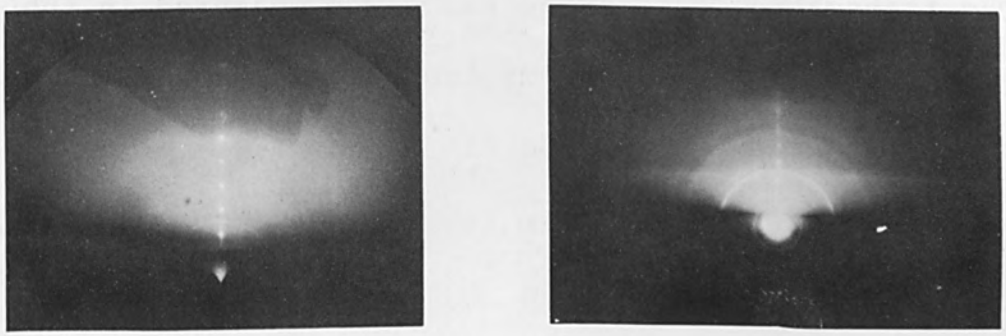

Titanium Zirconium

Fig. 6 Electron Diffraction Patterns of Oxidized Films

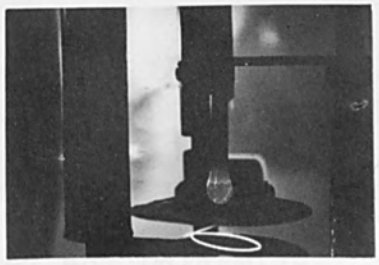

Fig. 7 Photograph of Silicon Molten Drop Evaporant

is of practical interest to contemplate the possibility of devising physically and chemically very stable film resistors by surface oxidation of deposited titanium or zirconium film.

(3) Silicon Films

Silicon thin films of the thickness of 2000 ~ 7000 Å were prepared in $1 \sim 2 \times 10^{-5}$ mmHg vacuum with evaporation rate of 0.5 Å/sec. Acceleration voltage was about 3 kv and electron beam current about 20 mA. Fig 7 is a photograph of a silicon drop in molten state as the source of continuous evaporation.

The transmittance of these films was measured in the visible and infrared region. Typical results are shown in fig. 8. The absorption edge of Si bulk crystal is at about 1.1μ, but that of Si thin film is at about 0.5μ as can be seen from curve I and II of fig. 8. Curve III of fig. 8 shows the transmittance of SiO thin film, absorption edge being at about 0.3μ. Comparison of these figures show that these Si thin films are partly oxidized and contain tolerable quantity of SiO or SiO_2.

The index of refraction can be calculated from the positions of transmission maximum and minimum which are caused by interference. Estimating the refractive index of Si films by the well-known simple relations which govern the

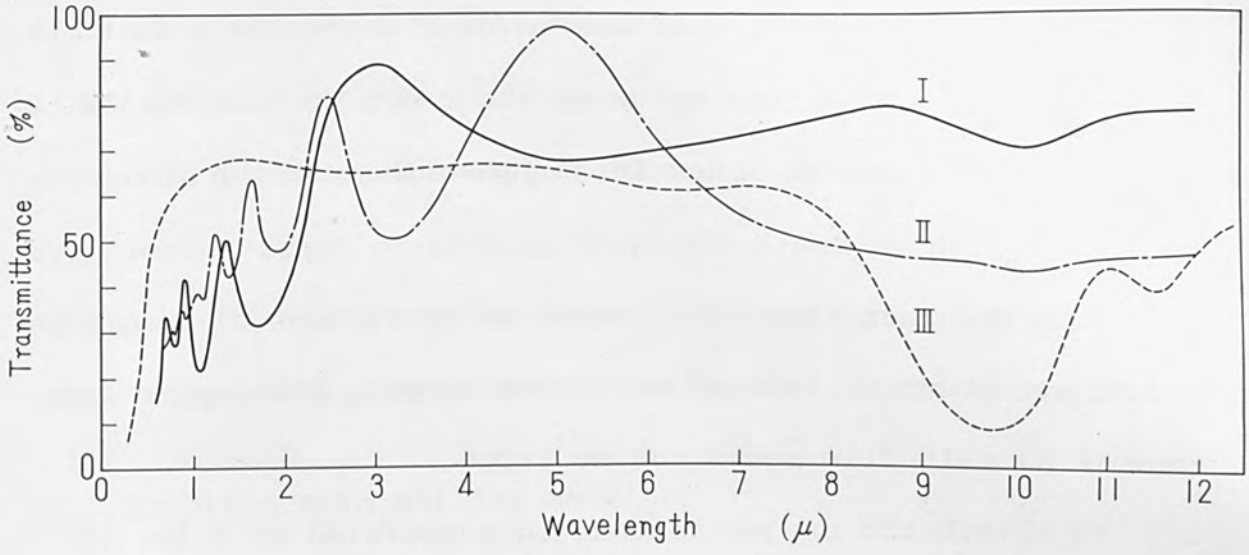

Fig. 8 The Transmission Spectra of Thin Films

I. Si Film : Thickness 3800 Å
II. Si Film : Thickness 6960 Å
III. SiO Film : Thickness about 1 μ

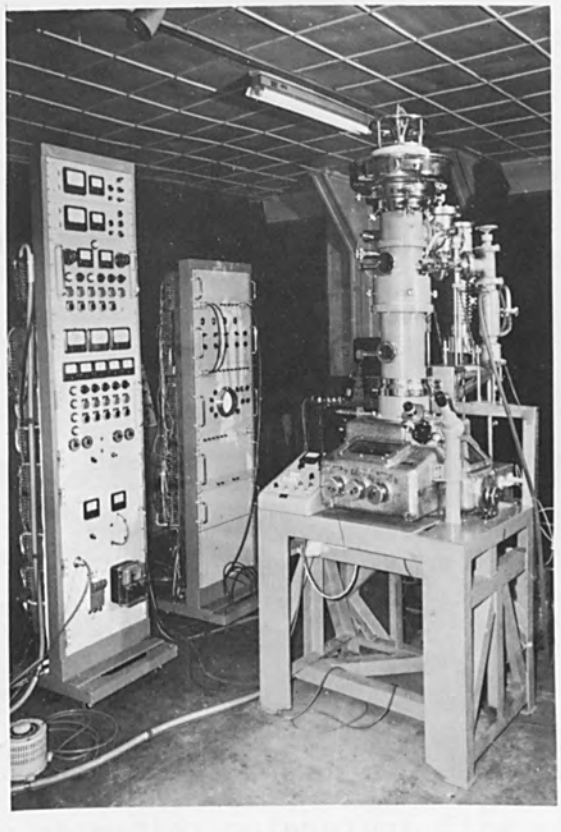

Fig. 9 Photograph of The Electron Beam Milling Machine of Our Laboratory

position of the maxima and minima in case where there is no absorption, we obtain the value of about 3.6 at 6000 Å, the thicker film having an index larger than that of the thinner film.

From the fact that the indices of refraction of SiO, SiO_2 and Si are about 2, 1.5 and 3.5 respectively, the oxygen content in Si thin film seems not so large.

To obtain the oxygen content in evaporated Si film, the infrared absorption band was analyzed. The number of Si-O oscillators can be determined from the equation (5),

$$No = \frac{9n}{(n+2)^2} \cdot \frac{3\mu c}{\pi e^2} \alpha_{max} H$$

where μ is the reduced mass of the oscillator, e is the net electric charge, n is the refraction index of the surrounding medium, α_{max} is the absorption coefficient at the band maximum and H is the half-width of the band.

On the assumption that n is 3.6 and e is 4.8×10^{-10}esu, the number of oxygen atom involved in the Si thin film is estimated at about 3×10^{-21} atoms/cm^3.

The result shows that the number of oxygen atoms is a few percent of the number of Si atoms, and that the oxygen content decreases with increasing thickness of the films. This may be due to the surface oxidation after deposition.

The number of oxygen atoms calculated from Curve III of

fig. 8 is about $3 \times 10^{22}/cm^3$ and that of the wafer crystal of Si is about $2 \times 10^{18}/cm^3$. These values are considered reasonable. To decrease the oxygen contents, either much higher evaporation speed of several hundreds Å/sec or higher vacuum of about 10^{-9} mmHg must be used. Construction of a high power electron gun type evaporator is now being contemplated.

II. Electron Beam Milling Machine

The studies on electron beam machining in Japan were started in 1960. Our laboratory constructed a tentative apparatus in collaboration with Japan Electron Optics Laboratory Co., Ltd. Similar apparatus are also being made by many other laboratories.

Our apparatus shown in fig. 9 consists of four units:

1. milling unit with an electron beam chamber, a machining chamber and evacuation system, (fig. 10).
2. high voltage supply.
3. electronic control panel with deflector control and pulse generator.
4. operation control panel with vacuum gauge, stabilizers of magnetic lens coil current, and indicators to show working condition of electron beam.

The electron beam chamber consists of an electron gun, 1st focusing magnetic lens, stigmator, electro-static deflection plates and 2nd focusing magnetic lens. The electron gun

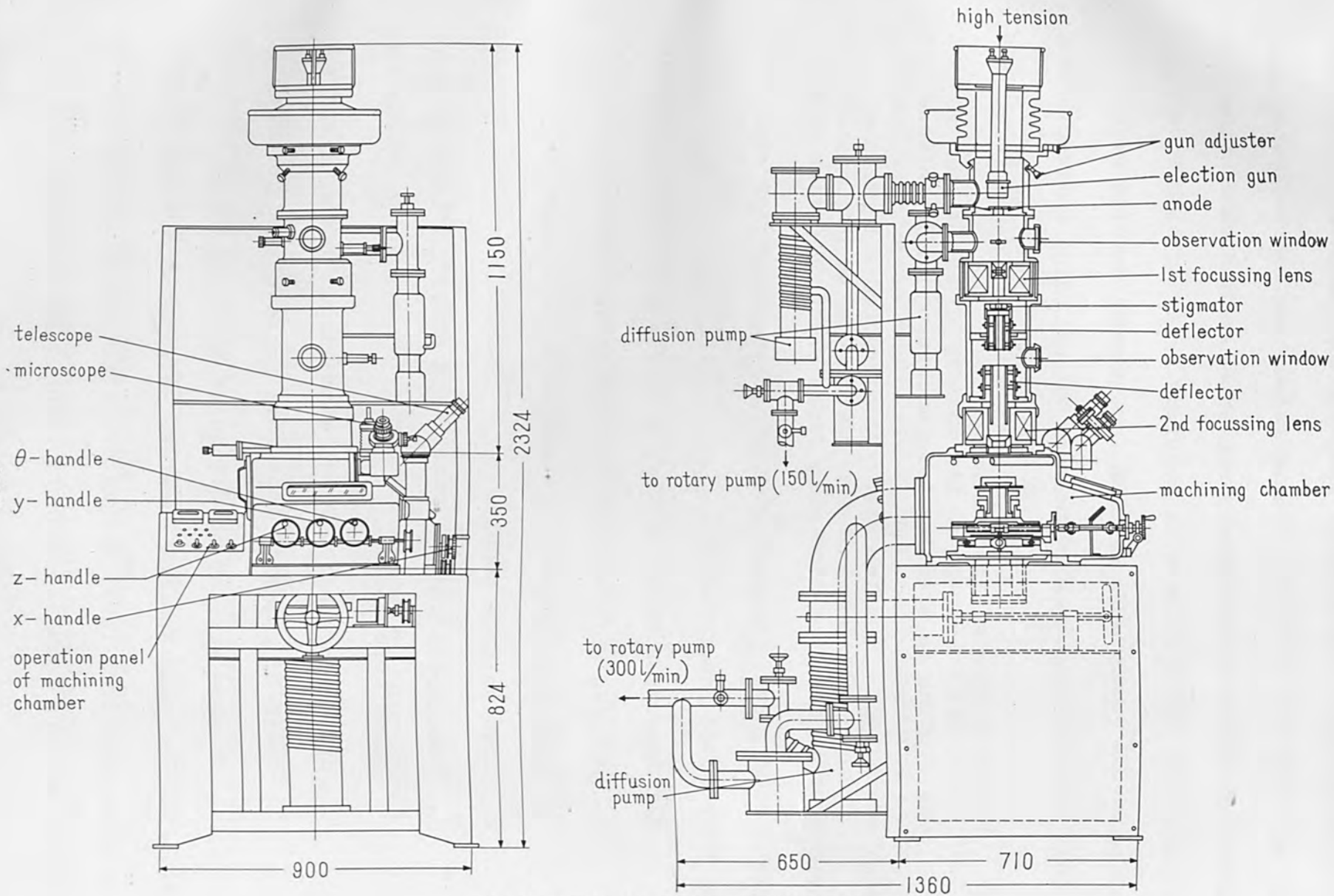

Fig. 10 Construction Diagram of Milling Unit

consists of a hair pin filament at negative high tension, a negative biased control grid, a positive biased control grid and an anode at earth potential. By the adjustment of biased potentials of the two grids, cross-over point of electron beam can be varied over a wide range.

The beam intensity is controlled by the bias potential of the negative control grid. Two electro-static deflectors aligned between the 1st lens and the 2nd lens are in cascade. The electron beam deflected by the 1st deflector is righted by the 2nd deflector, so that the beam always passes through the center of the 2nd lens with the deflection angle proportional to deflection potential. A detailed schematic diagram of the electron beam chamber is shown in fig. 11.

The work piece in the machining chamber can be moved in X, Y and Z directions, and turned to any azimuthal angle. All screws of these running mechanisms are controlled and independently with accuracy of one micron from outside of the vacuum chamber. A microscope of 100 and 200 magnifications is located between the 2nd lens and the work piece holder to observe the work piece.

Specification of the apparatus is as follows:

Beam diameter on work piece	50μ ~ 10μ
Beam current on work piece	0 ~ 3mA
Accelerating voltage	10 ~ 50kv

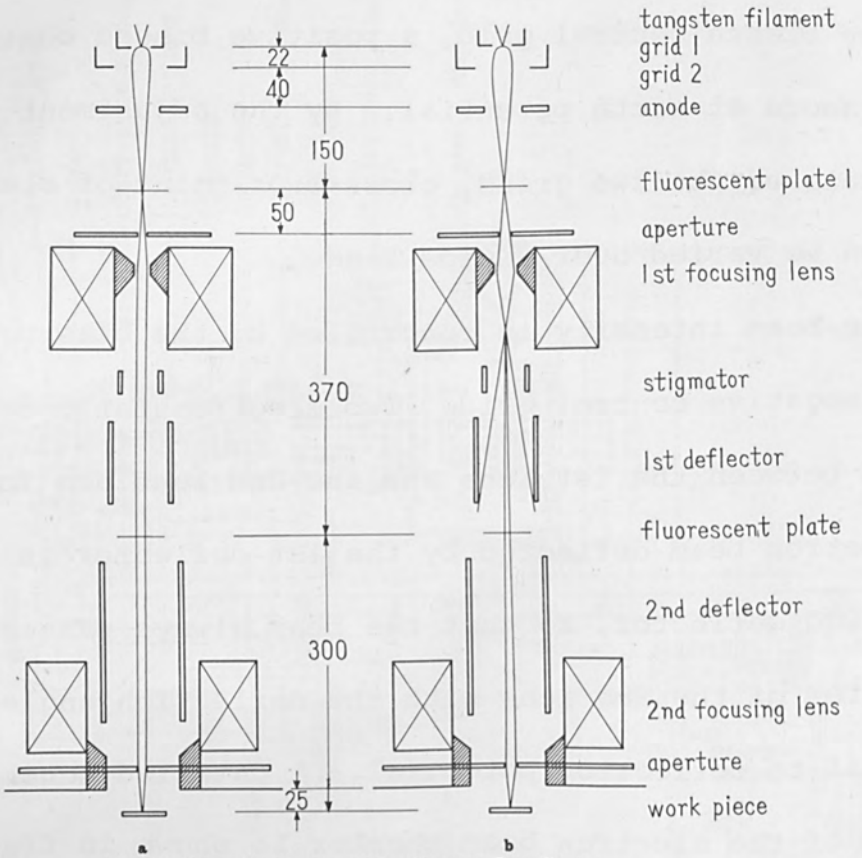

Fig. 11 Schematic Diagram of The Electron Beam Chamber Two types of electron beam focusing are possible to oftain high beam current (a) and sharp beam focusing (b) respectively.

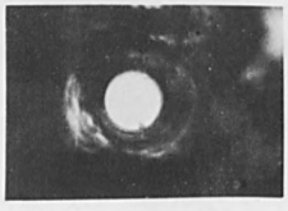

Fig. 12 Electron Beam Milling of 0.1 mm Thick Brass

Pulse duration : 50 msec
Pulse frequency : 10 cycle
Power of electron beam : 50 KV, 100 μA

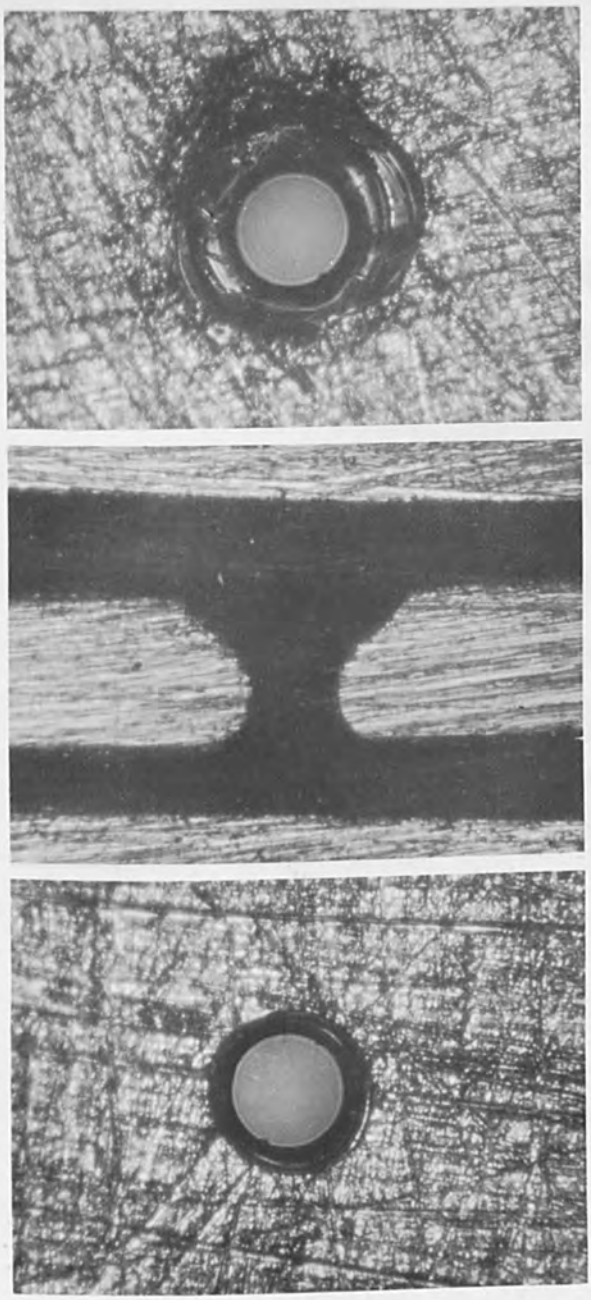

100μ

Fig. 13 Electron Beam Drilling of 0.15 mm Thick Molybdenum
a: entrance; b: cross section; c: exit
Pulse duration: 50μsec
Pulse frequency: 1000 cycle
Power of electron beam: 50 KV, 500μA

100μ

Fig. 14 Electron Beam Drilling of 0.5 mm Thick Stainless Steel
a: entrance; b: etched cross section; c: exit
Pulse duration: 50μsec
Pulse frequency: 5000 cycle
Power of electron beam: 50KV, 100μA

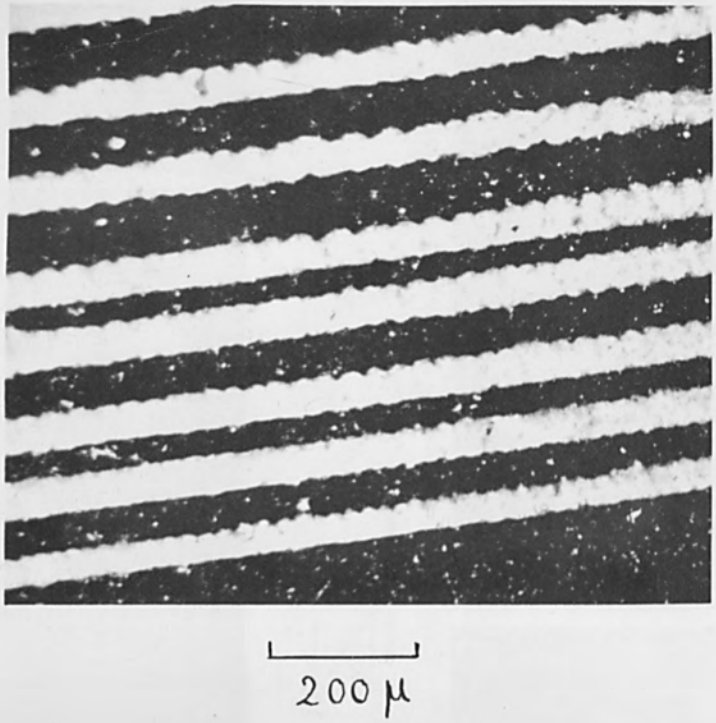

Fig. 15 Electron Beam Cutting of Evaporated Metal Film an Ceramic Substrate

Pulse duration : 50 μsec
Pulse frequency : 5000 cycle
Power of electron beam : 50 KV, 10 μA~20 μA

Attainable power density $> 10^7$ Watt/cm^2

The beam can be continuous or pulsed with frequencies of 1~ 5,000 cps and pulse duration of 50 μ sec ~ 500 msec, and deflected ± 1 mm to X and Y directions on work piece.

During the operation, vacuum of the electron beam chamber and of the machining chamber was about 5×10^{-5} and 5×10^{-4} mmHg respectively.

Our experience, obtained last year, is not enough to systematize the electron beam process. However, the application of the process to several materials such as stainless steel, molybdenum and sapphire, though still in an experimental stage, gave many interesting results.

For example, drilling of round holes of 30μ ~ 100μ through stainless steel and molybdenum plates of 0.2 ~ 0.5mm thickness was successful by pulse duration of 50 μ sec, frequency of 1,000cps ~ 5,000cps, beam current of about 300 μA and acceleration voltage of 50 kv. All holes drilled have a bell shape entrance and bell shape exit with a straight part of 1 ~ 10 times of the hole diameter. (Fig. 12, 13, 14).

Etch pattern of section showed the presence of melting zone around the drilled hole. (Fig. 14).

Ceramic materials such as glass and sapphire were cracked by localized thermal tension under the electron bombardment. However, drilling by low density bombardment at several tenth

μA was satisfactory.

Fig. 15 is an example of line cutting of a metal film deposited on ceramic substrate.

Our tentative apparatus has still many points to be improved and our second apparatus is now in the course of preparation.

References

(1) Namba, S., Reports I.P.C.R. (in Japanese), 35, 183 (1959).

(2) Namba, S., Tamura, H. and Yoshizawa, T., Reports I.P.C.R. (in Japanese), 35, 368 (1959).

(3) Namba, S. and Tamura, H., Reports I.P.C.R. (in Japanese) 36, 368 (1960).

(4) Namba S., Tamura, H. and Hirose, K., Sci. Papers I.P.C.R., 54, 353 (1960).

(5) Kaiser, W., Keck, P.H. and Lange, C.F., Phys. Rev., 101, 4 (1956).

ELECTRON BOMBARDMENT IN THIN FILM MICROCIRCUITRY PRODUCTION

By

David Wm. Moore
Manager
Lear, Incorporated
Santa Monica, California

ABSTRACT

This paper describes a production evaporator which will produce 80 - 500 thin film microcircuits in a two-hour cycle. Particularly stressed is the role of electron bombardment in the deposition of the resistive circuit elements.

A SYSTEM FOR THE PRODUCTION OF MICROCIRCUITS

It is now possible to produce thin film and hybrid microcircuits by a semi-automatic machine so that the component tolerances which are required for precision military systems are obtained. It is also possible to produce these microcircuitized systems for a cost which is considerably below that now considered average or normal for this type of equipment. In fact, the financial savings which can be expected with all types of microcircuitry are becoming known in the industry and, in effect, are the main reason for the unprecedented interest in this type of circuit fabrication. For years the scientific community has been aware of the availability of various forms of circuit miniaturization techniques. It has been possible for at least five years to make forms of microcircuitry which could enable a substantial size reduction and a corresponding increase in at least reliability. The cost of this type of circuit fabrication was, however, several times that of conventional circuit fabrication techniques. This increased cost precluded the use of microcircuitry for any use except the production of sample circuits to show in the right places. During the past year, possibly the last two years, it has become possible to make relatively inexpensive microcircuits. In fact, it can quite easily be shown how the use of microcircuit techniques can reduce the costs of some circuits by almost an order of magnitude. This now becomes an item of real and practical interest to all fabricators of electronic systems.

The extent to which this cost reduction potential has invaded the military thinking can be shown by the following experience which I had about six months' ago.

I had planned a visit to a large Air Force base to talk with the gentleman who is in charge of the development of advanced electronic packaging techniques. The purpose of my visit was to convince this gentleman that microcircuitry could be produced with present state of the art techniques for lower costs than cord wood or printed circuit board assemblies. I had come prepared to discuss the reasons for my convictions with him, and to try to get him to accept the reality of this situation. When I explained the purpose of my visit to him, he simply said, "I know it.". There was no need for any convincing on my part. I, obviously, was not the first visitor who had brought to him the "glad tidings". Now, the fact that I was received in this manner is extremely significant. It indicated that the cost reduction potential of the microcircuit processes is accepted. It means that the industry is aware that the advantages of the microcircuit (small size and weight, and greater reliability) are now combined with lower cost. This is in effect a revolutionary combination, and those of us in the field can feel the vanguard of this revolution right now. We are making so many quotations that it is becoming increasingly difficult to find the time to prepare them adequately. The requests for quotations are not just for five and ten of a circuit for sample quantities, but for really large quantities. Within the past month we have considered quantities of as high as 50,000 of a single type of circuit. Many of these inquiries are fishing expeditions. I do not expect anyone to order thousands of any microcircuit or microcircuitized system this year. I am sure, though, that they will next year. The trend has started, and it is irreversible.

I have dwelt perhaps more than I should in a short paper of this type on the cost reduction aspects of the microcircuitry production processes which we will be considering. This is justified, however, by the fact that the cost reduction potential is the greatest single factor which will get the microcircuit parade off to a good start. Without the cost reduction considerations, the microcircuit art would never get off the ground, so to speak, even for complex military systems.

As probably most of you know, there are several basic approaches to the fabrication of a microcircuit. We feel that for the immediate future, the really significant forms of microcircuitry will be the molecular circuit function, the thin film integrated circuit, and the hybrid circuit. The machine described in this paper will be usable for the thin film and hybrid microcircuitry systems.

Both the thin film integrated circuit and the hybrid circuit make use of thin film passive components and interconnecting wiring. These passive components and the associated wiring are produced by combinations of thin film materials which usually are deposited by carefully controlled vacuum deposition techniques. The vacuum deposition techniques are particularly adaptable to the microcircuit problem because they can be deposited through precision masks to produce directly and without hand adjustment, circuit components having the accuracies required for most types of military equipment. The mask through which the microcircuit is evaporated is the controlling factor, and it fortunately can be fabricated for a reasonable cost since it constitutes the bulk of the so called "production tooling" required for any microcircuit which goes into production.

The thin film microcircuit requires "add on" transistors and diodes. There are various forms which these transistors can assume, ranging from bare silicon chips to completely canned elements of the type which would be used in the more conventional printed circuit board techniques. These "add on" components determine to a large degree the production cost of any microcircuit, and account for probably 80 to 90 percent of the construction costs. They are also the portion of the integrated microcircuit most susceptible to damage from environmental exposure. Nevertheless, highly accurate and reliable integrated thin film circuits can and are being produced, and to my knowledge there is currently no other manner in which this can be accomplished.

The hybrid circuit is a new concept which, in effect, combines the solid circuit function and the thin film integrated circuit. The hybrid circuit is a thin film integrated circuit which has been deposited upon a silicon substrate into which the required active elements have been diffused. The circuit is deposited onto this silicon substrate instead of the normal dielectric substrate of glass or other suitable material. Being deposited upon a silicon substrate into which the active elements have already been diffused, the hybrid circuit is complete when it leaves the production evaporator. It is not necessary to add transistors to the hybrid circuit.

The cost aspects of the hybrid again are particularly interesting. Transistors diffused into the silicon substrate can be prepared for pennies apiece because the necessity for dicing the silicon and mounting the transistors is eliminated.

These handling costs are the most expensive part of transistor production, particularly for the extremely tiny units now being used for many of the thin film microcircuits. The hybrid circuit is a new concept, we are making some, others are also making some. Whether any precision hybrid microcircuits are in actual use, I do not know. But here again, it will not be too long until they will be.

The main advantage of the integrated thin film microcircuit and of the hybrid circuit is that the passive components can easily be deposited to the rather close tolerances which are necessary for military equipment. With the thin film circuit it is possible to exactly reproduce any conventional circuit, although significant gains are usually possible with careful and intelligent redesign. But in any event, the accuracy and the stability of the passive components, which are a must for any practical circuit, can be obtained from the thin film process.

Now, a thin film integrated or hybrid microcircuit is usually fabricated from three to five layers of thin film materials. Each of these layers must be deposited through a properly prepared mask in accurate registration with the underlying layers. The deposition process must be so handled that stable and accurate electrical characteristics are obtained from the film materials.

The films which are deposited are evaporated in a vacuum in the 10^{-6} mm region and at substrate temperatures of from 200 - 400° C. This combination of low pressure and high substrate temperature is what has presented the difficulties in depositing thin film circuitry at high production rates. To minimize

production costs it is necessary to accomplish as much as possible at one "pump down" and during one heating cycle.

The Lear high speed production evaporator has been designed to economically and rapidly deposit the film materials normally used in thin film and hybrid microcircuitry. This machine is quite flexible and can be set to meet a wide variety of material and application requirements.

As currently operating in our own facility, this machine will evaporate any of three different materials, through any of as many as five different masks, onto a total of 20 one inch square areas. This deposition is accomplished in a two hour time cycle.

Usually, the three materials would be a resistive alloy, a conductive alloy, and a dielectric film. This material combination would permit the deposition of the passive components normally used in thin film and hybrid microcircuitry. With these three materials, resistors, condensers, and the interconnections can be deposited.

Figure No. 1 is a photograph of this machine which is semi-automatic and particularly well adapted to both production line and development laboratory use. The critical operations of this machine are automatic, the non-critical operations are manual. For example, the resistance cutoff is extremely critical and is automatic. The vacuum pumping control is automatic so that an operator can attend more than one machine. Substrate indexing is manual, as are the various voltage adjustments for the evaporation sources and substrate

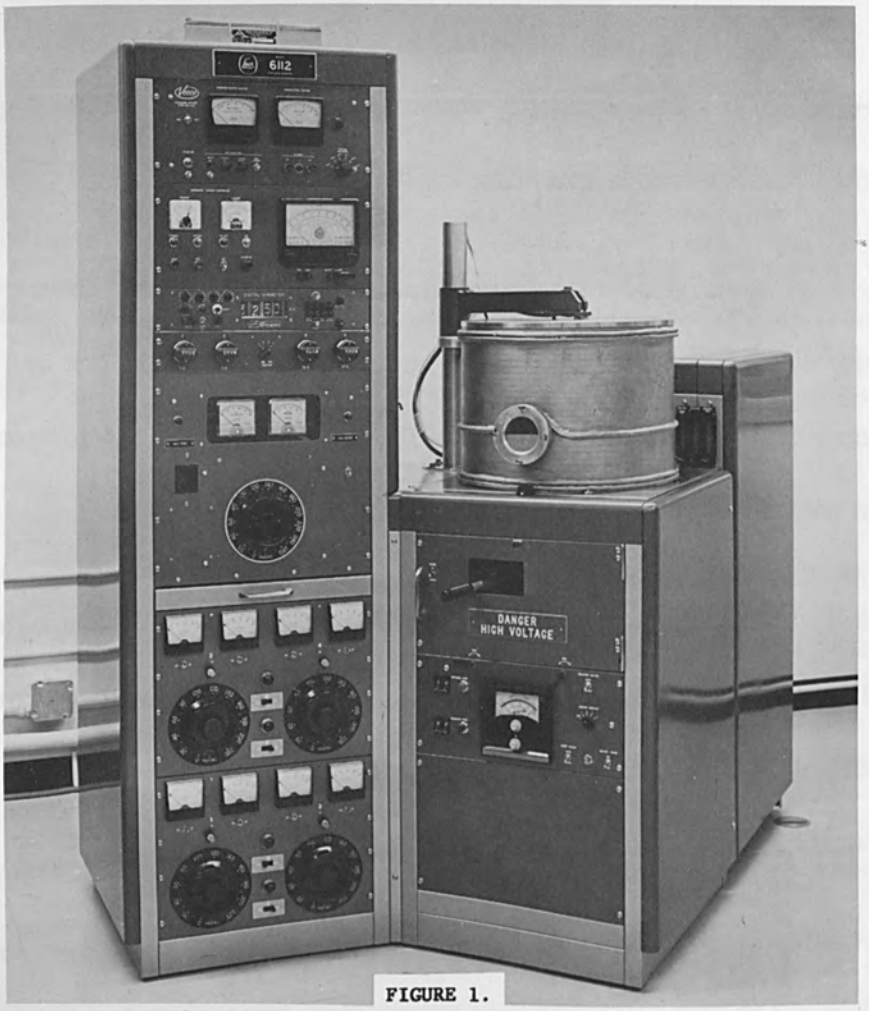

FIGURE 1.

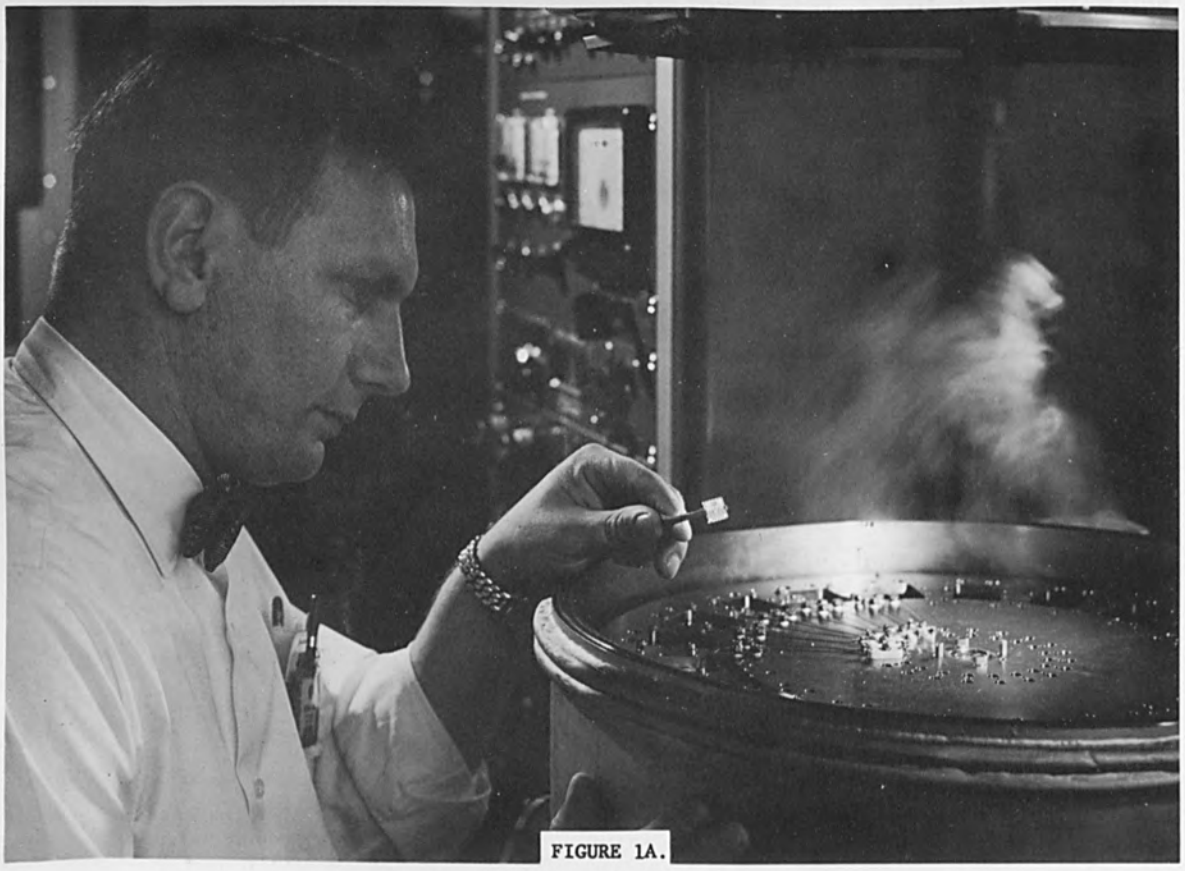

FIGURE 1A.

heaters. The use of manual adjustments and controls where such control will not adversely affect the operation of the machine substantially reduces the cost and complexity of this equipment and increases its operational reliability.

High speed oil diffusion pumps of advanced design with liquid nitrogen traps are employed to insure adequate pumping speed and a sufficiently low pressure during the evaporation of the film materials.

The deposition of all of the film materials required for a specific microcircuit in a single pump down contributes markedly to the consistency and reliability of the microcircuit, as well as to minimizing overall fabrication costs. Whenever more than one evaporation is required to produce a thin film component, there are always unknown and unpredictable effects due to surface contamination and possible film damage due to improper handling. These variables are eliminated by the single evaporation.

The operation of this high speed evaporator has been tailored to the requirements of the thin film production line and as such it forms the basis for a thin film facility. It is also adaptable to pilot line and laboratory use where its speed and flexibility can very substantially reduce the time required to develop experimental microcircuitry. We estimate that this type of machine would be as effective as 50 to 100 standard coaters.

The Lear Production Evaporator deposits any of three materials through five different masks and onto twenty different one inch square areas. This means that 20 five layer devices, or sets of devices, could be deposited in the two

hour cycle of this machine.

As an example, we can consider the fabrication of microcircuitry on one-half inch square glass substrates. This one-half inch square size has become widely used in our own facility and is a size upon which a substantial amount of microcircuitry can be deposited. Since the area of a one-half inch square substrate is only one-fourth of a square inch, four of these substrates can be placed in one of the one inch square areas in our machine. And, since there are 20 such areas, this machine can be loaded with a total of 80 one-half inch square substrates which it will process in a two hour cycle.

The following table shows the relation between substrate size and the number of microcircuits which this machine could process in two hours:

Substrate Size	Substrates Processed in Two Hours
1" x 1"	20
1/2" x 1/2"	80
1/4" x 1/4"	320
0.2" x 0.2"	500

The circuit yield would depend upon the circuit complexity and component tolerances and, to a degree, upon substrate size. We would estimate a yield of from 50 to 90 percent, the higher figure being characteristic of production runs of several hundred or more of the same circuit. Larger quantities would be required in the smaller substrate sizes to stabilize the production process.

At this writing there have not been large quantity requirements for microcircuitry of any type, so large quantity yields are a matter of estimation rather than of history.

The high speed evaporator would be used to deposit the passive components onto either the dielectric substrates of the thin film microcircuit, or onto the active substrate of the hybrid microcircuit.

Materials which can be evaporated from a filament, boat, chimney, or by electron bombardment can be deposited by the Lear high speed evaporator. For our immediate use we have this machine set up for the evaporation of nickel chromium alloy for resistors, (electron bombardment), beryllium copper for conductors (continuous feed boat), and silicon monoxide for dielectric films for condensers and circuit insulation (chimney). These three materials illustrate three different forms of evaporation which, incidentally, would handle most of the materials normally considered for microcircuitry. For complex films, where the vapor pressures of the constituents may vary widely, a flash evaporation source could be easily added.

Flexibility of this machine is assured by the ease with which materials can be changed and corresponding adjustments made in substrate temperature. Changes in materials or in processing techniques will not obsolete this machine since such changes can be quite easily accommodated.

The operation of this production evaporator is based upon a lazy susan principle in which the substrates are positioned adjacent to the particular mask through which the deposition is taking place and properly aligned. The lazy susan which is apparent in Figure 1A contains twenty one inch square areas through which the films can be deposited onto the substrates in twenty batches during the two hour cycle. The one inch square areas can be filled with as many substrates as they will hold. The design of the machine has been worked out so that the field uniformity over the one inch square area is adequate for the deposition of multiple circuits within this area. Control of the deposition is through a monitor slide for each one inch square area. The monitor slide is adjacent to the one inch square area, and while the deposition is taking place on the substrates, it is also taking place on the monitor slide. The monitor slide is in a position where the electrical resistance value of the pattern being deposited can be continuously monitored during the evaporation process. Then it is a rather simple matter to automatically stop the evaporation by means of a solenoid actuated shutter and suitable servo amplifier when the desired monitor slide resistance has been reached. Referring again to Figure No. 1, the panel with the digital ohmmeter contains the electronic equipment necessary to actuate the cutoff shutter when the desired value of monitor slide resistance has been obtained. The automatic cutoff feature is used for all film materials which are electrically conductive. The automatic feature frees the operator from having to be quite as careful in his operation of the machine and raises the yield considerably. Dielectric films are monitored by watching the interference color fringes build up as the film is being deposited. A periscope arrangement has

been built into the evaporator to enable the color fringe monitoring to be easily done.

Electron bombardment is used in our current machine to evaporate the resistive film which is a nickel chromium alloy. This electron bombardment consists of a molten anode drop of the material being evaporated surrounded by the tungsten cathode. A grid to control space charge is also included. This particular gun is of our own design and operates at 1500 volts and 300 - 400 milliamperes. The evaporation is upward, and one problem is that excess evaporated material which is deposited onto the masks and supporting fixtures sometimes falls back into the electron beam gun and shorts between the cathode and anode. We are designing a deflected beam gun into our new coaters so that the electron source is not in the vapor stream. This should prevent any material falling back into the gun and causing shorts and production delays while the gun is being cleaned. Deflected beam guns of the type manufactured by Temescal and Elion are being considered. In subsequent machines two of these deflected beam guns will be used; one for the resistive material evaporation and one for the evaporation of dielectric material. The electron beam sources are particularly well adapted for the continuous deposition required for a production machine.

Figures 2, 3, 4, 5 and 6 show the types of microcircuitry which can be deposited by this machine in final encapsulated form. Circuits of this type can now be made for less cost than conventional electronic systems, and offer substantial potential increases in reliability and life.

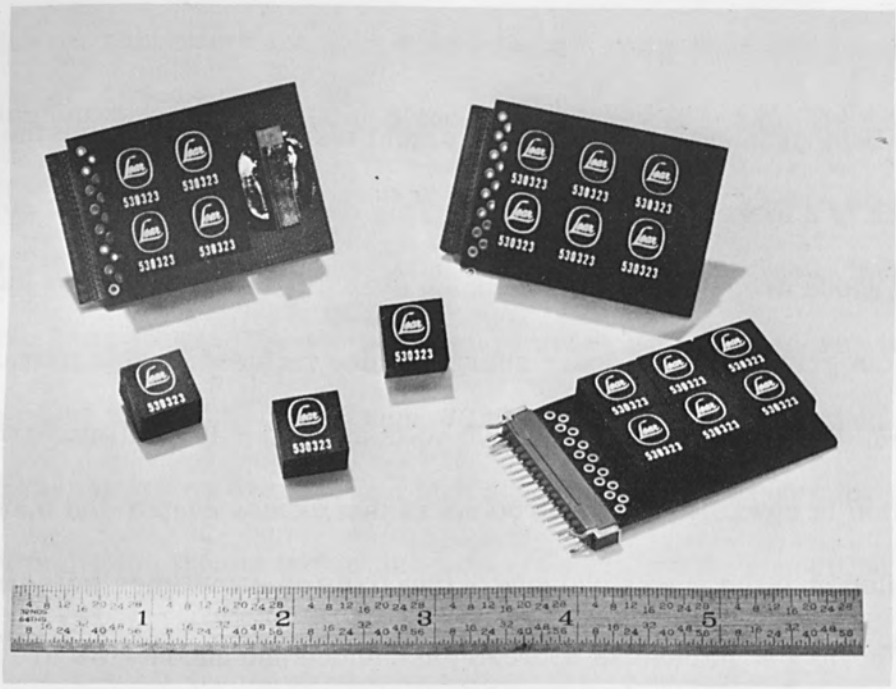

FIGURE 2.

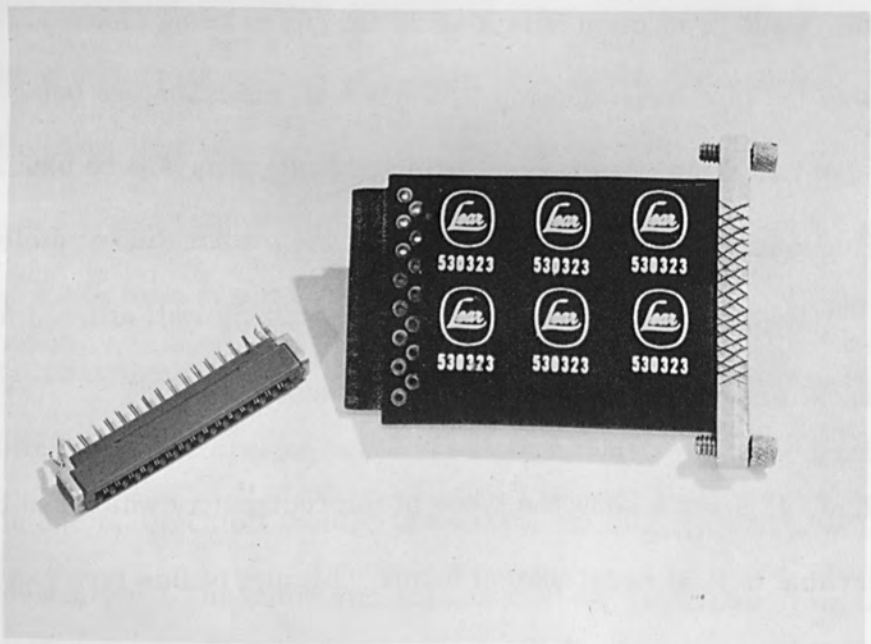

FIGURE 3.

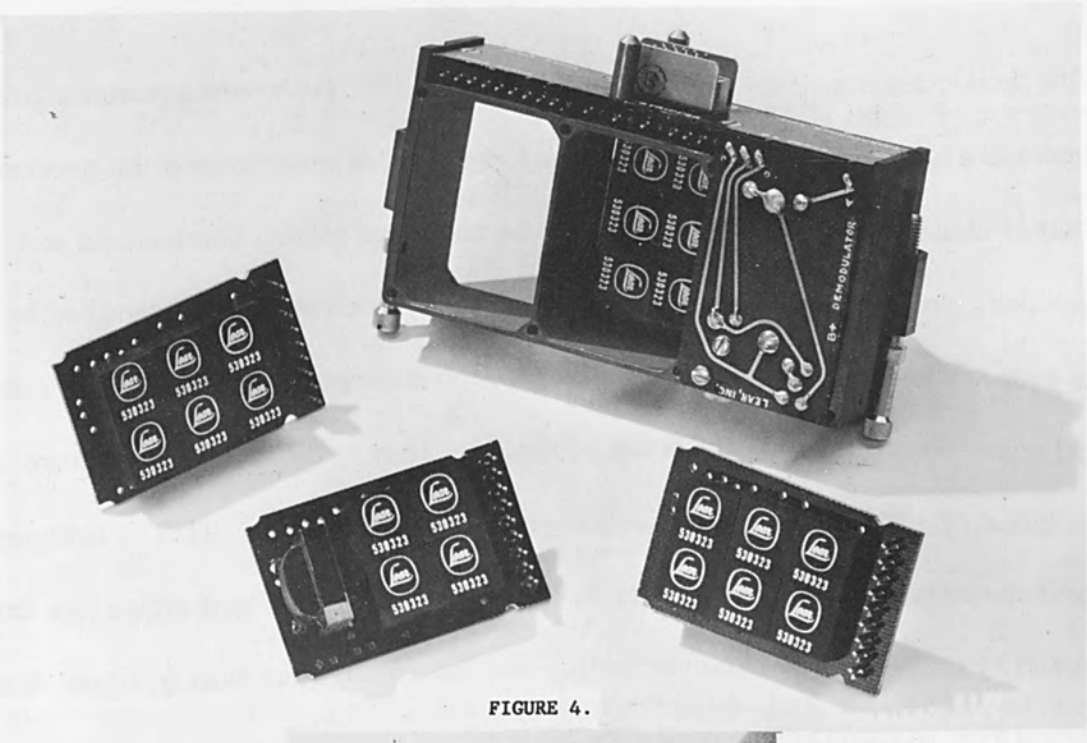

FIGURE 4.

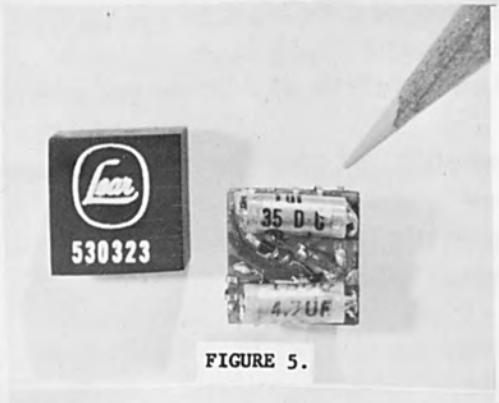

FIGURE 5.

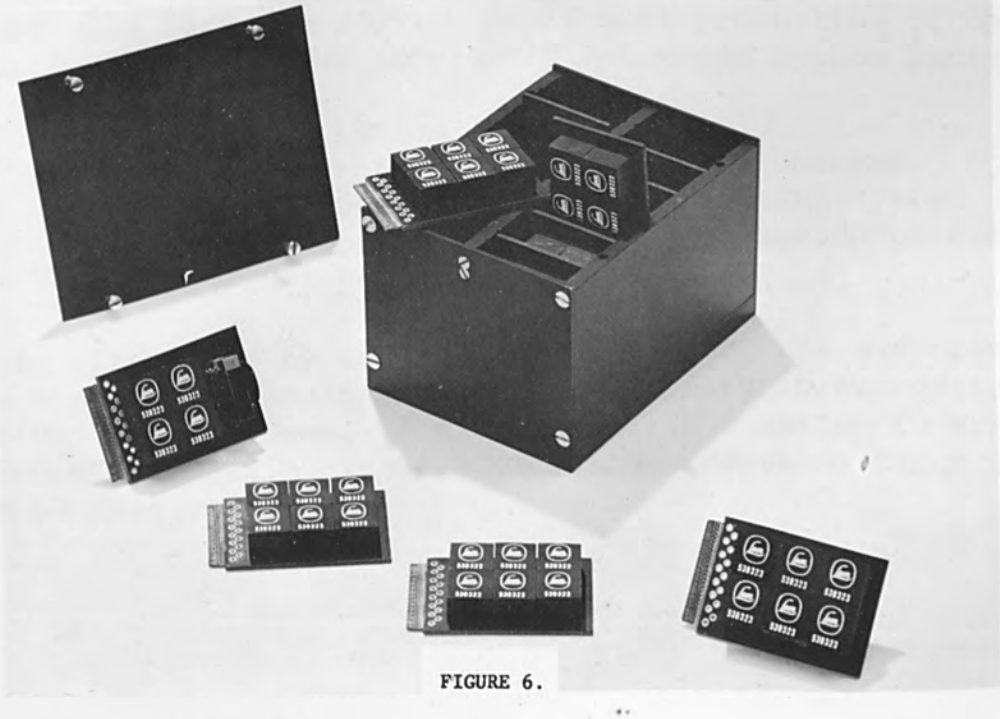

FIGURE 6.

With production machinery of the type described, the electronics manufacturer becomes a complete entity in himself and is not as dependent upon the procurement of electronic components. True - he has some add on components to consider, but the bulk of the circuit components he requires are deposited by the evaporation equipment in final form and mounted as they will be used in the equipment for which they are being produced. This is the radical departure in the industry - the manufacturer making his own components. This is bringing about the revolution in the industry because a manufacturer now either has this capability or he hasn't. And currently, and increasingly as time goes on, his competitive position will depend upon what he can do with microcircuitized packaging concepts. Manufacturers as a whole are realizing this now, and resulting upheaval is something of which we are all aware.

THIN FILM DEPOSITION PRODUCTION FACILITY

By

G. C. Riddle
Microsystems Electronics Department
Lockheed Missiles & Space Company
Sunnyvale, California

ABSTRACT

An electron-bombardment evaporator and associated equipment was developed to facilitate the formation of thin films for basic studies of thin film properties. The evaporator presents many advantages:

- o Evaporation of refractory materials
- o Close control of evaporation rate
- o Continuous, sustained, high evaporation rates
- o Multiple evaporations under one vacuum

From process control parameters determined during the initial development, a simultaneous, three-source evaporator, and related equipment, was built to provide rapid mass production of thin film electronic circuits. The completely automated system includes:

- o A three-station mask-holder
- o An efficient integral substrate-changer
- o A novel evaporation-rate monitoring system
- o A continuous sustained-rate three-source evaporator
- o Self-triggered cycle control

With this system the deposition of three different evaporant materials can be accomplished on the substrate in succession, rapidly under one vacuum. Application of the system to precision formation of thin film circuits in the Microsystems Electronics program is discussed.

A THIN-FILM DEPOSITION PRODUCTION FACILITY

Introduction

Many areas of research and development today are concerned with the properties of thin films: mechanical, electrical, magnetic, and optical. These films are formed by several processes: chemical, electro-chemical, vapor deposition, vacuum evaporation, sputtering, or spraying. One of the important phases in thin film investigation is the control of the many parameters that influence the film properties.

Although vacuum evaporation methods and processes have been in use since the 1930's, it has been only recently that the methods have been sufficiently improved and the instrumentation developed for precise process control.

Many materials can be deposited in thin film form by vacuum evaporation. These materials include metals, metal oxides, fluorides, sulfides, and other crystalline substances such as silicides. The only requisite is that the material evaporate or sublime without decomposing at the necessary temperatures and pressures.

The formation of thin films by vacuum evaporation requires a process that permits fine control of the many parameters involved. Process parameters that influence film properties include:

1. Absolute pressure during deposition.
2. Composition of residual gases.
3. Temperature of substrate during deposition.
4. Cleanliness of substrate surface.
5. Smoothness of substrate surface.
6. Material of evaporant.
7. Material of substrate.
8. Deposition (evaporation) rate.

9. Deposition time.

10. Post-deposition treatment.

11. Substrate-evaporant compatibility.

12. Temperature of evaporator.

The equipment needed to establish an electron-bombardment-type evaporation facility should have these desirable characteristics:

1. Permit evaporation of refractory materials.

2. Be flexible in specific arrangement to allow for several types of evaporant.

3. Permit several materials to be evaporated interchangeably under one vacuum.

4. Prevent contamination of evaporant by crucible or boat.

5. Permit sustained high evaporation rates.

6. Allow close control of evaporation rate.

7. Accurately monitor evaporation or deposition rates.

8. Allow control of substrate environment.

9. Be served by a vacuum system that is capable of maintaining an ultra high vacuum under evaporation conditions.

The evaporator developed to meet the needs of our research program exhibits all of these characteristics. In one arrangement multiple layers of different materials can be evaporated under one vacuum. Evaporation rates are monitored by a novel evaporation-rate meter, the operation of which is based on the model of the evaporant stream as an artificial dielectric system.

While this development effort has been conducted to aid us in our basic research of the properties of thin film materials, an extension of our present work capability is contemplated based on the findings of the development period. Actual production facilities are available only on an experimental scale.

Evaporator Design

An evaporant source was required that would provide a continuous stream of evaporant material for a sustained period. An excellent source for this use was developed using the cold sink type of electron-bombardment evaporator[1] which was successfully modified to permit a continuous supply of the evaporant material. Two arrangements were organized allowing the evaporant to be used in either wire or granulated form.[2]

In the wire form, the evaporant was fed through a small hole drilled along the axis of the cold sink and melted into a ball. The shape of the cold sink was also modified to that of a truncated cone to provide a minimum of heat loss. The arrangement is illustrated in Fig. 1 and is shown in Fig. 2 with the cover plate removed. This post or pedestal type of electron-bombardment evaporator has proven to be highly successful. Refractory materials such as tungsten, tantalum, and molybdenum were easily evaporated from this system, with sustained evaporations of from one to five minutes. It is interesting that these high-melting-temperature materials can be contained in a molten ball balanced atop the cooled copper post with little damage to the post and that the ball does not adhere to the post when allowed to cool.

To facilitate the evaporation of those materials which must be handled in powder, granular, or chunk form, an uncooled hearth type of evaporant holder was used. A lazy-susan arrangement was adapted to permit six hearths to be changed while still under vacuum. The arrangement is illustrated in Fig. 3 and is shown in Fig. 4. Later a circular groove turntable was adopted in place of individual hearths to provide a continuous evaporant source. By slowly rotating the evaporant-filled groove under the bombardment aperture, a high evaporation rate of crystalline material was sustained for up to seven minutes. The materials evaporated included chromium, silicon monoxide, magnesium fluoride,

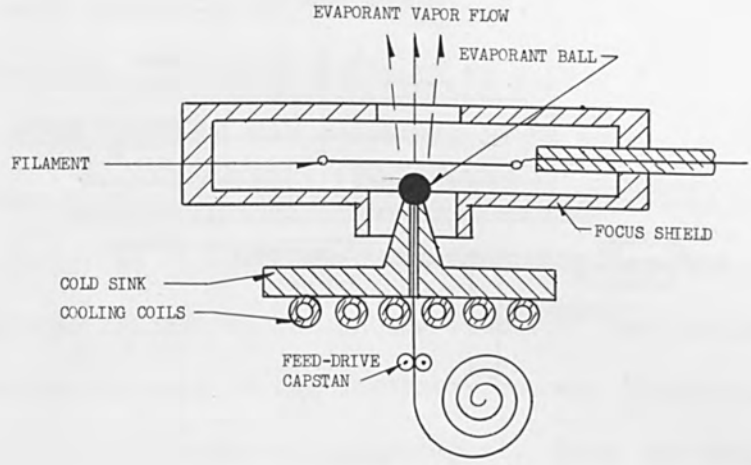

FIGURE 1

DIAGRAM OF PEDESTAL EVAPORATOR

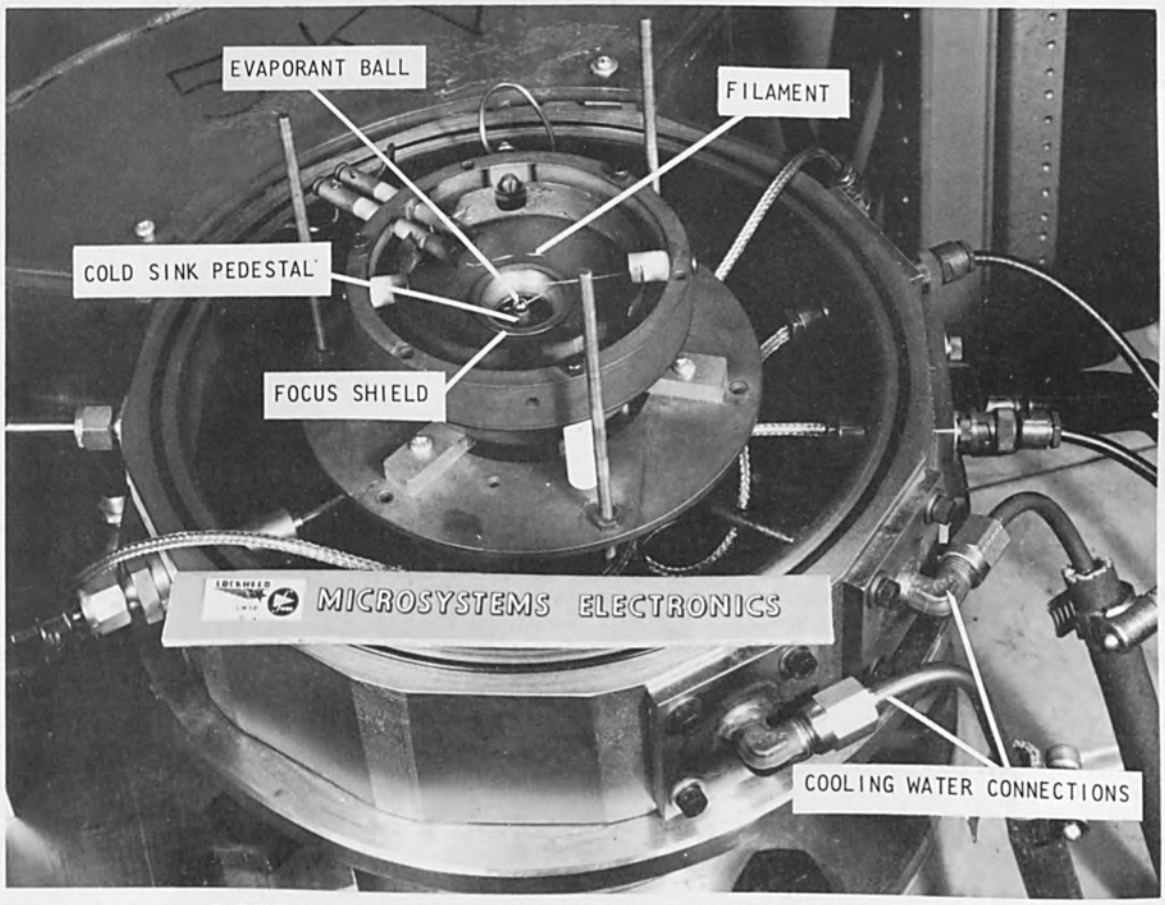

FIGURE 2 PEDESTAL EVAPORATOR WITH COVER PLATE REMOVED

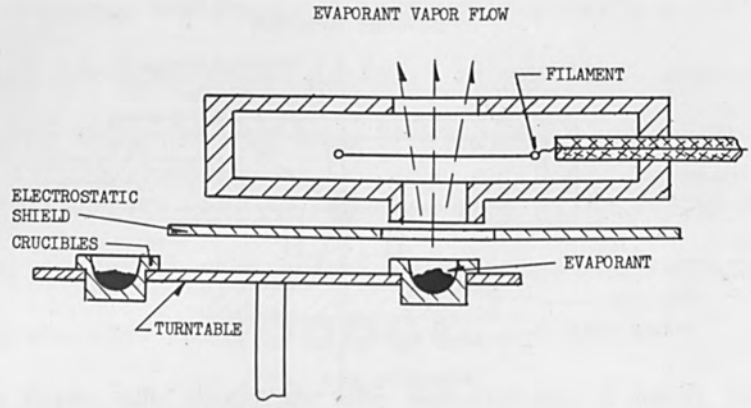

FIGURE 3

DIAGRAM OF LAZY-SUSAN EVAPORATOR

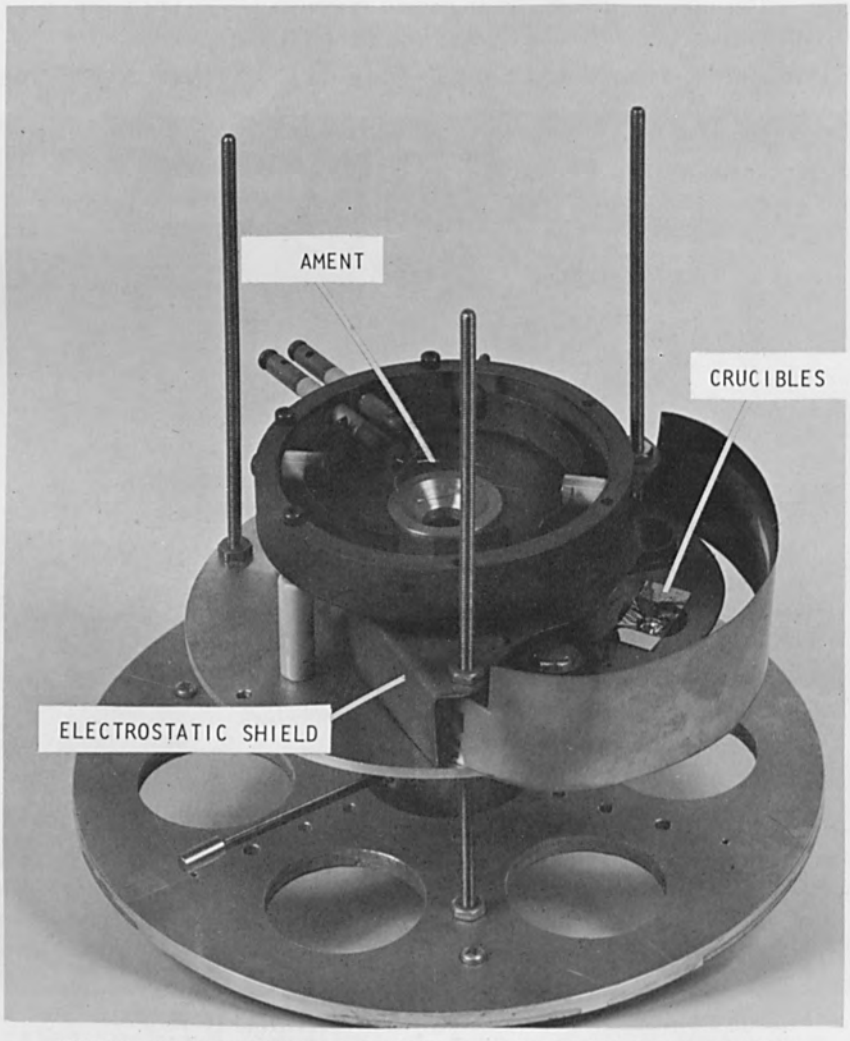

FIGURE 4 LAZY-SUSAN EVAPORATOR WITH COVER PLATE REMOVED

titanium diboride, zinc sulfide, cadmium sulfide, and zirconium silicide. Copper and gold were evaporated most easily by this arrangement.

Insulating materials such as silicon monoxide and cerium fluoride can be readily evaporated with the electron-bombardment heater because the insulating material becomes conducting as it is heated. When current is first applied to the material a surface charge is developed that causes deflection of the beam to the edge of the insulator, but as the evaporant boat heats up due to this deflected current the edge of the insulator becomes conducting and the heat slowly migrates to the center of the material. Once the heat has been distributed over the surface, the bombardment current can be increased to cause evaporation of the material.

Advantages of Bombardment Heating

Conventional evaporation methods use either a metal strip with a depression of some form to contain the molten material, or a coil of wire, each of which is heated directly by passing an electric current. While this method is the simplest to use, it has several disadvantages which are overcome by using electron-bombardment heating.

The ability to contain and evaporate the refractory and the reactive metals is one advantage. Refractory materials require such high temperatures for evaporation that usually the boat itself melts in the attempt. The reactive metals such as nickel, iron, cobalt, or combinations such as nichrome and karma when molten readily alloy with and dissolve the more common boat metals. These materials can be contained in graphite, alumina, or similar type crucibles, but however, a great amount of heating power is required in the process. In contrast, these materials can be easily evaporated from the pedestal evaporator by application of 300 watts of beam power (100 milliamperes at 3000 volts); see Fig. 5.

Another advantage is the more even heating that is obtained. When using a resistance heated boat to evaporate conducting materials such as copper or gold, extensive overheating of the boat occurs. As the material melts and flows to fill the boat, it shorts out the current through that portion of the boat. As a result the heating power is concentrated to the ends of the boat and evaporation occurs at the boundary between the evaporant liquid and the clean boat. As the liquid is evaporated, the point of evaporation moves across the boat in pursuit of the retreating evaporant boundary.

On the other hand, when using electron-bombardment heating, the evaporant is heated from the top surface at the area of beam contact and evaporation takes place from the same area. The surrounding melt flows to fill the area and maintain evaporation. Since the heating effect is independent of the resistance of the evaporant, a wide range of materials can be evaporated.

Another advantage is obtained when subliming materials such as chromium[3] and tellurium are evaporated. The evaporation occurs from the point where the heat is applied, and for resistance heated boats this point is on the bottom of the mass where the material makes contact with the hot boat. The sudden expansion of the evaporant tends to blow the remaining material out of the boat. These effects are absent using electron-bombardment heating; evaporation takes place from the top surface where the heat is applied, with a saving in time and material.

One most important advantage is that the pure evaporant material is not contaminated by the support when using the cooled pedestal as a hearth. The molten material makes a poor thermal contact with the hearth and does not wet the hearth surface. Some deposit occurs on the hearth surface from the evaporation, but this deposit is not re-evaporated. After several evaporations this deposit is of sufficient thickness that it can be peeled from the hearth.

Evaporation Rate Control

An interesting method of evaporation rate control was discovered while working with the wire-feed pedestal evaporator. It was found that for certain evaporator arrangements the molten ball stabilizes between one-eighth and one-fourth of an inch in diameter. If a rapid wire feed rate increases the ball diameter, the evaporation rate increases rapidly; if a slow feed rate permits the ball to decrease, the evaporation rate decreases sharply. This effect is considered to be due mainly to a change in the distribution of electron current between the ball and the post. Different chamber geometries do not exhibit this property.

This property can be useful in controlling the evaporation rate. Holding all other factors constant (acceleration voltage, bombardment current, etc.), the evaporation rate is dependent upon the evaporant-feed rate. An equilibrium condition will develop between the ball size, evaporation rate, and feed rate. Since the ball size will hold constant at any particular equilibrium condition, the evaporation rate will be directly proportional to the feed rate.

Another factor must be taken into account before the above property is applied: the included gases and other impurities in the evaporant feed wire. These impurities sometimes cause bubbling or sputtering of the molten ball as the wire is fed into it. Any surface being coated from the evaporation stands a chance of being splashed with a large drop of the evaporant. This effect can be minimized by feeding the evaporant intermittently, during which time the source is shuttered. The resulting evaporation rate is not constant; it slowly decreases during the cycle while no evaporant is being fed. However, the average evaporation rate is still proportional to the average feed rate.

Bombardment Evaporator Considerations

If bombardment power is to be controllable through filament emission

control, then the evaporator must be operated well within the temperature saturation region of the filament emission.[4] When working under this condition the current is relatively constant during wide changes of evaporator conditions.

On the other hand, if space charge limiting effects are permitted to develop, the current can be caused to vary widely by changes of conditions about the anode. Thus the power delivered to the ball will fluctuate widely by the influence of the evaporant vapor.

To insure that the bombardment process is always operating in the temperature saturation region, the acceleration voltages must be kept high enough to preclude space charge effects from developing.

It is easy to qualitatively determine if the bombardment process is temperature or space-charge limited. When operating in the temperature limited region a small change in filament voltage produces a large change in beam current, while a small change in acceleration voltage causes little change in beam current. However, when operating in the space-charge limited region, the effects are reversed. There is also a region where both types of current limiting occurs. This region corresponds to the "knee" of the emission curve as illustrated in Fig. 6.

Experimental data was taken on the performance of the ball evaporator under conditions of space charge limiting. Two sets of data were taken where only the radius of the filament, hence the anode-to-cathode spacing, was changed. The data are shown plotted on Fig. 7. In one condition evaporation commenced when the current increased above 50 milliamperes; in the other condition evaporation did not occur. The effect of the evaporant vapor on the space-charge limiting is seen as a deviation from the calculated curve. The calculated curves were determined from the equation

$$I = GV^{3/2}$$

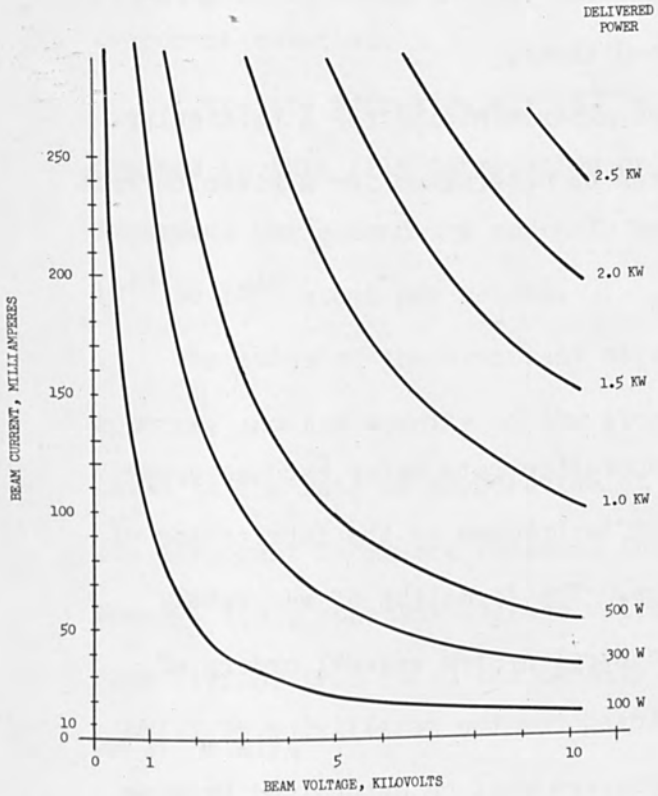

FIGURE 5

NOMOGRAPH OF EVAPORATOR BOMBARDMENT POWER

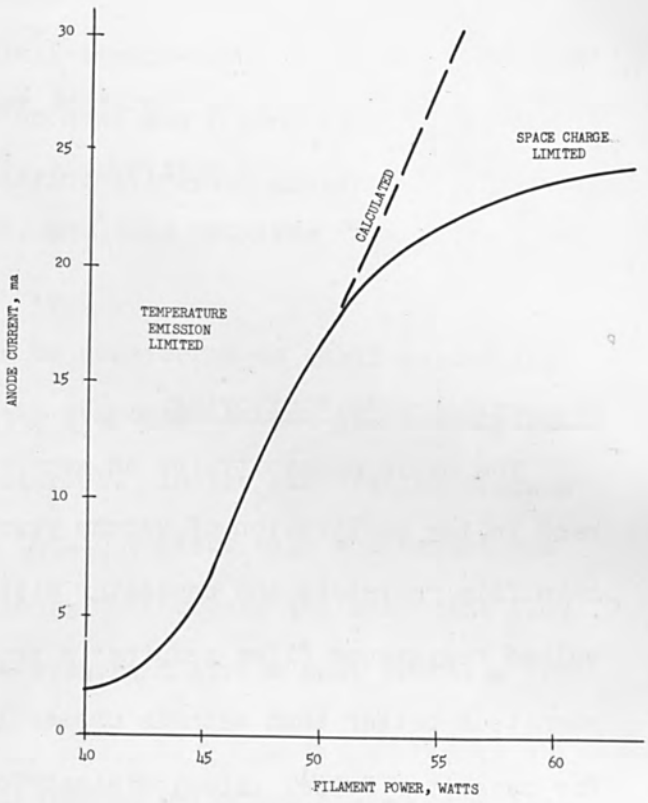

FIGURE 6

FILAMENT EMISSION CHARACTERISTIC

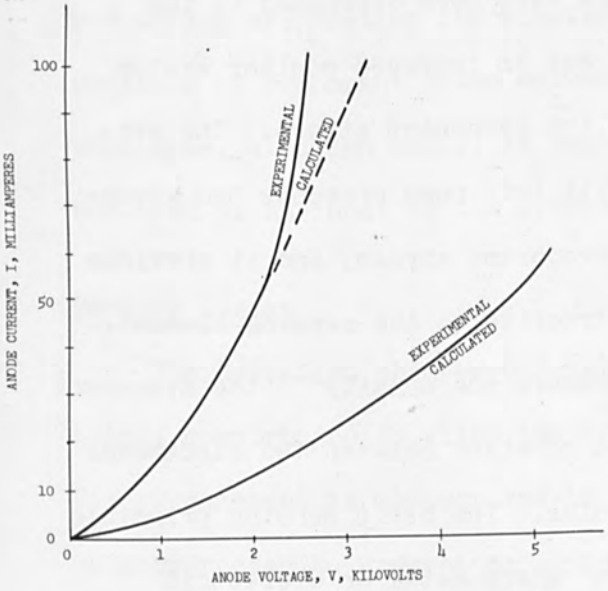

FIGURE 7

EFFECT OF EVAPORANT VAPOR ON SPACE CHARGE LIMITING

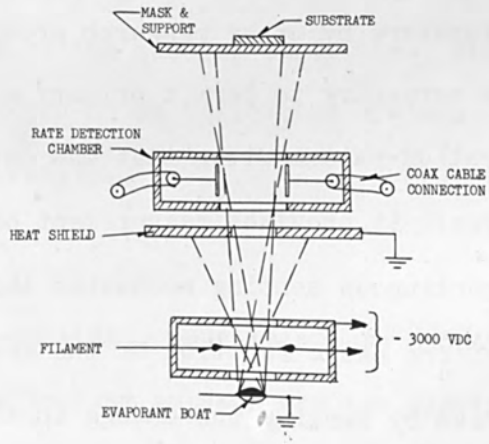

FIGURE 8

DIAGRAM OF DETECTION CHAMBER ARRANGEMENT IN EVAPORATOR

which is a general relationship that is applicable for any geometrical arrangement operating under space-charge-limited conditions.

Once the perveance G has been determined experimentally for a particular geometry, the minimum operating voltage V' can be determined for a given current by the equation

$$V' = I/G$$

Evaporation-Rate Monitoring

The basic necessity for an accurate evaporation-rate meter becomes apparent in the application of vacuum evaporation techniques to the fabrication of thin film resistors and capacitor dielectrics. The formation of accurately valued resistance films requires a process control system several orders of magnitude better than methods presently employed for the metallizing of films for capacitor foils. Also, dielectric thicknesses must be determined by some means before the counter electrode is applied. The deposition rate and the integral of the rate, the total deposit, is important for determining film stability, density, porosity, and adherence.

Several forms of secondary rate monitoring have been discussed in the literature by other research groups,[5,6,7,8] but an improved monitor system was necessary to permit primary monitoring of the evaporant stream. The evaporation-rate monitor that was developed to fill this need presents two advantages: it provides measurement of the total evaporant stream, and it provides a continuous sensing mechanism that is nondestructive to the sensing element.[9]

The basic function of the system is to measure the density of the evaporant stream by sensing the change in the dielectric constant between two electrodes caused by the presence of the evaporant molecules. The basic sensing principle involves the theory of "artificial dielectrics" where metal or dielectric spheres distributed in a space provide a relative dielectric constant of that

space greater than the empty space alone.[10] This design will operate for any evaporant material.

There are approximately 10^{14} atoms per Angstrom per square centimeter deposited in thin film fabrication processes. Deposition rates of 0.1 to 100 Angstroms per second are commonly employed, and this requires flow rates of 10^{13} to 10^{16} atoms per second.

The atoms of the evaporant stream can be considered as small conducting spheres, and the density of the atoms in the evaporant stream is directly related to the rate of evaporation of the material. In the evaporation process the evaporant atoms are released from the liquid surface with a constant net energy, i.e., constant average velocity; thus, to increase the evaporant flow rate (evaporation rate) the density of the evaporant stream must increase proportionately.

The sensing mechanism is a pair of electrodes which are placed such that the evaporant stream passes between them. The electrodes form a capacitor in one leg of an RF balanced-bridge circuit. The bridge is initially balanced before evaporation starts by adjusting the capacitance of the alternate leg, and during evaporation the unbalance of the circuit is due primarily to the presence of evaporant atoms between the plates of the sensing capacitor. This unbalance, although small, is amplified, presented on an indicating system, and used as an input to the process control circuits.

Monitor Design

The detection chamber consists of a well-shielded, parallel-plate capacitance, constructed to allow the evaporant flow to pass between the two electrodes. The arrangement is illustrated in Fig. 8. The chamber containing the electrodes is constructed to prevent capacitance changes due to spacing changes which would give an erroneous indication on the rate meter. The electrodes are completely

enclosed with all connections made with coaxial cable. The evaporant stream passes through a "chimney" aperture in the enclosure on the way to the substrate and thus becomes an artificial dielectric system between the capacitor electrodes.

The bridge circuit illustrated in Fig. 9 consists of the balanced center-tapped secondary of a driver transformer and two capacitors, C_1 and C_2, one in each leg of the secondary. The voltage appearing at the junction between the capacitors is the signal applied to the amplifier. In the actual circuit three other capacitors appear: one due to the capacitance of the coaxial cable between the driver transformer and the detection chamber, one lumped capacitance introduced to balance the latter and match the phase shift in each leg, and one due to the capacitance of the coaxial cable between the detection chamber and the amplifier.

Capacitance C_1 is the effective capacitance of the detector chamber including the stray effects of the chamber enclosure. The capacitance C_2 is a special vernier capacitor that varies between one and twenty picofarads. With all shields in place the balanced bridge developed a null of -93db.

The output of the balanced bridge is applied directly to the input of a high gain RF amplifier. The input is a high Q parallel tuned tank circuit which serves two purposes (other than selectivity): the inductance acts as a short circuit to any electron or ion current resulting from the fringe of the evaporant stream impinging on the detector electrode, and the resonance develops a high impedance by cancelling the input cable capacitance. This high impedance reduces the load on the bridge allowing more sensitivity at the null. The output voltage of the bridge is directly proportional to the evaporant density.

A 400 Kc oscillator drives a buffer amplifier which in turn drives the primary of a transformer, the secondary of which is part of the balanced bridge.

A three-stage single-tuned RF amplifier provides 90 db of gain for detection of the signal from the balanced bridge. A 10 db per step attenuator is included in the amplifier to provide scale changes. The output of the amplifier is rectified and the DC voltage is applied to a microammeter for rate indication. The DC voltage is also available for application to an integrator to determine total deposit.

Experimental Results

The balanced bridge has a very high sensitivity to any change of capacitance in the detector chamber. The degree of unbalance for various factors is as follows:

pencil-sized strip of tissue paper - 10 db

insulated length of #14 wire - 15 db

metallic evaporant stream - 20-60 db

The output of the RF amplifier must develop ten volts for full-scale deflection of the rate meter. This corresponds to a 20 db unbalance of the bridge. The 10 db/step attenuator in the amplifier provides scale changes to accomodate high evaporation rates.

The rate meter has been used in conjunction with both resistance heated evaporators and electron bombardment heated evaporators. Both sources perform satisfactorily with the rate detector, although the electron bombardment source must be carefully designed to reduce the effect of stray electrons and ions registering on the rate meter.(11)

Several initial tests were conducted to determine the accuracy of response of the rate meter to the evaporant stream.

First the correlation between indicated rate and amount deposited over a fixed period of time was checked. A Cahn Electrobalance was employed to weigh the specimen both before and after deposition. The Electrobalance has an

accuracy to within ten micrograms. Evaporations were conducted at a constant indicated rate for a set period of 10 seconds using copper as the evaporant. One-inch squares of aluminum foil were used as the substrate to keep total mass as low as possible and increase the percentage change. The data obtained from ten tests is presented on the graph of Figure 10.

After the mass-rate test the ability of the rate meter to predict the resistance of a deposited resistor was checked. A resistance pattern was deposited on a substrate and the resistance of the pattern was measured after deposition, using only the integrated rate to indicate the deposition limit. Five resistance strips were deposited on each substrate, and five substrates were deposited in succession while maintaining a continuous evaporation. The results of this test are presented on the graph of Figure 11. The variation of resistance from one strip to the other can be attributed to the nonuniformity of the mask pattern. It is the variation of the same strip from substrate to substrate that provides the reproducibility indication.

The average resistance of the group was taken as the basis for calculation of accuracy, and the percentage deviation from the average for each strip is presented on the graph of Figure 12. The maximum deviation is less than 20 percent, a tolerable amount in some circuit applications.

It is expected that further refinement of the evaporation apparatus with automatic monitoring control will improve the accuracy.

Thin Film Circuit Deposition

In the fabrication of evaporated thin film circuits there are only two process steps where accurate evaporation monitoring and control is really necessary. These steps are during the deposition of resistive elements and during the deposition of dielectric films for capacitive elements. During the remaining steps of the process, i.e., conducting strips, counter electrodes, etc., a

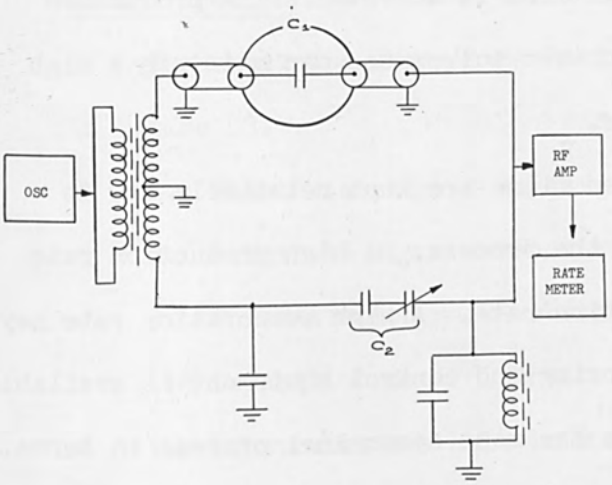

FIGURE 9

DIAGRAM OF BALANCED-BRIDGE
DETECTOR AND ASSOCIATED CIRCUITS

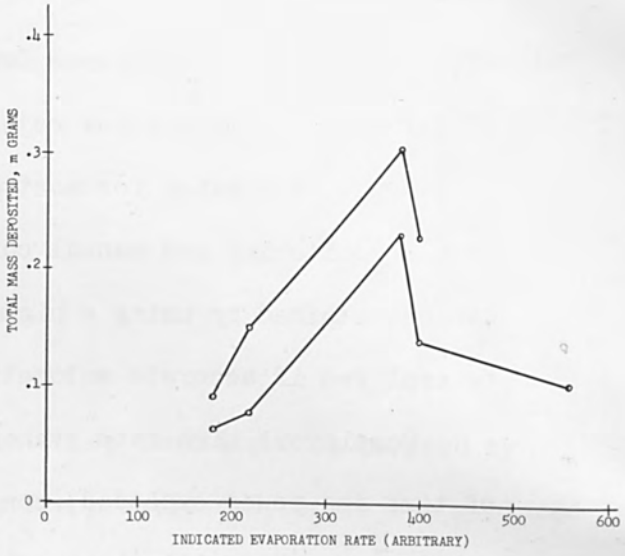

EVAPORANT MATERIAL: COPPER
DEPOSITION TIME : 10 SECONDS
EVAPORATOR TYPE : ELECTRON BOMBARDMENT
SOURCE TYPE : BOAT AND PELLET

FIGURE 10

MASS FLOW RATE TEST RESULTS

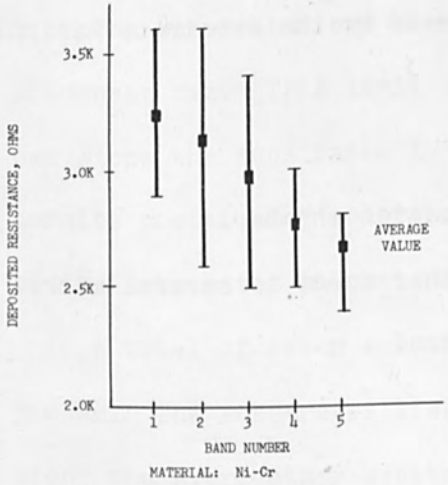

FIGURE 11

RESISTANCE DEPOSIT
CONTROL BY INTEGRATION OF INDICATED RATE

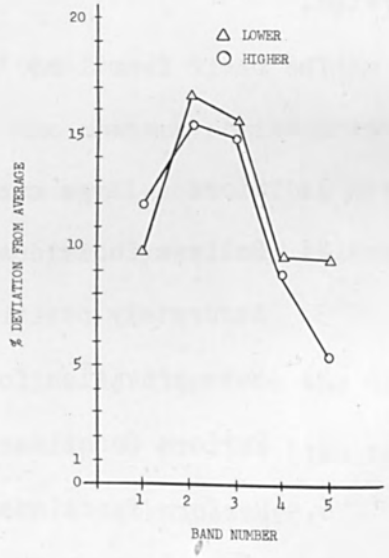

FIGURE 12

ACCURACY OF RESISTANCE DEPOSIT CONTROL

rather wide tolerance of deposition conditions is acceptable. A production process that makes allowance for the required tolerances can maintain a high production rate with a low reject factor.

Deposition rates for most evaporated films are kept relatively low to permit monitoring and manual control of the process. A high production rate can be obtained by using a high evaporation rate. A high evaporation rate may be employed if accurate automatic monitoring and control equipment is available.

Continuous high rate evaporation is the most economical process in terms of time and power expended, compared to volume of production, if a high speed substrate-mask positioning mechanism can be employed.

To meet the requirement for such a thin film deposition facility additional equipment was developed to work in conjunction with the electron-bombardment evaporator and evaporation rate meter. These include a substrate changer-positioner mechanism and a deposition control system. The deposition control system has been organized to permit a completely automated process control system.

The basic functions that need to be performed by the substrate manipulator are:

1. Store a large number of substrates.
2. Deliver individual substrates to deposition chamber.
3. Accurately position each substrate with respect to several masks.
4. Have provision for several mask stations.
5. Perform functions in minimum of space.
6. Perform functions in minimum of time.
7. Maintain proper substrate environment.

To perform these functions a novel mechanism was designed and constructed for the thin film research program.[12]

Changer Design

The substrate changer mechanism has four operating sections as illustrated in Figure 13.

1. Substrate storage magazine.
2. Substrate dispenser-positioner.
3. Three-station mask-substrate holder.
4. Deposition control shutters.

The substrates are held in a stack from which they are free to feed by gravity into the dispenser. The substrates are pre-cleaned before being placed in the magazine, and a heater arrangement maintains the substrates at an elevated temperature to effect a continuous outgasing of the substrate surface.

The substrate dispenser is a cam operated push rod that ejects the bottom substrate from the stack in the magazine. The cam is operated at a speed of one cycle per second, and one cycle of rotation is used intermittently to dispense each substrate. The substrates feed out in succession, the later substrates pushing those preceding.

The substrates are accurately positioned by the travel limit of the dispenser cam. This limit is adjusted such that the maximum position of the cam stops the substrates in the same exact position each cycle. This method permits positioning tolerances to be equivalent to the dimensional tolerance of the substrates which is ± 0.001 inch.

A total of seven substrates are held in the line leading from the dispenser. The substrates lie directly on the mask strip to provide high resolution; and every other substrate is positioned above a mask aperture.

The substrates are positioned by two fixed orthogonal reference edges and are held tightly to these edges by spring fingers. A strip heater maintains the substrates at elevated temperatures throughout the deposition process.

Photographs of this mechanism with the heater section removed are shown in Figures 14 and 15.

The three-station mask pattern as shown in Figure 16 is accurately dimensioned in one piece on a X10 scale and photo-reduced to insure close tolerances. The mask itself is photo-etched from 6-mil stainless steel. The three mask stations can represent different material patterns or an overlay of several patterns of the same materials for production of difficult patterns such as spiral coils or circles. As the substrates advance, they move in succession from one mask station to another, thus permitting several patterns to be deposited in succession.

Individual shutters are provided beneath each mask position to control the actual deposition time. These shutters are operated individually by electric solenoids actuated from the main control panel. The shutters permit individual deposition control for each mask station. They permit the evaporation process to be continuous, shuttering the mask opening from the evaporant stream during the one second required for substrate changing.

Automatic Cycling Process Control

Many process parameters have been determined during previous work with thin film materials. Methods of controlling these parameters have been developed during the design and construction of the equipment needed for the thin film investigation. A combined, completely automated process control system can be organized using the basic equipment modules presently available.[13]

The complete system is represented in block diagram form in Figure 17. Seventeen blocks are shown, each of which has an important process control function. The three main blocks indicate the physical grouping of the system units as shown in Figure 18.

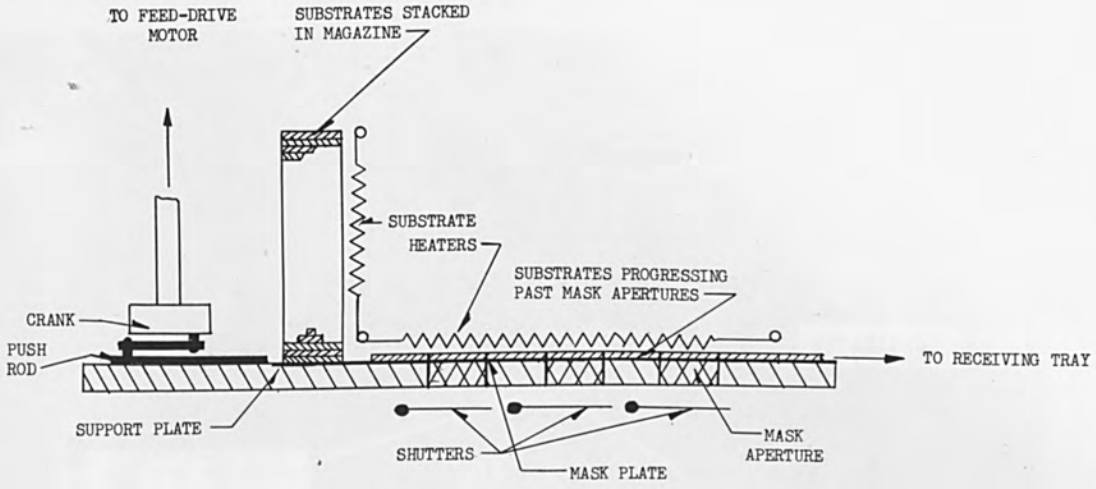

FIGURE 13

DIAGRAM OF SUBSTRATE CHANGER - POSITIONER MECHANISM

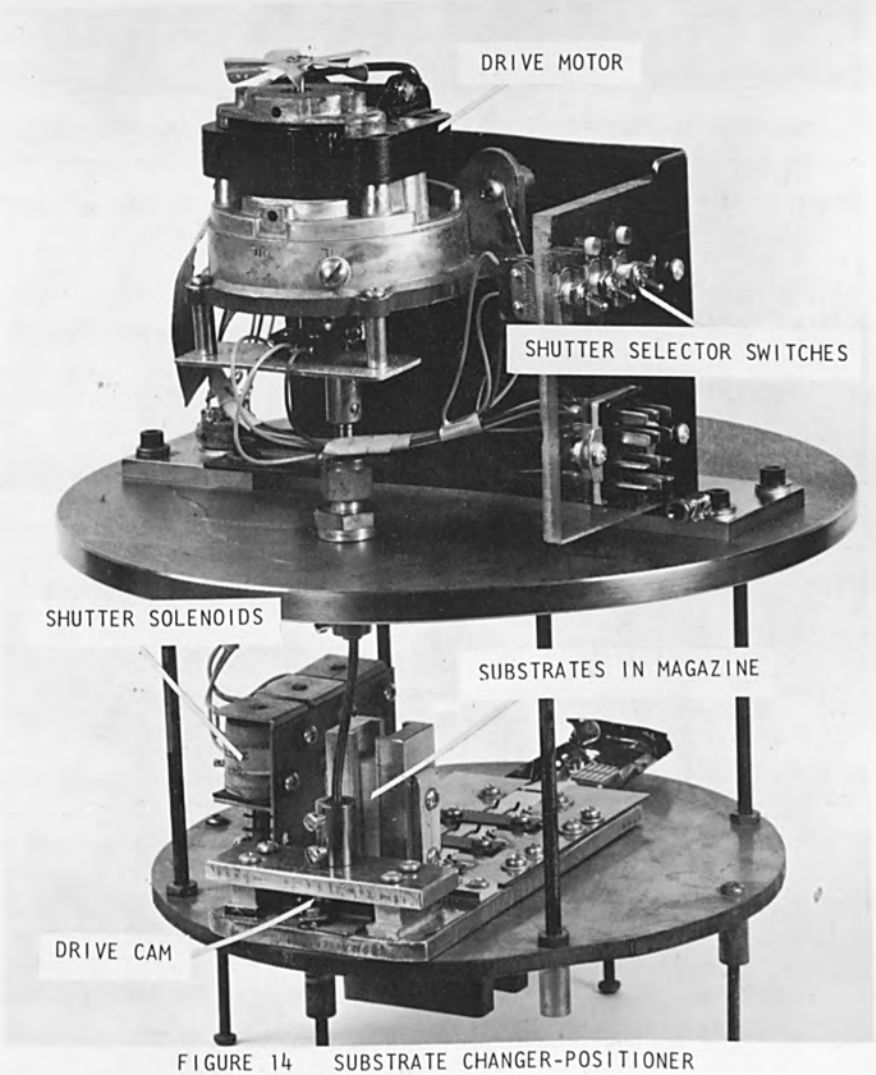

FIGURE 14 SUBSTRATE CHANGER-POSITIONER

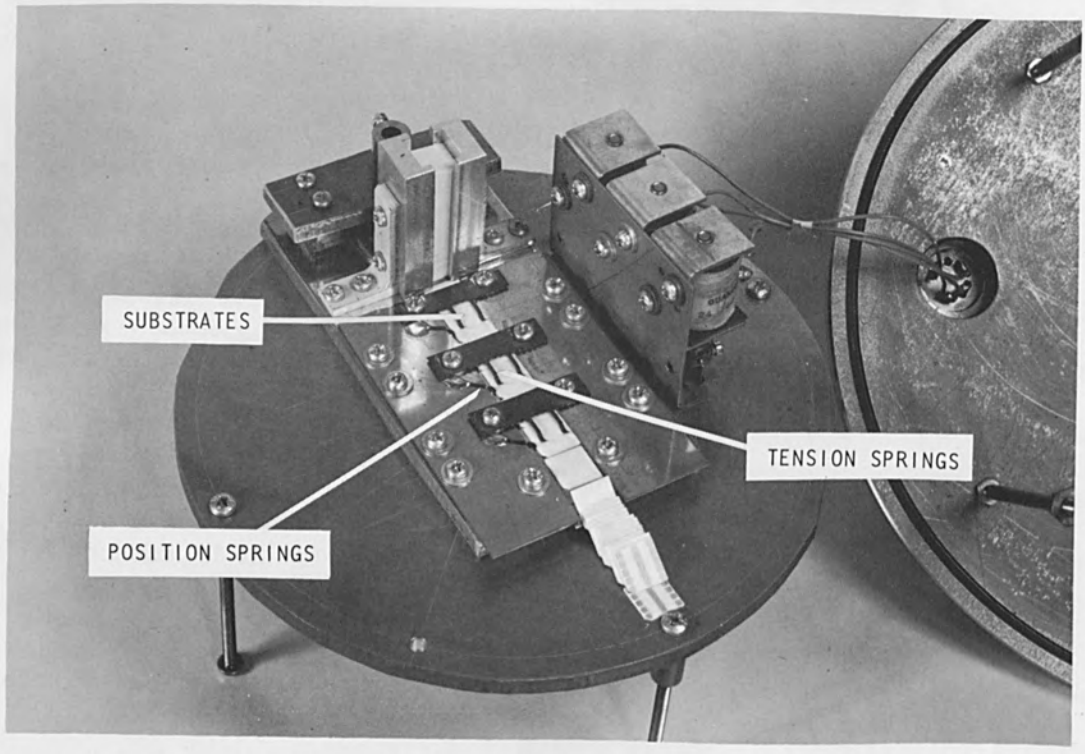

FIGURE 15 SUBSTRATE CHANGER-POSITIONER (SHOWING SOLENOIDS AND POSITIONING SPRINGS)

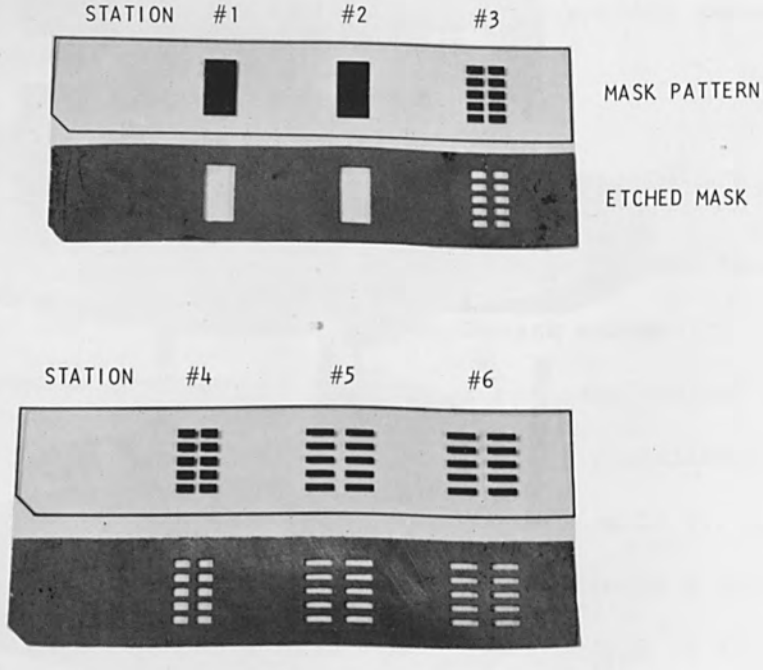

FIGURE 16 ILLUSTRATION OF THREE-STATION MASK PATTERNS AND MASKS

Over-All System

The control console contains all of the instrumentation required for deposition control and substrate changing, along with evaporation rate monitoring and control. These units are all interconnected to furnish feedback control of the process.

The process chamber contains all the mechanisms necessary for the performance of the evaporation and deposition process. The complete unit is designed to perform its function during a single pump-down of the chamber.

The evaporator power unit consists of the high voltage rectifier, filament power supply, filament emission control servo, and the high voltage metering circuits. The emission control servo is a closed loop within the power unit.

Control Console

The functions of the control console units shown in Figure 19 are as follows:

The substrate changer control provides power to the changer motor. This control receives a trigger pulse from the deposition control unit at the termination of deposition. This trigger pulse starts the changer motor which runs for one complete cycle and then stops. Upon stopping, the changer keys the deposition control unit which, if set for automatic cycle, restarts the deposition.

The deposition control unit is the main control unit. It receives information from several other units and controls the deposition shutters and substrate changer. In automatic cycle condition the rate-integrator limit triggers the termination of deposition, closing the deposition controlling shutters. This action also starts the changer mechanism and resets the integrator circuit. Upon completion of its cycle the changer mechanism keys the control unit to reopen the shutters and start the integrator. In manual cycle

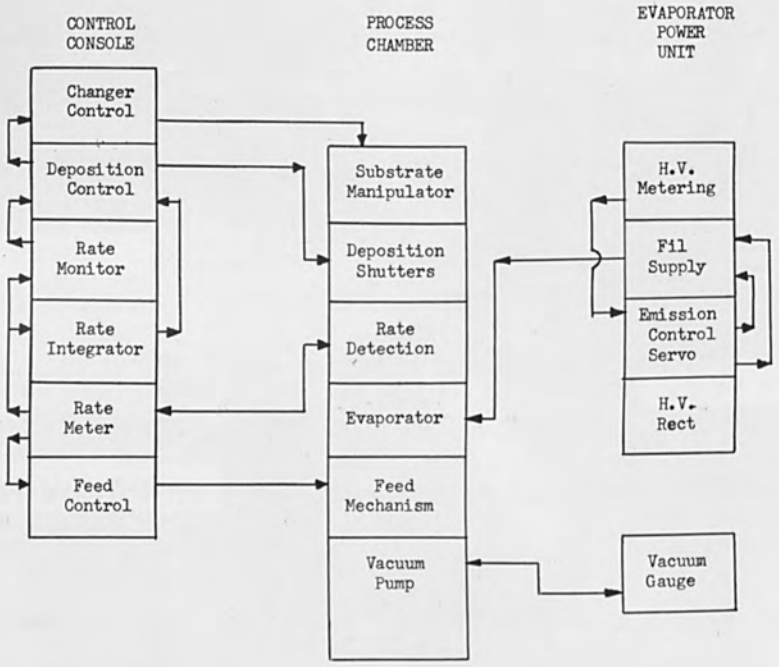

FIGURE 17 PROCESS CONTROL BLOCK DIAGRAM

FIGURE 18 PROCESS CONTROL EQUIPMENT ARRANGEMENT

condition these last actions are not performed. Manual override switches can start or stop any function at any time of the cycle.

The rate monitor is used to stop the deposition if the evaporation rate falls below a preset value. This function is used to insure reasonable accuracy of the rate meter and integrator. This unit also contains a resistance monitoring circuit as an auxiliary deposition control. The circuit can trigger the termination of deposition when the value of a monitored resistance being deposited becomes equal to that of a preset standard resistor.

The rate integrator receives a voltage from the evaporation rate meter and during the deposition time integrates this voltage to determine total deposit. An integration limit circuit can be preset to any fraction of the integrator meter scale and is able to stop deposition at that value. This function is the basis of the automatic cycle control. The integrator is reset during the one second required to change substrates, and integration begins when the shutters are opened again.

The evaporant feed control monitors the evaporation rate and through a servo amplifier adjusts the speed of the feed-drive motor to maintain a constant evaporation rate.

Process Chamber

The vacuum chamber shown in Figure 20 sits atop a high-speed vacuum-pump system. The system has a 1500 liter/sec oil diffusion pump backing a 15 liter liquid nitrogen trap baffle. Base pressure of 10^{-7} mm Hg can be obtained within five minutes from start of pumpdown.

The evaporator is the electron-bombardment heated type described earlier. Metal wire is continuously fed through the center of a copper post into a molten ball the size of which is determined by an equilibrium obtained between the evaporation rate and the feed rate.

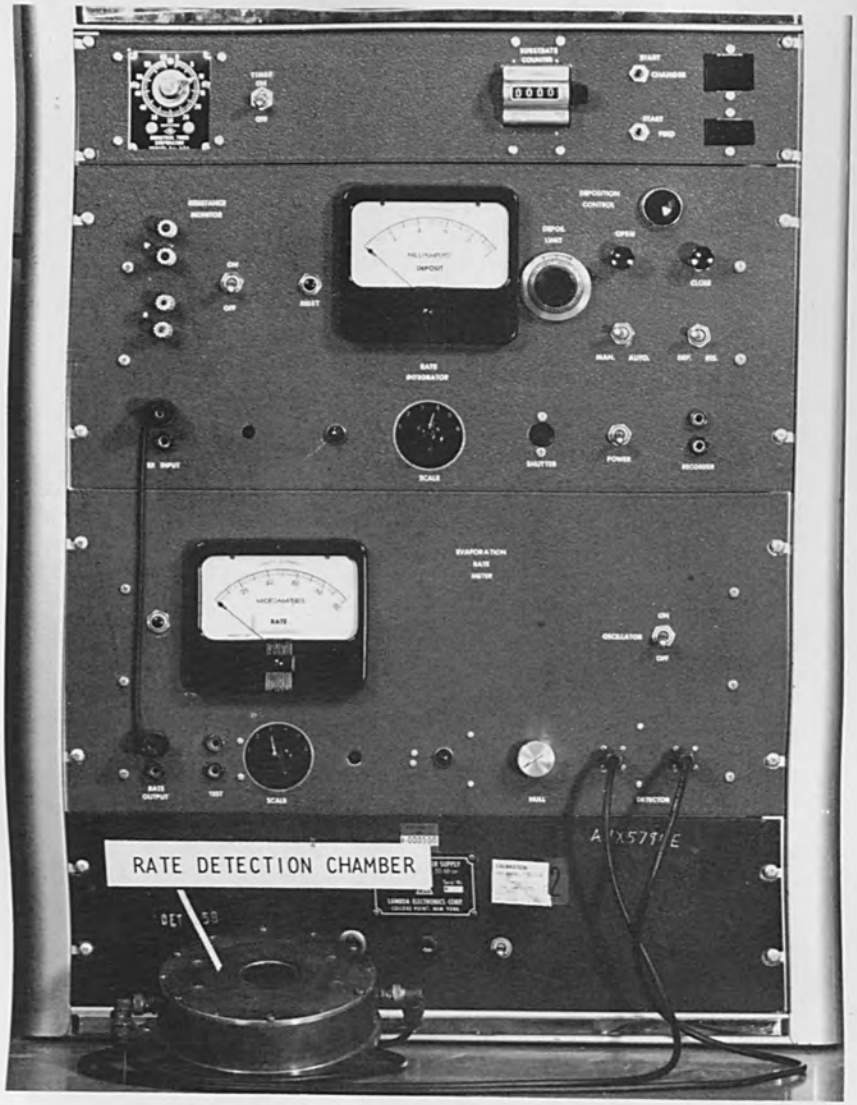

FIGURE 19 CONTROL CONSOLE

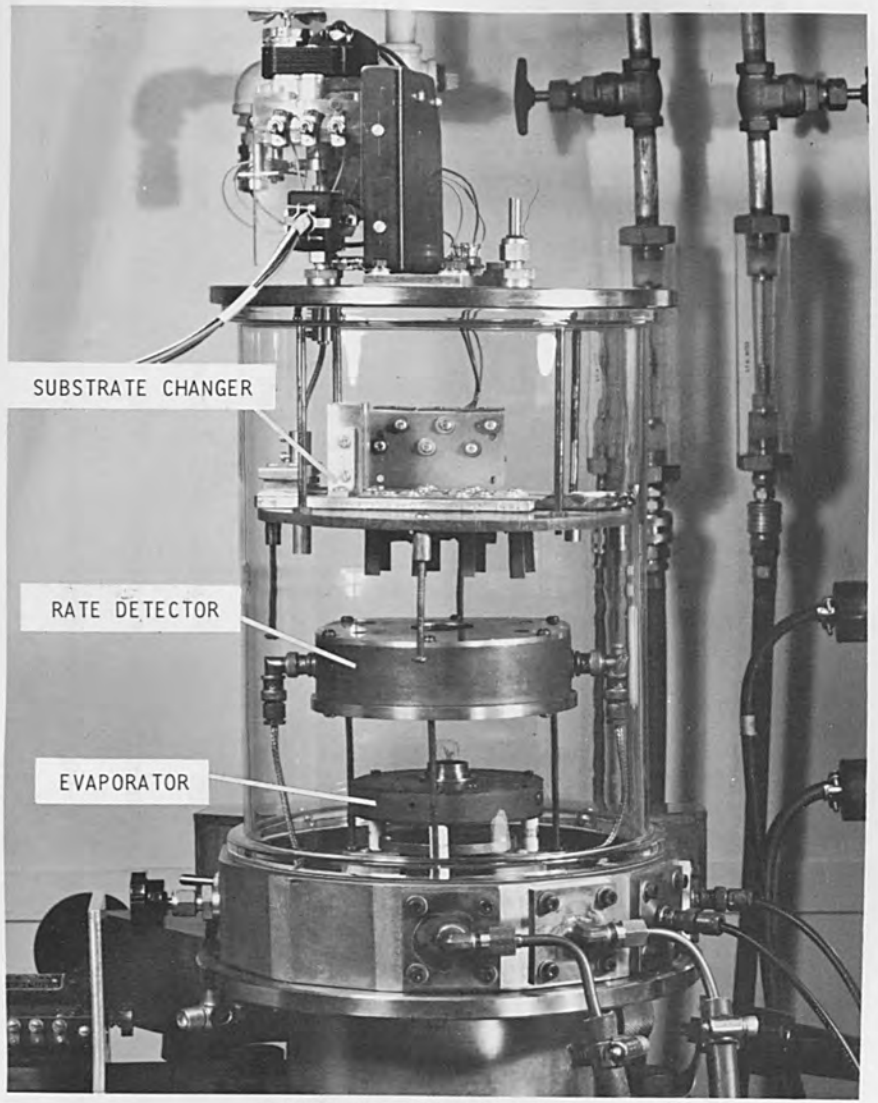

FIGURE 20 PROCESS CHAMBER

The evaporant feed mechanism is a capstan-type drive powered by a variable speed servo motor through a speed reducer mechanism. Speed of the evaporant wire is continuously variable from zero to one inch per second. This speed range is sufficient to provide the required evaporation rates. The feed rate is set by an adjustment on the control panel.

The rate detection chamber contains the sensing capacitance for the evaporation rate meter. The evaporant stream passes through the chamber on the way to the substrate.

The deposition shutters control the deposition time. Actuated from the control console by electrical solenoids, the three shutters control the deposition through three separate mask positions in the substrate holder. The three mask positions have been provided for the use of a simultaneous three source evaporator.

The substrate manipulator has been described previously. Substrates are pushed over the three mask positions in succession. The changer motor is powered from the control console and dispenses the substrates as each deposition is completed.

Evaporator Power Unit

The evaporator power unit provides the regulated power for the electron-bombardment evaporator. The high voltage rectifier can be manually set from zero to five kilovolts. The filament power supply can be set either manually or through an emission-control servo to control bombardment current.

The emission control servo is a magnetic amplifier system that maintains the emission current constant. Constant bombardment current provides constant heating power delivered to the evaporant ball, thus stabilizing the evaporation rate.

System Operation

The equipment must be initially set up and adjusted manually. Those adjustments necessary are integrator limit value, evaporation rate·feed rate, bombardment current and bombardment voltage. These settings are all done after the equipment has been assembled, connected, and the vacuum pumped.

The integrator limit is set to provide the correct amount of material that is required for the particular deposition. The deposition may be a resistance, a dielectric, or a conductor pattern. The integrator limit is determined by a calibration chart prepared for the various materials.

The bombardment voltage and current are set before the evaporant feed rate. The values of these settings have been determined from previous calibration tests as providing optimum evaporator operation.

The evaporant feed rate is then set to provide an adequate evaporation rate as indicated on the evaporation rate meter. The feed rate can then be controlled by the rate meter to maintain the evaporation rate at the desired value.

Once the evaporation process is in operation the deposition control circuits, the shutters and substrate changer can be exercised manually for one or two cycles to check operation. Then the automatic cycle switch is actuated and the system repeats the deposition cycle continuously.

The deposition control has only two sets of conditions when in automatic cycle program:

1. Deposition shutters open, changer drive stopped, integration on, deposition in progress.

When the integration reaches the preset limit, the control circuit is triggered to the alternate condition.

2. Deposition shutter closed, changer drive running, integration stopped and reset.

When the substrate changer has completed its cycle it triggers the control circuit to set up the initial conditions and recommence deposition.

The deposition control, therefore, is a self-triggered automatic cycle as opposed to a timer-programmed cycle.

The automatic cycling continues until either the deposition control is removed from automatic or the evaporation rate falls below a threshhold value (as would happen if the evaporant were exhausted), and the rate monitor stops the deposition.

Multiple-Source Evaporator

As a consequence of the process control parameters determined in the development program it is possible to construct an evaporator having several evaporant sources supplied by a single high voltage supply. Thus, a design has been completed for the construction of a three-source evaporator to be used with the substrate dispenser-positioner in conjunction with the three-station mask holder.[14] A three-barrelled evaporation rate detection chamber has also been constructed to be used with the three-source evaporator.

The three-source evaporator shown in Figure 21 has been constructed for use with one granular material and two wire materials. This arrangement has been assumed after consideration of the various materials to be deposited. With the consideration that the angle of incidence of the evaporant stream must be the same at each of the mask stations, the system is designed to make the direction of evaporant stream normal to each mask. This condition requires that the evaporator sources be spaced on the same interval as the mask stations which are spaced by the substrates.

The general arrangement of the evaporator is illustrated in Figure 22. The filaments are suspended between two copper posts which support the filament and connect the power. Each filament consists of two parallel strands

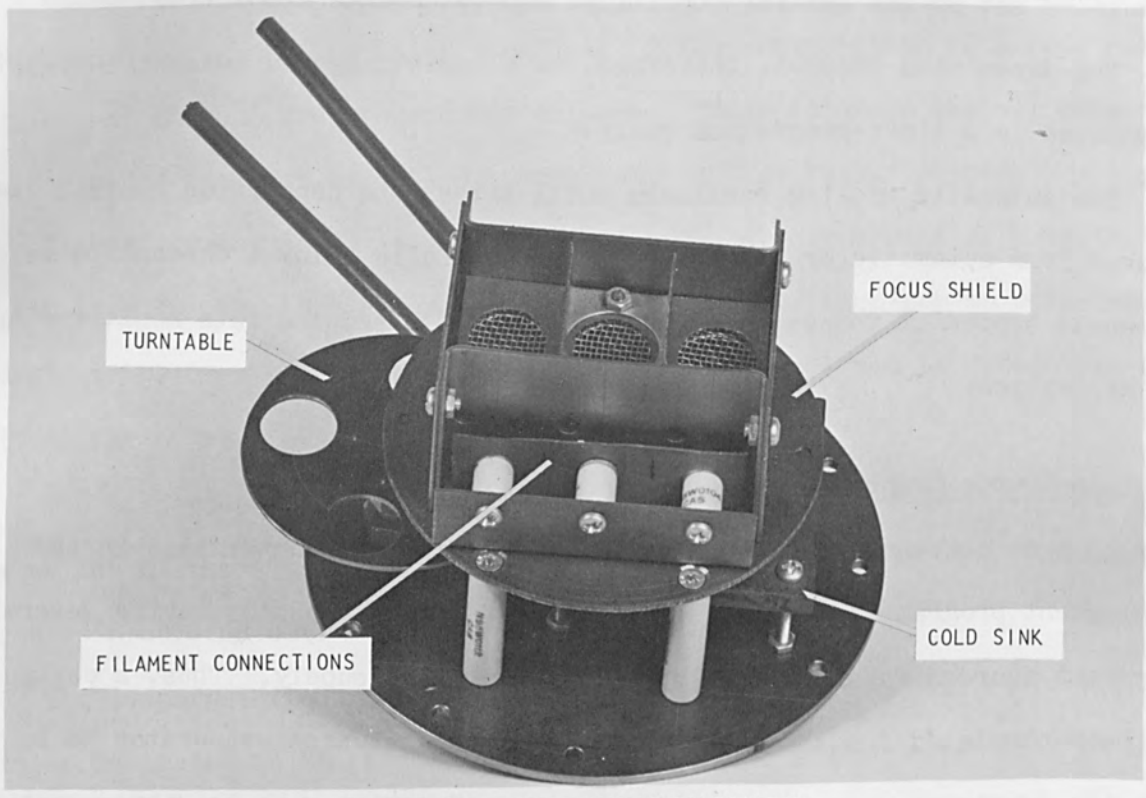

FIGURE 21 THREE-SOURCE EVAPORATOR

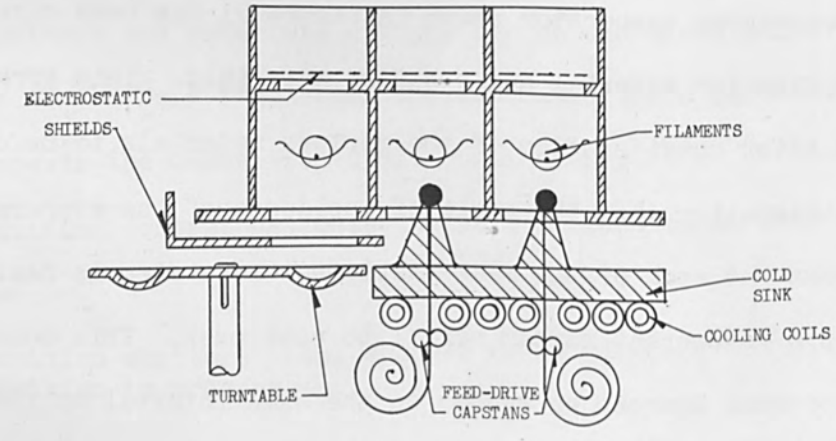

FIGURE 22

DIAGRAM OF THREE-SOURCE EVAPORATOR

of 5 mil tungsten wire. The filament power for each source will be controlled separately with a common acceleration voltage supplied by a high voltage rectifier. The evaporator shield is also connected to the high voltage terminal.

The three evaporant materials are fed by separate drive units. The turntable evaporator for the granular evaporant is geared to rotate slowly using the circular groove to hold the evaporant. Separate motor-driven capstans feed the evaporant wire (to the pedestal evaporators) from spool magazines into the molten ball atop the pedestal.

This evaporator will permit simultaneous deposition of three patterns, and in conjunction with the three-station masks and substrate changer, the patterns can be deposited successively. This simultaneous and successive deposition will provide a great saving of time and improve the efficiency of thin film fabrication processes.

REFERENCES

1. R. W. Berry, Electron Bombardment Evaporation of Tantalum for Thin Film Components, Proc. 3rd Symposium on Electron Beam Technology, pp. 358-366, Alloyd Electronics Corporation, 1961.

2. G. C. Riddle, MSE Electron Bombardment Evaporator, Lockheed Missiles & Space Company Tech Memo MSE/230-1, January 1962.

3. E. C. Drumheller, Silicon Monoxide Evaporation Techniques, 1960 Vacuum Symposium Transactions, pp. 306-312, Pergamon Press, Inc., 1961.

4. G. C. Riddle, Bombardment Evaporation Considerations, Lockheed Missiles & Space Company Tech Memo MSE/230-4, March 1962.

5. H. Schwarz, Method of Measuring and Controlling Evaporation Rates During the Production of Thin Films in Vacuum, 1960 Vacuum Symposium Transactions, pp. 326-332, Pergamon Press, Inc., 1961.

6. J. P. Reames, Methods of Electron Bombardment Heating for Deposition of Metallic Thin Films, 1960 Vacuum Symposium Transactions, pp. 219-223, Pergamon Press, Inc., 1961.

7. S. J. Lins and H. S. Kukuk, Resonance Frequency Shift Thin-Film Thickness Monitor, 1960 Vacuum Symposium Transactions, pp. 333-338, Pergamon Press, Inc., 1961.

8. D. S. Campbell and H. Blackburn, The Simultaneous Vapour Deposition of Two Component Systems, 1960 Vacuum Symposium Transactions, pp 313-318, Pergamon Press, Inc. 1961.

9. G. C. Riddle, A New Evaporation-Rate Monitor, Lockheed Missiles & Space Company Tech Memo MSE/230-3, January 1962.

10. J. Brown, Artificial Dielectrics, Progress in Dielectrics, Vol. 2, pp. 193-225, J. B. Birks and J. H. Schulman, Editors, Heywood & Co., 1960.

11. G. C. Riddle, Effect of Ionized Evaporant, Lockheed Missiles & Space Company Tech Memo MSE/230-2, January 1962.

12. G. C. Riddle, MSE Substrate Manipulator, Lockheed Missiles & Space Company Tech Memo MSE/220-1, February 1962.

13. G. C. Riddle, Automatic-Cycling Process Control, Lockheed Missiles & Space Company Tech Memo MSE/220-2, March 1962.

14. G. C. Riddle, Multiple Source Evaporator, Lockheed Missiles & Space Company Tech Memo MSE/230-5, March 1962.

VACUUM EVAPORATION BY ELECTRON BEAM - SOME ADVANTAGES AND LIMITATIONS IN THE FORMATION OF THIN FILM MICROCIRCUITS

By

William J. MacDonald
Advanced Development Engineer
Sylvania Electric Products Inc.
Waltham, Massachusetts

ABSTRACT

The electron gun presents a versatile means of evaporating a wide range of materials for use in thin film circuit deposition. Before full use of the gun can be obtained for this purpose, an operating technique must be established.

This paper will outline the electron beam technique being developed by Sylvania's Microelectronics Group. Factors such as permissible gun environment and changes in the evaporant pattern as the source material evaporates will be discussed.

"VACUUM EVAPORATION BY ELECTRON BEAMS -- SOME ADVANTAGES AND LIMITATIONS IN THE FORMATION OF THIN FILM MICROCIRCUITS"

INTRODUCTION

The electron gun has a definite place in the vacuum deposition of thin film microcircuits. The purpose of this paper is to describe some of the advantages and problems that Sylvania's Microelectronic Group has encountered while adapting the electron gun to the deposition of thin film resistor, capacitor, conductor, and insulator films.

In order to establish a frame of reference for the following discussion, a brief description of the film deposition techniques employing the electron gun will be given.

FILM DEPOSITION TECHNIQUES

Sylvania has two vacuum film deposition tasks underway in the Microelectronics Laboratory at the present time. Each employs the electron gun and each is contributing to our knowledge of the gun's operating characteristics.

The first technique involves the deposition of dielectric thin films. We are forming TiO_2, SiO_2, and Al_2O_3 films by the electron beam evaporation of Ti, Si, and Al in elemental form. Figure 1 shows a schematic of this evaporation technique. As can be seen in this figure, the electron beam is made to focus on a slug of Ti, Al, or Si. A calibrated leak is used to inject oxygen into the vacuum system. The chemical reactions shown, take place so that TiO_2, Al_2O_3 and SiO_2 deposit on the substrate. For example, a thin film capacitor can be deposited by the electron beam evaporation of titanium. The capacitor electrodes are made by evaporating titanium at a pressure of 5×10^{-6} mm Hg.

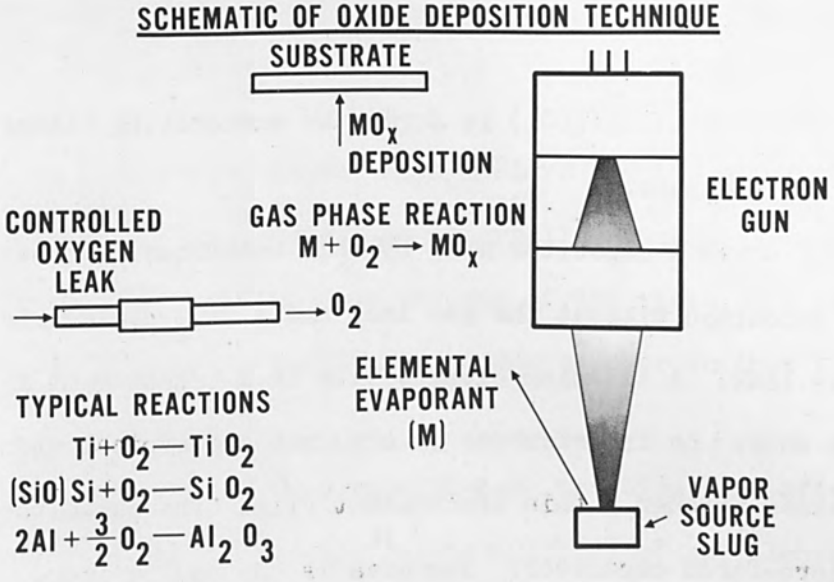

Figure 1 Schematic Diagram of Film Deposition by Gas Phase Reaction.

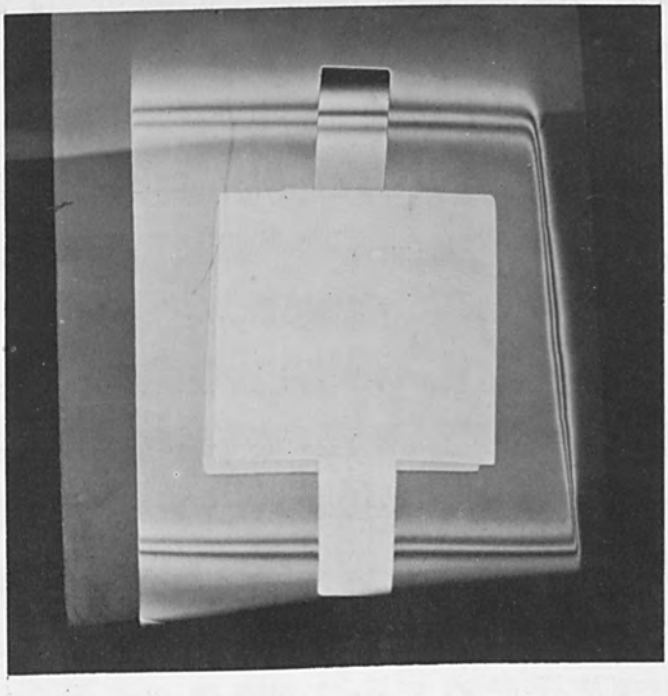

Figure 2 Vacuum Deposited Film Capacitor Containing Titanium Electrodes and a TiO_2 Dielectric Value 2 microfarads.

The capacitor dielectric (TiO_2) is formed by evaporating titanium at 5×10^{-4} mm Hg pressure.

Figure 2 shows a capacitor made by this technique. It has titanium electrodes deposited without the gas leak and a TiO_2 dielectric deposited with the gas leak. A titanium dioxide film is a transparent film. However, it shows the interference colors that are typical when white light is passed through a thin transparent film. The capacitor shown is a two micro-farad capacitor. Its area is one square inch.

Figure 3 shows the vacuum system in which this work is being done. It shows the electron gun, source material and the line through which oxygen is injected. The substrate holder and heater are partially hidden behind the electron gun. They are located beside and behind the gun's focus coil.

The vacuum system, is an ultra-high system that can readily attain pressures on the low 10^{-8} mm Hg pressure scale. The electron gun is a 6 KW unit with a maximum operating voltage of 20KV.

The second film deposition task now in progress in our laboratories concerns electron beam control and film monitoring. We are using the electron gun to controllably deposit the well known and often evaluated nichrome film resistor. Our goal is to use the gun to deposit nichrome film resistors to value and within a ±2% tolerance. In working toward this goal, we are learning which film deposition monitors are needed and we are improving upon and obsoleting an existing film deposition technique. We are currently vacuum depositing nichrome film resistors by filament evaporation in our microelectronics pilot plant facility.

Figure 4 pictures the vacuum system in which this correlation and control work is being done. It shows a second 6KW electron gun, an

eight position substrate holder with heaters and the nichrome slug upon which the gun is focused. An externally controllable shutter which permits film deposition at any one of the eight substrate positions has been taken out of the vacuum chamber so that the remaining fixtures could be seen.

We deposit nichrome resistors at each position, one after the other in succession, to determine the reproducibility of the electron beam evaporation technique. A resistance monitor at each substrate position is used to control the value of the resistors being deposited. For experimental simplicity, we are depositing two resistors at each position simultaneously through a fine line mask. In practice, as many as ten resistors are deposited through similar masks.

ADVANTAGES AND PROBLEMS OF EVAPORATION BY ELECTRON BEAMS

A. Control by Power Input

The first films that we deposited with the electron gun were made with a rather idealistic idea in mind. We wanted to determine how reproducibly nichrome film resistors could be made by simply controlling the power input to the electron gun. In this work, the gun was set up and focused before the desired evaporation was started. Then, the gun was turned on for a predetermined length of time. We found that we could make as many as five successive evaporations with reasonable success. Nichrome resistors deposited on a flame polished glass surface repeated to within 10% of a given value. Unfortunately, for reasons to be explained below, after every fourth or fifth evaporation, the resistance values obtained became more and more erratic with some being off by as much as 200%. In each case the resistance values became progressively lower.

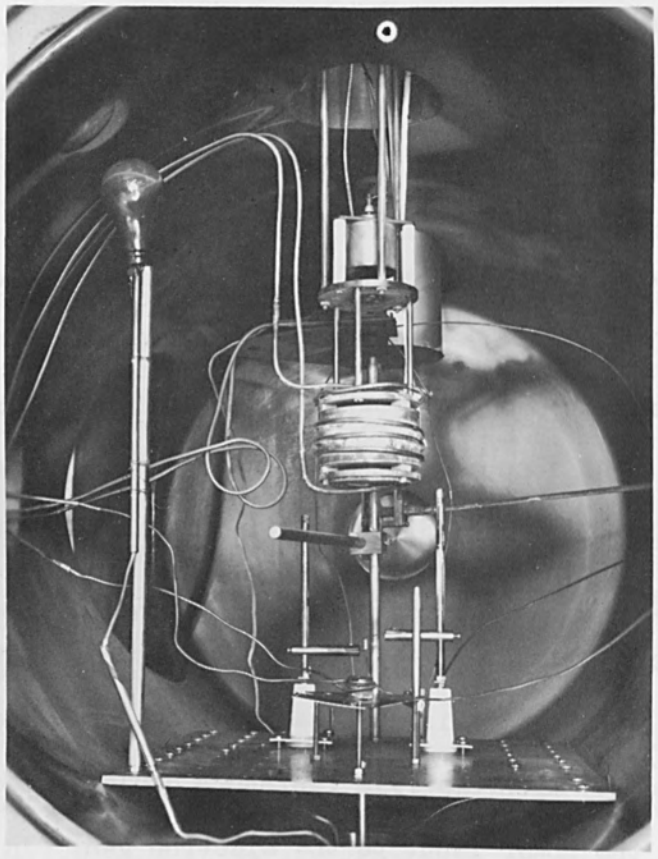

Figure 3 Vacuum System Used for Vacuum Film Deposition and Gas Phase Reaction.

Figure 4 Vacuum System and Tooling used to Make Controlled Nichrome Resistor Films by Electron Beam Evaporation.

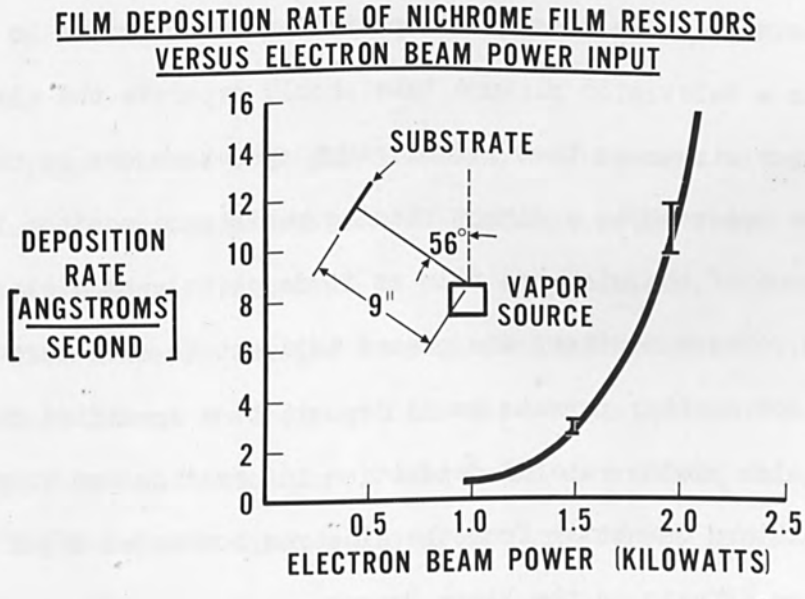

Figure 5 Deposition Rate of Nichrome V Versus Beam Power.

B. Evaporation Rate Monitor

These first tests showed that the electron gun was not yielding a constant evaporation rate. Accordingly, a standard ionization gauge was inserted into the vacuum chamber to read the rate of evaporation so that we could take steps to control the rate.

The electron gun had a considerable effect upon the ion gauge. We found that an electrically shielded gauge reads down scale toward the high vacuum end when the electron gun is operating. We think that this is caused by electrons streaming into the gauge and impinging upon the ion collector thereby reversing the direction of normal current flow in the collector circuit. The source of these electrons may well be the vapor source which probably emits secondary electrons in large quantities.

We have not had time to construct an ion gauge that could handle the large influx of electrons. However, the problem does not seem too difficult to solve. An electron trap similar in structure to the ion trap used in a television picture tube should separate the electrons from the vapor stream so that normal gauge operation can be obtained.

We have resorted to a direct reading resistance monitor to read the resistance of the nichrome film as it deposits upon a glass microscope slide. These monitors are placed adjacent to each circuit wafer. The resistance monitor permits us to deposit to a specified resistance value. It also yields rate of deposition information and knowledge of the vapor pattern emanating from the electron bombarded vapor source.

C. Beam Effects on the Vapor Source

A cylindrical piece of nichrome V is used in our work as the source of evaporant. This piece of metal is cut from a one inch diameter bar

in one inch lengths.

The first factor that we had to contend with was the matter of properly heat sinking this slug of metal. We quickly learned that it was necessary to water cool the target in order to maintain a constant diameter molten pool under the electron beam. A water cooling line hard soldered to the source accomplished the desired heat sinking effect.

The second factor that we noted was the ionization of the vapor stream. The vapor atoms collide with the electron beam as they come off the nichrome slug. As a result, a blue ion cloud forms just above the molten pool of metal. We haven't had an opportunity as yet, to determine how much of the vapor stream is ionized after it leaves this ion cloud. However, the rate at which film builds up on the gun parts which are out of the line-of-sight of the vapor stream indicates that the degree of vapor ionization is appreciable. These ions deposit on the gun by following the magnetic and electric fields generated by the electron gun.

If the vapor stream is highly ionized, as it seems to be, the electron beam yields ion deposition as opposed to the atomic or molecular deposition obtained with filament or boat evaporations. This could make a big difference in the two evaporation techniques. An ionized evaporant could change the mode of film deposition and growth. Additionally, the depositing ions could build up surface charges on the non-conducting substrate which would divert or attract later arriving evaporant.

We have noted one difference in the nichrome film resistors that we have made with the electron gun that may have something to do with

the ionization of the evaporant. An attempt has been made to remove the electron beam deposited film from the glass substrate with a hot aqua regia etch. The beam deposited films are much more etch resistant than are similar films deposited by filament evaporation. This difference indicates a structural or chemical difference between the films. We believe that the ionized electron beam evaporant may form a much more dense film than is obtained by filament evaporation which is indicated by its greater etch resistance. We have not had time to verify this idea as yet. However, we present it here to point out the fact that electron beam deposited film may be structurally very different from its filament evaporated counter-part because of the state of ionization during deposition. This is one idea that we intend to investigate fully.

A third factor effecting electron beam evaporation is the hole that the beam creates in the vapor source material by evaporation. As might be expected, the hole drilling by the beam causes the vapor pattern to become more directional. Deposition tests using our direct reading resistance monitor show that the width of the vapor pattern decreases as the hole grows in the vapor source. We noted this effect in our evaporation set-up after four or five evaporations. This explains the results obtained in our initial tests where we used only beam power and time to control the amount of material evaporated. The loss of film reproducibility was caused by the hole evaporated in the vapor source. We will either have to move our vapor source during evaporation, or design a new vapor source form factor to prevent the effects of hole drilling in future work.

One additional point can be made concerning the hole drilling caused by the electron beam. The vapor pattern distorts as it becomes more directional. On a first evaporation from a smooth surface using just one resistance monitor, resistor patterns have been simultaneously deposited at eight substrate positions, which were all equally spaced from the source slug, with a resistance spread of less than three percent. This spread in resistance values quickly increased as additional evaporations were made from the same spot on the surface of the vapor source. Our tests showed this spread to be in excess of ten percent by the third evaporation.

Our over-all aim in this work, as stated earlier, is to use the electron gun to make nichrome film resistors to a given value, reproducibly and to within narrow tolerance limits. Vapor pattern distortion must be eliminated if this aim is to be accomplished. At the present time, we are using a resistance monitor placed adjacent to the circuit wafer upon which resistors are being formed, to control the resistor depositions. By depositing upon each circuit wafer individually, we are able to obtain a ±2% tolerance on our resistors. The speed of the electron beam evaporation technique makes individual wafer deposition feasible. Monitoring as we do, the problem of vapor pattern distortion is circumvented.

A fourth factor that we have noted in our electron gun evaluation work was the film deposition rate versus electron beam power.

The curve shown in figure 5 was obtained as follows: The time to deposit a given resistance value was noted as a function of the beam power input. We assumed that the resultant films were of uniform thickness and to be 120 Angstroms thick. With these figures, we calculated

the deposition rate of each film and plotted the result versus the beam power used to deposit the film.

The small schematic sketch in figure 6 shows the evaporation geometry used to obtain this data. The deposition rates indicated are only true for this geometry. The beam spot diameter used was 0.125 inches.

At a 1.0 KW power input, the deposition rate was negligible being much less than one Angstrom per second. At 1.5 KW power input, the deposition rate increased to 2.6 Angstroms per second. This rate was reproducible in ten depositions to within 0.3 Angstroms per second.

At a power input of 2.0 KW, the resistor deposition rate rose rapidly to approximately 11 Angstroms per second. The reproducibility of the deposition rate at this power level was poor. The spread of rates in ten tests was 2.2 Angstroms per second.

Higher beam power inputs gave deposition rates too fast to control manually. However, electronic control of the gun may yield very fast yet reproducible film depositions.

Three conclusions can be drawn from this curve. First, the gun can provide a very wide range of deposition rates. Secondly, at moderately fast deposition rates, (2-4 Angstrom units per second of nichrome) the gun provides a well controlled rate. Auxilliary monitors are probably not necessary. Thirdly, at beam powers in excess of 2 KW, nichrome film resistor depositions can be made in a matter of a few seconds or less. We are now in the process of determining how reproducibly films can be made at the high deposition rates, having learned that nichrome resistors deposited at 2 Angstrom units per second can be made with a ±2% accuracy when a resistance monitor is placed adjacent to the

circuit wafer.

A fifth and last factor has been noted concerning the effects of the electron beam upon the vapor source. Nichrome V is a nickel-chromium alloy containing 80% nickel and 20% chromium. It is well known that fractional distillation occurs when this alloy evaporates from a filament or boat. Chromium has a higher vapor pressure than nickel at normal evaporation temperatures (1600°C). A number of evaporation tricks have been devised to overcome this problem when filaments and boats are used to heat the nichrome. We are learning whether the fractional distillation of nichrome occurs when it is evaporated by means of the electron beam.

A spectrochemical analysis has been obtained on the vapor source slug to see if a chemical change does occur in the metal area melted by the electron beam. The metal sample tested was taken from the surface of the melt area to a depth not exceeding 0.002 inches. The analysis showed that the chromium content in the melt area had not changed.

This result makes sense. The temperature of the melt area is significantly above the melting temperature of each metal constitutent. Therefore, the vapor pressure of the nickel and chromium and, thus, the evaporation rate of each would be quite high. The amount of fractional distillation,then, would be much less than that which occurs at lower temperatures. Efforts to obtain a spectrochemical analysis of the film itself have not yet been successful due to the extreme etch resistance of the film.

D. Electron Beam Evaporation at High Chamber Pressures

As described earlier, we are using the electron gun to deposit oxide films of titanium, aluminum and silicon. This is accomplished by vaporizing the element and oxidizing it as it travels to the substrate.

The tank pressure used in this work is varied between 10^{-4} and 10^{-3} mm Hg depending upon the type of film desired.

The electron gun will operate in this pressure region but not without difficulty. For example, we have found that approximately twice as much beam power is needed at 5×10^{-4} as is needed at 5×10^{-5} mm Hg to obtain a molten pool on a titanium vapor source. Ionization and beam scattering are sufficient to cause the electron beam to become visible in an oxygen pressure of 5×10^{-4} mm Hg.

A second problem encountered in using the electron gun is the 10^{-4} mm Hg pressure region is short cathode life. The oxidation mechanism yielding the oxide films also works on the tungsten filament which is the gun's cathode. The filament cathode quickly deteriorates in the oxygen atmosphere.

As might be expected, high voltage breakdown is also a trouble-some occurance in this pressure region. The system operates like a leaky electron tube. Because of these difficulties, we are now building a separately pumped gun chamber that will permit us to hold the pressure surrounding the gun to below 5×10^{-5} while the main tank pressure is running as high as one micron.

E. Summary

The electron gun has been found to be a versatile tool for thin film vacuum evaporation. Problems have been encountered with monitoring evaporation rates, with vapor pattern distortion and with gun performance at pressures in the 10^{-4} mm Hg pressure range. Each of these problems is being solved. Within a short period of time, electron beam evaporation should no more be difficult than filament evaporation and we will have gained the versatility and control provided by this new tool.

ELECTRON BEAM JOINING TECHNIQUES FOR ELECTRONIC PACKAGING

By

F. R. Schollhammer
Assistant Project Engineer

J. E. Cyr
Hamilton Standard Division
United Aircraft Corporation
Windsor Locks, Connecticut

ABSTRACT

This paper describes the progress to date of several unique and advanced electron beam welding applications which can be used in the construction and packaging of macro and micro-miniature circuitry.

The description of the different welding processes includes a discussion of lap and semi-butt welding and also a more recent process under development which fuses the ends of component leads directly into respective locations of a printed circuit. The resultant high-strength bonds created by any one of these different methods of electron beam welding offer a low-resistance electrical termination which can also serve as a hermetic seal. Laboratory data relative to strength, vibration, shock and electrical resistance are included. The hermeticity that can be achieved by electron beam welding is also cited in this paper.

ELECTRON BEAM JOINING TECHNIQUES FOR ELECTRONIC PACKAGING

INTRODUCTION

America's continuing efforts in space and defense programs are helping the nation's electronic industry sustain the growth that saw it move past the $10-billion mark in 1961 for the first time; industrial and consumer sales of electronic equipment are also adding to the strength. The industry's future rate of growth, however, will depend upon military spending and on how well the industry can meet the demands of the Space Age for smaller, lighter, and more reliable packaging. Although the electron beam has been in use since the discovery of the X-ray, the relatively recent introduction of electron beam technology as related to welding processes has provided the manufacturing breakthrough producers of macro- and microminiaturized components have been seeking.

Electron beam welding is accomplished by first producing an electron space charge, then accelerating the electrons, and focusing the beam on a workpiece. High energy beams are now being produced with power densities up to 10^{10} watts per square inch. With such concentrated energy and appropriate beam control, pulsing, and deflection devices, the Hamilton-Zeiss Electron Beam Welding Machine provides a most versatile and flexible welding tool. The success of this equipment in the electronics industry depends largely upon the creative design ability of engineers in designing supporting tools and fixtures. A considerable degree of success has been accomplished in this direction at Hamilton Standard, Division of United Aircraft Corporation. The electron beam has been used to weld macro- and microelectronic circuits, sometimes referred to as 3D Cordwood

and module construction, with considerable success.

The program discussed herein summarizes the electron beam welding of three different design approaches to the packaging of circuits presently in use, or in various stages of development. These approaches can be broadly categorized as:

1. The Cordwood concept.
2. Micro-element welding, or the module concept, as developed by the Hamilton Standard OMEC (Optimum Miniature Electronic Components) program as well as the micro-welding study sponsored by the Signal Corps.
3. Interconnections for thin film and solid circuits for which electron beam techniques provide an improved method of fabrication.

Since other papers[1] and articles[2] have cited the numerous advantages of welding over soldering, for electronic components this paper is limited to reporting the progress made with the Hamilton-Zeiss electron beam welder as a joining tool for constructing the packaging concepts outlined above.

DESCRIPTION OF EQUIPMENT

The electron beam machine used in these programs is the standard high-voltage (150 KV) Hamilton-Zeiss machine shown in Figure 1. Some of

---

[1]"Microelectronic Joining Techniques by Electron Beam Processes." Hamilton Standard, Division of United Aircraft Corporation, Windsor Locks, Connecticut, August 1961.

[2]"Metallurgical Considerations in Resistance Welding Electronic Component Leads", Space Technology Laboratories, Inc., Los Angeles 45, California.

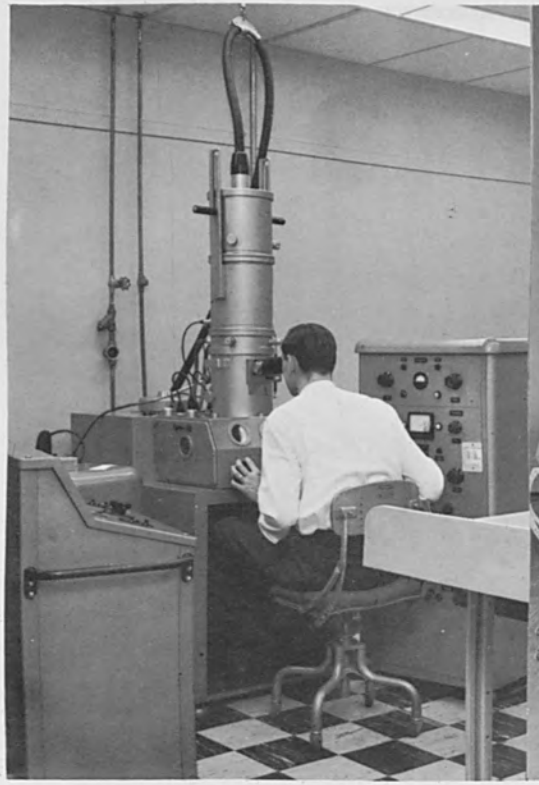

Fig. 1 Hamilton-Zeiss Electron Beam Welder

Fig. 2 Zeiss Electron Beam Welder

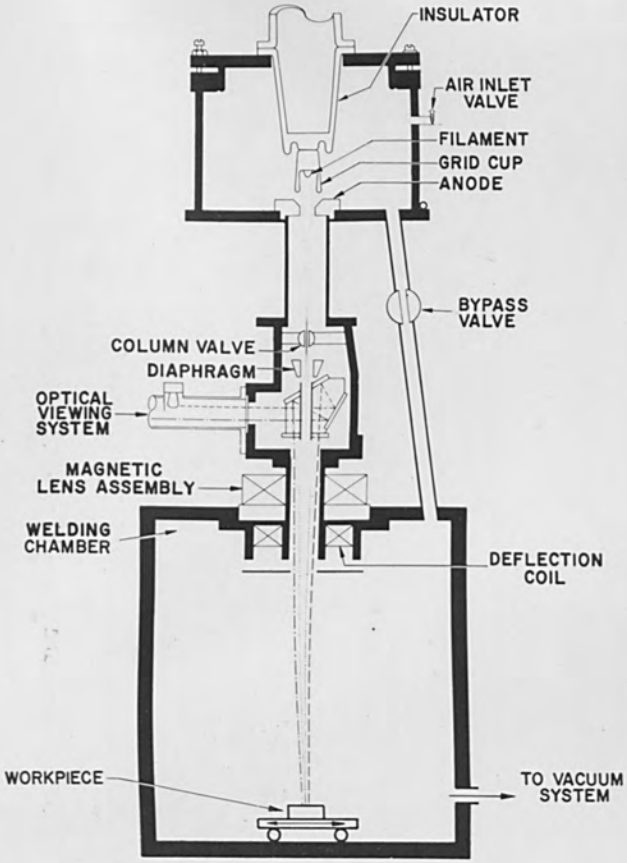

Fig. 3 Schematic, Hamilton-Zeiss Welder - Electron Gun Column

the earlier laboratory development work was accomplished with a high-voltage welder developed and manufactured by the Carl Zeiss Foundation and shown in Figure 2.

A schematic indicating the principle of operation of the Hamilton-Zeiss electron gun and electron optics is shown in Figure 3. The electron beam emitted by the electron gun is directed through the anode and then into the axis of the magnetic focusing lens. The lens focuses the beam onto the workpiece. Alignment of the welding to be made can be observed through a 20X or 40X microscope with built-in illumination. Below the magnetic lens is a system of magnetic coils which can deflect the beam over the workpiece as desired by the operator. The welding chamber contains a movable table which can be operated from the outside and on which one or more workpieces can be placed.

CORDWOOD PACKAGING DESIGN

The following description of the Cordwood concept, which involves the use of an end-welding technique or "rivet" welding, also includes a discussion of packaging modification designated as Tier construction.

BASIC CORDWOOD CONCEPT

Description of Packaging Concepts and Materials - End-Weld Process

The techniques discussed herein for component termination has been designated as the end-weld or "rivet" process. In this process the component leads are fed through holes in a metalized substrate with the leads trimmed close to the substrate as shown in Figure 4. To form the welded joint, the electron beam is impinged axially upon the end of the lead. This causes the lead to melt and join to the metalized surface, thus forming a rivet-like cap over the feed-through hole.

Since the beam is controlled so as not to impinge on the substrate

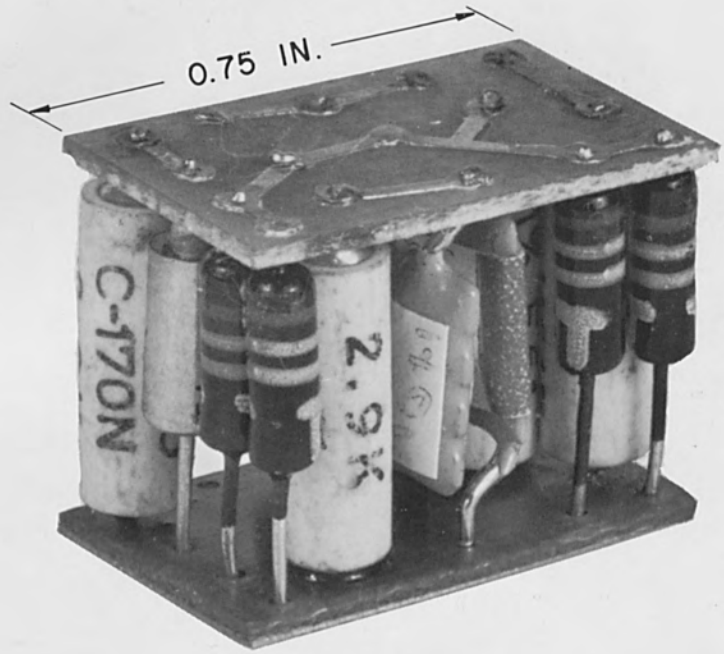

Fig. 4 Cordwood Assembly

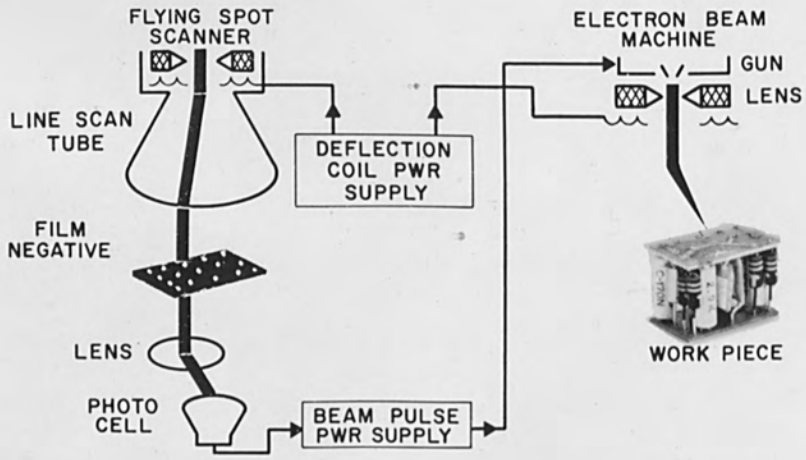

Fig. 5 Flying Spot Scanner Control for Electron Beam Deflection Welding

surface, there is no danger of damage to this surface. Interconnections can be made to the opposite side of the substrate by utilizing plated circuits interconnected with the feed-through hole. As no protrusions of leads or terminal pins are required, the small size of the welded cap permits a very compact arrangment of printed circuit interconnections.

With the captive-type configuration created by the rivet-like weld nugget, it is possible to retain the subheaders with the component leads. This eliminates the need for additional mechanical support.

Welding Methods and Fixturing

The Hamilton Standard electron beam machine can be actuated manually or automatically at a preselected beam repetition rate to weld component leads. With the exception of a few welds, the macro and micro welds were produced automatically every four seconds. This time period was sufficient to permit the operator to manually orient the weld joint in line with the electron beam. For most cases, the workpiece required movements of 0.100 inch or less between welds. For locations which required preinspection through the optical viewing system prior to welding, the beam pulse rate was switched from automatic to manual operation. However, it should be apparent that an automated system for beam and/or positional control would provide an extremely rapid operation, thus making the process not only feasible, but very attractive for automated welding of electronic devices.

One method utilized by Hamilton Standard for automating the beam consists of a Flying Spot Scanning system that permits indexing and welding of multiple module assemblies (Figure 5). The Hamilton Standard equipment incorporates provisions for deflecting the beam over a distance of approximately $\pm$ 0.3 inches in the "X-Y" plane; thus twenty-five welds can be produced in approximately one second with a pulse width of 15

milliseconds and a beam relocation time of 25 milliseconds. The method described also permits loading of assemblies in ambient, then processing them in a vacuum. Tape controlled operation is also entirely feasible and adaptable to the Hamilton equipment.

The exclusive optical viewing system of the Hamilton-Zeiss welder permits the operator to monitor the complete welding operation at all times through a 40X microscope. The operator can also manually position the workpiece to within 0.0005 inch of true position. The precise optics of the machine permit the beam to be positioned within 0.0002 inch of true position. In order to provide a uniform temperature distribution for each micro weld, the beam was deflected over the plane of the workpiece. This was accomplished by superimposing an a-c deflection on the d-c system. The a-c deflection control employs signal generators to drive the beam in the "X-Y" plane so that a sinusoidal, or other desired pattern, can be traced directly over the surface areas to be welded. (Reference Figure 28.)

Typical fixtures and devices used in the welding of Cordwood components are shown in Figures 6 and 7.

For the majority of the welds, the knife edge fixture shown in Figure 6 was sufficient. In some cases the use of polyethylene tape was the only fixturing required to weld components to their respective wafer assemblies. For example, transparent tape proved to be a very successful method for retaining minute leads to the top of the header pins. The result is illustrated in Figure 8. These welds were accomplished by pulsing the beam through the tape and welding the copper leads to the top of the steel header pins. A micrograph of the resulting weld revealed no sign of contamination from the tape itself. The reason for this becomes obvious when one considers that the tape consists of 1 mil of

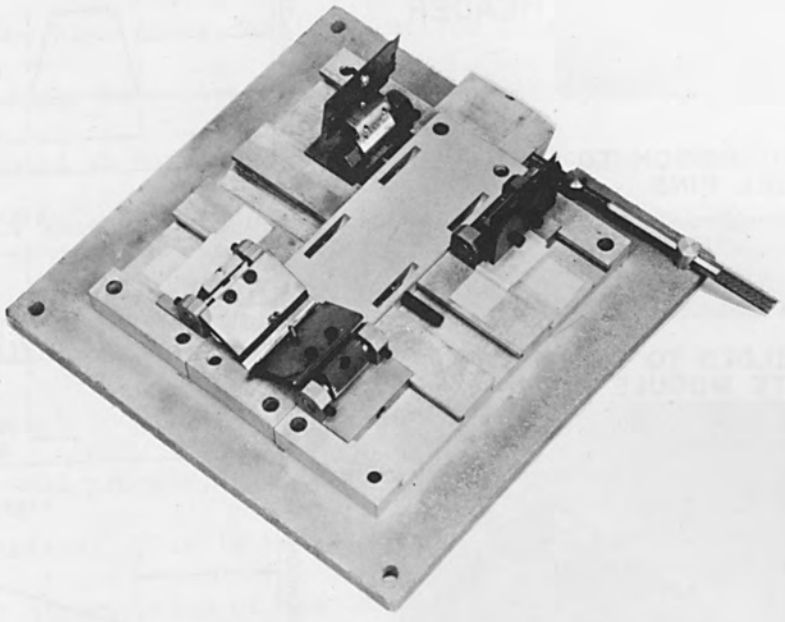

Fig. 6 Knife Edge Fixture

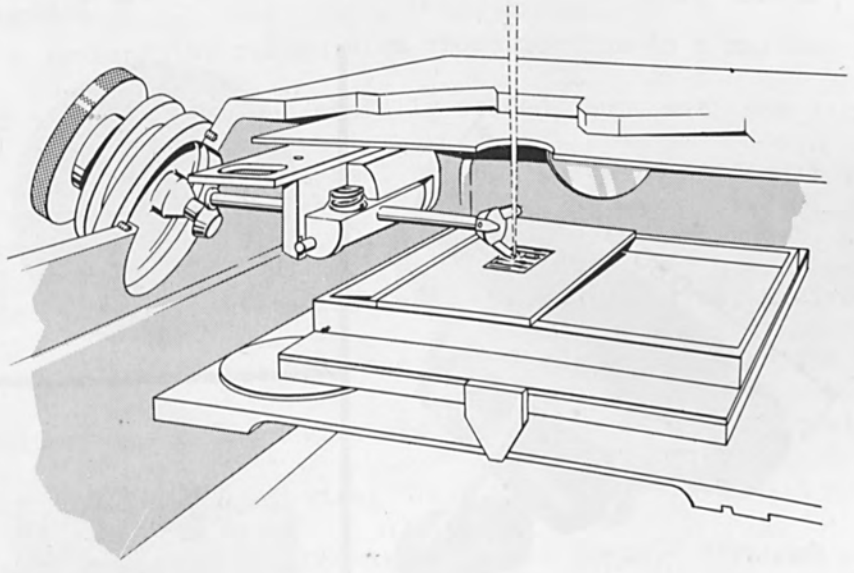

Fig. 7 Micromanipulator for Welding Microcomponents

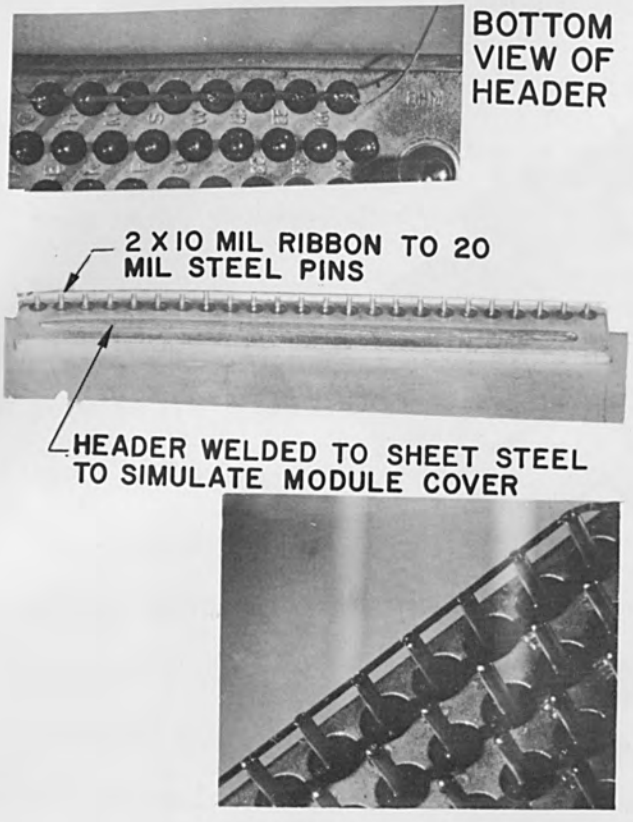

Fig. 8 Copper Leads Welded to Hermetic Header Pins

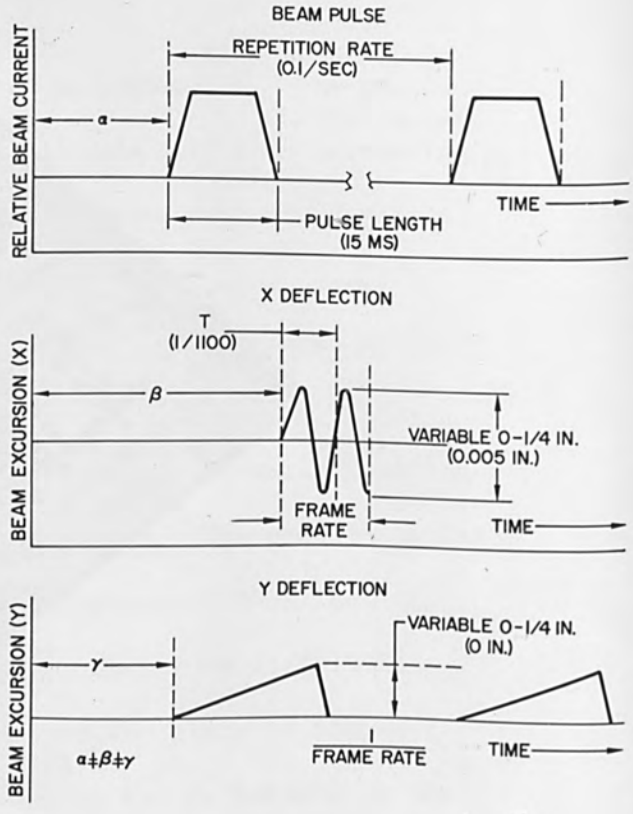

Fig. 9 Electron Beam Deflection Parameters

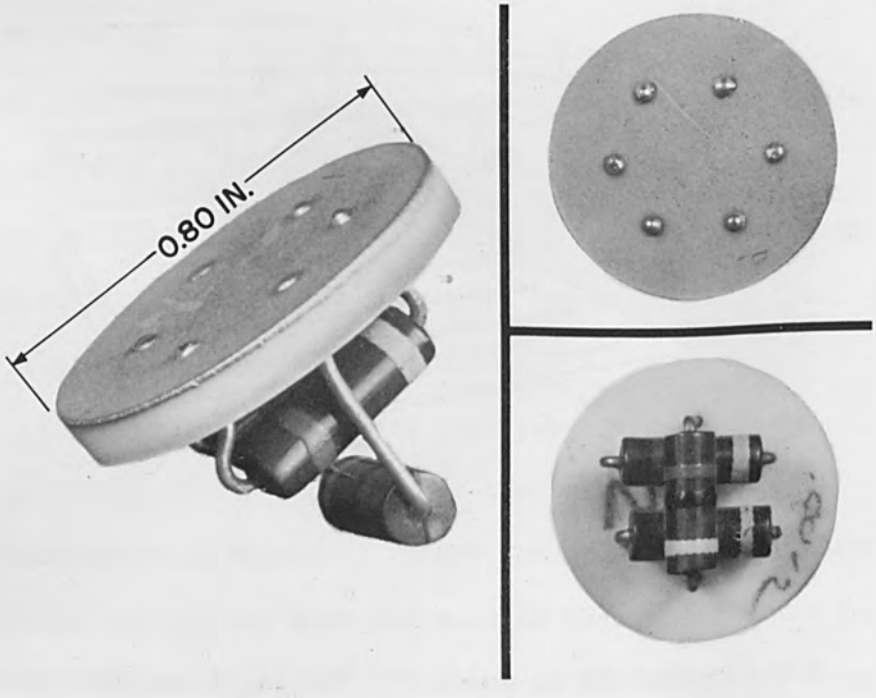

Fig. 10 End-Welded Miniature Component Assembly

Mylar, which evaporates immediately in the area impinged upon when subjected to the high power density electron beam

Although the end-weld concept is applicable to most materials, the tests conducted at Hamilton Standard utilized copper and nickel leads. Other metals which can be welded in a similar manner include gold, silver, platinum, and steel. Numerous alloys of the above metals have also been welded by electron beam processes.

Although the lead wire cross section does not have a major effect on the end-weld process, round wires were found to be more suitable for this application. This is because the shape of the beam is circular and a more even distribution of heat can be obtained. When using a rectangular lead, an essentially even heat flow can be attained by deflecting the beam in a pattern similar to the cross section of the rectangular lead, This is accomplished by using beam deflection parameters similar to those shown in Figure 9. It was found desirable to limit the length-to-width ratio of a rectangular ribbon wire cross section to a maximum of 3:1. Ratios of 5:1 have been successfully welded, but, with the larger deflection required, a homogeneous heat pattern was more difficult to achieve.

For small round wires, 0.032-inch diameter and under, a single undeflected beam pulse is sufficient. On larger wires, a circular deflection of approximately one-half the wire diameter produced the most effective results. The maximum wire size welded to date is approximately a 0.062-inch diameter copper wire. This wire was welded to 3 mils of nickel which was metalized to a 0.060-inch ceramic board. Stranded or braided wires can also be end-welded and are treated much the same as round wires. The resultant cap is identical to that of round wire.

Problems and Solutions

A number of substrate materials, metalizing processes, and plating metals have been investigated. The ideal metalizing process is one that exhibits the best adhesion to the substrate and that retains this adhesion when subjected to high welding temperatures. It may be readily deduced that as the lead wire melts and flows onto the plating, the plated surface rapidly assumes the temperature of the molten lead metal. If the metalizing is thin, 0.001 inch or less, and exhibits a high thermal conductivity, then the high weld temperatures will be rapidly transmitted to the inner surface of the metalizing. This could rupture the bond between the metalizing and the substrate material. However, this problem can be overcome by increasing the plating thickness, minimizing the weld schedule, or by selecting a plating material with lower thermal conductivity. If the mass of the lead wire is not great (0.015-inch diameter or less) in relation to the metal thickness (0.001 inch or more), then the residual heat of the molten metal lead is not sufficient to damage the metalized substrate surface.

To provide an acceptable end or "rivet" weld, the length of the lead wire extending beyond the surface of the substrate depends largely upon the amount of metal required to form the rivet cap. If the lead wire extension varied excessively from weld to weld, different energy settings would be required. Changes in energy setting could be compensated for by adjusting the energy to the minimum lead requirements and then providing an additional beam pulse when maximum lead lengths are encountered. This procedure was employed for prototype modules where, with manual operation, the operator could observe the discrepancies and correct the operation as mentioned.

For automated conditions, however, this process is not acceptable.

Further laboratory tests were made to determine an optimum lead protrusion length. It was found that an extension length of 1 1/2 to 3 wire diameters was sufficient to form a good cap that required no energy change. When a hermetic seal was required, laboratory experience indicated that it was best to keep the extension length close to the maximum limit.

In order to determine the allowable tolerances between the hole and equivalent wire diameter, tests were conducted in 25-mil alumina substrates having 0.025-inch diameter holes. Lead wires varying from 0.018 to 0.023-inch diameter were successfully welded. This represented an area of up to 2:1 (ratio of hole wire cross-section area). A wide tolerance of wire-to-hole diameter permits easy assembly techniques; these in turn facilitate manufacturing of jigs and fixtures for production processes.

The end or "rivet" weld technique also provides an additional unique welding advantage by providing a hermetic seal. Figure 10 illustrates a circular metalized alumina wafer to which 0.025-inch diameter copper wires have been end-welded through 0.032-inch diameter holes. When checked with a helium leak detector, leakage rates through the welded junctions showed less than 3×10^{-4} micron cubic feet per hour, or an equivalent 0.09 cubic centimeters per year. Since the detector will not register leakage rates lower than the above value, it can be assumed that leakage is primarily a function of the out-gasing rate of the material itself.

Results

Electron beam welding techniques are ideally suited for high density electronic packaging. The small, high strength, low resistance welded joint produced offers a near perfect termination technique that approaches the strength of the original materials. Since excessive force and high currents

are not applied to the leads during welding, the risk of component damage is essentially eliminated.

Another advantage of welding by electron beam is a high termination density that permits components to be stacked or log-piled. The package is assembled by inserting the component lead through its respective circuit hole and welding the component directly to the lower substrate surface. Since the welding process is so short (5-100 milliseconds), there is little heat effect outside the weld zone. Electron beam welding has been successfully conducted within 0.025 inch of the component itself. The packaging density for macro-and microminiaturization is, therefore, limited only by area required for the printed circuit interconnections and heat dissipation of the assembly.

In order to evaluate the strength of the welds produced for the Cordwood module, the specimen was vibration tested on an MB-2 shake table. The Cordwood module, as shown in Figure 10, was used. A broad band of random vibration was chosen to determine whether the electrical characteristics of the welds would change. The unit was tested by cycling (see Figure 11) at excitation frequencies from 50 to 2000 to 50 cycles per second, and at a constant acceleration level of 30g's in a 15-minute cycle. Upon completion of the test, component continuity and constant circuit characteristics were evident. Visual inspection of the welds revealed no evidence of structural failure.

To evaluate the strength of the completed joints, welds similar to those shown for the module of Figure 10 were tension tested. This is illustrated schematically in Figure 12. Values of approximately 2300 grams were achieved for 0.018-inch copper wires (Reference Table II, Appendix A). In all cases, failure of the interconnection occurred within the substrate or wire structure

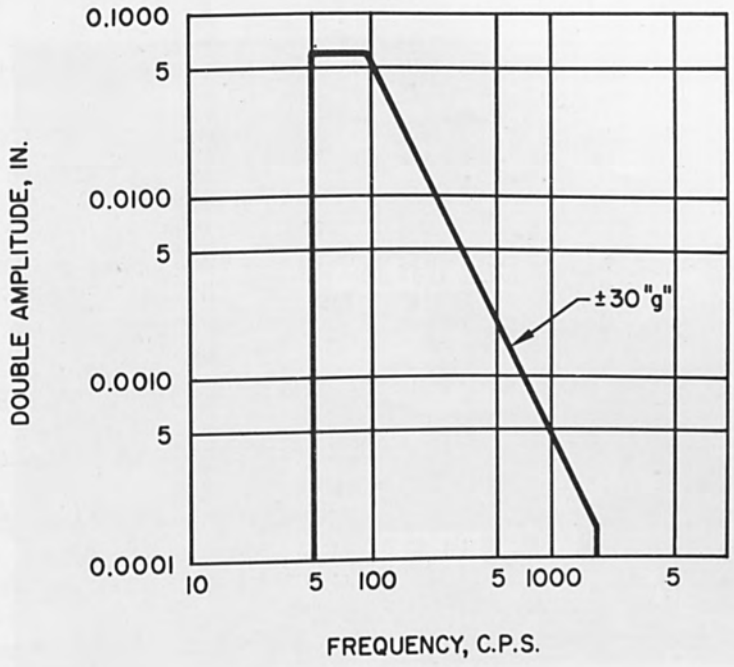

Fig. 11 Vibration Input Level for Cordwood Module

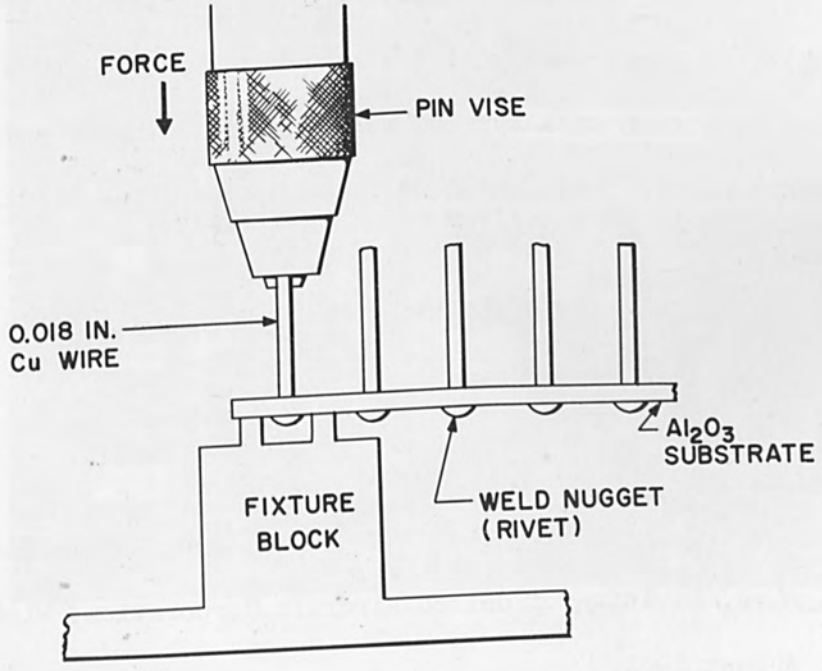

Fig. 12 Tension Test Schematic

itself and not at the joint.

Metallographic methods were utilized to determine the microstructures and type of bond attainable by electron beam welding of the Cordwood concepts. Since electron beam welding produced rapid melting and solidification of the material, a microstructure of small and essentially equiaxed grains is produced in the weld nugget as compared to the columnar-type grains produced by standard welding procedures. Some typical electron beam welds produced during the Cordwood investigations are shown in Figures 13 through 14. In addition to providing a strong mechanical bond, it is evident that a clearly defined alloy zone can also be found between the interface of the nickel, Kovar and copper wires. The absence of a heat-affected zone around the weld joint lends this process to Cordwood construction.

Figure 15 illustrates an electron beam weld between the steel cover and the header of the relay module shown in Figure 16. The weld zone is visible and penetrates well into the base metal. It is also interesting to note that this type of weld produced a hermeticity of 0.03 cubic centimeter per year without damaging the glass feedthrough interconnections.

Further mechanical and statistical evaluations of similar weld processes are described in Reference 3.

---

[3] "Microelectronic Joining Techniques by Electron Beam Processes". Hamilton Standard, Division of United Aircraft Corporation, Windsor Locks, Connecticut, August 1961.

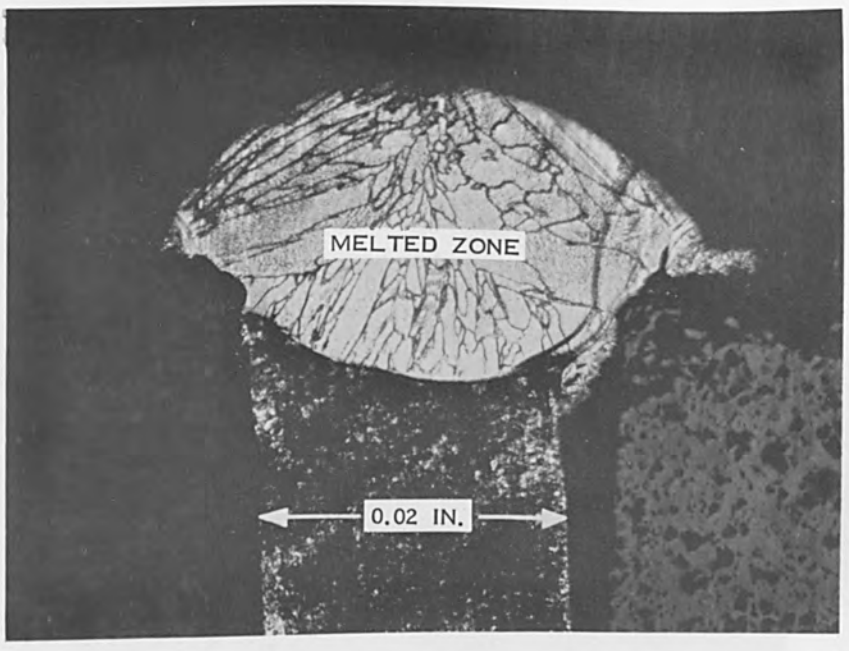

Etchant: 3 HNO_3, $2CH_3COOH$

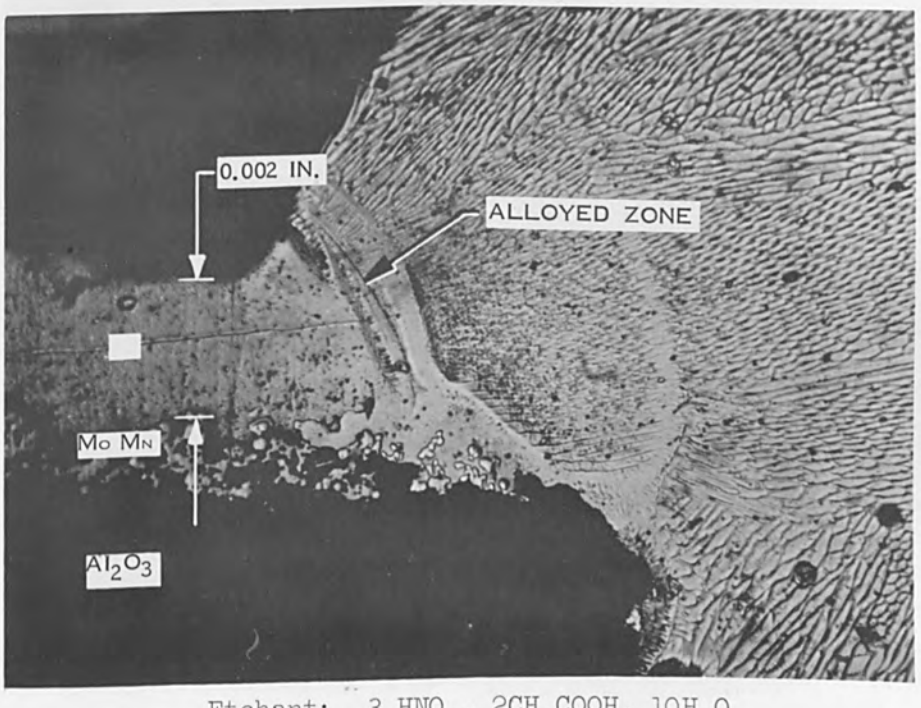

Etchant: 3 HNO_3, $2CH_3COOH$, $10H_2O$

Fig. 13 Kovar to Nickel - End Weld

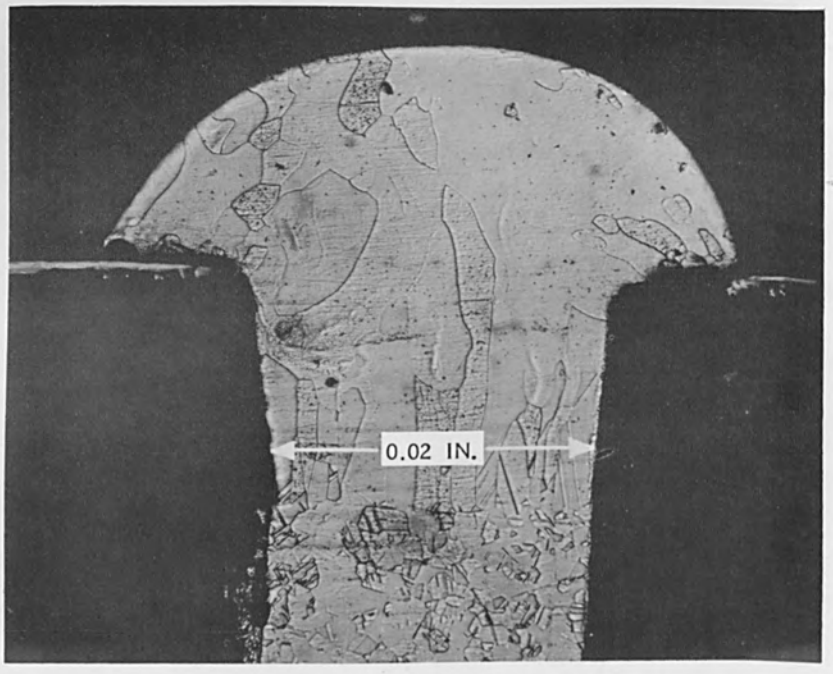

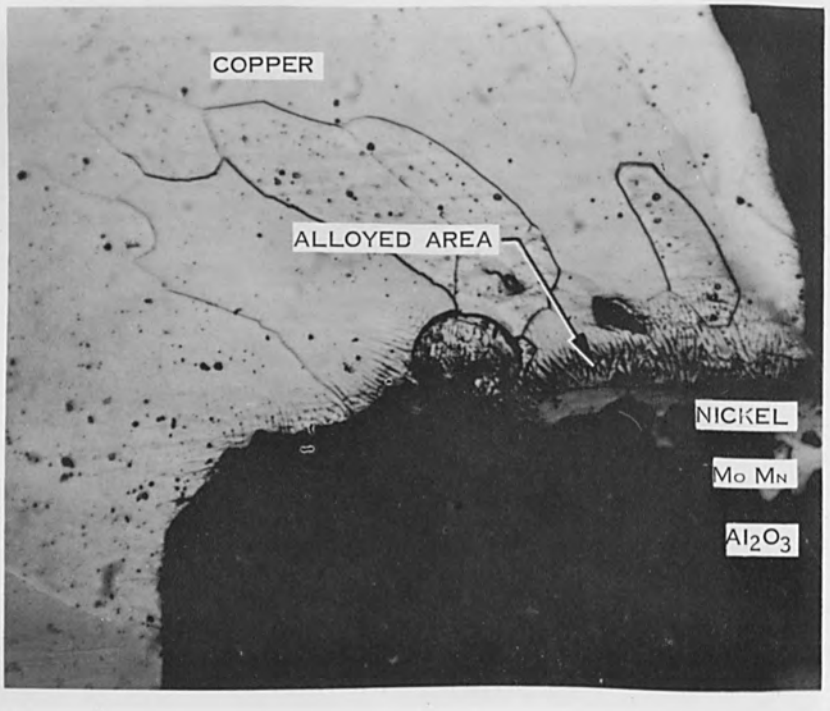

Etchant: 5 NH_4OH, 5H_2O, 2H_2O_2

Fig. 14 Copper to Nickel - End Weld

TIER CONSTRUCTION (Modification of Cordwood)

The following description of the Tier concept can be considered a modification of Cordwood construction. A discussion of these modifications and fabrication methods follows:

Description of Packaging Concepts and Materials

A variation of the Cordwood concept is the Tier concept as illustrated in Figure 17. As with the end-weld technique, metalized substrates were used for component termination. As indicated in Figure 18, the components were arranged in a predetermined configuration so that they extended approximately to the substrate rails or supporting strips. The leads were then welded to these rails by deflecting the beam over the end of the leads.

Welding Methods

Direct contact of the lead to the metalized surface is necessary when welding wires under 0.015-inch diameter. For larger size wires, it is desirable that contact be made between the wire and plated surface. However, a gap of two or three mils can be tolerated since the material flows to the metalized surface during the welding pulse increment.

Problems and Solutions

When the metalized plating was less than 0.001 inch, the beam deflection was restricted to the diameter or width of the lead wire, thus limiting the heat penetration and possible damage to the bond between the metalizing and substrate. For this application, closer tolerance of weld energy and beam deflection area was required.

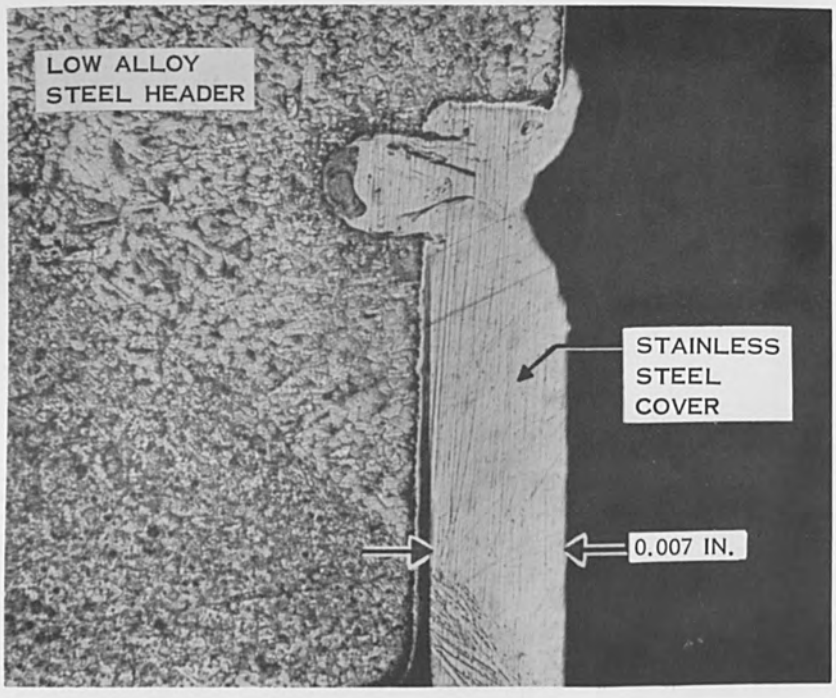

Fig. 15 Steel to Steel Micrograph Illustrating Hermetic Steel Header

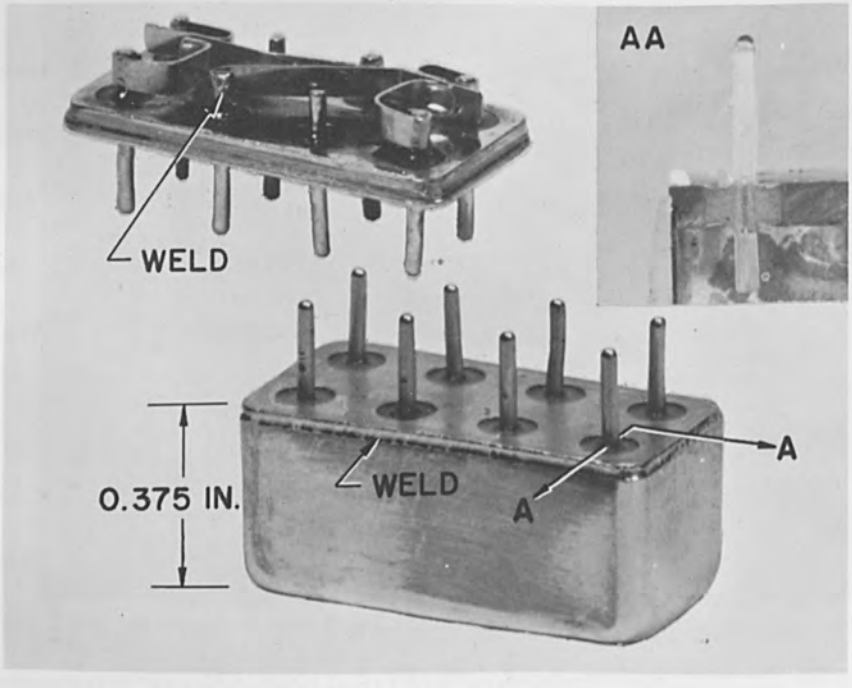

Fig. 16 Electron Beam Welded Relay Module

Results

Interconnections within each subassembly can be made by conventional methods, such as plated-through holes or by insulated micro jumper wires welded to pads. In the assembly concept illustrated (Figure 18), the tiers were nested and retained by external means. The tiers can either be stacked in a cavity and retained by mechanical means or wrapped with tape and inserted into a container. External connections for this illustration can be made with insulated copper wire welded to pads on the substrate, although it is feasible to use the riser wire concept illustrated in Figure 26 and described in a following section. It is worth noting that the selection of substrate material, metalizing, and plating was more critical for the Tier concept than for the end-welding concept

HAMILTON STANDARD MICROMINIATURE (OMEC) PROGRAM

Description of Packaging Concepts and Materials

The application of electron beam welding at Hamilton Standard to microminiaturization, designated as the OMEC program, is illustrated by the 8-bit digital adder shown in Figure 19. The adder consists of 20 aluminum oxide wafers to which 220 components have been welded. A typical wafer is shown in Figure 20. The total number of welds, including the mother board, the individual components on the wafers, and the construction and fabrication of the mother board assembly to the header, consisted of 1200 welds. In addition, the module cover itself was welded to the base header assembly. After welding the cover to the base plate, a vacuum or package hermeticity of 0.27 cubic centimeters per year leakage was achieved.

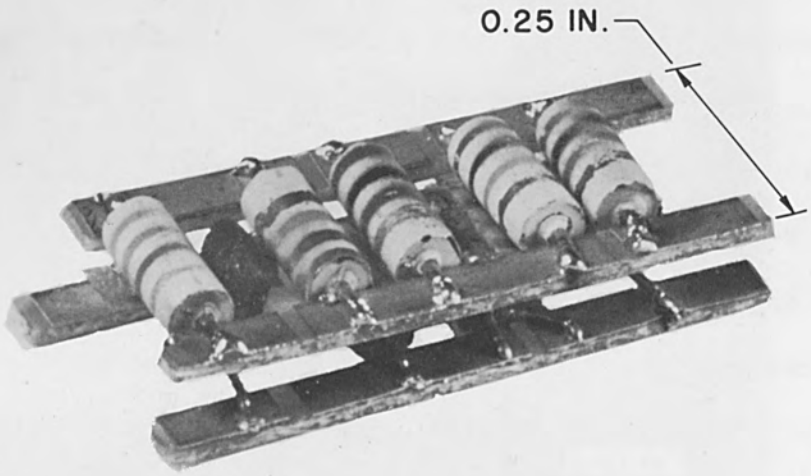

Fig. 17 Tier Module

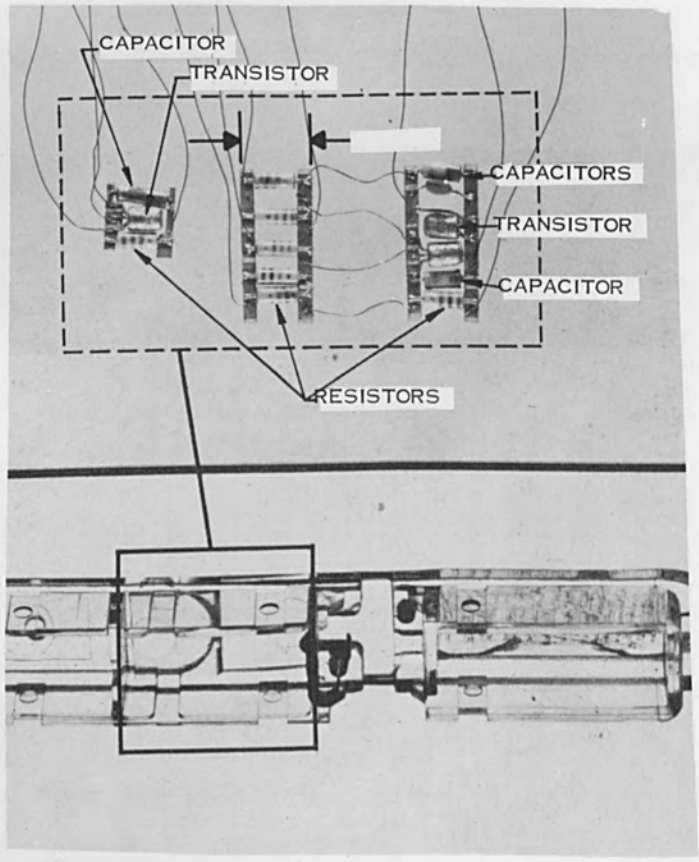

Fig. 18 Amplifier Module Note: Components in Top Photo Fit into Section Shown in Lower Photo

Welding Methods and Fixturing

The OMEC assembly shown in Figure 19 consisted of seven different circuits: inverter, flip-flop, and/or gate, two or gate, clock amplifier, two and gate, and multivibrator. The wafer used in the construction of this module consisted of (1/2-inch by 3/4 inch) 96 percent pure alumina oxide wafers. The circuits were produced by silk-screening techniques. A 0.5 to 0.8-mil moly-manganese coating was fired into the alumina over which nickel was electroplated to a thickness of approximately two mils. Standard transistor and micro-components obtained from PSI, King, and IRC were welded to the metalized circuits, Figure 20. The various materials that were used in the construction of this module, as well as the leas geometry of the components, and the required welding energy are referenced in Table I of Appendix A.

The fixturing required for the fabrication of OMEC packages were similar to that required for Cordwood. In those cases where the use of tape or simple knife edges was not practical, components were held in place by the micro-manipulator shown in Figure 7. Simple in its operation, this device was utilized for welding miniature three-mil transistor leads in all OMEC wafer circuits.

Results

In welding this package by electron beam techniques, the process not only indicated that micro leads could be welded to a metalized circuit and that a vacuum joint could be achieved, but also that micro welds along a coverheader assembly can be accomplished without damage to the glass hermetic seals. An illustration indicating the success of electron beam welding of a micro lead to a steel-glass hermetic pin can be seen in the center illustration of Figure 8.

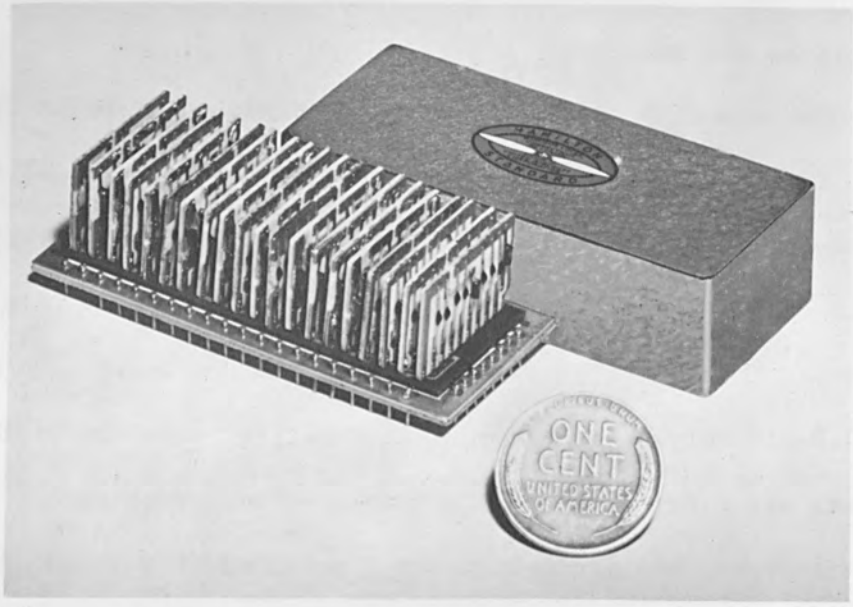

Fig. 19 OMEC 8 Bit Adder Assembly

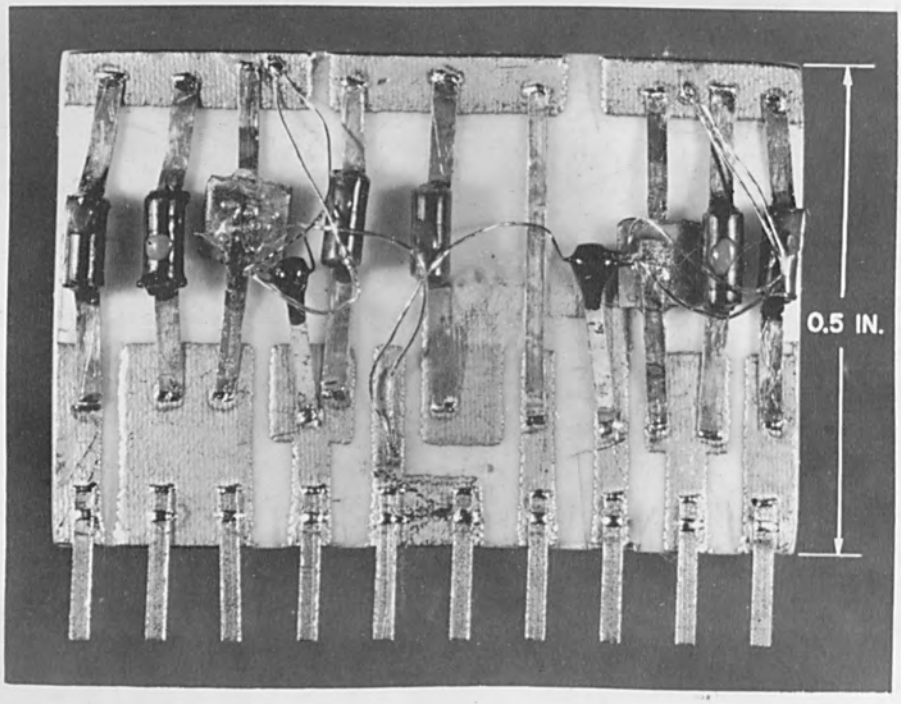

Fig. 20 Typical OMEC Wafer-Inverter

To further illustrate the capability of electron beam welding for module constructions, Figure 21 shows the technique used in constructing and fabricating wafer assemblies to a mother board. Each copper pin, or interconnection from the wafer assembly, was inserted into the mother board and extended approximately 0.010 inch above the plated surface. The leads were welded to the mother board circuit in a manner similar to that used for cordwood fabrication (i.e., directing the electron beam axially upon the end of the copper wire). By melting the copper wire and fusing the material directly to the nickel surface on the mother board, a strong low-resistance connection was accomplished. This process could also provide a hermetic seal, if so required. Laboratory experience has indicated no detrimental effect to the wafer assembly whether alumina oxide, glass, or Photoceram is utilized.

Figure 22 illustrates 2 x 10 mil copper ribbon welded to 1 mil copper plated epoxy substrate. As evident in the micrograph, fusion occurred only between the copper ribbon and plated material and did not damage the epoxy material. This again illustrates the fine control of machine adjustments that can be maintained during welding with the Hamilton-Zeiss equipment.

Figure 23 illustrates the feasibility of microminiature electron beam welding solder-coated copper leads to nickel-plated surfaces. These 0.010-inch diameter leads were welded in the same manner as the Kovar and copper leads which were welded for the OMEC and Cordwood programs. The weld strength obtained from these solder-coated leads compared favorably to the copper or gold-plated Kovar leads. During the welding process, the solder-coated material alloyed with the copper and nickel material, thus providing a strong bond to the wafer assembly itself.

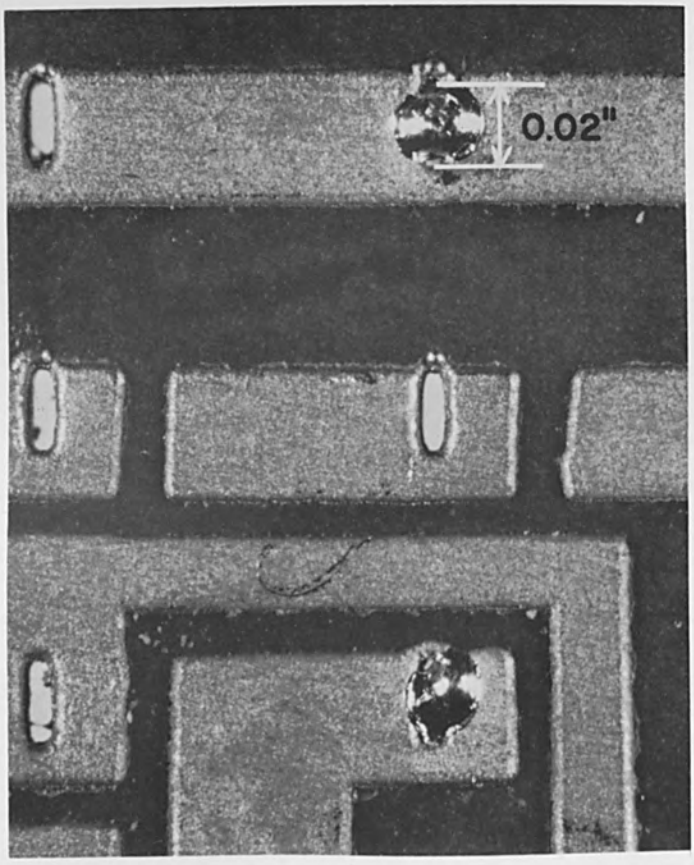

Fig. 21 OMEC End-Weld (Motherboard) Assembly

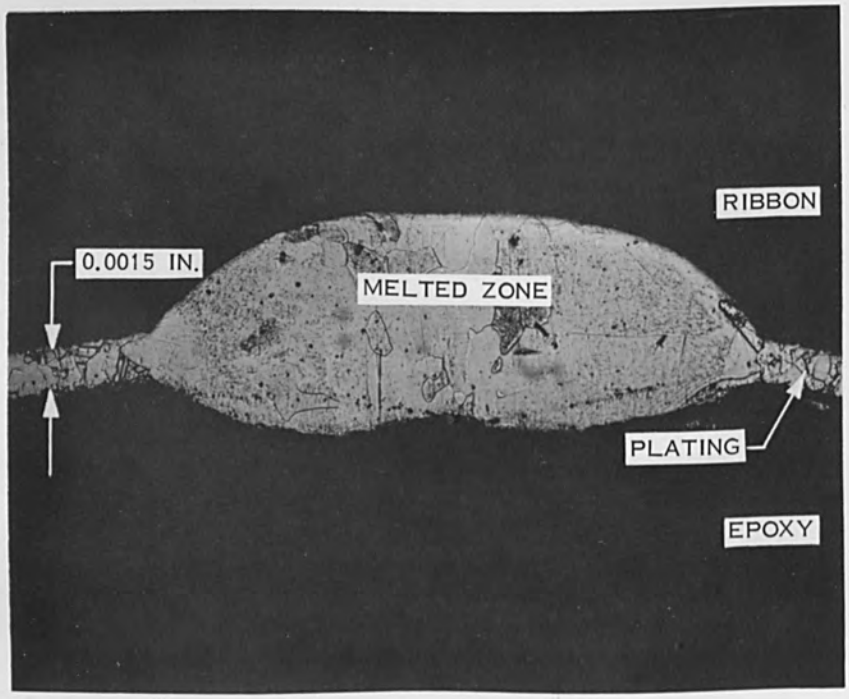

Etchant: $5H_2O$, $2H_2O_2$ (30%), $5NH_4OH$

Fig. 22 Copper to Copper Micrograph

Figure 24 demonstrates the welding of solder-coated copper to a circular steel hoop. Here it was necessary to hermetically seal the copper disc insert to the steel ring. Laboratory tests indicated that a hermeticity of 0.17 cubic centimeters per year was achieved.

Figure 16 shows a relay module assembly successfully welded and tested to a hermeticity of 0.03 cubic centimeters per year. The materials used in its construction consisted of a cold-rolled low alloy steel header assembly welded to a stainless steel cover. The low alloy steel was flashed with gold prior to welding. As evident from Figure 15, no distortion occurred and a minimum amount of gold flashing was evaporated. The heat-affected zone did not extend beyond 0.020 inch of the weld itself as evidenced by a microscopic examination of the finished product.

Figure 25 shows a one-mil platinum wire welded to a 25-mil copper terminal. In the design of this fuse circuit, it was extremely important to provide a junction which contained a low resistance value within specified limits. Measurements of the joint resistance indicated an essentially zero resistance value ($<$ 1 milliohm).

As is evident from the micrograph, fusion between the platinum and copper was complete. The copper-platinum interface area is actually larger in cross-section than the platinum wire. It is also interesting to note that for most welding processes welding of 1-mil platinum to 25-mil copper terminals would be most difficult, since the copper terminal provides a "heat sink"; that causes the terminal end of the platinum wire to ball up rather than to alloy to the copper material itself.

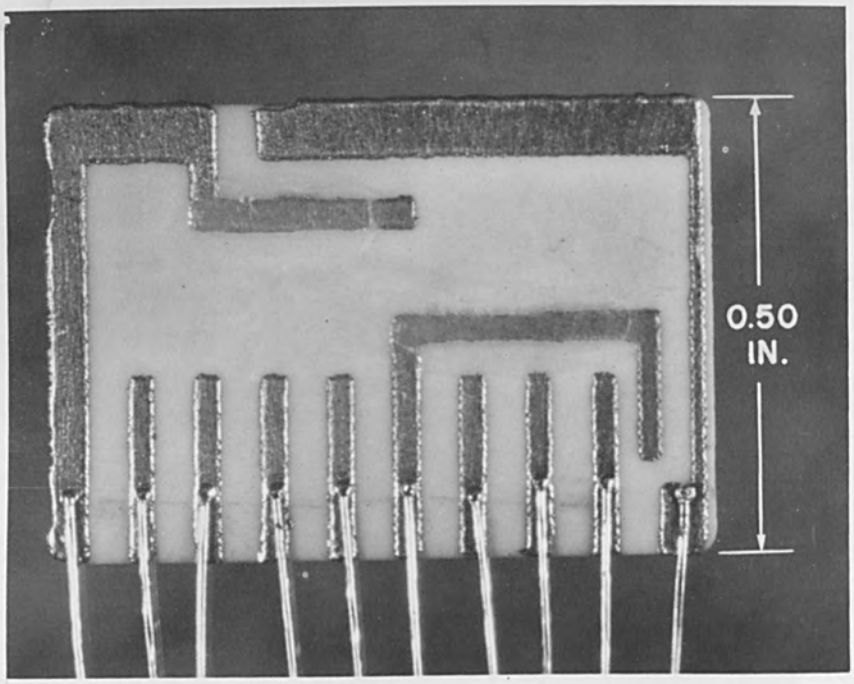

Fig. 23 Solder Coated 0.010-in Copper Leads Welded to 0.200-in. Nickel Plate

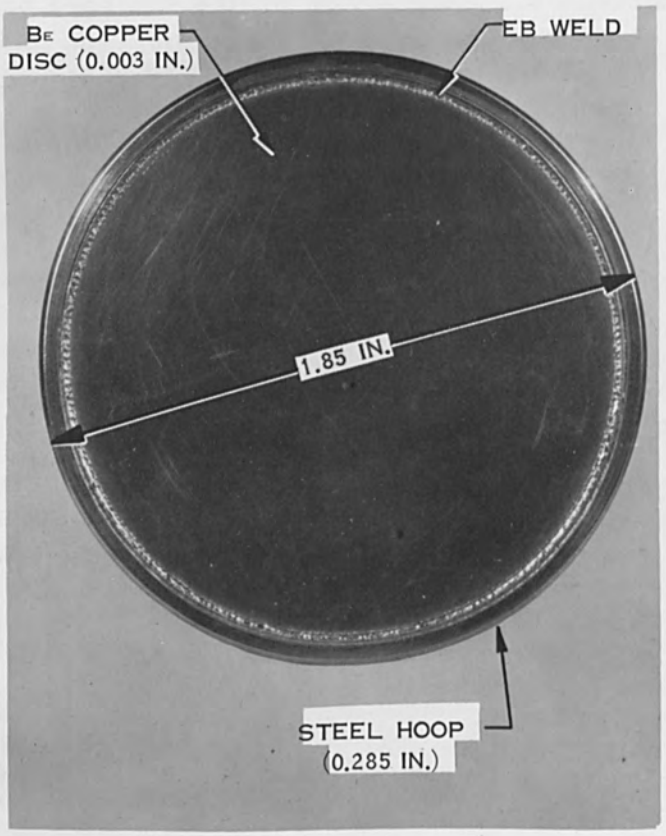

Fig. 24 Hermetic Seal Copper Disc Welded to Steel Hoop

SIGNAL CORPS MICROMINIATURE PROGRAM

Description of Packaging Concepts and Materials

The objective of the Signal Corps development program was to establish welded electrical connections having a termination density orders of magnitudes greater than that obtained with solder joints. The tests completed dealt with the investigation of welding 2 x 10 mil copper ribbons to metallized ceramic wafers. The study was primarily concerned with demonstrating the feasibility and reliability of electron beam welding conductor ribbons to wafers. This initial program was so successful that an enlargement of the program has been authorized by the Signal Corps and is now in process.

The extended program is concerned with welding conductor ribbons to multiple ceramic wafers. A termination density of 1600 welds per square inch must be demonstrated. As shown in Figure 26, this has been accomplished in part by welding 20 ribbon wires located on 25-mil centers to 10 wafers (.030 inches thick) located on 50-mil centers thus forming an initial termination density of 800 welds per square inch. The connections shown for these modules were produced on AL_2O_3 wafers to which 1 mil of nickel was electroplated over .0005 - .0008 inches of moly-maganese.

Welding Methods and Fixturing

To achieve the 1600 terminations per square inch, .010 inch thick alumina wafers will be used and located on 25-mil centers. Copper wire spaced on 25-mil centers will then be welded to the metallized wafers forming the required termination density. Prior to completing this phase, interconnections will be completed on all four surfaces of the module cube producing a total of 800 connections for a wafer module assembly

of approximately 0.60 x 0.60 x 0.25-inches.

The fixture concept used for the welding of these modules is a spring hold-down design shown in Figure 27. As indicated, the wafers can be readily installed by supporting them in a 3 point contact mode. The wires are kept in contact with the wafers by using the spring method of fixturing. This concept has demonstrated that the wires merely have to contact the wafer surfaces for electron beam welding. Since the welding is accomplished in 15 milliseconds, the minimum heat input essentially eliminates all warpage or distortion.

Problems and Solutions

All of the welds in this program required an effective weld nugget size of approximately 2×10^{-5} square inches. To accomplish this, the beam was deflected 10 mils at a frequency of approximately 250 cycles per second along the "Y" axis, which is perpendicular to the axis of the conductor ribbon. The resulting nugget which produced an average area of 15×10^{-5} square inches can be seen in Figure 28. Micrographs showed the alloying to be uniform throughout the interface of the weld structure. The welds completed during this program required a pulse width or beam on-time of 15 milliseconds.

For microminiature welding applications other than the Signal Corps, such as gold plated nickel, platinum-to-nickel, and Kovar, the pulse width had to be adjusted within an operating range of approximately 2-100 milliseconds. The accelerating voltage and beam current were also decreased (ref. Table I Appendix A).

Results

Results to date show that the weld resistance of these junctions is

less than 10 milliohms and that the strength of the weld nugget of the 2 x 10 mil copper ribbons is 280 grams or greater. The weld reliability being demonstrated by the Signal Corps contract is a minimum pull strength value of 220 grams in 100 thousand welds, and a weld resistance no greater than 1 milliohms in 100,000 welds.

Results of metallurgical evaluation tests can be seen in Figure 29, where a copper ribbon of 2 x 10 mil cross section was welded to a nickel plated aluminum wafer. A small defined alloyed zone is evident on the copper side of the interface. The thin dark line seen at the nickel-copper interface is a result of different reaction rates encountered during etching. This interfacial area is anodic to the nickel and thus etches faster. The resulting "valley" appears dark when observed microscopically, due principally to shadow effects.[4]

INTERCONNECTIONS FOR THIN FILMS AND SOLID CIRCUITS

As the state of the art for thin film and solid state fabrication advances, the problem of providing reliable interconnections from the film circuits becomes a more challenging problem. Laboratory tests completed to date indicate that the electron beam may provide the only satisfactory answer for fabricating a junction from the thin film to the respective carrying circuit.

The majority of the fixturing used in the fabrication of thin film interconnections is similar to the manipulator in Figure 8. This fixturing

---

[4] Kehl, George L., The Principle of Metallographic Laboratory Practices.

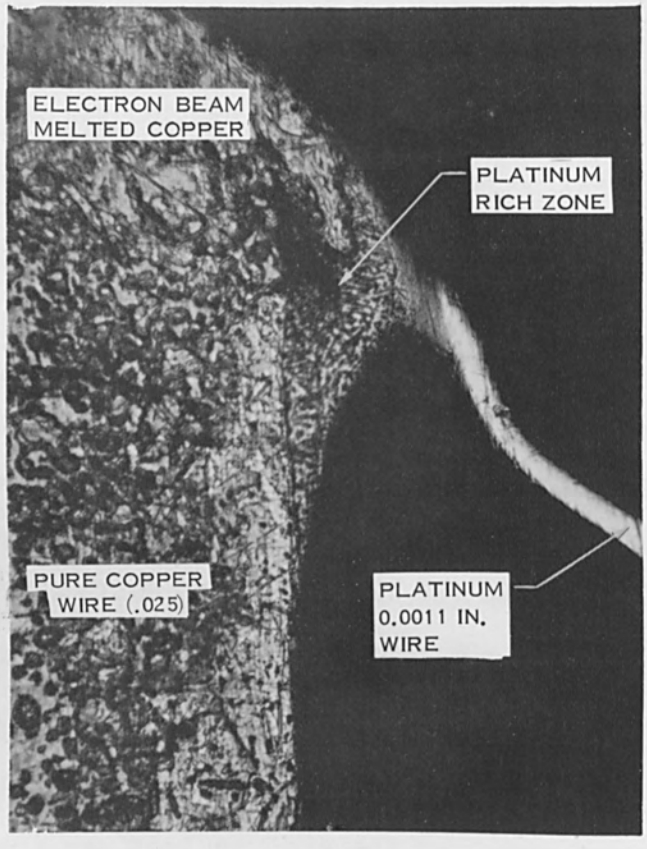

Fig. 25 Platinum to Copper Micrograph

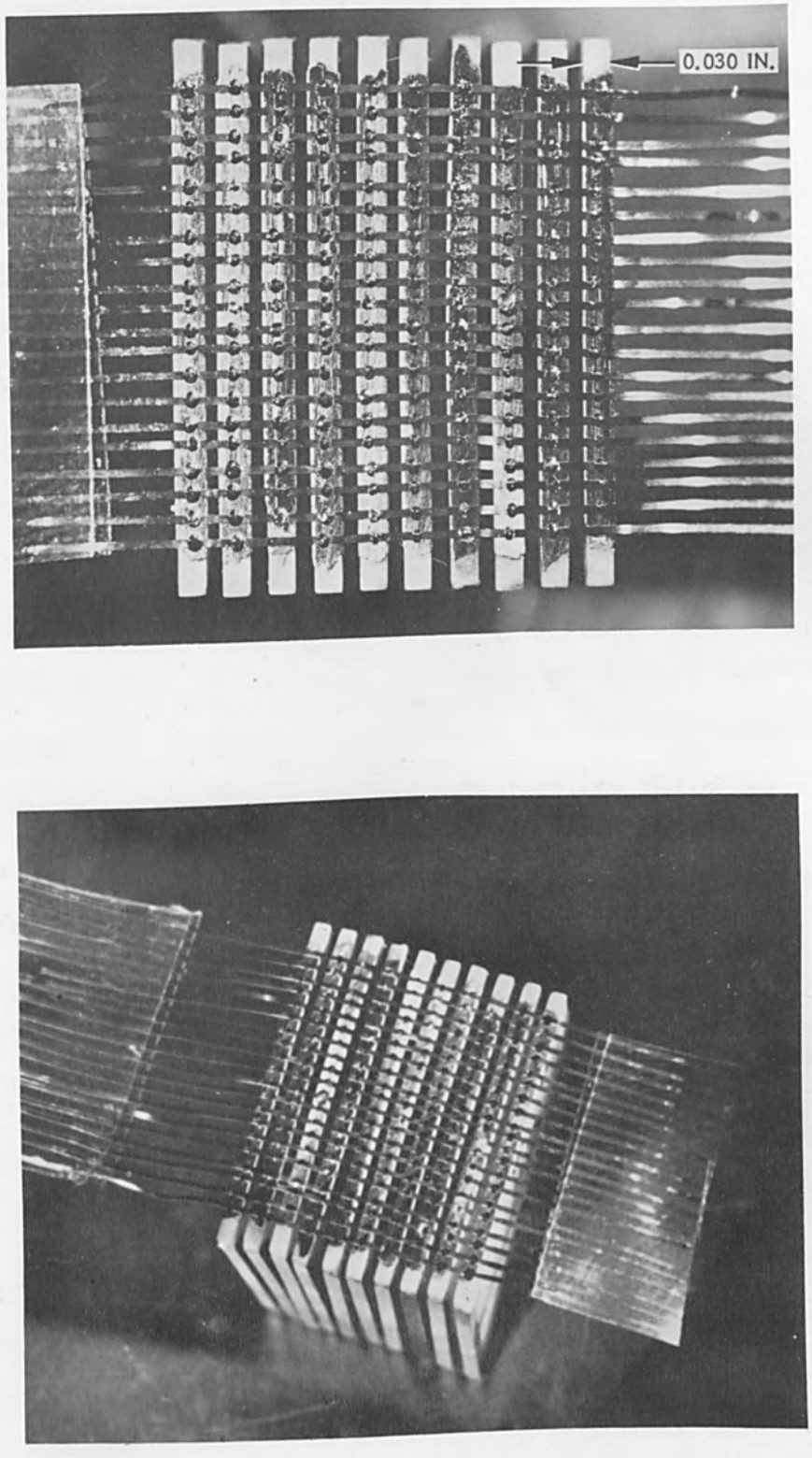

Fig. 26 Riser Wire Module - Signal Corps

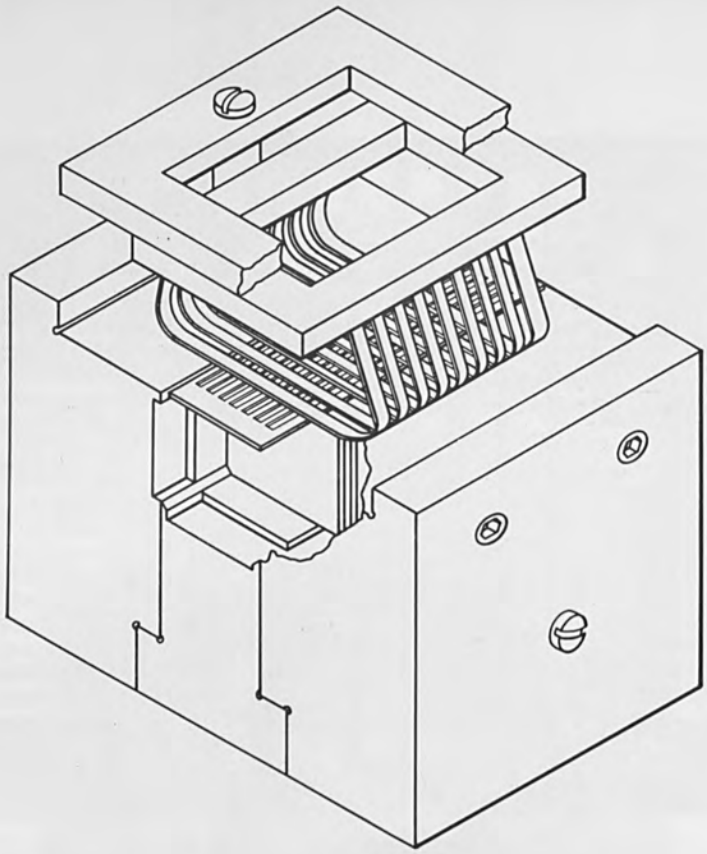

Fig. 27 Multiple Wafer Fixture - Signal Corps

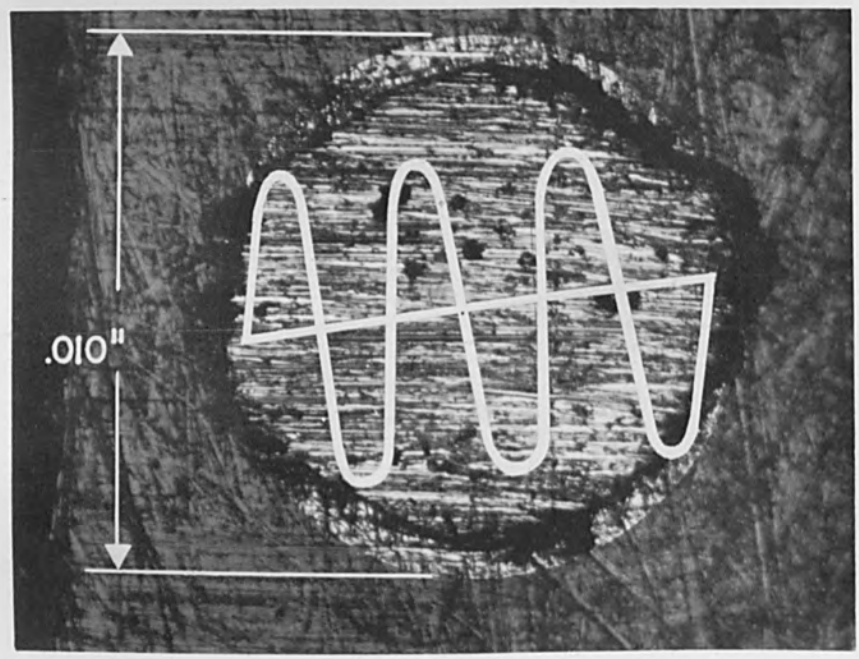

Fig. 28 Electron Beam Weld Nugget Area 0.002-in. x 0.010-in. Copper Interconnector Welded to Nickel on Alumina

consisted primarily of a microfinger through which the beam could be directly pulsed. In most cases the finger consisted of beryllium copper, which also served as a satisfactory "heat sink".

Some of the typical interconnection welds that have been made are shown in Figures 30 through 35. Figure 30 illustrates gold and Kovar tabs of one mil thickness welded onto copper plate electroplated with a gold deposition. The gold was vapor-deposited on quartz wafers. The thickness of the deposition and copper plate was approximately 500 and 30,000 Angstroms, respectively. Figure 31 indicates Kovar and gold leads of 0.5 mil thickness welded to 0.0002 inches of nickel plated on 3,000 Angstroms of chromium deposited on quartz. Figure 32 illustrates 0.0005-inch gold tabs welded directly to 2,500 Angstroms of gold deposited on quartz substrate. Electrical continuity for each of the interconnections was demonstrated. The resistance value measured was less than 0.5 milliohms for all cases. The resulting strength of the bond is illustrated in Figure 32 which shows that portions of the weld nugget were still retained on the thin film and quartz surfaces after the lead was pulled off.

Microscopic examination of some of the lead junctions indicated that some of the leads were occasionally welded to the quartz substrate, rather than to the film itself. However, even in these cases, electrical continuity was demonstrated. This was in all probability the result of surface wetting, and the dispersing of material over the thin film during solidification. It should also be noted that the heat affected zone around the respective wafer lead junctions was less than 0.005 inch. Inasmuch as this process demonstrates the feasibility of precision micro-welding, it lends itself to providing interconnections to solid state or thin film processes, since the remaining portion of the circuits are not subject

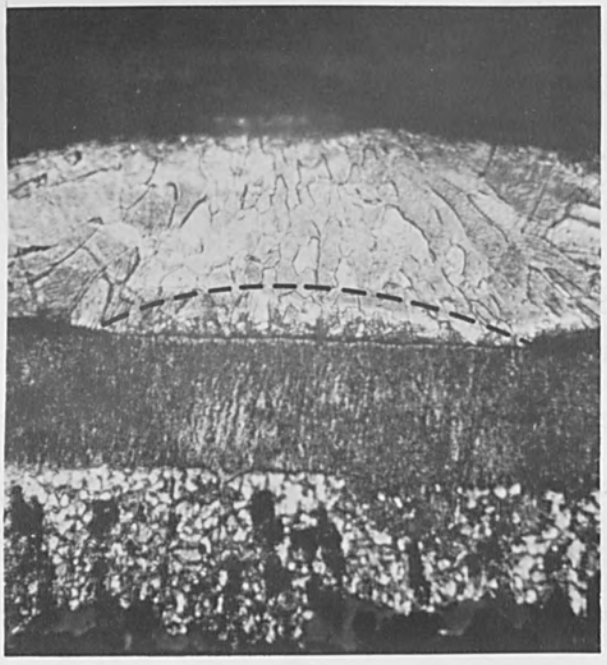

Fig. 29 Copper (0.002-in. x 0.010-in.) To Nickel (0.002-in.) Micrograph

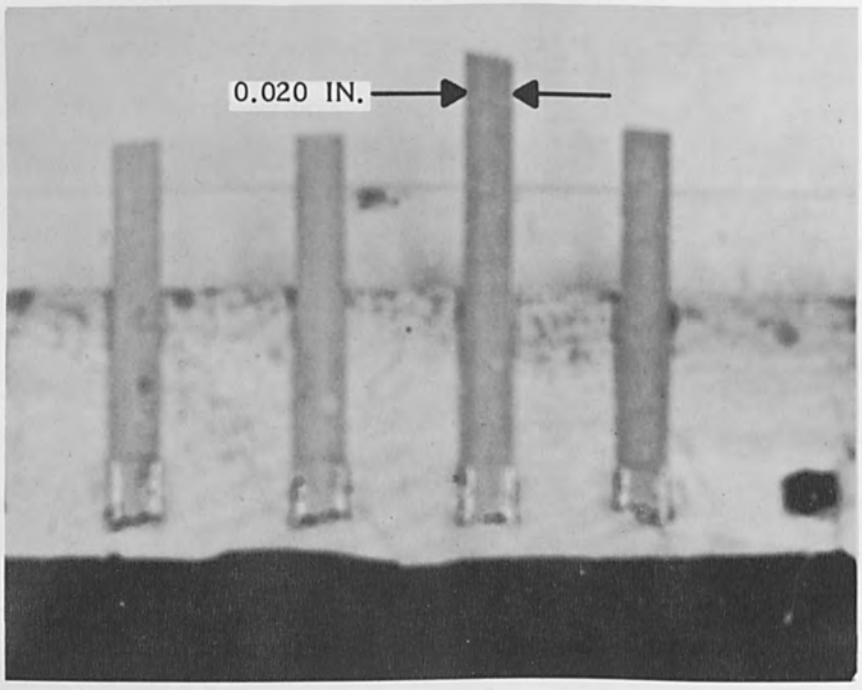

Fig. 30 Gold and Kovar Leads Welded to Copper Plate with Gold Deposition

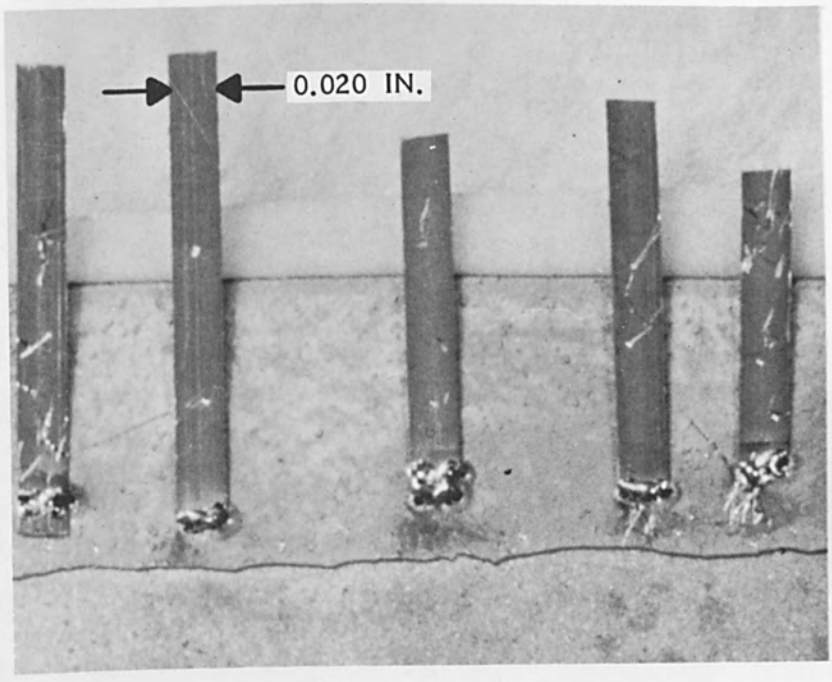

Fig. 31 Gold and Kovar Leads Welded
To 0.0002-in. Nickel

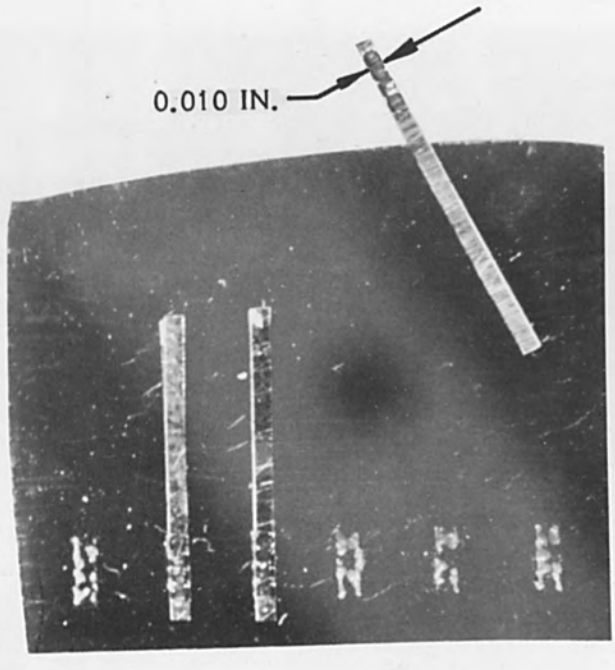

Fig. 32 Gold Tabs Welded to Gold Deposition

to heat damage. As an example, Figure 33 illustrates a 5 mil gold plated phosphor bronze lead that was flattened to one mil at its extremity before being electron beam welded to a copper film of 33,000 Angstroms. The copper film was deposited over 100 Angstroms of chromium on single crystal quartz substrate. Bronze leads of 0.5-mil thickness have also been welded to a 100 Angstrom thin film of cobalt deposited on glass.

Further work in the area of bonding leads to thin film is presently being investigated by depositing the thin film on the bottom side of the lead, as well as on the substrate. Here the lead is placed in contact with the thin film, then pulse-welded at very low energies. The pulse widths and welding duration are approximately 4.0 and 264 microseconds, respectively. The junction provided between the lead and the substrate in this case is actually a brazed joint, rather than a weld of the lead to the thin film.

The electron beam can also be used to weld miniature covers on solid state circuits; see Figure 34. This photograph illustrates a typical receptacle (Kovar) for a flip-flop solid state circuit to which a 0.003-inch thick Kovar cover was welded. The advantage of electron beam welding in this case is the production of a hermetic seal without damage to the internal solid state circuitry. A simulated functional block welded to a multi-layer board is shown in Figure 35.

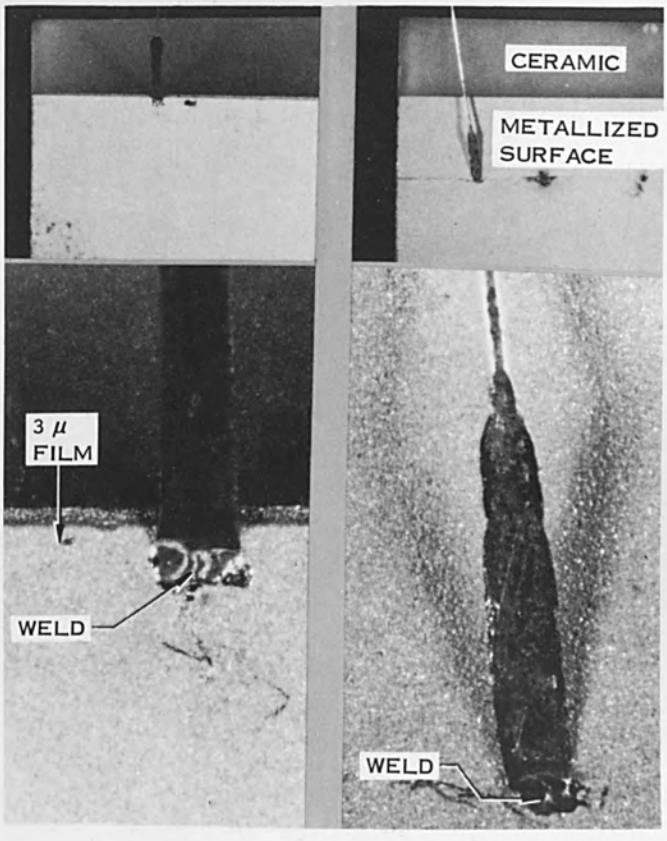

Fig. 33 Phosphor Bronze Lead Welded to Copper Film

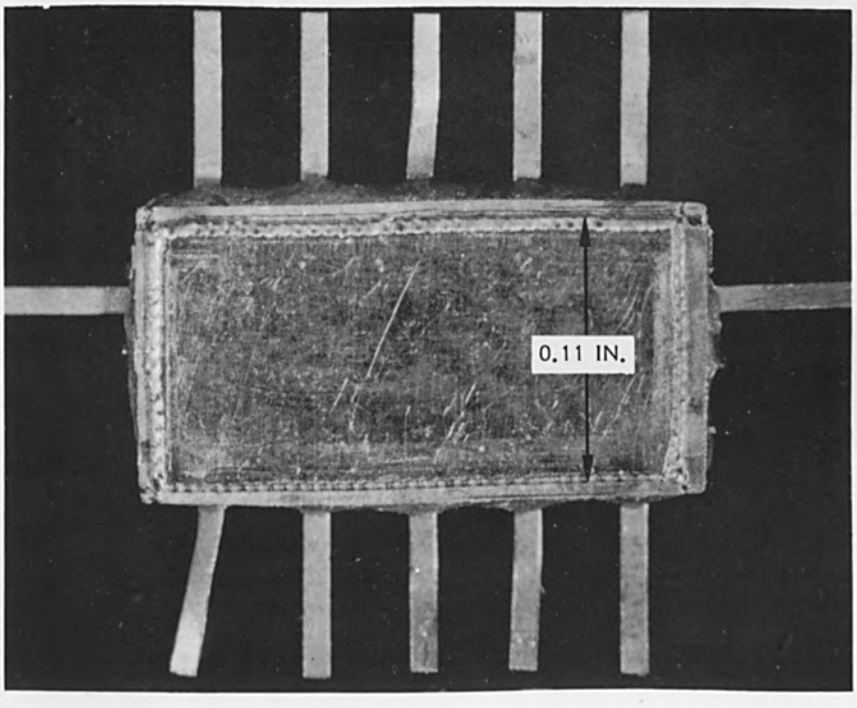

Fig. 34 Cover Welded to Solid State Receptacle

SUMMARY AND CONCLUSIONS

1. The microwelds investigated in the Signal Corps, Hamilton Standard OMEC, and Cordwood programs indicate that electron beam welding of miniature and micro miniature components with Hamilton-Zeiss high power density equipment is feasible and practical.

2. Mechanical and metallurgical properties of the investigated weldments were excellent. The data collected clearly indicate that microwelds provide a high degree of structural reliability necessary for micro-electronic or macro-electronic packaging.

3. The high packaging density attainable with electron beam welding makes this process highly applicable to thin film and solid state circuitry.

4. With the precise electron optics of the Hamilton-Zeiss electron beam welder, the beam spot size (heat-affected zone) can be accurately controlled. The use of this equipment, therefore, is ideally suited for welding heat sensitive microminiaturized components.

5. In addition to providing acceptable macro and micro welds, the electron beam can also be used to provide hermetic seals. This ability to produce a hermetic seal, a low resistance joint, and a high strength weld with one welding process, is a major technological advance for the micro-electronic industry.

6. As a result of these successful programs, Hamilton Standard has developed and will shortly market a combination micro-welding and cutting machine. This machine will permit the electronics industry to utilize more fully the new and advanced fabrication techniques described herein and in addition cut and drill precision miniature configurations into most metals and ceramics.

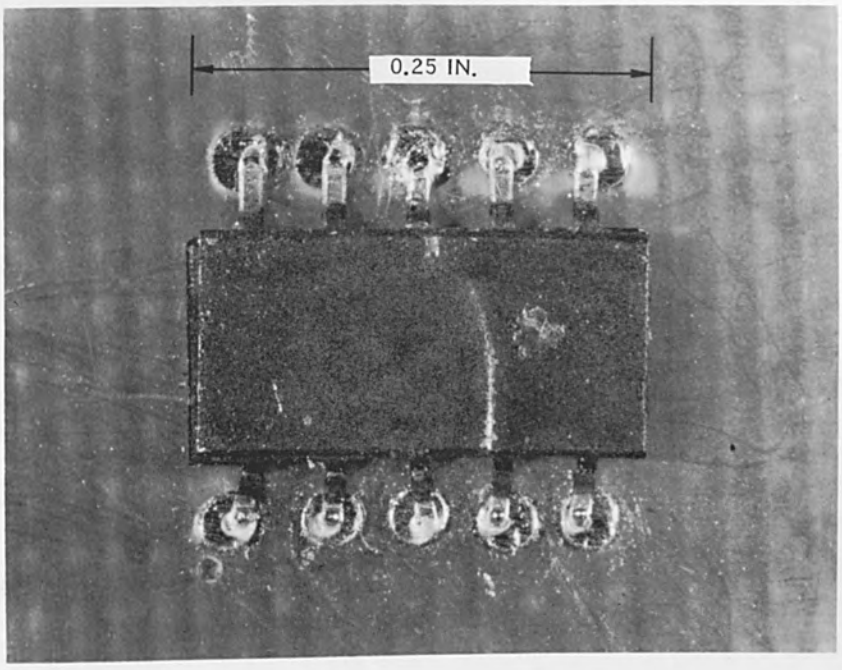

Fig. 35 Simulated Functional Block Welded to Multi-Layer Board

ACKNOWLEDGMENTS

The author wishes to express his appreciation to the following for their valuable help and cooperation in making this paper possible.

To J. Cyr for completing the microminiature welding specimens illustrated.

To R. Duhamel for completing the thin film interconnections.

To H. Hudolin for his assistance in performing many laboratory experiments.

Special thanks is also extended to the U. S. Army Signal Corps, Fort Monmouth, New Jersey, for permission to use their study data.

Appendix A

Table I

Typical Electron Beam Weld Energy Inputs

	KV	Ma	Pulse Width (MS)	Watt Secs.
Miniature Components				
0.032" Dia. Copper	80	0.5	100	4.0
0.025" Dia. Copper (tin coated)	65	0.5	100	3.25
0.020" Dia. Kovar	90	0.15	100	1.35
0.018" Dia. Kovar	85	0.5	20	0.85
0.016" Dia. Kovar	80	0.5	20	0.80
0.012" Dia. Kovar	65	0.5	20	0.75
0.015" Dia. Copper (tin coated)	70	0.5	20	0.70
0.010" Dia. Copper (tin coated)	60	0.5	20	0.60
0.011" x 0.032" Ni to 0.025" Dia. Gold Plated Dumet	90	0.4	10	0.36
0.011" x 0.032" Ni Ribbon to Motorola 2N 174 Copper Mesh	125	0.20	10	0.25
0.011" x 0.032" Ni to .016" Dia. Gold Plated Kovar	125	0.16	10	0.20
0.011" x 0.032" Ni to 0.025" Dia. Solder Coated Copper	125	0.16	10	0.20
Microminiature Components				
0.001" x 0.020" Kovar (with 0.001" gold plate)	90	0.10	15.0	0.135
0.003" x 0.030" Copper				
0.004" x 0.019" Kovar (with gold flash)				
0.002" x 0.010" Copper				

Table I (Continued)

Typical Electron Beam Weld Energy Inputs

	KV	Ma	Pulse Width (MS)	Watt Secs.
Microminiature Components				
0.001" Dia. Nickel (with 0.001" Gold Plate)	70	0.07	2	0.01
0.001" Platinum Wire to 0.025" Dia. Copper	125	0.18	5	0.11
0.001" x 0.030" Chrome Nickel	60	0.15	10	0.9
Interconnections for Thin Films, etc.				
0.001" Phosphor Bronze Lead to 100 Angstrom Cobalt Film	60	0.01	0.3	18×10^{-5}
0.0003" Kovar Ribbon	65	0.07	0.5	23×10^{-4}
0.0005" Au Tabs to 2500 A Gold Film	60	0.01	0.3	18×10^{-5}
0.001" Kovar Lead to .0005" Ni on Cr Film	60	0.03	1.0	18×10^{-4}
0.001" Kovar Lead to 0.0005" Ni on Au Film	60	0.03	1.0	18×10^{-4}
0.001" Gold Lead to Al film	60	0.01	0.3	18×10^{-5}
0.001" Gold Lead to Au Film	60	0.01	0.3	18×10^{-5}

APPENDIX A

TABLE II

END-WELD TENSION TEST TABULATION

No.	FORCE (LBS.)	REASON FOR FAILURE
1	4.7	No failure, pin vice slipped
2	3.9	Metalizing separated from ceramic
3	4.8	Metalizing failed
4	6.1	Ceramic Fractured
5	6.8	No failure, pin vice slipped
6	5.3	Metalizing failed
7	5.9	Ceramic fractured
8	4.2	Ceramic fractured
9	4.5	Metalizing failed

REFERENCES

1. Ceramic Industry 73 (4), 57, (1959).

2. Alcoa Aluminum Handbook, Aluminum Company of America, Pittsburgh, p. 39.

3. Gibbs, F. E., Private Communication, Kaiser Aluminum and Chemical Corporation, Spokane, Nov. 16, 1961.

4. Hokanson, H. A. and W. I. Kern, Electron Beam Welding of Molybdenum and Tungsten ASD TR 61-461, p. 25.

5. Passmore, E. M., Beryllium Joining WADC Sponsored Program, WADC Technical Report 59-695, Part II, p. 8.

6. MacPherson, B. M., and W. W. Beaver, Fusion Welding of Beryllium, WADD Technical Report 60-917, p. 12, 24-29, 38, 39, 54.

7. Hess, W. T., H. J. Lander, and S. S. White, Electron Beam Welding of Beryllium, Proceedings Third Symposium on Electron Beam Technology, Alloyd Corp., 1961, p. 185-187.

ELECTRON BEAM WELDING OF SINTERED ALUMINIUM

By

J. Van Audenhove
Research Scientist

M. Meulemans
Research Scientist

D. Tytgat
Assistant Research Director
Centre d'Etudes de l'Energie Nucleaire
Mol-Donk, Belgium

ABSTRACT

It is generally admitted that sintered aluminum, with different oxide contents, is difficult to weld and that it must be avoided to pass through the liquid state in the assembling techniques in order to save the interesting properties of the material.

Due to its higher energy concentration than in other welding methods, the use of electron beam welding for this task has been investigated. This presentation discusses this work in which C.E.N. and B. Precis guns were used.

ELECTRON BEAM WELDING OF SINTERED ALUMINIUM

A. INTRODUCTION

1. Sintered aluminium products (SAP[x] or Frittoxal[xx] in Europe, APM[xxx] in the U.S.A.) offer interesting possibilities for use as structural and canning materials in organic-cooled or organic-cooled and moderated reactor systems. Their high temperature strength, high thermal conductivity, low neutron absorption and excellent corrosion resistance in organic coolants make them attractive for operation at temperatures up to 450°C.

The improved elevated temperature strength is due to the dispersion strengthening effect of submicroscopic particles of aluminum oxide (Al_2O_3) in a matrix of aluminum. The strengthening effect is retained at elevated temperatures owing to the insolubility and high melting point of the dispersed phase, which blocks the movement of dislocations in the structure and opposes recrystallisation.

2. The manufacturing process of sintered aluminum products has been reviewed in some recent papers (3, 4, 5, 11).

SAP[x] - Protected trade name - A.I.A.G.V., Neuhausen, Switzerland

Frittoxal[xx] - Protected trade name - Tréfileries et Laminoirs du Havre (TLH) Paris, France

A.P.M.[xxx] - Protected trade name - Alcoa, U.S.A.

3. It is generally admitted that sintered aluminum with different oxide contents is difficult to weld and that it must be prevented from passing through the liquid state when assembling, in order to maintain the dispersed structure and the favorable properties of the material.

Various welding techniques have been described in the literature (flash-, spot-, pressure- and ultrasonic welding). Electron beam welding has been used in our laboratory. This technique has high energy concentration in comparison to other welding methods, and experience with such equipment existed at C.E.N. (9).

4. This research, done under Euratom contracts, has been conducted with close collaboration between the C.E.N. team and Euratom personnel of the Metallurgy and Ceramics Service at Saluggia, Italy.

B. ELECTRON BEAM WELDING WITH C.E.N. GUN

1. Description of the equipment.

Preliminary tests were made using equipment built at our laboratory which had been used to weld other types of materials, such Al, Cu, Ni, stainless steel, Mo, Nb, Ti, and Zr. (9).

This equipment is shown in fig. 1. A sketch of the electron gun is presented in fig. 2. The cathode has a hair-pin form and the electrons are electrostatically focused. The

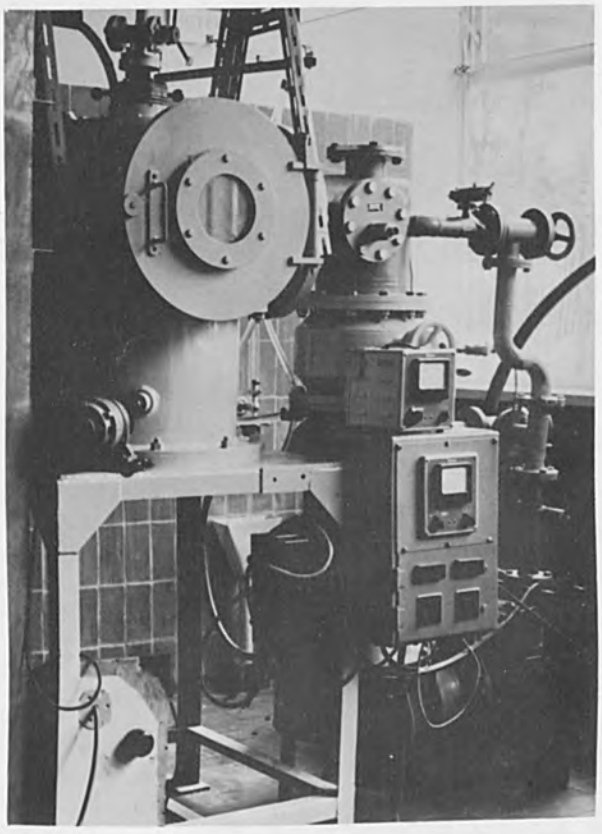

Fig. 1. Equipment used at the C.E.N. laboratory for welding.

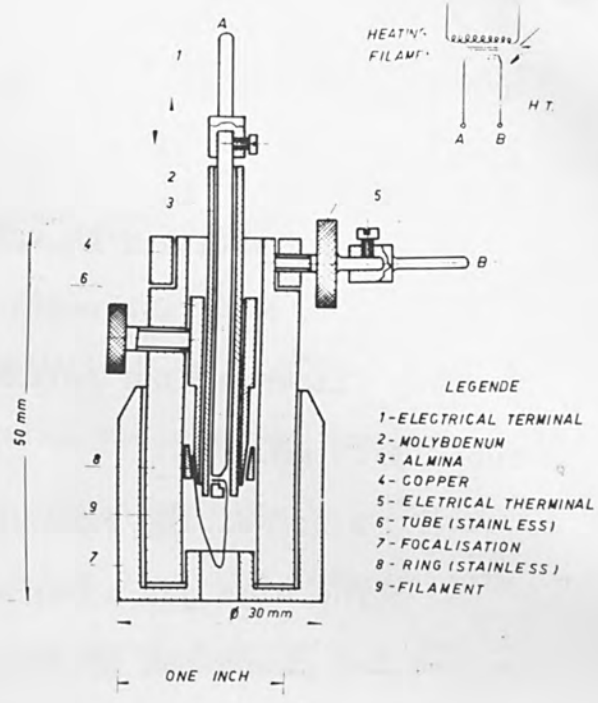

Fig. 2. Sketch of the electron gun.

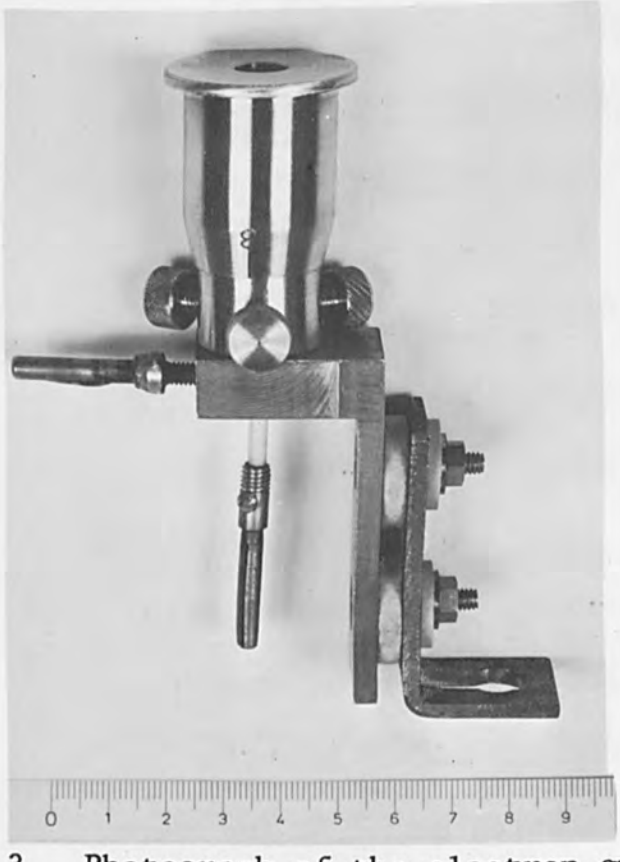

Fig.3. Photograph of the electron gun.

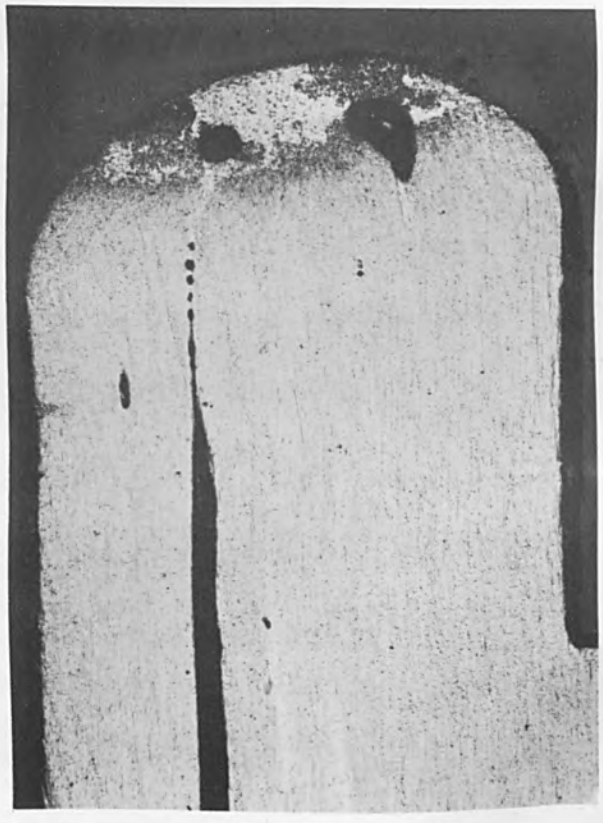

Fig.4. Undegassed S.A.P. after electron beam welding - Otto Fuchs material. X25

gun is shown in fig. 2. The specimen to be welded forms the anode.

2. Experiments with undegassed material.

2.1. Material used: manufactured by Otto Fuchs, Germany (licence AIAG Switzerland). SAP 865 (13% oxide). Tube 13/15 mm.

2.2. Welding experiments.

The high gas content (up to about 40 ml/100g) (6) caused two phenomena which limited the possibilities of welding by electron beam bombardment:

a) ionization (it leads to switch-off of the power supply),

b) metallic projections.

The weld bead has a dark outlook and shows many pits. The micrographic examination shows that the dispersed structure of SAP is no longer present. The aluminum contains many inclusions and porosity (see fig. 4).

3. Experiments with degassed material.

3.1. The degassing conditions were obtained by systematic tests conducted at 500°, 600°, and 625°C. Analysis of hydrogen in the gas was not possible. Degassing of Otto Fuchs' material was considered sufficient when no blistering or porosity occurred upon welding the SAP in the electron beam. This result was obtained by heating at 625°C for 24

hours under a vacuum of $1x10^{-4}$mm Hg (heating and cooling rates: 100°C/hour).

3.2. The welding conditions were: 25kV, 20-25 mA, 1.5 turn/20sec.

3.3. It has been possible to weld SAP by electron beam without formation of internal porosity and without complete transformation of the structure, as shown on fig. 5. The welds were leak-tight when tested using a helium leak-detector. The weld penetration is only 0.4 mm in a 1 mm thin can due to insufficient thermal concentration of the gun used.

C. ELECTRON BEAM WELDING WITH A GUN MANUFACTURED BY "B. PRECIS"[x] IN FRANCE.

1. The test combined two new factors:

a) A new gun was put at our disposal by Euratom (J. Briola). This electron gun is a PIERCE type gun of 3kW, in which the electrons are focused by a concentric electric field that is generated by the concentric arrangement of a spherical anode in a spherical cathode (13, 14, 15).

With this arrangement, the work piece is not the anode. This gun with added magnetic focalisation, permits a higher

---

x Firme "Precis B." 8, Boulevard Ménilmontant, Paris 20e, France

welded end. A thermocoax type heating element is placed inside the tube, close to the weld. The section of tube between the two enclosures is water cooled to protect the seals. The temperature of the seals is always measured 3 mm from the weld, by a thermocouple pressed against the tube by means of a small spring.

3.2. Test procedure.

a) Evacuate the second enclosure to 10^{-3} mm Hg

b) Pressurize the tube to 20 kg/cm^2 (value given by Euratom staff).

c) Heat the welded end of the tube at a constant rate, 12°C/minute until the leak detector indicates a break in the weld or in the tube.

4. Results

Two types of end plugs have been used: type A and type B (see fig. 9).

4.1. Type A end-plug.

A series of tests has shown that with precise mechanical positioning, it is possible to weld S.A.P. 960, 930, and 895 end plugs to tubes. The failure of the sealed tubes will occur at the side of the tube and not at the weld for short-term rupture tests at temperature. Temperatures reached are, on the average, 500°C, with 20 kg/cm^2 internal pressure. The metallograph of different SAP materials in

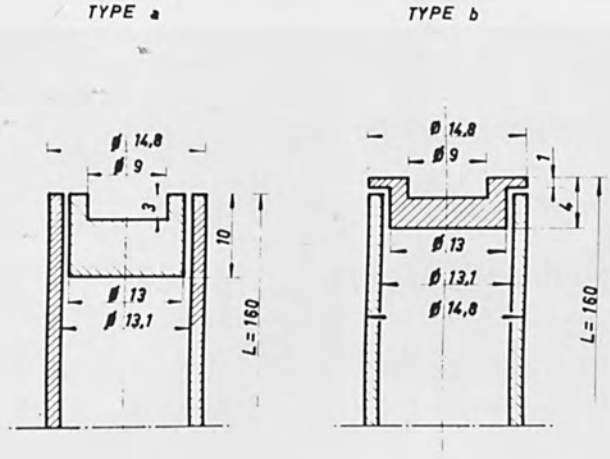

Fig.9. Sketch of the end-plugs - type a and b.

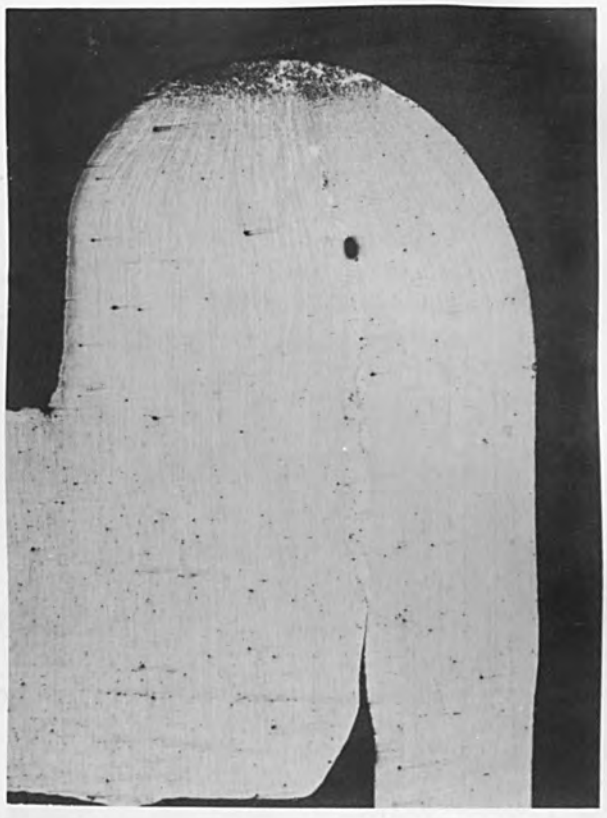

Fig.10. Type a - welding of S.A.P. 960 Montecatini. X25

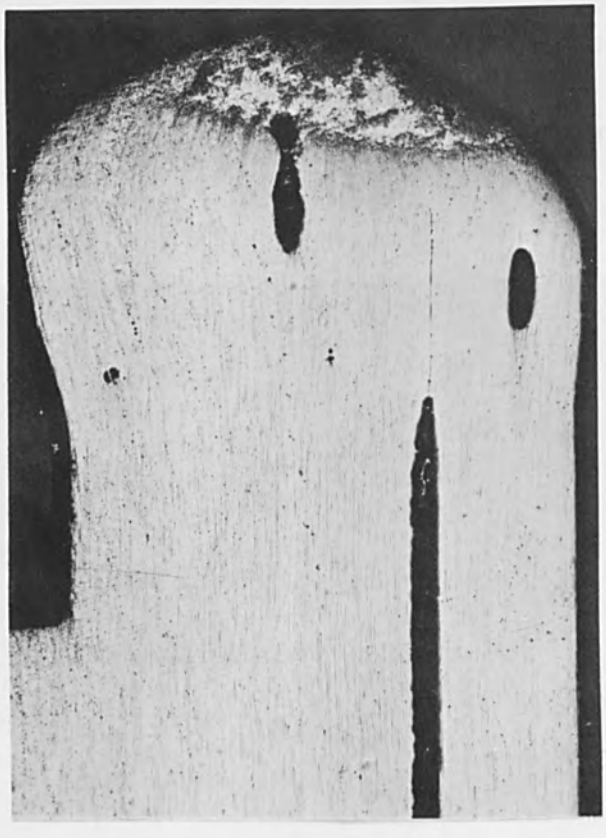

Fig.11. Type a - welding of S.A.P. 930 undegassed. X25

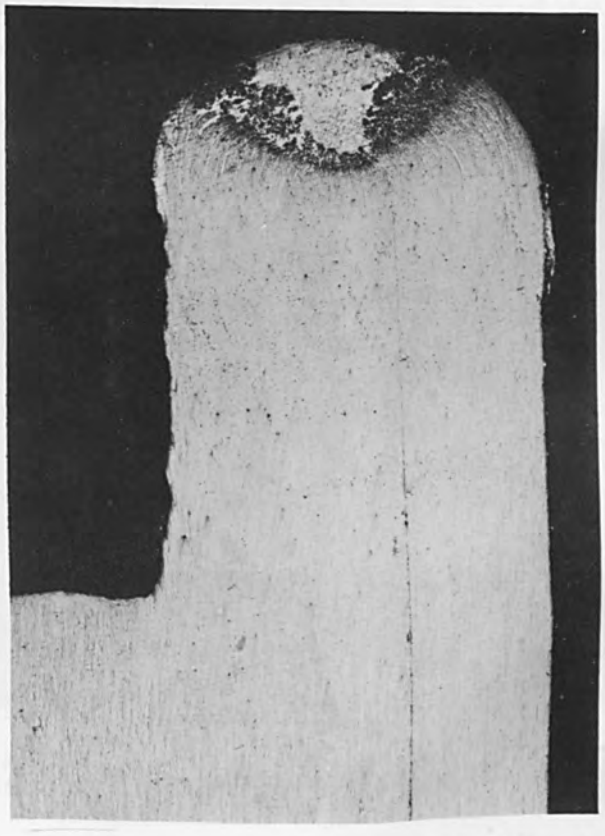

Fig.12. Type a - welding S.A.P. 930 degassed. X25

degassed and undegassed conditions is shown in fig. 10, 11, 12, 13 and 14.

It must be noted that SAP 930 and 895 have still to be degassed at 625°C for 24 hours or more, to avoid any blistering or porosity in the structure, mainly in the end-plug.

4.2. Type B end-plug:

Preliminary results indicate some improvement over the type A end-plug. (fig 15 and 16). The combination of pressure and lower temperatures appears to provide stronger joints.

5. Work under progress.

The procedure used will include a technique as described in reference 15, p. 51:
"...the successful procedure will involve sealing in a plug at the end of the tube followed by welding around the exposed bond line. The former should provide strength and the latter might ensure leaktightness." The report added: "This solution of the problem does not seem to have been selected at this time by any of the organizations in this field". In fact, it was selected!

D. CONCLUSIONS

1. Successful closure of S.A.P. tubes using an electron-beam welding technique has been possible for SAP 960, 930,

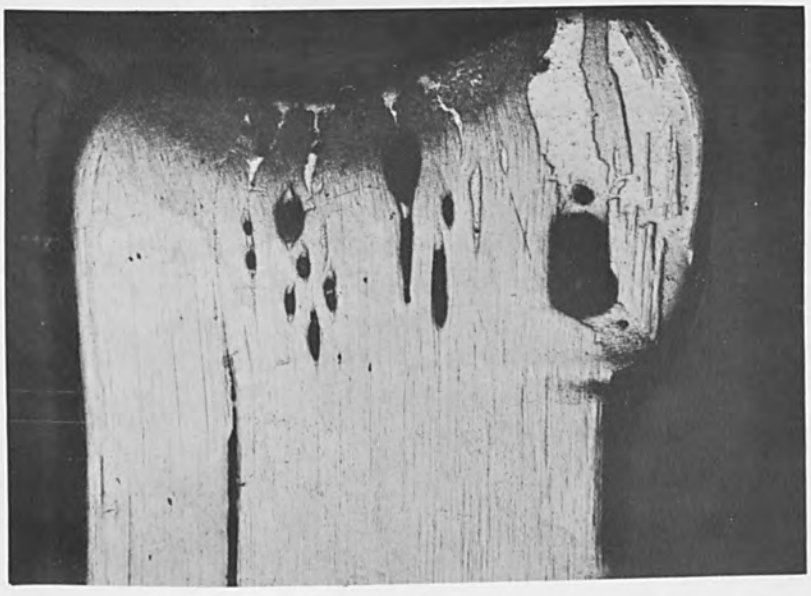

Fig.13. Type a - welding of S.A.P. 895 undegassed. X25

Fig.14. Type a - welding of S.A.P. 895 degassed. X25

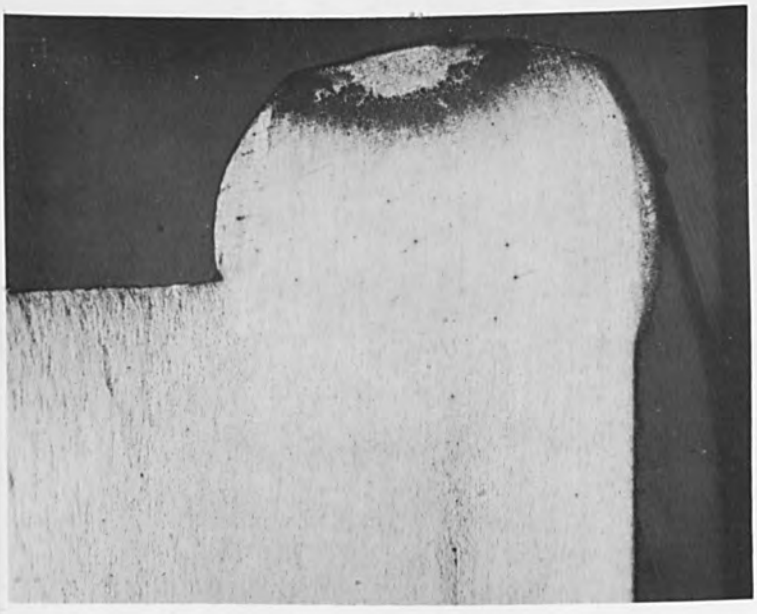

Fig.15. Type b - welding of S.A.P. 930 Montecatini. X25

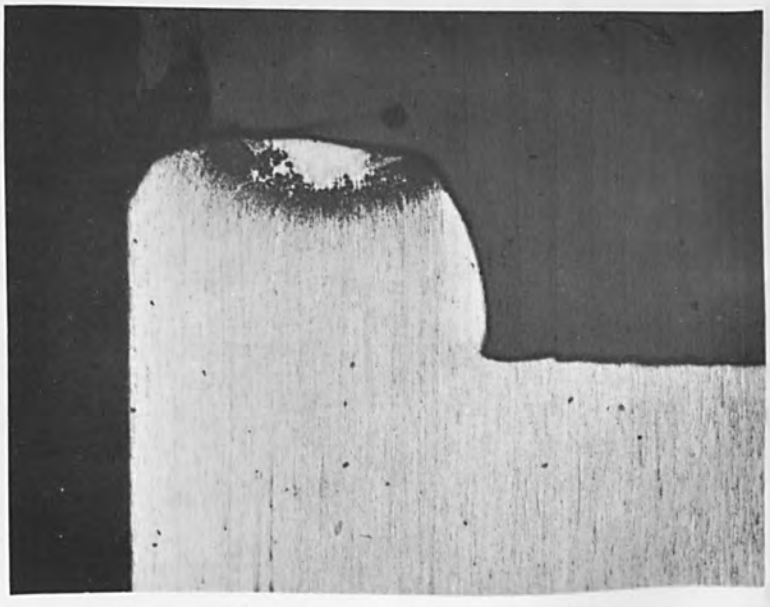

Fig.16. Type b - welding of S.A.P. 930 Montecatini. X25

and 895. High-temperature testing under pressure has been used to verify the quality of the welds.

2. Combination of pressure and welding should lead to high-quality closures equal to or superior to other types of welds because of the very high, localized heating.

3. Electron beam welding can be systematically used as a quality test for gas content of the material.

E. ACKNOWLEDGMENTS.

The authors thank G. Musso for the very fine metallographic work done, and P. Groeseneken for his technical help.

The collaboration with J. Briola and P. Jehenson of Euratom has been a permanent source of discussions, suggestions and stimulation.

ELECTRON BEAM WELDING OF SINTERED ALUMINIUM

List of Figures

BIBLIOGRAPHY

EUROPE

1) Bridoux C. and al, "Sintered aluminum powder as a canning material Nuclear Engineering, Vol. 6, n°60, p. 189 (May 1961).

2) Bridoux C. and al, "Soudage par étincelage de l'aluminium fritté utilisé comme matériau de gainage". Revue Métallurgie, Vol. 8, p. 695, aout 1961.

3) Boudouresque M.B. and Mann K.E. "Application of sinter aluminum as cladding material for fuel element". Symposium on fuel element fabrication with emphasis on cladding materials, Vienna, 10-13 May, 1960. Vol. 1, p. 145, Academic Press, London - New York (1961).

4) Mann K.E., Boudouresque M.B. "Sinter aluminum as cladding material for fuel element". Report CEA n°1993 - 1961.

5) Bloch E.A. "Dispersion strengthened aluminum alloys" Metallurgical Reviews 1961, Vol. 6, n°22, p. 193.

6) Hansen N. and al "Sintered aluminum powder for reactor applications" Riso Report n°13, May 1960.

7) Hansen N. and Eivind Adolph "The effect of heat treatments on the structure stability of sintered aluminum products", Riso report n°25, May 1960.

8) Schleicher H.W. and al "Contribution to the diffusion - and corrosion behaviour and creep strength of aluminum powder products" - Symposium on fuel element fabrication with emphasis on cladding materials, Vienna, 10-13 May, 1960, Vol. 2, p. 127. Academic Press, London - New York.

9) J. Van Audenhove and al. "Pratique du soudage par bombardment électronique appliqué aux métaux de gainage". Symposium on fuel element fabrication with emphasis on cladding materials, Vienna 10-13 May 1960. Vol. 1, p. 495.

10) Hug H. and Bichsel H. "Electron microscope investigation of S.A.P. structures", Metal Treatment and Forging, March 1961.

11) Gualandi D. and Jehenson P. "Improvements in the technology of S.A.P. for nuclear applications, particularly as canning material" Journées Nucléaires, Milan, December 1961.

12) Boghen J., Leymanie C. and Hérenguel J. "Influence des gaz résiduels sur les propriétés des produits frittés aluminum-alumine" - 5 éme Colloque de Metallurgie, les gaz dans les métaux. June 26-27, Saclay, France.

13) Sommeria J. "Communication aux Journées du Vide de Printemps 1961" Paris, France.

U.S.A.

14) Stohr J.A. "Electron Beam welding in France" - Proceedings third syposium on electron beam technology, Boston March 1961, p. 102.

15) Thum R.T. and al "A new electron gun", Vac. Symp. Transactions, 1959.

16) Friske W.H. "Interim Report on the Al powder metallurgy product development program", NAA-SR--4233, Jan. 15, 1960.

17) Kendall E.G. and Friske W. H. "Fabrication and Properties of APM products", Nuclear Metallurgy, Vol. VII, Symposium on Metallic Moderator and cladding Materials, A.I.M.E. (1960).

18) Kendall E.G. and al "Fabrication Development of APM fuel elements for organic cooled reactors", Nuclear Engineering, Vol. 6, n°67, p. 525, Dec. 1961.

19) A.N.L. Committee "Organic Nuclear Reactors: and evaluation of current development programs", ANL-6360, May 1961.

This bibliography does not pretend to be complete, as hundreds of papers have been published on S.A.P. or A.P.M. It collects some of the most recent publications easily available.

ELECTRON BEAM WELDING AT NORTH AMERICAN AVIATION

By

Gerald V. Anderson
Senior Research Engineer
North American Aviation, Inc.
Los Angeles, California

ABSTRACT

Preliminary tensile data for electron beam welds in PH15-7Mo stainless steel and titanium alloy 6Al-4V were obtained. It is possible to achieve nearly 100% of heat treated parent metal strength from welds made after heat treatment. Welds were made with depth-to-width ratios as high as 25 to 1. In addition, the amount of transverse weld shrinkage is less than .002 of an inch.

The precise control of the electron beam process makes it possible to join thick to thin material with practically no distortion in the thin member. The electron beam process also allows the joining of complex configurations without regard to minor variations in beam focal length. A sine wave web member was fillet welded to brazed honeycomb cap sections by laying the assembly on its side and allowing the beam to traverse the joint; following the hills and valleys of the seam. In addition, four butt welds in .030 inch thick stainless steel sheets have been made simultaneously from one side. These sheets were stacked on top of each other and were separated by a distance of one inch between each sheet.

Various types of sandwich structures, such as corrugated and egg crate, have been electron beam welded.

ELECTRON BEAM WELDING OF AEROSPACE STRUCTURES

In designing and building the X-15 rocket research vehicle and the XB-70 shown in Figure 1, North American Aviation is leading the way in Mach 3+ technology. Because of the high skin temperatures due to air friction at speeds above Mach 2.5, conventional materials and structures are no longer adequate. Weight, always an important factor in the aircraft industry, becomes even more critical as the design speed of the vehicle is increased. Thus new manufacturing and fabrication techniques that offer potential reductions in weight must be developed and exploited. We feel the electron beam welding process offers this potential.

Consequently, in mid-1960, the Los Angeles Division purchased two 150,000 volt electron beam welding machines. These machines, shown in Figure 2, are presently installed in the Research and Development Laboratory, however, very shortly they will be moved to our Palmdale facility where they will be used for making the final close-out welds on the wing to fuselage joints of the XB-70. I'll discuss this in more detail later.

Although most of our work has been on materials for the XB-70, at last count we had electron beam welded over 50 different materials and material combinations, see Figure 3.

Some of the remarkable tensile properties achieved in PH15-7Mo stainless steel by the electron beam process are illustrated in Figure 4. Butt welds were made in .030 to .250 inches thick panels, heat treated to 200,000 psi before welding. No filler wire was added. The weld

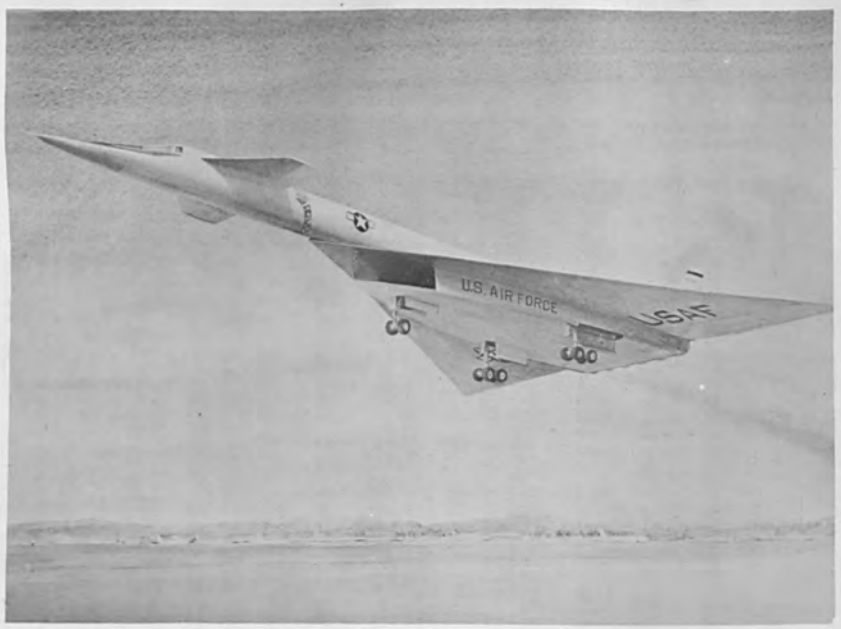

Figure 1. XB-70 Air Vehicle.

Figure 2. High Voltage Electron Beam Welding Machine.

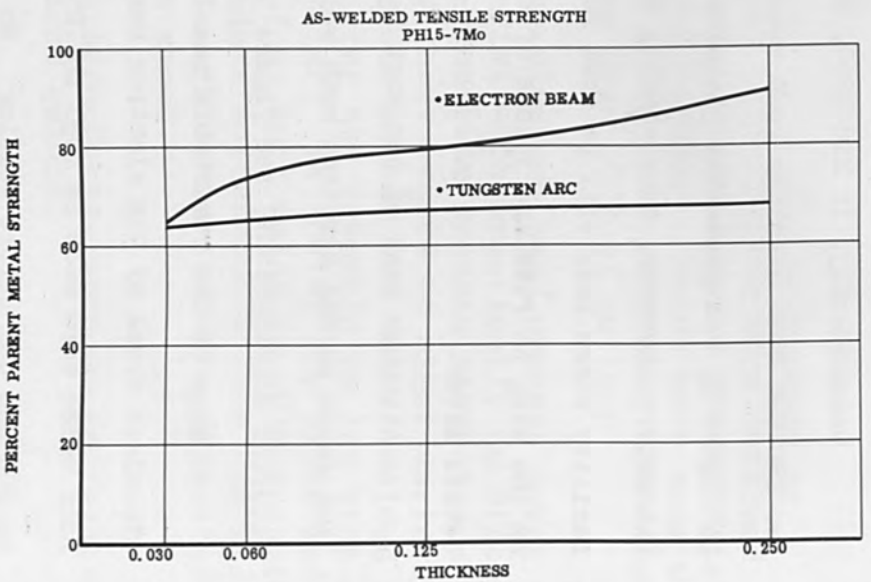

Figure 4. As Welded Tensile Strength - PH15-7Mo

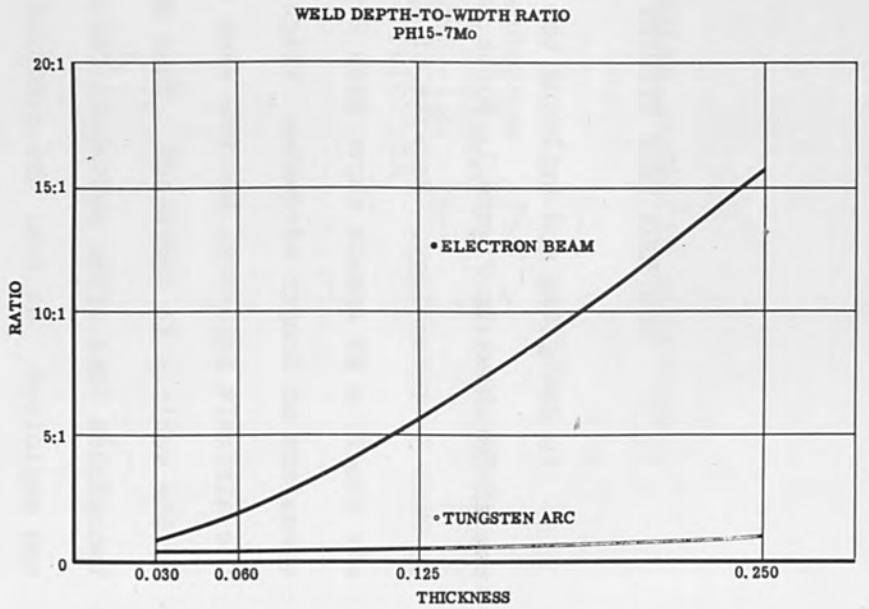

Figure 5. Weld Depth-to-Width Ratio -PH15-7Mo

Figure 3

MATERIALS THAT HAVE BEEN ELECTRON BEAM WELDED BY NORTH AMERICAN AVIATION, INC.

STEEL

PH15-7Mo
17-7PH
AM 350
301
302
321
347
4130
H-11
RENE 41
HASTELLOY

TITANIUM

6Al-4V
4Al-3Mo-1V
A110-AT

ALUMINUM

2024
6061

MISCELLANEOUS

BERYLLIUM COPPER
COBALT
CONETIC "AA"
COPPER
INCO 718
MAGNESIUM
NICKEL
N-155

REFRACTORY ALLOYS

UNALLOYED COLUMBIUM
Cb-1Zr
Cb-5Zr
Cb-8½Ti-1½Zr
Cb-10Ti
Cb-10Ti-5Zr
Cb-10Mo-10Ti
F-48
FS-82

UNALLOYED MOLYBDENUM
Mo-TZC
Mo-TZM
Mo-½Ti
UNALLOYED TANTALUM
UNALLOYED TUNGSTEN
UNALLOYED VANADIUM
UNALLOYED ZIRCONIUM
Zr-3Zl

COMBINATIONS

ALUMINUM TO COPPER
ALUMINUM TO STAINLESS STEEL
COLUMBIUM TO STAINLESS STEEL
COPPER TO STAINLESS STEEL
COPPER TO INCONEL
TUNGSTEN TO Mo-TZM

CERAMICS

ALUMINA
CORDIERITE
MOLYBDENUM DISILICIDE
ZIRCON

beads were machined flush with the parent metal before tensile testing at room temperature. There are two probable reasons for the apparent increase in strength exhibited by the thicker material. First, the weld and heat affect zone is extremely narrow and deformation of this partially annealed band is mechanically restrained by the unaffected parent metal. Second, since the width of an electron beam weld is practically the same for all thicknesses of material, the unaffected parent metal acts to an even greater degree as a restraint for the heavier gages than for the thinner.

We have made welds in material with a weld depth to width ratio as high as 25 to 1. Figure 5 illustrates the ratios obtained on the tensile specimens previously discussed. As in the preceding Figure a corresponding curve for tungsten-arc welds is shown also. The widths of the heat affected zones (including the welds) for various thicknesses of electron beam and tungsten-arc welded PH15-7Mo are shown in Figure 6. Here the widths are expressed as a function of the sheet thickness. Notice that for electron beam butt welds in .250 inch material the width of the heat affected zone is only 1/4 t or .080 inches wide. And, of course, since only a narrow band of material is heated and melted in the electron beam process, the amount of transverse weld shrinkage is extremely small. Figure 7 compares the amount of shrinkage for electron beam and tungsten-arc welds. It is interesting to note that for electron beam welds the amount of shrinkage is practically independent of sheet thickness.

Preliminary tensile data for electron beam welds in 6Al-4V titanium alloy showed 100 percent joint efficiency for welds in both the

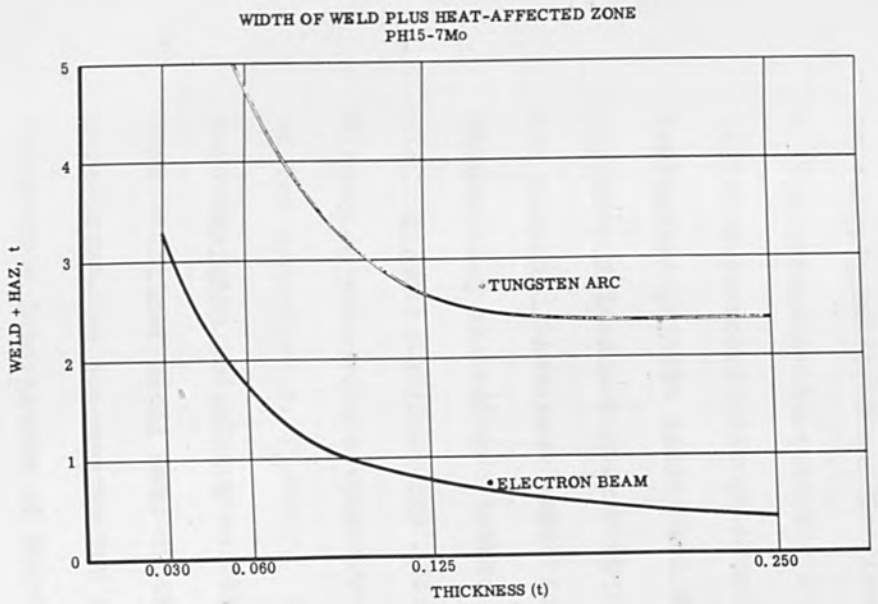

Figure 6. Width of Heat Affected Zone - PH15-7Mo

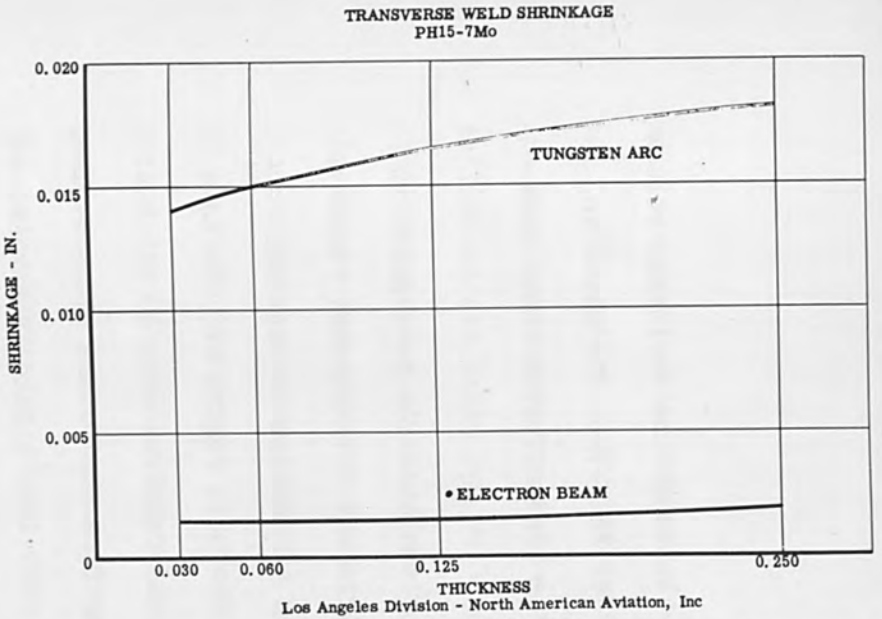

Figure 7. Transverse Weld Shrinkage - PH15-7Mo

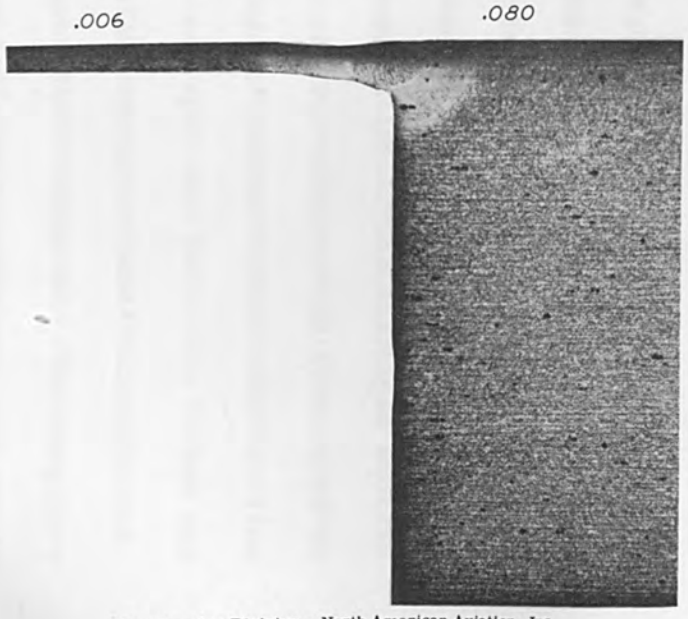

Los Angeles Division - North American Aviation, Inc

Figure 8. Thick to Thin Combination.

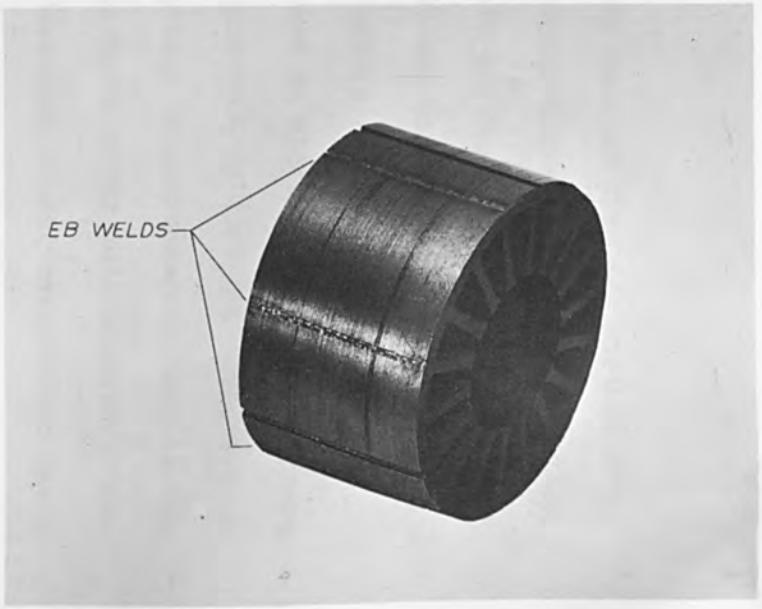

Figure 9. Stator Core Laminates.

as-welded and the heat treated condition. Although the shrinkage values for titanium welds were the same as those for PH15-7Mo, the depth to width ratios were less and the widths of the heat affected zones were slightly greater than those for PH15-7Mo.

The precise control of the energy of the electron beam makes it possible to join materials of radically different thicknesses. We have butt welded .006 foil to .080 sheet with no distortion in the foil member. A cross section of this joint is shown in Figure 8. The beam was directed at the top side of the joint and required only 40 watts of power to weld the pieces together. Welding from the bottom side resulted in an extremely large weld since the full .080 inch thickness was melted. In addition, it required 10 times more power to do it.

Figure 9 shows one type of the several small production parts now being electron beam welded for the XB-70. This part consists of silicon-iron laminates stacked together to make up the stator core assembly for electrical actuator motors. Conventional welding techniques for holding the laminates together at high rpm were unsuccessful. The uneven and inconsistent weld penetration and width resulted in non-uniform magnetic paths. The electron beam process allows the penetration to be controlled to within .001 to .002 inches and results in small uniform welds that do not adversely affect the magnetic properties of the core.

The electron beam process also allows the joining of complex configurations and neglects minor variations in beam focal length. Figure 10 illustrates a so-called sine wave web attachment to honeycomb panels. The usual method for joining this type of configuration is to

weld the cap section to the sine wave web from the opposite side of the cap. This method, referred to as blind-tee welding, requires critical tracking devices to trace the sine wave pattern. However, if the part is laid on its side, you no longer see a sine wave joint but a straight line that varies up and down in the vertical plane. The part shown in the figure was electron beam welded in just this manner. The beam was focused at about the midpoint of the sine wave height and then allowed to traverse the joint. No further adjustment was made as the beam moved up and down the hills and valleys of the seam. After welding, the honeycomb core was cut away and revealed no damage to the brazing alloy on the underneath side of the face sheet due to welding.

The electron beam welding process is capable of producing energy densities greater than 25 megawatts per square inch. Figure 11 shows a type of sandwich panel consisting of a sine wave web with flat sheets electron beam welded to it at the nodes. The part was then cut longitudinally down the center and subsequently rewelded by the electron beam. The beam welded not only both flat sheets simultaneously from one side, but also the sine wave member, following the contours of the web. Figure 12 further demonstrates the tremendous power concentration of the electron beam and the depth of field that is available with this process. Sine wave webs were electron beam welded to honeycomb panels in the manner described previously. Two of these specimens were then butted together with the sine wave members in the vertical plane. The electron beam was directed at the top of the upper honeycomb panel. The beam penetrated the top and bottom face sheets of the top panel and the top and bottom face sheets of the bottom panel making all four butt welds

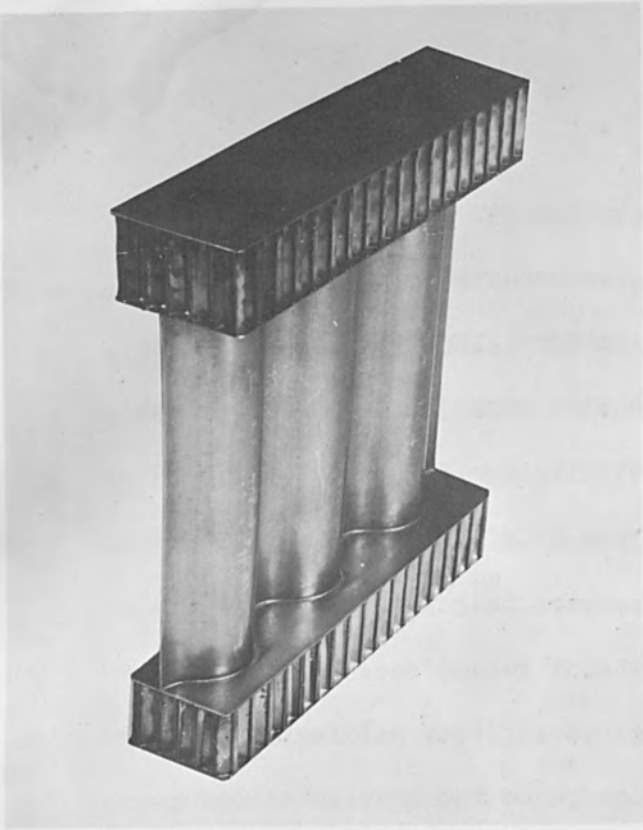

Los Angeles Division - North American Aviation, Inc

Figure 10. Sine Wave Specimen

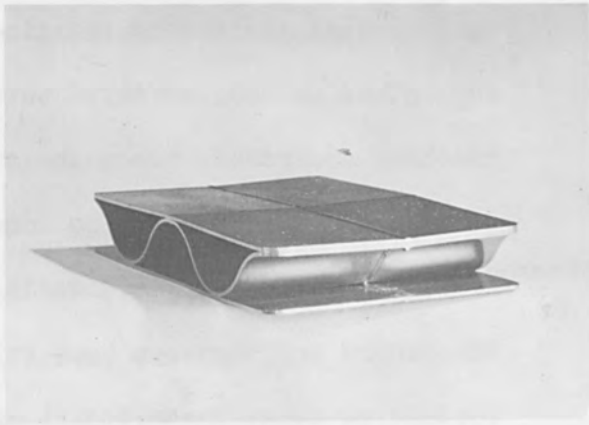

Figure 11. Simultaneous Three Weld Specimen

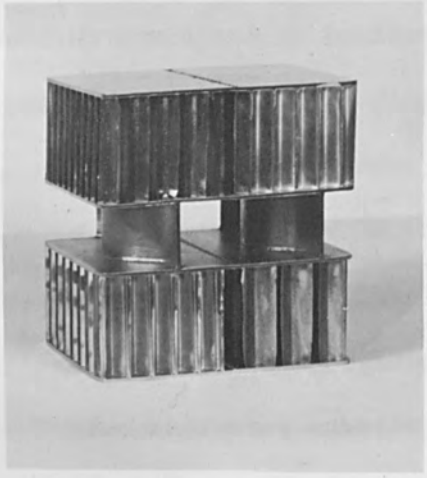

Figure 12. Simultaneous Four Weld Specimen

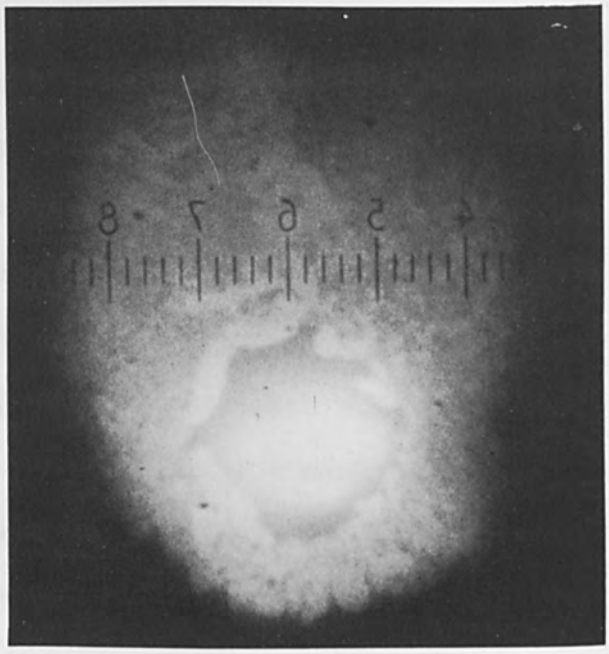

Figure 13. View Through Microscope - 40 X

simultaneously from one side. An interesting phenomenon was observed with the aid of a 40 power steromicroscope during this welding operation and is shown in Figure 13. The electron beam vaporized a small hole through the center of the molten weld metal allowing the beam to penetrate to the next joint. The hole was filled in again by the molten material as the beam moved along the joint. Figure 14 is a time exposure of this welding operation. Notice the interesting lines caused by the spatter of minute particles of molten metal.

A corrugated sandwich structure of columbium alloy FS-82, shown in Figure 15, has been electron beam welded. This structure consisted of .030 inch face sheets and corrugated core. The beam can be controlled to give either full penetration through both the face sheet and the core or through just the face sheet and into the core.

Another sandwich structure that has been welded is shown in Figure 16. This particular structure is made of 6Al-4V titanium alloy. The core consists of .020 inch thick by 1 inch high pieces slotted and fitted together much like the cardboard separators in an old fashioned egg crate. The .040 inch face sheets were electron beam welded to the core using the blind-tee technique. We have also made this type of structure in a molybdenum alloy.

Magnesium has been successfully electron beam welded also. The part, shown in Figure 17, is an AZ31B magnesium alloy float mechanism and consisted of butt welding a circular plug in a hollow ring. Suprisingly enough, there was no unusual amount of volitilization of molten metal. Magnesium is generally considered hard to weld by the electron beam process because of its high vapor pressure.

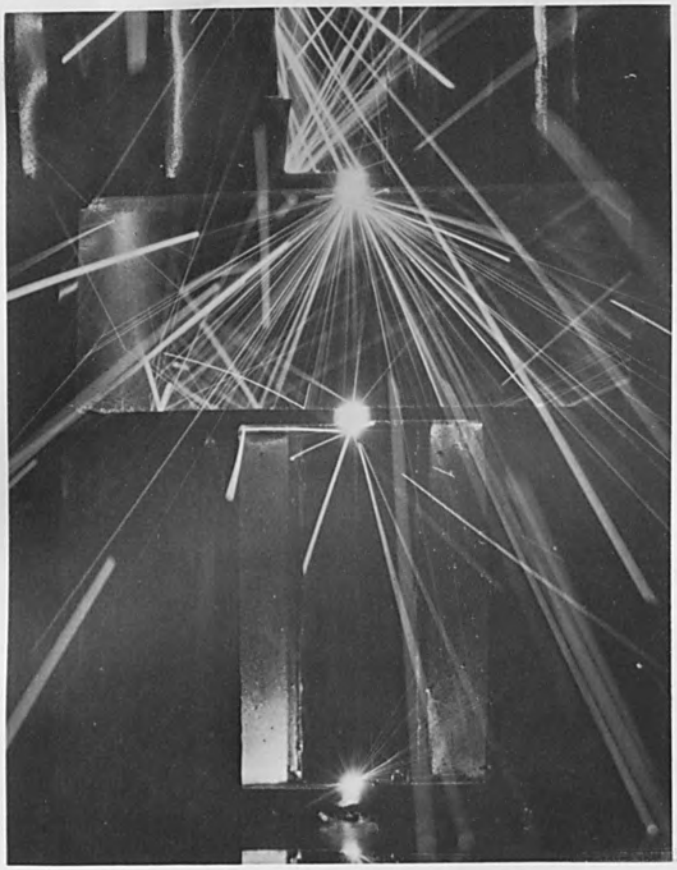

Figure 14. Time Exposure of Simultaneous Weld.

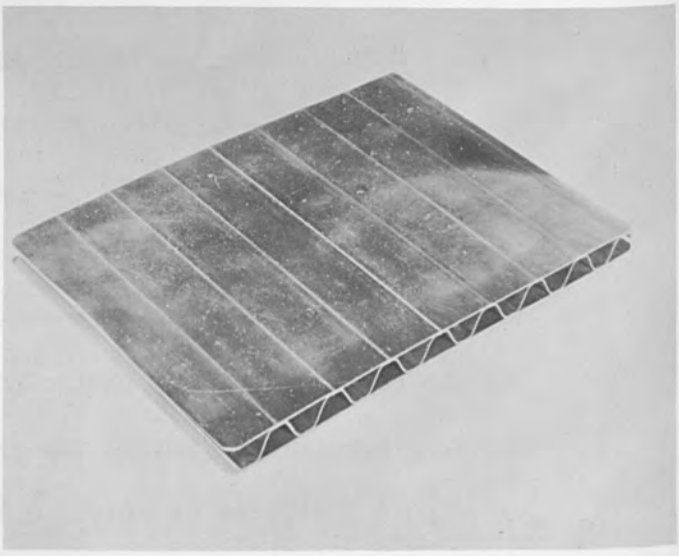

Figure 15. Columbium Corrugated Sandwich.

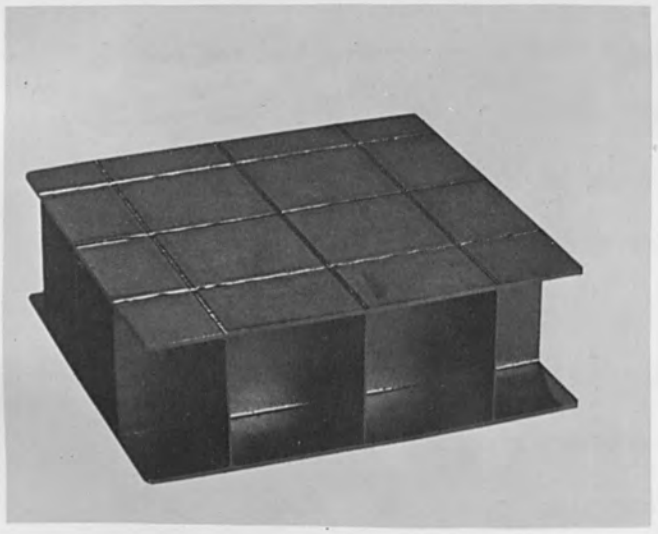

Figure 16. Titanium Egg Crate Sandwich.

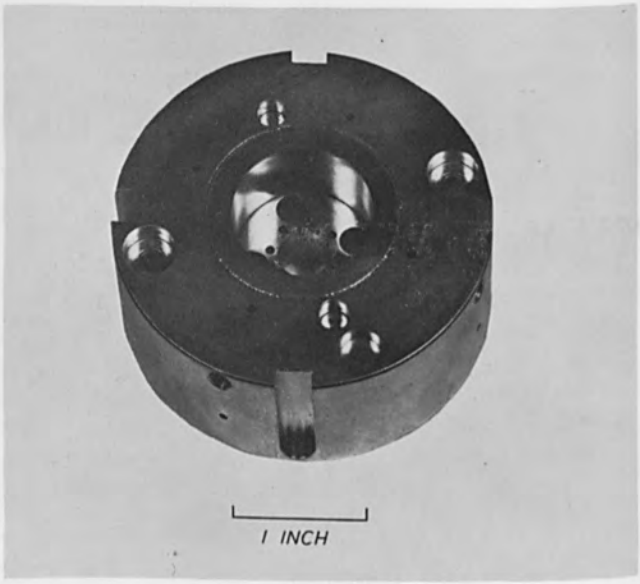

Figure 17. Magnesium Float Assembly.

Cursory studies have also been made of the weldability of various ceramic materials. Figure 18 shows four ceramic materials that have been successfully joined by the electron beam process. These samples were welded merely to see if it could be done. No physical tests were planned or intended at this stage.

Just recently, in the Research Laboratory, we have installed a 10 foot vacuum chamber for use with the electron beam process. The inside dimensions of this chamber, shown in Figure 19, are 3 x 3 1/2 x 10 feet. It is capable of welding parts as large of 1 1/2 feet high by 3 feet wide by 5 feet long. The time required to pump the chamber to 1×10^{-4} torr is approximately 6 1/2 minutes. It has a 300 cfm roughing pump and a 10 inch diffusion pump rated at 1400 liters per second. A periscope has been installed for remote viewing of the work. The interior of the chamber, Figure 20, shows the x-y table for moving the parts to be welded under the beam. The table speed is variable from 0 to 70 inches per minute.

We believe that no one type of system can adequately do every job. Therefore, we are investigating the feasibility of using low voltage equipment for some of our applications. At the present time we are evaluating in the laboratory a 30 Kv unit manufactured in Southern California. This system is shown in Figure 21. One advantage of this type of equipment is its small size. To date the results appear very encouraging.

North American Aviation has developed a method whereby electron beam welding can be used for fabricating parts too large to fit into standard vacuum chambers. A small, portable, half-shell type clamp-on

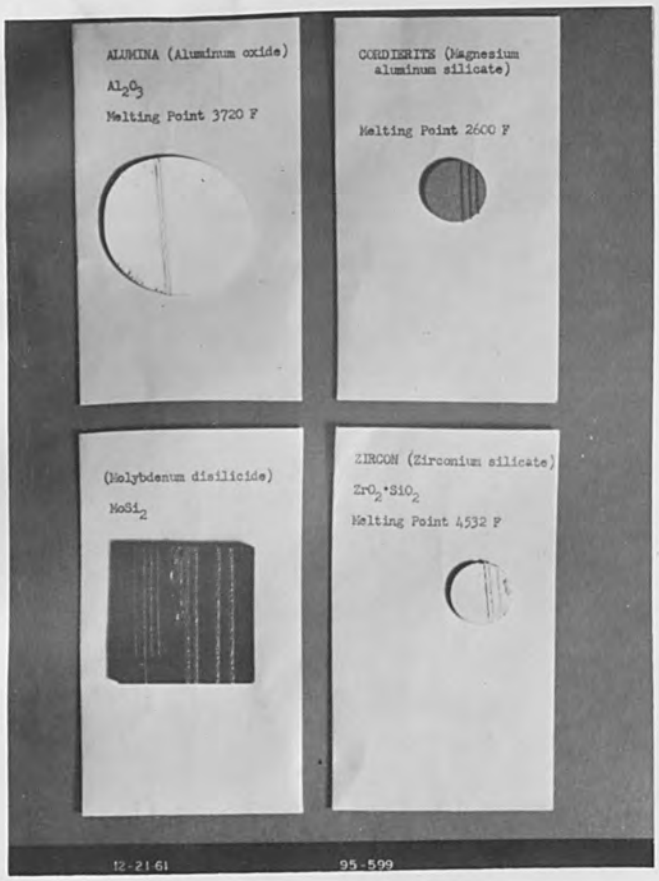

Figure 18. Welded Ceramic Materials.

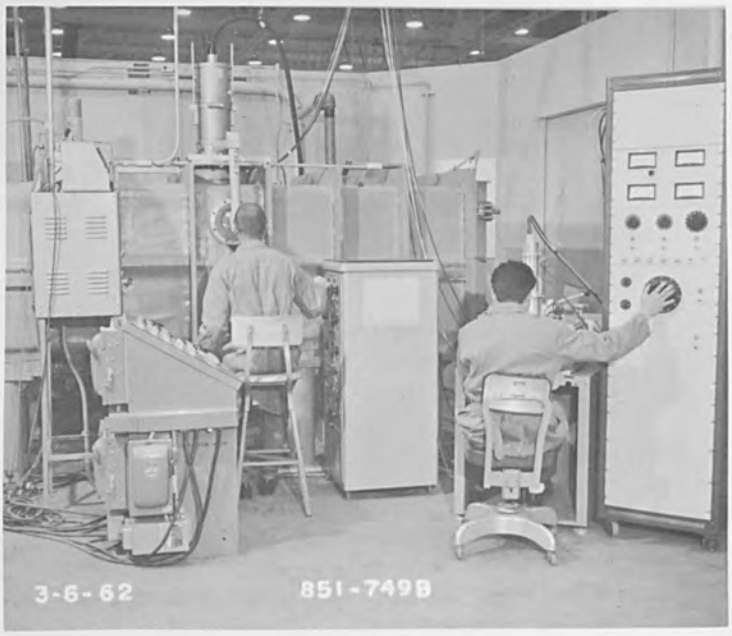

Figure 19. Exterior View of Ten Foot Vacuum Chamber.

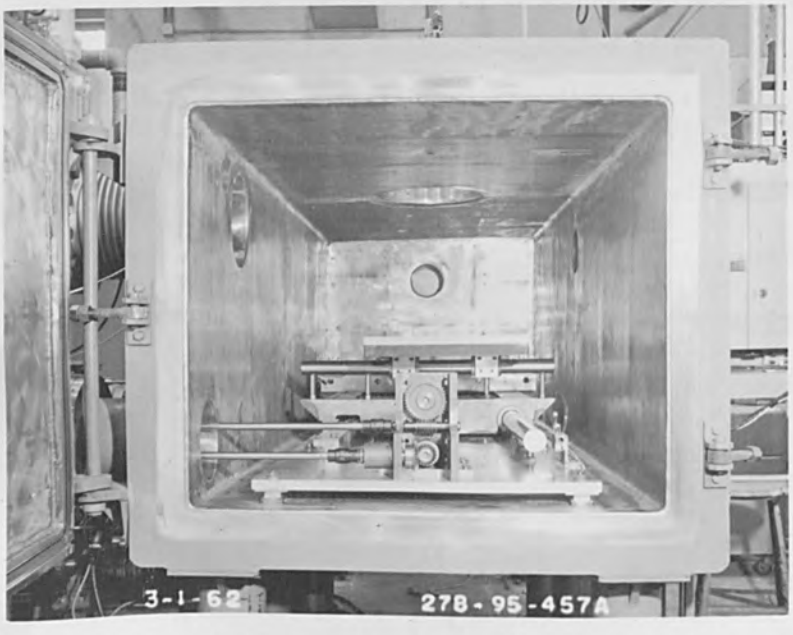

Figure 20. Interior View of Ten Foot Vacuum Chamber.

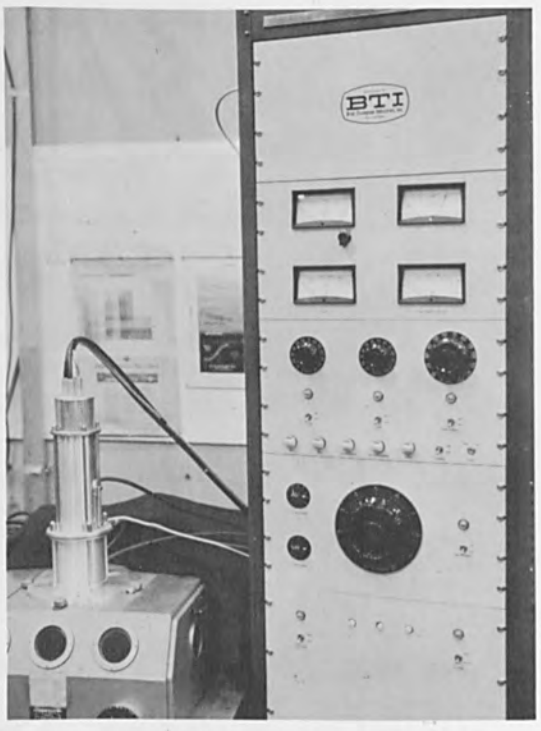

Figure 21. Low Voltage Electron Beam Welding Equipment.

Figure 22. Prototype Portable Vacuum Chamber.

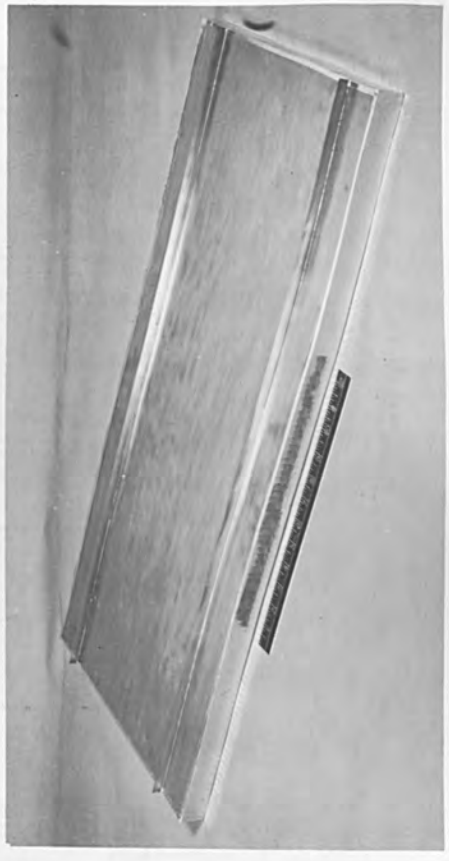

Figure 23. Tee Attachments to Honeycomb Panel.

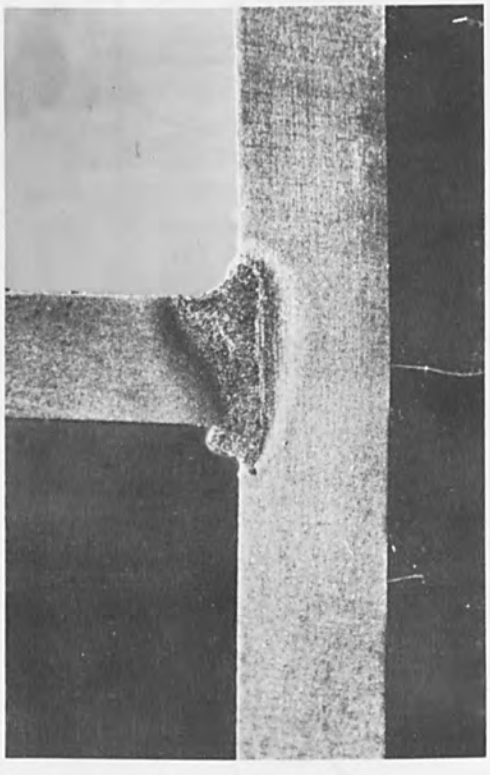

Figure 24. Electron Beam Fillet Weld.

Figure 26. Photomacrograph of Simulated Wing to Fuselage Weld.

Figure 25.

WING TO FUSELAGE JOINT

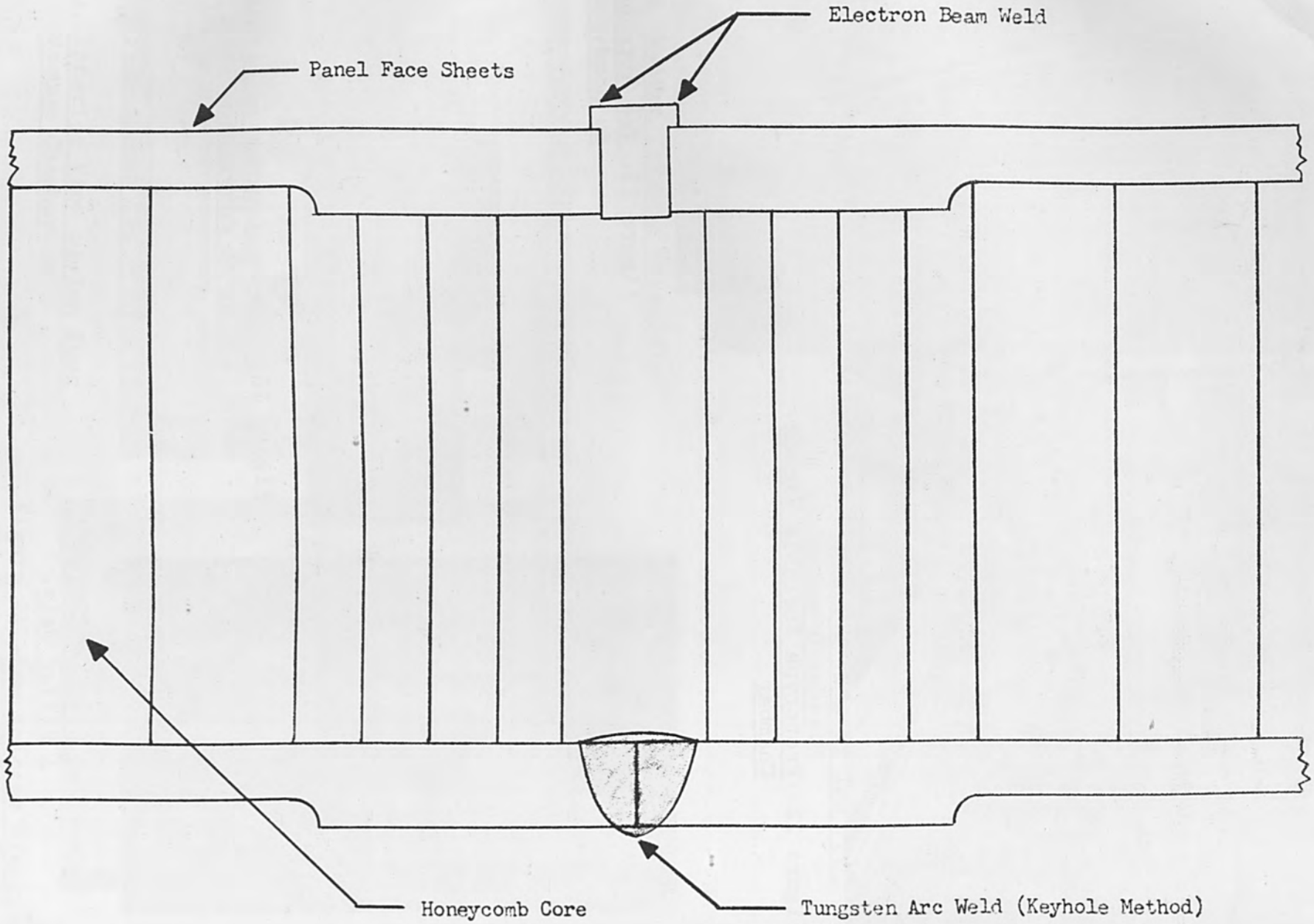

chamber is fitted over the part to be welded and the cavity is evacuated. In this manner the work piece acts as the bottom half of the chamber. The first laboratory prototype chamber, which was developed for attaching tee members to brazed honeycomb panels, is shown in Figure 22. The electron gun is mounted on a lid that slides along the top of the chamber. At the completion of the weld the vacuum is released and the chamber is moved to a new position, evacuated again, and the weld is continued. Figure 23 shows a honeycomb panel to which two tee members have been attached by electron beam fillet welding using the portable chamber. This panel, longer than the chamber, required the repositioning of the chamber at least once along each weld. Figure 24 illustrates the type of fillet weld possible with the electron beam process. This sample, welded from one side in the standard vacuum chamber, shows the shallowness of the heat penetration in the face sheet possible with this process.

North American Aviation has enough confidence in the feasibility of the portable chamber concept, that in order to reduce weld shrinkage and distortion, we are going to use the electron beam process for making the final closeout weld on the wing to fuselage joint of the XB-70. A sketch of the cross section of this joint is shown in Figure 25. The bottom face sheet will be tungsten-arc welded by the keyhole method. A tee shaped filler strip will be placed in the gap, a portable chamber clamped over the joint, and the area will be evacuated. Electron beam welds will be made on each side of the filler strip on both upper and lower outer mold line surfaces. A macrosection of this type of weld is shown in Figure 26.

In summary, the electron beam welding process is rapidly moving out of the laboratory stage into production. There are many applications where it offers tremendous advantages over conventional welding techniques and some areas where it is the only process that will do the job. However, electron beam welding is not a cure-all. Many times designers, carried away with the uniqueness of the method, demand electron beam welding where more conventional joining processes would do just as well.

ELECTRON BEAM WELDING OF ALUMINUM, BERYLLIUM, AND ALUMINA

By

H. A. Hokanson
Assistant Project Engineer

W. I. Kern
Metallurgical Engineer

S. L. Rogers
Development Installation Engineer
Electron Beam Department
Hamilton Standard Division
United Aircraft Corporation
Windsor Locks, Connecticut

ABSTRACT

Results of a program directed at electron beam welding of high-strength aluminum alloys, of pure beryllium, and of alumina to itself and to metals are reported in detail.

Welding was conducted with a 3 KW high-voltage, high-power density electron beam welding machine. The range of machine parameters utilized in the aluminum welding program were: accelerating voltage to 150,000 volts, beam current to 20 milli-amperes, and travel speeds to 120 inches per minute. Additionally, various beam oscillation and pulsing conditions were employed.

Alloys welded were 7075 and 6061 aluminum, 85%, 96% and 99.5% alumina, and commercially available beryllium. Initial investigations were concentrated on the development of optimum welding techniques for each material. For the aluminum, particular emphasis was placed on (1) inducing wettability by destruction of the oxide coating in the weld bead area and (2) reduction of fusion-induced annealing or overaging by minimizing energy input through the use of minimal beam diameter and maximum possible welding speeds. For the alumina welding both to itself and to metals, primary emphasis was placed on eliminating cracking by the use of controlled pre and post-heating. The major emphasis in the beryllium welding was placed on producing welds of maximum strength and ductility by minimizing energy input to the fusion zone.

ELECTRON BEAM WELDING OF ALUMINA, ALUMINUM, AND BERYLLIUM

INTRODUCTION

This paper reports recent results of work being conducted on the electron beam welding of three materials - alumina, aluminum, and beryllium - at Hamilton Standard Division of United Aircraft Corporation. The welding programs from which the data were taken are still in progress; therefore the reported information will be supplemented, and perhaps modified, by future results. Since the alumina, aluminum, and beryllium programs were conducted as completely independent programs, the details of each investigation are discussed in separate sections.

EQUIPMENT

Except for provisions for preheating during the alumina welding, the welding equipment was essentially the same for all three of the investigations. The equipment, Figure 1, was a Hamilton-Zeiss high-power-density electron beam welding machine rated at three kilowatts, with accelerating potentials to 150,000 volts negative and beam currents to 20 milliamperes. Beam spot size can be controlled by electromagnetic focusing to a diameter of less than 0.010 inch. The principles of formation, acceleration, and focusing of electron beams are well known. However, to provide a thorough understanding of the techniques used in the welding programs, features of the equipment which were of particular importance in performing the welding are discussed below.

A schematic of the electron gun is illustrated in Figure 2. The electrons are formed and accelerated and the initial focus is determined by the triode-type electron gun in the upper portion of the schematic. The triode gun design permits regulation of the beam current independent of the accelerating potential. Thus beam current can be continuously varied from zero to 20 milliamperes at any accelerating potential. The grid also permits pulsing of the beam by the cyclic variation of grid voltage.

Weld location is precisely controlled by the use of optics designed so that the workpiece is viewed coaxially with the electron beam at magnifications of 20 or 40 power. The optics not only permit exact location of the beam impact point but also permit viewing of the joint during welding. This is of particular value in studying the phenomena occurring at the time of the actual formation of the weld.

Another feature of the electron gun which was used extensively during the welding programs is the electromagnetic beam deflection system. Excitation of deflection coils with an a-c electrical signal induces beam deflection at corresponding frequencies and wave shapes to a maximum amplitude of $\pm$ 0.25 inch. The deflection system supplies the capability of increasing the equivalent beam diameter with a wide variety of a-c signal patterns and thereby provides wide control of heat distribution to the workpiece. Another important use of the deflection coils is the programming of the beam about a circle by excitation of the coils with two 60-cps sine waves 90 degrees out of phase. By simple potentiometer adjustment,

Figure 1: Hamilton-Zeiss
Electron Beam Welding Machine

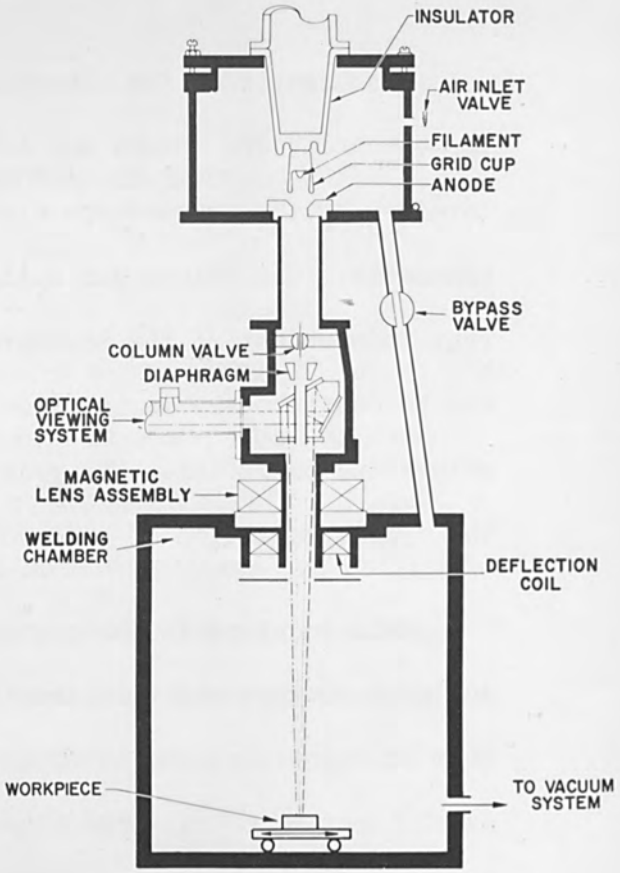

Figure 2:
Welding Machine Schematic

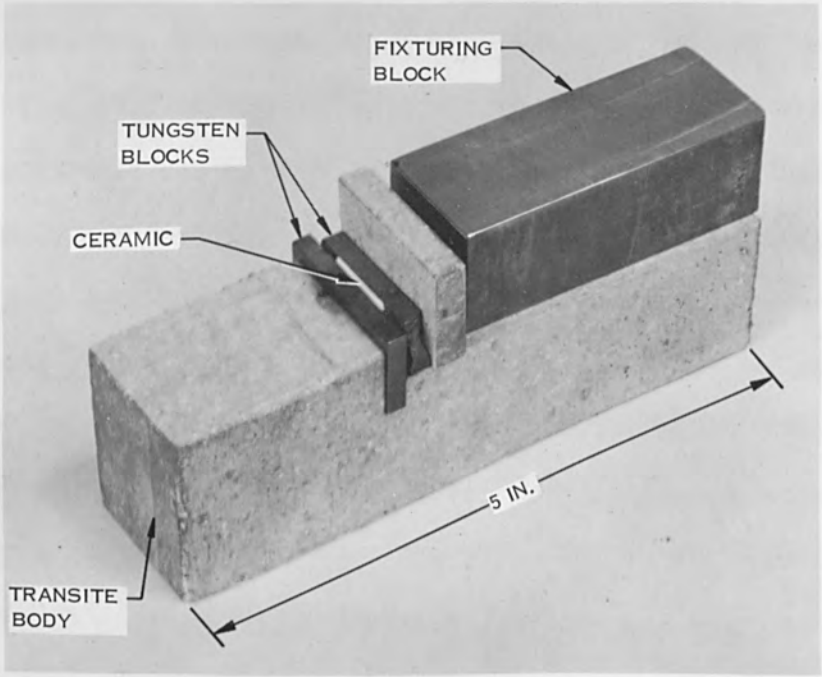

Figure 3: Fixture for Electron Beam Preheating of Al_2O_3

the diameter of the circle can be infinitely varied up to approximately 0.5 inch.

ALUMINA WELDING

Background

Ceramic materials are being used extensively by the electronics industry in the construction of power electron tubes, microwave windows and similar components. The advantages of ceramics in these applications include high dielectric strength and superior elevated temperature properties. These advantages have not been fully realized because of difficulties in joining separate ceramic sections into structurally sound, vacuum-tight components. Current metallized and brazed joints present problems of matching thermal expansion. Further, brazed joints exhibit lowered arcover thresholds and reduced useful service temperatures. Also, the joints are subject to electrode capacitance effects which limit electrical performance.

Electron beam welding is one of the few methods available for direct fusion welding of ceramics. Actual welding of ceramics is attractive for it will minimize many of the difficulties associated with brazing. Gas or plasma torches can fuse certain ceramics; however these methods lack the precise controllability and cleanliness available with electron beam techniques. Because of these considerations, a program was initiated to develop and evaluate electron beam welding procedures for the joining of ceramic materials, including alumina, quartz, and magnesia, to themselves and to metals. Preliminary information from the alumina phase of the welding program

is reported in this portion of the paper.

Experimental Procedure

Alumina materials studied in this program include 85% and 96% grades and Lucalox[1], an extremely high-purity aluminum oxide. Residuals contained in the 85% and 96% aluminas were calcium and magnesium oxides and glassy-phase materials. The alumina materials were in the form of wafers in thicknesses of 0.010 inch, 0.025 inch and 0.030 inch.

Welding techniques were established by an investigation of the effects of welding conditions on weld characteristics. Welding parameters investigated included accelerating voltage (55 to 130 KV), beam current (0.05 to 3.0 ma), welding speed (5 to 30 ipm), longitudinal and transverse beam oscillation (0 to $\pm$ 0.050 inch at 60 cps to 500 cps), and preheating (ambient to 3300 F).

The study of the relationships between welding parameters and weld-zone characteristics was supported by several evaluation techniques. Determination of cracking was based on dye-penetrant inspection and on visual examination at high magnifications. Relative joint strength was determined by flexural bend testing. Hermeticity of the joints was confirmed by helium leak checking. By far the most useful tool in studying the welding process was the optics system of the welding machine, which permitted close examination of the actual welding process. This was extremely useful in studying the origin and propagation of cracks.

A requirement for preheating and controlled cooling was immediately

apparent from very early results. Without preheating, welds invariably showed evidence of cracking. Therefore, two preheating techniques were devised—electron beam heating and resistance heating.

The fixture used for preheating with the electron beam is shown in Figure 3. Specimens for edge welding are sandwiched between the tungsten blocks and held in place by the metal slab. Preheating is accomplished by impinging the beam on the tungsten blocks. Beam power is increased until the desired temperature is reached. Then the beam is adjusted to the required conditions and the weld is made. Although welding results were encouraging using beam preheating, inadequate heating and cooling control prevented the achievement of reproducible results. A particular problem was the delay time involved in changing from preheating conditions to welding conditions.

Resistance preheating techniques yielded much more precise control. Excellent results were obtained with the small furnace illustrated in Figure 4. The heating element is a tungsten filament wound on a zirconia coil form. Multiple heat shields of tantalum and molybdenum surround and cover the unit except for a small opening at the top to allow optical viewing and welding. Weld specimens are supported on a tungsten platform inside the coil form. Maximum temperature attainable with the furnace is 3300F. Direct-current electrical power is used to reduce field effects on the electron beam.

Results and Discussion

A representative edge weld produced in the program is illustrat-

ed in Figure 5; a typical butt weld is shown in Figure 6. For both types of welds, the results of the investigation to date indicate that the major factors controlling weld quality are accelerating voltage, beam current, welding speed, preheating temperature, and cooling rate after welding.

For a given beam power at a given welding speed, relatively high-voltage (90 KV), low current (2 ma) beams gave the most satisfactory welds. This appeared to be the case for welds produced both with and without transverse beam oscillation. As beam currents were increased (to 10 ma) and voltage was dropped (to 55 KV) less satisfactory welds resulted. Examination of the welding process through the optics indicated that the solidification phenomena with lower-voltage beams was non-uniform. This resulted in rough and irregularly undercut weld beads with heavy evidence of cracking. Because of the extreme difficulty in producing meaningful photographs of weld cracks, no illustrations of defective welds are included.

With regard to welding speed, best results were achieved at higher travel rates. Lower speeds (15 ipm) produced a glassy structure such as that illustrated in the 96% alumina of Figure 7. No cracks are evident in the weld zone; however, flexural testing indicated that glassy welds are relatively weak. The tendency toward formation of glassy welds increases in the less pure aluminas.

Figure 8 illustrates a weld made in identical material as in Figure 7 and at an identical beam power. The increased welding speed

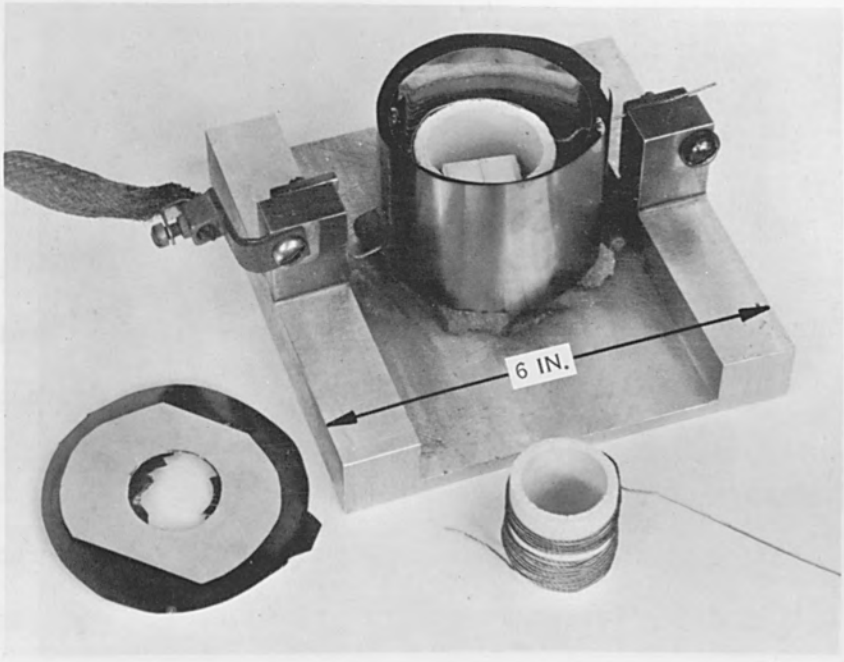

Figure 4: Resistance Furnace for Controlled Heating of Al_2O_3

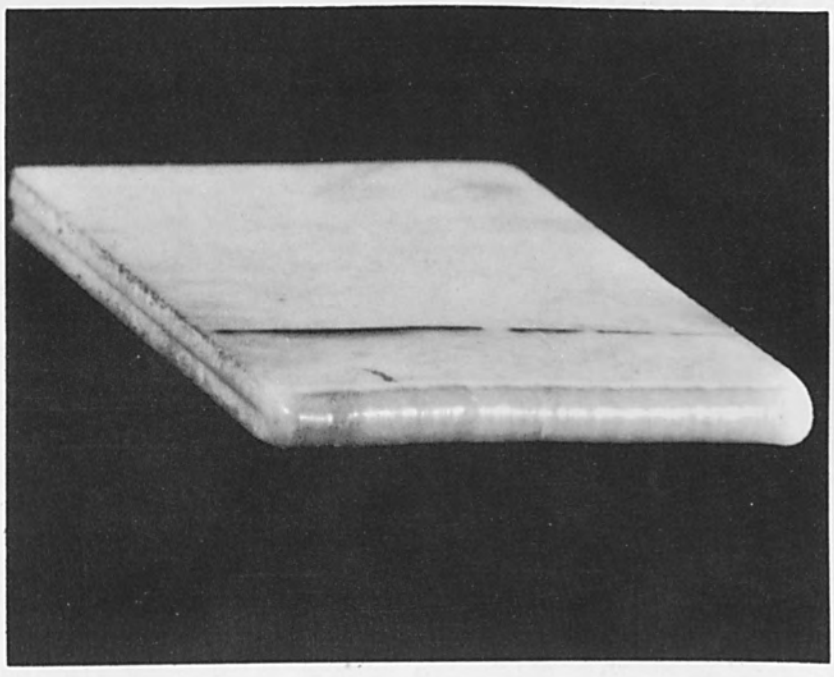

Figure 5: Edge-Welded Al_2O_3

(30 ipm) has limited glass formation. Both welds of Figures 7 and 8 were made with 1800°F preheat. The advantage of higher welding speed appears to result from the decreased time the weld zone is above the 1800F preheat temperature. This limits the time available for segregation of the glassy constituents and for grain growth.

Despite the high thermal-shock resistance of alumina, preheating and controlled cooling were very important in limiting crack formation. Preheating temperatures of at least 1800 F were required for the 96% alumina and temperatures above 2000F appeared to be necessary for welding of the Lucalox. Cooling rates of greater than 50 F induced cracking at temperatures above 1200 F. Below 1200 F cooling rates were less critical.

Flexural bend testing of welded ceramics indicated that relatively good joint strengths can be obtained. Under simple beam bending the base ceramic achieved a surface stress of approximately 50,000 psi. Electron beam welded joints withstood as much as 19,700 psi. Retention of 40% of the base strength is very promising for the early stages of the program. Further work should lead to even better results.

Alumina to Metals

Limited tests were also conducted on the joining of alumina to metals. Using techniques similar to those used in the pure alumina welding, crack-free joints have been produced between 96% alumina and tungsten, molybdenum, and columbium. Undoubtedly the successful

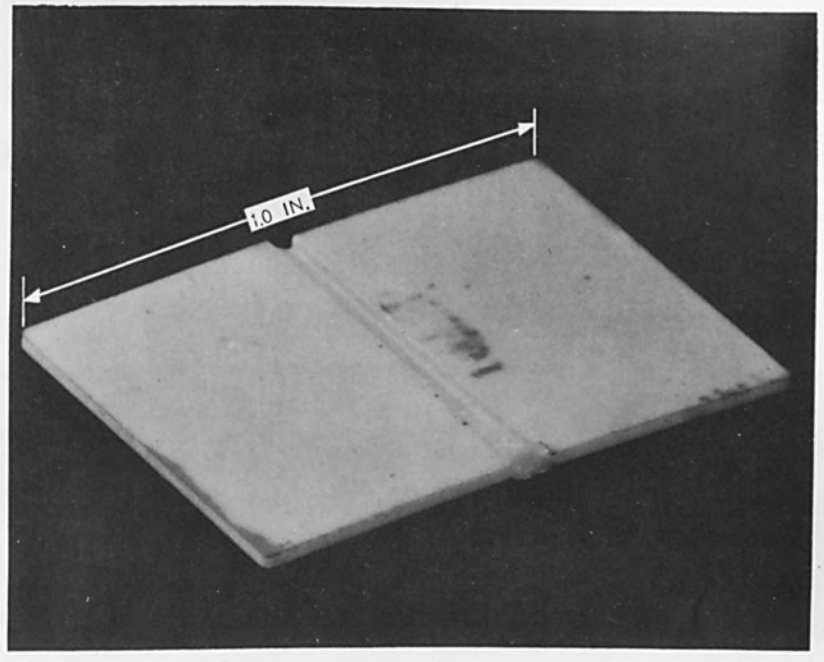

Figure 6: Butt-Welded Al_2O_3

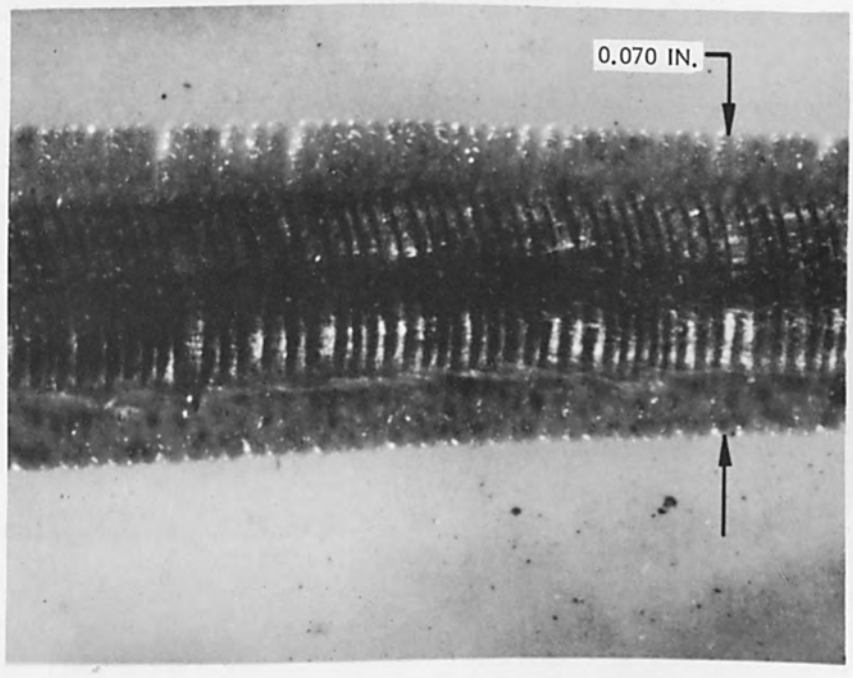

Figure 7: Al_2O_3 Weld-Bead Surface

(1800F preheat, 90 KV, 2 ma, 15 ipm, 0.040" transverse oscillation)

ALUMINUM WELDING

Background

Conventional fusion welding techniques for most aluminum alloys are well established and yield satisfactory results in many applications. However certain aluminum alloys, particularly the 7000 series, are very difficult to join by normal fusion welding methods. Moreover, even with the readily weldable alloys, such as 6061, conventional fusion welding is sometimes unsatisfactory for a particular application because of unacceptable distortion, excessive heat input, or related problems.

Many of the difficulties allied with conventional fusion welding are associated with factors which are minimized by electron beam welding. The extreme localization of the weld zone by high-voltage electron beam welding in combination with the low total energy input should not only minimize distortion but should also inhibit deterioration of mechanical and metallurgical properties. Therefore a program was initiated to develop and evaluate electron beam welding techniques for aluminum. Results obtained from the 7075 portion of the program, as well as a practical application of electron beam welding of aluminum, are presented in this portion of the paper.

Experimental Procedure

The work was conducted on 0.062-inch Alclad 7075 aluminum sheet. Welding was conducted in the T6, W and O tempers[2]. All welds were produced by butt welding flat specimens perpendicular to the sheet rolling direction. No filler materials were employed; furthermore no

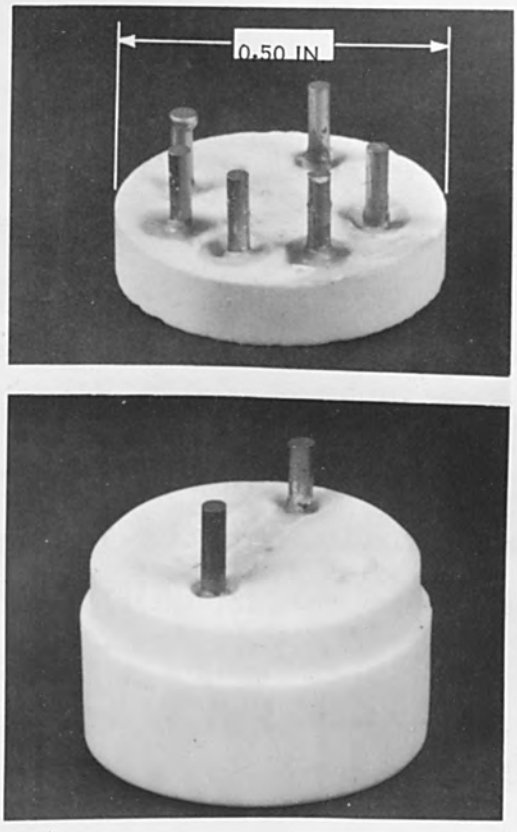

Figure 10: Electron Tube Molybdenum Feed-Throughs

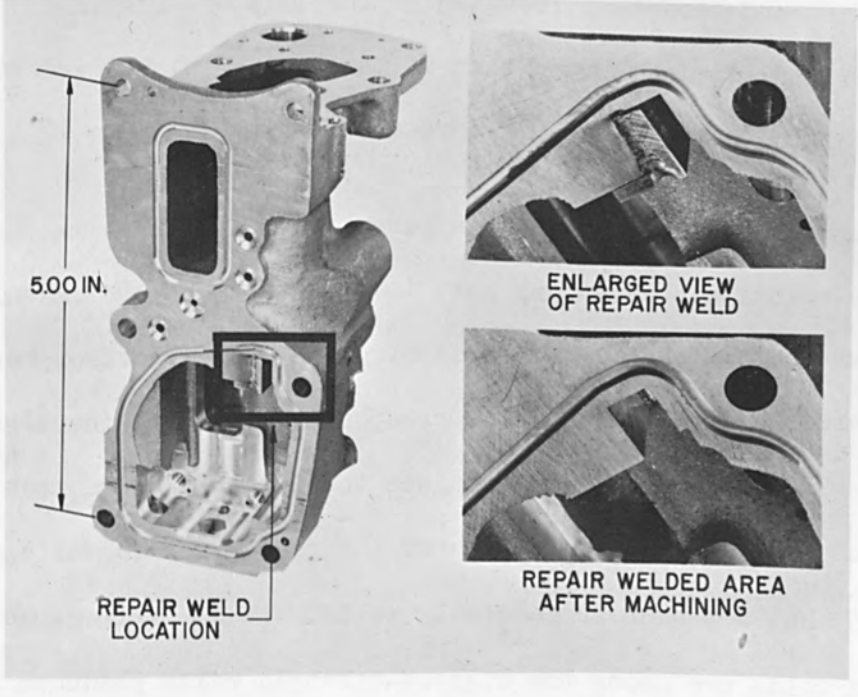

Figure 11: Repair Welding of Aluminum Castings

pre or post-heating was used. After welding, the specimens in the T6 temper received no further heat treatment; those in the W temper were aged to T6; and the welds in the O temper were solution treated and aged to T6. Following welding and heat-treating, the welds were subjected to visual and radiographic inspection for cracks and porosity. Then the specimens were tensile and bend tested. The transverse bend tests were conducted with a deflection rate of 0.5 inch per minute, a bend radius of 0.062 inch (equal to the sheet thickness) and a span between supports of 1.00 inch.

Results and Discussion

Visual and radiographic inspection of the welds indicated no incidence of cracking or porosity. The high purity of the vacuum welding environment undoubtedly contributed to this favorable condition. The tensile-test and bend-test results for the 7075 are listed in Table 1. For comparison, typical properties of the base metal and recently reported data[3] for conventional welding are also included.

Referring to Table 1, it is apparent that the welds in the 7075 that were solution treated and aged to T6 retained approximately 90% of the base-metal tensile and yield strength. The electron beam weld results are far superior to the corresponding tungsten-inert-gas (TIG) results. This is not surprising since the TIG welds were made with non-heat-treatable 4043 filler. However, the comparison is valid, since the 7075 alloy has not been successfully welded without filler, and the 7075/4043 welds are among the highest-strength welds produced to date.

TABLE 1

TENSILE AND BEND RESULTS FOR ELECTRON BEAM

WELDED 7075 ALUMINUM

SPECIMEN CONDITION	ULTIMATE STRENGTH (psi)	YIELD STRENGTH (psi)	ELONGATION (% in 1 in.)	ELONGATION (% in 1/4 in.)	BEND ANGLE AT FAILURE (degrees)
EB welded in T6, Tested as Welded	50,500	43,300	2.0	8.0	-
	51,100	43,200	2.0	8.0	-
	-	-	-	-	41
	-	-	-	-	46
EB welded in W, Aged to T6	49,400	44,000	4.0	12.0	-
	50,700	44,000	2.0	8.0	-
	-	-	-	-	37
	-	-	-	-	26
Welded in O; Heat-treated to T6	70,500	61,000	6.0	8.0	-
	69,700	59,700	6.0	8.0	-
	-	-	-	-	28
	-	-	-	-	27
O Base Metal	32,000	14,000	17	-	90
T6 Base Metal	76,000	67,000	11	-	58
TIG Welded in T6 4043 Filler Tested as Welded	37,000	29,000	2	-	-
TIG Welded in T6 Reheat-Treated to T6	44,800	29,100	4	-	-

Results from the 7075-T6 welds that were tested as-welded indicate that the strengthening effects of precipitation hardening were partially destroyed by the welding process. However, comparison with the base-metal data shows that complete annealing did not occur. In fact, the results are again superior to the corresponding TIG weld results.

The tensile results from the 7075 welded in the W temper and subsequently aged to T6 indicate that the weld did not completely respond to aging. Apparently, thermal effects of the weld pass altered the weld-zone metallurgy to a condition that was not totally receptive to solid-solution precipitation. Response to precipitation hardening after welding should increase with increased welding speeds, because less time at temperature would inhibit deterioration of the metallurgical conditions needed for the precipitation reaction.

The tensile-elongation and bend-test results indicate good ductility for all welds. A direct comparison with the base-metal ductility is difficult because of the unique weld-zone shape. This is particularly apparent from the as-welded 7075-T6. Since failure occurred in the weld at a strength below the base-metal yield strength, negligible elongation occurred in the surrounding base metal, and all of the strain was absorbed by the narrow weld zone. Thus the reported elongation values are extremely sensitive to the gauge-length measurement. Note that the bend-test results indicate that the as-welded 7075-T6 joints were the most ductile of the three conditions, a fact not apparent from the one-inch tensile-elongation values.

Aluminum Repair Welding

The low energy input in combination with the extremely localized

heating available from electron beam welding makes the process an ideal tool for repair welding of aluminum components. A representative example of repair welding is illustrated in Figure 11.

A slot, illustrated in the close-up, was machined to too wide a dimension in over 100 cast aluminum jet engine fuel control housings Since the slot served as a guide for an actuating lever, correct dimensions were required. The error was discovered after all other machining operations had been completed; therefore, conventional repair welding would have distorted nearby critical dimensions out of tolerance.

Each slot was repaired by electron beam welding oversize pads of 6061 aluminum into the slot. After welding, the slot was machined back to the correct dimension. Six castings were repaired in each machine pump-down by use of the fixture illustrated in Figure 12. This gave a rate of over 20 castings repaired per machine hour.

In review it can be seen that repair welding was successful because of two of the major advantages of electron beam welding. First, low energy input minimized distortion; second, the precise controllability of the process combined with the 20 x optical viewing permitted exact location of the beam on the desired seam (thereby taking advantage of the low energy input).

Summary

The results of our aluminum welding program to date indicate that high-voltage electron beam welding is a feasible technique for the joining of aluminum alloys. Of particular interest are the favorable

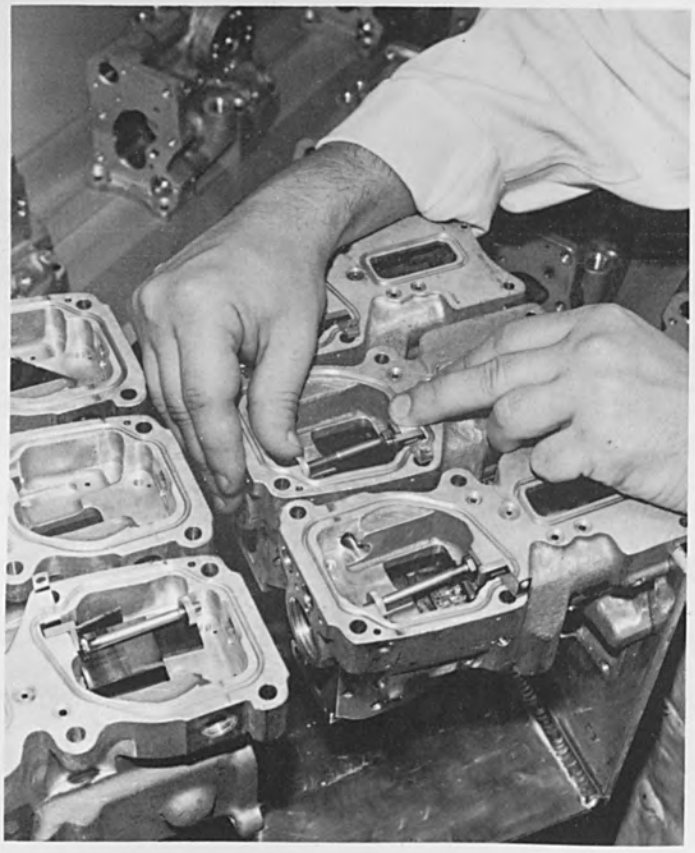

Figure 12: Fixturing of Castings for Repair Welding

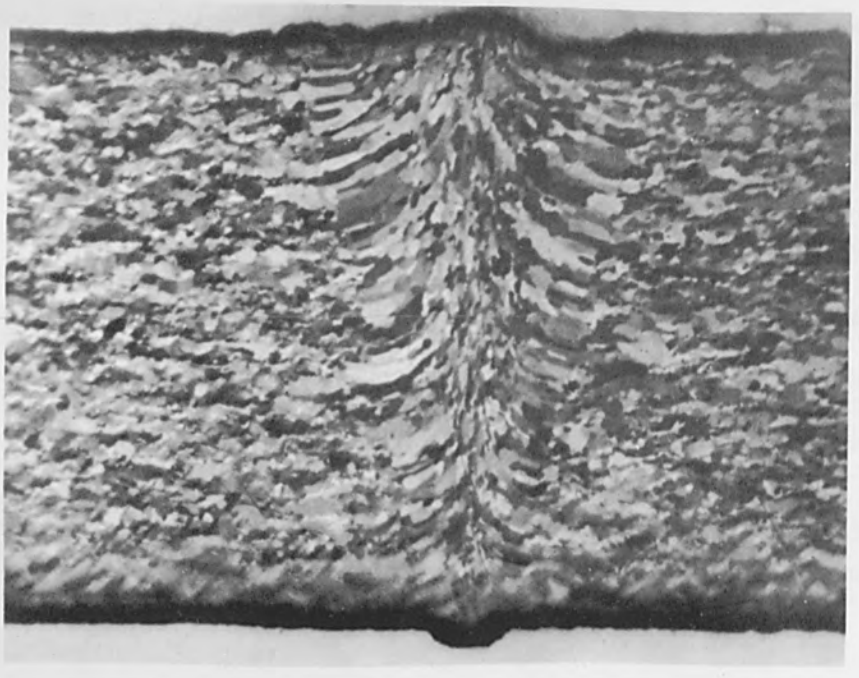

Figure 13: Weld Cross-section in 0.040-in. Beryllium
(110 KV, 2.5 ma, 15 ipm, 0.015-in. beam)

results obtained from 7075, a very difficult alloy to weld by normal techniques. The tensile results, though limited, indicate a probability of retaining full base-metal properties if the welds are completely heat-treated. There also appears to be a possibility of attaining a significant percentage of T6 strength by simple low-temperature aging after welding. The repair welding application demonstrates the successful application of the process to aircraft hardware.

BERYLLIUM WELDING

Background

Beryllium, with its low density, high modulus of elasticity, and high specific heat, is being used to an increasing extent in aerospace applications. However, use of beryllium for structural applications has been impeded, in part by the lack of satisfactory welding techniques for the production of sound and reliable joints. Conventional fusion welding techniques have been hindered by contamination, cracking, hot-shortness, and related problems, all of which have led to low room-temperature strength and poor ductility. Some success has been realized with brazing and braze welding techniques; however, brazed joints have limited applications due to the difference in the melting point of the braze metal and the beryllium.

In view of the difficulties encountered in welding and brazing beryllium by conventional techniques, and based on the excellent success of high-voltage electron beam welding in the joining of other hard-to-weld materials such as tungsten and molybdenum , a program was initiated under the sponsorship of the Aeronautical Systems Division,

Air Force Systems Command, United States Air Force, to develop and evaluate high-voltage electron beam welding techniques for beryllium. The data reported herein was taken from a preliminary phase of this program. Further work will certainly lead to improved techniques for electron beam welding of beryllium.

Experimental Procedure

The beryllium material used in this program was 0.040-inch thick QMV-grade beryllium sheet, manufactured by the Brush Beryllium Company and supplier by the Aeronautical Systems Division to Hamilton Standard. Preliminary welding was performed on specimens 1.5 inches long, and weldments for test consisted of butted specimens with four inches of continuous weld bead. All material was carefully cleaned before welding by a technique suggested by the material supplier.

Welding techniques for butt joints were developed through an evaluation of the effects of machine parameters on visual weld quality. Parameters studied included: accelerating voltages of 60 to 120 KV; beam currents of 1.5 to 20 ma; travel speeds of 15 to 80 ipm; beam oscillation of zero to 0.250 inch; and beam pulsing between 1 and 3000 cps with on-times of 0.50 to 10 millisecond.

Evaluation of the welds was based on normal inspection procedures and mechanical testing. All welds were visually inspected for cracks, undercutting, bead roughness, and related defects. Metallographic examination was used to study the effects of welding parameters on weld-zone grain structures. Tensile testing of the butt welds was conducted at room temperature and at 1000F.

Results and Discussion

Good results have been obtained in electron beam welding of beryllium by using moderately high power densities and slow welding speeds. When welding speeds are increased, or when extremely high power densities are used, highly columnar grain growth leads to weld cracking.

Figure 13 illustrates a cross-section of a beryllium weld produced with 110 KV, 2.5 ma, and 15 ipm. Beam diameter was 0.015 inch. Although the grain pattern is somewhat columnar, the results are encouraging because of the extremely narrow weld zone.

A more randomly oriented but wider fusion zone is illustrated in Figure 14. Moderating the power density by decreasing the voltage to (65KV) and increasing the beam diameter (to 0.020 inch) has induced a larger weld zone. However the grains are relatively small in size and show little evidence of columnar growth. It appears that welding conditions somewhere between those used for the welds of Figures 13 and 14 should develop the desired narrow, but randomly oriented weld zone.

The weld in Figure 15 was produced with conditions similar to those used for the weld of Figure 14. However, the total energy input was somewhat higher. As in the weld of Figure 14, the fusion zone is relatively wide, but now columnar grain growth is evident at the boundaries of the weld zone.

Long lead times involved in obtaining metallographic information on the welds made it necessary to initiate tensile testing before the

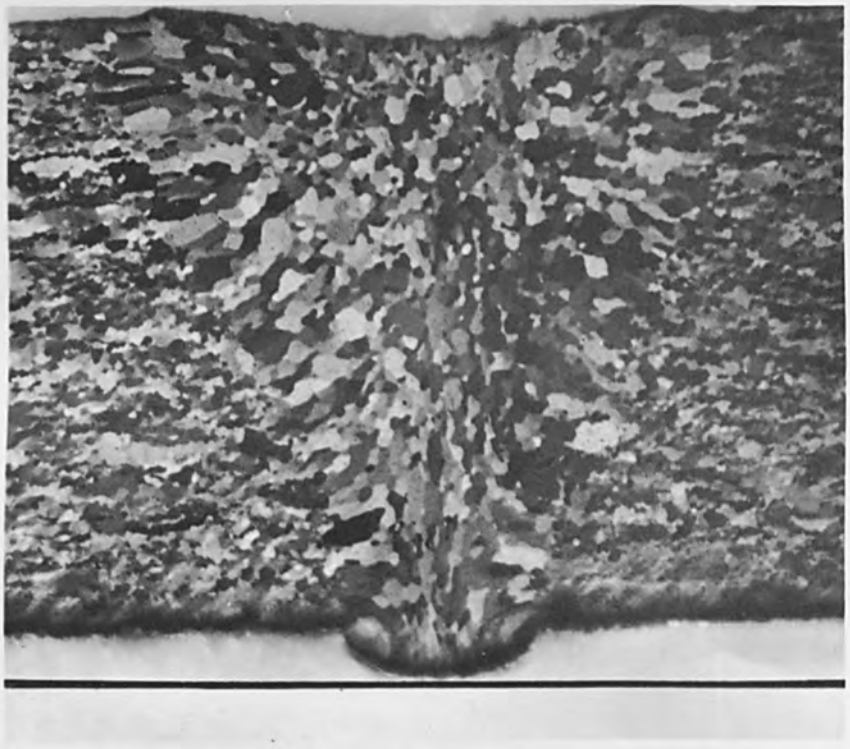

Figure 14: Weld Cross-section in 0.040-in. Beryllium (65 KV, 4 ma, 15 ipm, 0.020-in. beam)

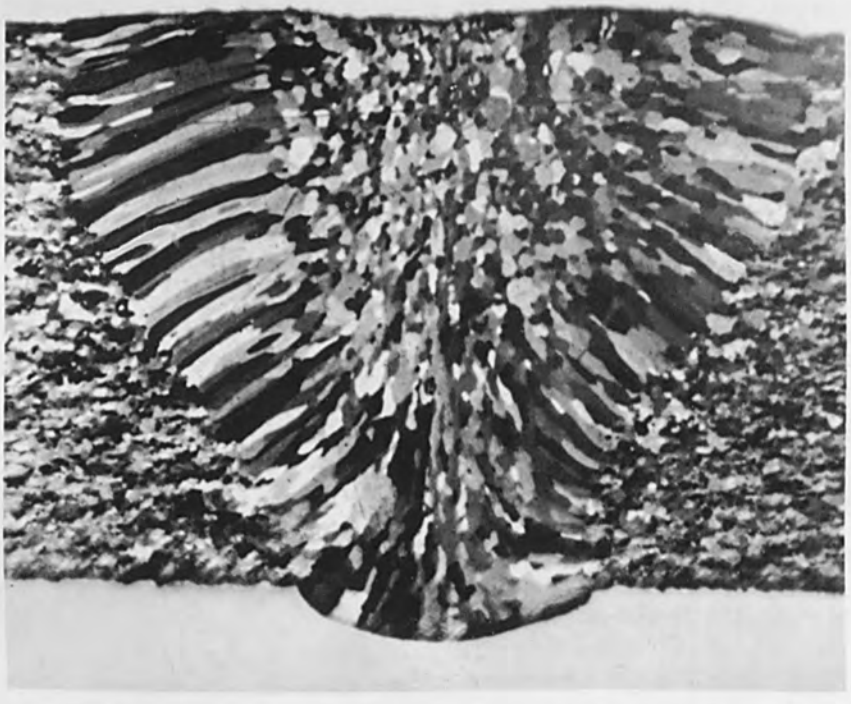

Figure 15: Weld Cross-section in 0.040-in. Beryllium (75 KV, 6 ma, 15 ipm, 0.020-in. beam)

metallographic evaluations were completed. Therefore, the welds of Figure 15 were selected for tensile testing solely on the basis of visual appearance. Figure 17 illustrates an over-all view of a typical welded specimen, and Figure 18 shows a close-up view of the bead surface and root.

As mentioned above increasing the welding speed led to highly columnar grain structures. Figure 16 illustrates the effect of welding at a fast speed with a beam of relatively high power (120 KV, 7 ma, and 80 ipm). The weld zone assumes the classical wedge shape associated with high-energy-density electron beam welding; however, the fusion grains are columnar and highly oriented. This condition, in general, induces low strength and ductility. In fact, a crack is present down the entire centerline of the weld.

The weld shown in Figure 19 was produced with relatively high power (120 KV, 7 ma, and 80 ipm) and longitudinal beam oscillation. Experience with tungsten welding[4] has shown that this type of deflection creates a more randomly oriented grain structure in the fusion zone, leading to very good weld strength. However, essentially no improvement was realized when this technique was applied to beryllium.

Circular beam oscillation has been used with good success in the welding of aluminum. The circular motion of the beam tends to break up the oxide film and also induces random grain growth. However, welding beryllium with circular oscillation offered no improvement in grain quality; as seen in Figure 20. Increased effective spot size has made the

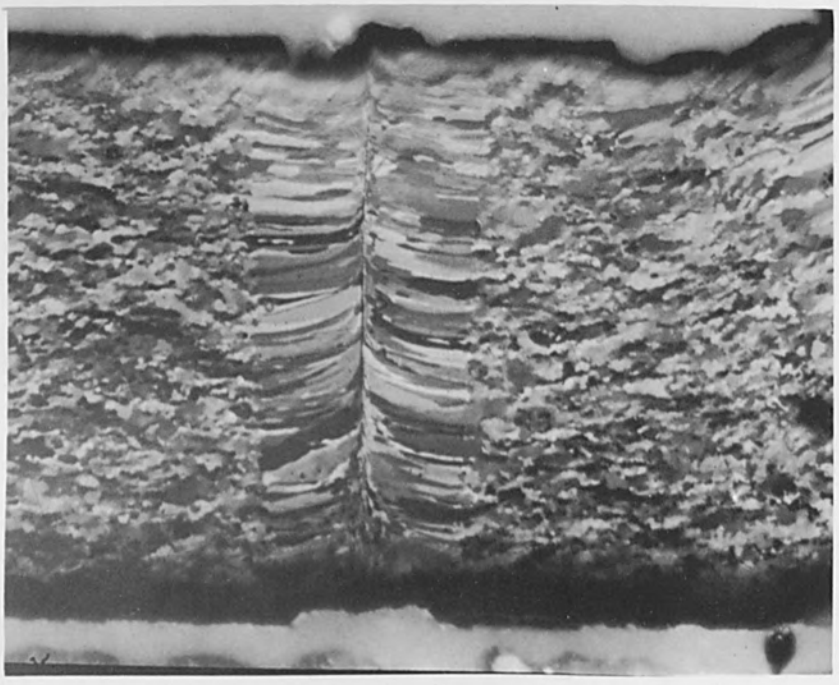

Figure 16: Weld Cross-section in 0.040-in. Beryllium (120 KV, 7 ma, 80 ipm)

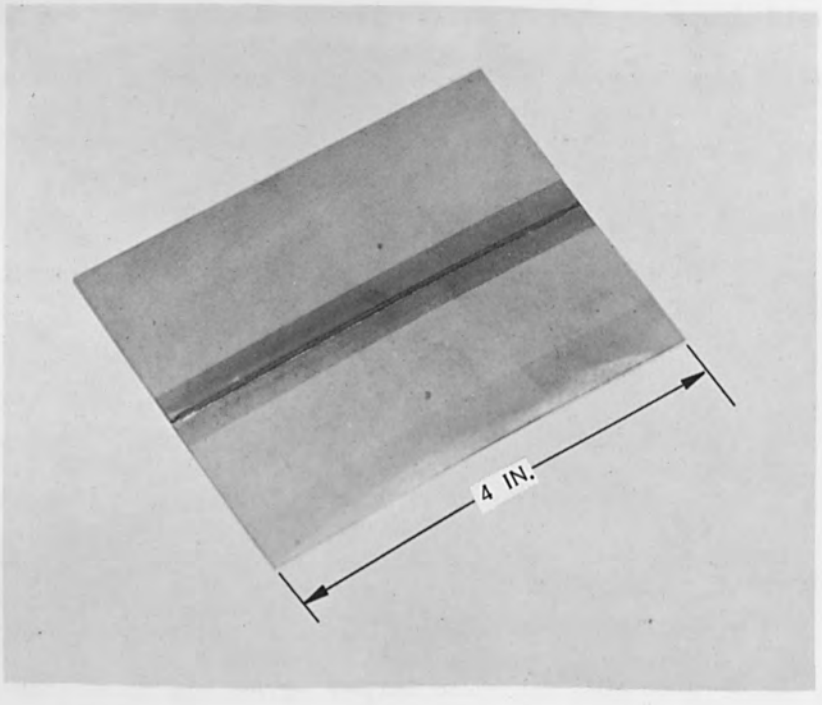

Figure 17: Butt-welded Beryllium

Figure 18: Beryllium Weld-Bead Surface and Root

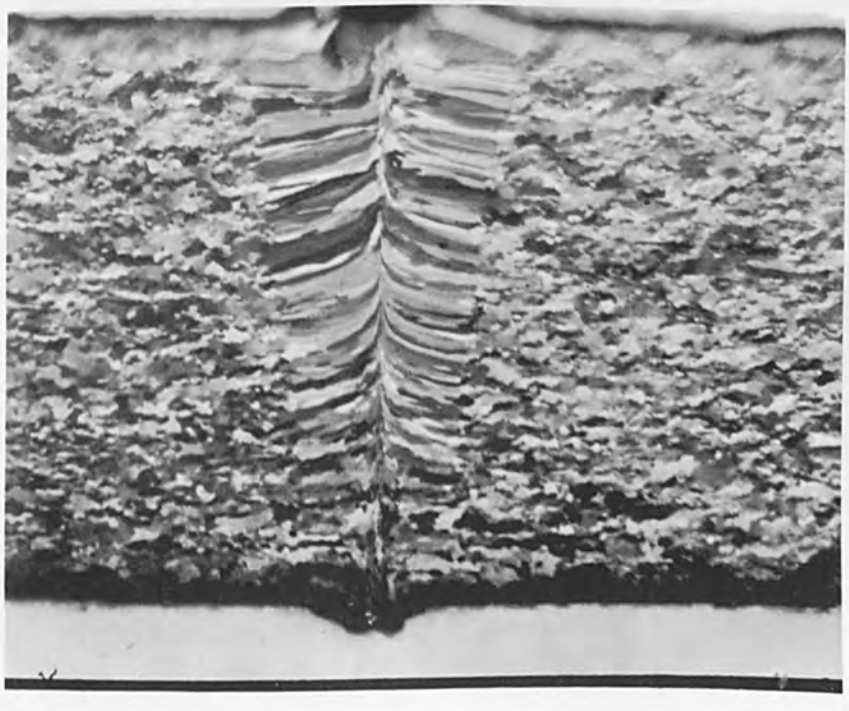

Figure 19: Weld Cross-section in 0.040-in. Beryllium (120 KV, 7 ma, 80 ipm, longitudinal oscillation)

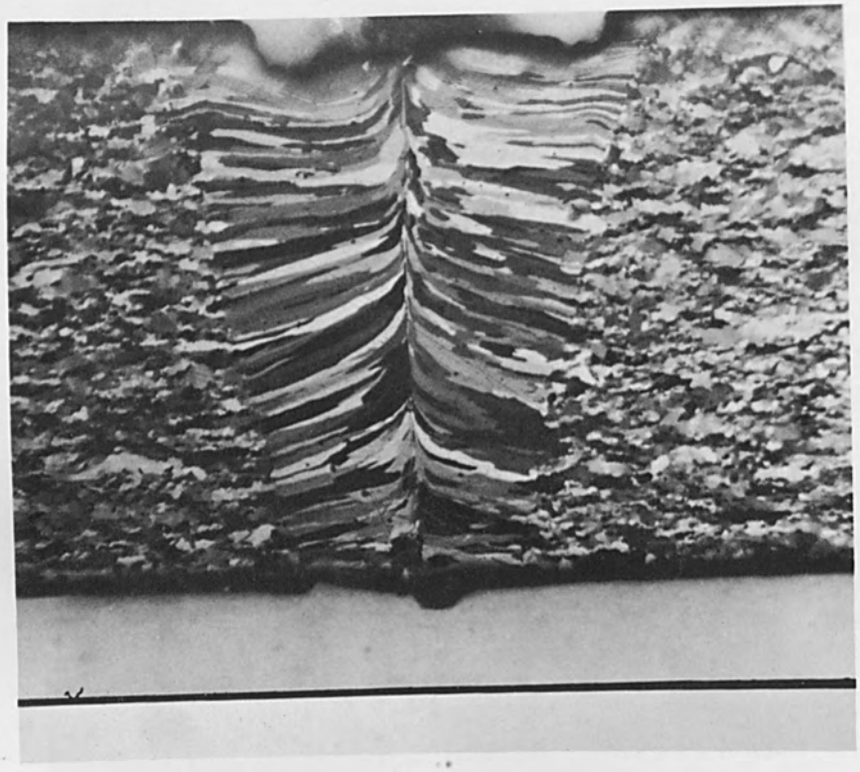

Figure 20: Weld Cross-section in 0.040-in. Beryllium (120 KV, 7 ma, 80 ipm, circular oscillation)

weld-zone width still relatively large.

The columnar grain structure resulting from welding at fast speeds with a beam of relatively high specific power is to date unexplainable. Experience with metals other than beryllium has always indicated a decrease in grain size and orientation with increasing welding speeds. Beryllium, the exception, exhibits the opposite effect.

It appears that due to a combination of its high thermal conductivity and high specific heat, beryllium is extremely sensitive to thermal input. The fast cooling rate associated with the low-energy input from welding with relatively high-power-densities and fast travel speeds results in severe weld cracking along grain boundaries. This is due primarily to the high orientation of the columnar grains towards the center of the weld zone. With TIG welding it has been reported[5] that the tendency towards hot-tearing decreases with slower welding speeds and increased preheat.

It appears that controlled cooling is required to produce the optimum weld-zone microstructures. This is accomplished by moderating the power density and decreasing the welding speed. Of course the ideal weld-zone would be small in over-all size while exhibiting a fine-grained, random microstructure. The results illustrated in Figure 13 indicate that such a weld structure is attainable by the use of moderately high voltages in combination with lower beam currents, while maintaining the slow welding speeds. Therefore, current efforts are being concentrated in this area.

Results obtained from tensile testing the beryllium welds at room temperature and 1000F are listed in Table 2. For comparison, parallel results obtained from the base metal are also included. It is apparent that the room-temperature ultimate strength of the electron beam welds is consistently about 65 percent of the base-metal strength. However, the base-metal strength is considerably higher than that reported in other beryllium welding investigations[6,7]. Thus, even with the 35 percent drop in ultimate strength, the electron beam welds have strengths among the highest reported.

At 1000F, even though all of the welded specimens failed in the welds, the base-metal and weld ultimate and yield strengths are essentially the same. Similar trends have been reported for TIG welding, but again, perhaps because of the higher base-metal strength, the actual strength values for the welds at 1000F are among the highest reported.

Ductility appears to be the property that has suffered most from the welding process. However, it should be noted that in weld fractures a very high proportion of the strain is absorbed within the very narrow weld zone. Thus a very high degree of local ductility could be masked by the overall measurement. Bend-test results, presently in progress, are expected to yield more meaningful ductility information.

As mentioned during the discussion of the metallographic studies, the conditions selected for welding of the tensile specimens were based on visual examination of the weld bead and were <u>not</u> based on metallographic evaluations. Thus the data cannot be interpreted as being representative of optimum electron beam welds in beryllium. In fact, metallographic work conducted after the tensile testing indicated that better

TABLE 2

TENSILE RESULTS FOR ELECTRON

BEAM WELDED BERYLLIUM

SPECIMEN CONDITION	TEST TEMPERATURE (F)	ULTIMATE STRENGTH (psi)	YIELD STRENGTH (psi)	ELONGATION (% in 1 in.)
EB Weld	80	43,400	None	0
EB Weld	80	44,400	None	0
EB Weld	80	47,200	43,900	0.5
EB Weld	1000	25,600	23,400	3.5
EB Weld	1000	24,700	23,800	3.5
EB Weld	1000	24,700	23,400	3.5
Base	80	70,100	42,500	18
Base	80	70,200	41,700	20
Base	80	68,100	42,600	14
Base	1000	25,600	24,400	16
Base	1000	25,600	25,000	20
Base	1000	24,700	24,500	17

mechanical properties are to be expected with somewhat different welding conditions. Further testing of welds of superior grain structures is planned.

Summary

The results of the beryllium welding study indicate that high-strength welds can be produced by high-voltage electron beam welding techniques. Contrary to almost all other metals, fine grain size and random grain orientations in beryllium electron beam welds are not dependent on fast welding speeds. Instead, best results to date have been achieved with relatively low welding speeds (15 imp). Further evaluation of the relationships between grain structure and welding conditions is required to develop welds of optimum quality.

ACKNOWLEDGEMENTS

The authors wish to express their appreciation of the contributions of Messrs. J. L. Cutler and L. E. Lubin to the experimental work conducted for this paper. In addition, the authors wish to thank Messrs. J. W. Meier and R. A. Schnubel and Dr. R. F. Donovan for their helpful suggestions in the preparation of the manuscript.

THE ELECTRON BEAM POST HEAT TREATING OF ELECTRON BEAM WELDMENTS

By

S. S. White
Supervisor
Materials Joining
Alloyd Electronics Corporation
Cambridge, Massachusetts

R. Bakish
Director of Research
Alloyd Electronics Corporation
Cambridge, Massachusetts

ABSTRACT

Mechanical testing of electron beam post heated weldments produced in electron beam welded solutionized sheets, solutionized and rolled sheets, and aged sheets of titanium alloys shows that impact data remain essentially the same as for those found in weldments not post heated. Tensile tests show an increase in strength over non-post heat treated welds, and are equal to or very close to base metal strength. Incremental strain readings of heat treated welds are not significantly less than those of non-heat treated welds, but are more uniform. Similarly, simultaneous stress-strain curves of fusion and base metal zones show that such curves can be nearly matched by such post heating, although serious mismatch may occur in non-post heat-treated welds. Thus essentially uniform mechanical properties can be achieved.

THE ELECTRON BEAM POST HEATING OF ELECTRON BEAM WELDS

INTRODUCTION

The advantages of electron beam welding several titanium alloys, high strength steels and molybdenum have been shown to be related to both gas content of the fusion zone and total heat input. In particular, it has been shown that, over a wide range of weld widths, titanium alloys show substantially no change in strength and generally have strengths which are of the 150,000 - 165,000 psi ultimate strength range. In other words, fusion zones in electron beam welded titanium alloys consistantly have approximately the same strength as solutionized base plate.[1]

It has been further shown that the Department of Defense titanium sheet rolling alloys vis. the 5Al-2 1/2 Sn alloy, the 16V-2 1/2 Al alloy, the 6Al-4V alloy, the 4Al - 3Mo-IV alloy, and the 13 1/2V - 11Cr-3Al alloy, have increasing impact resistances with increasing weld width for constant fusion zone grain size and condition of heat treatment. Further, these impact resistances are generally all higher than found in solutionized or hardened base plate. This has been related to hydrogen content wherein it has been shown that as weld width increases hydrogen content decreases.[1]

It has been shown, also that ultimate strengths for titanium alloys are primarily dependent upon the grain size of the fusion zone and this accounts for the consistent strength levels over a wide range of fusion zone geometry.[1] Incremental strain readings showed a general loss of ductility caused by welding as opposed to the ductility measurements present in a sheet prior to welding.[1] Usually losses were most severe in the heat affected zone immediately adjacent to the fusion zone. Certain alloys, notably, the 4Al-3Mo-1V alloy exhibited significant loss of ductility even in the fusion zone.[1] However, the incremental strains reported are still of engineering use since they generally run at least 5 to 10% even in the most severe cases of low strain reporting.

The ability to obtain titanium weldments of strengths equal to solutionized base plate with very high impact resistances is encouraging. However, it would be even more desirable to have titanium fusion zones of higher strengths compatible with strengths of solutionized and rolled plate or plate otherwise hardened and still retain high impact resistance, while perhaps increasing the weldment incremental strain values. Since impact resistance is a function of hydrogen content as well as conditions of heat treatment, these higher properties might be realized by heat treating an entire

assembly. However, heat treating an entire assembly necessarily involves not only considerable expense for very large heat treating furnaces for large parts such as missile casings and considerable time involved with attendant expenses, but, perhaps even more important, often results in extensive deformation when applied to large assemblies.

Thus, it would be very advantageous to be able to post-heat treat in the same weld fixturing directly after a welding pass only fusion and high temperature heat affected zones produced in hardened sheet. Thus, a fully heat-treated weld in fully hardened sheet might be produced with little distortion, quite rapidly, and at very low cost. Such an approach has been tried by Lefas[2] wherein cast iron was joined using a carbon welding arc, and oxyacetylene torches were used to post-heat treat the weld area. The same approach was attempted by White et al.[3] wherein an induction coil trailing a tungsten arc torch was used to post-heat treat weldments in the all beta titanium alloy (13 1/2V-11Cr-3Al). In both cases, the rate of heat input from these secondary non-melting heat-treating sources was too low to effect substantial aging or annealing as desired.

The electron beam is a highly efficient heating tool wherein electrons emitted from a gun actually penetrate several thousandths of an inch into a material before any

melting or substantial heating begins. Thus it seemed quite feasible to use a non-melting pulse from an electron beam gun as a secondary heating source. This could be accomplished in the form of a second gun travelling behind the first melting or welding gun or it could be accomplished by low power density generated from the very same gun that performed the welding operation, constituting a second pass. This procedure was applied to determine the precise feasibility of the technique when utilized with the 5Al-2 1/2 Sn alloy, the 6Al-4V alloy, the 4Al-3Mo-1V alloy, and the 13 1/2V-11Cr-3Al alloy. The alloys were either in the solutionized, or solutionized and rolled conditions prior to welding. In addition, work was also done with material in the solutionized and aged condition prior to welding.

EXPERIMENTAL PROCEDURE

Weldments in different alloys involve an infinite number of heat affected zone peak temperatures at varying distances from the edge of the fusion zone which will be either relatively hard or soft, depending on the alloy in question. It was, therefore, necessary to develop a post-heating tool which would be quite versatile in terms of both peak temperature distribution from the edge of the fusion zone as well as actual peak temperature in the center line of the fusion zone.

Peak temperature locations were determined using the temperature sensitive lacquer technique (tempilac).[1] In this procedure, temperature sensitive lacquers, each corresponding to a specific peak temperature, and each melting within plus or minus 1% of that peak temperature, are painted transversely to the welding direction. The peak temperature locations resulting from either the welding operation (if these stripes are painted prior to welding) or the peak temperature locations subsequent to post heating (if the stripes would be applied before post-heating but after welding could be determined and the loci of these peak temperatures compared.

The subject materials were obtained in 1/8" nominal sheet thickness since this sheet thickness was felt to be of practical interest to missile and airframe manufacturers. Using such materials two limiting variations of the post heating technique were evolved. In the first technique a non-melting low power density E.B. pulse was used as a second weldment pass following the first E.B. fusion welding pass. However, the power density involved was only slightly less than that required for melting.

Using the peak temperature equations of Adams[4] as recommended by Lander et.al.[1] it can be shown that the reciprocal of the difference between any peak temperature

and room temperature is directly proportional to the distance from the edge of the fusion zone, when such heat flow is primarily of a two dimensional nature. For either two or three dimensional heat flow, linear relationships are evolved when this reciprocal temperature factor is plotted against the square of the distance from the edge of the fusion zone.[1] Reference to Figure 1 will show the result of this first technique of post heating. It may be seen that a relatively narrow width of heat affected zone resulting from this post heating was obtained and that very high peak temperatures were obtained. The data are shown as least mean square lines and the seeming discrepancy between top and bottom side temperatures, namely that the bottom surface temperature was higher than that of the top is nevertheless in keeping with much of the previous work done with these particular alloys.[1] Thermocouple measurements were also taken to check peak temperature locations during E.B. welding. A good agreement was obtained, and thermocouples than used primarily to determine time at centerline peak temperature.

The second variation in this technique involved designing a post-heat treatment such that a relatively wide width of heated material and low centerline peak temperature would be obtained. In other words, having obtained by the first method a means of achieving a high centerline peak

temperature and having only small distances from the edge of the fusion zone affected, the evolution of a technique which would yield the opposite of this should allow conditions to be set between these two limits to achieve any desired peak temperature distribution within the plate. More diffuse heat input was achieved by using an even lower power density beam, i.e. a beam having the same power settings as utilized for welding but a considerably larger spot size, and by using several post-heating passes of the beam to slowly bring the joined portion of the assembly up to the desired centerline peak temperature. Figure 2 shows the results of using this technique. It will be noticed that the use of multiple passes and of a power density even less than that of the first limiting parameter allowed a more uniform peak temperature between the top and bottom sides to be produced. In fact, it was generally found that the same peak temperature, within experimental limits, was obtained for these runs. It should also be noted that the horizontal axis is ten times that represented in Figure 1 and still the subject curve in Figure 2 has much less of a slope than the curves of Figure 1, so that much more material was heated by multiple pass technique.

In an effort to determine just how precise the post heating technique could be, temperature sensitive lacquers

were painted on a specimen prior to welding and the results of these peak distributions are plotted in Figure 3. Knowing these peak temperature distributions, a post heat-treatment was then designed to reproduce as closely as possible these two curves represented in Figure 3, without melting the plate. The results of this experiment are presented in Figure 4. Comparing Figure 4 to Figure 3, it will be seen that the peak temperature distributions and the maximum center line peak temperature are essentially the same in both cases although no melting occurred during the post heat-treating operation.

On all material which was welded in the solutionized condition or the solutionized and rolled condition, it was decided to use a centerline post-heat peak temperature which would be close to the lowest temperature attainable for constant temperature heating through plate thickness, for absolute distortion minimization.

Also temperatures close to this particular peak temperature had to be maintained for at least 1/4" - 1/2" on either side of the weld in order to embrace all of the high temperature heat affected zones. In this way aging might be induced into the weld fusion zone and high temperature heat affected zones. Consequently, aging might compensate for any loss of strength from the solutionized and rolled

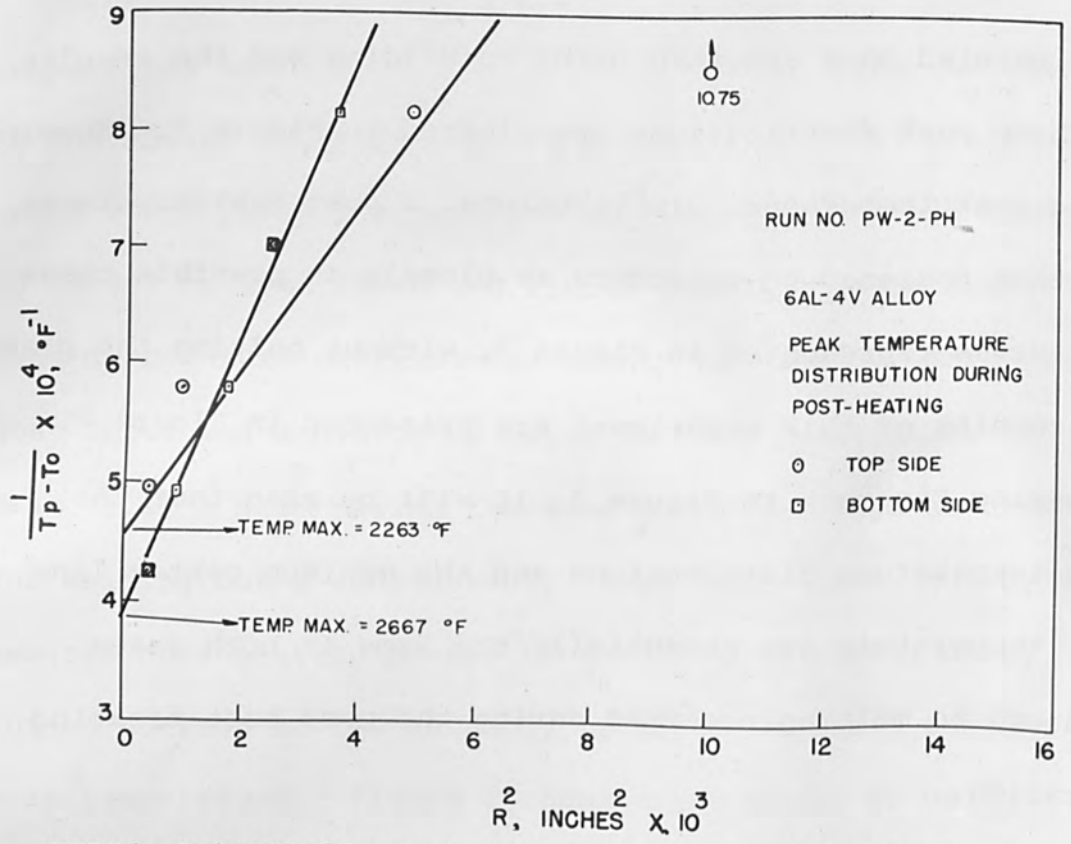

FIGURE 1 - Reciprocal of Temperature Difference vs R^2

T_p - Peak temperature at R
T_o - Initial temperature of plate
R - Distance from fusion zone edge to peak temperature location

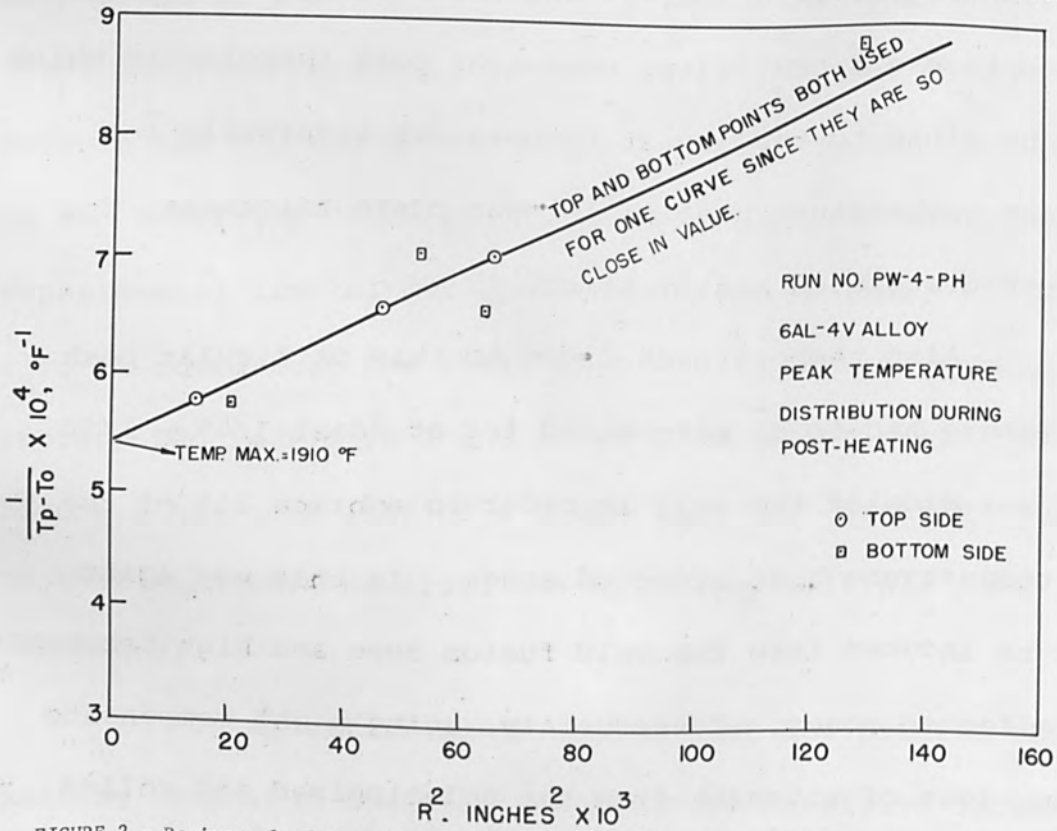

FIGURE 2 - Reciprocal of Temperature Difference vs R^2

T_p - Peak temperature at R
T_o - Initial temperature of plate
R - Distance from fusion zone edge to peak temperature location

condition to the welded condition. The lowest possible centerline peak temperature which would allow relatively constant temperature conditions to exist from the top to the bottom of the plate was approximately 1600°F. Thus, all solutionized and welded plate was post-heat treated with at least an 1800°F centerline peak temperature. In order to achieve this particular peak temperature and the desired temperature distribution, it was found a three pass technique of heating was required. All post heating conditions yielded temperature distribution plots similar to those of Figure 2, for centerline peak temperatures up to 2200°F, for all materials in all conditions of heat treatment or hardness used. Higher centerline peak temperatures were achieved in two passes, yielding approximately the same peak temperature distribution. For ease of reference in the remainder of this report, such conditions will be referred to only by centerline peak temperature.

The alloys which were aged prior to welding were those that could be aged commercially, vis, the 6Al-4V alloy, the 4Al-3Mo-1V alloy, and the 13 1/2-11Cr-3Al alloy. These were subjected to post heating after aging and welding as well as post heating after solutionizing and welding. When these alloys were used in the aged condition for post heating a variety of post heat temperatures were applied to them to

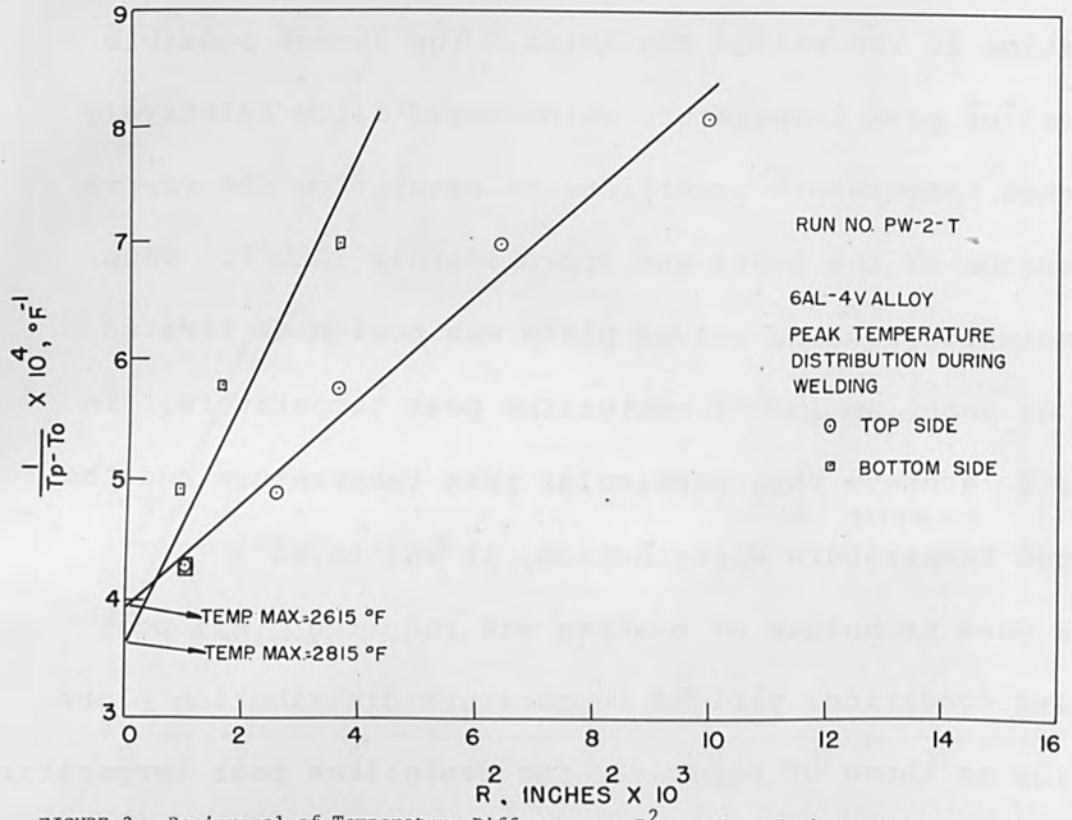

FIGURE 3 - Reciprocal of Temperature Difference vs R^2

T_p - Peak temperature at R
T_o - Initial temperature of plate
R - Distance from fusion zone edge to peak temperature location

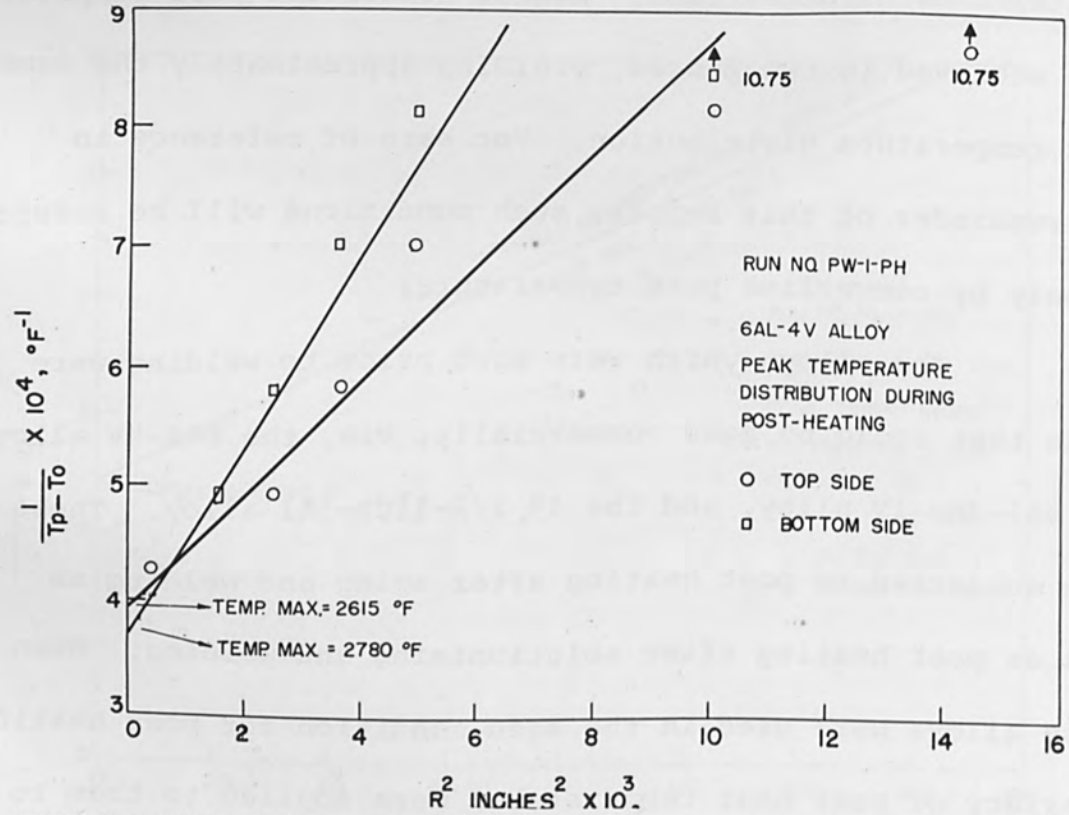

FIGURE 4 - Reciprocal of Temperature Difference vs R^2

T_p - Peak temperature at R
T_o - Initial temperature of plate
R - Distance from fusion zone edge to peak temperature location

determine the influence of post heating on overaging of plates, impact resistance, and strain. For ease of reference in the remainder of this report, material aged prior to welding is referred to as "hardened" material. Material in the solutionized, or solutionized and rolled condition prior to welding is given no special identification.

Welding conditions for these materials were 14,000 volts, 200 milliampers, and 8-10 inches per minute travel rage, depending on the alloy used and the particular thickness of sheet (one for each alloy) used. With a gun efficiency of approximately 65%, approximately 10,000-15,000 joules per inch were utilized for the welding operation. Post heat-treating was carried out at the same settings, with the exception that spot size was increased from that of the minimum available during the welding operation (approximately 0.030 inch) to a more diffuse spot (0.070-0.100 inch). Under these conditions, a time-temperature relationship showed that a particular spot on the weldment centerline was at its peak temperature during post heating for approximately 5 seconds and was quickly raised to this temperature and rapidly cooled from it. Although 1800°F considerably above the solution-izing temperature for these alloys, a 5 second exposure should be insufficient to allow solutionizing, but should result in significant aging, perhaps equivalent to a 10 hour hold at 900°F.

For each condition of post heat-treatment, transverse tensile bars were prepared from the welds. Transverse tensile bars were also taken from the as-welded specimen, i.e. the specimens having no post heat-treatment and from the unwelded base plate for comparison. Thus, for each alloy, three tensile comparisons generally of the base plate, as-welded condition,

and post heat-treatments at 1800°F, 2000°F, 2200°F and occasionally at 2500°F were made. These flat tensile bars were ground to A.S.T.M. flat tensile bar specifications. The 2" long by 1/2" wide reduced gage section was subjected to the photogridding process.[5] This process originally developed by the Watertown Arsenal Laboratories allows an accurate grid of 0.001 inches wide lines arranged in square array, 0.049" on a side to be photographed directly onto the specimen.[5] Since the photographic emulsion has a very low elastic limit, the entire plastic strain of a specimen throughout all of its metallurgical portions can be readily determined by measurement of these grids before and after testing. In this way, any portion of the weldment which would suffer a serious loss of ductility, or experience a large increase in ductility could be delineated. This would

be impossible using standard 1" or 2" gage length measurements which may be quite meaningless for a weldment in which the entire width of weld and heat affected area may be less than one-eighth of the gage length.

Impact properties of most of these various conditions were also determined. The specimen used was a Charpy bar in all dimensions except that of its thickness which was the thickness of the sheet being used.[6] In the case of actual weldments or post heated weldments, the thickness would be that which resulted after any crown, fillet or other deviation from flatness had been removed by machining. Charpy V-notch specimens of sheet thickness are quite adequate for determination of the total quantities of crack propagation energy, crack initiation energy and specimen bending energy. The specimen can, however, be modified by the introduction of a natural fatigue crack at the base of the notch, as has also been introduced by the Watertown Arsenal Laboratories.[1,7] The natural fatigue crack allows strictly crack propagation energy to be measured, since it has been shown that the energy determined on an energy per area basis is independent of specimen geometry,[8] and since the energy to reinitiate a natural fatigue crack at the base of the notch is essentially zero. The natural fatigue crack

is introduced by exposing specimens to several thousand reversals on a standard fatigue machine. Depth of the crack can be controlled to within several thousandths of an inch. In the subject program, the crack was controlled to within 0.050 inch $\pm$ 0.010 inch. In addition, the area through which the crack propagated was measured on every specimen subsequent to fracture. Impact energy readings thus determined on an area basis bear a 1:1 relationship with the Gc test of Irwin and Kies.[7,9] Not only does this technique yield the lowest possible impact resistance number available (and, therefore, the safest value in engineering terms), it yields a value which is meaningful for weldments, since they fail from existing stress risers, be they infinitely sharp cracks which are undetected or be they other metallurgical or mechanical notches.

Since one of the most important aspects of the subject research was to determine means of producing specimens which would have essentially the same properties in the fusion zone and base plate areas, a new technique of tensile testing has been introduced. Use has been made of miniature strain gages (o.015 inches - 0.030 inches in gage length). Such a strain gage can be placed directly on a fusion zone and second one on the base metal. In

this way, the simultaneous stress-strain curves which these two areas generate when the entire specimen is loaded can be recorded, allowing the dynamic plastic behavior as determined by the incremental strain readings to be determined. The use of the miniature strain gages allows the moduli of elasticity to be compared, the extent of true elastic strain occurring in regions which show no plastic strain can be determined, and the relative magnitudes of residual stress either in weld or base metal as a result of either welding or post heating can be determined.

A. The 5Al-2 1/2 Sn Alloy

Although this alloy is not generally considered to be an age-hardenable alloy and is used only in the solutionized condition, electron beam weldment strengths are generally in the neighborhood of 120,000-125,000 psi ultimate strength as shown in Figure 12 and as determined in the previous study. This alloy is often supplied at this strength; however, the original material supplied for this study had been cold worked by rolling such that its strength was approximately 142,000 psi ultimate strength. Thus, an attempt was made to age this material using an 1800°F post heat temperature.

Figure 5, presents a summary of the ultimate strengths determined from various testing conditions, it

may here be seen that all fractures took place in the base metal or heat affected zone, and that base metal strength was achieved. The moduli of elasticity which were determined for this particular alloy series show no change from the standard value of approximately 16×10^6 psi.

Figure 6 shows the percent elongation per 0.050" in unwelded 5Al-2 1/2 Sn alloy base plate.

In Figure 7, the incremental strain readings for weldment tested without post heat-treatment are shown. It may be seen that a significant amount of plastic elongation has been lost in the fusion and heat affected zones. However, the total elongation is still quite excellent with a very large amount of plastic strain available to the overall weldment. Figure 8 shows incremental strain readings for the weldment post heat-treated at 1800°F.

The impact resistance of unwelded material is shown in Figure 9 as a function of testing temperature. All the data points are from specimens that did not fracture, but elected to bend regardless of the depth of notch, showing the extreme toughness of this material in the as-welded condition.

A previous study using this very same material[1] did not show such results, with material having approximately the same impact strength in the welded as in the

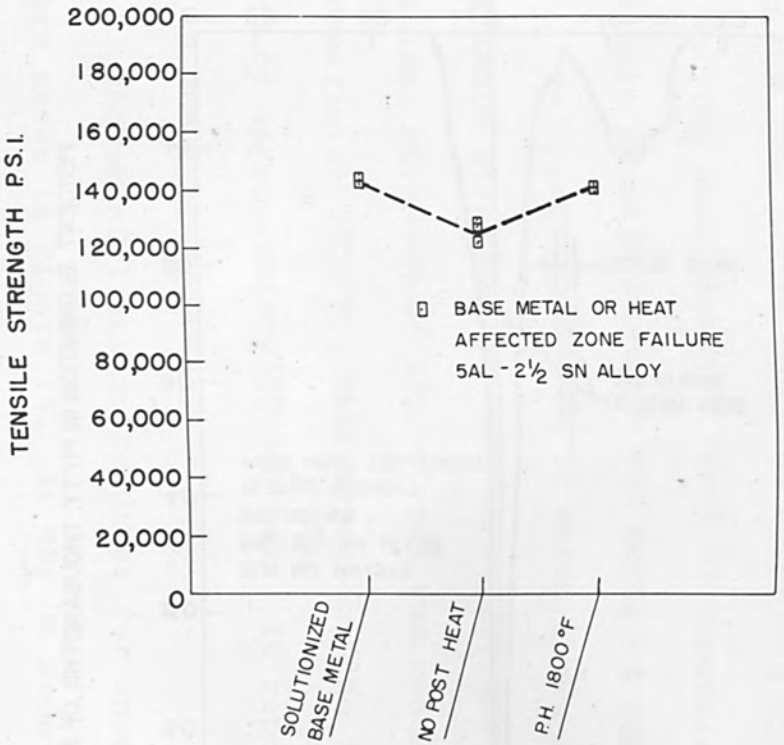

FIGURE 5 - Ultimate tensile strength for various testing conditions for the 5Al-2½Sn alloy.

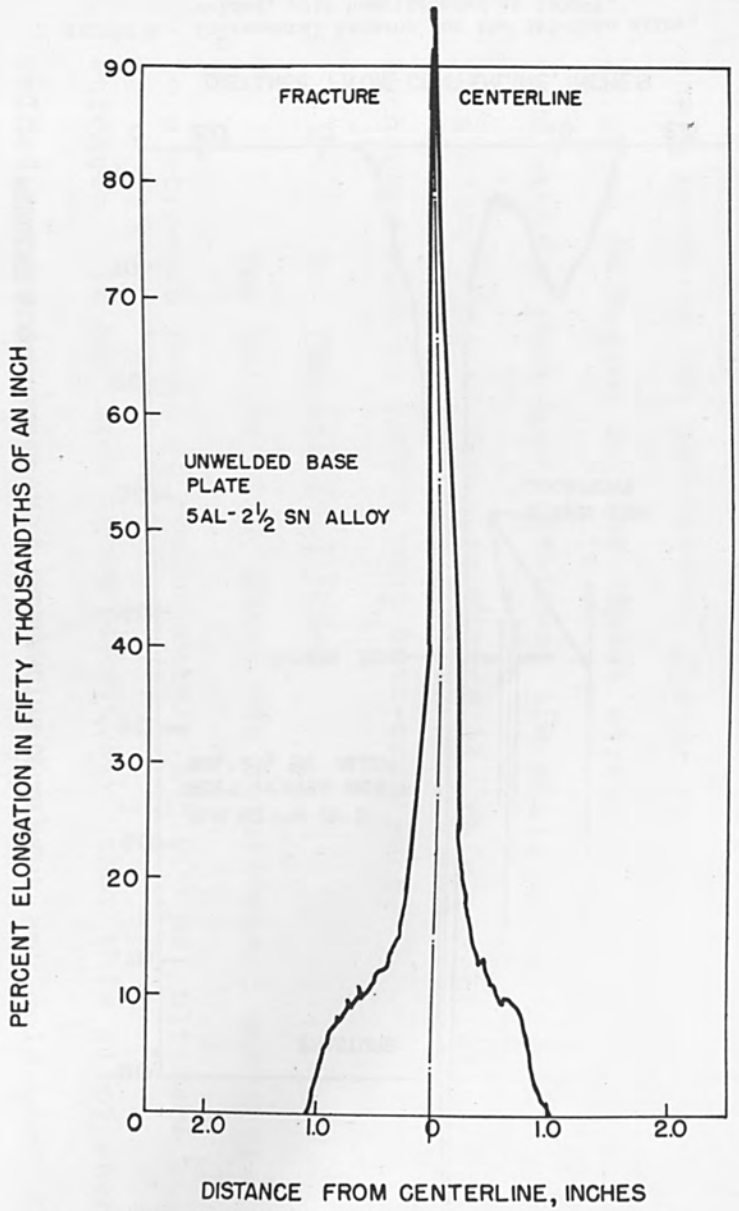

FIGURE 6 - Incremental strains for unwelded 5Al-2½Sn alloy.

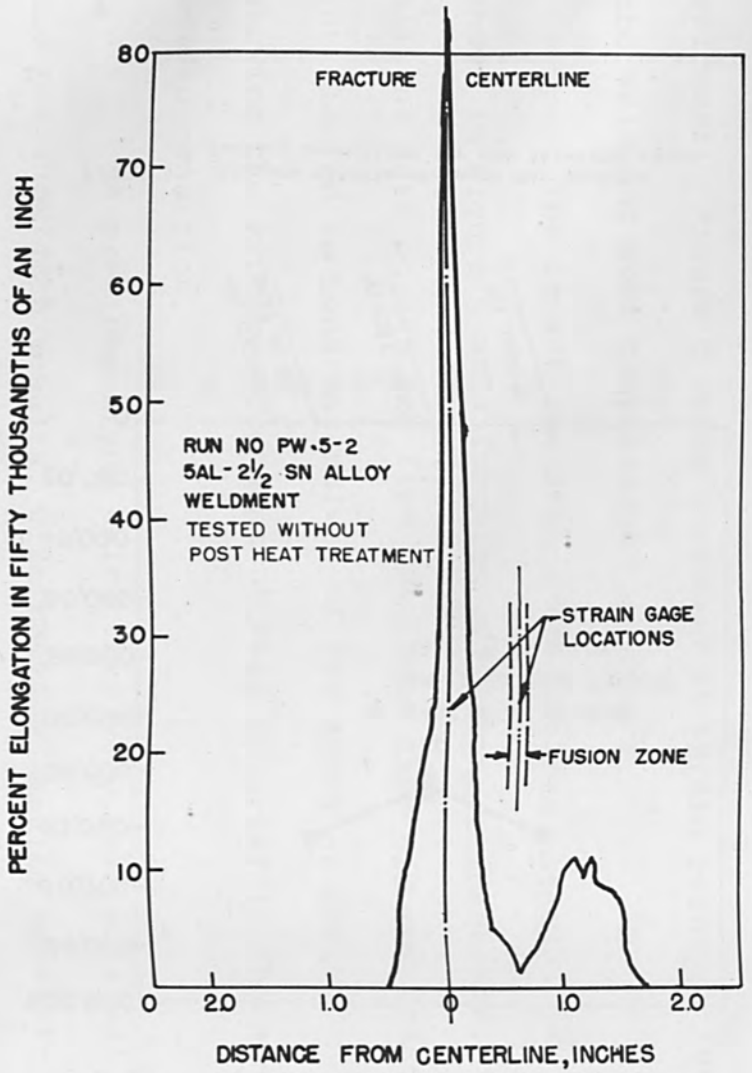

FIGURE 7 - Incremental strains for 5Al-2½Sn alloy, welded, no post heat-treatment.

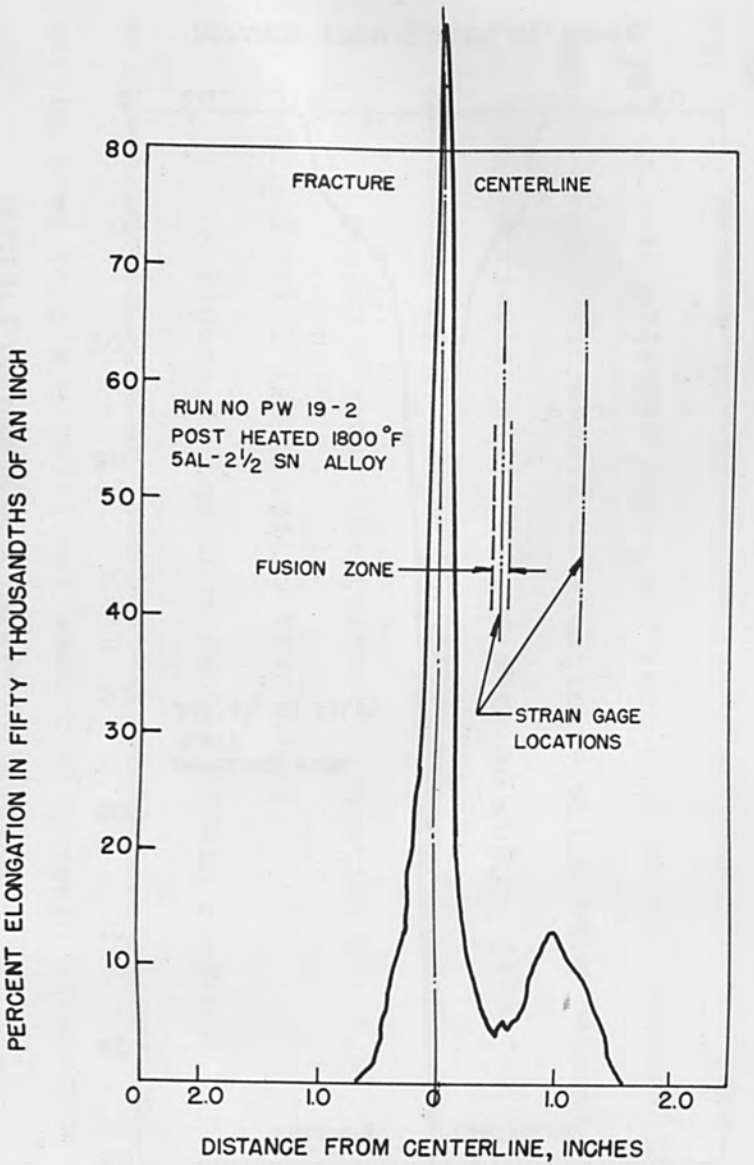

FIGURE 8 - Incremental strains for the 5Al-2½Sn alloy, welded, post heat-treated at 1800°F.

unwelded condition. All specimens failed from the infinitely sharp notch in the pre-cracked Charpy specimen.[1] However, as shown in Figure 10, the impact strengths of the weldment made without post heat-treatment are still quite high for this alloy and, as shown in Figure 11, this essentially unchanged with an 1800°F post heat-treatment.

B. The 6Al-4V Alloy

The 6Al-4V alloy plate was solutionized and rolled to a strength level of approximately 185,000 psi ultimate strength. It has been shown previously[1] that this alloy when welded in the solutionized condition without any cold work applied has strengths of approximately 150,000 psi ultimate strength, which is essentially the same as the strength realized in the base plate. Several as-welded specimens have been tested and the same strength level of approximately 149,000 psi ultimate tensile strength was obtained for 3 specimens.

Reference to Figure 12 which shows a summary of the ultimate strengths of various conditions shows that the original strength of 180,000 psi was reached by post heat-treating at 1800°F. This represents an increase in strength of approximately 30,000 psi. It represents little change in modulus as shown in Figure 13.

Incremental strain readings for unwelded base plate are shown in Figure 14. It may be seen by comparing

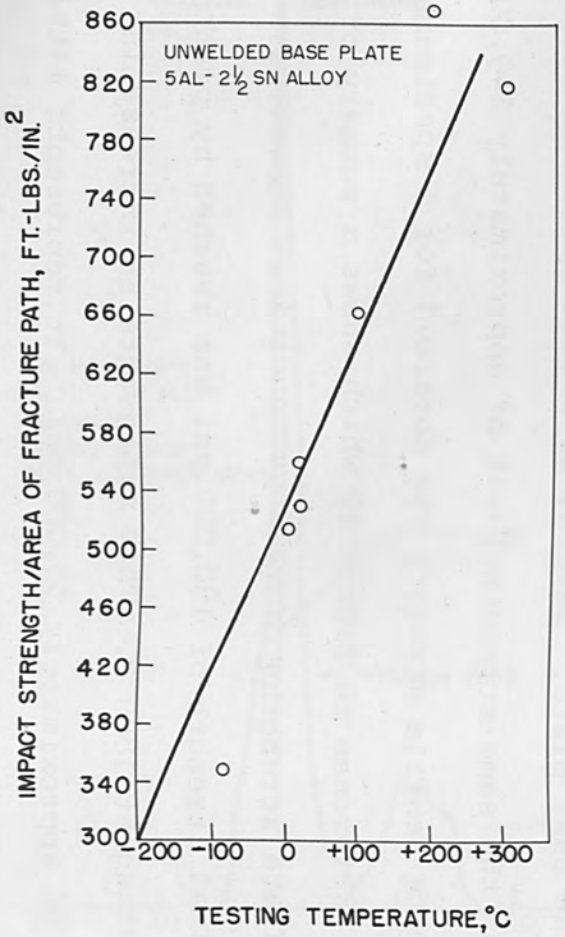

FIGURE 9 - Impact resistance for unwelded 5Al-2½Sn alloy as a function of testing temperature.

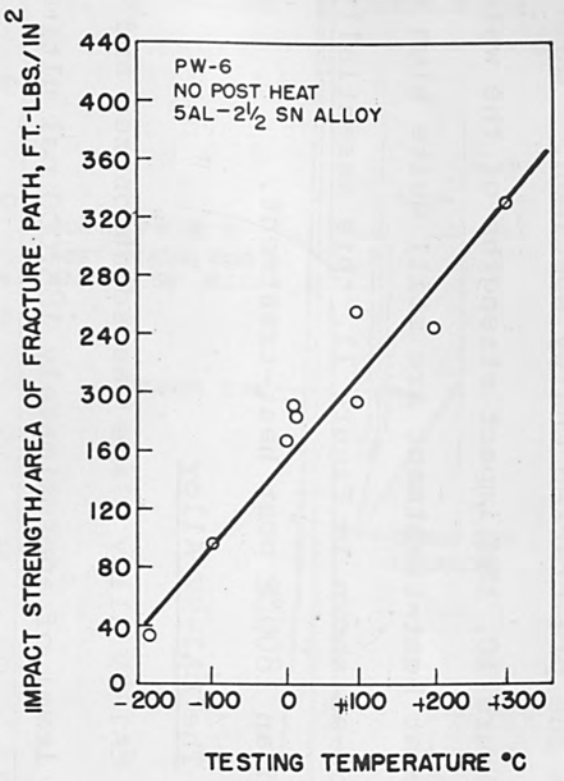

FIGURE 10 - Impact resistance for 5Al-2½Sn alloy, welded, no post heat-treatment, as a function of testing temperature.

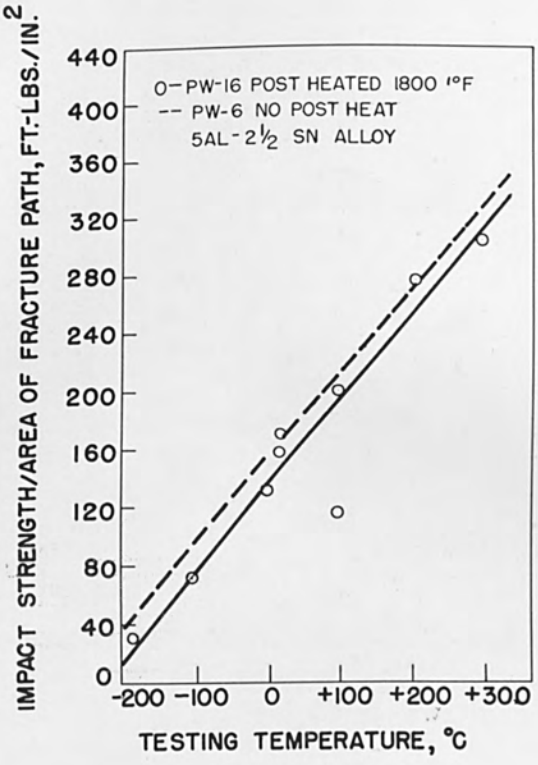

FIGURE 11 - Impact resistance for 5Al-2½Sn alloy, welded, post heat-treated at 1800°F, as a function of testing temperature.

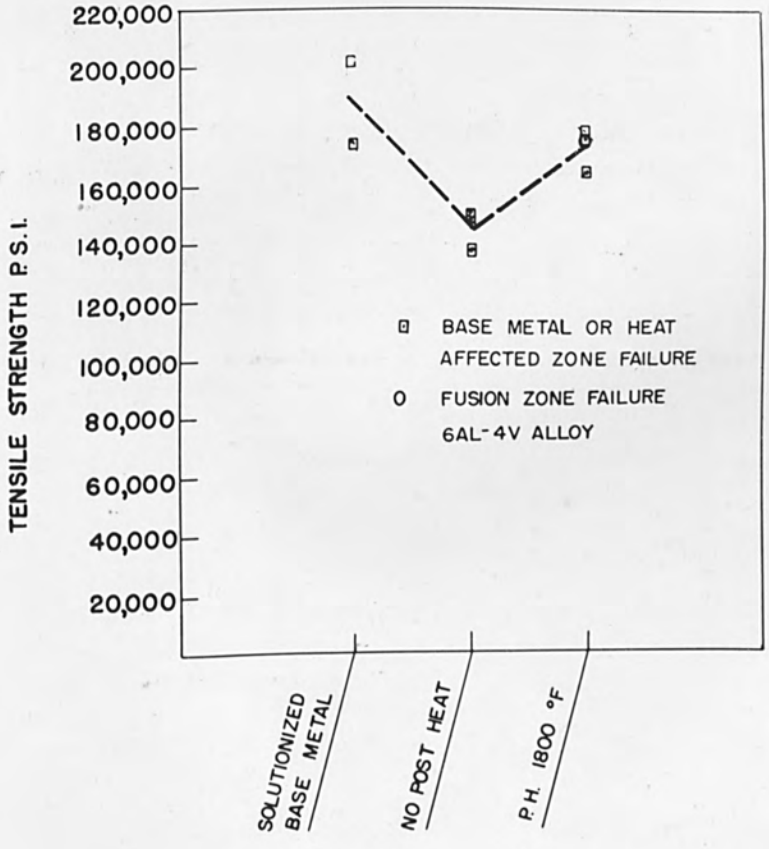

FIGURE 12 - Ultimate tensile strength for various testing conditions for the 6Al-4V alloy.

with Figure 15, which represents the incremental strain readings of a weldment tested without post heat-treatment, that plastic elongation has been lost throughout most of the weldment in the various metallurgical zones particularly in the fusion zone and very high temperature heat affected zones. The same condition was found to occur in a previous study using base plate which had not been worked prior to welding.[1] Figure 16 shows the incremental strain readings for a weldment which has been post heat-treated at 1800°F. Comparing these data with those of the previous figure it will be seen that there is very little, if any, loss in plastic elongation as a consequence of post heating and the elongation has been possibly increased in the fusion zone and high temperature heat affected zones. There is also a general tendency for more uniform elongation throughout the entire specimen.

Figure 17 shows the impact strength of the unwelded base plate as a function of testing temperature and Figure 18 shows the impact strength of the welded condition without post heat-treatment as a function of testing temperature. It can be seen that the welding operation with its softening effect (and its reduction in hydrogen content) has significantly increased the impact resistance. Perhaps of greater importance, however, is the fact that Figure 19 shows

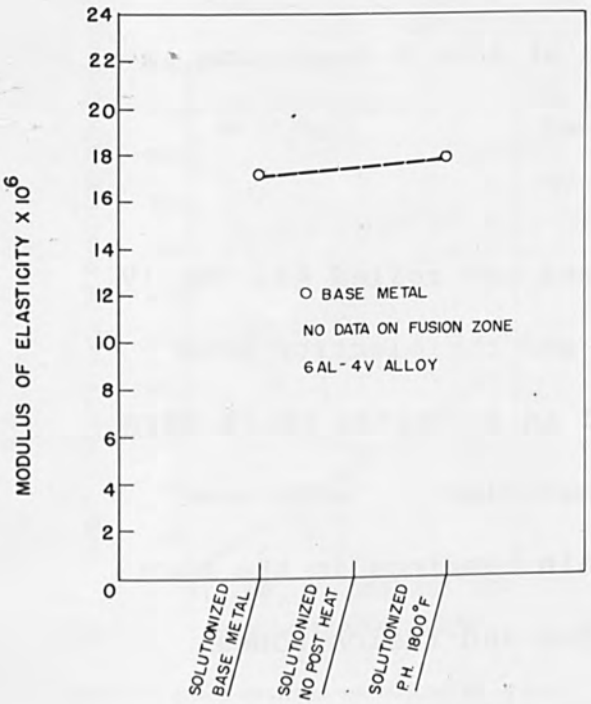

FIGURE 13 - MODULUS OF ELASTICITY FOR VARIOUS TESTING CONDITIONS FOR THE 6A1-4V ALLOY.

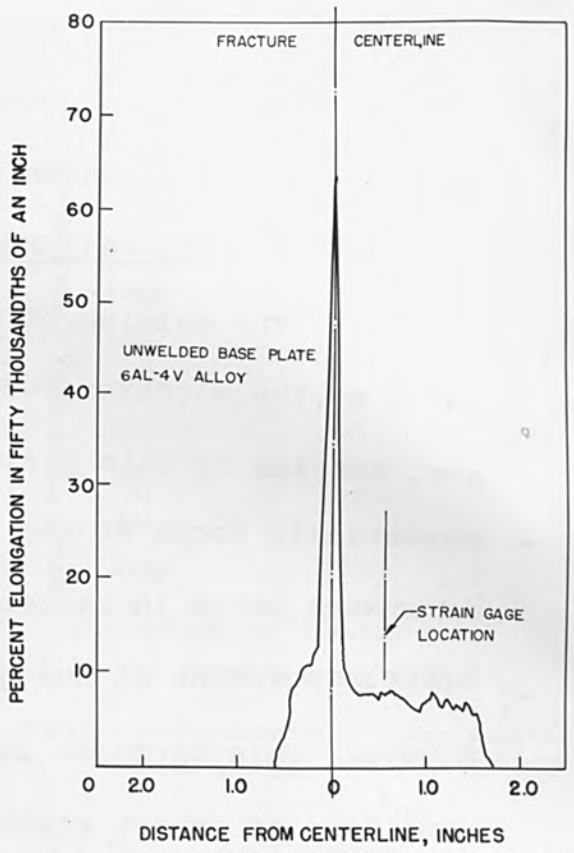

FIGURE 14 - INCREMENTAL STRAINS FOR UNWELDED 6A1-4V ALLOY.

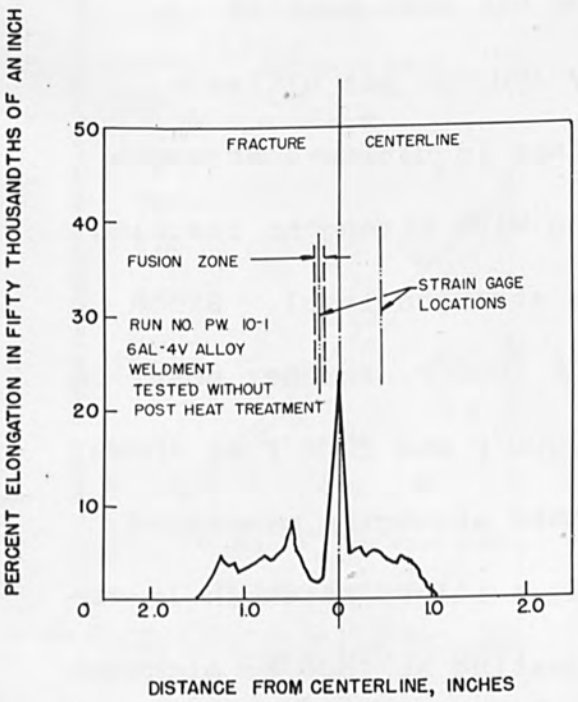

FIGURE 15 - INCREMENTAL STRAINS FOR 6A1-4V ALLOY, WELDED, NO POST HEAT-TREATMENT.

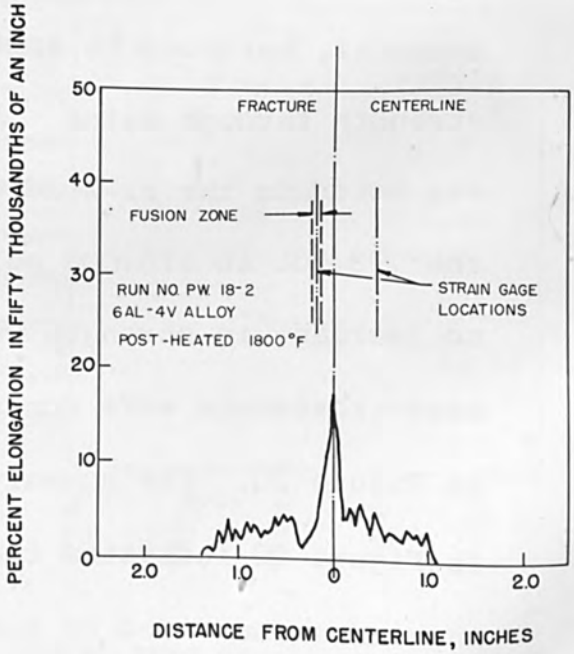

FIGURE 16 - INCREMENTAL STRAINS FOR THE 6A1-4V ALLOY, WELDED, POST HEAT-TREATED AT 1800°F.

essentially no change between the as-welded condition and the as-welded and post heat-treated at 1800°F condition insofar as impact strength is concerned.

C. The 4Al-3Mo-1V Alloy

The welding of solutionized and rolled 4Al-3Mo-1V alloy by the electron beam process and the electron beam post heating of this again resulted in strengths which were essentially those of the unwelded material with some increases noted in incremental strain readings in the more brittle portions of the heat affected and fusion zones. However, this increase in strain and stress was attended by some loss of impact strength in all likelihood due to severe microstructural changes induced by the post heat-treatment.

Attention was focused upon the same heat of material, hardened to approximately 190,000 psi ultimate strength through aging. A slight loss in ultimate strength was noted in the as-welded condition with strengths reaching the 170,000 to 175,000 psi ultimate strength level. Since no increase in strength was noted at 1800°F, further post heat-treatments were conducted at 2000°F and 2200°F as shown in Figure 20. The summary of ultimate strengths presented in Figure 20 indicates that possibly a slight strength lowering was encountered by post heat-treating at 1800°F, although there is also an indication that this strength loss is no

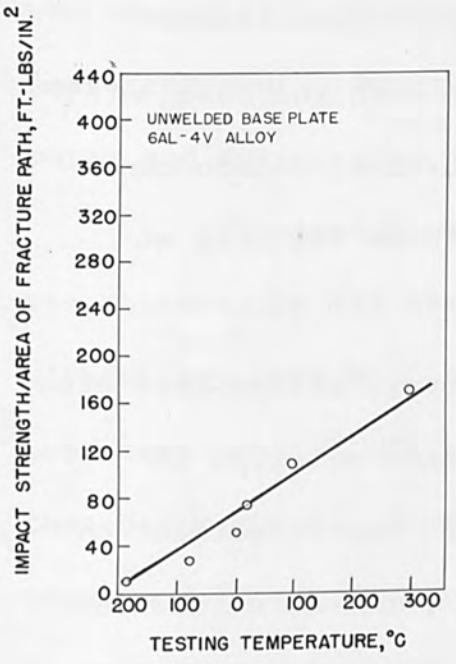

FIGURE 17 - IMPACT RESISTANCE FOR UNWELDED 6A1-4V ALLOY AS A FUNCTION OF TESTING TEMPERATURE.

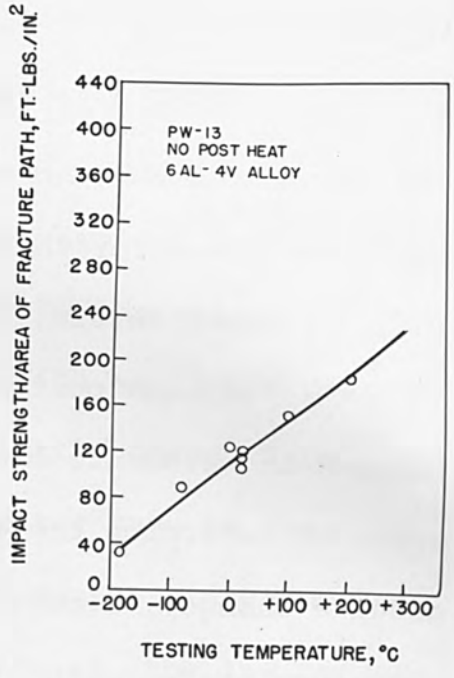

FIGURE 18 - IMPACT RESISTANCE FOR 6A1-4V ALLOY, WELDED NO POST HEAT-TREATMENT, AS A FUNCTION OF TESTING TEMPERATURE.

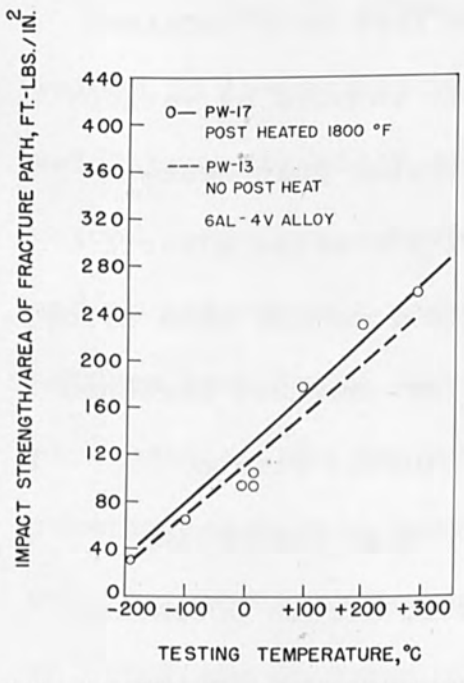

FIGURE 19 - IMPACT RESISTANCE FOR 6A1-4V ALLOY, WELDED, POST HEAT-TREATED AT 1800°F, AS A FUNCTION OF TESTING TEMPERATURE.

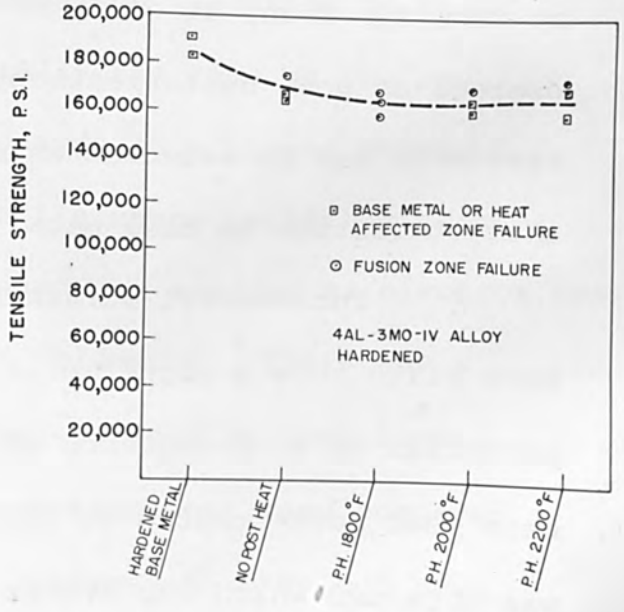

FIGURE 20 - ULTIMATE TENSILE STRENGTH FOR VARIOUS TESTING CONDITIONS FOR THE HARDENED 4A1-3Mo-1V ALLOY.

longer apparent when the material was post heat-treated at 2200°F. With fractures occurring in both the base metal and the fusion zone no definite metallurgical reason can easily be given for the occurrence of these failures at these strength levels.

Various post heat-treatment temperatures were also imposed on weldments made in this hardened material in order to determine the influence of post heat-treatment on modulus change. Figure 21 shows the dependence of modulus upon post heat-treatment temperature for both the solutionized base metal runs and the hardened base metal runs. In the former case identical moduli were obtained with an 1800°F post heat and in the latter case they were obtained at 2200°F. Thus, at equal stress levels induced by various degrees of post heat-treatment, a particular post heat-treatment may be selected which will give similar elastic characteristics in base metal and fusion zone for this alloy.

Incremental strain readings for unwelded hardened base plate show a significant loss of plastic strain potential as a consequence of welding. When assemblies were post heat-treated at 2200°F, plastic strain potential was obtained which was higher than that obtained in the non post heat-treated condition and at a strain level which

was essentially the same as that obtained without any post heat-treatment. Again, this occurred with matching base metal and fusion zone moduli.

The impact resistance of the unwelded base plate was essentially the same as that shown by the weldment without any post heat applied to it. With an 1800°F post heat-treatment, there was relatively little change from this basic curve. However a significant change in the generated impact curve became more obvious at higher post heat-treatment temperatures. In particular, the low temperature portion of the curves had been significantly raised.

D. The 13 1/2V-11Cr-3Al Alloy

The 13 1/2V-11Cr-3Al alloy was electron beam welded in the solutionized and unworked condition to yield weld strengths which are essentially the same as the unwelded material. There was no change in ultimate strength and no appreciable change in tensile characteristics between base metal and fusion zones was noticed as electron beam post heating was applied to such weldments. There was a substantial strain loss caused by the welding operation when weldments having no post heat-treatment were compared in total and incremental strain readings to unwelded base plate. However, incremental strain values are substantially

increased by post heat-treating with higher post heat-treatment temperatures yielding increasing amounts of plastic incremental strain. Using a 2500°F post heat-treatment, incremental strain readings essentially compatible with those of unwelded base plate were attained. The impact resistance of as-welded fusion zones was compatible with that of unwelded base material.

This same heat of material was aged to the 180,000 psi ultimate strength level. General softening induced by the heat of welding was not alleviated through post heat-treatment by the electron beam for any of the post heating conditions utilized, as was found to be the case of the aged 4Al-3Mo-1V alloy. There was again a general trend towards slightly lower ultimate strengths with increasing post heat temperature. No aging could be definitely distinguished in the microstructures of these weldments. It would be expected that this alloy should have a slower aging response to electron beam post heating than the previous three alloys discussed, since this alloy has the slowest response of all the DOD titanium alloys insofar as aging is concerned. This particular alloy is generally aged at 900°F for 90 hours. Consequently, it would probably be most difficult to effect aging in this alloy through short time,

high temperature passes, even multiple passes. However, as shown in Figure 22, electron beam post heating does allow less of a discrepancy between base metal and fusion zone moduli to be obtained.

Although electron beam post heat-treatment did not restore strength losses caused in hardened 13 1/2V-11Cr-3Al alloy sheet by electron beam welding, moderate amounts of post heat (as low as 1800°F) substantially improved the impact resistance of the weldment without adversely affecting the stress or strain of the as-welded condition. Post heat-treating also allowed more uniform elastic modulus condition to be achieved in base plate and in fusion zone.

CONCLUSIONS

1. The electron beam has been shown to be a practical tool for the post heating of electron beam fusion and heat affected zones in titanium alloys of 1/8" thickness.

2. A technique for determining the simultaneous stress-strain characteristics of different metallurgical portions of a weldment has been developed.

3. Ultimate strengths of electron beam weldments in solutionized and rolled titanium alloy plate may be obtained in fusion and heat affected zones by electron beam post heating. By this technique, weldment strengths of the 180,000 psi ultimate strength level have been produced.

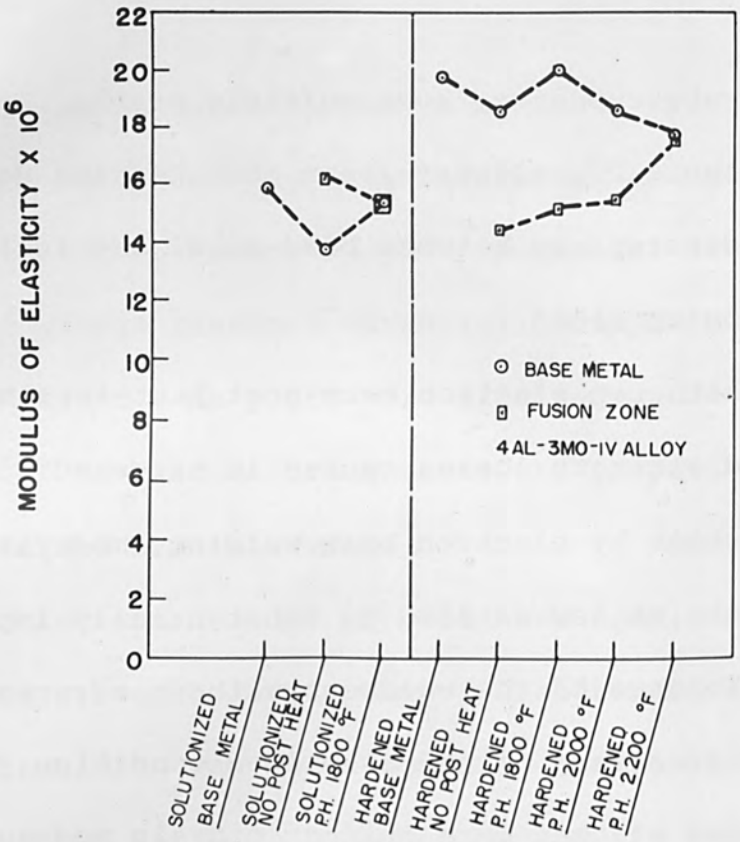

FIGURE 21 - Modulus of elasticity for various testing conditions for the hardened 4Al-3Mo-1V alloy.

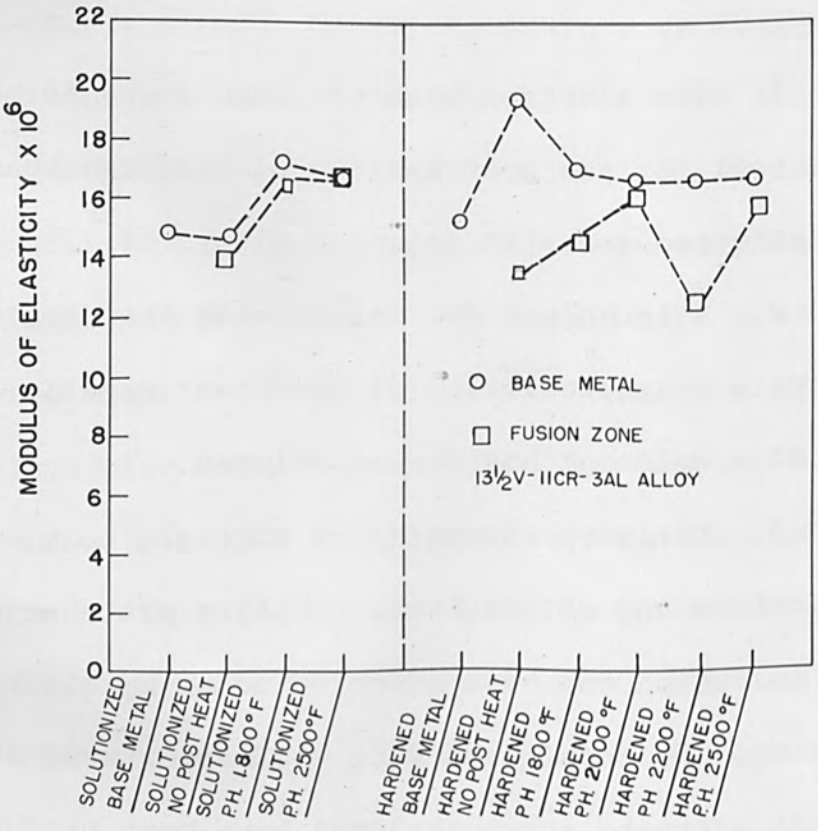

FIGURE 22 - Modulus of elasticity for various testing conditions for the hardened 13½V-11Cr-3Al alloy.

4. Electron beam post heating does not decrease impact resistances in electron beam fusion zones produced in solutionized and rolled 5Al-2 1/2 Sn alloy or 6Al-4V alloy sheet.

5. For solutionized and rolled sheet, electron beam post heating of electron beam weldments increases incremental strains for the 4Al-3Mo-1V alloy, causes no change from the high strains of the 5Al-2 1/2 Sn alloy, and causes more uniform incremental strains to be obtained for the 6Al-4V alloy, as compared to electron beam weldments not post heat-treated.

6. Ultimate strengths of electron beam weldments in solutionized plate that has not been cold worked are equivalent to that of unwelded material even in the absence of electron beam post heat-treatment.

7. Electron beam post heating of electron beam welds in solutionized 13 1/2V-11Cr-3Al alloy increases incremental strains to essentially those of base plate values.

8. Electron beam post heating of electron beam welds in solutionized 13 12/V-11Cr-3Al alloy does not decrease fusion zone impact resistances which are essentially equivalent to those of unwelded material.

9. Solutionized and aged plates when electron beam welded cannot be hardened to unwelded base plate strengths.

However, post heating increases impact resistances above those of unwelded plate and increases strains above those of weldments not electron beam post heated.

10 Moduli of elasticity in base metal and fusion zones of electron beam welds can be matched by electron beam post heating for titanium alloys in any condition of heat-treatment or hardness prior to welding.

ACKNOWLEDGMENTS

The authors gratefully acknowledge the sponsorship of the U.S. Army Ordnance Department. In particular, we wish to thank our supervisory agency, the Watertown Arsenal Laboratories, for permission to publish this report, and to Mr. Donald Buffum, Project Supervisor, for his technical help and for expediting work done outside our laboratory.

We also acknowledge with deep appreciation the fine contributions to this report made by Messrs. C.J. Viall, J.S. Di Pesa and C. Cann of the Alloyd Electronics Staff, and Mr. L. Phaneuf, formerly of the Alloyd Electronics Staff. Their help in the preparation of welds, and thermal and mechanical testing has been of great value.

BIBLIOGRAPHY

1. Lander, H.J., Hess, W.T., Bakish, R. and White, S.S., "Electron beam Welding of Rocket Casing Materials", Proc. 3rd Symposium on Electron Beam Technology P. 189, R. Bakish, Editor, Boston, Massachusetts.

2. Lefas, R., "The Carbon Arc Welding of Cast Iron", S.M. Thesis, M.I.T., Department of Metallurgy, 1958.

3. White, S.S., D'Andrea, M.M., Jr., and Hartbower, C.E., unpublished research at the Watertown Arsenal Laboratories, 1959.

4. Adams, C.M., Jr., The Welding Journal, 37, (5), p. 210-S, 1958.

5. Hartbower, C.E., "Fusion Welding High-Strength Titanium Sheet", Proc. Sagamore Conference, 1960.

6. Orner, G.M., and Hartbower, C.E., "Sheet Fracture Toughness Evaluated by Charpy Impact and Slow Bend", The Welding Journal, Research Supplement, 40, (5), 405-S to 416-S, 1961.

7. Orner, G.M., and Hartbower, C.E., "Transition-Temperature Correlations in Constructional Alloy Steels", The Welding Journal, Research Supplement, 40, (10), 459-S to 467-S, 1961.

8. Orner, G.M., "Effect of Specimen Geometry on Charpy Low-Blow Transition Temperatures", Watertown Arsenal Laboratories Report No. WAL TR 112/87-6; also The Welding Journal, Research Supplement, 38, (8), 315-S, 1959.

9. Irwin, C.R., Kies, J.A. and Smith, H.L., "Fracture Strengths Relative to Onset and Arrest of Crack Propagation", ASTM Proc. 58, 1958.

alloyd electronics corporation
CAMBRIDGE 42, MASSACHUSETTS